

VOLUME 3

PROCEEDINGS

ELEVENTH INTERNATIONAL CONFERENCE ON THE BEARING CAPACITY OF ROADS, RAILWAYS AND AIRFIELDS

Edited by
Inge Hoff, Helge Mork and Rabbira Garba Saba



 **CRC Press**
Taylor & Francis Group



ELEVENTH INTERNATIONAL CONFERENCE ON THE BEARING CAPACITY OF ROADS, RAILWAYS AND AIRFIELDS, VOLUME 3

Proceedings of the 11th International Conference on the Bearing Capacity of Roads, Railways and Airfields – Volume 3 comprises the third part of contributions to the 11th International Conference on Bearing Capacity of Roads, Railways and Airfields (2022). In anticipation of the event, it unveils state-of-the-art information and research on the latest policies, traffic loading measurements, in-situ measurements and condition surveys, functional testing, deflection measurement evaluation, structural performance prediction for pavements and tracks, new construction and rehabilitation design systems, frost affected areas, drainage and environmental effects, reinforcement, traditional and recycled materials, full scale testing and on case histories of road, railways and airfields. This edited work is intended for a global audience of road, railway and airfield engineers, researchers and consultants, as well as building and maintenance companies looking to further upgrade their practices in the field.



Taylor & Francis

Taylor & Francis Group

<http://taylorandfrancis.com>

PROCEEDINGS OF THE ELEVENTH INTERNATIONAL CONFERENCE ON THE BEARING
CAPACITY OF ROADS, RAILWAYS AND AIRFIELDS, 28-30 JUNE 2022, TRONDHEIM,
NORWAY

Eleventh International Conference on the Bearing Capacity of Roads, Railways and Airfields, Volume 3

Edited by

Inge Hoff & Helge Mork

Norwegian University of Science and Technology, Trondheim, Norway

Rabbira Garba Saba

Norwegian Public Roads Administration, Trondheim, Norway



CRC Press

Taylor & Francis Group

Boca Raton London New York Leiden

CRC Press is an imprint of the
Taylor & Francis Group, an **informa** business

A BALKEMA BOOK

CRC Press/Balkema is an imprint of the Taylor & Francis Group, an informa business

© 2022 selection and editorial matter, Inge Hoff, Helge Mork & Rabbira Garba Saba; individual chapters, the contributors

Typeset by Integra Software Services Pvt. Ltd., Pondicherry, India

The right of Inge Hoff, Helge Mork & Rabbira Garba Saba to be identified as the authors of the editorial material, and of the authors for their individual chapters, has been asserted in accordance with sections 77 and 78 of the Copyright, Designs and Patents Act 1988.

The Open Access version of this book, available at www.taylorfrancis.com, has been made available under a Creative Commons Attribution-Non Commercial-No Derivatives 4.0 license.

Although all care is taken to ensure integrity and the quality of this publication and the information herein, no responsibility is assumed by the publishers nor the author for any damage to the property or persons as a result of operation or use of this publication and/or the information contained herein.

Library of Congress Cataloging-in-Publication Data

A catalog record has been requested for this book

Published by: CRC Press/Balkema
Schipholweg 107C, 2316 XC Leiden, The Netherlands
e-mail: enquiries@taylorandfrancis.com
www.routledge.com - www.taylorandfrancis.com

Volume 1:

ISBN: 978-1-032-12044-7 (Hbk)

ISBN: 978-1-032-12068-3 (Pbk)

ISBN: 978-1-003-22288-0 (eBook)

DOI: 10.1201/9781003222880

Volume 2:

ISBN: 978-1-032-12049-2 (Hbk)

ISBN: 978-1-032-12070-6 (Pbk)

ISBN: 978-1-003-22289-7 (eBook)

DOI: 10.1201/9781003222897

Volume 3:

ISBN: 978-1-032-12052-2 (Hbk)

ISBN: 978-1-032-12074-4 (Pbk)

ISBN: 978-1-003-22291-0 (eBook)

DOI: 10.1201/9781003222910

Table of contents

Preface	ix
Organizing committee	xi
<i>Evaluation of deflection measurements</i>	
Influence of driving speed on Traffic Speed Deflectometer data – Field test and parameter study	3
<i>C. Podolski & M. Čičković</i>	
FWD time-history data for the evaluation of concrete slab stability	13
<i>C. Van Geem</i>	
Estimating asphalt concrete strains in airport pavements using geometric property of the pavement surface deflection basin from heavy weight deflectometer tests	22
<i>H. Kazmee, N. Garg & L. Ricalde</i>	
Comparison of RAPTOR measurements with falling weight deflectometer deflections using backcalculation	33
<i>S.S. Madsen & N.L. Pedersen</i>	
Indication of viscoelastic behaviour of asphalt pavements using FWD time history data	45
<i>Z. Boros & J. Komacka</i>	
<i>Reinforcement of structural layers</i>	
Ultra-thin whitetopping for asphalt pavement rehabilitation: The influence of the interlayer in the properties of the double-layered system	57
<i>M. Pasetto, A. Baliello, G. Giacomello & E. Pasquini</i>	
Laboratory fatigue assessment of large geocomposite-reinforced double-layered asphalt concrete beams	65
<i>P. Jaskula, D. Rys, M. Stienss, C. Szydlowski, M. Golos & J. Kawalec</i>	
<i>Structural design systems for new construction and rehabilitation</i>	
Calibration of mechanistic-empirical flexible pavement damage models	77
<i>A.T. Papagiannakis, E. Alrashydah & A. Masad</i>	
Design of full depth reclamation of low volume roads	87
<i>S. Agardh, C. Ossbahr & V. Perez</i>	

Structural evaluation and performance prediction for pavements and tracks

PEHKO-project – using bearing capacity analysis as a tool for proactive maintenance of paved roads	99
<i>T. Herronen, A. Hiekkalahti, A. Matintupa, T. Saarenketo & P. Varin</i>	
The influence of asphalt/base modulus ratio on strain mode reversal in flexible pavements	108
<i>M. Foshee & D. Timm</i>	
Permanent deformation and fatigue damage interaction in asphalt concrete using energy approach	118
<i>M. Alamnie, E. Taddesse & I. Hoff</i>	
Impact of the bearing capacity and settlement ratio of track bed on the structural performance and fatigue life of bituminous tracks	128
<i>M. Sol-Sánchez, F. Moreno-Navarro, J.M. Castillo-Mingorance, M.C. Rubio-Gámez, E. Tomás-Fortún & V. Pérez-Mena</i>	
Proposed damage risk assessment of pavement subsurface cavities using the rolling dynamic deflectometer	138
<i>J.M.V. Flores, T.S. Tran, W.S. Lee, K.D. Kim, C.A. Elipse, A.O. Madlangsakay & H.J. Lee</i>	
Flexible pavement performance with lime treated bases	150
<i>M.I. Souliman, N.R. Bastola & M.H. Elshaer</i>	
Machine learning solutions for development of performance deterioration models of flexible airfield pavements	159
<i>A.Z. Ashtiani, S. Murrell, R. Speir & D.R. Brill</i>	
Evaluation of subgrade mechanistic-empirical permanent deformation models in the response of a railway slab track	168
<i>A. Ramos, A.G. Correia, R. Calçada & P.A. Costa</i>	
Follow up on reduced thickness of asphalt concrete layers on a performance specifications contract	178
<i>C.A. Lenngren</i>	
New backcalculation method to obtain viscoelastic properties of asphalt pavement from HWD tests	188
<i>J.-M. Roussel, M. Broutin, H. Di Benedetto & C. Sauzéat</i>	
Microwave deep healing of road pavements: preliminary numerical results	198
<i>F.G. Praticò, S. Zumbo, M.T. Bevacqua & T. Isernia</i>	
Investigation of local rail track deterioration due to sleeper support condition variation	207
<i>N. Lillin, D. Rudisch, S. Freudenstein, F. Mitlmeier, F. Kotter & C. Moormann</i>	
Sleeper contact modelling in asphalt overlayment trackbeds	220
<i>P. Jørgensen, R.N.H. Perslev & E. Levenberg</i>	
Analytical study on structural remaining life of airfield pavement using FWD	228
<i>F.V. Soto & R. Pacheco-Torres</i>	
Analysis of evaluation and assessment procedures for the application of the TSD on asphalt pavements	236
<i>M. Čičković</i>	

International roughness index model for jointed reinforced concrete highway pavements: An artificial neural network application	246
<i>S. Sultana, Y. Najjar, H. Yasarer, W. Uddin & R. Barros</i>	
Composite pavement roughness modeling for LTPP wet freeze climate region using machine learning	256
<i>R. Barros, H. Yasarer, W. Uddin, S. Sultana & Y. Najjar</i>	
Prediction of asphalt pavement responses under moving loads with non-uniform tire footprints using the Fourier finite layer method	266
<i>G.C. Falla, C. Weise, S. Leischner, M. Oeser & F. Wellner</i>	
Compressive strength of concrete using different field-curing methods	275
<i>P. Solanki & H. Xie</i>	
Pavement structural performance: Predicting remaining life using rapid non-destructive testing	282
<i>G. Salt, L. Grimshaw & A. Marradi</i>	
Numerical modelling of the evolution of differential settlement of railway tracks	291
<i>C. Charoenwong, D.P. Connolly, P.K. Woodward, P. Galvín & P.A. Costa</i>	
 <i>Utilization of traditional and recycled materials</i>	
E* master curve parameters as indicators of cracking susceptibility of mixtures with recycled asphalt shingles	303
<i>F. Leiva & A. Taylor</i>	
Laboratory study of soil-cement manufactured with RAP for its application as a sustainable and high-performance base in asphalt pavements	313
<i>F. Moreno-Navarro, M. Sol-Sánchez, G. García-Travé, R. Tauste-Martínez, M.C. Rubio-Gámez, C. Rodríguez-López, M. Hernández-Pérez & J. Gambín-Peñalver</i>	
Fundamental study on combined aging for warm-mixed asphalt and RAP-WMA mixtures using SATS conditioning	322
<i>M. Iwama & K. Hayano</i>	
Bio-based emulsifiers for pavement material: Emulsion formulation and cold asphalt mix properties	332
<i>F. Lévenard, V. Gaudefroy, C. Petiteau, E. Chailleux, I. Capron & B. Bujoli</i>	
Characterization of multiple recycled reclaimed asphalt incorporating polymer modified bitumen	341
<i>I. Widyatmoko, A. Subhy, C. Ojum, A. Khojinian, R. Hudson-Griffiths, D. Giles & M. Simms</i>	
Selection of sand gradations and proportions for sand-bentonite mixtures of fine-grained soil	351
<i>G. Verma & B. Kumar</i>	
Preparation of artificial aggregate to be used in the asphalt mixture	360
<i>G. Liu, M. Ding, H. Xing, H. Huang, G.A. Kasimova & H. Chen</i>	
Aspects concerning the structural evaluation of non-conventional pavements	370
<i>V. Papavasiliou & A. Loizos</i>	
Manufacturing and characterization of asphalt binders designed on the bases of polymer modified bitumen with cement by-pass dust and fly ash	380
<i>R. Merijs-Meri, J. Zicans, T. Ivanova, R. Berzina, A. Bernava, M. Žiganova, A. Ābele & V. Haritonovs</i>	

Bearing capacity behavior of base course reinforced with woven geotextile <i>K. Sato, T. Fujikawa, C. Koga, Y. Wakabayashi, M. Shimazaki, K. Hirakawa, J. Hironaka & Y. Isobe</i>	387
Study of the mechanical behaviour and self-cementing properties of recycled crushed concrete aggregates <i>C. Wang, C. Chazallon, S. Mouhoubi, P. Hornych & P. Jing</i>	398
High content of Reclaimed Asphalt Pavement (RAP) in asphalt mixtures – optimal use of rejuvenators <i>T. Jørgensen, T.H. Fiske & R. Telle</i>	407
Polymer modified bitumen for runways containing 60% recycled asphalt <i>C.P. Plug, A.H. de Bondt, F.R. Bijleveld & G. van Uden</i>	418
Effect of bio heating oil from biodiesel production on rheological behaviour of bitumen <i>M. Cabette, J. Pais & R. Micaelo</i>	426
Investigating the use of fly ash for sustainable asphalt binders <i>R. Melaku, S. Ness, D. Gedafa & N. Suleiman</i>	436
Comparison of field and laboratory mix performance <i>J. Liu, R. Melaku, D. Gedafa & N. Suleiman</i>	445
Design and evaluation with balanced performance of recycled asphalt concrete <i>M.-C. Liao, J.-W. Shi, W.-H. Gao & M.-T. Hung</i>	454
Resilient and permanent deformation of foam glass aggregates assemblies <i>E.L. Pérez-González, J.-P. Bilodeau, P. Segui & G. Doré</i>	463
Stabilization of expansive clays using recycled glass <i>R. Barros, H. Yasarer & Y.M. Najjar</i>	471
Assessment of construction and demolition waste materials for sublayers of low traffic rural roads <i>S. Pourkhorshidi, C. Sangiorgi, D. Torreggiani & P. Tassinari</i>	480
Utilization of fly ash as a filler in cold bituminous emulsion mix <i>D. Prasad, S.K. Suman, B. Singh, N. Saboo & A. Kathuria</i>	491
Estimation of durability of new surface courses using accelerated load test and expert's opinions <i>B. Kalman, D. Lo Presti, G. Di Mino, K. Mantalovas, E. Keijzer, T. Pary, L. Neves & R. Kleizienė</i>	502
Performance characteristics of pavement sub-base containing steel slag <i>M. Panda, S. Barik, S.S. Mishra, P. Kar & P.K. Bhuyan</i>	511
Author index	519

Preface

Bearing capacity is not an easy term to define. It is used to express the traffic load a pavement structure can withstand without showing severe damage. It is not a measure of the ultimate structural strength that will cause a failure state for a single vehicle if exceeded. The ultimate strength of a pavement is normally significantly higher than the bearing capacity. For rehabilitation projects, the bearing capacity is becoming more and more important, and it is a challenging task for an engineer to determine the remaining bearing capacity of a structure and how this capacity could be further utilized.

This conference is the eleventh in the series started in Trondheim 1982 and arranged at four-year intervals under the title Bearing Capacity of Roads and Airfields, BCRA. At the sixth conference in Lisbon, Portugal, railway tracks was added as the third important component. The acronym is since then BCRRA. The conference has been organized at five cities in addition to Trondheim (1982, 1990, 1998, 2005 and 2013): Plymouth, UK (1986), Minneapolis, USA (1994), Lisbon, Portugal (2002), Champaign, USA (2009) and Athens, Greece (2017).

The BCRA/BCRRA conferences have contributed to creating and sharing knowledge in this area through more than 2000 papers and an even higher number of participants in the conferences.

The organizing committee would like to express gratitude to all that have participated in making this conference possible.



Inge Hoff
Chair of the organizing committee



Taylor & Francis

Taylor & Francis Group

<http://taylorandfrancis.com>

Organizing committee

Inge Hoff, *Norwegian University of Science and Technology (NTNU), Trondheim, Norway*
Helge Mork, *Norwegian University of Science and Technology (NTNU), Trondheim, Norway*
Rabbira Saba, *Norwegian Public Roads Administration (SVV), Trondheim, Norway*
Leif Bakløkk, *Norwegian Public Roads Administration (SVV), Trondheim, Norway*



Taylor & Francis

Taylor & Francis Group

<http://taylorandfrancis.com>

Evaluation of deflection measurements



Taylor & Francis

Taylor & Francis Group

<http://taylorandfrancis.com>

Influence of driving speed on Traffic Speed Deflectometer data – Field test and parameter study

C. Podolski

Bundesanstalt für Straßenwesen (BASt), Bergisch Gladbach, Germany

M. Čičković

HELLER Ingenieurgesellschaft mbH, Darmstadt, Germany

ABSTRACT: In contrast to the Falling Weight Deflectometer (FWD), the Traffic Speed Deflectometer (TSD) operates without traffic safety measures, stressing the examined pavement by simply rolling over it. Measurements are usually performed at speeds of up to 80 km/h. Due to the horizontal speed of the truck, in contrast to other bearing capacity measuring methods, visco-elastic material behaviour and inertial effects can also be observed. This raises the question whether the horizontal speed of the truck influences the measurement results. The results are important for TSD data assessment as well as for operational issues in high-trafficked areas or in-town measurements.

For these purposes, various field tests were conducted with the BASt-owned TSD evaluating varying horizontal speeds (20-90 km/h, increments of 10 km/h). The measurements were performed at selected test sites with different bearing capacity levels. Based on these data, the effect of speed on various indicators related to bearing capacity, such as SCI_{300} and deflections has been assessed in detail. The study has been supplemented with an analytical parameter study using the 3D-Move algorithm. The results of the parameter study confirm the findings of the field test: In the speed range from 20 km/h to 90 km/h, the effects of the horizontal speed on the measurement results (for example the SCI_{300}) are marginal. The analysis of the 10 m values showed no significant change in the SCI_{300} with respect to horizontal speed. The model calculations in 3D-Move showed that only from horizontal speeds below 20 km/h the applied load becomes almost static and thus a different material behaviour is addressed. It can therefore be assumed that measurement results that lie within the permissible horizontal speed window (40-80 km/h) specified by the manufacturer are nearly unaffected by the horizontal speed of the truck.

Keywords: Traffic Speed Deflectometer (TSD), asphalt pavement, parameter study, bearing capacity measurements, 3D-Move

1 INTRODUCTION

The Traffic Speed Deflectometer (TSD) was developed in Denmark at the end of the last century with the aim of detecting deformations at high speed (Rasmussen 2002). The measuring system is installed on a truck (incl. all associated instrumentation, see Figure 1). Thus, the recording of the bearing capacity at a speed of approx. 80 km/h is possible. The measuring beam must be resistant to bending and torsion, and its temperature profile must be as uniform as possible in order to

ensure equal conditions for the correction of the individual Doppler laser data (Forschungsgesellschaft für Straßen- und Verkehrswesen (FGSV) 2015).

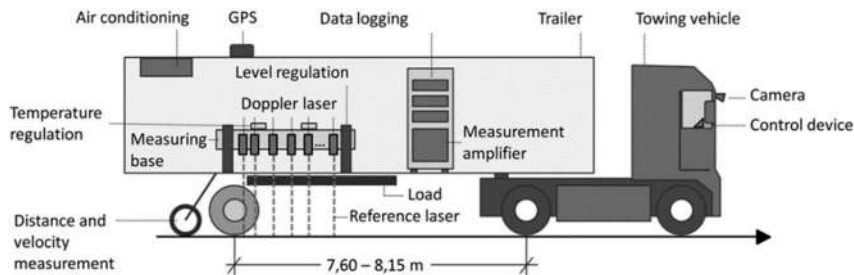


Figure 1. Principle sketch of the TSD (Forschungsgesellschaft für Straßen- und Verkehrswesen (FGSV) 2017).

The principle of data acquisition of the TSD is based on the Doppler effect, i.e. the wavelength of the emitted light beam is different than the wavelength of the immitted (reflected) light beam. Thus, the oblique speed of the deformation can be recorded. In order to measure only the deformation speed, exact knowledge of the inclined position of the Doppler laser and the horizontal speed is necessary. The inclined position is measured with the aid of a reference laser. In addition, acceleration sensors and gyroscopes are used to record the movements during data acquisition. The horizontal speed of the vehicle is recorded by a hodometer and is used to calculate the vertical speed (i.e. the deformation speed) (Hildebrand et al. 2000).

Since all load-bearing capacity measured values and derived characteristic values depend on the test performance and the framework conditions existing at the time of the measurement, a standardisation to reference framework conditions is indispensable. In the course of other load capacity measurement procedures, measured values and/or back-calculated characteristic values are standardised on the basis of the following framework conditions:

- Force impact or load
- Temperature (asphalt core temperature)

Correction functions are usually available for this purpose, with which raw or characteristic values can be standardised to a reference level with the aid of the conditions present in each case.

A further parameter that significantly influences the measured values is the horizontal speed of the vehicle, i.e. the driving speed. Since the speeds of other bearing capacity measuring methods are either constant or negligibly low, influences from the dynamics of the load and the resulting inertial effects are also negligible. However, this is not valid for the TSD. Due to the phase-shifted deformation maximum alone, which is significantly dependent on the horizontal speed (apart from the material under investigation), a standardisation to a reference speed or at least a consideration of different speed scenarios is indispensable.

BECKEDAHL ET AL. [2016] investigated the influence of speed on load capacity parameters. Three different speeds were measured on a test section:

- $v_1 = 40 \text{ km/h}$
- $v_2 = 60 \text{ km/h}$
- $v_3 = 80 \text{ km/h}$

Only D_0 was examined as a comparative parameter. It was shown that D_0 increases with decreasing measuring speed. There is no significant difference between the values for D_0 at 60 km/h and 80 km/h, while the value for D_0 at $v_1 = 40 \text{ km/h}$ is significantly higher (Beckedahl et al. 2016). Similar findings were already noted in 2006 for parameter SCI_{300} (Krarp et al. 2006). These statements are contradicted by BALTZER ET AL. [2010], who were unable to

find any differences for D_0 in serial tests with the same speed classes. This is attributed to the fact that these measurements were carried out in Australia and the bound layers are much thinner than in Central Europe. Therefore, visco-elastic effects may not occur to the same extent and the influence of speed disappears (Baltzer et al. 2010).

Currently there is no standardisation procedure that takes the measuring speed into account. The only thing to be ensured is that the data acquisition is carried out at a speed of $v > 40$ km/h. Furthermore, the measuring speed is not taken into account in the standardisation of the data (Forschungsgesellschaft für Straßen- und Verkehrswesen (FGSV) 2020).

For this reason, the influence of the travelling speed of the TSD on load capacity parameters was investigated in the present work.

2 METHODS AND DATA

The following part explains the overall approach of the parameter study. In a first step, the procedure for simulating the mechanical behaviour of the pavement is described. Subsequently, the procedure for the in-situ measurements is described.

2.1 *Simulating the mechanical behaviour of pavements in 3D-Move*

In order to be able to simulate loads and thus carry out parameter studies with varying framework conditions in terms of environment and material properties, the continuum-based finite layer analysis programme 3D-Move (Asphalt Research Consortium 2013) was used. The programme can simulate the response of a multi-layer system to a stress at constant speed by Fourier transformations and can also illustrate the visco-elastic material properties of asphalt layers (Siddharthan et al. 1998; Zafir et al. 1994). Due to the fact that both the visco-elastic material behaviour and a constant travelling speed can be simulated, a simulation of a TSD crossing and the resulting deformation is possible (Nasimifar et al. 2015).

In the present study, a load of 50 kN is applied onto the pavement with a pressure of 0.862 MPa. The output of 3D-Move is the stress and strain state as well as the resulting deformations in all coordinate directions for a considered point. It is important to note that the output deformation is in the time domain, i.e. it is an Euler representation of the deformation. In order to change to the Lagrange representation, a conversion must be made with the aid of the travelling speed and information concerning the distance of the starting point from the marked point.

The unbound layers are represented by means of a linear-elastic material behaviour, while asphalt layers can also be calculated visco-elastically. When defining the material properties of the unbound layers, it is possible to choose from a catalogue of pre-defined materials or to directly set the Young's modulus E , the Poisson's ratio μ , the damping factor D , the density ρ and the thickness d . The density ρ and the thickness d are also one of the input values when defining the material parameters of the asphalt. When defining the visco-elastic properties there are two different possibilities: Either laboratory parameters are used, which come from the Master Curve test and the Dynamic Shear Rheometer (DSR). The second possibility is to use the Witczak model, which describes the dynamic modulus of elasticity $|E^*|$ of the asphalt based on material properties of the bitumen used and volumetric properties of the asphalt mix. Therefore, testing parameters are also used here to describe the mechanical properties of the asphalt. However, this does not include a split tensile strength threshold test of no-threshold, as these results are regressively simulated by the volumetric properties of the asphalt.

For the parameter study, the two superstructures from Figure 2a. and Figure 2b. were selected, whereby for the superstructure according to Figure 2a., a favourable and an unfavourable state were simulated for the stiffness of the unbound layers by varying the Young's modulus. The construction according to Figure 2b. was carried out with a constant stiffness of the unbound layers. The asphalt core temperature was assumed to be constant and was set at $T = 20$ °C. The varied parameters are listed below:

- > Young's modulus of the unbound layers E_0
 - $E_{0,1} = 275 \text{ MPa}$
 - $E_{0,2} = 60 \text{ MPa}$

Table 1. Travelling speeds of the TSD (parameter study in 3D-Move).

	v_{TSD} [km/h]	v_{TSD} [km/h]	v_{TSD} [km/h]	v_{TSD} [km/h]			
v_1	1.6	v_5	32.2	v_9	64.4	v_{13}	128.8
v_2	8.0	v_6	40.2	v_{10}	72.4	v_{14}	160.9
v_3	16.1	v_7	48.3	v_{11}	80.5		
v_4	24.1	v_8	56.3	v_{12}	96.6		

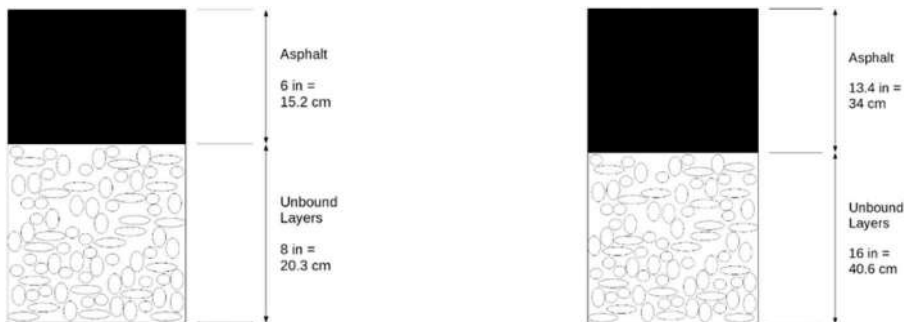


Figure 2. a. Cross section of the superstructure corresponding to the load class Bk1.0; b. Cross section of the superstructure corresponding to the load class Bk100.

The result of these simulations are deflections in the time domain that need to be converted into a Lagrange representation in order to obtain a deflection bowl. Characteristic bearing capacity values can be calculated by means of the deflection bowls. In this case, the change of the SCI_{300} (see Figure 3) and the deflection at the load centre D_0 (see Figure 3) were considered in relation to the travelling speed of the TSD.

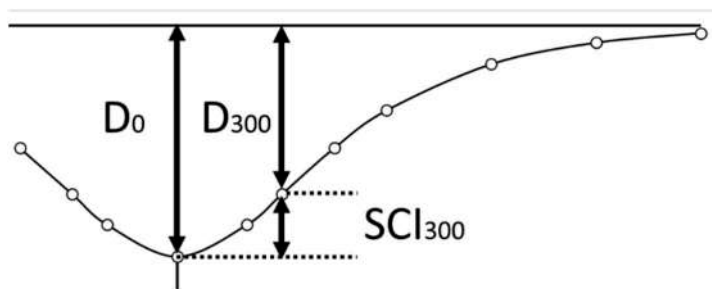


Figure 3. Schematic illustration of the SCI_{300} (Forschungsgesellschaft für Straßen- und Verkehrswesen (FGSV) 2020).

2.2 On-site parameter study

All field tests were carried out on an oval course at Aldenhoven Testing Center (ATC) in Germany in May 2019. The oval course's road length is about 2 km depending on the lane of driving. All measurements were conducted in the middle lane (see Figure 4). The pavement of the oval course is a rather stiff construction with an asphalt top layer. The construction of the underlying layers was unknown at the time of data analysis.

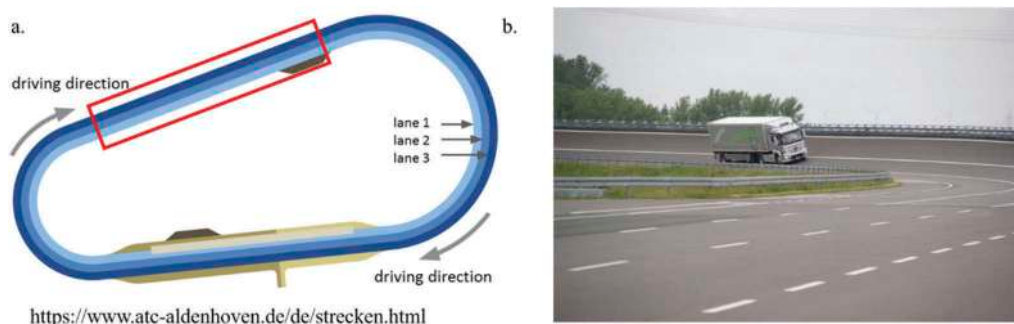


Figure 4. a. Oval course test site at Aldenhoven Testing Center (ATC), Germany. Only data from the indicated section (box) was used for analysis. b. BAST TSD on oval course.

Only data from the straight section on the northern side of the test track was used for analysis to ensure constant travelling speed of the measuring vehicle and to avoid an uneven load distribution in the inclined curve sections. The selected section was about 350 m long (Figure 4a, see indicated area). Measurements were carried out at travelling speeds between 20 km/h and 89 km/h and repeated in mixed order. The varied velocities are listed below (in ascending order):

Table 2. Travelling speeds of the TSD (on-site measurements).

	v_{TSD} [km/h]		v_{TSD} [km/h]		v_{TSD} [km/h]		v_{TSD} [km/h]
v_1	20.0	v_5	45.0	v_9	65.0	v_{13}	85.0
v_2	30.0	v_6	50.0	v_{10}	70.0	v_{14}	89.0
v_3	35.0	v_7	55.0	v_{11}	75.0		
v_4	40.0	v_8	60.0	v_{12}	80.0		

During measurements, air temperatures were stable between 14 °C and 15 °C, road temperatures varied between 23 °C and 26 °C (surface) but were mostly stable around 25 °C with prevailing cloudy and dry weather. Data that was collected during rainfall later in the day was eliminated for this analysis which led to the elimination of data collected at 55 km/h, 65 km/h, 75 km/h, and 85 km/h. Additionally, the selected data was analysed for homogeneous values of deflections (D_0 and SCI_{300}) to ensure higher reliability of the data. Figure 5 shows a small decrease of deflection values in the beginning of the test section (distance: 0 m – 100 m) changing to a more stable distribution towards the end of the section (distance: 100 m – 350 m). Only the data showing a stable distribution is used for data analysis in this work (distance: 100 m – 350 m).

3 RESULTS AND DISCUSSION

In this part, the results of the on-site measurements and simulations are being presented and critically analysed, summarising the most important conclusions. With these conclusions

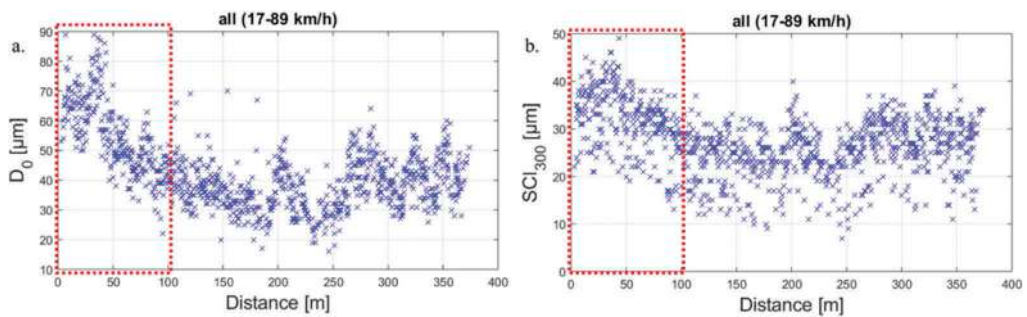


Figure 5. a. D_0 , and b. SCI_{300} on selected straight test section (all measured travelling speeds). Data show a decrease of deflection parameter values at distances between 0 m – 100 m (box). This data was eliminated from the data set for further analysis.

formulated, the focus shall turn to interactions and links of the on-site measurements with the theoretical calculation of the mechanical behaviour of the pavement, in order to stipulate the lessons learnt from these parameter studies.

3.1 Simulating the mechanical behaviour of pavements in 3D-Move

First of all, the differences in the shape of the deflection bowl should be considered. Figure 6 shows the three groups of deformation bowls. Differences can be seen depending on the travelling speed, but they are not too obvious. Only in the almost static load condition a clearer differentiation of the respective deformation set from the other deformation sets can be seen. All in all, the relation of the absolute values of the deflections, depending on the thickness of the asphalt layers as well as the Young's modulus of the unbound layers, is consistent: The greatest deflections occur at low thickness of the bound layers and low stiffness of the unbound layers.

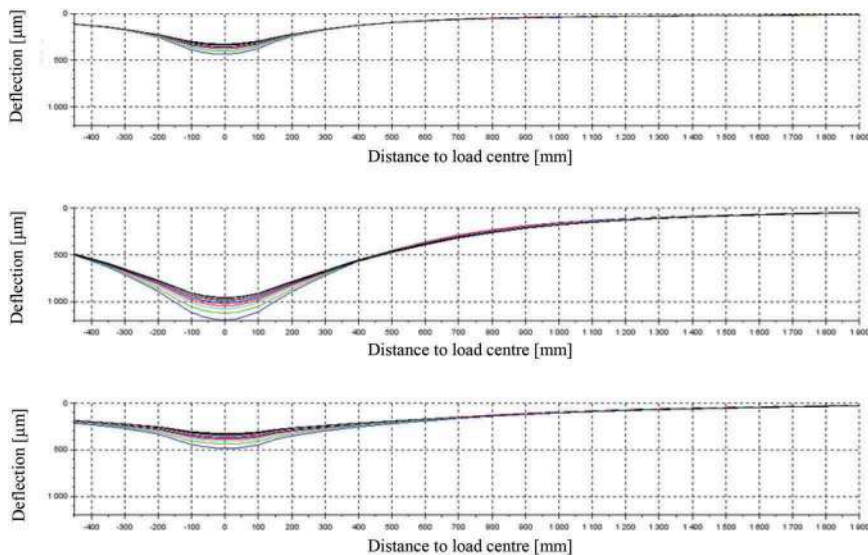


Figure 6. Deflection bowls calculated with the aid of 3D-Move (a. load class Bk1.0 and high stiffness of the unbound layers, b. load class Bk1.0 and low stiffness of unbound layers, c. load class Bk100).

With these deflection bowls it was possible to calculate characteristic bearing capacity values. As mentioned above, SCI_{300} and D_0 were chosen for this purpose. In order to show the sole effect of the driving speed of the TSD on the quantitative expression of the characteristic values, relative values were calculated and presented for the two bearing capacity parameters. The reference value for calculating the relative values is the quantitative characteristic at $v = 80$ km/h. Figure 7 depicts the course of the relative bearing capacity values as a function of the travelling speed of the TSD.

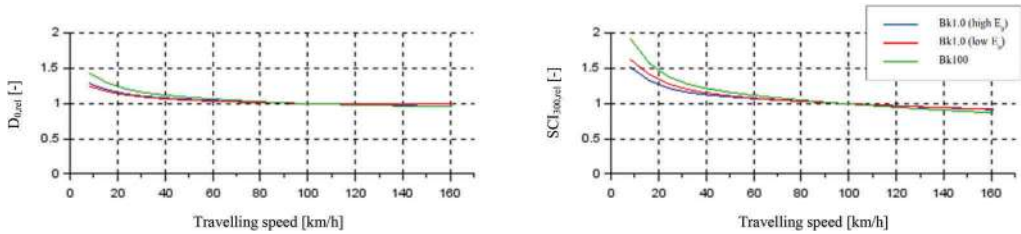


Figure 7. Relative characteristic bearing capacity values as a function of travelling speed (a. D_0 , b. SCI_{300}).

The parameter study shows that the travelling speed of the TSD does have an influence on the quantitative characteristics of the bearing capacity values, but only from a speed range below 20 km/h. If the travelling speed of the TSD is within the speed window specified by the manufacturer (40 km/h to 80 km/h), the influence of the speed on the bearing capacity values is negligible. The stiffness of the unbound layers has no influence in the relative consideration of the change of the bearing capacity values. It should be noted that an associated parameter study of the interaction with the influence of the temperature was not carried out here.

3.2 On-site parameter study

The selected data was analysed for deflection parameters D_0 and SCI_{300} at different speeds. Figure 8 shows D_0 at different speeds with corresponding mean values and standard deviations. The numbers do not show any significant changes in D_0 . Figure 9a. depicts D_0 mean values as a function of travelling speed, and the linear regression fit (red line), Figure 9b. shows the regression of the mean values and the standard deviation as error bars. Although the regression line suggests a slight decrease of D_0 values with increasing travelling speed, it must be brought to attention that D_0 values are very small in this case.

The same pattern is obvious for SCI_{300} : SCI_{300} values are also very small and do not show any significant changes with increasing travelling speed (see Figure 10 and Figure 11). The linear regression fit is almost constant.

It must be noted that the pavement of the test site was rather stiff and produced only small deflections resulting in very low values for D_0 and SCI_{300} . Even for travelling speeds below 40 km/h there is no obvious change in deflection parameters. Furthermore, the subsurface structure and composition of the pavement was unknown at the time of data analysis. GPR data that was also obtained during the measurements was not yet evaluated at the time of data analysis, but could give some insight into what makes this pavement a “stiff” pavement. Additionally, it could also reveal the degree of homogeneity of the pavement in general. Although the driver of the measuring vehicle focused on keeping the vehicle in the same wheel track, there could still be some variance resulting in slightly varying deflections.

Slope values and other SCI values were not considered in this study but should be analysed in the future to get a better picture of the deflection bowl produced by the measuring vehicle. Due to the ongoing pandemic at the time of data evaluation, planned measurements on weaker pavements could not be carried out. Deflection values from weaker pavements are

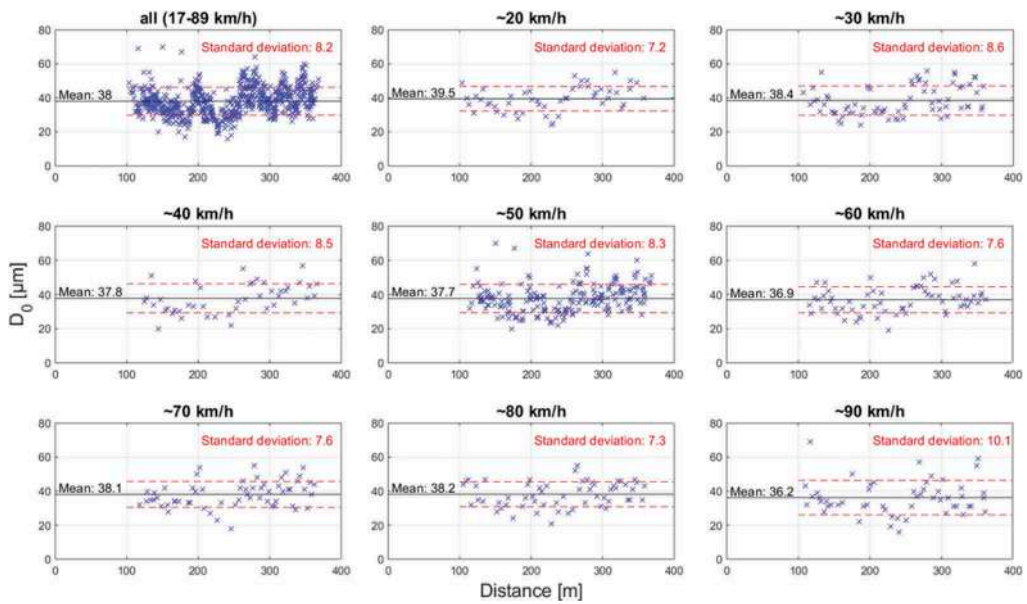


Figure 8. Distribution of bearing capacity value D_0 as a function of distance at different travelling speeds. Black and red (dashed) lines indicate corresponding mean values and standard deviation, respectively.

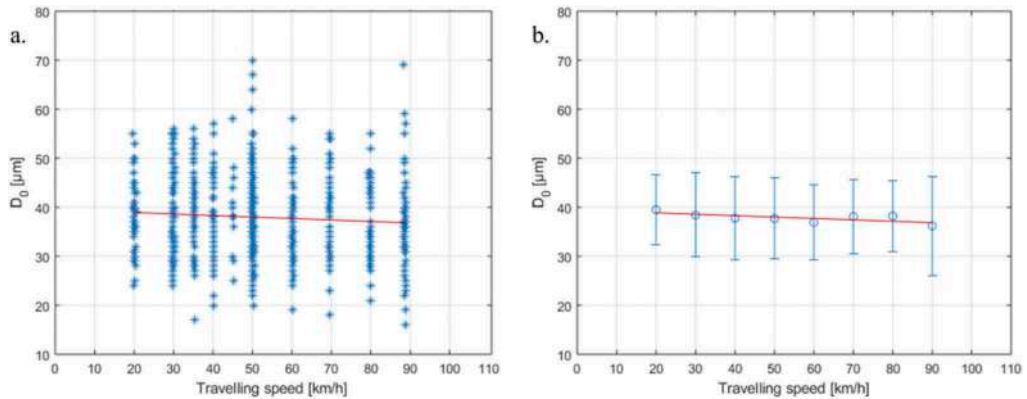


Figure 9. Bearing capacity value D_0 as a function of travelling speed. Red lines indicate linear regression fit for a. all data, and b. mean values. Error bars in b. show standard deviation of D_0 at different travelling speeds.

expected to give more insight into pavement behavior depending on travelling speed, especially at lower velocities.

3.3 Comparison

The comparison of the parameter study in 3D-Move and the in-situ measurements shows that the effects of the speed of the TSD are very small or hardly existent. The parameter study in 3D-Move showed an influence from speeds below $v = 20$ km/h. The real measurements could also not show any speed dependence for the load-bearing capacity parameters D_0 and SCI_{300} but are subject to very high scattering due to the comparatively stiff mounting, which the statistical

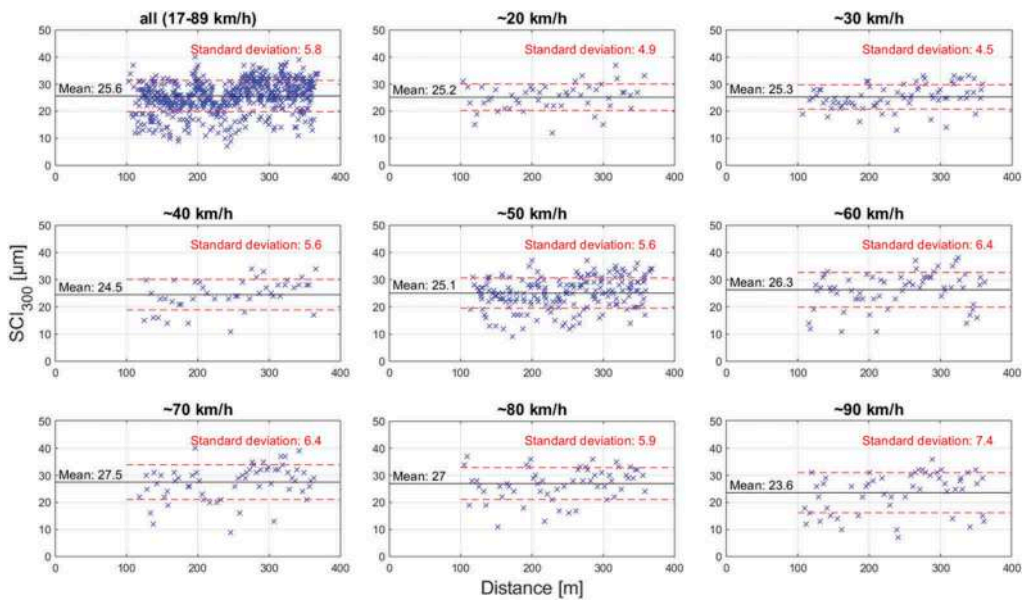


Figure 10. Distribution of bearing capacity value SCI_{300} as a function of distance at different travelling speeds. Black and red (dashed) lines indicate corresponding mean values and standard deviation, respectively.

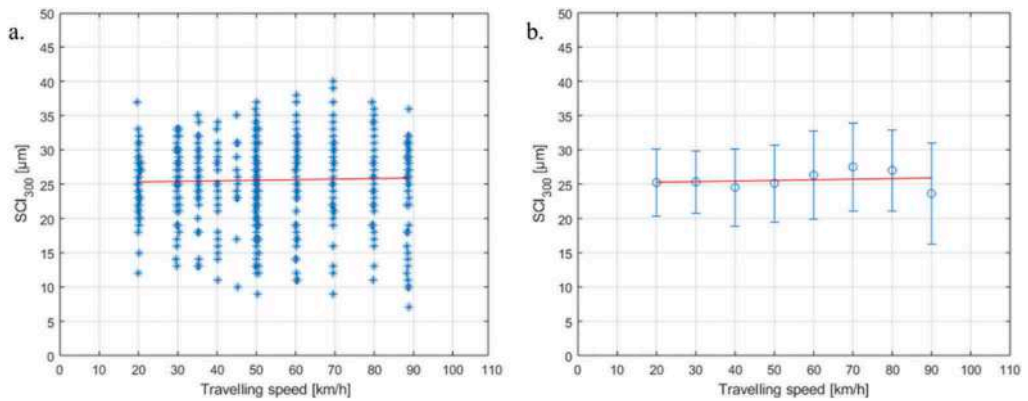


Figure 11. Bearing capacity value SCI_{300} as a function of travelling speed. Red lines indicate linear regression fit for a. all data, and b. mean values. Error bars in b. show standard deviation of SCI_{300} at different travelling speeds.

analysis of the results showed. In principle, however, it can be stated that an influence of speed on load-bearing capacity values could not be proven with either analysis method.

4 CONCLUSION

The data obtained in the field study show no significant change in deflection parameters with increasing travelling speed. For stiff pavements like German motorways, it seems to be safe to also use data for deflection analysis that was obtained at low travelling speeds (20 km/h – 40 km/h), e.g. in high-trafficked areas. Due to the rigid character of the analysed pavement,

no conclusion can be drawn for weaker pavements from the on-site parameter study. The analytical parameter study suggests an influence of travelling speed on bearing capacity parameters at very low speeds (below ~20 km/h). The authors emphasize that tests were conducted in a very narrow temperature range. Future field tests should preferably include measurements over a wider range of temperatures to evaluate the same parameters with varying visco-elastic effects.

The authors highly recommend additional field studies on weaker pavements including low and very low driving speeds. Especially in rural areas, travelling speeds can be very low due to traffic and speed limits in towns and villages. Results from these measurements are expected to give valuable information as to whether the range of driving velocities specified by the manufacturer can be expanded to lower speeds.

ACKNOWLEDGMENT

This report is based on parts of the research project carried out at the request of the Federal Ministry of Transport and Digital Infrastructure, represented by the Federal Highway Research Institute, under research project No. 04.0318/2018/MRB. The authors are solely responsible for the content.

REFERENCES

- Asphalt Research Consortium (2013): 3d-Move. Version 2.1. Reno.
- Baltzer, Susanne; Pratt, David; Weligamage, Justin; Adamsen, Jens; Hildebrand, Gregers (2010): Continuous Bearing Capacity Profile Of 18,000 Km Australian Road Network In 5 Months. Melbourne (24th Arrb Conference).
- Beckedahl, Hartmut J.; Koppers, Stefan; Balck, Henning; Skakuj, Marek (2016): Vergleich Verschiedener Kontinuierlich Messender Systeme Zur Bestimmung Der Tragfähigkeit Von Verkehrsflächen Aus Asphalt Auf Netzebene. Schlussbericht Zum Fe 04.0276/2013/Egb. Wuppertal.
- Forschungsgesellschaft Für Straßen- Und Verkehrswesen (Fgsv) (2015): Arbeitspapier. Tragfähigkeit Von Verkehrsflächenbefestigungen. Teil B 5: Schnell Fahrendes Messsystem Traffic Speed Deflectometer (Tsd). Gerätebeschreibung, Messdurchführung (Ap Trag Teil B 5). Köln: Fgsv-Verlag.
- Forschungsgesellschaft Für Straßen- Und Verkehrswesen (Fgsv) (2017): Working Paper. Bearing Capacity Of Asphalt Pavements. Part B 5: Fast Moving Measurement System. Description Of Equipment, Taking Measurements (Ap Trag Part B 5 E). Köln: Fgsv-Verlag.
- Forschungsgesellschaft Für Straßen- Und Verkehrswesen (Fgsv) (2020): Arbeitspapier. Tragfähigkeit Von Verkehrsflächenbefestigungen. Teil C 5: Traffic Speed Deflectometer (Tsd). Auswertung Und Bewertung - Asphaltbauweise (Ap Trag Teil C 5). Köln.
- Hildebrand, Gregers; Rasmussen, Søren; Andrés, R. (2000): Development Of A Laser-Based High Speed Deflectograph. In: Shiraz D. Tayabji Und Erland O. Lukanen (Hg.): Nondestructive Testing Of Pavements And Backcalculation Of Moduli. Proceedings Of The "Third International Symposium Nondestructive Testing Of Pavements And Backcalculation Of Moduli", Held Seattle, Washington, On 30 June - 1 July 1999. Fredericksberg: American Society For Testing And Materials (Astm) (Astm Stp, 1375), S. 457–469.
- Krarup, J. A.; Rasmussen, Søren; Aagaard, Lisbeth; Hjorth, Poul G. (2006): Output From The Greenwood Traffic Speed Deflectometer. Canberra (22nd Arrb Conference).
- Nasimifar, Mahdi; Siddharthan, Raj V.; Rada, Gonzalo R.; Nazarian, Soheil (2015): Dynamic Analyses Of Traffic Speed Deflection Devices. In: *International Journal Of Pavement Engineering* 18 (5), S. 381–390.
- Rasmussen, Søren (2002): Development Of A High Speed Deflectograph. Danish Road Institute. Roskilde (Report 117).
- Siddharthan, Raj V.; Yao, Jian; Sebaaly, Peter E. (1998): Pavement Strain From Moving Dynamic 3d Load Distribution. In: *Journal Of Transportation Engineering* 124, S. 557–566.
- Zafir, Zia; Siddharthan, Raj V.; Sebaaly, Peter E. (1994): Dynamic pavement-strain histories from moving traffic load. In: *Journal of Transportation Engineering* 120, S. 821–842

FWD time-history data for the evaluation of concrete slab stability

C. Van Geem

Belgian Road Research Centre, Brussels, Belgium

ABSTRACT: In the case of a pavement with concrete slabs, faulting of two consecutive slabs can be measured with the Faultimeter. This instrument fixed on a tripod and placed across a joint, measures the maximal relative movement B of the adjacent slabs while the 11 tons rear axle of a truck slowly passes by. Movement B is the sum of maximum B_1 observed for the oncoming axle and maximum B_2 observed when the axle moves on the slab behind the joint. The Falling Weight Deflectometer (FWD) is also used for the analysis of load transfer efficiency (LTE) over joints and for void detection under a slab. Results of studies at BRRC about the use of these devices for the evaluation of the stability of concrete slab pavements were published previously. In particular when comparing the results of these devices, it was noticed that sometimes the FWD identified low LTE where the Faultimeter indicated small relative slab movements. In that respect, FWD and Faultimeter are complementary.

However, these previous studies did not consider the time-history data collected by the FWD. In this contribution we report on further investigations where we do include the FWD time-history data. We will present new gained insights on the interpretation of the FWD data and how they compare to the Faultimeter data. A displacement observed by the geophones of the FWD when the charge is dropped on the slab after the joint correlates well to B_2 . A similar correlation can be established for the displacement observed by the geophones of the FWD when the charge is dropped on the slab before the joint and B_1 , except in cases where the LTE is extremely low. This observation and its consequences for the evaluation of faulting will be elaborated in the paper.

Keywords: Concrete slab road, FWD, time-history, faulting, LTE

1 CONCRETE SLABS, FAULTIMETER AND FWD

Many secondary and rural roads in Belgium have concrete slab pavements, often without dowels. After many years of service, one of the expected degradations of the concrete slab roads is the faulting between slabs. The pumping mechanism leads to increasingly large voids or cavities under the slabs. Slab faulting has a negative effect on the road condition itself and can over time cause more severe damage to the slabs themselves. Faulting also generates noise which is a concern for road users and local habitants.

1.1 Load Transfer Efficiency (LTE)

The FWD is a well-known measuring device used for the evaluation of the bearing capacity of roads and the ways in which it is used are well described, e.g. in (Van Gurp et al. 2005). For the use of the FWD on concrete slab pavements and indicators for the assessment of faulting and void detection we can refer to (Crovetti and Darter, 1985) and (Khazanovich and Gotlif, 2003).

For the assessment of the load transfer efficiency (LTE) at a joint between two adjacent concrete slabs of a road pavement, the foot of the FWD is placed tangent to the joint and geophones are positioned at both sides of the joint. The LTE is defined as the ratio (in percent) between the deflection $D_{u(i)}$ measured by the geophone at 300 mm from the place of impact on the unloaded slab and the deflection D_l measured by the geophone at the foot of the FWD on the loaded slab: $LTE = D_{u(i)}/D_l \cdot 100\%$. For the configurations and positioning of the geophones as illustrated in Figure 1, $D_{u(i)}$ is deflection $D^a(300)$ when the impact is on the approach slab and $D_{u(i)}$ is deflection $D^b(-300)$ when the impact is on the leave slab. For a comprehensive overview of the technique, we refer to (Khazanovich and Gotlif, 2003).

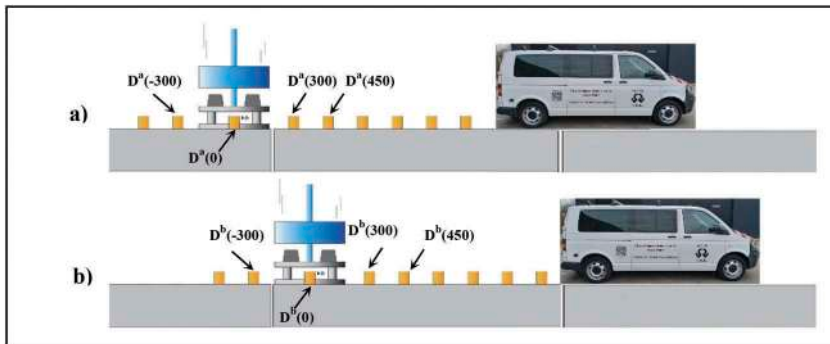


Figure 1. The Falling Weight Deflectometer positioned at a joint (a: drop on the approach slab, b: drop on the leave slab).

In (Perez and Van Geem, 2010) we typically applied a force impact of about 40 kN and under these conditions an LTE value of 70 % was considered as the critical value below which the load transfer over the joint is judged insufficient. In (Perez and Van Geem, 2010b) another configuration was used as well: we placed the foot of the FWD on the leave slab in such a way that the joint is in between geophones $D^c(-450)$ and $D^c(-300)$. This configuration is illustrated in Figure 2. In this case, LTE was defined as $D^c(-450)/D^c(-300) \cdot 100\%$.

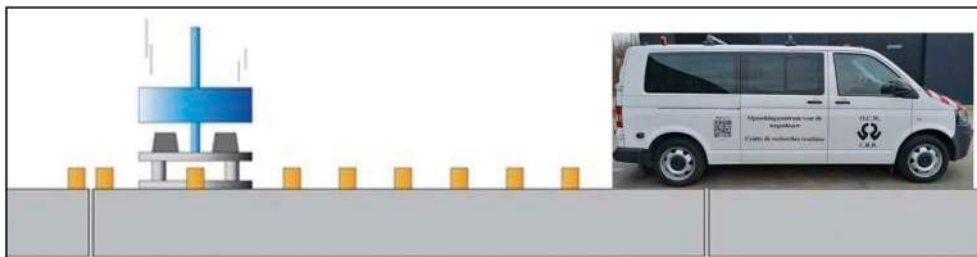


Figure 2. The Falling Weight Deflectometer positioned at a joint between geophones at -300 and -450 mm from impact.

1.2 Void detection

For void detection, (Crovetti and Darter, 1985) presented a method where the FWD is placed near the joint in the same manner as for the LTE evaluation, but measurements are repeated for three different drop heights and thus for three different force impacts. These measurements

give rise to three points on a graph with the force on the X-axis and the deflection D_l under the foot of the FWD on the Y-axis. The “straight line” with equation $y = m x + b$ optimally close to these three points (the best-fit) will cut off the Y-axis at b . When this value is too big ($b > 75 \mu\text{m}$), it is often said that a void is present. Whereas for $b < 50 \mu\text{m}$ it is generally accepted that no void is present (Crovetti & Darter, 1985). Different opinions can be found for b in the range between 50 and 75 μm . In (Perez and Van Geem, 2010) we typically applied forces of approximately 40, 50 and 60 kN.

Another interesting indicator is the difference between the deflections measured on both sides of the joint: $DIF^{(i)} = D_l - D_{u(i)}$, where D_l is the deflection measured under the impact. For $DIF^{(a)}$ when the FWD is placed before the joint $D_{u(a)}$ is deflection $D^a(300)$ measured by the geophone at 300 mm from the place of impact whereas for $DIF^{(b)}$ when the FWD is placed after the joint $D_{u(b)}$ is deflection $D^b(-300)$ measured by the geophone at -300 mm from the place of impact. We also defined $DIF^{(c)} = D^c(-300) - D^c(-450)$. The $DIF^{(i)}$ value could give an indication of the presence of a void.

Note that in the procedure for FWD measurements near a joint the FWD applies its force to one of the slabs only (since FWD measurements are done at standstill).

1.3 Faulting, pumping and voids

Faulting is the relative movement of two adjacent slabs. The movement generated by the loads of traffic can induce the formation of voids under the slabs by a pumping effect. The direction of the traffic has a decisive effect on the nature of the pumping, so that when a cavity is formed at a joint, the cavity first occurs under the leave slab. When a cavity is formed under the approach slab, the cavity is also present under the leave slab. The slab movements can be observed and measured by the Faultimeter (Figure 3).

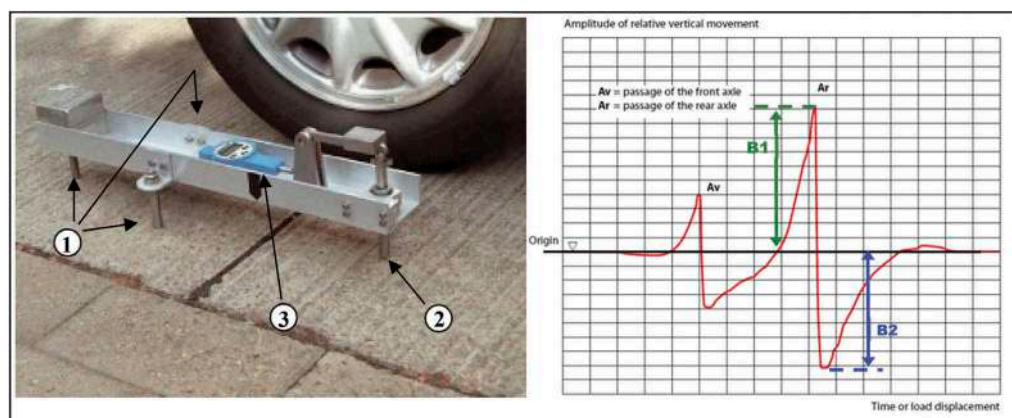


Figure 3. Faultimeter and typical measurement obtained with it (images as in (BRRC Fiche N59)).

The Faultimeter is put over the joint between adjacent slabs and records the relative measures the relative movements of the slabs while the 11 tons rear axle of a truck slowly passes from the approach slab to the leave slab (cf. Figure 3). The Faultimeter measures the physical behaviour of the faulting itself and Figure 3 shows its mechanism. The device consists of a stand with three supports (1) and a movable pin (2) serving as the fourth support. A transmission system connects this pin to a dial gauge (3), which indicates the magnitude of the movement in thousands of mm. Figure 3 also shows a typical measurement obtained with the device. The part of the curve relating to the front axle is not taken into account. For the 11 tons rear axle two maximums can be observed. The first one (B1) can be measured when the load is on top of the slab before the joint and the second one (B2) when the load is on top of the slab after the joint.

The indicator B used in Belgium is the sum of the two maximal vertical displacements B1 and B2 measured by the Faultimeter during the passage of a rear axle. It is widely accepted that the slabs are not stable when the value for $B = B1+B2$ is greater than 0.7 mm. It is also widely accepted that the slabs are stable when the value for B is lower than 0.5 mm. Another indicator which can be retrieved from this type of measurement is the final value of the gauge. If the final value of the gauge (after the slabs have been relieved) is the same as before the measurement, the slabs have returned to their initial position. If the gauge registers a residual value, the slabs are interlocked with each other.

Note that in the measurement procedure for the Faultimeter the approach and leave slabs are loaded consecutively by the moving truck. After the truck left the approach slab, that slab slowly moves back upward while the leave slab is pushed down. The measurements with the Faultimeter thus depend on the load applied to both slabs.

2 PREVIOUSLY PUBLISHED OBSERVATIONS

A correspondence between load transfer efficiency measured with an FWD and the faulting parameter $B = B1 + B2$ measured with a faultimeter was previously described and visualized in a graph in (Perez and Van Geem, 2010). We show the same graph again in Figure 4. One area shows that good load transfer efficiency implies small or inexistent faulting. Another area shows that important faulting implies bad load transfer efficiency. A third area, however, shows that bad load transfer efficiency can also occur at places where no significant faulting is observed.

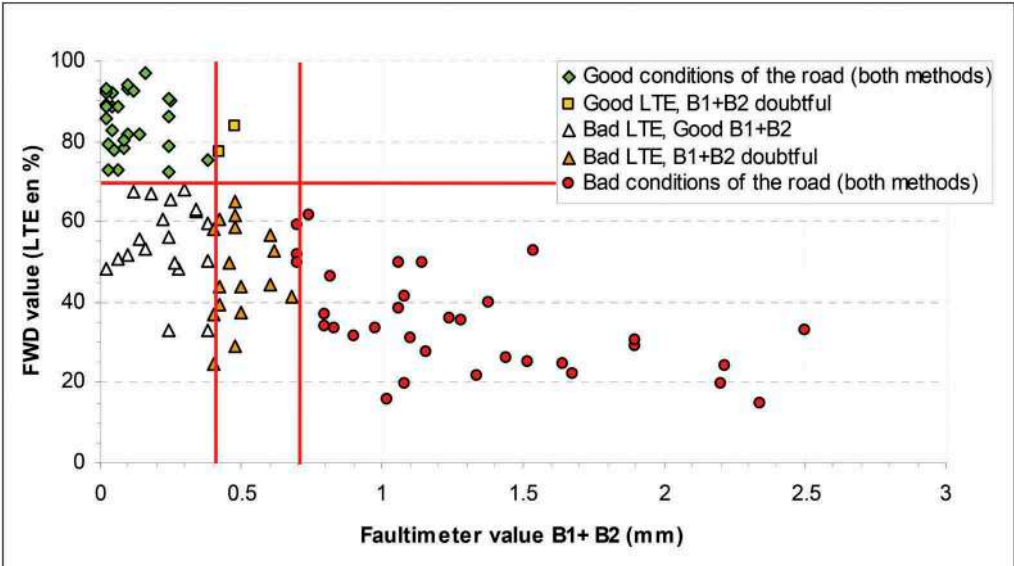


Figure 4. Correspondence between FWD and Faultimeter as presented on Figure 4 in (Perez and Van Geem, 2010).

Some other observations were reported as well. In (Perez and Van Geem, 2010), a good correlation between indicators $DIF^{(b)}$ and B2 are reported but is not found between $DIF^{(a)}$ and B1. The same paper reports on the effect of fractioning and rolling of slabs (done for stabilising of faulting slabs before an overlay with a bituminous layer). A better relationship was found between $DIF^{(c)}$ and the indicator “b” for void detection used in (Crovetti and Darter, 1985).

Based on the examples reported in (Van Geem and De Myttenaere, 2009), the LTE measured with the FWD applying a force on the approach slab is very similar to the LTE measured with the FWD applying a force on the leave slab and in case of (near) perfect load transfer, the value of LTE lies between 81 and 90%.

3 NEW INSIGHTS

In the last few years, more routine cases allowed us for more data collection on concrete slab pavements. These incited us for deeper analysis of this kind of data and we report here on new insights.

3.1 Symmetry of the deflection bowl

With the deflection bowl we mean that we look at the maximal deflection reported by each of the individual geophones. That is, for the FWD equipped with 9 geophones we look at 9 values on the deflection bowl.

When the FWD is positioned in the middle of a slab, we would expect an almost perfect symmetry of the deflection bowl. Experience with measurements on stations in the middle of slabs confirm that the measured deflection values $D(-300)$ and $D(300)$ at equal distance of the centre if impact are always almost equal. When the FWD is positioned near a joint, this symmetry is no longer observed.

For measurements near joints, geophones are positioned at 300 mm in front of the centre of impact and at 300 mm behind the centre of impact. Let us denote symmetry $S = D(-300)/D(300)$, then for a perfectly symmetrical deflection bowl we would have $S = 1$. In Figure 5 we plotted LTE and DIF against S for a road section with 39 joints. For the graph on the left the FWD was positioned on the approach slab, for the graph on the right the FWD was positioned on the leave slab. Clearly, symmetry degrades with decreasing LTE in a univocal way. Also an increasing DIF is well correlated with decreasing symmetry.

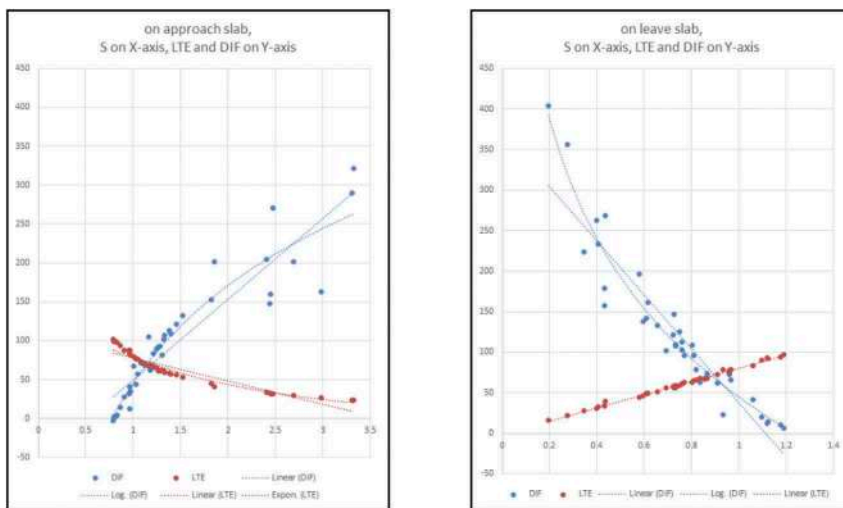


Figure 5. Symmetry against LTE and DIF at 39 joints, measured on approach and on leave slabs.

Hence, both load transfer over the joint and the presence of a cavity under the slabs can explain the asymmetry of the deflection bowl.

We made a further observation on the shape of the deflection bowl obtained when the FWD is positioned in the configuration illustrated in Figure 2. In that case, the geophone measuring 300 mm behind the centre of impact is still on the leave slab, the same slab as where the force is applied. We almost always have $D^{(c)}(-300) > D^{(c)}(0)$, which means that at $D^{(c)}(-300)$ we observe a movement of the end of the slab as a whole rather than a temporary local deformation (or deflection) of the concrete slab (as in the case of a measurement in the centre of the slab).

3.2 Time-history data on slabs

When looking more closely to the definition of B1, one would expect that B1 corresponds to the maximum difference M between the registered responses (as in the time-history data) of the two geophones used for the definition of $DIF^{(a)}$. This maximum difference is only approximately equal to $DIF^{(a)}$. So we hoped that B1 measured with the Faultimeter corresponds more to M registered by the FWD and that this would give a better correlation than the correlation we sought before between B1 and $DIF^{(a)}$. But computations on a data set of FWD measurements did not lead to a correlation between M and B1 at all, as illustrated by the graph on the left in Figure 6 where we plotted M against B1 for a small data set of stations near joints.

Note that from the definition of B2, the starting point of the vertical displacement of the slabs during a measurement with the Faultimeter is not an unloaded situation: the truck passing by the Faultimeter is unloading the approach slab only at the moment when it starts loading the leave slab. In the case of measurements with the FWD, the initial state is one where both slabs are unloaded before the FWD applies a force to one of the slabs. The conditions of the measurement with Faultimeter and FWD are different and so we do not expect to find a value in the time-history data of the FWD that corresponds to B2. Computations on a data set of FWD measurements indeed did not lead to a correlation between M and B2 either. This is illustrated in the graph on the right in Figure 6 for the same data set of stations near joints.

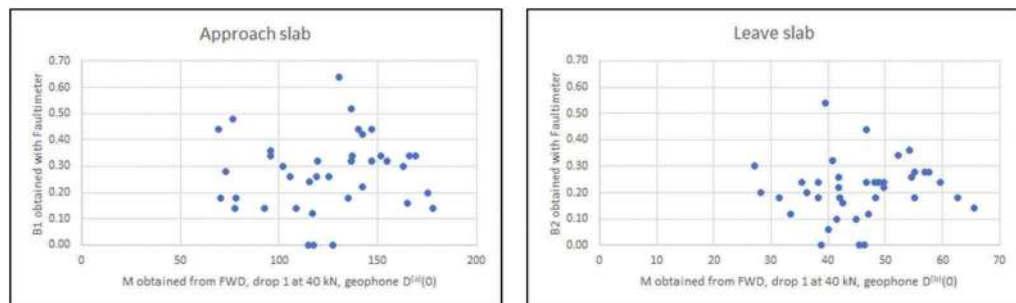


Figure 6. Attempt to simulate Faultimeter data from FWD time-history data.

When looking at the time-history curves of the FWD, two parameters are often considered as important: the area englobed by the curve and the orientation of the straight line through the origin of the graph and the point furthest away on the curve. When a pavement is in perfect condition, the dissipated energy is small at every depth so that the englobed areas are quite small. Also, the slopes of the straight lines vary slightly and monotonously in function of the distance to the centre of impact. However, when there is some deterioration of the pavement structure, there appear to be larger variations between the time-history curves of consecutively aligned geophones (which we call “jumps” in the following). Shapes of the time-displacement curves can show dramatic “jumps” for geophones on opposite sides of a joint and may be a sign of the presence of voids. This is illustrated in Figure 7, representing two stations near different joints on the same road section. In both cases the load plate was positioned tangent to the joint on the leave slab. One station had insufficient LTE of 57% slabs move little when

measured with the Faultimeter. For that station, the graph on the left of Figure 7 shows a relatively small “jump” between the blue curve of geophone D(0) and the yellow curve of geophone D(300) on the other side of the joint. The second station had a worse LTE value of only 42% and the Faultimeter measured important relative movements of the slabs. The graph on the right in Figure 7 shows a much bigger “jump” between the blue and yellow curves of the geophones at opposite sides of the joint. The main difference between the two joints is the slab movement (and hence the potential presence of a cavity).

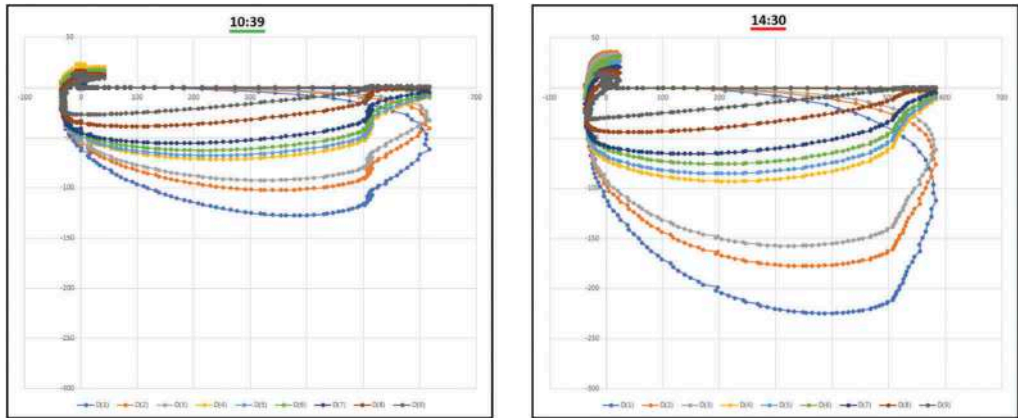


Figure 7. Time-history curves with FWD on leave slab (left: LTE = 57%, B1+B2 = 0.24, right: LTE = 42%, B1+B2 = 0.86).

In (Sybilski et al., 2009) a bouncing in the time-history data is reported to be an indicator for debonding of interlayers in the case of a bituminous pavement. This inspired us to having a look at the potential presence of a bouncing when there is a cavity under the leave slab. The “Interlayer Bond Index” I_{bond} was defined in (Sybilski et al., 2009) as follows:

$$I_{bond} = \frac{D_{end} - D_{min}}{D_{max}} \cdot 100\%$$

where D_{end} is the deflection value registered at the end of the run after 600 ms, D_{min} is the lowest deflection value during the run of 600 ms, and D_{max} is the highest deflection value during the run of 600 ms. In case the lowest deflection value is not observed, D_{min} is to be taken equal to D_{end} . When no 60 Hz filter is applied to the data, D_{max} is the deflection that is usually reported as the deflection measured by the geophone, D_{min} represents the importance of the rebound whereas D_{end} marks the cut-off at the end of the time window of 600 ms.

In order to evaluate this indicator, we computed its value for a data set of FWD measurements where we applied 6 consecutive drops on each station: the first 2 drops with a force of 40 kN, then 2 drops of 50 kN, followed by 2 drops of 60 kN. Applied to measurements on concrete slabs in the vicinity of a joint, we observed that the returned value of I_{bond} increases with increasing force and that for two consecutive drops with the same force the value of I_{bond} at the second drop is significantly lower than at the first drop. This is shown in the graph at the left of Figure 8, where we plotted the values for I_{bond} for the six consecutive drops at one station. This might be a “settlement” effect that can only be observed in the time-history data, since the maximal deflections are very similar for two consecutive drops at the same force.

The comparison between Faultimeter data (B1+B2) and I_{bond} show no correlation. This is illustrated by the graph on the right in Figure 8, where we compared I_{bond} computed for the second drop at 40 kN with Faultimeter data on 38 stations in the vicinity of joints on the

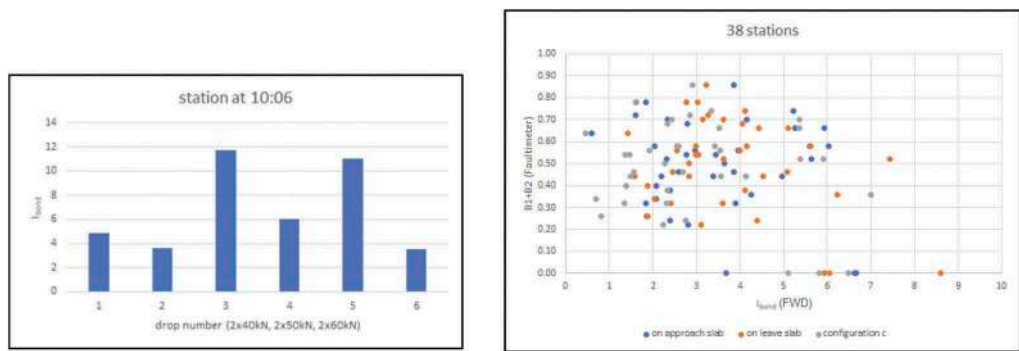


Figure 8. Evaluation of joints with the Interlayer Bond Index.

same road section and for the three configurations of the FWD (cf. Figure 1 and Figure 2). The graph we made with the data from the first drop at 40 kN gives the same kind of spreading. The comparison between I_{bond} and $\text{DIF}^{(c)}$ again gives a wide spreading and no correlation.

4 CONCLUSIONS

In the case of a pavement with concrete slabs, the evaluation of faulting, load transfer efficiency and the presence of cavities at joints is part of the evaluation of the structural condition of the pavement. The FWD can be and is used for such evaluations with indicators such as LTE and DIF. In this contribution we reported on several other interpretations of data collected with the FWD, including the time-history data and we compared these data with results obtained with the Faultimeter (a device that measures the relative movement of adjacent slabs when a truck is passing by). We tried to find a trace of the relative movement of adjacent slabs in the time-history data of the FWD but failed.

The comparison of the shape of the hysteresis curves computed for the different geophones positioned at opposite sides of a joint seem to give an indication on the presence of a cavity. The attempt to use the Interlayer Bond Index for an easy detection of a cavity was not successful. However, we also observed that for two consecutive drops with the same force this indicator gives a much smaller value at the second drop than at the first drop, although the maximum deflection of both drops is the same. This indicates that the shape of the time-history data for the two consecutive drops is not the same.

Both observations on the shape of the time-history curves is of interest because it shows that the time-history data contain more information than the simple deflection values and the indicators LTE and DIF derived from them.

REFERENCES

- BRRC Fiche N59. *Meting van het opwippen van betonplaten met de faultimeter*, (in Dutch), <https://brcc.be/sites/default/files/2021-10/N59.pdf> (last visited on 1 March 2022).
- Crovetti, J.A and Darter, M.I., 1985. *Void Detection for Jointed Concrete Pavements*, Transportation Research Record 1041, Transportation Research Board, National Research Council, Washington, D.C.
- Khazanovich, L. and Gotlif, A., 2003. *Evaluation of Joint and Crack Load Transfer*, Final Report, FHWA-RD-02-088.
- Perez, S., Beeldens, A., Maeck, J., Van Geem, C., Vanelstraete, A., Degrande, G., Lombaert, G. and De Winne, P., 2009. *Evaluation des stabilisations de dalles en béton au moyen du FWD et du Faultimètre*, Belgian Road Congress, Ghent, Belgium (in French).
- Perez, S. and Van Geem, C., 2010. *Evaluation by FWD and Faultimeter of Concrete Slabs Stability*. Proceedings of the 11th International Symposium on Concrete Roads, Sevilla, Spain.

- Perez, S. and Van Geem, C., 2010b. *FWD on concrete roads: Load Transfer Efficiency, Faulting and Bearing Capacity*. 6th European FWD User's Group Meeting, Sterrebeek, Belgium.
- Sybilski, D., Mechowski, T. and Harasim, P., 2009. *Evaluation of effectiveness of FWD use for assessment of pavement interlayer bonding*. Proceedings of the 8th International Conference on the Bearing Capacity of Roads, Railways and Airfields, Champaign (Illinois), USA.
- Vanelstraete, A., Maeck, J., Beeldens, A., Perez, S., De Visscher, J., Vervaecke, F., Van Geem, C., Lombaert, G., Lak, M. A. and Degrande, G., 2009. *Trillingsgecontroleerd stabiliseren van betonplaten voor duurzame asfaltoverlagingen met scheurremmende lagen*, Belgian Road Congress, Ghent, Belgium (in Dutch).
- Van Geem, C. and De Myttenaere, O., 2009. *Premature failure of slab pavements at heavily trafficked industrial sites*, Proceedings of the 8th International Conference on the Bearing Capacity of Roads, Railways and Airfields, Champaign (Illinois), USA.
- Van Gurp, C.A.P.M. et al., 2005. *COST 336, Use of Falling Weight Deflectometers in Pavement Evaluation*, Final Report of the Action, Main Report, 2nd Edition, April 2005.

Estimating asphalt concrete strains in airport pavements using geometric property of the pavement surface deflection basin from heavy weight deflectometer tests

H. Kazmee

Applied Research Associates, Inc., Egg Harbor Township, NJ, USA

N. Garg

National Airport Pavement & Materials Research Center, WJHTC, ATRD ANG-E262, Federal Aviation Administration, Atlantic City, USA

L. Ricalde

Applied Research Associates, Inc., Egg Harbor Township, NJ, USA

ABSTRACT: Tensile strain at the bottom of the asphalt concrete (AC) layer is an important pavement response and is related to the fatigue life of AC layer. The AC strains can be measured using strain gauges placed at the bottom of the AC layer during construction. In a mechanistic-empirical design framework, the fatigue damage algorithms rely on tensile strains from mechanistic models. In absence of strain gauges, prediction of such strains with mechanistic models and subsequent estimation of fatigue life can be misleading for in-service pavements and overlay designs owing to the unknown extent of damage governed by load and environment-related factors. This paper lays out a simplified method to estimate AC strains using a deflection basin parameter (shape factor) known as Area Under Pavement Profile (AUPP) from heavy/falling weight deflectometer (HWD/FWD) tests. AUPP is calculated from surface deflections obtained from routine HWD/FWD tests. The concept was developed in the early '80s using ILLI-PAVE (finite element program) and verified/refined using FWD test data from Mn/ROAD project. As part of a research study conducted at FAA's National Airport Pavement & Materials Research Center (NAPMRC), HWD tests were performed over AC pavements with embedded AC strain gages during Test Cycle 1 (TC-1). The surface layer of test pavements included Hot Mix Asphalt (HMA) and Warm Mix Asphalts (WMA). WMA was produced using a chemical additive Evotherm. The paper will present the relationship developed between AUPP and AC strains.

Keywords: Fatigue, Strain, HWD, AUPP, HMA, WMA

1 INTRODUCTION

Falling weight deflectometer (FWD) is the most widely used tool for pavement structural evaluation at both network and project level pavement management systems for highways (Nasimifar et al. 2016; Noureldin et al. 2003). Such evaluation involves impulse loading and subsequent measurement of surface deflections at different offsets. Conventional analytical techniques primarily focus on the backcalculation of pavement layer moduli from the measured deflections using layered elastic analyses (LEA). These back-calculated moduli are also used for the design of pavement overlays (Wang et al. 2020).

Besides the backcalculation, these deflections can be formulated into certain geometric indices known as deflection basin parameters (DBP). Previous studies have correlated these DBPs to critical pavement responses (Thompson 1989a; Thompson and Elliott 1985). Majority of those studies documented critical pavement responses such as tensile strain at the bottom of asphalt concrete (AC) layer derived from numerical techniques involving linear elastic analyses (LEA), and finite element analyses (FEA) accommodating stress-dependent material properties (Losa et al. 2008; Ma et al. 2019), etc. Thompson (1989) and Hill (1988) introduced the area under pavement profile (AUPP) as a viable DBP for the prediction of tensile strain at the bottom of the AC layer. Researchers used the ILLIPAVE finite element program to create a synthetic database of DBPs and associated critical pavement responses. Later on, Garg (1997) verified the developed correlations with critical pavement responses from instrumented MnROAD test sections.

Heavyweight deflectometer tests are conducted on airfield pavements as an integral tool to the pavement management systems. Contrary to the FWD tests, impulse loads are raised to simulate aircraft traffic conditions during the HWD tests. Like studies on highways, soft computing techniques with a synthetic database of pavement responses have also been used for mechanistic interpretation of airfield pavements. Therefore, previous studies involving HWD tests on airfield pavements offer scarce information on measured critical pavement responses.

Although the prediction models for critical pavement responses have been developed under simulative controlled conditions using LEA and FEA, inherent assumptions of those mechanistic models often limit the accuracy of predicted responses. Furthermore, the true extent of load-induced damage in a functional airfield pavement cannot be assessed correctly using those mechanistic models. Considering these issues, the current study investigated the effect of load and environment on pavement surface deflections with HWD testing on instrumented full-scale pavement structures. Statistical correlation was developed to predict tensile strain at the bottom of the AC layer from the AUPP parameter.

2 OBJECTIVE AND SCOPE

The primary objective of this paper is to outline a simplified methodology to estimate tensile strain at the bottom of the asphalt concrete (AC) layer relating a specific deflection basin parameter measured with routine heavyweight deflectometer (HWD) testing in airfield pavements. Accordingly, the tensile strain responses measured from instrumented pavement sections were correlated to the HWD AUPP index for three different load levels. The instrumented test sections used were constructed during Test Cycle 1 at the FAA National Airport Pavement and Materials Research Center (NAPMRC). Six 74.7 m (245 ft) long test lanes were constructed, each encompassing three full-scale test sections. Twelve strain gauges were installed beneath the asphalt concrete layer in each of the test sections. HWD tests were conducted on top of the embedded sensors for functionality assessment. In addition to the correlation, this paper also highlights the effect of load level, pavement temperature, and AC mix types on the observed tensile strain values. Note that this paper only discusses the load-induced tensile strains which have also been frequently referred to as strain responses.

3 DESIGN OF PAVEMENT STRUCTURES

During test cycle 1 (TC-1), six test lanes were constructed at FAA's National Airport Pavement and Materials Research Center (NAPMRC). Table 1 summarizes the mix types and designed layer thicknesses used in TC-1. All the test lanes had the same layer thicknesses. Using the FAA Rigid and Flexible Iterative Elastic Layered Design (FAARFIELD) procedure, the pavement structure was designed to contain the load and temperature-induced permanent deformation in the surface layer only. Additional details can be found elsewhere (CSRA and ARA 2017b).

The four test lanes in the outdoor area of NAPMRC were paved with four different mixes consisting of two different binder grades. The asphalt concrete (AC) mixes in lanes 1 and 2 were produced at a reduced temperature in conjunction with a chemical additive to replicate warm mix asphalt (WMA). The AC mix in lane 1 was prepared with a polymer-modified binder having a performance grade (PG) of 76-22; whereas lane 2 was paved with a neat binder (PG64-22) AC mix. Lanes 3 and 4 were constructed with traditional hot mix asphalt (HMA) comprising PG76-22 and PG64-22 asphalt binders, respectively. Indoor test lanes 5 and 6 were paved with the same polymer-modified warm and hot mixes as used in outdoor lanes 1 and 3, respectively. Each of the test lane was further subdivided into three distinct sections namely: North, Center, and South. Those full-scale test sections were trafficked with different combinations of tire pressure and temperature. Details on the trafficking condition are beyond the scope of this paper and have already been covered elsewhere (Garg et al. 2018).

Table 1. Mix Types and Designed Layer Thicknesses in TC-1.

Test Lane	Mix Type	Placement Area	Layer Thicknesses		
			Asphalt Concrete	P-209 Base	P-154 Subbase
1	WMA PG 76-22	Outdoor	12.7 cm (5 in.)	30.5 cm (12 in.)	30.5 cm (12 in.)
2	WMA PG 64-22				
3	HMA PG 76-22				
4	HMA PG 64-22				
5	WMA PG 76-22	Indoor			
6	HMA PG 76-22				

4 LAYOUT OF STRAIN GAUGES

Figure 1 exhibits the typical instrumentation layout in the North and South sections of each test lane. Judging the scope of this paper, the discussion in this section will only be limited to the layout of asphalt strain gauges (ASG). Conventional H-bar type ASGs were procured from four different manufacturers. Three out of the four ASG types had a full-bridge configuration whereas the remaining one had a quarter-bridge configuration. The operational range of the strain measurements among the gauge types varied between ± 1500 to ± 3000 $\mu\epsilon$. Further details on the strain sensors can be found elsewhere (CSRA and ARA 2017a). Six ASGs were symmetrically embedded beneath the asphalt concrete layer on both sides of the earth pressure cell (EPC-A). The longitudinal strain gauges (LSG) were placed at a center-to-center distance of 61.0 cm (24 in.) along the centerline. Transverse strain gauges (TSG) numerically identified with numbers 1 and 4 were installed approximately 50.8 cm (20 in.) away from the transverse centerline. TSG's 3 and 6 were placed 40.6 cm (16 in.) apart from the centerline. TSG locations were aligned with certain offsets of a normally distributed traffic wander sequence. Further details on the wander sequence can be found elsewhere (Kazmee et al. 2019a).

5 FUNCTIONALITY TESTS WITH HEAVYWEIGHT DEFLECTOMETER

Instrumentation has been widely used for performance evaluation and model validation in numerous accelerated pavement testing studies. The efficacy of those instrumentations heavily relies on proper installation and periodic monitoring of the sensor functionality. During TC1, the functionality of the sensors was similarly checked at three different stages:

- a. Pre-installation resistivity check,
- b. Post-construction functionality tests with heavyweight deflectometer (HWD), and
- c. Pre-traffic response testing at three different wheel loads.

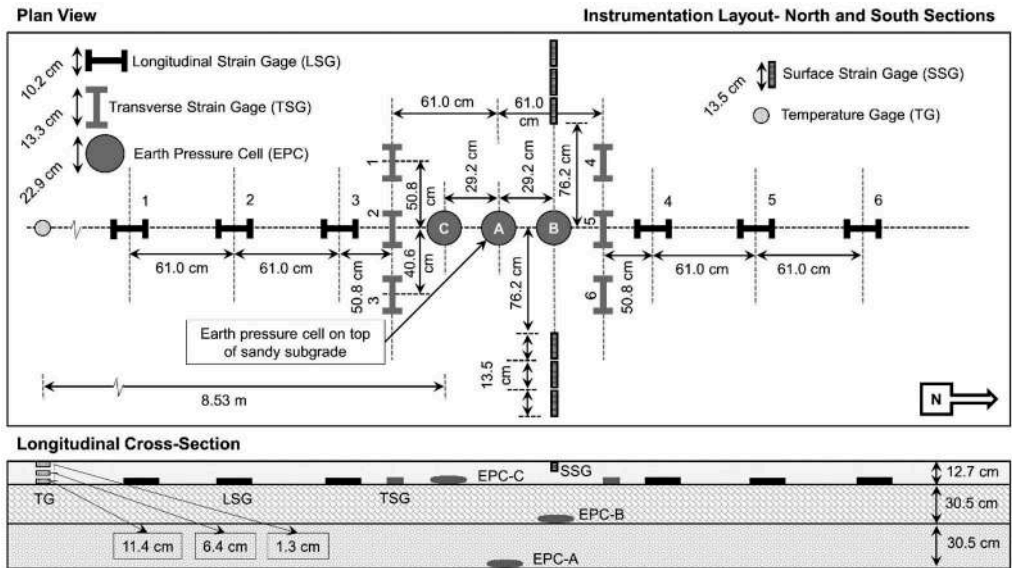


Figure 1. Layout of instrumentation in North and South sections of Test Cycle 1.

The functionality of the embedded sensors was verified with HWD impulse loads on each of the sensors. Each HWD test consisted of a 160.1 kN (36-kip) seating drop followed by three impulse loads of 53.4, 106.8, and 160.1 kN (12, 24, and 36 kips), respectively. Corresponding surface deflections were measured with seven geophone sensors spaced at an interval of 30.5 cm (12 in.). Regardless of the sensor orientation, the series of deflection sensors were always aligned with the central bar of the strain gauges during the HWD tests. Associated sensor responses were recorded with the NAPMRC data acquisition system and any residual responses at the beginning of the HWD test event were subtracted to minimize the noise. The sampling frequency rate for data acquisition was set to 400 Hz so that the entire spectrum of transient sensor responses induced by impulse load could be recorded. Figure 2 (a) shows the deflection basin observed during the sensor verification test with an impulse load of 160.1 kN (36-kip) on pavement surface designated with the sensor identification tag LSG-3 in Lane 2 North section. Figure 2 (b) shows the tensile strain recorded throughout the respective sensor verification test at three different load levels. As shown in the top left corner of Figure 2 (b), tensile strains presented in this paper were estimated from the difference between the peak strain at respective impulse load and the residual strain threshold from the prior drop. Sensor responses from the seating drops were not included for further analyses.

Note that the selected load levels in this study were considerably higher than those used in falling weight deflectometer tests for the structural elevation of highways at project levels. This was intended to reflect the airfield traffic condition. The higher load levels were also anticipated to result in higher deflection. Considering this, the conventional area under pavement profile (AUPP) index was modified to incorporate all the sensors used for the measurement of surface deflections. To this end, theoretical breakdown of the parameter has been presented in Figure 2 (a) and can be mathematically derived as:

$$AUPP = 1/2 \times \{11D_0 - 2 \times (D_1 + D_2 + D_3 + D_4 + D_5) - D_6\}$$

where:

D_0 = Center deflection,

D_1, \dots, D_6 = Deflections measured at 305, 610, 914, 1219, 1524 and 1829 mm (12, 24, 36, 48, 60 and 72 in.), respectively.

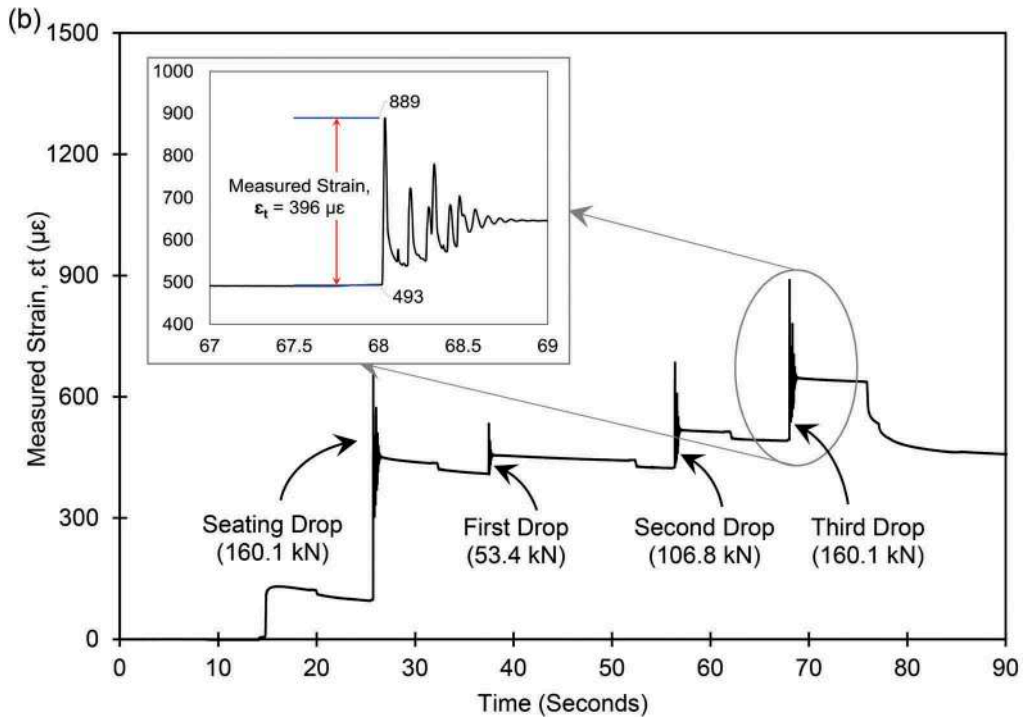
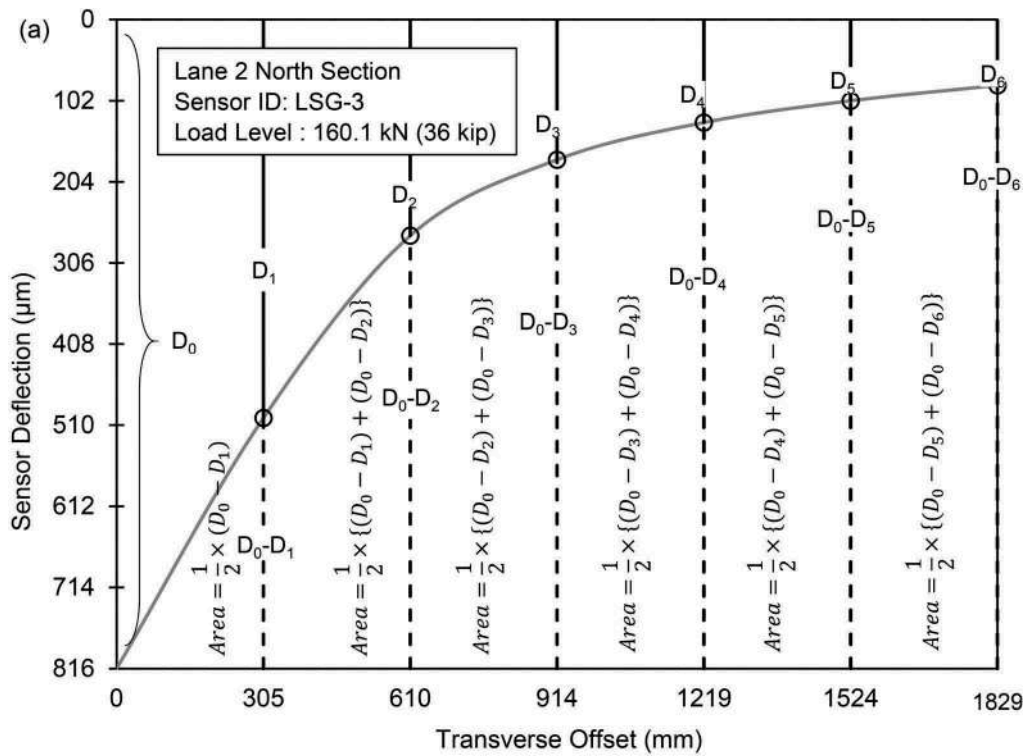


Figure 2. (a) Deflection basin from sensor verification test on LSG-3 with 160.1 kN (36-kip) load drop; (b) Sensor responses from the sensor verifications test at three different load levels.

6 AREA UNDER PAVEMENT PROFILE AND TENSILE STRAIN

The following subsections briefly discuss the effect of load level, pavement temperature, and asphalt concrete mix types on the interaction between AUPP and tensile strain measured from the installed gauges. Strain responses exceeding 1,500 microstrains ($\mu\epsilon$) were discarded considering the mixed operational range of installed ASG's. After the exclusion, a total of 330 observations was used for parametric investigation and development of DBP-based prediction model for tensile strain.

6.1 Effect of load level

Figure 3 shows the variation of tensile strains with the AUPP parameter at three representative HWD load levels. An increase in loading resulted in higher surface deflection and associated AUPP values. Recorded tensile strains also increased proportionately with the AUPP values. Hill (1988) documented a strong correlation between flexural stiffness of the asphalt concrete layer and the AUPP index. Previous numerical studies have correlated the tensile strain and AUPP index on a logarithmic scale (Garg 1997; Kim and Park 2002). Considering this, the documented strain responses were correlated to the AUPP values using a simplified power model that could also be deduced as a logarithmic model. This way, the AUPP parameter derived from the deflection basin would reflect the AC stiffness at respective load level and pavement temperature without the need for extensive laboratory characterization or computationally expensive mechanistic analyses.

Summary statistics of the linear regression on the logarithmic model are presented in Table 2. The median value of the residuals is close to 0. Distribution of the 1st and 3rd (1Q and 3Q) quartile values, as well as the minimum and maximum residuals, clearly substantiate the assumption of homoscedasticity for linear regression. Both t- and P- values for the slope parameter indicate the coefficients associated with AUPP are not equal to 0 and a strong correlation exists between the independent and dependent variables. With a single numerator, the critical F-statistics for a significance level of 0.05 are 3.87 and 3.86 with degrees of freedom denominators at 300 and 500, respectively (Field et al. 2012). The F-statistic presented in Table 2 is substantially higher than the critical thresholds listed above. This alongside the coefficient of determination at 0.79 indicates a robust correlation between the AUPP parameter and the tensile strain at the bottom of asphalt concrete.

Table 2. Summary Statistics of the Log-Linear Model.

Residuals:				
Min	1Q	Median	3Q	Max
-0.34346	-0.07721	-0.00775	0.07865	0.34238
Estimate of Model Parameters:				
<i>Coefficients</i>	<i>Estimate</i>	<i>Std. Error</i>	<i>t- Value</i>	<i>Pr(> t)</i>
Intercept (a)	-0.82568	0.0895	-9.225	< 2e-16
Slope (b)	0.97302	0.02782	34.98	< 2e-16
Goodness of Fit:				
Residual Standard Error: 0.112 on 328 degrees of freedom				
Multiple R ² : 0.7886, <i>Adjusted R²: 0.788</i>				
<i>F-statistic: 1224</i> on 1 and 328 DF, p-value: < 2.2e-16				

Issues like material variability, variation in pavement temperature, asphalt concrete thickness, material types, and achieved in-place density were anticipated to be reflected by this deflection basin index since the AUPP formula accounts for representative surface deflections influenced by underlying pavement structural layers over a longitudinal span of 1829 mm (6 ft). The interactions

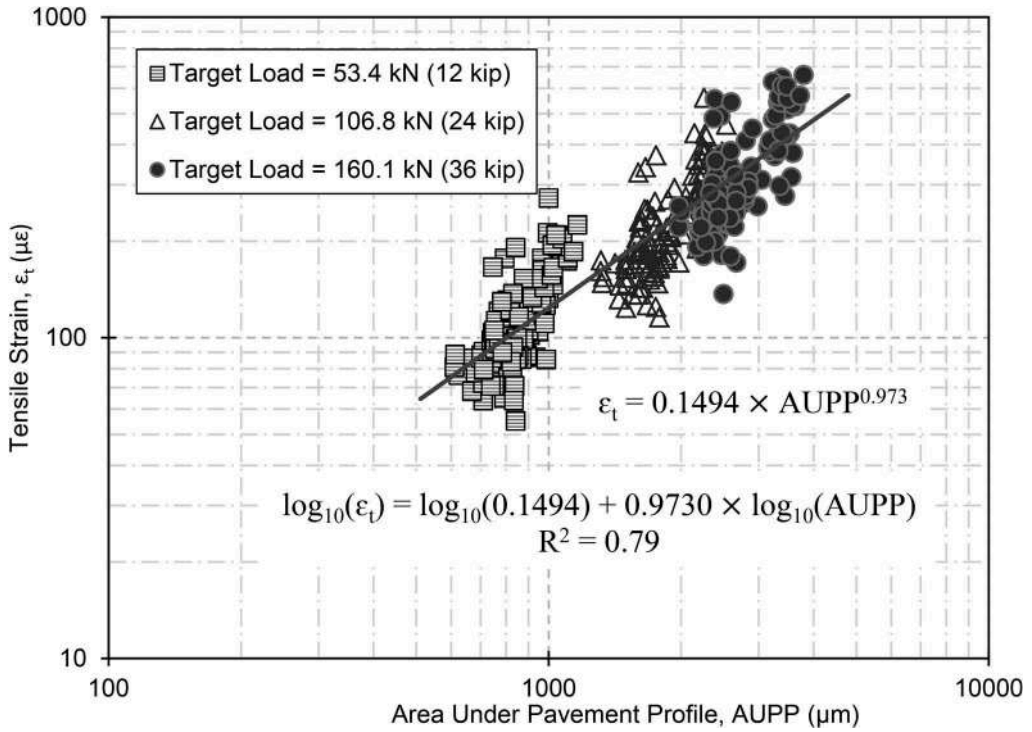


Figure 3. Variation of tensile strain with load levels.

among pavement temperature, material variability, and AUPP indices are further investigated in the ensuing sub-sections to corroborate the assumption.

On the other hand, the relative spread of tensile strains also appeared to increase with the increase in load level. As shown in Figure 2(b), the cumulative strain from the consecutive impulse loads can reach the limiting strain threshold ($\pm 1,500$ microstrains ($\mu\epsilon$)) set by the asphalt strain gauge manufacturers. As a result, tensile strains estimated from the cumulative strain magnitude at 160.1 kN (36-kip) load level seemed to exhibit the highest variability. An assumption is made that the HWD load plate was centered over the strain gage (marked on the pavement surface using survey data). However, any shift in the strain gauge position due to paving operations can also contribute to the increased spread in strain values at higher loads.

6.2 Effect of temperature variation

Effects of pavement temperature on the HWD deflection basin and respective tensile strains are shown in Figure 4 (a) and 4 (b), respectively. Notably temperatures at the mid-depth of the asphalt concrete layers were estimated using the BELLS3 equation (Lukanen et al. 2000) for routine testing methods which can be mathematically written as:

$$T_d = 0.95 + 0.892 * IR + \{\log(d) - 1.25\} \{-0.448 * IR + 0.621 * (1 - day) + 2.63 * \sin(hr_{18} - 15.5)\} + 0.042 * IR * \sin(hr_{18} - 13.5)$$

where:

T_d = pavement temperature at depth, d (°C),

IR = infrared surface temperature (°C),

d = depth at which AC temperature is being predicted (mm),

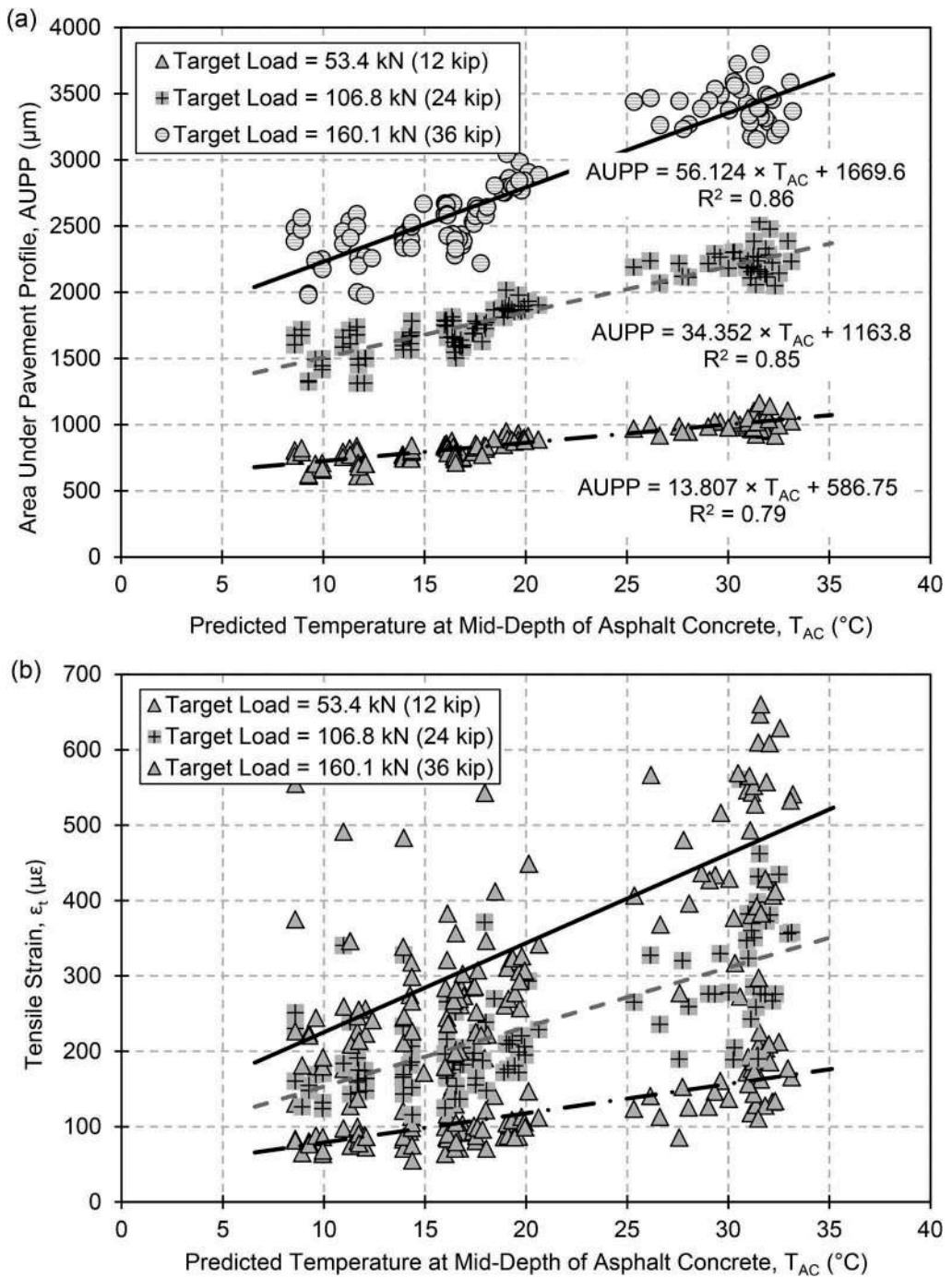


Figure 4. Effect of temperature on (a) AUPP and (b) tensile strain.

$I\text{-day}$ = average air temperature the day before testing ($^{\circ}\text{C}$),

Sin = sine function on an 18-hr clock system, with 2π radians equal to one 18-hr cycle and

hr_{18} = time of day calculated using 18-hr AC temperature cycle.

Since field coring is an intrusive and time-consuming method for the determination of asphalt concrete thickness, design thicknesses are often used for network and project level analyses of the structural capacity of the corresponding pavement structure. On a similar note, the mid-depth of the asphalt concrete layer was assigned to be 6.4 cm (2.5 in.) based on TC-1 design thickness. As-built construction thickness of the asphalt concrete layers in respective test lanes and locations were not used.

In project level testing, temperature readings are generally acquired through HWD mounted infrared sensors. Precise temperature measurements with embedded thermocouples are not feasible in operational runways or taxiways. Hence, the widely used BELLS3 temperature prediction model was used even though pavement temperature data from embedded thermocouples existed for some of the sections. Since the prediction model was designed to be shade-adjusted and indoor test lanes consistently exhibited lower surface temperature, the effect of enclosure on the predicted temperatures for the indoor lanes was anticipated to be minimal.

Temperature dependency of visco-elastic material was evident from the AUPP deflection basin parameter. An increase in temperature led to higher center deflection during the HWD tests and as a result, the area under the pavement profile also increased for all three load levels. Observed AUPP values were correlated to the pavement temperatures at mid-depth using linear regression. The slope of the linear trendlines appeared to be steeper with the increment in load levels. The coefficients of determination (R^2) for the linear relationships between pavement temperature and AUPP parameter at different load levels were consistent with each other. Figure 4 (b) highlights the effect of temperature on tensile strain accumulation. Like the observation from AUPP indices, the slope of linear trends for tensile strains got steeper with increasing load levels.

6.3 Effect of asphalt concrete mix types

Figure 5 summarizes the tensile strain responses against the AUPP indices for individual mixes used to construct the TC1 test lanes. The solid black color data points represent the neat binder (PG64-22) AC mixes. The circular data points with white and grey shades designate the indoor test lanes with PG76-22 warm and hot mixes, respectively. The outdoor test lanes with similar mix types were identified with hashed rectangular and triangular markers. Overall, the hot and warm mixes exhibited a similar magnitude of strains with respect to the binder grades. The PG64-22 mixes consistently exhibited higher AUPP values and corresponding tensile strains compared to their polymer-modified counterparts. Laboratory characterization of these mixes revealed that the polymer-modified mixes had higher stiffness than the neat binder mixes (Kazmee et al. 2019b). With higher resistance to load and temperature-induced deformation, the PG76-22 mixes performed better in terms of lower AUPP values and tensile strains. Observations from the HWD functionality tests were also consistent with the tensile strain trends observed during the temperature-controlled traffic tests (Kazmee et al. 2019a).

7 CONCLUSIONS

Six full-scale test lanes were constructed at FAA's National Airport Pavement and Materials Research Center (NAPMRC) to investigate the feasibility of warm mix asphalt for airfield flexible pavement applications. Each lane was subdivided into three full-scale test sections instrumented with asphalt strain gauges. Series of heavyweight deflectometer (HWD) tests were conducted on all those sensors to assess their functionality. Strain responses acquired from those tests revealed that both the AUPP parameter and tensile strain increased with the increase in applied load and pavement temperature. AC mixes comprising of polymer-modified mixes consistently exhibited lower values of AUPP index and tensile strains compared to their

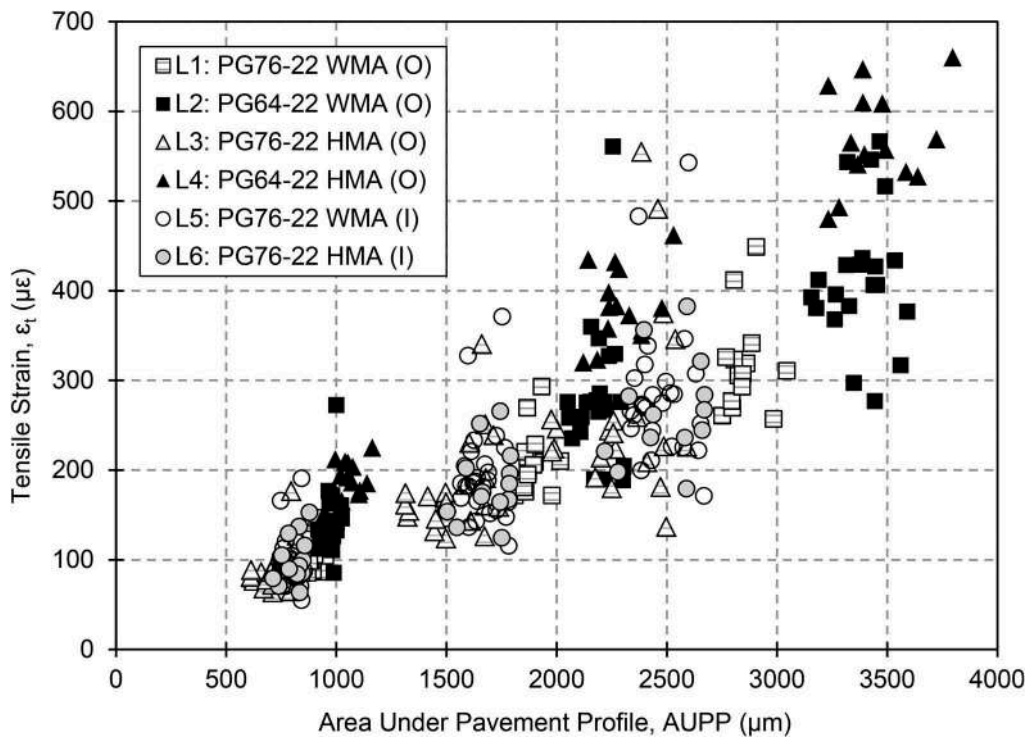


Figure 5. Variation of tensile strain with asphalt mix types.

neat binder counterparts. Since the temperature variation, material variability, and load level were reflected through the relative change in AUPP indices, a simplified power model was proposed for the prediction of tensile strain at the bottom of the AC layer using the AUPP index solely. The proposed model exhibited satisfactory goodness of fit in terms of R^2 value.

REFERENCES

- CSRA, and ARA. (2017a). *National Airport Pavement and Material Research Center (NAPMRC) Test Cycle 1 (TC1) Instrumentation and Traffic Test Report (Volume 2)*. Washington, DC, USA.
- CSRA, and ARA. (2017b). *National Airport Pavement and Material Research Center (NAPMRC) Test Cycle 1 (TC1) Design and Construction Report (Volume 1)*. Washington, DC, USA.
- Field, A., Miles, J., and Field, Z. (2012). *Discovering Statistics Using R*. SAGE Publications Ltd, Washington, DC.
- Garg, N. (1997). "Mechanistic-Empirical Evaluation of the Mn/ROAD Low-Volume Road Test Sections." University of Illinois at Urbana-Champaign.
- Garg, N., Kazmee, H., Ricalde, L., and Parsons, T. (2018). "Rutting Evaluation of Hot and Warm Mix Asphalt Concrete under High Aircraft Tire Pressure and Temperature at National Airport Pavement and Materials Research Center." *Transportation Research Record: Journal of the Transportation Research Board*, SAGE PublicationsSage CA: Los Angeles, CA, 1–11.
- Hill, H. J. (1988). "Early Life Study of the FA409 Full-Depth Asphalt Concrete Pavement Sections." University of Illinois at Urbana-Champaign.
- Kazmee, H., Garg, N., Knieriem, R., Gerke, J., and Villafane, W. (2019a). "Aircraft Tire Pressure and Pavement Temperature Effects on HMA and WMA Strains." *Proceedings of the International Airfield and Highway Pavements Conference 2019*, I. Al-Qadi, H. Ozer, A. Loizos, and S. Murrell, eds., American Society of Civil Engineers, Chicago, IL, 322–332.

- Kazmee, H., Garg, N., Tomlinson, C., and Ricalde, L. (2019b). "Warm Mix Asphalt (WMA) for Airport Pavements – Relating Laboratory Test Results to Performance Under Accelerated Pavement Testing (APT)." *Journal of the Association of Asphalt Paving Technologists*, 88, 30p.
- Kim, Y. R., and Park, H.-G. (2002). *Use of Falling Weight Deflectometer Multi-Load Data for Pavement Strength Estimation (Report No. FHWA/NC/2002-006)*. Raleigh, NC.
- Losa, M., Bacci, R., and Leandri, P. (2008). "A statistical model for prediction of critical strains in pavements from deflection measurements." *Road Materials and Pavement Design*, Taylor & Francis Group, 9, 373–396.
- Lukanen, E. O., Stubstad, R. N., and Briggs, R. C. (2000). *Temperature Predictions and Adjustment Factors for Asphalt Pavement (Research Report No. FHWA-RD-98-085)*. McLean, VA.
- Ma, L., Li, M., Pang, J., and Huang, C. (2019). "Evaluation of Transverse Cracks for Semi-Rigid Asphalt Pavements using Deflection Basin Parameters." *Transportation Research Record: Journal of the Transportation Research Board*, SAGE Publications Ltd, 2673(2),358–367.
- Nasimifar, M., Thyagarajan, S., Siddharthan, R. V., and Sivaneswaran, N. (2016). "Robust Deflection Indices from Traffic-Speed Deflectometer Measurements to Predict Critical Pavement Responses for Network-Level Pavement Management System Application." *Journal of Transportation Engineering*, American Society of Civil Engineers (ASCE), 142(3), 04016004.
- Noureldin, A. S., Zhu, K., Li, S., and Harris, D. (2003). "Network Pavement Evaluation with Falling-Weight Deflectometer and Ground-Penetrating Radar." *Transportation Research Record: Journal of the Transportation Research Board*, National Research Council, 1860(1),90–99.
- Thompson, M. (1989a). "ILLI-PAVE Based NDT Analysis Procedures." *Nondestructive Testing of Pavements and Backcalculation of Moduli*, ASTM International, 100 Barr Harbor Drive, PO Box C700, West Conshohocken, PA 19428-2959, 487-487–15.
- Thompson, M. R. (1989b). "Area Under the Pavement Profile to Predict Strain." FWD Users Group Annual Meeting, Indianapolis, IN.
- Thompson, M. R., and Elliott, R. P. (1985). "ILLI-PAVE-based response algorithms for design of conventional flexible pavements." *Transportation Research Record*, (1043), 50–57.
- Wang, H., Xie, P., Ji, R., and Gagnon, J. (2020). "Prediction of airfield pavement responses from surface deflections: comparison between the traditional backcalculation approach and the ANN model." *Road Materials and Pavement Design*, Taylor and Francis Ltd.

Comparison of RAPTOR measurements with falling weight deflectometer deflections using backcalculation

S.S. Madsen

Road Survey Technology (RST), Ramböll, Malmö, Sweden

N.L. Pedersen

Department of Mechanical Engineering, Technical University of Denmark, Kgs. Lyngby, Denmark

ABSTRACT: Continuous deflection measurements are gaining increased interest due to the benefit of effectively measuring large networks. However, a pavement responds differently to a continuously moving load than to an impulse load from a Falling Weight Deflectometer (FWD) which has been the industry standard for structural testing for decades. Several approaches have been taken to assess the level of agreement between the two types of deflection measurement devices. This is important for road authorities for which deflection measurements provide a basis for maintenance decisions.

This paper presents a viscoelastic and dynamic model able to simulate both a moving wheel and an impulse load, and hence generate a link between continuous deflection devices and FWD. The model can be used to perform backcalculation of continuous deflection measurements to obtain pavement properties. These properties are then used as input to the model to simulate an FWD experiment. The output is FWD deflections corresponding to what an FWD would have measured at the place where the continuous deflection measurements were reported. This procedure is applied to RAPTOR measurements collected at a city road in Copenhagen, Denmark. The calculated corresponding FWD deflections were compared with actual FWD measurements collected on the same day. The results show a good agreement of the center deflection, but also outer deflections agree well. The viscoelastic properties obtained in the backcalculation of RAPTOR measurements were in good agreement with the FWD deflection time histories.

Keywords: Rapid Pavement Tester (RAPTOR), Falling Weight Deflectometer, Rolling Wheel Deflectometer, viscoelasticity, Finite Element Method

1 INTRODUCTION

Structural capacity of pavements is usually evaluated by deflection measurements performed by a Falling Weight Deflectometer (FWD), which applies a stationary impulse load on the pavement. In recent years, there has been an increasing interest in applying high speed continuous deflection measurements for network level applications. Examples of continuous deflection devices are the Traffic Speed Deflectometer (TSD) and the Rapid Pavement Tester (RAPTOR), which continuously measure the pavement response due to a constant loading from the wheel moving on the pavement. These devices overcome the limitation of an FWD since they operate at traffic speed and require no traffic disruptions. However, the response of the pavement due to the continuously moving load is different than the pavement response to

an FWD impulse load. Due to the viscoelastic nature of asphalt concrete the pavement response under a moving load is delayed in time resulting in an asymmetric deflection basin around the loading wheel. The dynamic FWD impulse load generates a wave transmitted through the pavement structure, and thus inertia becomes significant (see e.g. Maina et al. (1996) and Cao et al. (2019b)). Deflections obtained from a continuous deflection device can therefore not be expected to be the same as deflections measured by an FWD.

Given that the FWD has been industry standard for several decades there is an interest in assessing the level of agreement between measurements performed by the two types of devices. This is important for road authorities and pavement design engineers since deflection data provides a basis for maintenance decisions. Some previous effort in doing such comparisons include Shrestha et al. (2018), Březina et al. (2017) and Elseifi et al. (2012) in which a comparison of the center deflection provided by FWD and continuous deflection devices is considered. They all find a good agreement for the trends from the different devices, but varying deviation in the magnitude of the deflections. Another study by Katicha et al. (2014) compared surface curvature index (SCI) and base damage index (BDI) between the Traffic Speed Deflectometer (TSD) and the FWD, and found that differences between the two devices could be significant.

Another approach to compare continuous deflection measurements with FWD deflections is through a numerical model. Elbagalati et al. (2018) developed an Artificial Neural Network (ANN) algorithm to statistically convert TSD measurements to corresponding FWD deflections (See also Zihan and Elseifi (2019)). The drawback of ANN is the need for a large amount of data for training and validation of the model. Since the difference in pavement response from the two types of measurement devices depends a lot on layer properties it can be difficult to ensure that the data set used for training and validation of the model is in fact representative for conversion of new data.

The present paper presents a dynamic and viscoelastic numerical pavement model that is able to simulate the pavement response both due to a moving load and an impulse load. In that sense the model can represent the pavement response from both continuous deflection measurement devices and FWD, and can thus be considered as a link between the two deflection responses. This is done by performing backcalculation of continuous deflection measurements to obtain pavement properties. These pavement properties are then applied in the simulation of an FWD experiment to obtain corresponding FWD deflections, i.e. what an FWD would have measured. This approach is applied to continuous deflection measurements collected by a RAPTOR. Figure 1 illustrates the concept of backcalculation of RAPTOR measurements and forward prediction of corresponding FWD deflections.

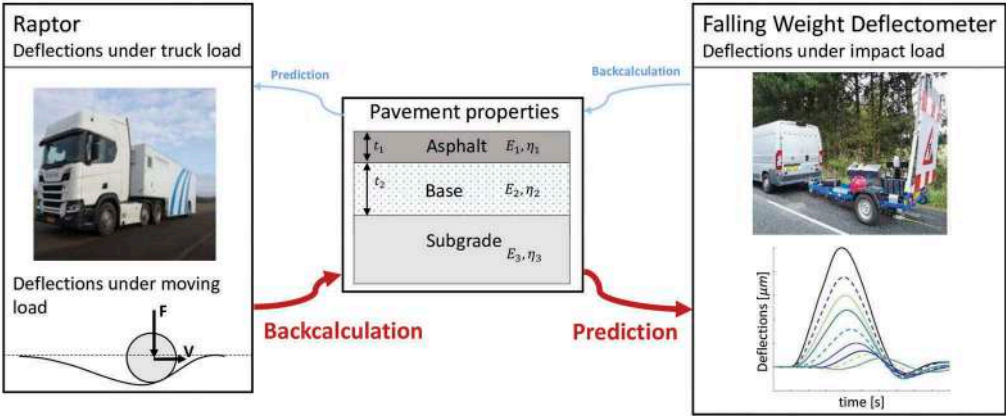


Figure 1. RAPTOR and FWD concept.

Another advantage of the model is that it is capable of evaluating surface deflections directly below the wheel. No continuous deflection measurement devices available today is able to measure the pavement response below the loading wheel. FWD deflection basins reveal that the deflection response in many cases decreases rapidly within the first 2-300 mm from the center of the loading plate. Similar behavior would be expected from a moving wheel. Furthermore, the corresponding FWD deflections obtained from backcalculation of continuous deflection measurements can be included directly in a pavement management system in the same way as the user would import FWD measurements. This way continuous deflection measurements are well integrated with existing historical FWD data applied for remaining life calculations.

2 RAPID PAVEMENT TESTER (RAPTOR)

RAPTOR is a continuous deflection measurement device developed by Dynatest, which measures the pavement response continuously while moving at traffic speed. It consists of a custom designed truck trailer loaded by 10 ton on the rear axle. Inside the trailer, 12 line lasers are mounted on a stiff carbon fibre beam close to the rear wheel. Each laser measures the distance to the pavement surface. These measurements are combined to provide the RAPTOR Deflection Indices (RDI), which are used to obtain the mechanical properties of the pavement. The lasers are positioned from 1.5 m behind the wheel up to 3.6 m in front of the wheel.

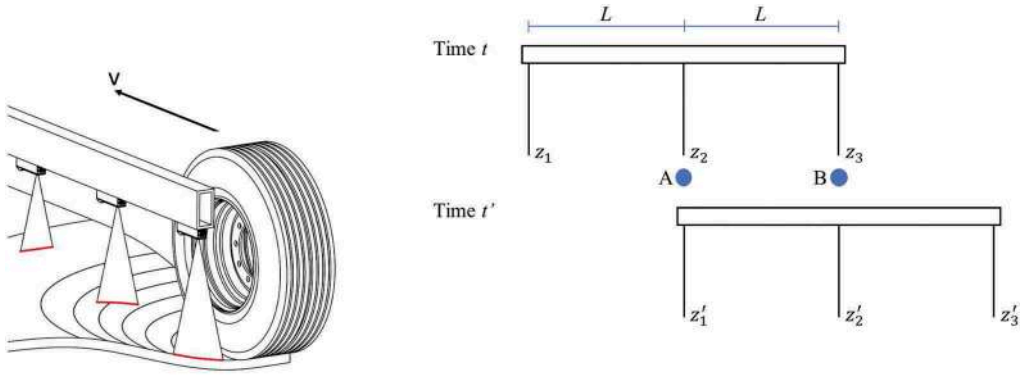
The line lasers measure 1280 points on a 200 mm wide line transverse to the driving direction as depicted in Figure 2a. Each laser measurement is a summation of three contributions; a reference height, h , from the laser to the undeflected pavement surface, the pavement deflection d_i below laser i and a contribution r_j from the texture at point j on the pavement surface. Reference height and texture can be eliminated by combining the measurements from three equidistantly spaced lasers in two different instances of time based on a principle similar to the Harr algorithm Harr and Ng-A-Qui (1977). The Harr algorithm relies on the possibility to measure the same spot on the pavement surface by two different lasers. The fact that the lasers installed on the RAPTOR measure a wide line ensures the possibility of finding the same spot on the pavement twice. An image recognition technique is applied in order to locate the same spot on the pavement.

While the RAPTOR moves, small changes in the angle between the beam and the reference plane can occur. This angle change adds a fourth contribution to the laser measurements. For this reason the original Harr algorithm would require four laser measurements combined in order to isolate pavement deflections. However, the angle change is measured by gyroscopes mounted on the beam and can therefore be accounted for without including a fourth laser for calculation of the RDI.

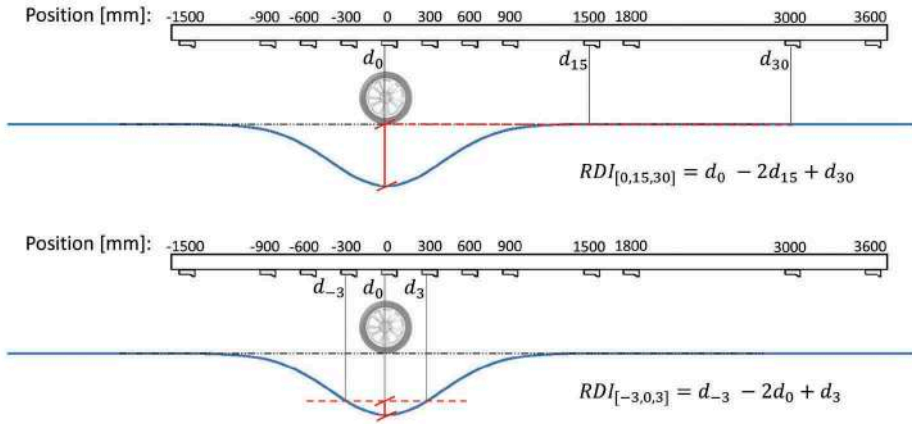
2.1 Calculation of RAPTOR Deflection Indices (RDI)

Let z_1 , z_2 and z_3 be measurements at time instance t from laser 1, 2 and 3 equidistantly spaced by length L . The order of the lasers should be such that laser 1 is the rearmost, laser 3 is in front, laser 2 is in the middle. When the beam has moved distance L , another set of measurements $z_{1'}$, $z_{2'}$ and $z_{3'}$ at time t' is recorded. At time t' laser 1 sees the same point A as was seen by laser 2 at time t , i.e. $z_{1'}$ and z_2 includes the same texture r_A (see Figure 2b). Subtraction of reading z_2 from $z_{1'}$ eliminates texture r_A at point A. Similarly measurement $z_{2'}$ and z_3 includes the same reading of the texture, r_B at point B and subtraction of z_3 from $z_{2'}$ eliminates texture r_B . The equations for the measurements collected at point A and point B at time t and t' as well as the differences between t' and t are listed in Table 1. A subtraction of the two equations in the last column eliminates the reference heights yielding the RAPTOR Deflection Index

$$RDI_{[1,2,3]} = d_1 - 2d_2 + d_3 \quad (1)$$



(a) Laser mounting on beam. (b) RAPTOR measuring principle.



(c) RAPTOR Deflection Indices (RDI).

Figure 2. RAPTOR measuring principle and laser setup.

Table 1. Equations for laser readings at time t and t' .

Measurement at time:	t	t'	
Point A:	$z_2 = h + r_A + d_2$	$z_{1'} = h' + r_A + d_1$	$z_{1'} - z_2 = (h' - h) + d_1 - d_2$
Point B:	$z_3 = h + r_B + d_3$	$z_{2'} = h' + r_B + d_2$	$z_{2'} - z_3 = (h' - h) + d_2 - d_3$

Measurements from any three lasers on the beam can be combined to calculate a RDI as long as they are equally spaced. In order to distinguish between RDIs coming from different laser combinations, the subscription indices 1, 2 and 3 in Equation (1) are replaced with indices for the position of the lasers with a reference to 0 at the position right next to the loading wheel. Negative indices will thus refer to lasers positioned behind the wheel, while positive indices refer to laser positions in front of the wheel. For instance an RDI calculated from the three lasers positioned by the wheel, 1500 mm and 3000 mm in front of the wheel is named $RDI_{[0,15,30]}$. The indices refer to the position with the unit 10^2 mm in order to keep the notation as short as possible.

In case of a narrow deflection basin where the deflection 1500 mm and 3000 mm ahead of the loading wheel are close to zero, $RDI_{[0,15,30]}$ would correspond to the actual deflection of the pavement below the laser next to the loading wheel as illustrated in

Figure 2c. Another example is $RDI_{[-3,0,3]}$, which is a combination of lasers positioned by the loading wheel, 300 mm behind and 300 mm in front of the loading wheel. To illustrate the relationship of the quantity of $RDI_{[-3,0,3]}$ to the deflection basin seen by the lasers, one can draw a line between the deflection seen by the first and the last laser, i.e. from 300 mm behind to 300 mm in front of the wheel (see the red dashed line in Figure 2c). The distance from this line to the deflection seen by the middle laser, in this case the laser right by the wheel, corresponds to $-\frac{1}{2}RDI_{[-3,0,3]}$.

3 DYNAMIC AND VISCOELASTIC PAVEMENT MODELING

This section presents a pavement model able to simulate both a moving load (such as RAPTOR) and an impulse load from an FWD. Such a model needs to represent both viscoelastic and dynamic analysis.

Asphalt is a viscoelastic material, which means that it exhibits both elastic and viscous behaviour when undergoing deformation. Both the elastic and the viscous characteristics changes under different loading and temperature conditions. Asphalt can be characterized by its mastercurve representing the elastic and viscous properties under all load and temperature conditions. Thus the elastic and viscous property can be found in the mastercurve for any specific condition of load and temperature. A constitutive model able to represent the viscoelastic behavior under a large range of temperature and loading time or frequencies requires a certain amount of model parameters. One of such models with fewest parameters is the Huet Sayegh model, which has a total of 6 model parameters. A continuous deflection device would measure the pavement response under one load and temperature condition. For the purpose of backcalculation there would only be information in the measurements about the asphalt properties under the specific measurement condition. So in order to represent the asphalt behavior under one such condition, a simple constitutive relation representing elastic and viscous characteristics is sufficient to capture the viscoelastic behavior exhibited due to the moving load. In this paper the Kelvin-Voight model is adopted. The constitutive relationship between stress and strain for a Kelvin-Voight material consists of an elastic part and a viscous part

$$\sigma = \mathbf{C}\varepsilon + \eta\mathbf{C}\dot{\varepsilon} \quad (2)$$

where σ is the stress tensor, ε and $\dot{\varepsilon}$ are the strain and strain-rate tensors, respectively, \mathbf{C} is the constitutive tensor and η denotes material damping. For small strains $\mathbf{e} = \frac{1}{2}(\nabla\mathbf{u} + (\nabla\mathbf{u})^T)$ where \mathbf{u} is the displacement vector and ∇ is the gradient operator. Assuming isotropy, the constitutive tensor is governed by two parameters: Young's modulus E and Poisson's ratio ν . The pavement is modeled as a fully bonded layered structure.

The governing equation of motion is given by the second law of Newton Cook et al. (2002)

$$(\nabla^T \sigma)^T = \rho \frac{\partial^2 \mathbf{u}}{\partial t^2} \quad (3)$$

where ρ is the mass density and \mathbf{s} refers to the stress defined in Equation (2). The Finite Element method is applied to solve for the pavement response. For this purpose, the equation of motion (3) is multiplied by a virtual displacement $\tilde{\mathbf{d}}$ followed by integration over the volume. Reformulation using the divergence theorem yields

$$\int_S \tilde{\mathbf{d}}^T \sigma \mathbf{n}_z dS - \int_V \tilde{\varepsilon}^T \sigma dV = 0 \quad (4)$$

where S and V denote integration over surface area and volume, respectively, and \mathbf{n}_z is a unit vector indicating the vertical direction of the external load. Introduction of shape functions into Equation (4) yields the governing equation in matrix form

$$\mathbf{M}\ddot{\mathbf{U}} + \mathbf{Z}\dot{\mathbf{U}} + \mathbf{K}\mathbf{U} = \mathbf{F} \quad (5)$$

in which \mathbf{M} is the mass matrix \mathbf{Z} is the damping matrix, \mathbf{K} is the stiffness matrix and \mathbf{U} is the vector of nodal deflections. \mathbf{F} represents the external load from the moving wheel. The (\cdot) and $(\ddot{\cdot})$ represents ones and twice differentiation in time, respectively.

In this paper, the moving load is assumed to move at constant speed under constant loading. In this case the inertia effects on the pavement response becomes negligible as long as the the speed of the moving vehicle does not come close to soil wave propagation speed, which most often would require much higher vehicle speed than regular traffic. That means that the simulation of the moving load can be simplified by leaving out the inertia part of the governing equation, leaving it to be

$$\mathbf{K}\mathbf{U} + \mathbf{Z}\dot{\mathbf{U}} = \mathbf{F} \quad (6)$$

On the other hand, inertia becomes important when modeling an FWD impulse load as the impulse generates a wave that propagates in time through the pavement structure. However, the FWD experiment is symmetric (contrary to the moving load experiment). In that sense the FWD simulation can be simplified by solving the equation in axisymmetric coordinates yielding a much faster computation time. That coordinate transformation is relatively simple and is described in Madsen and Levenberg (2018)..

The asphalt viscosity is determining for the shape of the deflection basin under a moving load. An increase in asphalt viscosity increases the asymmetry of the deflection basin. If the viscosity is $\eta = 0$, the asphalt concrete is purely elastic and the basin becomes symmetric. An increase in asphalt viscosity parameter also causes a decrease in the deflection magnitude. The influence of asphalt viscosity is illustrated in Figure 3. Viscoelasticity also have an important impact on the deflections occurring from an impact load on the pavement. The delay in deflection response is increased as well, which can be seen in the deflection time histories recorded by an FWD. However, since the deflection basin is drawn by selecting the peak values in the deflection time histories, this effect is not clearly seen in an FWD deflection basin.

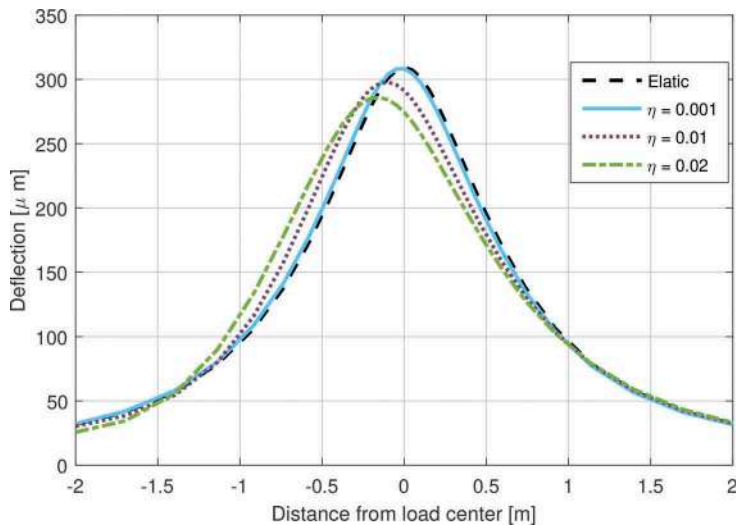
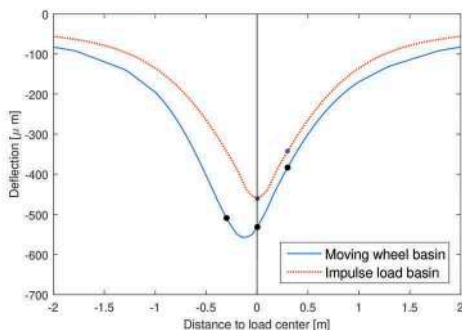


Figure 3. Influence of viscous parameter of the asphalt concrete layer on the deflections occurring from a moving load.

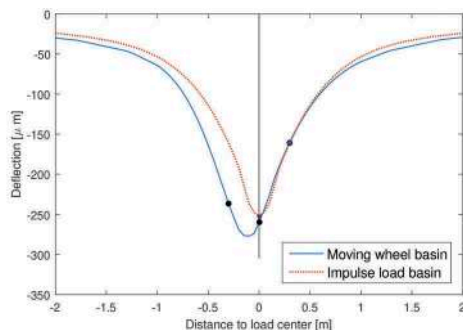
3.1 Comparison of moving wheel deflection basin with FWD deflection basin

As mentioned in the introduction, previous research have found that it can be difficult to make an empirical correlation between deflections measured by a continuous deflection device and an FWD. This section illustrates with a couple of examples the reason why. The differences between a deflection basin from a moving load and that of an impulse load is highly dependent on material properties of the different layers in a pavement structure. Figure 4 shows two numerical examples of deflection basins obtained under a moving load and from an impulse load calculated for the same pavement structure. The examples are calculated for a pavement with 200 mm asphalt concrete overlying a soft subgrade (Figure 4a) and a stiff subgrade (Figure 4b), respectively. The asphalt concrete has a Young's modulus of $E_{AC} = 2000$ MPa and a viscous parameter of $\eta = 0.01$, which is within the range of realistic values presented in literature. The x-axis indicate the distance to the load center where '0' refer to the position directly below the load. The moving load basin is clearly asymmetric around the load center and the maximum deflection no longer occurs at the load center, but behind. How far behind depends on the viscosity of the asphalt concrete as shown in Figure 3. The deflection basin due to the impulse load is symmetric. The black points indicate the deflection at the load center as well as 300 mm in front of and behind the load center, which clearly illustrate that deflections from a moving wheel are larger behind the wheel compared to in front of the wheel. The difference between moving wheel deflection basin and FWD basin is dependent on the material properties. The moving wheel basin in Figure 4a is considerably larger than the FWD basin both at the load center and at the outer part of the basin. The maximum moving load deflection is $557\mu\text{m}$ and occurs approximately 100 mm behind the center of the wheel. This is 21% more than the maximum impulse load deflection of $460\mu\text{m}$. The outer deflections occurring due to a moving load is larger as well, in this case $115\mu\text{m}$ 1500 mm in front of the wheel compared to $79\mu\text{m}$ at the impulse load basin corresponding to 45% greater deflections in the case of a moving load. In case of a stiffer subgrade (Figure 4b) the front part of the moving wheel basin compares closely with the impulse load basin. However, the maximum deflection is still around 10% larger and the outer deflection at 1500 mm in front of the load is approximately 20% larger.

A common index calculated from FWD surface deflection is the Surface Curvature Index $SCI_{300} = D_0 - D_{300}$ with D_0 as the center deflection and D_{300} the deflection 300 mm from the load center. In the case of a moving load where the deflection basin is asymmetric, there exist two different values of SCI_{300} ; one in front of the wheel and another one behind the wheel. For the example in Figure 4a the SCI_{300} in front of the wheel is $SCI_{300}^{front} = 148\mu\text{m}$, which is about 20% bigger than $SCI_{300}^{FWD} = 117\mu\text{m}$ calculated for the impulse load basin. Behind the wheel $SCI_{300} = 22\mu\text{m}$, which is way smaller. SCI_{300}^{front} calculated for the example in Figure 4b is



(a) Soft subgrade



(b) Stiff subgrade

Figure 4. Deflection basin under moving load plotted together with FWD deflections basin both of them simulated using the same pavement properties: 200 mm asphalt concrete (AC), $E_{AC} = 2000$ MPa, $\eta = 0.01$ and either stiff ($E_{sub} = 222$ MPa) or soft ($E_{sub} = 80$ MPa) subgrade.

only slightly larger than SCI_{300} for the impulse load basin, while SCI_{300}^{back} is about 25% of the magnitude.

3.2 Backcalculation

In a backcalculation process the RAPTOR Deflection Indices are calculated from the deflection response obtained from the pavement model using a set of model parameters as input and the objective is to minimize the difference between measure RDI and modeled RDI. The objective function is the root mean square error

$$\psi = \sqrt{\frac{1}{N} \sum_{i=1}^N (d_i - \bar{d}_i)^2} \quad (7)$$

where \bar{d} are the measured quantities, d are modeled quantities and N is the total number of quantities. The set of model parameters that gives the minimum value of the objective function and thereby the best fit between modeled and measure RDI are considered the properties of the tested pavement. Each layer in the pavement structure has a number of model parameters such as Young's modulus, E , viscosity, η , Poisson's ratio ν , density ρ and layer thickness h . That is a total of 5 parameters for each layer and thus for multiple layers the number of parameters to backcalculate quickly increases. For backcalculation it is an advantage to limit the number of unknowns in order to ensure a more robust solution and lower the computational time. Some of the parameters have a limited influence on the pavement response. For instance, the influence of material density is small and is set to $\rho = 2400 \text{ kg/m}^3$ for the asphalt concrete and $\rho = 1800 \text{ kg/m}^3$ for the subgrade (see also Chatti et al. (2004) and Cao et al. (2019a)). Also Poisson's ratio is fixed to $\nu = 0.35$ for both types of layers.

In this paper a two layer structure is considered, however the model can represent any number of layers. The thickness of the asphalt concrete layer is assumed to be known. The remaining parameters are elastic moduli and viscosity of each layer. Damping in sub layers is considerably smaller than damping in asphalt concrete, typically an order of magnitude smaller. A sensitivity analysis of subgrade damping supports the limited influence on the deflection response. For this reason the damping in the subgrade is fixed to $\eta_{sub} = 0.001$. If a two layer structure is considered then the remaining model parameters are elastic modulus of asphalt and sublayer, E_{AC} and E_{sub} , as well as asphalt viscosity, η_{AC} .

3.3 Corresponding FWD deflections from RAPTOR measurements

All laser based continuous deflection devices measure the pavement response next to the wheel since it is not yet possible to measure directly below the load as it is done with the FWD. However, the pavement deflection decreases while moving away from the load center. The actual deflection of the pavement at the center of the load can be found using a proper pavement model. Using such model enables the entire deflection basin around the wheel to be evaluated. FWD measurements have been conducted and applied in pavement management systems all around the world for several decades. With this pavement model it is possible to simulate what an FWD would have measured based on continuous deflection measurements. In that sense, agencies can easily add corresponding FWD deflections in their system with historical FWD deflections.

The model parameters obtained through backcalculation of RAPTOR Deflection Indices are used as input to a simulation of an FWD experiment. An actual FWD load is used as the external load input to the model. The output from the simulation is the deflection time histories corresponding to what an FWD would have measured on that particular pavement. The maximum value of the time histories are used to describe the deflection in the traditional FWD distances from the load center: 0, 200, 300, 450, 600, 900, 1200, 1500, 1800 and 2100 mm. The entire procedure can be outlined in the following two steps

Step 1 Backcalculate RAPTOR Deflection Indices (RDI) to obtain pavement properties.

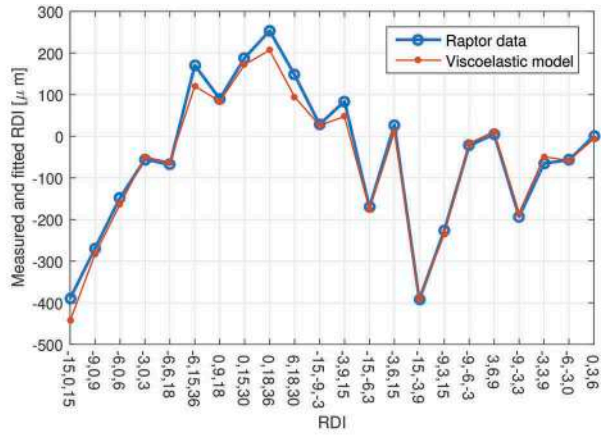
Step 2 Calculate corresponding FWD deflections using the backcalculated pavement properties as input.

4 FIELD EXPERIMENT WITH RAPTOR AND FWD

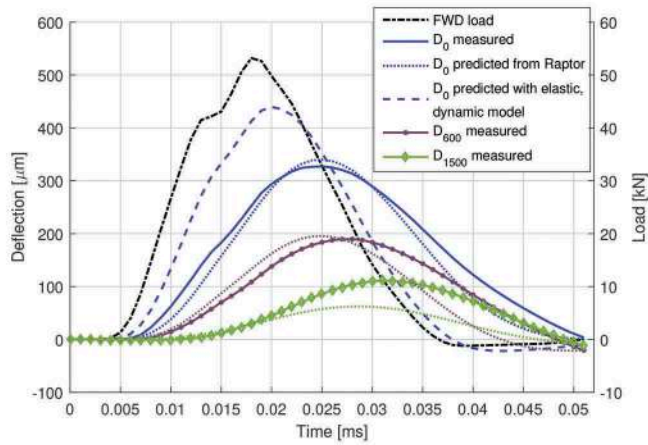
Measurements with RAPTOR and FWD were conducted consecutively on a 3.5 km pavement section in the city of Copenhagen in Denmark. RAPTOR measurements were reported as average values over 10 m distance and FWD measurements were collected with 25 m spacing except for a 200 m missing part between station 600 m and 800 m. The model was applied to calculate equivalent FWD deflections from the collected RAPTOR measurements as described by the two steps in the previous section. For this purpose a 3D Finite Element model of size 120 m in the driving direction, 60 m in the transverse direction and a depth of 20 m is used. A large domain is used to eliminate any influence from the boundary. The loading wheel is moved across the surface of the mesh at a constant speed of 50 km/h, which was around the driving speed of the RAPTOR during collection of the measurements. All six wheels of the truck and trailer are considered in the model.

The RAPTOR deflection indices are calculated using Equation (1). All 22 possible RDI were calculated and used in the backcalculation to fit the RDI measured at a specific station. Figure 5a shows an example of such best match between measured and modeled RDI. A closer look at the RDI values reveal that the viscoelastic nature of the pavement response is captured in the RDI measurements. Consider two RDI calculated using deflection sets mirrored around the load center, for instance $RDI_{[-6,-3,0]}$ and $RDI_{[0,3,6]}$. $RDI_{[-6,-3,0]}$ is calculated using the deflection measured by the wheel center together with the deflections measured 300 mm and 600 mm behind the wheel, while $RDI_{[0,3,6]}$ is calculated using measured deflections at the same distances from the loading wheel, but on the opposite side (in front of the wheel). For a symmetric deflection basin $RDI_{[-6,-3,0]} = RDI_{[0,3,6]}$ because they are calculated symmetrically on each side of the load center. In Figure 5a $RDI_{[-6,-3,0]} = -57\mu\text{m}$ and $RDI_{[0,3,6]} = 1\mu\text{m}$, which shows that the deflection basin is clearly not symmetric. A similar behavior is found in the example deflection basins in Figure 4. Looking at the moving wheel basin in for instance Figure 5 an almost straight line could be drawn between the load center and 600 mm in front of the wheel. That would give an $RDI_{[0,3,6]}$ close to zero. Contrary the basin is curved looking from the load center and 600 mm behind the load and therefore $RDI_{[-6,-3,0]} > 0$.

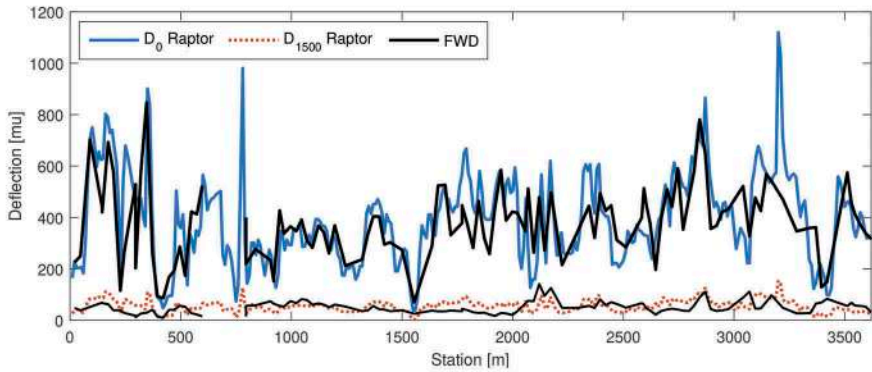
The backcalculated properties were then used as input to a simulation of an FWD experiment following step 2 in the previous section. The output is the corresponding FWD deflection time history as it would look like if the FWD had been measuring instead. The result is shown in Figure 5b as the dotted lines. On top of these the measured FWD deflection histories recorded at the same point on the road is illustrated with solid lines. The deflections D_0 , D_{600} and D_{1500} in the graph corresponds to the pavement response at the load center, 600 mm and 1500 mm from the load center. These three deflection graphs illustrate the agreement between RAPTOR predictions and FWD measurements both at the load center, in the middle and far out in the deflection basin. The measured FWD load, which was also given as input to the model, is plotted in the graph as the black solid line. The figure shows a good agreement between deflection histories predicted from the RAPTOR and those actually measured by the FWD. That means that the pavement properties backcalculated from the RAPTOR are in good agreement with the FWD. In particular it is worth noting that the time delay in deflection histories is predicted correctly as well meaning that the viscous property of the asphalt was successfully backcalculated. This is important because the viscosity of asphalt has a significant influence on the pavement response. Both in terms of the RAPTOR deflection basin becoming asymmetric, but it also has a significant influence on FWD deflection time histories. To illustrate this, the same FWD experiment was simulated using the properties backcalculated from RAPTOR except that the viscous property was set equal to zero, simplifying the model to elastic, dynamic analysis. The calculated D_0 is plotted in the same graph



(a) Modeled and measured RDI.



(b) FWD deflection time histories predicted from RAPTOR with FWD recordings on top.



(c) D_0 and D_{1500} predicted from RAPTOR with FWD measurements on top.

Figure 5. RAPTOR backcalculation and FWD prediction compared with FWD measurements.

with a dashed line for comparison. This shows the big difference in both magnitude and time delay occurring from leaving out the viscoelastic effect.

D_0 and D_{1500} predicted from RAPTOR are plotted in Figure 5c with the FWD measured D_0 and D_{1500} plotted on top. An overall good agreement is obtained between RAPTOR predicted deflections and FWD measurements. Both below the load center, but also further out in the deflection basin, which is important for getting information about subgrade structural conditions. Deviations between modeled and measured FWD can partly be explained by load variations in the RAPTOR has not been taken into account. The load is assumed constant at 50 kN as load measurements were not available for those measurements.

5 CONCLUSION

This paper presented a dynamic and viscoelastic model able to simulate the pavement response due to a moving load as well as an impulse load. The application of the model is to perform backcalculation of continuous deflection measurements and use the obtained pavement properties as input to simulate the corresponding FWD deflections. That yields a tool to obtain FWD equivalent deflections of a pavement with close spacing. The purpose of this is to generate a link between the well known FWD, which has been industry standard for measuring pavement structural response and the newer continuous deflection measurement devices. The corresponding FWD deflections can be compared with FWD deflections obtained on the same pavement with the purpose of verifying the collected continuous deflection measurements.

Previous efforts of direct comparison of measurements have showed difficulties in creating an empirical relationship between the two devices. This paper presents a couple of examples illustrating the reason for this. The examples show that the pavement response in the two different test situations is highly dependent on the properties of the tested pavement.

The model was applied to a field example where a city road in Copenhagen was measured by the continuous deflection device RAPTOR and an FWD. The RAPTOR measurements were backcalculated and the pavement properties were used to forward simulate the corresponding FWD deflections. A comparison with measured FWD deflections showed a good agreement between the two measurement devices.

ACKNOWLEDGEMENT

This work is supported by the Innovation Fund Denmark through the grant ‘AWAPAVE’. RAPTOR and FWD experiments were collected by Dynatest. The RAPTOR development team consists of: Jack Larsen, Mathias B. Andersen, Vagn Johansen, Lars K. Hansen, Soren Rasmussen, Stine S. Madsen and Albert N. Comes.

REFERENCES

- Ilja Březina, Josef Stryk, and Jiří Grošek. *Using traffic speed deflectometer to measure deflections and evaluate bearing capacity of asphalt road pavements at network level*. Iop Conference Series. Materials Science and Engineering, 2360 (1):0012102 (7pp), 2017.
- Dandan Cao, Yanqing Zhao, Wanqiu Liu, Yuhua Li, and Jian Ouyang. *Comparisons of asphalt pavement responses computed using layer properties backcalculated from dynamic and static approaches*. Road Materials and Pavement Design, 200 (5):0 1114–1130, 2019a.
- Dandan Cao, Yanqing Zhao, Wanqiu Liu, Yuhua Li, and Jian Ouyang. *Comparisons of asphalt pavement responses computed using layer properties backcalculated from dynamic and static approaches*. Road Materials and Pavement Design, 200 (5):0 1114–1130, 2019b.
- Karim Chatti, Yigong Ji, and Ronald Harichandran. *Dynamic Time Domain Backcalculation of Layer Moduli, Damping, and Thicknesses in Flexible Pavements*. Transportation Research Record: Journal of the Transportation Research Board, 18690 (1):0106–116, 2004.
- R.D. Cook, D.S. Malkus, and M.E. Plesha. *Concepts and applications of finite element analysis*. Wiley, 2002.

- Omar Elbagalati, Momen Mousa, Mostafa A. Elseifi, Kevin Gaspard, and Zhongjie Zhang. *Development of a methodology to backcalculate pavement layer moduli using the traffic speed deflectometer*. Canadian Journal of Civil Engineering, 450 (5):0377–385, 2018.
- Mostafa A. Elseifi, Ahmed M. Abdel-Khalek, Kevin Gaspard, Zhongjie Zhang, and Said Ismail. *Evaluation of Continuous Deflection Testing Using the Rolling Wheel Deflectometer in Louisiana*. Journal of Transportation Engineering, 1380 (4):0 414–422, 2012.
- M. E. Harr and Ng-A-Qui. *Noncontact Nondestructive Determination of Pavement Deflection Under Moving Loads*. Technical Report FAA-RD-77-127, Federal Aviation, 1977.
- Samer W. Katicha, Gerardo W. Flintsch, Brian Ferne, and James Bryce. *Limits of agreement method for comparing TSD and FWD measurements*. International Journal of Pavement Engineering, 150 (6):0532–541, 2014.
- Stine Skov Madsen and Eyal Levenberg. *Dynamic backcalculation with different load-time histories*. Road Materials and Pavement Design, 190 (6):01314–1333, 2018.
- James W. Maina, Hiroshi Yokota, and Kimiaki Maki. *Difference of Results Between Dynamic and Static Analyses of FWD Data*. Journal of Pavement Engineering, Jsce, 1:0 65–71, 1996.
- Shivesh Shrestha, Samer W. Katicha, Gerardo W. Flintsch, and Senthilmurugan Thyagarajan. *Application of Traffic Speed Deflectometer for Network-Level Pavement Management*. Transportation Research Record: Journal of the Transportation Research Board, 26720 (40):0 348–359, 2018.
- Zia U. A. Zihan and Mostafa Elseifi. *A Mechanistic Approach to Utilize Traffic Speed Deflectometer (TSD) Measurements into Backcalculation Analysis*. Technical Report FR 612, Louisiana State University, 052019.

Indication of viscoelastic behaviour of asphalt pavements using FWD time history data

Z. Boros & J. Komacka

STRABAG – TPA, Bratislava, Slovakia

ABSTRACT: The methodology developed for the determination of the phase angle of pavement from a FWD time history data is described. The verification of the methodology based on FWD time history resulting from the measurements on the test section representing a semi-rigid and flexible pavement demonstrated the phase angle varies along the section. A slight decrease of phase angle with increasing temperature was mostly observed. The repeated loading by traffic (fatigue) has a marginal effect on the change of the phase angle.

Keywords: FWD, time, history, pavement, deflection, phase, angle, temperature, fatigue

1 INTRODUCTION

The permanent deformation of asphalt pavement in the form of rut is an important problem from traffic safety point of view. The rapid worsening due to the increase in the intensity of heavy trucks and the prolongation of periods with high temperatures of asphalt layers has led to many research projects.

The importance of choosing suitable bituminous binder is evident from design manuals (AASHTO MP1, 2000; Asphalt Institute, 2003; Hunter, R. N. et al., 2015); or research papers (Mugume and Kakoto 2020; Karki et al., 2022). The insufficient ability of basic tests of bituminous binders (penetration, softening point) to distinguish them from the viewpoint of future rutting resistance of asphalt has led to the development of new test methods for bituminous binders that would be able to characterise the viscoelastic behaviour of bituminous binders at high temperatures (AASHTO M 320, 2017; Eurobitume 2022). The shear complex modulus test (AASHTO T 315, 2020) has found a wide application, allowing to characterize the behaviour of tested binder at different temperatures and loading frequencies. The time lag between a load force and strain of sample during the test, that is subsequently transferred to a phase angle, is considered as a parameter representing viscoelastic behaviour of bituminous binder enabling together with the complex modulus to distinguish the susceptibility of binder to a plastic deformation (Rowe 2009; Wen and Wang 2019).

As a bituminous binder is only one of asphalt components, the findings on bitumen were verified also on asphalts. The empirical tests in wheel tracking devices were supplemented by new fundamental tests, that were developed to investigate the rutting resistance of asphalts under various test conditions. Results of various tests (uniaxial or triaxial tests on cylindrical specimens or stiffness and fatigue tests on specimens of different shapes) confirm the viscoelastic behaviour of bitumen is transferred to the asphalt mixture and, similarly as for bitumen, can be identified via the phase angle between a load force and strain of sample (Maggiore et al. 2014; Guo et al. 2021). The results of complex modulus tests (Xu and Solaimanian 2009) conducted on 20 different asphalt concrete mixtures performed at 4 test temperatures (4.0 - 40.0 °C) by applying the

compressive uniaxial sinusoidal loads at 6 frequencies (0.1 - 25 Hz) for each temperature proved the phase angle increases with increasing temperature or decreasing frequency. The same findings emerged from the study (Ali et al. 2016) focused on the dynamic response of various asphalt concrete mixtures (four wearing and four base course). Specimens were subjected to uniaxial sinusoidal loading. The tests were conducted at temperatures of 4.4 - 54.4 °C and frequencies of 0.1 - 25 Hz. A slight contradiction with the relatively clear conclusions regarding the effect of temperature on the phase angle values can be found in (Clyne et al. 2003). It was found out the phase angle increases with the increase of test temperature from -20 °C to 20 °C, but for 40 °C and 54 °C the phase angle decreases with the increase of the test temperature. This could be an indication of aggregate interlock effects.

Individual asphalt mixtures are tested separately in all laboratory tests enabling assessment their viscoelastic behaviour. Generally, asphalt mixtures used in asphalt layers of pavement (wearing, binder and base) have different viscoelastic behaviour (Ramirez Cardona et al. 2015). However, in pavement, all asphalt layers work together. In addition, they are supported by underlying layers and subgrade. Moreover, the load generated by wheel(s) of passing vehicles produces a stress state that differs from that used in laboratory tests.

Considering this, the question is what behaviour of whole asphalt pavement is and what is an effect of viscoelastic behaviour of asphalt layers. To investigate (verify) this, a load test of a pavement is necessary and a load force with a pavement response must be recorded in the same time scale for the determination of the phase angle of a pavement. Measurements performed by Falling Weight Deflectometers (FWD) are one of possibilities of pavement load test. Moreover, FWD output data (time history) contains the values of load force and pavement deflection in time intervals. Therefore, the presented study was performed with following objectives:

- to analyse whether time history of FWD provides sufficient data for the determination of phase angle of pavement and, if so, to propose an appropriate methodology to determine the necessary inputs;
- based on FWD measurements performed on an experimental test site to investigate the variability of phase angle and an effect of temperature of asphalt layers and repeated loading (fatigue).

As the duration of FWD loading impulse varies depending on the FWD manufacturer (European Commission 2005), the next objective of the study related to investigation of this effect on the phase angle values.

2 METHODOLOGY

A FWD time history consists of a load force and deflections values in the time scale (Figure 1). They increase from initial values to maximum and decrease to final values. Basically, the time history is an overview of trend of FWD load force and the response of a pavement.

The time lag between the peak of FWD load force and the peaks of deflections can be seen in Figure 1 (the area “B”). The time lag between the FWD load force and the deflections can also be identified at the beginning of the time history (the area “A”). Existing time lag of a FWD load force and pavement deflections can be considered as an analogy of the lag of relative deformation (strain) of sample behind the applied force (stress) in laboratory mechanical tests based upon stress-strain relationship (Figure 2). This lag is the base for the determination of phase angle (φ) which is used as an indicator of viscous (or elastic) properties of the evaluated material. According to (Biligiri et al. 2010), the phase angle is simply the angle at which strain (ϵ_0) lags stress (σ_0) and this is mathematically expressed as

$$\varphi = \frac{t_i}{t_p} * 360, \quad (1)$$

where t_i is time lag between a cycle of stress and strain (s) and t_p is time for a stress cycle (s). The formula (1) is valid for the tests with the load cycle corresponding to the sinusoidal waveform. However, the trend of load force in the FWD test has the haversine waveform (approximately) and the load is applied in the half-cycle time interval. Therefore, the total range of wavelength is between 0 and 180° and the multiplication by 180 must be used instead of 360 to calculate the phase angle.

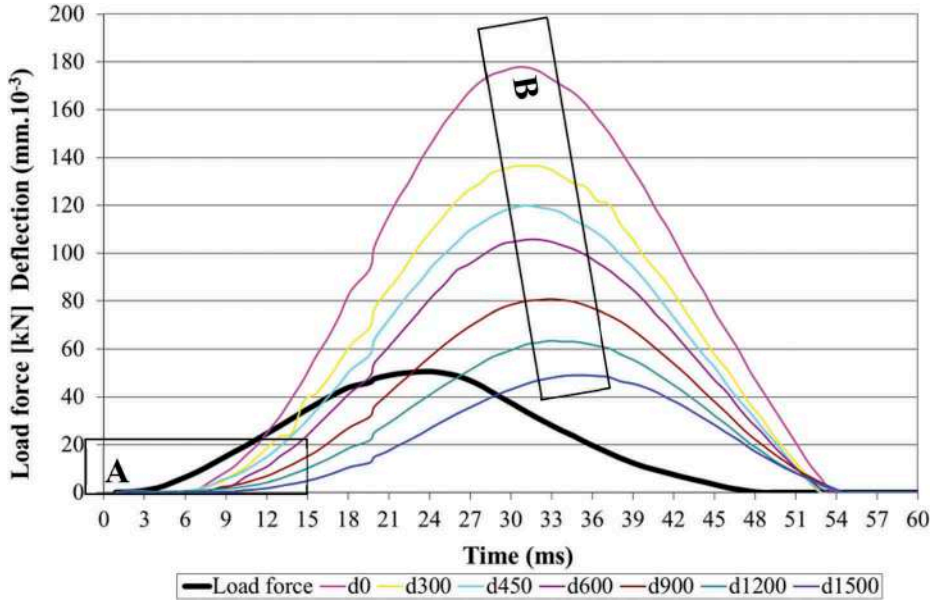


Figure 1. Example of FWD time history.

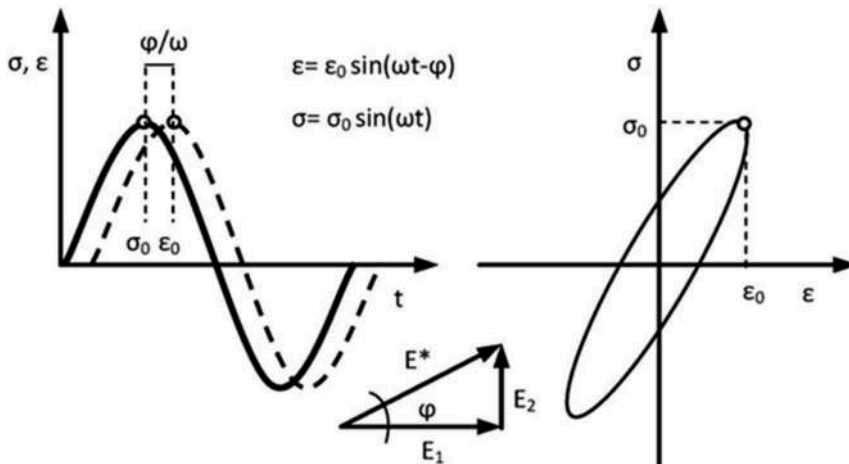


Figure 2. Stress and strain during cyclic dynamic tests of viscoelastic materials.

To determine the phase angle of pavement, the time lag of a cycle of stress and strain (t_i) resulting from laboratory tests can be replaced by time lag of a load force and deflection from FWD tests. However, only the lag of the FWD load force and the deflection at the centreline of the load area (d_0) is relevant for this purpose and time history at other sensors, spaced out of load plate, must be excluded. As for time for a stress cycle (t_p), the duration of the FWD load pulse may be used for calculations.

The determination of time lag of the load force and the deflection at the centreline of the load area (d_0) and the duration of the FWD load pulse relates to an accuracy problem of FWD time history. As it was presented in (Komačka 2017), there is a slow change of load force and deflection values in the beginning of the time history with the same values in consecutive time intervals. The similar situation occurs in area of maximum values. Usually, the same maximum values repeat several times, but the change in the load force and deflection values is easier to identify.

To solve the problem with the repeated values of load force and the deflection d_0 in the beginning of time history and in the range of maximum values, the following procedure was proposed and used. The upward and downward trend of FWD load force and deflection d_0 (blue dots in Figure 3) was replaced by a line passing through the linear part of the rising and falling part of the FWD load force and deflection d_0 trend (red lines in Figure 3). The start and end time (t_s , t_e) of the adjusted trend was determined as the value at which the line intersects the horizontal (time) axis.

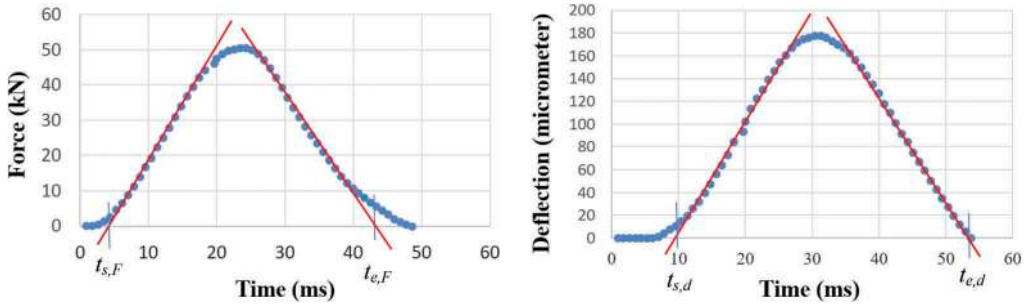


Figure 3. Determination of start and end time of the adjusted trend of FWD load force and the deflection d_0 .

Subsequently, based on the adjusted start time of deflection trend ($t_{s,d}$) and FWD load force trend ($t_{s,F}$), the time lag of these two variables was calculated as

$$t_{i,s} = t_{s,d} - t_{s,F} \quad (2)$$

The adjusted FWD loading time was calculated from the start and end time of FWD load force as

$$t_{p,FWD} = t_{s,F} - t_{e,F} \quad (3)$$

The time lag of the FWD load force and the deflection d_0 was also determined using the range of their maximum values. The problem of repeating values at successive time intervals was solved based on the assumption that the middle of the time range of maximum values is the exact time at which the maximum value is reached. It was calculated as:

$$t_{m,F(d)} = (t_1 + t_2)/2 \quad (4)$$

where t_1 is time of the first maximum value of FWD load force or deflection (s) and t_2 is time of last maximum value of load force or deflection (s).

Thereafter, the time lag of the maximum of FWD load force and the deflection d_0 was calculated as

$$t_{i,m} = t_{m,d} - t_{m,F} \quad (5)$$

Comparing the time lags of the load force and deflection d_0 calculated from start time of its trends ($t_{i,s}$) and the range of their maximum values ($t_{i,m}$) it was found, they are significantly different. Considering the problematic trend of FWD load force and deflection d_0 at the beginning of the time history and the used adjustment of trends, it was decided to use the time lag calculated from the range of maximum values ($t_{i,m}$) for the determination of the phase angle of pavement. This was calculated using the modified formula (1) as

$$\varphi = \frac{t_{i,m}}{t_{p,FWD}} * 180 \quad (6)$$

3 EXPERIMENTAL

The proposed methodology for determination of the phase angle of asphalt pavement was verified on the test section consisting of two types of pavement. To investigate the effect of temperature and traffic, measurements were performed in two paths within the width of the traffic lane at different times of the day.

3.1 Test section and conditions

The measurements were performed on a 300 m long section of speedway. According to the traffic census, the intensity of heavy vehicles is more than 5500 per 24 h. The thickness of pavement and its layers is the same. The only difference is in the material of subbase layer. At the beginning and end of the section, there is a hydraulically bound subbase layer (semi-rigid pavement). Between them (approx. at chainage of 110 - 205 m) there is an unbound subbase layer (flexible pavement).

Measurements with two deflectometers (FWD Dynatest and FWD Kuab) with the different loading pulse duration (approx. 20 ms and 45 ms respectively) were performed to monitor short-term loading. The difference in the loading pulse duration could mean the load frequency is different. Considering the observed change in a phase angle due to test frequency in laboratory test (e.g., Clyne, T. et al. 2003, Guo, L. et al., 2021), a possible difference in phase angle resulting from the measurements made by FWD with different loading time (frequency) was investigated.

As the section has been in operation for a long time, measurements were made in the right wheel track of passing vehicles and between wheel tracks to investigate the effect of long-term loading (fatigue). The measurements by FWDs were not performed at the exact same testing points. There was a slight difference in the longitudinal and transversal direction.

Measurements were performed three times a day at the different temperature of asphalt pavement surface (measured by infrared sensor of FWD). The distance of the deflectometers during the measurement was minimal to ensure the same temperature.

Table 1. Time intervals of measurements and temperature of pavement surface.

Position	right wheel			between tracks		
	time	7.00-8.00	10.00-11.00	13.00-14.00	8.00 - 8.30	11.00-11.30
temperature	20 - 22 °C	28 - 31 °C	34 - 40 °C	23 - 27 °C	30 - 33 °C	37 - 42 °C

3.2 Results and discussion

The phase angles of pavement determined from the time lag of the FWD loading force and the deflection in the centre of load (d_0) according to the methodology given in the previous chapter are shown in Figure 4. The difference among the phase angles determined from the measurements of both deflectometers is evident. The lower values of the phase angles were determined from the measurements of the FWD Dynatest, which has a shorter duration of the

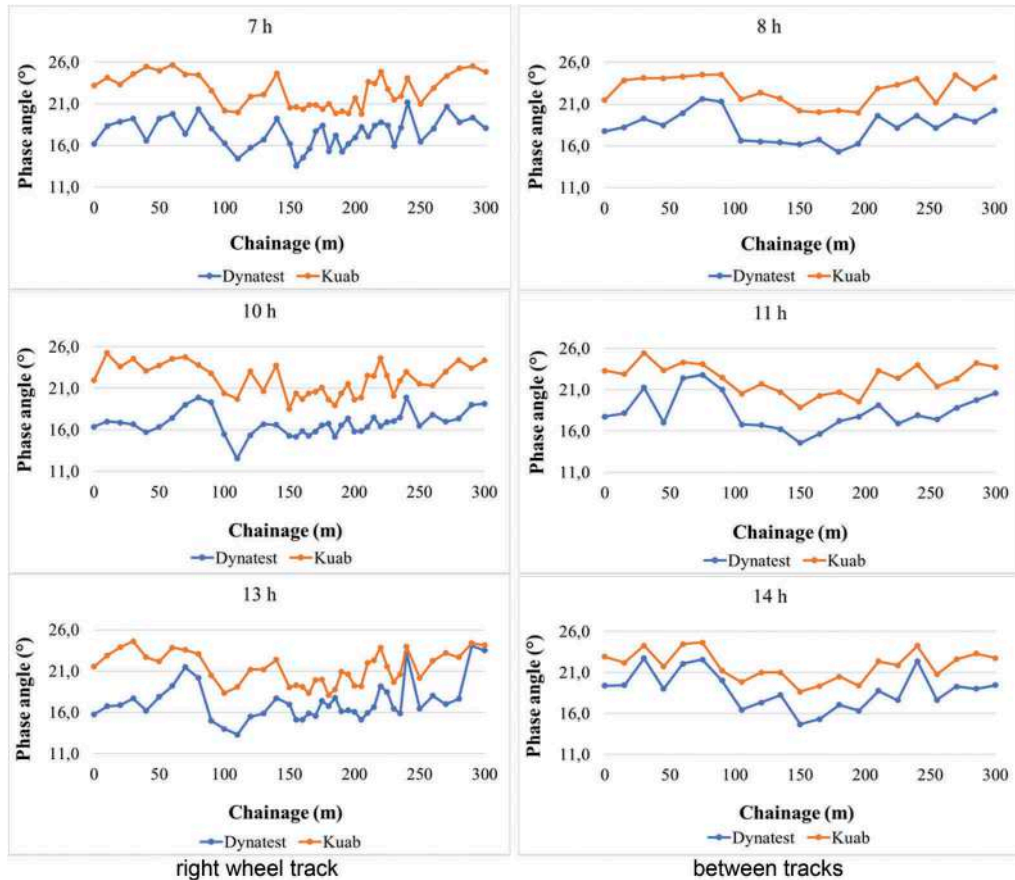


Figure 4. Phase angles determined from the time histories of FWD Dynatest and FWD Kuab.

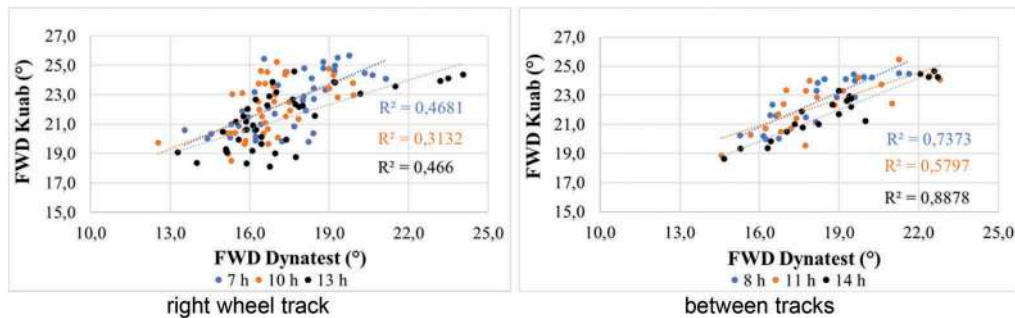


Figure 5. Correlation of phase angles determined from time histories of FWD Dynatest and FWD Kuab.

load impulse. The trend of the phase angle values along the length of the section is approximately the same, but the correlation was only partially confirmed. The coefficients of determination in Figure 5 have a wide range, but, in general, they confirm the existence of a relationship of phase angles. It is also necessary to keep in mind the previously mentioned non-identical position of the load plate at a given station.

The difference in the type of the lower base layer can be identified from the values of the phase angles along the section. The phase angles of flexible pavement are lower, which is more visible in the phase angles resulting from the measurements between the wheel tracks.

As for the effect of temperature on the change in the value of phase angles, the situation is not entirely clear. As it is evident from Table 1, the surface temperature of asphalt pavement increased during the measurements. However, when the increase in the pavement surface temperature (calculated relative to the temperature at 7 h (in the right wheel track) or at 8 h (between wheel tracks)) is plotted against the change in phase angle (Figure 6), no clear trend is observed. The changes in the phase angle in the right wheel track (blue colour) and between wheel tracks (red colour) due to the raised temperature have positive but also negative value. The changes are mostly in the range from $+2^\circ$ to -3° regardless the difference in the increase of the pavement surface temperature. Perhaps, a slight trend can be observed for the phase angles determined from the Kuab measurements. With a more significant increase in surface temperature (12-18 °C), the change in phase angle is mostly negative, i.e., as the temperature of the asphalt pavement surface increases, the phase angle decreases.

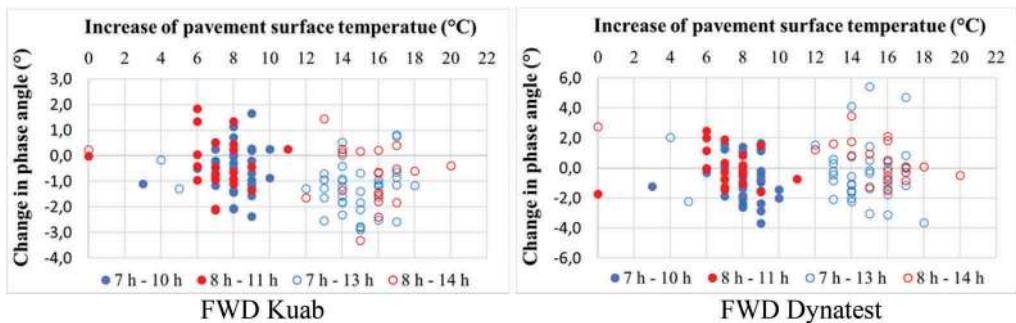


Figure 6. Change in phase angle due to pavement surface temperature changes.

The effect of long-term traffic intensity (fatigue) on the change in phase angle was assessed using the values in the right wheel track of passing vehicles and between wheel tracks (Figure 7). The measurements in the right wheel track and between tracks were time-shifted by about 1 h. This led to the different pavement surface temperature (Table 1). As the effect of temperature on the change in the phase angle was identified as negligible over the test temperatures range, no corrections were made before the comparison.

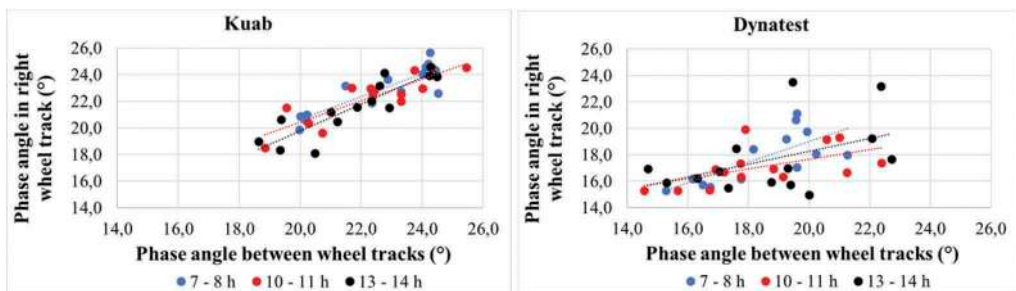


Figure 7. Relation of the phase angles in the right wheel track of passing vehicles and between wheel tracks.

The differences in the phase angles determined from FWD Kuab measurements performed in two positions within the width of a lane are not very large. When the values of individual pairs are compared it is mostly less than 2°. Using the regression line (the blue, red, and black dotted lines in Figure 7), no or very small difference in the phase angles in the right wheel track and between tracks can be stated.

A lower consistency among the phase angles can be observed for the values derived from the FWD Dynatest measurements (especially for the measurements performed between 10 - 11 h and 13 - 14 h). Some differences reach 4 - 5 °. However, the regression lines show the negligible difference (max 1°) for the phase angles determined for the period 7 - 8 h. For the other two periods and the phase angle up to 18°, no significant difference can also be stated.

4 CONCLUSIONS

The following conclusions can be drawn from the analysis and evaluation of time histories of Falling Weight Deflectometers (Kuab and Dynatest) focusing on the indication of viscoelastic behaviour of asphalt pavements:

- a time history of FWD provides sufficient data to determine the inputs (time lag of FWD load force and the deflection in the centreline of FWD load plate and FWD loading time) that are needed to determine the phase angle characterizing the viscoelastic behaviour of pavement;
- a phase angle varies along the section, the differences reach several degrees;
- the value of phase angle is related to the duration of the FWD load impulse; a lower phase angle is determined for a shorter load impulse;
- the changes in the phase angle due to the increase in the pavement surface temperature (approx. from 20 °C to 40 °C) were mostly in the range from +2° to -3°;
- no clear trend in the phase angle change is evident for the phase angles derived from the FWD Dynatest time history;
- over the tested range of pavement surface temperatures, a slight decrease in phase angle (up to 3°) could be supposed for the phase angles derived from the FWD Kuab time history when the increase in the pavement surface temperature is approximately 12 °C to 18 °C;
- the values of the phase angle in the track of the right wheel of passing vehicles and between wheel tracks are very similar; considering the intensity of heavy vehicles passing the tested section and the number of years of operation, it can be stated, the repeated loading (fatigue) generated by long-term traffic intensity has marginal effect on the change in the phase angle.

REFERENCES

- AASHTO M 320, 2017. *Standard Specification for Performance-Graded Asphalt Binder*. Washington, DC: American Association of State Highways and Transportation Officials.
- AASHTO MP1, 2000. *Standard specification for performance graded asphalt binder*. Washington, DC: American Association of State Highways and Transportation Officials.
- AASHTO T 313, 2019. *Standard Method of Test for Determining the Flexural Creep Stiffness of Asphalt Binder Using the Bending Beam Rheometer (BBR)*. Washington, DC: American Association of State Highways and Transportation Officials.
- AASHTO T 314, 2012. *Standard Method of Test for Determining the Fracture Properties of Asphalt Binder in Direct Tension (DT)*. Washington, DC: American Association of State Highways and Transportation Officials.
- AASHTO T 315, 2020. *Standard Method of Test for Determining the Rheological Properties of Asphalt Binder Using a Dynamic Shear Rheometer (DSR)*. Washington, DC: American Association of State Highways and Transportation Officials.

- Ali, Y. et al., 2016. *Investigation of factors affecting dynamic modulus and phase angle of various asphalt concrete mixtures*. Materials and Structures, Vol. 49 (2016), pp. 857–868. doi.org/10.1617/s11527-015-0544-3.
- Asphalt Institute, 2003. Superpave performance graded asphalt binder specification and testing: Superpave series No.1 (Third Revision). Asphalt Institute.
- Biligiri, K. P., Kaloush, K., Uzan, J. (2010). *Evaluation of asphalt mixtures' viscoelastic properties using phase angle relationships*. International Journal of Pavement Engineering, 11(2),143–152. doi:10.1080/10298430903033354
- Clyne, T. et al., 2003. *Dynamic and resilient modulus of MN/DOT asphalt mixtures*. Final report MN/RC – 2003-09.
- El Atrash, K., Assaf, G., 2019. Evaluating factors influencing asphalt road construction quality in high temperature condition (case study). Journal of Civil Engineering, Science and Technology 10(1):75–81, doi: 10.33736/jcest.1203.2019.
- Eurobitume, 2022. Testing. <https://www.eurobitume.eu/technical/testing/> (visited on 14/02/2022).
- European Commission, Directorate General Transport, 2005. *COST 336 Use of Falling Weight Deflectometers in Pavement Evaluation*. Final Report of the Action, Main Report, 2nd Edition.
- Guo, L. et al., 2021. *Comparative Study on Complex Modulus and Dynamic Modulus of High-Modulus Asphalt Mixture*. Coatings 11(12):1502, doi: 10.3390/coatings11121502
- Hunter, R. N. et al., 2015. The Shell Bitumen Handbook (Sixth edition).
- Karki, P. et al., 2022. *Performance-graded asphalt binder selection catalog for asphalt overlays*. Construction and Building Materials, vol. 319, doi.org/10.1016/j.conbuildmat.2021.126012.
- Komačka, J., 2017. *An accuracy problem of the FWD time history with regard to the application of the SASW method*. Civil and Environmental Engineering, vol. 13, issue: 2, pp. 120–124, doi: 10.1515/cee-2017-0016.
- Maggiore, C. et al., 2014. A dissipated energy comparison to evaluate fatigue resistance using 2-point bending. Journal of Traffic and Transportation Engineering, 1(1),49–54. doi:10.1016/s2095-7564(15)30088-x.
- Mugume, R., Kakoto, D., 2020. *Effect of Inappropriate Binder Grade Selection on Initiation of Asphalt Pavement Cracking*. Sustainability 2020, 12(15), 6099, doi.org/10.3390/su12156099.
- Ramirez Cardona, D. A. et al., 2015. Viscoelastic Behaviour Characterization of a Gap-graded Asphalt Mixture with SBS Polymer Modified Bitumen. Materials Research, 18(2),373–381. doi:10.1590/1516-1439.332214
- Rowe, G., 2009. Phase angle determination and interrelationships within bituminous materials. Advanced Testing and Characterization of Bituminous Materials. Taylor & Francis Group, London, 2009, ISBN 978-0-415-55854-9.
- Wen, Y., Wang, Y., (2019). High-Temperature Rheological Properties of Asphalt Binders with Polymeric, Warm-Mix, and Rubber Particulate Additives. Journal of Materials in Civil Engineering, 31(3), 04018404. doi:10.1061/(asce)mt.1943-5533.0002589
- Xu, Q. and Solaimanian, M., 2009. *Modelling linear viscoelastic properties of asphalt concrete by the Huet_Sayegh model*. International Journal of Pavement Engineering, vol. 10, No. 6 (2009), pp. 401–422.



Taylor & Francis

Taylor & Francis Group

<http://taylorandfrancis.com>

Reinforcement of structural layers



Taylor & Francis

Taylor & Francis Group

<http://taylorandfrancis.com>

Ultra-thin whitetopping for asphalt pavement rehabilitation: The influence of the interlayer in the properties of the double-layered system

M. Pasetto, A. Baliello, G. Giacomello & E. Pasquini

Department of Civil, Environmental and Architectural Engineering, University of Padova, Padova, Italy

ABSTRACT: The use of concrete overlays in asphalt pavements could be an effective and economical alternative to the common rehabilitation solutions. The Ultra-Thin Whitetopping (UTW) technique consists in the casting of a thin concrete slab (from 50 to 100 mm) over damaged wearing courses in order to limit the high level of distresses typical of the Asphalt Concrete (AC) pavements. Otherwise, the efficiency of such system is strictly related to the interlayer bonding developed between the existing bituminous surface and the concrete overlay: in fact, the degree of adhesion between materials of different nature could be not sufficient to guarantee the structural continuity of the layers, thus it can cause differential expansions and contractions due to vehicular and thermal loads, as well as excessive stress-strain state within the structure. The present paper illustrates a laboratory study aimed at evaluating the experimental performance of double-layered systems prepared with the same UTW and asphalt concrete but with different interlayers. In particular, direct bond tests were executed to identify the shear performance of four different interfaces (plain, with bituminous tack coat emulsion, with bituminous tack coat emulsion and gravel, brushed AC). The same systems were also tested to determine the stiffness characteristics through 3-point bending tests. Mainly, the characteristics of the selected interface deeply influenced the structural behavior and the failure mechanism of the UTW-AC systems. With respect to the other alternatives, plain asphalt concrete used as laying surface for UTW gave the best results in terms of shear resistance and stiffness.

Keywords: Ultra-thin whitetopping, interlayer bond, shear strength, flexural stiffness

1 INTRODUCTION AND OBJECTIVE

Road rehabilitation practices are gaining popularity because of the progressive reduction of new constructions and the general financial straits that promote wise maintenance strategies. In recent years, whitetopping has been diffused as maintenance strategy for distressed asphalt pavements. Such intervention consists in the casting of a Portland Cement Concrete (PCC) layer over existing Asphalt Concrete (AC) wearing courses. By using standard thickened slabs over old pavements, conventional whitetopping is intended as a reinforcement designed and constructed following the typical criteria for concrete materials. In the case of Ultra-Thin Whitetopping (UTW), reduced thicknesses (from 50 to 100 mm) are used to produce overlays that result in small square-shaped slabs with substantially-near joints (Balbo and Rodolfo 1998). In the US, first successful UTWs dated back the early 1990s; then, several studies and installations pushed towards its prompt diffusion worldwide (Gucunski, 1998). This happened

mainly thanks to the involved benefits principally related to the long durability and the substantial cheapness (Abhijith and Mahendra 2018).

However, despite the development of the early researches, actual scientific community is still investigating to strictly determine the role of the many variables affecting the efficacy of UTW systems. In particular, it must be considered that the thin UTW elements have to face vehicular and thermal loads over reduced areas, even in high-stressed pavements. This implies the need of specific design concerning the selected materials and their mechanical performance, but also regarding all the secondary aspects, e.g., the joints, the interaction with the near asphalt portions and the interlayer bonding with the existing AC.

In this regard, it is quite recognized that PCC-AC boundary represents a critical zone because of a possible poor shear strength, at least with respect to traditional AC-AC interface. Indeed, the hypothetical reduction of the interlayer bonding must be also advised when considering the presence of distresses responsible of possible slippage failures (Pasetto et al. 2019). Thus, the paper presents a laboratory study aimed at evaluating the role of the PCC-AC interface in the case of UTW overlay applied above asphalt pavements. In particular, interlayer bond properties of four different interfaces were tested in order to understand how their working mechanisms and failures can affect the global performance of the UTW pavement.

2 MATERIALS AND METHODS

UTW overlays were reproduced in the laboratory by manufacturing different double-layered structures. Four systems were obtained using the same mixtures (for upper and lower layers) but varying the interfaces. The lower layers, prepared with a dense-graded AC20 complying with the Italian technical prescriptions, intended to simulate a typical road binder course (UTW application was simulated over a milled road surface, in which the wearing course was removed). UTW overlays were made by a Portland cement concrete (cement type: II/B-LL 42.5 R), whose design followed a literature example for such mixes (Jayakesh and Suresha 2018). Properties of mixes are detailed in the Tables 1 and 2.

The four studied interfaces were prepared in such conditions: i) plain (code P); ii) with bituminous tack coat emulsion (C60B2) dosed at 0.3 kg/m² of residual binder (code E); iii) with the same bituminous emulsion and a 4/8 mm gravel (code EG); iv) with brushed surface of the lower asphalt layer (coded B). In particular, the latter case (B) implied a mechanical abrasion to simulate a partially-raveled/damaged existing AC. For each system, cylindrical 150 mm-diameter samples were created firstly compacting at 160 °C a 70 mm AC layer through the shear gyratory compactor (SGC) at fixed target voids of 5.0%. Once cooled, AC surfaces were treated with the selected interface and then, if needed, they were left at rest for proper emulsion breaking (E and EG cases). Finally, samples were placed in ad-hoc formworks and a 70-mm thick layer of PCC was casted and vibrated. Moreover, prismatic samples were obtained compacting 50 mm-high slabs of AC for the first layer (EN 12697-33). Then, slabs were cut in samples (100 mm x 400 mm plan dimensions) to be treated with the selected interface. Finally, prismatic formworks were used to cast the PCC above the AC specimen (50-mm thick UTW layer). Figure 1 summarizes the produced specimens.

The first characterization part was aimed at analyzing the interface properties whereas the second one concerned the study of the mechanical properties (namely, the stiffness) of the double-layered systems. Shear Bond Tests – SBT (prEN 12697-48) were carried out using the cylindrical specimens to determine the interlayer shear strengths τ_{max} . Three sample replicates for each configuration were tested at 28 days curing and 25 °C test temperature, applying the nominal deformation speed of 0.85 mm/s to the moving layer. Even the lack of a normal load during test, SBT was considered suitable to identify the maximum shear strength at failure that represents the interface performance (Romanoschi, 1999) (minimum τ_{max} is commonly prescribed by technical specifications for interlayer performance of road pavements). Prismatic specimens were used to perform 3-Point Bending (3PB) tests at 25 °C. Sample beams (100 mm-wide, 100 mm-high and 400 mm-long) were subjected to a central constant load rate of 50 N/s in bending configuration (supports located at 40 mm from the external edges). The

load progression and the corresponding central displacement were recorded to construct the load-displacement curves (three replicates for each configuration). Flexural stiffness modulus E_f was calculated using the first linear part of the obtained curves.

Table 1. Characteristics of the AC20 mix used for lower binder courses.

Grading of limestone aggregate								
Size [mm]	20	12.5	8	4	2	1	0.25	0.063
Passing [%]	100	97.1	77.7	48.5	31.9	21.6	11.8	7.1
Bitumen properties								
Non- modified (Pen: 50/70 – Soft. point: 59 °C) dosed at 6.00% by agg. weight								
Mixture properties								
Target voids: 5.0%			MQ: 4.79 kN/mm			ITS: 0.70 MPa		

Table 2. Characteristics of PCC mix used for UTW overlays.

Component dosages [kg/m ³]							
Cement	CA*	FA**	Water	Water/Cement	S***	Air	
400	1127	721	152	0.38	2.10	2%	
Mixture properties							
R _{ck} (14 days): 38.67 MPa				R _{ck} (28 days): 43.11 MPa			
* CA: coarse limestone		** FA: fine limestone		***S: superplasticizer			

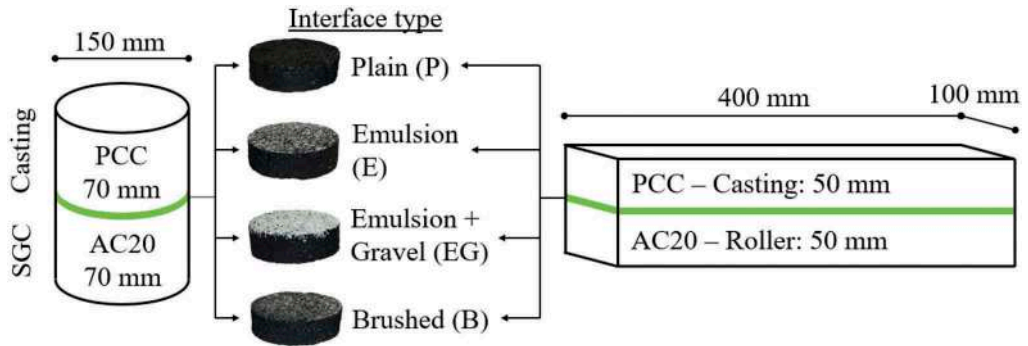


Figure 1. Scheme of double-layered specimens produced in the laboratory.

3 RESULTS AND DISCUSSION

3.1 Interface shear performance

The evolution of the interlayer shear stress τ with the deformation s is depicted in Figure 2a (curves are intended as the average of three test replicates for each system type). Distinct interlayer shear strength τ_{max} were identified: P interlayer (AC without treatment) owned the greater resistance (it exhibited the higher mean τ_{max} equal to 0.955 MPa). P and B values were also in line with literature strengths assumed by common bituminous interfaces between AC layers and tested in similar conditions (Ferrotti et al. 2016). On the contrary, the presence of tack coat emulsion (E or EG) seemed to negatively affect the interface bonding: this is probably due to its bituminous nature, not fully compatible with the PCC constituting the UTW. In the interface with gravel (EG), τ_{max} was highly compromised with respect to the plain case.

Actually, shear strengths given by E and EG resulted also inconsistent with the main technical prescriptions for interfaces of upper pavement layers (requirement limits at least of 0.6-0.7 MPa). The shape of the curves indicated a fast decrease of the shear stress after the failure for P and B interfaces; E and EG showed less steep post-peak trends reasonably because of the viscous effects given by the bituminous emulsion.

The same indications can be collected analyzing Figure 2b, where the maximum deformations d_{max} (at peak) and the shear stiffness moduli k (τ_{max}/d_{max} ratios) are depicted. B samples showed parameters of 80-85% with respect to those of P specimens: such a general trend also accorded with other findings presented in similar literature (Lopez-Carreno et al. 2017). Therefore, the brushing of the surface did not seem strictly suggested to improve the characteristics of the interfaces.

Final considerations about the selected cases were done proposing also a preliminary pavement calculation in order to determine the effective stress field of a representative whitetopping system: considering the thin layer of the concrete overlay (50 mm), experimental interlayer strengths were compared with the shear stresses due to a standard vehicular load at the interested depth. Using the linear elastic theory, the pavement was modelled at 25 °C assuming the following structure (from the top surface): i) a concrete overlay ($E = 20000$ MPa, $\nu = 0.15$); ii) an asphalt layer ($E = 3000$ MPa, $\nu = 0.35$); iii) a granular base ($E = 300$ MPa, $\nu = 0.30$). The subgrade was assumed as a soft soil owing $E = 30$ MPa and $\nu = 0.30$; all interfaces were presumed fully bonded. Shear (τ_{xz}) and vertical (σ_{zz}) stresses within the pavement were computed at different longitudinal positions (x) and depths (z) by considering a single tire loading a circular area ($D = 126$ mm) and imposing a vertical load of 30 kN. A surface friction coefficient f equal to 0.8 was assumed to determine the tangential load applied by the moving wheel: this led to consider a horizontal force of 24 kN applied at the $x = 0$ coordinate.

The schematic view of the pavement is shown in Figure 3. Results of the comparison are depicted in Figure 4. Here, the stress state of the pavement at 50 mm of depth (UTW-AC interface) and at distances x_i from the loading centerline (see the black line) is represented in the Mohr's plane together with the interface shear strengths experimentally found (see the points along the y-axis). Namely, the failure of the interface should be hypothesized when its bond strength is not sufficient to resist the shear stresses transmitted by the vehicles.

Based on the represented trends, it is evident that, whatever the rate of increase of τ_{max} as a function of σ_{zz} (dashed lines), the identified τ_{max} seemed always able to avoid the possible delamination of the upper layer eventually caused by the traffic tangential forces. Really, considering all the simplifying assumptions of the model (fully bonded elastic layers, single wheel, constant temperature, etc.), E and EG interfaces, which resulted quite close to the failure domain, should be probably attentioned to bypass possible structural and functional issues.

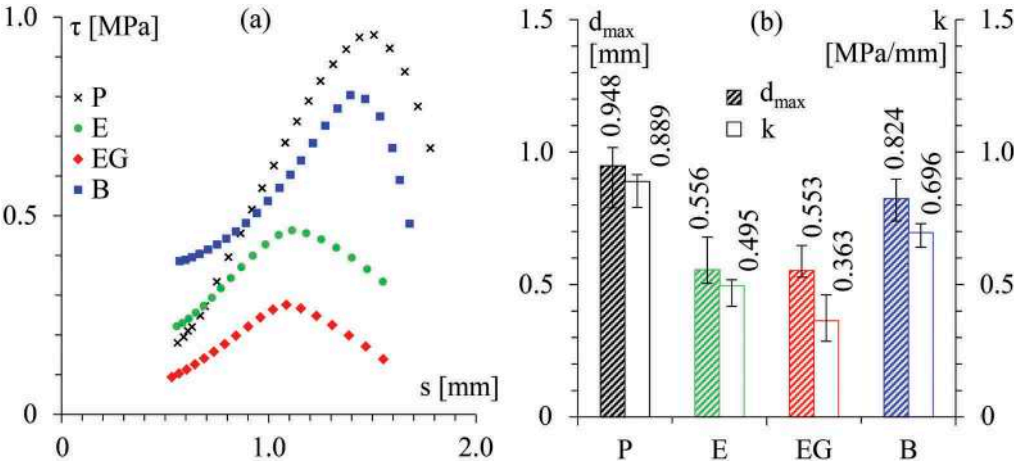


Figure 2. SBT results: τ vs. s (a) and d_{max} , k (b) for the selected interfaces.

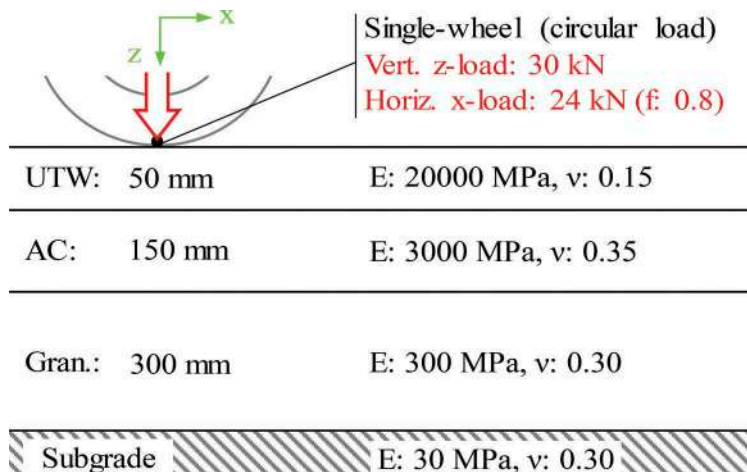


Figure 3. Scheme of the pavement model assumed in the study.

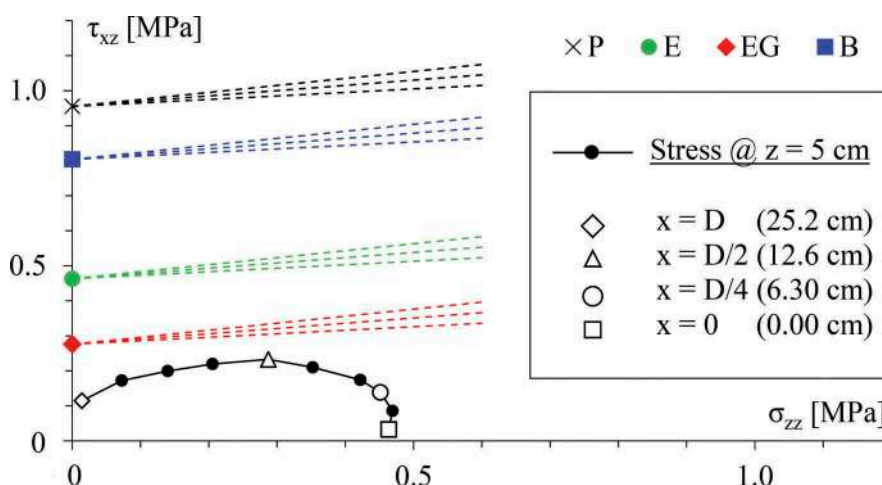


Figure 4. Results of modeling expressed in terms of shear stresses vs. failure domain.

3.2 Mechanical properties of UTW-AC double-layered systems

Mechanical properties of systems deduced by 3PB tests were firstly assessed plotting the load-displacement curves (P vs. d). According to literature (Canestrari et al. 2012), the typical shape obtained is indicative of the failure mechanism suffered by specimen. After a quasi-linear first part, the peak load P_{max} is reached: here, the first failure point is generally assumed since the first crack occurs. The trend after d_{max} (i.e., the displacement corresponding to P_{max}) is used to first characterize the interface behavior, then that of the global system. Based on such theoretical approach, two distinct areas under the curve can be identified; these ones are referred to: i) the initial ability to absorb energy up to the first crack (“ D ” area); ii) the same concern related to the total curve up to the final breaking point (“ T ” area). The described approach is schematized in Figure 5a. The load-displacement experimental results are presented in Figure 5b whereas some comparison between P_{max} , D and T values are depicted in Figure 6.

Principal findings indicated different load peaks for each system, with greater P_{max} for P and B cases: D energy resulted hierarchically in accordance with P_{max} values, with comparable results for P and B, as well as with sensibly lower amounts for E and EG (only 60-70% of the reference

P system). After the quasi-linear parts, distinct responses were found. Progressively considering P, B, EG and E, more and more rapid decreases were visible: this gave an index of the system ductility after P_{max} due to the interface working mechanism. Namely, P and B systems presented a very gradual load decrease that suggested a good ability to retain a residual flexural resistance; on the contrary, emulsion-based samples (above all E) exhibited a more pronounced post-crack fragility. These results also affected the global system strength, and this was demonstrated by the final value of the T energy (E and EG had about halved T with respect to P or B).

Considering the wide utilized toughness index I_{tot} (i.e., the T/D ratio between the area under the curve up to the final deflection and that up to first crack), the abovementioned considerations are confirmed (I_{tot} equal to 4.02, 2.76, 3.05 and 5.59 for P, EG, E and B, respectively). Really, the distinct responses of emulsion-based samples were assessed in deep; effectively, a visible debonding of the bituminous interfaces was observed after the load peak during the test. Therefore, the reduced performance of such systems was ascribed to a disrupted failure mechanism verified on the samples because of the lower bond strength (see SBT results). In this sense, Figure 7 represents the two failure mechanisms encountered during the tests (Type A for P and B systems, Type B for E and EG ones).

Finally, mean stiffness moduli E_f were also calculated based on the presented data (see Table 3). Effectively, E_f results seem to indicate the same hierarchic response of the systems deduced by the previous analysis. However, it was understood that the simple analysis of

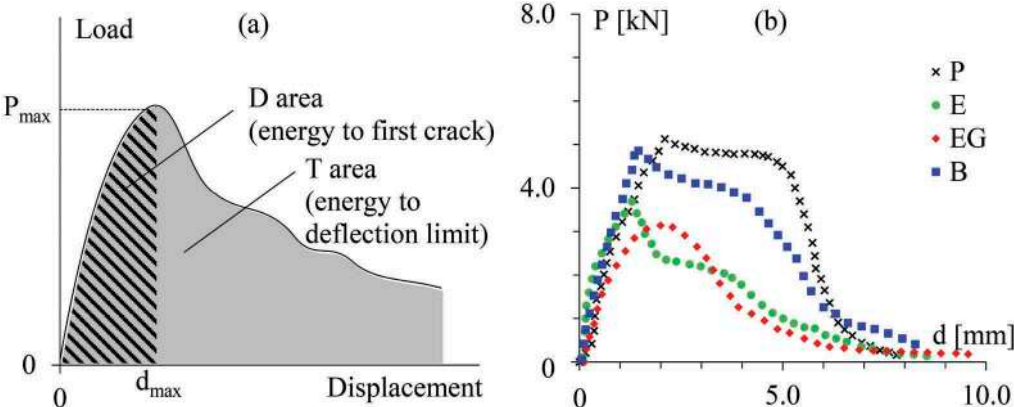


Figure 5. P vs. d curves: theoretical approach (a) and experimental results (b).

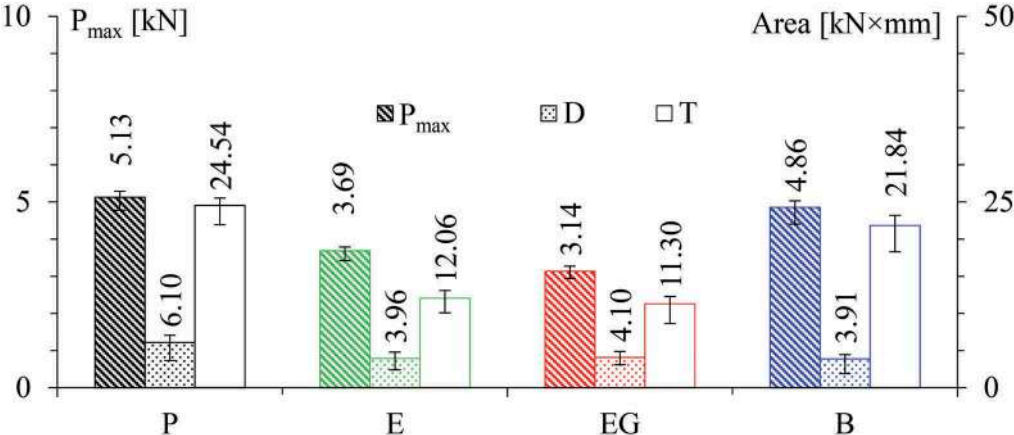
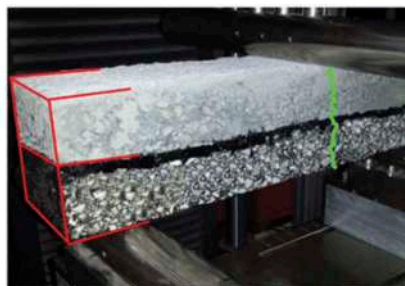
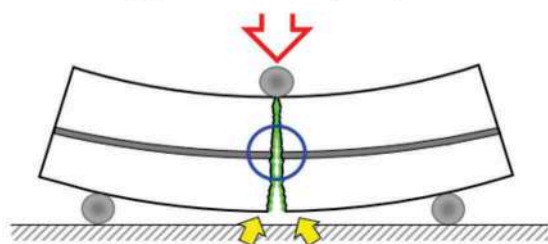


Figure 6. Flexural parameters determined for the tested systems.

Failure: Type A - Dual-layer system failure



Failure: Type B - Interface failure

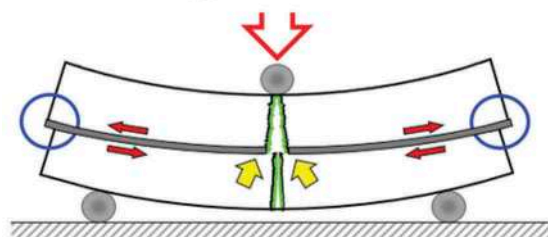


Figure 7. Typologies of failure for the tested systems.

Table 3. Flexural stiffness moduli of the studied samples.

System	P	E	EG	B
E_f [MPa]	242	279	249	358

stiffness E_f was not able to accurately describe the real mechanical characteristics of systems since substantial information about the post-crack phase and the ductility cannot be obtained by such parameter (in fact, it was verified that some samples, despite appreciable modulus E_f , presented fragile failure because of inadequate bond strength at the interface).

4 CONCLUSIONS AND FURTHER RESEARCH

The study dealt with the role of different PCC-AC interfaces for UTW rehabilitation. Double-layered systems with four interlayer configurations were studied in terms of shear bond strength and flexural responses. Based on the obtained results, it was found that interfaces deeply affected system performance. More specifically:

- the use of bituminous emulsion between cement and asphalt concrete was rather unsuitable, even if integrated with fine gravel;
- among the tested solutions, the direct placing of UTW over AC was the most effective one (the AC surface treatment with brushing did not seem to imply significant differences – it definitely did not improve the system characteristics);
- the interface properties influenced the flexural failure mechanisms of samples: systems with low interface bond strength (see emulsion-systems) showed some interlayer delamination (interface failure);
- the simple assessment of flexural stiffness modulus was not completely able to predict the real mechanical characteristics of double-layered systems because no advices about the post-crack phases and the ductility/fragility can be collected.

Further investigations could improve the study including different interface alternatives, also considering that interlayer properties should depend on the combined effect of traffic and temperature, thus on the subsequent rigidity of the AC lower layers. In turn, additional efforts should be spent to replicate in the laboratory asphalt concrete surfaces able to accurately simulate a deteriorated wearing course subjected to UTW overlays applied for road maintenance.

REFERENCES

- Abhijith, C.C. and Mahendra, S.P., 2018. *Effect of bonding layer and admixtures on performance of ultra thin white topping*. Journal of Mechanical and Civil Engineering, 15(4),17–25.
- Balbo, J.T. and Rodolfo, M.P., 1998. *Concrete requirements for ultra-thin concrete overlays (whitotopping) for flexible pavements*. Proceedings of Eight International Symposium on Concrete Roads, 1–7.
- Canestrari, F., Pasquini, E., and Belogi, L., 2012. *Optimization of geocomposites for double-layered bituminous systems*. Seventh RILEM International Conference on Cracking in Pavements, 1229–1239.
- Ferrotti, G., D’Andrea, A., Maliszewski, M., Partl, M.N., Raab, C., Sangiorgi, C. and Canestrari, F., 2016. *Inter-laboratory shear evaluation of reinforced bituminous interfaces*. Eight RILEM International Symposium on Testing and Characterization of Sustainable and Innovative Bituminous Materials. 309–321.
- Gucunski, N., 1998. *Development of a design guide for ultra thin whitotopping (UTW)*. The State University, New Jersey, 1–49.
- Jayakesh, K. and Suresha, S.N., 2018. *Experimental investigation of interface treatment technique on interface shear bond fatigue behaviour of ultra-thin whitotopping*. Construction and Building Materials, 161, 489–500.
- Lopez-Carreno, R.D., Pujadas, P., Cavalaro, S.H.P. and Aguado, A., 2017. *Bond strength of whitotoppings and bonded overlays constructed with self-compacting high-performance concrete*. Construction and Building Materials, 153 835–845.
- Pasetto, M., Pasquini, E., Giacomello, G. and Baliello, A., 2019. *Innovative composite materials as reinforcement systems for asphalt pavements: an experimental study*. Road Materials and Pavement Design, 20(2),617–631.
- Romanoschi, S.A., 1999. *Characterization of pavement layer interfaces*. Louisiana State University, Louisiana, 1–236.

Laboratory fatigue assessment of large geocomposite-reinforced double-layered asphalt concrete beams

P. Jaskula, D. Rys, M. Stienss & C. Szydlowski

Faculty of Civil and Environmental Engineering, Gdansk University of Technology, Gdansk, Poland

M. Golos

Tensar International Limited, Blackburn, Lancashire, UK

J. Kawalec

Faculty of Civil Engineering, Silesian University of Technology, Gliwice, Poland

Tensar International s.r.o., Cesky Tesin, Czech Republic

ABSTRACT: Geosynthetic reinforcement of asphalt layers has been used for several decades. Evaluation of the influence of these materials on pavement fatigue life is still ongoing, especially for new types of geocomposites. This paper presents the evaluation of fatigue performance of large asphalt concrete beams reinforced with a new type of composite in which square or hexagonal polypropylene stiff monolithic paving grid with integral junctions is bonded to polypropylene non-woven paving fabric. Unreinforced samples were used as reference. Fatigue testing was performed in the scheme of four-point bending test (4PB-PR) in the controlled strain mode at +13°C. Test results were analysed in several aspects, including the standardised approach based on stiffness reduction, but also using critical strain at one million cycles. A new parameter – relative increase in fatigue life – was introduced in the analysis as well. On the basis of the obtained results, it can be concluded that the evaluated composites will have evident positive effect on pavement performance and may contribute to a several fold increase in fatigue life of pavement structure. More benefits in terms of pavement bearing capacity are expected in the case of reinforcement of thick and new asphalt pavements. The use of hexagonal geogrid resulted in greater improvement of fatigue resistance than composites with square geogrid.

Keywords: grid reinforcement, fatigue of asphalt pavements, four-point bending test, crack propagation, reflective cracking

1 INTRODUCTION

Reinforcement of asphalt pavements with geocomposites improves bearing capacity effectively, as proved in numerous previous studies (Brown, 1985; Correia, 2014; Graziani et al., 2014). The benefits are notably visible when geocomposites are used in rehabilitation of old, cracked pavement sections (Canestrari et al., 2013; Pasquini et al., 2013; Zieliński, 2013). However benefits are clearly observed in the field (Al-Qadi, 2006; Ragni et al., 2020; Spadoni et al., 2021), the literature still lacks a detailed description (Solatiyan et al., 2020) of the quantified contribution of geocomposite reinforcement to an increase in bearing capacity or reduction of crack propagation of asphalt pavements. Importantly, geocomposites are installed on

top of an existing pavement during placement of new layers and provide different functions according to the type of geosynthetic used (Nguyen et al., 2021; Shukla & Yin, 2004).

The main objective of the presented studies was to evaluate the probable contribution of the new type of geocomposite to extension of bearing capacity, reduction of crack propagation and overall fatigue life extension of asphalt pavement. The evaluation was conducted on the basis of laboratory fatigue tests of double-layered asphalt specimens in four-point bending scheme.

2 METHODOLOGY

2.1 *Experiment planning*

It is expected that reinforcement of asphalt layers with grid geocomposites should increase the fatigue life and delay crack propagation in asphalt pavements. Therefore, double-layer asphalt mixture systems were subjected to cyclic loading in order to determine their fatigue performance. Reference systems consisted of two layers of asphalt concrete, AC 11 W for the lower layer and AC 16 W for the upper layer, bonded with tack coat (Jaskula et al., 2021). Reinforced systems were prepared using same asphalt concrete mix design; the only differences consisted in the implementation of geogrid reinforcement at layer interface and application of a higher quantity of asphalt emulsion used for tack coat. Results obtained for reinforced systems were compared to results obtained for reference system in order to obtain the relative increase in fatigue life. Two groups of specimens were considered: plain and with notch. The idea of testing plain specimens was to simulate the effect of reinforcement in a new pavement structure, where geocomposite may contribute to transfer of tensile stresses and delay crack formation. Notched systems were tested in order to simulate the effects of reinforcement in a rehabilitated pavement, where cracks have already formed in the lower layer and geocomposite prevents reflecting cracking.

2.2 *Laboratory testing in 4PB scheme*

Fatigue testing was performed in the scheme of four-point bending test on prismatic specimens (4PB-PR). A novel aspect of the approach was the use of significantly larger beams consisting of two layers of asphalt mixture with composite reinforcement and emulsion tack coat at their interface. Since such tests may be significantly affected by the size effect, the specimens were larger than those used in typical procedures of fatigue testing with the 4PB-PR scheme. The adopted width of the sample (170 mm) was based on the assumption that the width of the geogrid placed between asphalt layers in the sample must include at least 2 full pitches (both square and hexagon) of geogrid. The distance between axes of the end supports equalled 740 mm. The distance between axes of the loading supports equalled 247 mm. Due to load set-up (bottom loading actuator) of the testing equipment, the specimens had to be placed in clamps of the testing machine in an inverted position in comparison to their natural arrangement in the pavement (i.e., the 30 mm of the lower AC 11W asphalt mixture and the reinforcement grid facing upwards). The loading actuator bent the beam upwards, so the location of the compression and tension zones within the specimen reflected real conditions. The test was performed in a climatic chamber at a constant temperature of +13 °C, which is the equivalent temperature adopted in the design of flexible pavements in Poland (Judycki et al., 2017; Pszczola, 2019). A view of the test equipment with marked dimensions of specimen and frame is presented in Figure 1.

Beams were subjected to cyclic loading that caused a sinusoidal change in strain from 0 to the pre-set maximum value. The following maximum strain values were adopted: 400, 500, 600, 700 and 800 μ strain. For each strain level and for a given type of reinforcement, a single specimen was tested. Bending was forced only in one direction, so that the grid would function in the zone subjected to tension, like in a full-scale pavement structure. The loading frequency equalled 1 Hz. The maximum number of loading cycles equalled 300,000, which resulted in the maximum testing time of 84 hours per test.

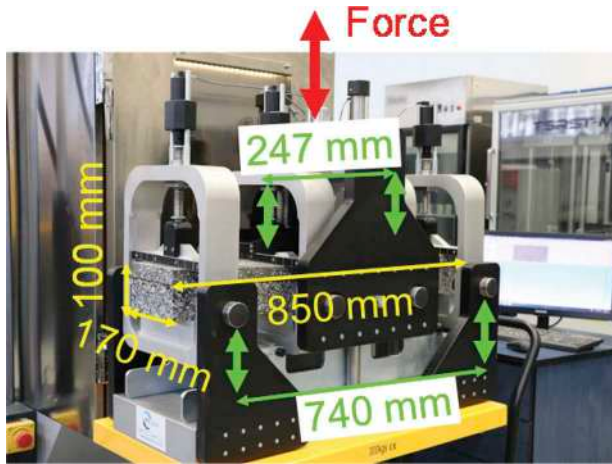


Figure 1. 4PB Equipment used for laboratory testing of double-layer specimens.

2.3 Methodology of analysis of the test results

During the fatigue testing of asphalt mixtures in the controlled pre-set strain mode, the consecutive cycles result in a gradual decrease in the stiffness modulus (and, therefore, the stress induced in the specimen), which is indicated by the continuous decrease in the force needed to induce the adopted strain level. The obtained results were analysed in terms of the initial stiffness, the number of cycles to failure, fatigue curves, strain at one million load cycles and relative increase in fatigue life. A detailed description of the parameters is given below.

Pre-set tensile strain [-]: maximum strain of the extreme tension fibres of the cross section, in the case of homogenous isotropic material. In the performed fatigue tests with controlled strain mode this value is constant for the duration of the entire test. The value of tensile strain is calculated on the basis of vertical deflection measured at the centre of the beam by a LVDT sensor. In fact, the value of ε_t is a theoretical value, since beams are not homogenous and consist of two asphalt layers with various values of stiffness modulus. Moreover, partial slippage occurs at the interface between two layers. Therefore, the strain was defined in this study as “pre-set”, which means that it is the value set in the UTM software and real value of tensile strain differs from the pre-set value.

$$\varepsilon_t = 12 \frac{\delta \cdot h \cdot 10^6}{3S_w^2 - 4L_w^2} \quad (1)$$

where:

ε_t : peak pre-set tensile strain, constant value for the duration of the entire test,

δ : vertical peak deflection at the centre of the beam [mm],

h : beam height (100 mm),

S_w : support span width (740 mm),

L_w : loading span width (247 mm).

Stiffness S [MPa]: equivalent to the stiffness modulus of the system in a given loading cycle in the test. Stiffness in any given cycle may be calculated from (2). This parameter was excluded from the analysis in the first cycles of test due to the rapid decrease in stiffness under loading during the first stage of the test. In the presented research, the initial stiffness S_{ini} was calculated using the data from the 100th cycle.

$$S_i = \frac{\sigma_i}{\varepsilon_i} \quad (2)$$

where:

S_i : stiffness in the i -th cycle of the test,

σ_i : maximum tensile stress in the i -th cycle.

Fatigue life N_f [-]: number of cycles to fatigue failure of the specimen. Different approaches are used regarding the limit of fatigue life. The most popular definition of fatigue failure, which was also assumed in these studies, is the moment at which the stiffness S_i decreases to 50% of the initial stiffness S_{ini} .

Fatigue curve: determined by the N_f fatigue life results obtained at various strain levels. The curve enables the evaluation of the system's fatigue life at any given strain level, even outside of the tested range. The general form equation of the curve is as follows:

$$\varepsilon_i = A(N_f)^b \quad (3)$$

where:

ε_i : pre-set tensile strain,

A : slope of the fatigue curve,

b : coefficient based on the obtained fatigue test results,

N_f : fatigue life of the system.

Strain at one million load cycles ε_6 : parameter based on the fatigue curve, equivalent to the strain level at which the system's fatigue life equals one million load cycles (Corté & Goux, 1996). This parameter is used for characterisation of asphalt mixtures in terms of fatigue resistance. Higher ε_6 strain level indicates better fatigue performance of the mixture (or the entire tested layered system).

Relative increase in fatigue life RI [%]: function delivered from equation (3), expressing the increase in fatigue life of the reinforced systems in comparison to the reference systems at a given tensile strain. The formula (4) was used to calculate the values of RI.

$$RI = \frac{N_{f,mod}}{N_{f,ref}} = A_{ref}^{\frac{-1}{b_{ref}}} A_{mod}^{\frac{1}{b_{mod}}} (\varepsilon_i)^{\frac{b_{mod}}{b_{ref}}} \quad (4)$$

where:

RI: relative increase in fatigue life,

$N_{f,mod}$: fatigue life of the system reinforced with a given type of geogrid,

$N_{f,ref}$: fatigue life of the reference system,

A_{ref}, b_{ref} : coefficients obtained from the fatigue curve of the reference system,

A_{mod}, b_{mod} : coefficients obtained from the fatigue curve of the geogrid-reinforced systems,

ε_i : tensile strain.

3 MATERIALS AND SPECIMEN PREPARATION

Tests were performed on double-layered specimens prepared in the following scheme:

- bottom layer made of asphalt concrete AC 11 W 35/50 for levelling courses,
- upper layer made of asphalt concrete AC 16 W 35/50 for binder courses.

Asphalt concretes were designed and produced at the Road Research Laboratory of the Gdansk University of Technology in accordance with the EN 13108-1 standard and Polish technical guidelines WT-2:2014 for medium traffic KR3-4. The mineral mixture was composed of crushed gneiss/granite aggregate and mineral limestone filler. Effective bitumen content equalled 11.9% and 11.5% by volume, and air voids equalled 4.6% and 4.5%, in AC 11 W and AC 16 W, respectively.

Geogrid composites used in this research were produced by Tensar, Blackburn, Lancashire, UK. Two types of composite reinforcement were tested:

- composite interlayer AR-GN, i.e. square aperture geogrid bonded to non-woven fabric,
- composite interlayer AX5-GN, i.e. hexagonal geogrid bonded to non-woven fabric.

Both structural paving composites consist of two components: (1) a polypropylene stiff monolithic paving grid with integral junctions and (2) a polypropylene non-woven paving fabric. The grids used in the described composites perform the structural reinforcement function (R) of the asphalt interlayer. The tensile strength of the reinforcement was 20×20 kN/m for the square grid and 16×20 kN/m for the hexagonal grid, with a peak strain of approximately 11% in the longitudinal and transverse directions at maximum load, when tested in accordance with EN ISO 10319. The non-woven fabric used in both types of composites functions as a bonding layer during installation. Another function provided by the non-woven fabric is moisture interlayer barrier (B). The described fabric has a residual bitumen retention of approximate 1.5 kg/m^2 . Unit weight of the grid component is approximately 225 g/m^2 (square) and 210 g/m^2 (hexagonal), while the unit weight of the fabric component is 130 g/m^2 . Both composites are visible in Figure 2 (step 4).

Bitumen emulsion for surface treatments with designation C 69 B3 PU (Bitunova, Warsaw, Poland) was selected to be applied as tack coat. The emulsion was produced from 100/150 neat bitumen, whose content equalled 69%. The residual bitumen amount after emulsion decay equalled to 0.2 kg/m^2 for unreinforced systems and 1.2 kg/m^2 in case of reinforced systems. Higher content of tack coat is necessary when composite is applied, to ensure proper inter-layer bonding and stress relief function. It has to be emphasised that introducing a composite between two asphalt layers causes partial loss of inter-layer bonding, despite the higher amount of tack coat. Formation of specimens was conducted in six successive steps, which are visualised in Figure 2:

Step 1 – assembly of wooden moulds with internal dimensions of $250 \times 135 \times 1000$ mm,

Step 2 – laying and compaction of the lower asphalt layer AC 11 W, the height of layer after compaction equalled 45 mm.

Step 3 – application of tack coat of bitumen emulsion C 69 B3 PU.

Step 4 – installation of geogrid composites.

Step 5 – laying and compaction of the upper asphalt layer AC 16 W, the height of layer after compaction equalled 90 mm.

Step 6 – sawing of testing beam from the compacted specimen to the final specimen dimensions $170 \times 100 \times 850$ mm.

Step 7 – preparation of a 10 mm notch in the middle of beam length in the lower asphalt layer.

Preparation of unreinforced, reference beams was carried out in the same way, except for step 4 (installation of geogrid composites – which was omitted) and a different amount of emulsion application.

4 TEST RESULTS

The decrease in the stiffness modulus in following cycles is presented on a log-log scale in Figure 3. The results obtained for the same $600 \mu\text{strain}$ load mode were selected as an example. Figure 3 enables comparisons between the reference system without reinforcement and the systems with geogrid reinforcement, both in the case of plain and notched specimens. Typically, for specimens of single asphalt mixture, three stages of stiffness modulus decrease are distinguished: (1) initial phase, which is characterised by a rapid decrease in stiffness, mostly due to the effect of thixotropy, (2) phase of damage accumulation, when stiffness decreases gradually, (3) stage of failure, when stiffness decreases rapidly due to macro-crack formation. Reference system with plain specimen confirms these typical stages; for the specimen shown in Figure 3 the third phase begins around the 100 000th cycle. The third phase of failure was not observed for reinforced plain specimens until the 300 000th cycle.

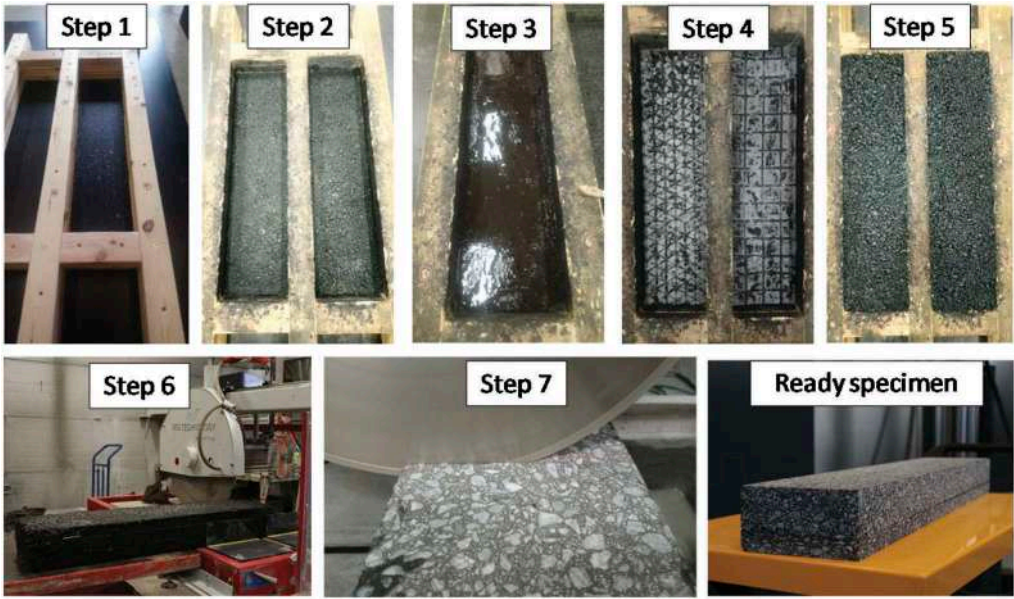


Figure 2. View of the successive steps of specimen fabrication.

In the case of all the notched systems, macro-cracks are already initiated in the lower layer. Stiffness of the reference system decreases gradually, which means that cracks penetrate from the lower layer to the upper layer. Failure of the system occurs much faster than in the case of plain specimen. In contrast, when specimen is reinforced with geogrid, the rate of decrease in stiffness is rapid at the beginning and around the 4000th cycle the rate decreases. It means that the crack propagates in the lower layer, but when it reaches the level of geocomposite reinforcement it does not pass to the upper layer. Consequently, notched systems reinforced with geocomposites remained in the second phase until the end of test (300 000 cycles). The chart presented in Figure 3 as well as visual observation of the tested specimens clearly shows that cracks did not penetrate from the lower layer to the upper layer when geocomposite reinforcement was used in the system.

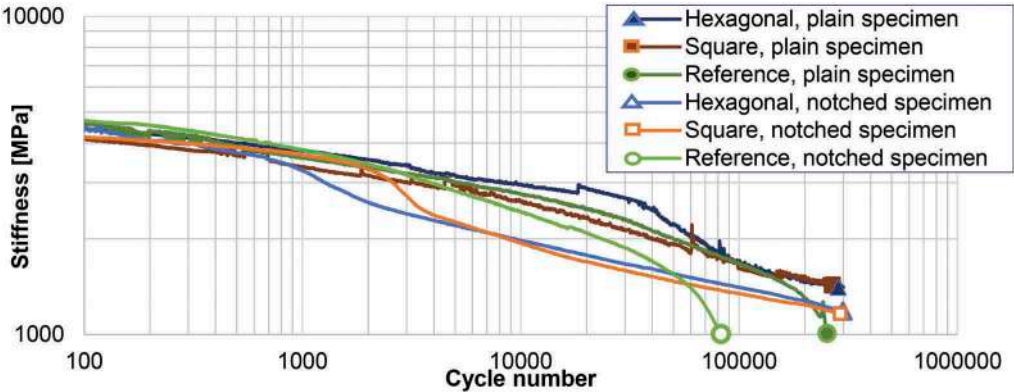


Figure 3. Comparison of the decrease in stiffness of plain and notched specimens during successive fatigue cycles at constant 600 μ strains load mode.

The results of fatigue tests expressed by the number of cycles N_f until decrease in stiffness to 50% of the initial value are presented in Figures 4 and 5 for plain and notched systems, respectively. The regression functions of fatigue curves were calculated using the least square method, and the power model (equation (3)) was used. The fatigue curve parameters A and b are given in Figures 4 and 5. They are also summarised in Table 1.

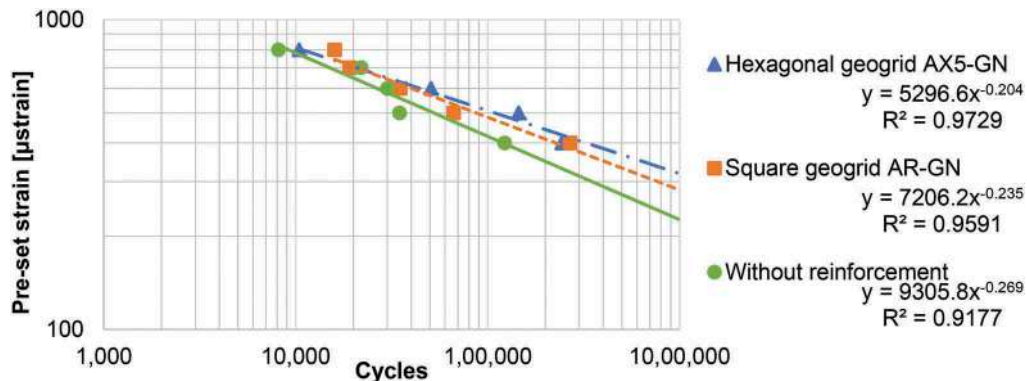


Figure 4. Fatigue model chart for double-layered asphalt beams without notch.

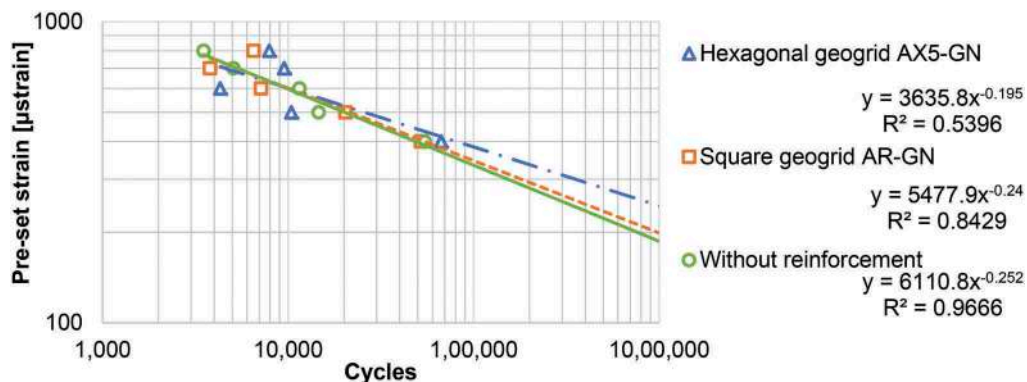


Figure 5. Fatigue model chart for double-layered asphalt beams with notch.

Table 1. Coefficients of fatigue curves.

	System	A	b
Plain specimens	Reference (without reinforcement)	9305.8	-0.269
	Reinforced with square geogrid	7206.2	-0.235
	Reinforced with hexagonal geogrid	5296.6	-0.204
Notched specimens	Reference (without reinforcement)	6110.8	-0.252
	Reinforced with square geogrid	5477.9	-0.240
	Reinforced with hexagonal geogrid	3635.8	-0.195

It was observed that at higher levels of pre-set strain fatigue life of reinforced systems was comparable to that of the reference unreinforced system. Differences are more visible at lower levels of pre-set strains, where higher fatigue life was observed for reinforced systems.

Power models fit to test results very well in the case of all the plain specimens and the reference notched system, as expressed by the high value of $R^2 > 0.9$. The fatigue life model of the notched reinforced systems does not fit the experimental data equally well. Fast crack propagation in the lower layer and delamination of two asphalt layers caused by crack propagation may be the reason of high variability in the observed values of fatigue life of the notched reinforced systems. However, a deeper analysis of the outliers visible in Figure 5 (e.g. for 600 μ strains) leads to analysis of the decrease in stiffness in subsequent load cycles (see Figure 3). The criterion of a 50% decrease in stiffness modulus was adopted for determination of fatigue life for all systems, but the process of fatigue is different in the case of non-reinforced notched system and reinforced notched systems. After failure of the lower layer, the stiffness of the whole system decreases rapidly, but then the geocomposite activates itself, which results in a lower rate of stiffness decrease, as shown in Figure 3.

The fatigue curves were used to calculate the strain at one million load cycles ϵ_6 . The results are presented in Figure 6. Higher values of ϵ_6 obtained for the reinforced systems both in the case of plain and notched systems express higher fatigue performance of those systems.

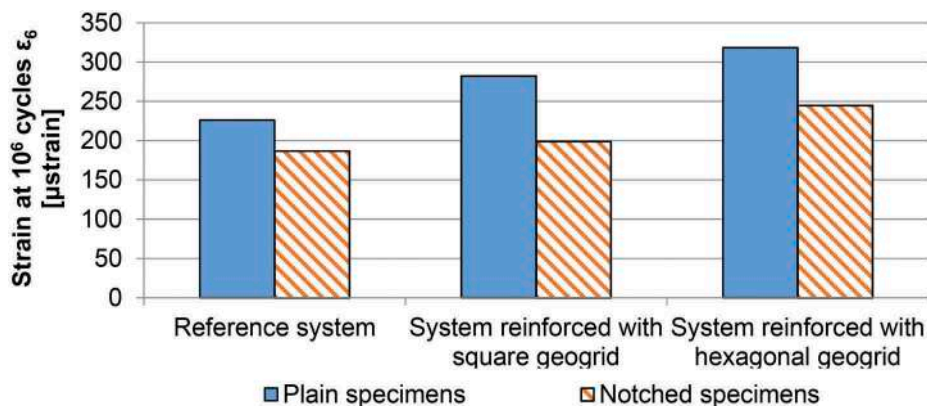


Figure 6. Critical strains at 10^6 cycles and relative change in critical strain.

5 IMPACT OF GEOCOMPOSITE REINFORCEMENT ON BEARING CAPACITY OF ASPHALT PAVEMENT

The bearing capacity of asphalt pavement is directly related to fatigue life of asphalt layers. The relative increase in fatigue life of double-layered systems was calculated according to equation (4). Coefficients A and b used in equation (3) were determined on the basis of regression coefficients summarised in Table 1. Figure 7 presents the results of relative increase in fatigue life RI for tensile strains from 80 to 200 μ strains. Plots presented in Figure 7 were developed on the basis of extrapolation of models given in Figures 4 and 5, which generates some uncertainty in the presented values. Nevertheless, it can be stated that application of hexagonal geogrids causes a severalfold increase in fatigue life. Reinforcement with square geogrids is less efficient than reinforcement with hexagonal geogrids, but it increases the fatigue life up to 4 times in comparison to the reference systems.

The assumed levels of tensile strain correspond to the values which occur at the bottom of the asphalt layers in pavement structure loaded by wheels of a heavy vehicle. Determination of tensile strain at the bottom of the asphalt layers is a complex process, as it depends on several factors. However, some general dependencies can be formulated. Tensile strain decreases when: 1) axle load decreases, 2) total thickness of the asphalt layers increases, 3) elastic modulus of the

subbase and subgrade increases, 4) stiffness of the asphalt layers increases (e.g. due to a decrease in temperature and an increase in vehicle speed). Since the experiment was performed in laboratory, fatigue life of the systems as well as the pre-set tensile strains do not correspond to the values representative for the entire pavement structure. A shift factor should be used between the fatigue life obtained for systems tested in laboratory and the fatigue life of pavement structure. It is expected that the shift factor for the reference system is around 20 (e.g. shift factor for Asphalt Institute fatigue criteria equals 18.4). The shift factor for reinforced systems is unknown. Nevertheless, the relations between the increase in fatigue life of reinforced pavements and reinforced beams tested in laboratory conditions remain the same – they are presented in Figure 7.

Figure 7 shows evidently that reinforcement of pavement with geocomposites improves its bearing capacity. Reinforcing with hexagonal geogrids is more beneficial than reinforcing with square geogrids. When reinforcement is used in plain systems, which simulate new pavements, the relative increase in fatigue life is greater than in the case of notched systems, which simulate rehabilitated pavements. More beneficial effects of pavement reinforcement are expected for thicker pavements, where tensile strains at the bottom of asphalt layers caused by traffic loads are lower.

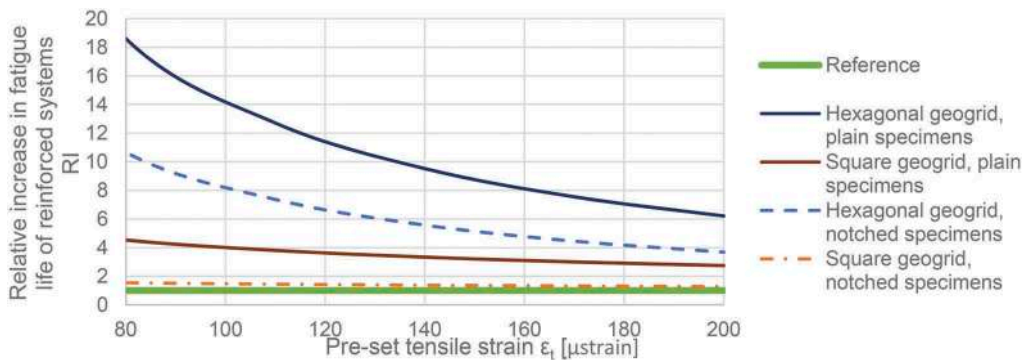


Figure 7. Relative increase in fatigue life of double-layered reinforced systems.

6 CONCLUSIONS

Analysis of the results of fatigue tests, which were performed on reference (unreinforced) systems and systems reinforced with geocomposites (both on plain and notched specimens), leads to the following conclusions:

- Strengthening the pavement structure with geocomposites increases both their load-bearing capacity and overall fatigue life.
- In the presented study, polypropylene stiff monolithic paving grids with integral junctions thermally bonded to polypropylene non-woven paving fabric were tested. For such geocomposites, the shape of the grid has an impact on fatigue life of the reinforced system. More beneficial effects are observed for hexagonal geogrids.
- The relative increase in fatigue life of the reinforced systems depends on the level of tensile strain at the bottom of the asphalt layers.
- More benefits in terms of pavement bearing capacity are expected in the case of reinforcement of thick, new asphalt pavements, where tensile strains at the bottom of the asphalt layers are lower and fatigue cracks have not been initiated yet.
- Using reinforcement in pavement structure postpones cracks formation in the upper layers.

- When using geocomposite reinforcement (i.e. geogrid bonded to paving fabric) one should expect that overall stiffness can be slightly reduced, as a consequence of slight differential movement between asphalt layers and geocomposite.
- Introducing geocomposite reinforcement between asphalt layers can also affect shear strength of interlayer bonding, but this should not have detrimental effect on overall pavement performance.

Future theoretical studies should be focused on solving the uncertainty in relationships between pre-set tensile strain in fatigue tests and tensile strain at the bottom of the asphalt layers in real pavement structure, as well as on the probable shift factor between results obtained from laboratory fatigue tests and fatigue life of pavements structures.

REFERENCES

- Al-Qadi, I. L. (2006). Pavement Interlayer System Mechanisms : Separation, Reinforcement, and Reflective Cracking Control. *Chinese Society of Pavement Engineering*, 73.
- Brown, S. F. (1985). Polymer grid reinforcement of asphalt. *Journal of Asphalt Paving Technology*, 54, 18–41.
- Canestrari, F., Belogi, L., Ferrotti, G., & Graziani, A. (2013). Shear and flexural characterization of grid-reinforced asphalt pavements and relation with field distress evolution. In *Materials and Structures*. <https://doi.org/10.1617/s11527-013-0207-1>
- Correia, N. de S. (2014). *Performance of flexible pavements enhanced using geogrid- reinforced asphalt overlays*. University of Sao Paulo, Brasil.
- Corté, J.-F., & Goux, M.-T. (1996). Design of pavement structures: the French technical guide. *Transportation Research Record*, 1539, 116–124. <https://doi.org/10.3141/1539-16>
- Graziani, A., Bocci, E., & Canestrari, F. (2014). Bulk and shear characterization of bituminous mixtures in the linear viscoelastic domain. *Mechanics of Time-Dependent Materials*. <https://doi.org/10.1007/s11043-014-9240-x>
- Jaskula, P., Rys, D., Stienss, M., Szydowski, C., Golos, M., & Kawalec, J. (2021). Fatigue Performance of Double-Layered Asphalt Concrete Beams Reinforced with New Type of Geocomposites. *Materials*, 14(9), 2190. <https://doi.org/10.3390/ma14092190>
- Judycki, J., Jaskuła, P., Pszczola, M., Ryś, D., Jaczewski, M., Alenowicz, J., Dołycki, B., & Stienss, M. (2017). New polish catalogue of typical flexible and semi-rigid pavements. *MATEC Web of Conferences*, 122. <https://doi.org/10.1051/mateconf/201712204002>
- Nguyen, M. L., Hornych, P., Le, X. Q., Dauvergne, M., Lumière, L., Chazallon, C., Sahli, M., Mouhoubi, S., Doligez, D., & Godard, E. (2021). Development of a rational design procedure based on fatigue characterisation and environmental evaluations of asphalt pavement reinforced with glass fibre grid. *Road Materials and Pavement Design*, 22(S1), S672–S689. <https://doi.org/10.1080/14680629.2021.1906304>
- Pasquini, E., Bocci, M., Ferrotti, G., & Canestrari, F. (2013). Laboratory characterisation and field validation of geogrid-reinforced asphalt pavements. *Road Materials and Pavement Design*, 14(1), 37–41. <https://doi.org/10.1080/14680629.2012.735797>
- Pszczola, M. (2019). Equivalent temperature for design of asphalt pavements in Poland. *MATEC Web of Conferences*, 262, 05010. <https://doi.org/10.1051/mateconf/201926205010>
- Ragni, D., Montillo, T., Marradi, A., & Canestrari, F. (2020). Fast falling weight accelerated pavement testing and laboratory analysis of asphalt pavements reinforced with geocomposites. *Lecture Notes in Civil Engineering*, 48(May), 417–430. https://doi.org/10.1007/978-3-030-29779-4_41
- Shukla, S. K., & Yin, J.-H. H. (2004). Functions and Installation of Paving Geosynthetics. *3rd Asian Regional Conference on Geosynthetics*, 314–321.
- Solatiyan, E., Bueche, N., & Carter, A. (2020). A review on mechanical behavior and design considerations for reinforced-rehabilitated bituminous pavements. *Construction and Building Materials*, 257, 119483. <https://doi.org/10.1016/j.conbuildmat.2020.119483>
- Spadoni, S., Ingrassia, L. P., Paoloni, G., Virgili, A., & Canestrari, F. (2021). Influence of Geocomposite Properties on the Crack Propagation and Interlayer Bonding of Asphalt Pavements. *Materials*, 14(5310), 1–18.
- Zieliński, P. (2013). Investigations of Fatigue of Asphalt Layers with Geosynthetics. *Archives of Civil Engineering*, 59(2). <https://doi.org/10.2478/ace-2013-0013>

Structural design systems for new construction and rehabilitation



Taylor & Francis

Taylor & Francis Group

<http://taylorandfrancis.com>

Calibration of mechanistic-empirical flexible pavement damage models

A.T. Papagiannakis & E. Alrashydah

School of Civil and Enviro. Engineering, University of Texas at San Antonio, USA

A. Masad

Department of Civil Architectural and Enviro. Engineering University of Texas at Austin, USA

ABSTRACT: This paper presents a concise approach for calibrating the damage models in the TxME, a mechanistic-empirical flexible pavement design model developed for Texas. The models calibrated are rutting, bottom-up fatigue cracking, and transverse (thermal) cracking. Pavement performance observations from the Texas Department of Transportation (TxDOT) maintained Data Storage System (DSS) were used for this purpose. Prior to calibration, Analysis of Variance (ANOVA) was used to establish similar groups of sections in terms of structural, traffic and environmental conditions. For the rutting model, the layer calibration coefficients weighed plastic deformations linearly, hence it was possible to establish them by minimizing the sum of the squared errors (SSE) between the estimated and observed surface (i.e., total) rutting. For the fatigue cracking model, calibration focused on the transfer function between the accumulated fatigue damage and the observed fatigue cracked area. For the transverse cracking model, the exponent of the pavement life ratio $\frac{P}{m}$ was established through curve-fitting on transverse cracking observations. In general, the calibration resulted in significant quality of fit improvements.

Keywords: M-E design, calibration, rutting, cracking

1 INTRODUCTION

TxME was developed for the Texas Department of Transportation (TxDOT) as a tool for the mechanistic-empirical analysis of flexible pavements (Zhou et al. 2010). The framework of the TxME has some similarities to the AASHTOware® Pavement Mechanistic-Empirical Design (PMED) (AASHTO 2020), but in general, the flexible pavement damage functions used are different.

The TxME predicts distresses versus time, given material, environmental, and traffic data inputs. It consists of computer software with a graphical user interface that allows specifying pavement type, pavement layer properties, site location, and traffic spectra. The location allows the user to select environmental data from Texas weather stations near the design site. Traffic is characterized in terms of load spectra consisting of average annual daily truck traffic (AADTT), vehicle classification distributions (VCD), monthly adjustment factors (MAF), and axle load distributions (ALD) by axle configuration. Material properties can be input as either

fundamental properties (e.g., asphalt concrete master curves, soil-water characteristic curves) or index properties (e.g., resilient moduli, plasticity indices). Traffic inputs can be customized with site-specific load spectra information or approximated using built-in default values.

The TxME incorporates damage functions for the plastic deformation of the pavement layers that add to surface rutting, bottom-up fatigue cracking and transverse (i.e., thermal cracking). There is a need to calibrate these damage functions, so they accurately predict field observations.

There is an abundance of literature on mechanistic-empirical pavement damage model calibration. Their majority deals with the calibration of the PMED and it is part of State agency efforts to implement this pavement analysis approach. Recent examples include Arizona (Darter et al. 2014) and Georgia (Von Quintus et al. 2015). These efforts utilized multiple PMED runs and performed statistical analyses to minimize the errors between predictions and observations. A “split-sample” approach was used for this purpose, whereby calibration factors are established using a subset of the data (i.e., roughly 85%), and the accuracy of the calibrated models is verified using the remaining data subset. This provides an unbiased test of the fit quality of the calibrated damage models.

Other calibration efforts include those of North Carolina (Kim et al. 2011) and Iowa (Ceylan et al. 2013). One of the innovations introduced by these efforts involves the use of finite differential expressions to quantify the sensitivity of model estimates to pavement design input (Ceylan et al. 2013). Another is the use of error minimization solvers that allow a single step fitting of calibration constants. This is possible where the calibration constants weigh linearly the mechanistic predictions. An examples of this approach is the work by Kim et al. (2011) for the North Carolina DOT.

2 OBJECTIVES

The objective of this paper is to present a concise methodology for calibrating and validating the damage functions in the TxME. The goals of the calibration are to:

- Minimize bias (i.e., minimize the differences between distress predictions and observations) and
- Maximize quality of fit (i.e., minimize the squared differences between distress predictions and observations).

This study utilized Texas-specific data to calibrate and validate the rutting, bottom-up fatigue cracking, and transverse (thermal) cracking models in the TxME. Its findings were presented by Masad et al. (2021). This paper provides a summary of these findings.

3 TXME DAMAGE MODELS

The TxME includes pavement damage models for layer rutting, bottom-up asphalt concrete fatigue cracking and transverse (i.e., thermal) cracking. These are described below in tabular format (Table 1). The variables involved are defined below:

- N_i and N_p are the number of strain cycles to fatigue cracking initiation and propagation, resp. and k_i, k_p are the corresponding calibration factors.
- FD is the amount of fatigue damage accumulated.
- K values are stress intensity factors, A and n are the Paris law cracking constants and k values are calibration factors for each of the three cracking modes, i.e., tension, shear and torsion.
- D is the reflective damage accumulated.
- ρ is the length of time (months) it takes for the sum of the transverse crack increments $\sum^A C$ to accumulate to a length equal to the thickness of the asphalt concrete layer h_{AC} , m is the month number, while B and β are calibration constants.

Table 1. TxME pavement damage functions.

Damage Function	TxME Damage Model
AC Fatigue Life N_f	$N_f = k_i N_i + k_p N_p$
AC Fatigue cracking (bottom-up) FC	$FC = \frac{100}{1 + e^{C \log FD}}$
Strain endurance limit	Singular value (e.g., 70) or distribution
Reflection cracking increments ΔC and reflective cracking rate RCR	$\Delta C = k_1 A(K_b)^n + k_2 A(K_s)^n + k_3 A(K_r)^n RCR = \frac{100}{1 + e^{C_1 \log D}}$
Transverse (thermal) cracking increments ΔC and cracked amount CA	$\Delta C = kA(\Delta K)^n CA = \frac{100B}{e^{0.693147}(\rho/m)^{\beta}}$
AC rutting RD	$RD = \sum_m k_f \int_0^{N_i} (U_i^+ - U_i^-) \mu_i N^{-\alpha_i} dN_f = f_1(T)f_2(E)f_3(h_{OL})$
Base/subgrade rutting RD	$RD = k \int \Delta U \mu N^{-\alpha}$

- ΔU are differences in deflections for each sub-layer i estimated as the deflection at the top of the sublayer minus that at its bottom (i.e., $U_i^+ - U_i^-$).
- μ and α are plastic deformation material properties and k are calibration factors for the AC and the granular layers and,
- f is a rutting correction function for temperature, AC stiffness and AC layer thickness.

All the variables involved are in US customary units. It is noted that these damage functions are, in general, different from the ones incorporated into the PMED.

4 PAVEMENT PERFORMANCE DATA USED

Two pavement performance databases were considered, namely, the Texas Long Term Pavement Performance (LTPP) database and the Data Storage System (DSS) database maintained by TxDOT (Walubita et al. 2014). The DSS contains data for over 120 sites that are 152-304 meters (500-1000 ft) long. Data collection began in 2011. It includes data for both existing and newly constructed flexible pavement sites of various structural configurations and base materials located on roadways of different functional classes. Statistical comparisons between the Texas LTPP and the DSS revealed that the two databases are drastically different in terms of the type of pavement survey data collected, the material properties available and the age of the sections monitored. Therefore, it was decided not to combine the two databases and use only the DSS data for calibrating the TxME damage models.

Three broad flexible pavement categories were considered, namely new pavements, overlaid pavements, and perpetual pavements. Each category was further subdivided by base type, namely non-stabilized, lime or binder stabilized, and cement stabilized. Each pavement group was assigned letters A, B . . . to G, as follows:

- A, B, C: New construction with unbound, cement-treated and binder/lime stabilized base, respectively,
- D, E, F: Overlaid with unbound, cement-treated and binder/lime stabilized base, respectively and,
- G: Perpetual (i.e., most sites in this category had cement-treated bases).

Data availability reduced the number of sites available to 77. The structural characteristics of these sections were as follows:

- Asphalt concrete thicknesses ranged from 5.08 to 57.15 cm (2 to 22.5 inches).
- Base layer thicknesses ranged from 15.24 to 62.23 cm (6 to 24.5 inches).
- Subgrade resilient moduli ranged from 57.22 to 851.5 MPa (8.3 to 123.5 ksi).
- AADTT values ranged from 8 to 11,460 vehicles/day.

Summary statistics for the three measured distress, are given in Table 2. Additional details can be found in the report documenting this study (Papagiannakis et al. 2020).

Table 2. Summary statistics for the measured distresses.

Measured Distress	Number of Sections	Number of Observations	Minimum	Maximum	Mean	Standard Deviation
Rutting (mm)	77	454	0	8.89	2.45	2.02
Fatigue cracking (%)	19	125	0	38.40	6.21	5.26
Transv. cracking (m/km)	20	125	0	716.67	186.05	137.06

5 MODEL CALIBRATION APPROACH

Model calibration involved two main steps. First, the TxME simulations were carried out using the default calibration factors and errors were estimated with respect to the field observations. These errors were analyzed using Analysis of Variance (ANOVA) to establish groups of sections exhibiting statistically similar behavior in terms of structural, environmental or traffic factors. Second, for each of the section groups established, a split-sample approach was used, whereby a random 85% of the sections was selected for calibration and the remaining 15% used for validation. The actual calibration approach used varied by distress type, but their objectives were common, namely minimize bias (i.e., minimize the sum of the differences between distress predictions and observations) and maximize the quality of fit (i.e., minimize the sum of the squared differences between distress predictions and observations).

5.1 Rutting model

The main challenge in calibrating the rutting model was that observations were available only for surface rutting, which is the sum of the plastic deformations in each of the deformable pavement layers (i.e., asphalt concrete, base, and subgrade). However, observing the models for predicting the plastic deformation in each layer (Table 1) reveals that the calibration factors k_{AC} , $k_{granular}$ and $k_{subgrade}$ are simple linear weights to the layer plastic deformations in computing the total surface rutting. As a result, a single TxME simulation for each section sufficed for back-estimating the term $\int \Delta U \mu N^{-\alpha}$ for each layer in each month. This in turn, allowed estimation of the three calibration factors simultaneously by minimizing the sum of the squared errors (SSE) in surface rutting (i.e., estimated surface rutting minus observed surface rutting squared) using the generalized reduced gradient (GRG) error minimization approach. The MS Excel® Solver was used for this purpose using a range of calibration coefficients between 0.1 and 10.

5.2 Fatigue cracking model

Preliminary TxME sensitivity analysis of the fatigue cracking predictions with respect to the three calibration coefficients revealed that only C has an effect. The reason is that the factors k_i and k_p seem to have been treated as constants in the TxME software. As a result, the calibration process focused on calibrating the transfer function between fatigue damage FD and the percent of the wheel path area cracked FC . This was done by back-estimating FD using the software default C value of -7.890 through:

$$\log(FD) = \frac{\ln\left(\frac{100}{FC} - 1\right)}{C} \quad (1)$$

Subsequently, C was fitted by minimizing the errors between the back-estimated $\log(FD)$ and the observed FC using the GRG error minimization algorithm. For this analysis, only 19 sections with non-zero fatigue cracking observations could be used (i.e., could not take the logarithm of zero). The curve fitting algorithms built into MATLAB® were used as an alternative yielding similar calibration coefficients. The MATLAB® iteratively reweighted least-squares

approach, referred to as bi-square, was used for fitting the sigmoidal curve between observed FC and $\log(FD)$.

5.3 Transverse cracking model

The calibration coefficients to be determined were k , B and β with default values of 0.5, 42.24 and 1.1854, respectively. The coefficient k weighs linearly the predicted crack increments ΔC (Table 1) and hence, it affects the rate of their accumulation and the length of time it takes for their sum to reach the thickness of the asphalt concrete layer. By definition, the specific month m when this takes place is ρ and hence, at this point the ratio $\frac{\rho}{m}$ equals 1. Furthermore, at this point, the Cracked Amount CA becomes $50B$, i.e., the denominator of the CA transfer function (Table 1) becomes 2, regardless of the value of the exponent β . For the default B value of 42.24, $50B$ equals 2,114 ft/mile (400 m/km), which is the consensus maximum length of transverse thermal cracks expected per mile. As a result, it was decided not to alter B , but focus on the calibration in establishing the values of k and β that generated TxME estimates best fitting the observed transverse cracking amounts. For this purpose, only 20 sites with non-zero transverse crack observations were used.

Sensitivity analysis of the transverse cracking model suggested that the coefficient k weighing the crack increments needs to be increased, while the exponent β of the CA transfer function needs to be decreased from their default values (i.e., 0.5 and 1.1854, respectively). A multitude of TxME simulations were conducted using the calibration dataset by selecting a wide range of coefficients. In these simulations, k ranged from 0.1 to 170, while β ranged from 1.1854 to 0.1. The resulting standard error S_e in predicting transverse cracking (CA) was plotted versus k and β . A surface was fitted through these prediction errors using the cubic spline interpolation approach. It revealed that the effect of β is by far more significant than the effect of k in reducing prediction errors. The minimum standard error was obtained for values of $k=0.1$ and $\beta=0.3$ and amounted to 124 m/km (654 ft/mile), which was much lower than the 800 m/km (4,226 ft/mile) obtained with the TxME default values. The effect of k was further explored by analyzing its effect on transverse cracking prediction error S_e and bias while keeping $\beta=0.3$, which is the minimum value established earlier. These results suggested that increasing the value of k , decreases the standard error but increases the bias. Therefore, it was decided to maintain the value of k at the default value of 0.5 and estimate the value of β by minimizing the sum of squared errors between the back-estimated $\frac{\rho}{m}$ values and the observed transverse cracking CA (Table 1) using:

$$\rho = \left[\frac{\ln\left(\frac{100B}{CA}\right)}{0.693147} \right]^{1/\beta} \quad (2)$$

Where, $B = 42.24$. The curve fitting for establishing the exponent β was done with MATLAB®.

6 CALIBRATION AND VALIDATION RESULTS

6.1 Rutting model

Preliminary ANOVA of the surface rutting prediction errors before calibration (i.e., using the TxME default calibration factors) revealed that at 95% confidence, there was no significant statistical difference between pavement groups A, B, and C, which were combined and labeled as A*. There was, however, a difference between groups A*, D, E, F and G. Further analysis demonstrated that the pavement group, the AADTT volume and the subgrade modulus M_r were statistically significant (Table 3). Further analysis demonstrated that pavement type and AADTT were significant and so was their interaction. Given the small number of sections available, it was decided not to fragment the data set any further. Accordingly, pavement sites

were grouped by pavement type and AADTT level for calibration purposes. It should be noted that boundaries for the various variables were selected to create roughly pavement sub-groups of similar sample size.

Table 3. ANOVA of rutting prediction errors before calibration by structural, traffic and environmental factors.

Group by	Criteria	F	P-value	F-critical
Pavement Type	A*, D, . . . , G	4.229	0.0003	2.118
Subgrade M_r (MPa)	≤ 207 >207	4.344	0.0376	3.862
AADTT	≤ 500 >500	19.86	1.05E-05	3.862
AC thickness (mm)	≤ 127 >127	0.0205	0.886	3.864
Min Temp. ($^{\circ}$ C)	≤ 20 >20	0.4822	0.4877	3.862
Climatic zone	Moderate Warm Cold	0.0089	0.991	3.0165

A*= Combined pavement types A, B and C

The calibration dataset of 77 sections was randomly split into a calibration and a validation subset (i.e., roughly 85% and 15% of the sections, resp.) For the calibration dataset there was a reduction in bias and standard error for all these sections. For the validation dataset, there was a reduction in bias for 5 out of the 9 pavement sub-groups and a reduction in standard error S_e for 6 out of the 9 pavement sub-groups.

Following this analysis, the calibration was repeated for all 77 sections by pavement sub-group and for all subgroups together. The resulting calibration factors and the associated prediction bias and error statistics are shown in Table 4. The improvements resulting from the calibration are shown in Figures 1 and 2, which plot the before and after calibration prediction bias and S_e , respectively. Overall, the calibration factors fitted resulted in reductions in bias and S_e of 71% and 19%, respectively, compared to those obtained with the TxME software default calibration factors. Figure 3 shows an example of the quality of fit improvements as a result of the rutting model calibration.

Table 4. Recommended layer rutting calibration factors and quality of fit statistics.

Statistic	Group A*		Group D		Group E		Group F		Group G		All Groups	
	≤ 500	> 500	≤ 500	> 500	≤ 500	> 500	≤ 500	> 500	≤ 500	> 500	≤ 500	> 500
Obs.	91	47	63	50	16	8	81	51	5	42	256	198
Bias	-0.211	-0.541	-0.152	0.061	-0.759		0.061	-0.008	-	0.102	-0.142	-0.267
SSE	0.176	0.465	0.278	0.129	0.156		0.173	0.065	-	0.263	0.818	1.497
S_e	1.115	2.527	1.676	1.288	2.050		1.173	0.904	-	2.009	1.435	2.207
k_{AC}	0.100	0.243	0.577	0.100	0.737		0.692	0.795	-	1.291	0.632	0.696
$k_{granular}$	0.861	0.100	0.100	0.286	n/a		0.100	0.100	-	1.881	0.368	0.100
$k_{subgrade}$	2.088	10.000	10.000	5.249	10.000		0.100	5.329	-	2.209	1.043	3.604

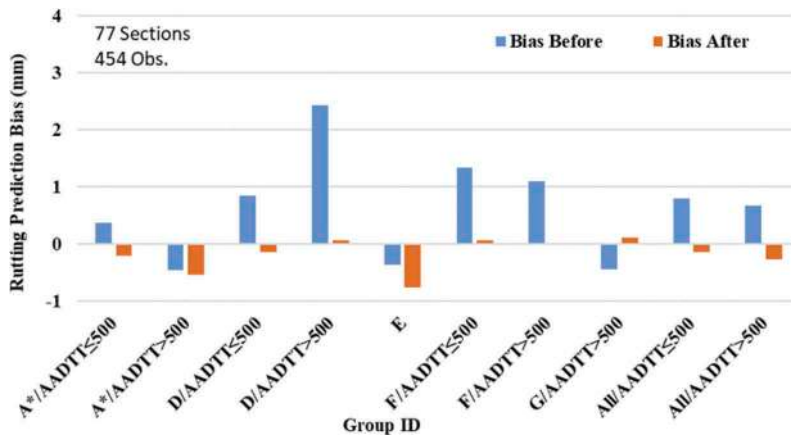


Figure 1. Rutting prediction bias before and after calibration; All sections analyzed.

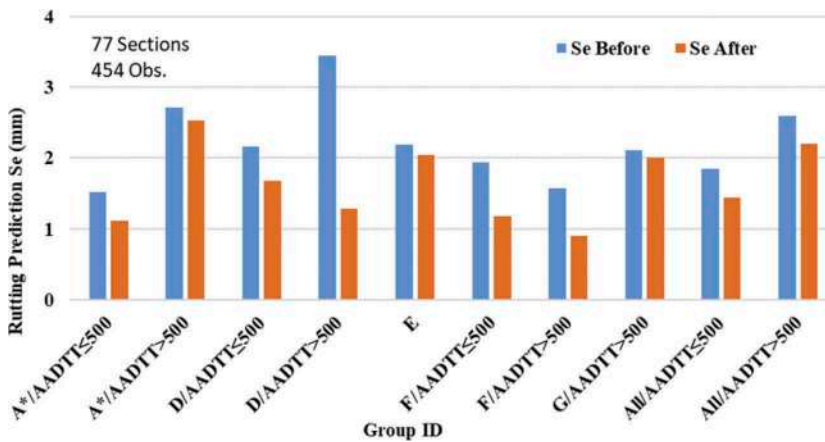


Figure 2. Rutting prediction standard error before and after calibration; All sections analyzed.

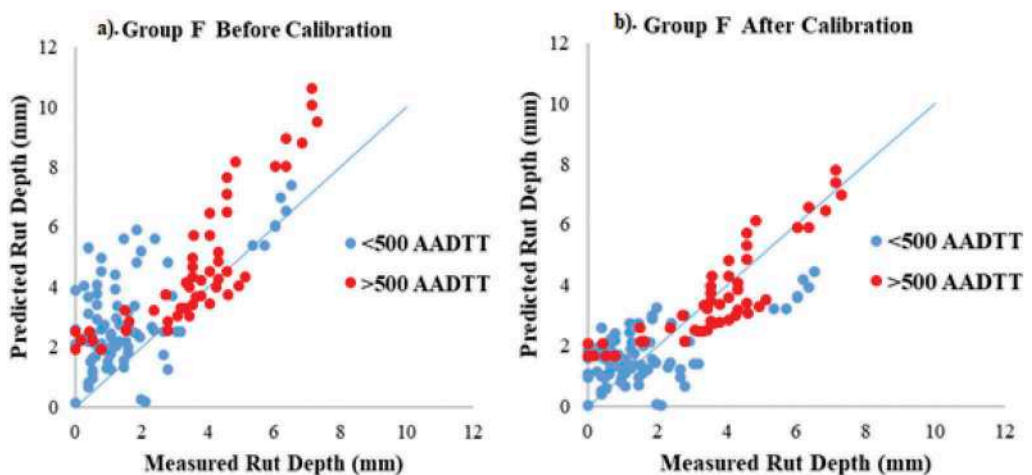


Figure 3. Example of measured versus predicted rutting before (a) and after (b) calibration; Pavement Type F (i.e., overlaid with a binder or lime treated base over granular base).

6.2 Fatigue cracking model

The ANOVA of fatigue cracking prediction errors revealed that the subgrade resilient modulus M_r and the base thickness are the only statistically significant factors affecting fatigue cracking (Table 5). Further ANOVA considering all pavement types as one group revealed that the effect of the interaction between the subgrade M_r and the base thickness is not significant, while the effect of subgrade M_r is marginally significant. As a result, the 19 sections with non-zero fatigue cracking observations were divided into two groups, one with $M_r \leq 207$ MPa (30 ksi) and the other with $M_r > 207$ MPa (30 ksi). The fatigue cracking predictions were not affected at all by the constants k_i and k_p (Table 1). As a result, the calibration focused on the exponent C . A sigmoidal curve was fitted using MATLAB® by minimizing the error between the back-estimated log(FD) and the observed fatigue cracked area FC (Equ. 1).

Table 5. ANOVA of fatigue cracking prediction errors before calibration.

Type of subgrouping	Criteria	Number of Sections	F	P-value	F_{crit}
Pavement type	A, ..., G	19	1.430	0.229	2.453
Subgrade M_r (MPa)	≤ 207	11	3.801	0.054	3.924
	>207	8			
AADTT	≤ 500	10	1.514	0.221	3.924
	>500	9			
AC Thickness (mm)	≤ 127	6	0.830	0.364	3.924
	>127	13			
Base Thickness (mm)	≤ 254	6	3.960	0.049	3.924
	>254	13			
Min temperature (°C)	≤ 20	9	0.888	0.348	3.924
	>20	10			
Climatic Zone	Moderate	5	2.106	0.126	3.077
	Warm	9			
	Cold	5			

Table 6 summarizes the quality of fit statistics for the calibration dataset and the verification dataset. It suggests that the validation data set has a comparable fit to the validation dataset. The quality of fit improvements resulting from the calibration are shown in Figure 4.

Table 6. Fatigue cracking calibration coefficients and fit statistics.

Group ID	Subgrade $M_r \leq 207$ MPa		Subgrade $M_r > 207$ MPa	
	Calibration (85%)	Validation (15%)	Calibration (85%)	Validation (15%)
Num. of obs.	45	12	49	10
Bias (%)	0.022499	0.042549	0.017556	0.001810
SSE	0.266667	0.051891	0.028036	0.000328
Se/Sy	0.010363	0.012557	0.010480	0.009999
Se (%)	0.076980	0.065759	0.023920	0.005723
Sy (%)	7.428012	5.236752	2.282475	0.572372
C	-3.0815		-5.3406	

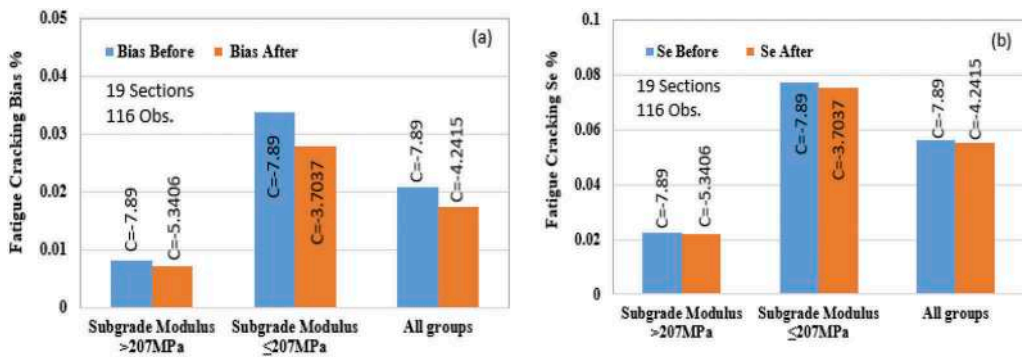


Figure 4. Fatigue cracking bias (a) and S_e (b) before and after calibration.

6.3 Transverse cracking model

ANOVA revealed that none of the factors considered (e.g., pavement type, asphalt concrete thickness, binder PG, environmental conditions, and so on) were statistically significant in predicting transverse (i.e., thermal) cracking. As a result, all 20 pavement sections with non-zero observations were analyzed as a single group. The value of the transverse cracking calibration factor β (Equ. 2) was established as 0.3663 by fitting a curve to the back-estimated life ratio $\frac{\rho}{m}$ and the observed transverse cracking data using MATLAB®. The quality of fit could be improved by the ability to adjust the life ratio $\frac{\rho}{m}$ so it is close to the desired 1.0 value when 50% of the maximum transverse cracking is achieved (i.e., 400 m/km). This was not always the case however, suggesting the need to revise the transverse cracking model. The fitted β value resulted in significant reductions in bias and S_e as shown in Figure 5.

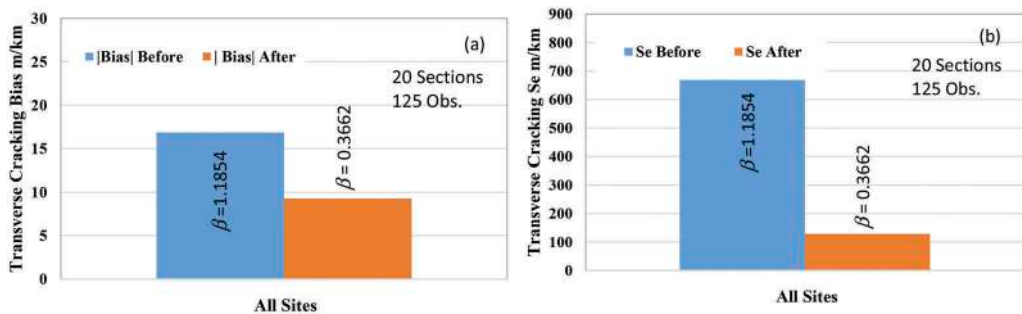


Figure 5. Transverse cracking bias (a) and S_e (b) before and after calibration.

7 CONCLUSIONS

- ANOVA allows establishing pavement subgroups with similar prediction error characteristics by pavement distress type. The corresponding calibration factors by subgroup yield more accurate predictions (i.e., reduced bias and standard error) than those obtained for all subgroups combined.
- Closed-form calibration was feasible, where calibration factors weigh linearly the mechanistic damage predictions. This was the case for the TxME rutting and fatigue cracking models. This approach established statistically the relative contribution of the plastic deformation of individual layers to the total pavement surface rutting.

- Calibration of the fatigue cracking model resulted in an overall reduction in bias and S_e by 16% and 2%, respectively compared to those estimated with the original default factors.
- Calibration of the transverse cracking model resulted in an overall reduction in S_e by 62% but an increase in bias by 75% compared to the values estimated with the original default factors.

REFERENCES

- AASHTO, Mechanistic-Empirical Pavement Design Guide-A Manual of Practice, American Association of State Highway and Transportation Officials, 3rd Edition, August 2020.
- Ceylan, H., Kim, S., Gopalakrishnan, K., & Ma, D. (2013). Iowa calibration of MEPDG performance prediction models (InTrans Project 11-401). Ames, IA: Iowa State University.
- Darter, M. I., Von Quintus, H., Bhattacharya, B. B., and Mallela, J. (2014). Calibration and implementation of the AASHTO mechanistic-empirical pavement design guide in Arizona (No. FHWA-AZ-14-606). Arizona. Dept. of Transportation. Research Center.
- Kim, Y. R., Jadoun F. M., Hou T., and Muthadi N. (2011), Local Calibration of the PMEDG for Flexible Pavement Design, Final Report for Project FHWA\NC\2007-07.
- Masad, A.E, E. Alrashydah and, A.T. Papagiannakis (2021), Preliminary Calibration and Validation of the Texas Mechanistic-Empirical Flexible Pavement Design, International Journal of Pavement Engineering, Taylor & Francis, May 20 2021 p. 1–13.
- Papagiannakis, A. T., Masad A. E., Alrashydah, E., Von Quintus, H. and Bink, W. (2020). Calibration and Validation of Flexible Pavement M-E Design Using Texas Data, Project 46-8MTIA007 Final Report.
- Von Quintus, H., Darter M.I., Bhattacharya B.B. and Titus-Glover, L. (2015). Implementation and calibration of the PMEDG in Georgia, Final Report FHWA/GA-014-11-17.
- Walubita, L. F., Hassan, R., Lee, S. I., Faruk, A. N., Flores, M., Scullion, T., . . . & Nazarian, S. (2014). Data collection and population of the database (The DSS and RDSSP) (No. 0-6658). Texas A&M Transportation Institute.
- Zhou, F., Fernando, E. and Scullion, T. (2010). Development, Calibration, and Validation of Performance Prediction Models for the Texas M-E Flexible Pavement Design System Technical Report: 0-5798-2, Texas Transportation Institute, College Station, TX 77843–315.

Design of full depth reclamation of low volume roads

S. Agardh, C. Ossbahr & V. Perez

Ramboll, Sweden

ABSTRACT: Old low volume roads are often made from local materials. Therefore, the gradation curve of the unbound materials in the pavement is often not according to new regulations, which often results in low bearing capacity. One way to improve the quality of existing materials, and thereby save natural resources, is to do a Full Depth Reclamation with mechanical stabilization.

The objectives of this project were to develop a tool to design amount and type of added material for the mechanical stabilization and to find a method to evaluate the effect on bearing capacity and material quality of a Full Depth Reclamation with mechanical stabilization. Theoretically it should be possible to calculate the resulting gradation curve after the rehabilitation based on the gradation curves of existing and added materials. In practice it is hard to predict the gradation curve of crushed asphalt. Also some crushing, especially of larger particles, can occur during the milling process that will affect the resulting gradation curve. Suggestions on how to deal with this are presented.

Full Depth Reclamation at four different low volume roads in Sweden has been studied where gradation curves before and after the reclamation has been compared. FWD measurements has also been carried out. The study showed that, according to the FWD measurements, there were no immediate improvement in bearing capacity. However, the variance of bearing capacity was much smaller after the maintenance. On one of the roads new FWD measurements were done after two years. Then the bearing capacity had improved considerably.

Keywords: Full Depth Reclamation, Gradation curve, Bearing capacity, Mechanical stabilization

1 INTRODUCTION

Full Depth Reclamation (FDR) is a technique where the full thickness of the bound materials is milled and mixed with the underlying material and often with some added material for stabilization. Three different kinds of stabilization are often used (Nielsen, o.a., 2007):

- Unstabilized
- Mechanical stabilization
- Chemical stabilization
- Bituminous stabilization

The stabilization methods can also be combined. The most used stabilizers are bitumen and cement (Xiao, Yao, Wang, Li, & Amirkhani, 2018) and a lot of research has been done on those stabilizers. This paper only deals with the less common mechanically stabilized FDR, where crushed aggregate is added to stabilize the existing base course, and no chemical or bituminous materials are added.

1.1 Objective

The main objective of this project was to develop a method to evaluate the effect of FDR while planning maintenance of low volume roads and to make a tool for the design of mechanical stabilization. The parts presented in this paper deal with prediction of the gradation curve of the finished material and effect of the FDR on bearing capacity.

2 MECHANICAL STABILIZATION

The purpose of FDR is to create an unbound base layer of good quality based on existing road materials. By using existing material transports are minimized which will save both costs and environment (Bemanian, Polish, & Maurer, 2006). Mechanical stabilization means that only unbound granular materials are added to improve the existing material. In this study only crushed rock is added as stabilizer, but other materials, e.g. crushed concrete, crushed asphalt or foam glass can also be used (Nielsen, o.a., 2007).

The FDR can be done by either one or two millings. With two millings first the existing asphalt is milled together with existing base course, then the stabilizer material is placed on the road before a second milling. With one milling the stabilizer material is placed on the asphalt surface and is then milled together with the asphalt and base course.

Mechanically stabilized FDR is most suitable on roads with aged asphalt layers (Nielsen, o. a., 2007) where structural capacity needs to be improved (Morian, Solaimanian, Scheetz, & Jahangirnejad, 2012). A new asphalt layer on a cracked asphalt will often soon result in cracks in the new layer. Then it's often better to mill the existing asphalt before the new layer is put on (Nielsen, o.a., 2007). Even if the existing base layer is of poor quality with, for instance, too much fine material, the result of the FDR can be quite good with a properly done mix design (Bladh, 2014).

To be able to make a good design of the stabilization it is important to know the properties of the existing materials in the road. Tests that often are recommended are sieve analysis, Plasticity Index (PI), maximum dry density, sand equivalence and optimum moisture content (Nielsen, o.a., 2007). Some of these tests are mainly for designing chemical stabilization. For mechanical stabilization information about particle sizes is most important.

An important factor in the obtained material from the FDR is the crushed asphalt. With thick asphalt the teeth on the milling machine mill will wear faster. Therefore, FDR is usually only used on roads with relatively thin asphalt layers since. According to (Taha, Ali, Basma, & Al-Turk, 1999) the CBR decrease with higher amount of RAP in the mix, with CBR 65 with 20% RAP to CBR 27 with 80% RAP. Similar results were obtained by (Cooley, 2005), but when the stiffness was measured in that study the lowest stiffness was obtained with 25% RAP.

How many material tests that needs to be taken from a road varies with the homogeneity of the road. Swedish Transport Administration recommends one test for each km (Trafikverket, 2010). Another example of recommendations is one test each 400 m or one test each 1600 m on homogenous roads (New York Department of Transportation, 2015). In addition to the tests taken before it can be a good idea to continuously make new material tests during construction to be able to adjust the material design.

3 METHOD

3.1 Studied road segments

For the project 12 different road segments in different parts of Sweden where FDR had been performed were studied. On most of the segments not enough measurements of good quality had been performed during construction to evaluate the result in a good way. The project had limited possibilities to make completing measurements and due to the time schedule of the project it was not possible to do any extra measurements before the FDR was performed.

Therefore, only road segments where a thorough investigation already had been done, especially before the measure, could be chosen for this project.

Four different segments in different parts of Sweden were found that could be used. The length of the segments varied from 6 to 30 km

Segment A is a small road in the middle of Sweden trafficked by approximately 200 vehicles per day. FDR with mechanical stabilization with particle size 16/32 was done. FWD measurements were performed both before and after the FDR.

Segment B is trafficked by approximately 300 vehicles per day. The FDR was done in two steps where first the asphalt layer was crushed together with underlying base course. Then, in the second step, mechanical stabilization was done with particle size 16/32. This road didn't get a new bituminous layer but was transformed into a gravel road. FWD measurements were performed both before FDR and on the gravel surface course after the measure. Sieve analysis of the materials was done before FDR and after each milling.

Segment C is a larger road than the others with a traffic of approximately 1500 vehicles per day. Unlike the other roads it has a known history and was built with modern material specifications. This means that the conditions were more homogenous than at the other segments. Sieve analysis was done both before and after milling.

Segment D is trafficked by approximately 300 vehicles per day. After FDR the new surface layer consists of an open graded aggregate where bitumen emulsion was poured into the voids (grouted macadam). Both FWD measurements and sieve analysis were done before and after the FDR.

Table 1. Summary of the road segments used in this study.

Road segment	Measure	FWD	Sieve analysis
A	Milled once with added macadam. New bituminous layer	Before, after and after 2 years	-
B	Milled twice: 1. Asphalt and base course 2. With added macadam. New gravel surface course	Before and after	Before, after first milling and after second milling
C	Milled once with added macadam. New bituminous layer	-	Before and after
D	Milled once with added macadam. New layer with penetration macadam	Before and after	Before and after

For most of the tests the samples for gradation curves were taken on different locations before and after the FDR, but in total 30 material tests were supposed to be carried out at the same spot.

3.2 Bearing capacity

On three of the studied segments Falling Weight Deflectometer (FWD) measurements has been carried out both before and after the FDR. Calculating bearing capacity from FWD measurements can be done in many ways. In the Swedish regulations for FWD investigation (Trafikverket, 2020) a Bearing capacity Index (BI) is used. It is based on calculated asphalt strain:

$$BI = \frac{1000}{\varepsilon_a} \quad (1)$$

The asphalt strain is calculated with:

$$\varepsilon_a = 37.4 + 0.988D_0 - 0.553D_{300} - 0.502D_{600} \quad (2)$$

Where

D_i = deflection at distance i mm from load centre

4 RESULTS BEARING CAPACITY

This chapter is based on FWD measurements from segments A, B and D. On these segments, FWD measurements were carried out both before and after FDR. On segment A new measurements were also carried out two years after the FDR.

On segment B no new asphalt layer was laid after the FDR. Instead a gravel surface course was used. Therefore, no Bearing capacity Index (BI) could be calculated for this segment. Instead, the surface modulus is presented in Table 2.

Table 2. Bearing capacity Index (BI) before and after FDR. For segment B surface modulus (MPa) is presented.

	Segment A before	After	Segment D before	after	Segment B Before	after
median	2,17	1,98	2,95	2,95	236	222
95-percentile	1,44	1,61	1,73	2,27	153	141
COV	18 %	10 %	30 %	16 %	28 %	43 %

As can be seen in Table 2 the median bearing capacity didn't increase for any of the three segments. It seems that the bearing capacity will decrease because of the FDR.

On segments A and D the variation of the bearing capacity decreased and the road became more homogenous. An example of that is shown in Figure 3.

For segment B the variation increased. One possible reason for that could be that before the FDR the road had an asphalt surface course and after the FDR there was a gravel surface course. It is possible that the variation in an unbound material often is larger than in a bound material.

In the measurement of segment A after two years the median BI had increased to 2,52. That means an increase of 25%. The variation was still almost the same as directly after the FDR (COV=11%).

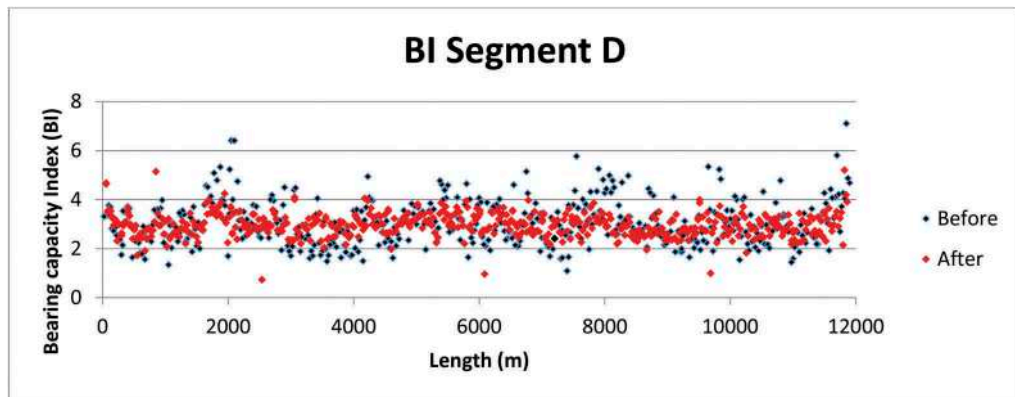


Figure 1. Bearing capacity measurements for segment D before and after FDR.

5 RESULTS GRADATION CURVE

This chapter is based on measurements from segments B, C and D.

5.1 *Crushing of asphalt during milling*

If the old pavement, down to milling depth, consists of an asphalt layer and a base course, and macadam is added for the FDR, the gradation curve after the FDR can, theoretically, be calculated with

$$K(after) = a_{old\ BC} \cdot K(oldBC) + a_{crushed\ asphalt} \cdot K(crushed\ asphalt) + a_{macadam} \cdot K(macadam) \quad (3)$$

Where

$K(i)$ = Gradation curve fore layer i

a_i = proportion of layer i

This equation is often used to determine amount and type of added macadam. A problem is that it is hard to predict the gradation curve of the crushed asphalt. For segments B, C and D sieve analysis has been done both before and after the milling of the asphalt layer. The gradation curves of the old base course, the added macadam and the final results are known for these segments. The only unknown part of the equation is then the gradation curve for the crushed asphalt. Therefore, a theoretic gradation curve for the crushed asphalt can be calculated.

The theoretic gradation curve for the crushed asphalt was calculated for all sections where test samples have been taken both before and after milling (total number of sections: 30). For many sections the theoretical gradation curve was unrealistic with values below 0%, values above 100% and curve tilting in wrong direction. Even though the tests before and after FDR are supposed to be taken at the same spot, in reality the difference can probably be a few meters. In addition, the material is moving during the milling process, so the samples are not taken from the exactly same material. Since the asphalt layer in most cases is only a small part of the total milled material (around 25%) a small error in the other materials will lead to a large error in the calculated curve for the asphalt material. The average theoretical asphalt gradation curve for the three road segments is shown in Figure 2.

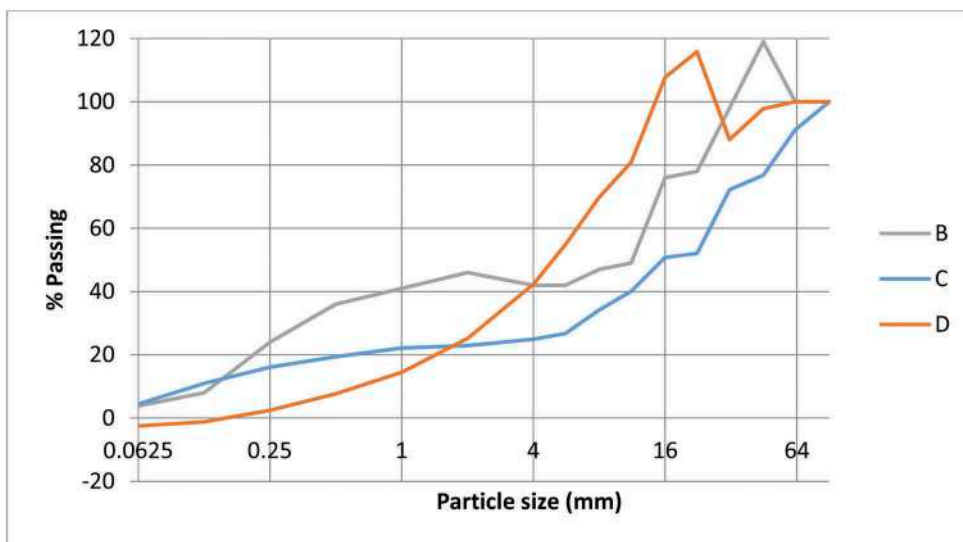


Figure 2. Average theoretical gradation curve for the crushed asphalt for the different segments. Note that there are values both below 0 and above 100.

Since the variation in calculated gradation curve for the crushed asphalt is large, it is hard to determine a general gradation curve. It seems though that not much material is crushed to sizes below 0.063 mm, with an average value of 1.6%.

5.2 Crushing of aggregate during milling

For segment B the FDR was done in two steps where the first step was milling of asphalt and base course. In the second step macadam was added. This means that the second milling is just blending of materials. With Equation 3 the theoretic gradation curve after the second milling can be calculated. The calculated gradation curve together with the measured gradation curve after milling can be seen in Figure 3.

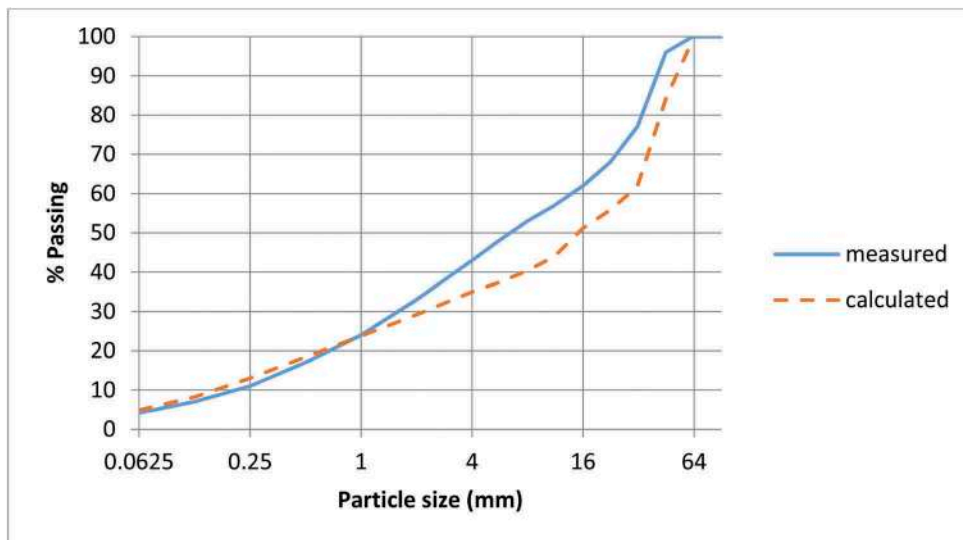


Figure 3. Measured and calculated gradation curve after second milling on segment B.

For particles smaller than 1 mm the calculation seems to match the calculated values, but for the rest of the curve it seems as the real material has more fine particles and less coarser particles than expected. The reason for this is probably crushing of the larger particles. It seems as some of the large particles (>8 mm) has been crushed to size 1-8 mm.

6 RECOMMENDATION ON DESIGN OF MECHANICAL STABILIZATION

The most important part in designing the mechanical stabilization is to determine amount and type of material to use for the stabilization. The base for those decisions can be calculations with Equation 3. However, the results in chapter 5 shows two problems doing that:

- It is hard to determine the gradation curve of the crushed asphalt
- Some particles will be crushed during the milling.

Often the material design is done without taking these problems into consideration and still get reasonable results (Bladh, 2014). For the studied segments the difference between calculated and measured gradation curve with this method is shown in Figure 4. The result seems to be good for smaller particle sizes, but not for larger particles.

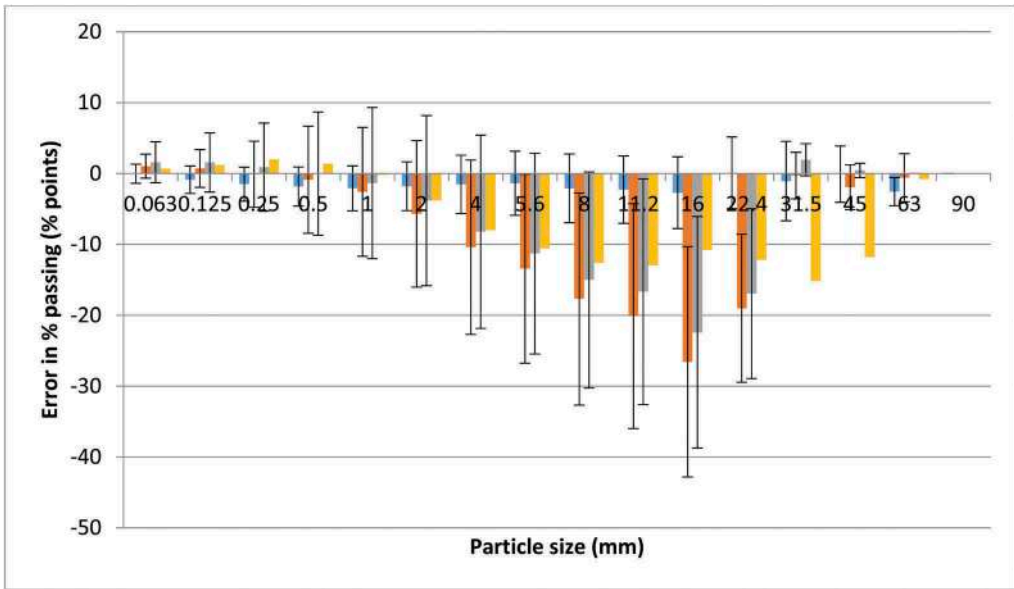


Figure 4. Difference between calculated and measured gradation curve after FDR for the different segments. The error bars show one standard deviation.

The theoretical gradation curves obtained for the crushed asphalt in this project show a large variation. A possible reason for this can be variation in asphalt types, asphalt quality and/or asphalt thickness along the segments (Haque, 2014). The type and condition of the milling machine can also affect the result of the milling (Sebesta & Scullion, 2016). Therefore, it is hard to give recommendations of the best way to deal with this. Based on average values from the calculations in chapter 5.1 a gradation curve according to Table 3 is suggested. This curve needs further validation. It is possible that the curve should be based on type of asphalt, and maybe asphalt thickness, and not just one curve for all types.

Table 3. Recommended grading curve for the crushed asphalt.

Sieve size (mm)	Passing (%)
0.063	0
0.125	1
0.25	6
0.5	11
1	20
2	33
4	52
5.6	64
8	82
11.2	96
16	100

Dealing with crushing of the unbound particles can be done in many ways. A simple way to do so is to just increase the calculated passing percentage with a certain number. According to this study it seems that crushing only occur for larger particles. Therefore, an increase,

according to the numbers in Table 4, is suggested. This is mostly based on measurements from segment B. These numbers need more validation.

Table 4. Recommendations on increasing of calculated passing % because of crushing of particles during milling.

Sieve size (mm)	Increase in percentage points
2	5
4	10
5.6	10
8	10
11.2	10
16	10
22	10
32	5

Some samples from Segments A, B and C were saved for validation of the suggested method for the material design of the mechanical stabilization. Calculations of the gradation curve were made both with and without taking gradation curve of crushed asphalt and crushing into consideration (Table 5).

Table 5. Difference between measured and calculated gradation curves after FDR (percentage points).

	Segment A	Segment B	Segment C
RMS with Equation 3	1.6	11.5	9.7
RMS with Equation 3 and recommendations above	5.4	2.6	2.2

For two of the segments the improvement was quite big, but for the samples from segment A the RMS actually increased when the gradation of crushed asphalt and crushing of particles was taken into consideration.

7 DISCUSSION

According to this study there doesn't seem to be an immediate increase of the bearing capacity of the road after an FDR with mechanical stabilization. However there seems to be an improved bearing capacity with time. On one of the segments a follow up measurement of bearing capacity was done after 2 years whereas the measured bearing capacity index had increased with 25%. An evaluation of the effect of the FDR on bearing capacity should therefore probably not be done immediately after the measure. The effect of the FDR can probably better be seen after a few years.

In this paper recommendations about the material design of a mechanical stabilization is shown. The study was performed only on real roads. No special test setup was done to get controlled circumstances. To be able to make a solid study some demands on the measurements done on the segments had to be made. This narrowed down the number of road segments in the study. The recommendations have only been validated on samples from the same segments that were used to obtain the recommendations. Therefore, further validation is needed.

ACKNOWLEDGEMENTS

This project was funded by the Swedish Transport Administration. Special thanks to Agne Gunnarsson for all discussions during the project and for the help of both finding suitable study road segments and to retrieve data from them.

REFERENCES

- Bemarian, S., Polish, P., & Maurer, G. (2006). *State-of-the-Practice on CIR and FDR projects by Nevada DOT*. Transportation Research Board.
- Bladh, A. (2014). *Infräsning - En metod för att förstärka vägar med bärighetsproblem*. Lund: Lunds universitet.
- Cooley, D. A. (2005). *Effects of Reclaimed Asphalt Pavement on Mechanical Properties of Base Materials*. Brigham Young University.
- Haque, R. (2014). *Thickness Variability Effects on The Properties of Unstabilized Full Depth Reclaimed Aggregates*. Halifax, Nova Scotia: Dalhousie University.
- Morian, D. A., Solaimanian, M., Scheetz, B., & Jahangirnejad, S. (2012). *Developing Standards and Specification for Full Depth Pavement Reclamation*. Harrisburg, PA: The Pennsylvania Department of Transportation.
- New York Department of Transportation. (2015). *Design and Construction Guidelines for Full Depth Reclamation of Asphalt Pavements*. New York: New York Department of Transportation.
- Nielsen, N., Hauser, B., Preber, T., Sebaaly, P., Johnston, D., Huft, D., & Bang, S. (2007). *Quality Base Material Produced Using Full Depth Reclamation on Existing Asphalt Pavement Structure*. Washington, DC: Federal Highway Administration.
- Portland Cement Association. (2005). Full-Depth Reclamation: Recycling Roads Saves Money and natural Resources. Portland Cement Association.
- Sebesta, S., & Scullion, T. (den 1 February 2016). In-depth reclamation? - States need to do more to assure FDR quality. *Roads & Bridges*, ss. 38–41.
- Taha, R., Ali, G., Basma, A., & Al-Turk, O. (1999). Evaluation of Reclaimed Asphalt Pavement Aggregate in Road Bases and Subbases. *Journal of the Transportation Research Board*, 1652, 264–269.
- Tosovic, S., & Rosic, B. (2010). *Deep cold recycling procedure for road rehabilitation*. The Highway Institute, Republic of Serbia.
- Trafikverket. (2010). *Förstärkning av vägar - infräsning av makadam i befintligt bärlager*. Borlänge: Trafikverket.
- Trafikverket. (2020). *Utvärdering av vägkonstruktioners bärighet med fallviktsapparat*. Trafikverket.
- Xiao, F., Yao, S., Wang, J., Li, X., & Amirhanian, S. (2018). A literature review on cold recycling technology of asphalt pavement. *Construction and Building Materials*, 579–604.



Taylor & Francis

Taylor & Francis Group

<http://taylorandfrancis.com>

*Structural evaluation and performance
prediction for pavements and tracks*



Taylor & Francis

Taylor & Francis Group

<http://taylorandfrancis.com>

PEHKO-project – using bearing capacity analysis as a tool for proactive maintenance of paved roads

T. Herronen, A. Hiekkalahti, A. Matintupa, T. Saarenketo & P. Varin
Roadscanners Oy, Rovaniemi, Finland

ABSTRACT: Challenges with paved Finnish public roads due to declines in budgets has caused an increase in pavement deterioration rates and budget backlog. PEHKO-project was established to solve this problem using innovative road asset management concepts. The idea of the project is to improve maintenance and strengthening practices used on the Finnish paved road network in such a way that productivity increases, road condition stays at its current level or even improves with lowered annual costs. This goal will be achieved by focusing on three targets: 1) Improving daily maintenance, 2) utilizing new non-destructive testing technologies, such as GPR, TSD, lidar and 3D-accelerometers in the diagnostics and 3) changing maintenance policies from reactive to proactive. Annually, PEHKO-project collects high accuracy rutting information with lidar and calculates exact rut growth rates. When this data is combined with GPR data and bearing capacity analysis, it is possible to determine root causes of rut growth and design rehabilitation operations in the most cost-effective manner. Additionally, through the combination of TSD deflection data and GPR pavement thickness data, road sections with critical pavement strain can be located and repaired before they fail and lifetime of the road increases significantly at lesser costs. After 2021, PEHKO-project has been underway for six years and the preliminary results are very promising. Right from the start it was possible to identify the weakest links that were cutting down pavement lifetime and increasing lifecycle costs. These critical sections covered only 10-20% of the overall length, but their impact on annual paving costs was up to 50%. Deficiencies were found in pavement structures and daily maintenance operations. Structural problems are related to too thin pavements and to the effects of heavy trucks on road sections with soft subgrade soils. Maintenance deficiencies were mainly associated with poor drainage and inadequate winter maintenance.

Keywords: Pavement, daily maintenance, savings, life cycle costs, proactive maintenance

1 GENERAL

Since 2015 Roadscanners has been testing a new road asset management concept in Finland in three road districts: Lapland and Central-Finland from 2015 and Uusimaa from 2018 (Figure 1). Based on the findings and recommendations of the EU funded ROADDEX-project, the idea and goal for the PEHKO-project, has been to improve the practices and policies in paved road maintenance and management (Saarenketo et al. 2019). The PEHKO-project's goal is to enhance the productivity of road maintenance operations and processes and to improve the condition of the paved road network or keep them at the same condition level with less resources. This goal will be achieved by focusing on three targets:

- 1) Improving the daily maintenance, especially drainage and winter maintenance standards for paved roads (Matintupa et al. 2020). This will lead to increased pavement lifetimes and lower annual paving costs.
- 2) Applying new non-destructive testing technologies, such as GPR, TSD, Lidar and 3D accelerometers, in the diagnostics of paved roads. These techniques allow engineers to focus their rehabilitation and maintenance measures exactly on the problem sections and address the root cause of the problems rather than just treating the symptoms– and waiting for the problem to reappear in the same location.
- 3) Changing maintenance policies from reactive to proactive maintenance. This will mean that maintenance crews fix the potential problem sections before serious pavement damages appear.

In the PEHKO project Roadscanners has been responsible for the project design, data collection and analysis as well as making recommendations for maintenance measures and pavement program and design.



Figure 1. Pilot areas of PEHKO-project.

Now when the PEHKO project has been under way for six years in the first two areas, the preliminary results of the project have been promising. Right from the start it was possible to identify the weakest links that were reducing pavement lifetime and increasing lifecycle costs. These critical sections, spread all over the network, covered only 10-20% of the length, but impacting the annual paving costs up to 50%. Deficiencies were found in both in pavement structures and daily maintenance operations. Structural problems could be addressed to too thin pavements or to the effects of new heavy trucks on road sections with soft subgrade soils. Maintenance deficiencies were mainly associated with poor drainage and inadequate winter maintenance (Tapio et al. 2016).

2 DATA COLLECTION AND ANALYSIS PRINCIPLES

Collecting the functional and structural data from the whole PEHKO road network is made by using GPR, lidar, 3D accelerometer, digital videos, and Traffic Speed Deflectometer (TSD) technology. Everything is bound together with high accuracy positioning. Data collection is carried out with Road Doctor Survey Van (RDSV) at one drive (Figure 2), except TSD data, which is collected with specific test truck. Traffic Speed Deflectometer technique (Figure 3) uses laser doppler velocimeters to measure pavement response of a 10-ton trailer axle at a traffic speed of 5 – 80 km/h. From the deflection velocity the deflection under the loading wheel is calculated. Average deflections are presented and analyzed at specified intervals and

in this project 10m interval was used. The latest TSD versions enable deflection measurements also behind the loading wheel, which allows evaluation if the pavement response is elastic or visco-elastic. The benefits of TSD, compared to FWD systems, is that it collects data in traffic speed without any disruption to traffic flow and it simulates the impact of a real truck tire. The dense point interval allows also precise diagnostics. TSD has proven to be very effective in network level evaluations.

Ground Penetrating Radar (GPR) is a non-destructive survey method that can be used in surveying roads, railways, bridges, airports, environmental objects, etc. Its main advantage is the continuous profile over the road structures and subgrade soils. It is fast and cost-effective, and it is becoming increasingly important survey tool especially on the structural evaluation of low volume roads. A further advantage in road surveys is that it is not intrusive to other traffic using the road (Saarenketo 2016).

Lidar or laser scanning is a surface mapping technique where the distance of a point is calculated from the travel time of a laser beam from the laser scanner to the target and back. When the laser beam angle is known, and beams are sent out in different directions from a moving vehicle with a known position, it is possible to make a 3D surface image, or point cloud, from the road and its surroundings. In the point cloud with millions of points, every point has an x, y and z coordinate and reflection, or remission, characteristics (Saarenketo et al. 2012).

Accelerometer is a device that measures acceleration forces in 3D. Modern measurement units can be combined with gyroscopes and other sensors to offer better accuracy and measurement possibilities. When a vehicle drives over a road with roughness, the accelerations to the car tire are recorded by the 3D accelerometer assembled to the rear axle of the survey vehicle.

Annually high accuracy rutting information is collected in PEHKO-project and rut growth rates are calculated. When this data is combined with GPR data and bearing capacity analysis, it is possible to determine root causes of rut growth and design rehabilitation operations in the most cost-effective manner (Herronen et al. 2015). Additionally, through the combination of TSD deflection data and GPR pavement thickness, road sections with critical pavement strain can be found and repaired before they fail and lifetime of the road increases significantly at a lesser cost.



Figure 2. Roadscanners Road Doctor Survey Van. GPR antennas mounted in the front, lidar system, IMU, GPS and the cameras on the roof.



Figure 3. Traffic speed deflectometer truck, IBDIM Poland.

3 PRINCIPLES OF BEARING CAPACITY DATA ANALYSIS

In pavement design or programming the key factor is return on capital with pavement investments over a long term. General trend is moving towards thicker pavements, because trucks are getting heavier due to environmental and economic pressure. Also, super single tires, and higher tire pressures are used to reduce emissions and costs. In renovation, design measures will be focused on much shorter sections than earlier; the goal is to build more homogenous pavements against pavement fatigue and through that, achieve longer lifetimes. The root cause of the problem will always be fixed instead of fixing the symptoms (Saarenketo 2017).

Effect on daily maintenance consist of improvement of problematic drainage sections and ensuring that they remain in good condition, because dry road structure is much stronger than wet (Berntsen and Saarenketo 2005). Laser scanner data can be utilized to monitor drainage in an objective way, for example measuring the level of the ditch bottom or mapping verges. Drainage around private access road junctions has been recognized to be big problem and improvement in their maintenance standards has been important to ensure bearing capacity of the road stays in good level also on these spots (Aho and Saarenketo 2006). New winter maintenance standards have also been implemented because of need for removal of snow on road shoulders early enough (rather too early than too late) to ensure working drainage when the snow is melting.

In PEHKO-project the basic analysis of GPR and TSD data consist of calculating following parameters: BCI (Base Curvature Index), SCI (Surface Curvature Index), horizontal strain of pavement bottom, subgrade moduli values, thickness of pavement and total thickness of road structure. Surface Curvature Index (SCI) and Base Curvature Index (BCI) can be very useful in determining rutting modes (Dawson and Kolisoja 2004). SCI-value is calculated by subtracting the d_{200} deflection value (or in some countries the d_{300} mm) from the d_0 deflection value. This parameter gives information of stiffness of pavement and top part of unbound base course and through this it is indicative for Mode 1 rutting, where the deformation takes place in the asphalt and/or unbound base course. BCI-value is calculated by subtracting the d_{1200} deflection value from the d_{900} value and is an excellent indicator of how a road structure spreads wheel load over weak subgrade. If the BCI is high, it predicts either Mode 2 rutting, where the deformation takes place in pavement structure/subgrade interface. It can indicate also pumping problems (ground water is pumped into the road structure). One of the most important and useful parameters in proactive maintenance is (horizontal) strain of pavement bottom. This

strain value is calculated from FWD or TSD data together with GPR data. On good road sections strains will stay constant at a level of 200 or less, but in sections with deformation problems and pavement damage these strains can increase to a level of 300 – 400 microstrain and more, as the road approaches the end of its working lifetime (Saarenketo et al. 2020).

4 THE PAVEMENT STRAIN VALUE

4.1 Calculation and principles of pavement strain value

Estimation of pavement strain can be calculated from the FWD or TSD measurements using formulas developed by Swedish National Road Administration (Trafikverket). Pavement strain without temperature correction is calculated using following formula:

$$\varepsilon_a = 37,4 + 0,988*d_0 - 0,553 * d_{300} - 0,502 * d_{600}$$

where

d_r = deflection at a distance of r [mm] in front of the load point

Bitumen in pavement is viscoelastic and the transformations in pavement therefore depend on the temperature. Temperature correction using the Swedish formula is done to a standard temperature of +10 °C. Temperature correction is done using following formula:

$$\varepsilon_{a,10} = \frac{\varepsilon_{a,T}}{\left(\frac{T}{10}\right)^{3,08*10^{-8}*h_1^2*d_0}}$$

where

T = pavement temperature during measurement

h = pavement thickness [mm]

4.2 The use of pavement strain value in analysis

In PEHKO-project the goal of using pavement strain values is to find road sections that are approaching the end of their lifetime. These sections have not yet started to deteriorate quickly and have not developed cracking that will increase the distress rate of the road. If this kind of sections can be identified and repaved before cracking is visible, new pavement will increase lifetime significantly more compared to paving over a cracked surface.

Figure 4 shows the basic relationship between pavement strain and number of heavy axles that the road has left in its lifetime. As the pavement strains get higher than ~300 μ strain, the fatigue and cracking of the road start to increase rapidly and fairly small number of heavy axle passes leads to high increase in pavement strain and further to macrocracking.

The strain values depend also on the type of the bitumen used. A generalized classification of pavement strain used in PEHKO-project is presented in Table 1.

Even short section with high risk of rapid rut growth and pavement distress can be identified with combination of TSD and GPR. In Figure 5 the pavement thickness compared to TSD strain values the correlation can be clearly seen.

4.3 Indications of strain values

TSD-measurements done in PEHKO areas 2015 and 2020 have given good, measured information about the effect of different paving measures to the strain values and the expected lifetime they predict. Figure 6 shows that the remix overlays (REM, UREM, REMO), which do not increase or only slightly increase pavement thickness, do not also decrease the pavement strain values as much as the other pavement types, which also increase pavement thickness.

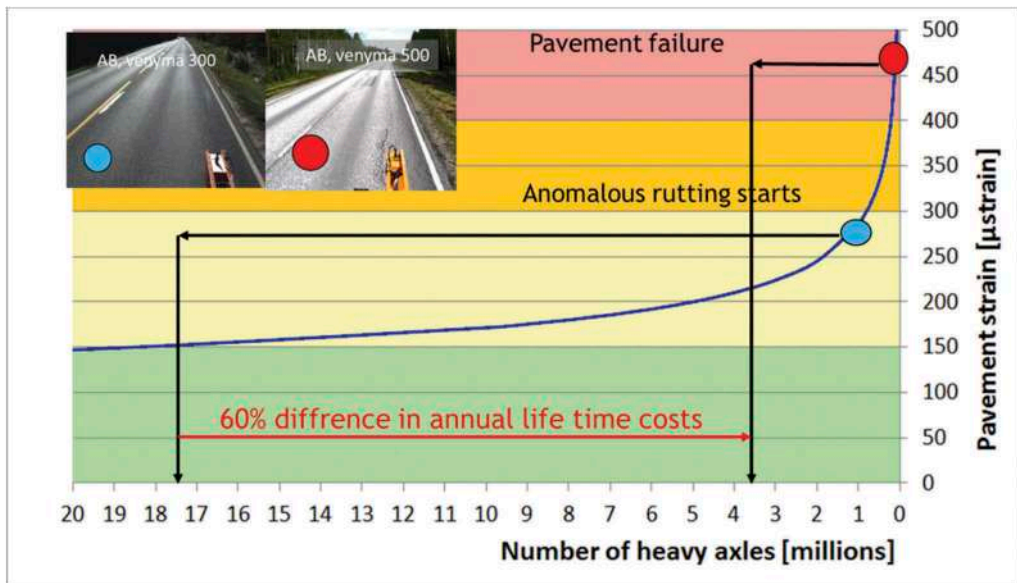


Figure 4. Principled relationship between pavement strain and number of heavy axes left in the road lifetime according to Finnish AC fatigue model. Red and blue dot represent the two measured pavement strain examples shown in the photos. Arrows represent the increase in lifetime, if the same type of paving is done in both scenarios.

Table 1. Pavement classification based on strain values for soft and hard bitumen used in PEHKO-project in Finland.

	Hard bitumen	Soft bitumen
<i>Excellent</i>	<100	<200
<i>Good</i>	100–200	200–300
<i>Satisfactory</i>	200–300	300–450
<i>Alarming</i>	300–450	450–600
<i>Damaging</i>	450–600	600–800
<i>Lost</i>	>600	>800

As written above, if the pavement strain is already very high and severe distress is visible on the road, it is usually already too late to add a new overlay on top of the old pavement. In this case and if the pavement is relatively thin, mix milling of the old pavement can be a good solution to homogenize the structure before paving a new pavement. If the pavement is thick, milling or remixing before new overlay is improving the top surface integrity. Structural problems, such as problems with the soft subgrade (BCI) or overall thickness or problems with the drainage, should be also fixed.

5 BASE CURVATURE INDEX

5.1 Calculation and principles of BCI

BCI-value is a useful parameter that can be easily calculated from FWD or TSD data (Figure 7). It is calculated by subtracting the d_{1200} deflection value from the d_{900} value. Usually, no temperature correction is needed.

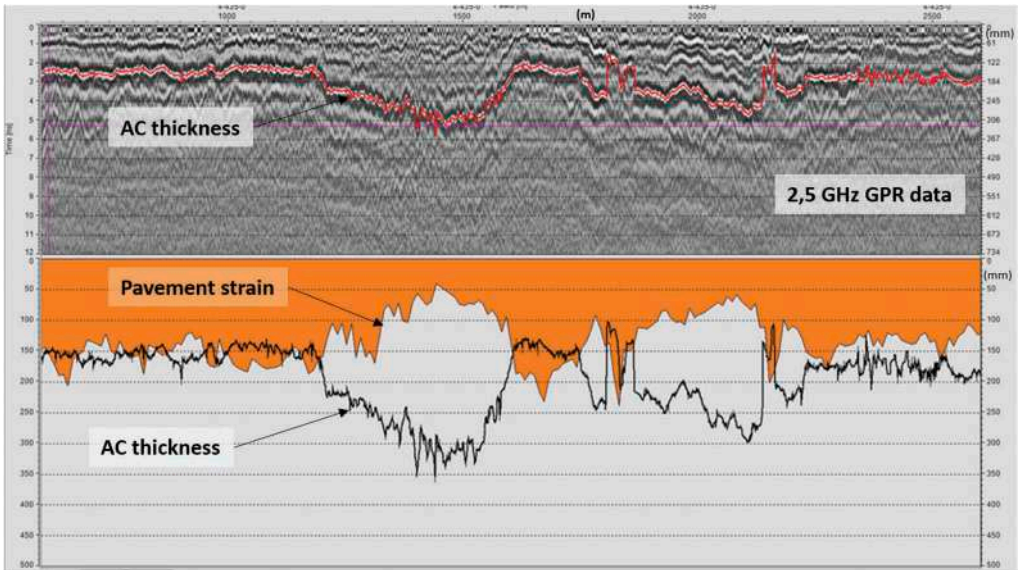


Figure 5. GPR pavement thickness and TSD strain values from a PEHKO-road. Above GPR b-scan, below TSD strain value (orange) and depth corrected pavement thickness from GPR. Correlation between two separate methods and parameters is clear.

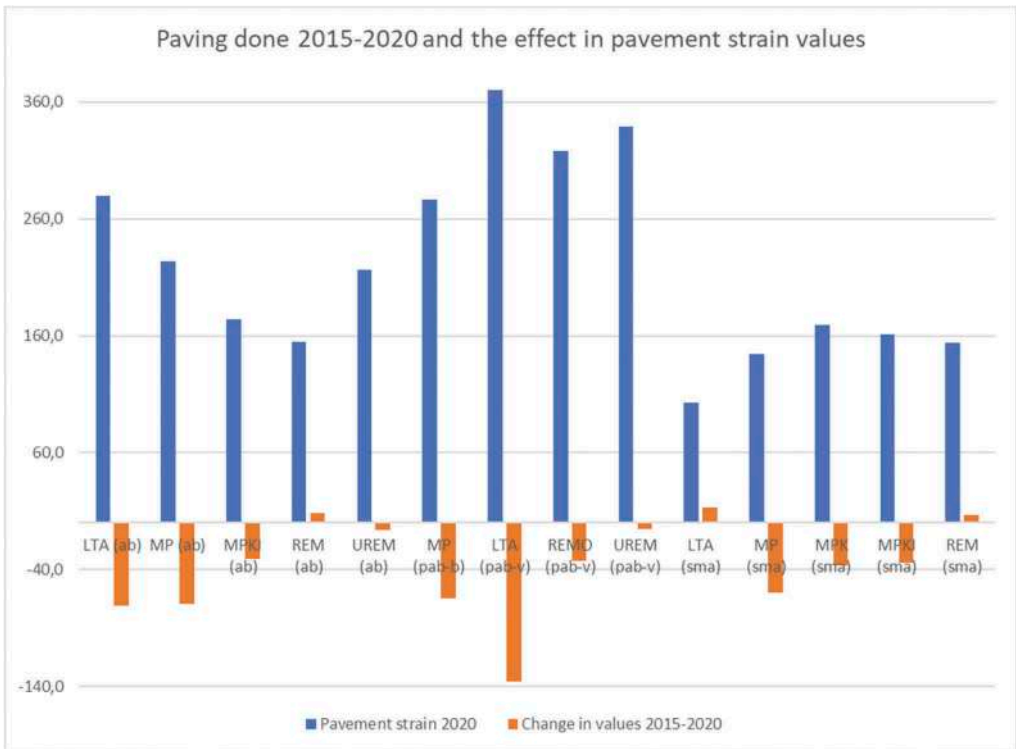


Figure 6. Division of pavement strain values on different pavement types.

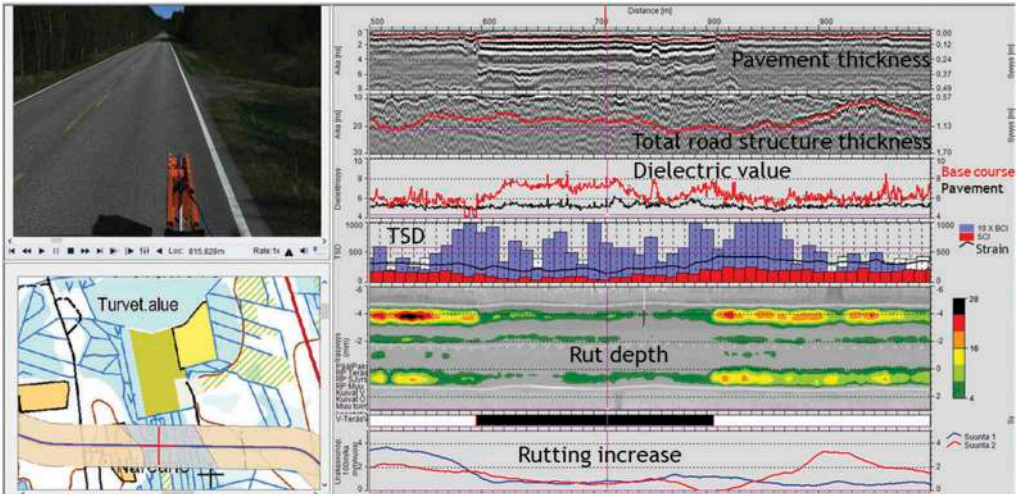


Figure 7. Example of different analyses done in Road Doctor-software. TSD-data shows that the BCI-values (blue bars in the middle show 10xBCI) are high (about 50-100). GPR data shows that the road structure has old steel net installed in at about 20cm depth in the base course between 600-800m distances. Steel net is performing very well, but outside the steel net, rutting depth map shows mode 2 rutting and edge deformations caused by the weak subgrade and the road structure not spreading the wheel load well enough.

BCI-value depends on the type of the subgrade as well as the road structure itself. The Table 2 shows the effect of subgrade on the average BCI (and SCI and strain) values in PEHKO Uusimaa area.

Table 2. Different TSD parameters on different types of subgrades. Based on subgrade map provided by Geological Survey of Finland.

Subgrade	Bedrock	Gravel	Sand	Sandy Moraine	Silt	Clay	Peat	Gyttja
BCI	21	22	24	24	27	33	50	52
SCI200	93	97	118	135	139	137	113	97
Ea10	172	171	203	227	235	229	187	187

5.2 The use of BCI in analysis

If the BCI is high, it usually indicates either Mode 2 rutting or pumping problems. Generalized classification of BCI used in PEHKO-project is presented in Table 3.

Table 3. The guidelines of BCI-values for road condition classification.

Excellent	Good	Satisfactory	Passable (potential problems)	Poor	Extremely poor
<10	10-30	30-40	40-60	>60	>80

5.3 Indications of BCI values

If high BCI-values are caused by pumping or drainage related problems, the lowered bearing capacity can possibly be fixed easily and cost effectively by improving drainage. However, many times high BCI is caused by poorly performing road structure that does not spread the wheel load well enough over a weak subgrade. Sometimes BCI can be improved simply by increasing pavement thickness, but many times the pavement has been already suffered from

cracks and roughness. It is proven also in PEHKO-project that one of the most cost-effective ways to fix soft subgrade related problems has been to install steel grid into the road structure (inside unbound base course), in depth of 20-25 cm from the surface.

6 SUMMARY AND CONCLUSIONS

During first six years of PEHKO-project, lots of different kind of research and new innovations have been tested related to improved pavement structure performance. In a long-term project it is easy to follow how the chosen solutions and innovations are performing. Information of pavement lifetime costs can be calculated and verified in real road network. If the annual maintenance costs are increasing, it is possible to recognize the critical parameters affecting that.

Bearing capacity analysis, based on TSD data supported by GPR, has been one of the key tools in making decisions related to proactive maintenance of pavements. Together with other NDT-survey data utilization makes this process even more effective. It is important to react to arising problems before they are visible by human eye. For example, strain values indicate very well the condition and state of fatigue in current pavement. However, proactive maintenance could sometimes show senseless for public audience: it can be a problem to explain to road users why good-looking roads are paved instead of clearly damaged roads.

REFERENCES

- Aho, S. and Saarenketo T., 2006. *Managing Drainage on Low Volume Roads*. Executive summary, Roadex III Project.
- Berntsen, G. and Saarenketo T., 2005. *Drainage on Low Traffic Volume Roads*. Problem description, improvement techniques and life cycle costs, Roadex II Project.
- Dawson, A. and Koliisoja, P. (2004). Permanent Deformation. ROADEX II project report.
- Herronen, T., Matintupa, A. and Saarenketo T. 2015. Experiences of Integrated Analysis of TSD, GPR and Laser Scanner Data. Proceedings of International Symposium on Non-Destructive Testing in Civil Engineering (NDT-CE) 2015.
- Matintupa A., Pyhähuhta M. and Saarenketo T., 2020. *Drainage of Low Volume Roads*. eLearning package, ROADEX Network.
- Saarenketo, T., 2016. Experiences of integrated GPR and Laser Scanner analysis – We should not only look down but also around. Proceedings of the 17th Nordic Geotechnical Meeting Challenges in Nordic Geotechnic 25th – 28th of May 2016, Reykjavik.
- Saarenketo, T. 2017. What New Technologies can Provide to Intelligent Road Asset Management. Proceedings of the 29th International Baltic Road Conference, 28-30 August 2017, Tallin.
- Saarenketo, T., Matintupa, A., Kourim, B., (2012). Experiences with New Technologies in Road Problems Diagnostics. Proceedings of EPAM 2012 Conference, Malmö, Sweden.
- Saarenketo, T., Munro, R. and Matintupa, A. 2019. PEHKO Project, Implementing recommendations for rural road asset management in Finland. Proceedings of the International Symposium on Cold Regions, ISCORD 2019. Oulu, Finland June 17- 19.
- Saarenketo T., Pyhähuhta M. and Munro R., 2020. *Permanent Deformation*. eLearning package, ROADEX Network.
- Tapio R., Lehtinen, J., Ylinampa, J. and Saarenketo, T. (2016). “PEHKO Project 2015-2025, increasing the productivity of paved road management in Finland” Proceeding of EAPA Conference, Prague 2016. Digital Object Identifier (DOI): dx.doi.org/10.14311/EE.2016.144

The influence of asphalt/base modulus ratio on strain mode reversal in flexible pavements

M. Foshee & D. Timm
Auburn University, USA

ABSTRACT: Horizontal tensile strain at the bottom of the asphalt concrete in a flexible pavement is a primary design parameter, used to predict bottom-up fatigue cracking, in most modern mechanistic-empirical thickness design approaches. Designers typically simulate static loading events using layered elastic theory to make the strain prediction which represents peak tension relative to a zero baseline level. However, in reality, dynamic loading events usually cause the pavement to experience a compressive strain inflection point prior to tensile peak strain in the direction of travel. This type of response has been shown to contribute to the initiation and propagation of transverse cracks but has yet not been fully investigated. Furthermore, in some cases, the mode will shift from predominantly tensile to predominantly compressive strain. This research utilized four instrumented full-scale flexible pavement sections at the National Center for Asphalt Technology (NCAT) Pavement Test Track to study the inflection-peak relationship and the mode reversal phenomenon. The data were collected on a weekly basis over 17 months. Eight-axle trucks traveling at 72 kph were used to induce the strain events and, though complete strain histories were gathered, the analysis focused on the mode and magnitude of the inflection point and peak strain level as the axles passed over the strain gauges. Consistent trends were found in the ratio of peak to inflection point strain levels and layered elastic analysis confirmed these findings and demonstrated the impact of layer properties on whether the strain was tensile or compressive.

Keywords: asphalt, strain, instrumentation

1 INTRODUCTION

Pavements are often instrumented at accelerated pavement test facilities to directly measure critical pavement responses to improve the fundamental understanding of structural responses to external loadings. In flexible pavement experiments, asphalt strain gauges (ASGs) are usually placed at the bottom of the asphalt concrete (AC) to measure tensile strains induced through bending action under loading. These strain events, whether directly measured or simulated, are primary inputs to modern mechanistic-empirical pavement design approaches, such as the Mechanistic-Empirical Pavement Design Guide (ARA, 2004), to facilitate thickness design through empirical transfer functions that predict bottom-up fatigue cracking. Normally, the strain measurement or prediction represents a peak tensile response relative to a zero baseline (i.e., no loading) that does not consider the entire strain response of a passing wheel load.

In reality, flexible pavements experience both compressive and tensile strain under a moving wheel load. Figure 1 depicts a typical strain response under an 8 axle tractor-triple trailer truck measured in an instrumented full-scale flexible pavement section at the National Center

for Asphalt Technology (NCAT) Test Track. Key points on the first (steering) axle have been highlighted and represent:

1. Baseline (0 strain) before axle arrives
2. Compressive inflection strain just before axle is directly above ASG
3. Peak tensile strain when axle is directly above ASG
4. Compressive inflection strain as axle departs gauge
5. Return to baseline before tandem axle arrives

These five critical points repeat themselves, for the most part, for each of the remaining axles as the truck passes over the gauge. Previous studies have shown that the strain amplitude, measured vertically from Point 2 to 3, rather than simply the peak strain, measured vertically from point 1 to 3, helps explain the development of cracks transverse to the direction of travel (Timm and Priest, 2008).

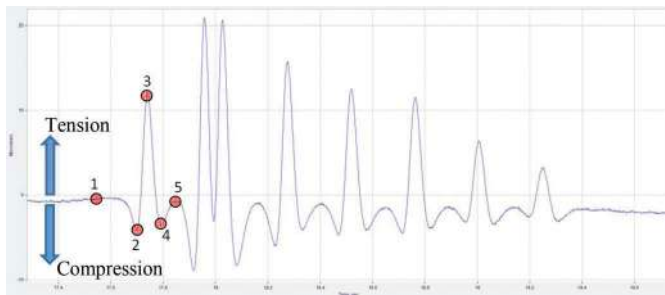


Figure 1. Measured dynamic pavement response (Timm, 2016).

Figure 1 is representative of typical flexible pavements consisting of AC over unbound granular materials over the subgrade soil. However, recently constructed sections at the NCAT Test Track with stabilized foundation layers have shown a dramatically different behavior under certain conditions where the strain response changes mode from tensile to compressive as depicted in Figure 2. The dashed series in Figure 2 is from a cold weather condition and resembles Figure 1 in shape, if not magnitude. The solid series, measured during warm weather, shows the pavement experiences predominantly compressive responses with tensile inflection under the same truck loading. Furthermore, the pavement seems to experience a small increase in strain (tension) when the axle is directly over the gauge. This is especially apparent in the

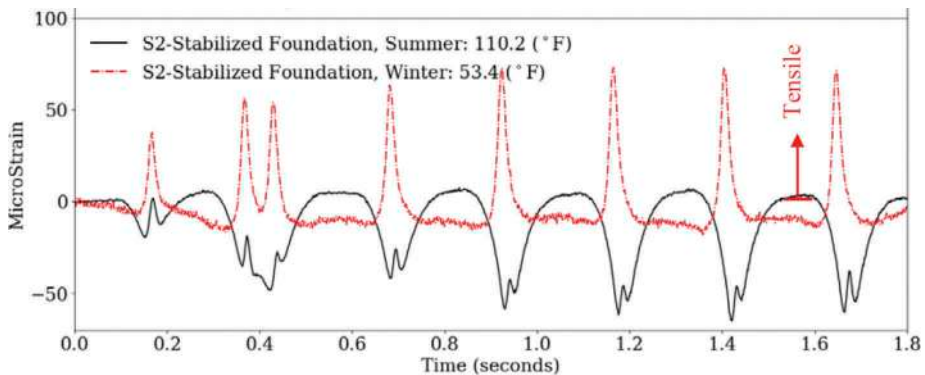


Figure 2. Measured dynamic strain response in a stabilized foundation section (Nakhaei and Timm, 2021).

last five axle events. Since the primary difference between the two conditions was pavement temperature, the mode change is likely due to variations in the AC modulus.

Despite the previous investigations (Timm and Priest, 2008; Nakhai and Timm, 2021) and general understanding developed thus far, there is a need to further investigate the strain reversal phenomenon and discuss the potential impacts on flexible pavement design. Specific issues include quantifying the relationship between inflection and peak strain values and determining under what conditions the fundamental mode (tensile or compressive) is achieved.

2 OBJECTIVE AND SCOPE OF WORK

Given the background and needs described above, the objectives of this study were to:

1. Characterize the relationship between inflection and peak strain levels.
2. Identify the conditions under which predominantly tensile or compressive strain occurs.

These objectives were accomplished by analyzing measured inflection and peak pavement responses from four instrumented pavement sections at the NCAT Test Track collected weekly over 17 months. Mechanistic simulations were also conducted in WESLEA on a hypothetical pavement section to validate the trends observed in the measured data.

3 TEST SECTIONS AND FIELD MEASUREMENTS

Figure 3 depicts the full-scale pavement cross sections and depth of embedded asphalt strain gauges used in this investigation. Two sections (N4 and S12) were sponsored by the Virginia Department of Transportation (VDOT) in 2012. Both sections featured cold central plant recycled (CCPR) asphalt as a base asphalt layer, but S12 also included a base layer that was cement-stabilized in place. The CCPR sections had a dense graded Superpave mix on top of the CCPR and both were topped with a stone matrix asphalt (SMA). The Mississippi DOT (MDOT) sponsored section S2 in 2018, which featured cement and lime-stabilized base (SB) layers beneath four lifts of dense-graded Superpave mixtures. S2 was also unique in that

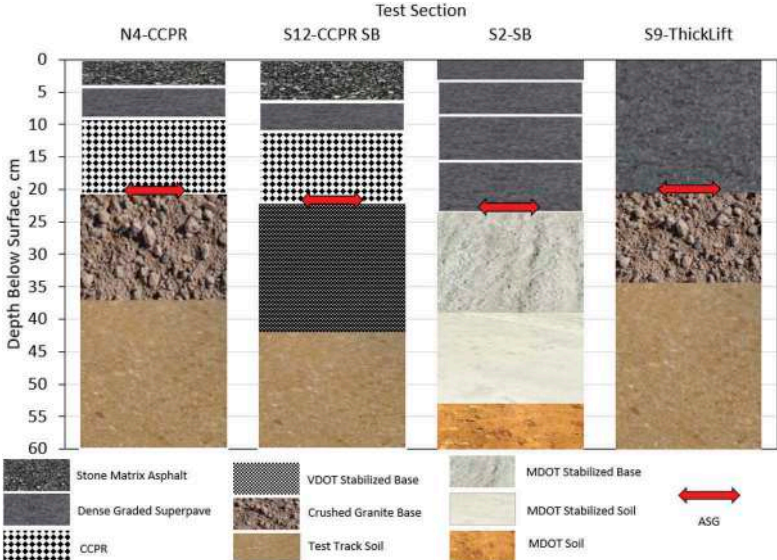


Figure 3. Test sections.

a subgrade material was imported to the Test Track from Mississippi, rather than using the native Test Track soil as with the other sections. Section S9 was sponsored by the South Carolina DOT (SCDOT) in 2018 and was constructed as a single AC thick lift over the same granular base and subgrade as Section N4. Details regarding the various asphalt mixtures, substructure materials and construction are beyond the scope of this paper, but have been documented elsewhere (Diefenderfer et al., 2016; McCarty, 2019). It is also important to point out that only sections N4 and S12 were part of a common experimental design, while the other two sections were part of separate independent studies. However, they were selected to provide a wide range of cross sections and materials in this investigation.

The strain gauges depicted in Figure 3 were embedded during construction and were oriented to measure strain in the direction of travel. Sections N4 and S12 had an array of 6 ASGs centered around the outside wheelpath, while Sections S2 and S9 had an array of 12 gauges, also centered around the outside wheelpath. Details regarding the instruments and installation have been previously documented (Diefenderfer et al., 2016; McCarty, 2019).

Strain measurements made on a weekly basis between November 29, 2018 and May 27, 2020 under repeated truck loadings are included in this paper. Signals such as those shown in Figures 1 and 2 were measured from which inflection and peak strain values were extracted. Typically, 15 to 20 truck passes, with the vehicles moving at approximately 72 kph, were gathered on a particular testing date. The data were sorted according to axle type (steer, tandem, single axles) and only data from the single axles were used in this analysis, as they represent the vast majority of pavement response measurements. Furthermore, only the best hit from among the 6 (CCPR sections) or 12 (S2, S9 sections) strain gauges for each axle pass was analyzed. Finally, the data were sorted into either peak tension or peak compression events as depicted in Figure 4, with the inflection and peak points characterized accordingly. Relationships between the inflection and peak measurements were developed on a section-by-section basis.

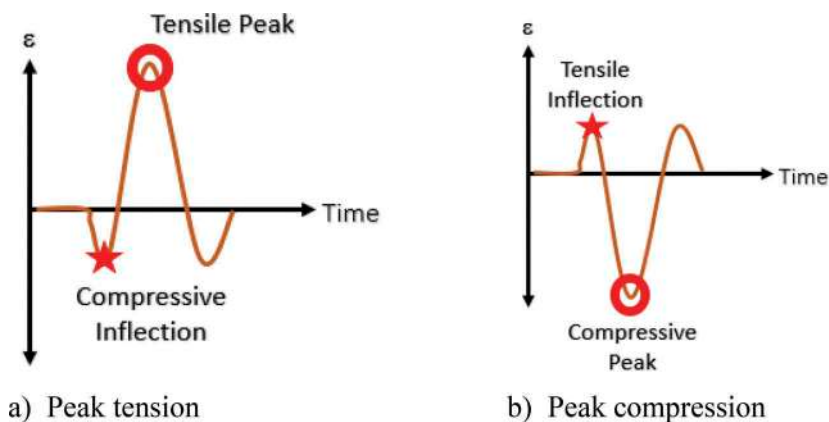


Figure 4. Measured strain event Categories.

Figure 5 plots the peak tensile strain versus the compressive inflection strain for each test section, representing the condition depicted in Figure 4a. Included in each plot are linear trendlines, forced through the origin, where the slope represents the ratio between peak tensile strain and compressive inflection strain. Also in each plot are the total number of data points (N). It is important to note that Figures 5a and 5b (unbound base layer pavements) have axes spanning three times those of the stabilized sections (Figures 5c and 5d). This was expected since the stabilized foundations should limit the amount of bending relative to the other sections, which was readily apparent.

Very strong relationships between peak tensile and compressive inflection strains were observed in all four sections. The R^2 were higher (>0.9) for the unbound sections (Figures 5a and 5b) and somewhat lower (>0.6) for the stabilized foundation sections (Figures 5c and 5d).

The peak and inflection responses are obviously linked and consistent within a section over a wide range of conditions, as the change in strain values within a section stem primarily from changing pavement temperatures ranging from 4C to 50C over the 17 month collection period. As the pavement stiffness changed due to temperature changes, both the measured inflection and peak strains were affected at a consistent rate. Finally, it is important to note that the slope of the trendlines were between -3 to -3.5 for the unbound sections while the stabilized foundations had slopes between -2 to about -2.5. Again, this difference is likely due to the bending restraint provided by the stabilized foundation in S2 and S12 which will be further explored in the following section. In all cases, the amount of inflection strain is significant and as demonstrated previously (Timm and Priest, 2008) should be considered in pavement design since it helps explain the orientation and development of cracking.

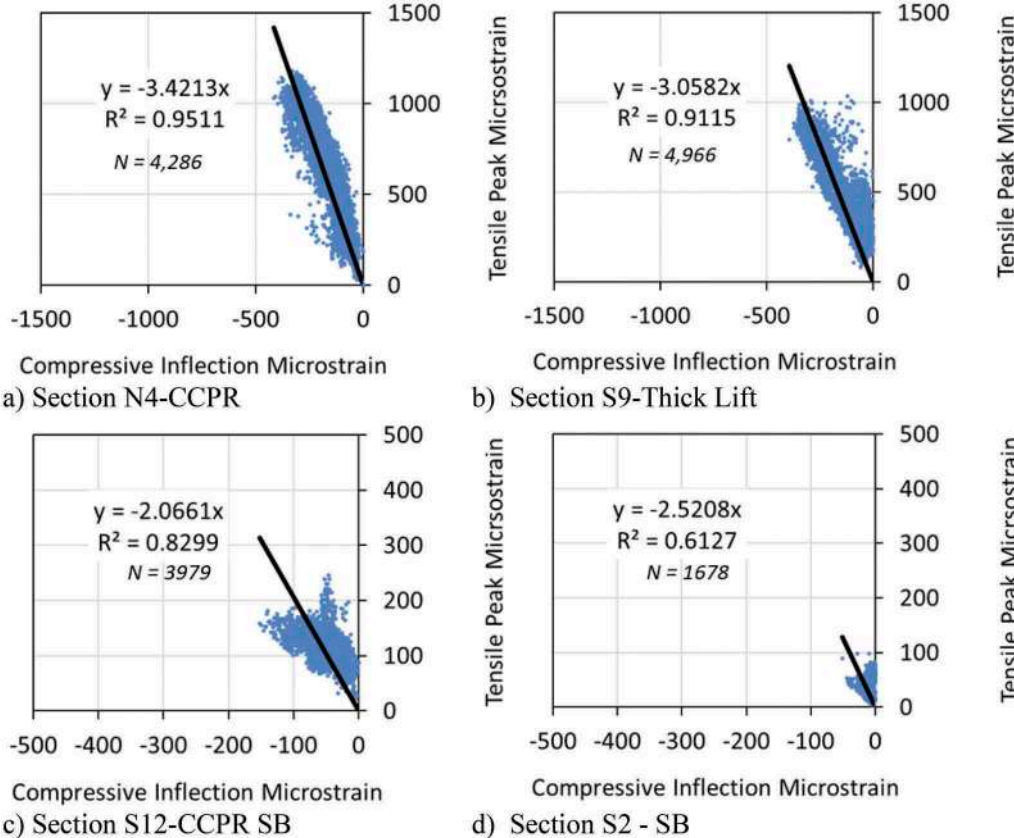


Figure 5. Measured peak tensile strain versus compressive inflection strain.

Figure 6 plots the peak compressive strain versus the tensile inflection strain for each test section, representing the condition depicted in Figure 4b. Like Figure 5, trendlines have been added as well as the number of data points in each graph. The drastically fewer data points between Figures 5 and 6 indicate this condition occurs much less frequently than peak tensile strain. The magnitude of strain level is also much lower for the compressive case than the tensile case, as evidenced by the axis scales. However, much like Figure 5, when peak compression occurs there is again a strong relationship ($R^2 > 0.85$) for three of the four sections. The exception is S2, which has a relatively low R^2 . In this case, it appears that peak compressive strain may be unrelated to the tensile inflection. This will be further explored in the mechanistic

modeling section below. It is also interesting to note that the unstabilized foundation sections (Figure 6a and 6b) have the lowest trendline slopes, while the stabilized foundation sections (Figures 6c and 6d) are the largest. This is opposite of the trends in Figure 5. Again, mechanistic modeling will help better understand these observations.

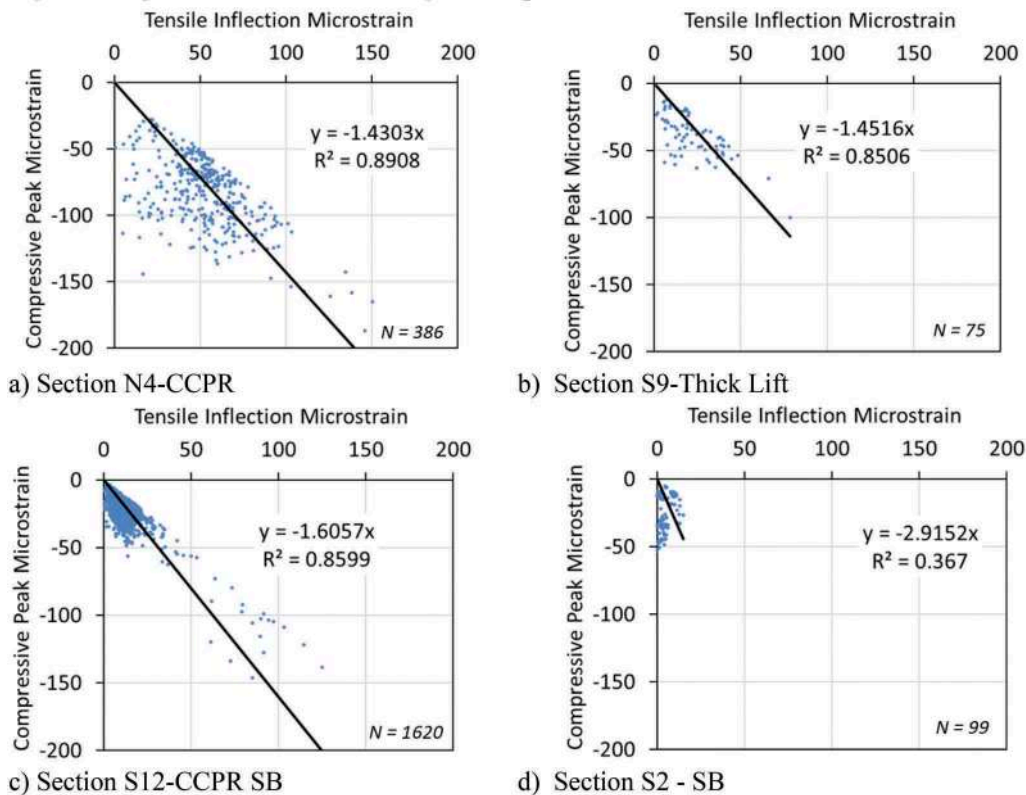


Figure 6. Measured peak compressive strain versus tensile inflection strain.

4 MECHANISTIC MODELING

To better understand the measured data shown in Figures 5 and 6, a series of layered elastic analysis pavement simulations were conducted using WESLEA for Windows (Version 3.0). Since the trends observed in the measured data were thought to derive primarily from the modulus of the pavement layers, it was decided to create a hypothetical pavement cross section and conduct a sensitivity analysis, where the modulus of the AC and base layers were varied to generate various strain responses from which inflection and peak points were extracted. The goal was not to generate specific strain events to match against those measured in Figures 5 and 6 but rather to develop a general understanding of how modulus values influence the shape and magnitude of the strain response.

To this end, a three-layer pavement was set up in WESLEA consisting of 17 cm of asphalt over 15 cm of base over the soil. Table 1 contains the AC and base modulus values used in the factorial sensitivity analysis while the subgrade modulus was fixed at 207 MPa. Since there were seven values for each layer, a set of 49 simulations were conducted where some combinations would resemble the unbound foundation sections (AC modulus > base modulus) and

other combinations would resemble the stabilized sections (AC modulus < base modulus). The load was simulated as an 89kN single axle with single tires (44.5 kN/tire) and contact pressure of 690 kPa. Strain computations were made at the bottom of the asphalt at 2.54 cm (1 inch) offset intervals to a distance of 124 cm (49 inches) from the load center in the direction of travel to resemble the strain signals depicted in Figures 1 and 2, which plot strain versus time.

Table 1. AC and base modulus values used in sensitivity analysis.

Layer Modulus, MPa	
Asphalt	Concrete
13,790	20,684
10,342	13,790
6,895	6,895
5,171	3,792
3,447	689
2,068	517
689	345

Figure 7 shows strain data generated through WESLEA for an unstabilized base layer ($E_2 = 345$ MPa) with each series representing a different E_1/E_2 ratio computed from the values given in Table 1. For example, the $E_1/E_2 = 2$ series represents the $E_1 = 689$ MPa and $E_2 = 345$ MPa condition which very much resembles the strain depicted in Figure 1. As expected, as the asphalt stiffens relative to the base (E_1/E_2 increases), there is less bending action and both the peak tensile strain and compressive inflection strain decrease, but the strain never switches mode to predominantly compressive with a tensile inflection point.

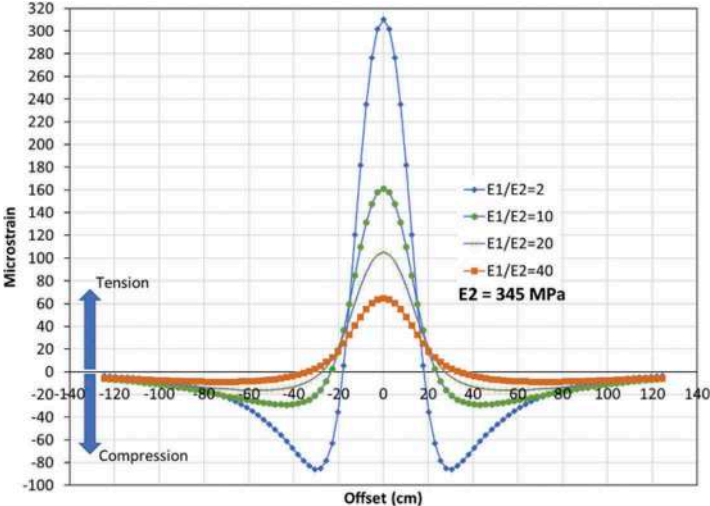


Figure 7. Unbound base simulated strain levels with varying E_1/E_2 and $E_2 = 345$ MPa.

In contrast, Figure 8 contains similar data as Figure 7 but for a stabilized base layer ($E_2 = 6,895$ MPa). The figure shows that the primary response flips from tensile to compressive at $E_1/E_2 = 0.1$, which is very soft asphalt relative to the base layer. The other series indicate

decreasing strain levels as the asphalt softens, which is counterintuitive because softer asphalt is generally related to greater bending (as seen in Figure 7), but in this case it appears the stabilized foundation is providing greater levels of restraint as the asphalt softens. This effect was also observed in earlier studies (Nakhaei and Timm, 2021). It is notable that the traces very much resemble those depicted in Figure 2, even including the small positive increase in strain at the bottom of the E1/E2 = 0.1 trace.

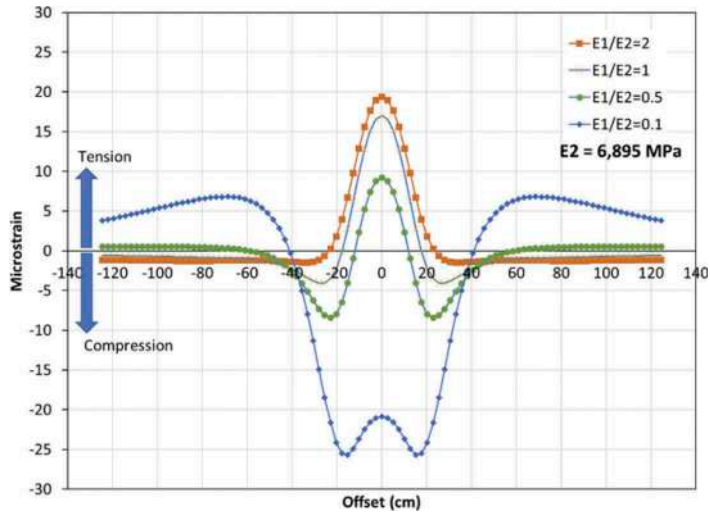
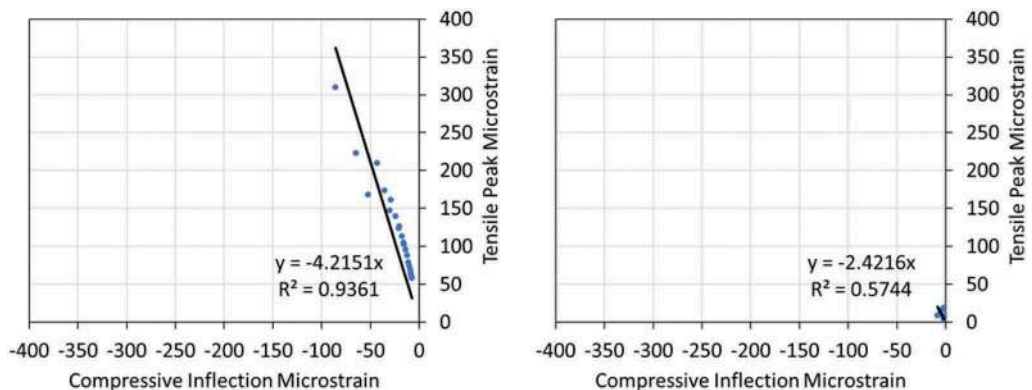


Figure 8. Stabilized base simulated strain levels with varying E1/E2 and E2 = 6,895 MPa.

Figures 7 and 8 demonstrated that modular ratio and whether a pavement had a stabilized base were critical factors in the resulting strain response. These simulated strain traces, in addition to all those generated through the full factorial generated from the Table 1 modulus values, were used to find the magnitude and mode (tensile or compressive) of each simulated strain event. Figure 9 plots these peak tensile events for unstabilized (Figure 9a) and stabilized (Figure 9b) conditions. As demonstrated in Figures 5a and 5b, there is a relatively stable



a) Unstabilized Base ($E_2 \leq 3,447$ MPa)

b) Stabilized base ($E_2 \geq 6,895$ MPa)

Figure 9. Simulated tensile peak versus compressive inflection strain.

linear trend between tensile peak and compressive inflection for the unbound base condition (Figure 9a) as well as a similar slope on the trendline, though slope in Figure 9a is admittedly higher. In contrast, Figure 9b (stabilized base condition) had remarkably lower strain levels, a considerably smaller trendline slope and lower R^2 , all of which was consistent with Figures 5c and 5d. In this manner, the layered elastic simulations again confirmed the measured pavement responses.

Figure 10 plots the simulated cases where the peak was in compression and the inflection point was tensile. This only occurred when the E2 modulus exceeded 6,895 MPa (i.e., stabilized base) with the exception of one case where E2 was 5,171 MPa, but the modular ratio (E1/E2) was 0.18. In all cases, the modular ratio was 0.5 or below. This again demonstrates that the primary mode is driven by whether there is a stabilized base and only occurs in extreme conditions when E1 is much less than E2, which happens at higher temperatures.

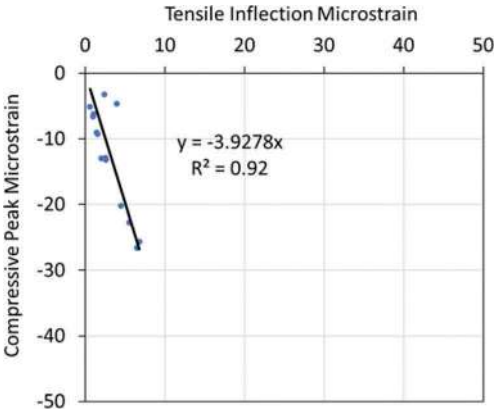


Figure 10. Simulated compressive peak versus tensile inflection strain.

5 CONCLUSIONS AND RECOMMENDATIONS

This study focused on quantifying the relationship between peak and inflection strain levels and determining when the mode reverses, under live truck loading and simulated using layered elastic analysis. Based on the data presented herein, the following conclusions and recommendations are made:

1. A linear relationship exists between the inflection and peak strain under dynamic loading in a flexible pavement and appears to be largely derived from the relationship between the asphalt and base modulus.
2. The magnitude of the inflection strain is significant and should be considered in structural pavement design, since earlier studies (Timm and Priest, 2008) demonstrated the importance in the orientation and development of cracking.
3. Under certain conditions, where the base modulus far exceeds the AC modulus, which can be found in stabilized base pavements at higher pavement temperatures, the bending strain may convert to predominantly compressive. Since the strain mode is in compression, and relatively low, this behavior is likely inconsequential from a pavement design perspective. However, previous studies (Nakhaei and Timm, 2021) have found that generating compression at the bottom of the AC in a stabilized foundation pavement could force maximum tension to occur at shallower depths. Since mixes placed at shallower depths are not often designed with cracking resistance in mind, they may be more prone to cracking so the conditions contributing to this effect are important to understand and quantify, as done in this paper.

REFERENCES

- ARA, Inc., ERES Consultants Division, 2004. *Guide for Mechanistic-Empirical Design of New and Rehabilitated Pavement Structures*. Final report, NCHRP Project 1-37A. Transportation Research Board of the National Academies, Washington, D.C. <http://www.trb.org/mepdg/guide.html>.
- Diefenderfer, B.K., Diaz-Sanchez, M.A., Timm, D.H., and Bowers, B.F., 2016. "Structural Study of Cold Central Plant Recycling Sections at the National Center for Asphalt Technology (NCAT) Test Track. Final Report VTRC 17-R9, Virginia Transportation Research Council.
- McCarty, Carolina A., 2019. *Early Characterization and Performance of a Flexible Thick Lift Pavement*. MS Thesis, Auburn University.
- Nakhaei, M. and Timm, D., 2021. Middle-Up Cracking Potential in Flexible Pavements with Stabilized Foundations. *Proceedings of the 100th Annual Transportation Research Board*, Washington, D.C. and under review for the Transportation Research Record.
- Timm, D.H., 2016. Key Concepts in Dynamic Signal Processing from Instrumented Pavement Sections. *5th International Conference on Accelerated Pavement Testing*, San Jose, Costa Rica, September 19 – 21.
- Timm, D.H. and Priest, A.L., 2008. Flexible Pavement Fatigue Cracking and Measured Strain Response at the NCAT Test Track. *Proceedings of the 87th Annual Transportation Research Board*, Washington, D.C.

Permanent deformation and fatigue damage interaction in asphalt concrete using energy approach

M. Alamnie & E. Tadesse

Department of Engineering Sciences, Civil and Structural Engineering, University of Agder, Grimstad, Norway

I. Hoff

Department of Civil and Transport Engineering, Norwegian University of Science and Technology, Trondheim, Norway

ABSTRACT: The interaction of fatigue and permanent deformation is very complex phenomenon and little attempt is made on this topic. This paper presents an investigation on the interaction of the two damages using the energy approach. Laboratory tests were conducted for both fatigue and permanent deformation on two different asphalt concrete in a sequential test procedure. A new failure criterion is proposed based on the dissipated energy ratio (DER). The proposed criterion for permanent deformation gives more damage indicator (inflection points) than the conventional flow number/strain rate criterion. The sequential test procedure is also found economical that can be standardized. From the study, strain hardening (pre-deformed) accelerates fatigue cracking susceptible. Similarly, high fatigued samples are more prone to permanent deformation than new samples. The energy approach is convenient for potential coupling of fatigue and permanent deformation interactions.

Keywords: Permanent deformation, fatigue, dissipated energy ratio, sequential test

1 INTRODUCTION

As asphalt concrete pavement is subjected to repetitive loads, different damage modes develop over its lifetime. Fatigue cracking and permanent deformation are the two dominant pavement damage mechanisms. One of the distinguishing features of fatigue and permanent deformation is the loading mode. In fatigue damage, cracks grow perpendicular to the tensile loading direction, whereas in permanent deformation, wing cracks can develop parallel to the load direction (Dyskin et al., 2003). The influence of temperature is another crucial factor in distinctive damage evolution. Fatigue is critical at intermediate and low temperatures. On the other hand, permanent deformation is high-temperature damage. At elevated temperatures, the critical energy threshold that causes fatigue cracking increases (or the mixture relaxes faster). Consequently, more energy is needed to initiate crack (Onifade et al., 2015, Sangpetngam et al., 2003). On the other hand, plastic flow and aggregate re-orientation dominate at high temperatures. Traditionally, bottom-up cracking of the asphalt concrete layer was the primary fatigue damage mechanism. However, experimental and field observations showed that top-down cracking due to tire compression is also the mechanism for fatigue damage (Pellinen et al., 2004, Roque et al., 2004). Crack initiation in compression occurs when the viscoplastic strain hardening reaches saturation at the flow number (FN).

The damages in asphalt concrete evolve through energy dissipation due to viscous flow leading to *fatigue cracking* and plastic flow for *permanent deformation* (Widyatmoko et al., 1999), and some part of the energy is transferred into heat (Di Benedetto et al., 2011). The energy dissipation caused material ductility exhaustion, hardening, and viscoplastic flow. Different energy-based failure criteria were proposed using the classic energy balance principle (Ghuzlan and Carpenter, 2000, Anderson et al., 2001, Shen et al., 2006, Korsunsky et al., 2007). The existing models treat fatigue and permanent deformation damage independently, and the complex interaction between the two damage modes is still not well researched. One of the limitations is the lack of an integrated testing protocol for fatigue-permanent deformation interaction. Some attempts can be found in literature, such as an Indirect Tension (IDT) testing for deformation and fracture (Bahadori et al., 2015) and a haversine loading waveform in fatigue tests (Liu et al., 2020, Gupta and Atul Narayan, 2019). The haversine load is used because it can be decomposed into pure creep (for permanent deformation part) and pure sinusoidal (fatigue part) components. However, the creep-recovery behavior cannot be captured with such approaches.

Moreover, field and laboratory observations have shown that fatigue cracking accompany permanent deformation (rutting) (Lundstrom et al., 2007, Pellinen et al., 2004). In addition, the same load causes both damages, and strain-hardening and cracking can develop simultaneously at intermediate temperatures. Therefore, the independent treatment of the two damages is an oversimplification and far from the actual condition. The pavement is more susceptible to fatigue cracking in the cold seasons, and micro-cracks can initiate. These pre-existing cracks can significantly accelerate the permanent deformation at high pavement temperatures in hot seasons. The inverse is true that viscoplastic strain hardened during the hot season is more susceptible to fatigue cracking in cold seasons. Both damages are critical at intermediate temperatures. Hence, the independent treatment of the two damages sets clear limitations for the mechanistic pavement design.

In this paper, an attempt is made to investigate the effect of fatigue on permanent deformation and vice versa using an energy approach. Several asphalt concrete samples were tested for fatigue (F) and permanent deformation (PD) in a Sequential Test (ST) procedure. The tests were performed in two different orders: the F-PD and PD-F sequences. A new energy-based failure criterion is proposed and validated using experimental data from two different asphalt mixtures.

2 ENERGY-BASED MODELS

The dissipated energy in a cyclic load is the area under the stress-strain hysteresis loop. In a cyclic creep-recovery test, material hardening grows, irrecoverable viscoplastic strain accumulates, and the hysteresis loops shift horizontally (Figure 1a). On the other hand, the idealized hysteresis loop in the cyclic fatigue test causes stiffness reduction and phase angle increment with negligible viscoplastic strain (hysteresis loops do not shift horizontally) (Figure 1b). Nevertheless, the stress-strain hysteresis in simultaneous damage conditions could evolve in a complex manner due to hardening-softening, healing, etc. The dissipated energy (DE) is expressed by the following integral, where $\sigma(t)$ is the stress function and $\frac{\partial \varepsilon(t)}{\partial \tau}$ is the strain rate.

$$DE = \int \sigma(t) \frac{\partial \varepsilon(\tau)}{\partial \tau} dt \quad (1)$$

The DE in fatigue and permanent deformation damages can be computed using the appropriate stress and strain rate functions in Equation 1.

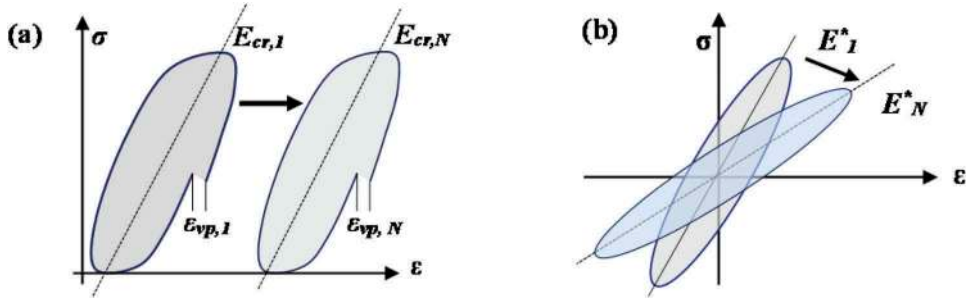


Figure 1. Schematic – stress-strain hysteresis loops (a) creep-recovery (b) tension-compression fatigue.

2.1 Fatigue failure criterion

For a strain-controlled fatigue test with sinusoidal strain wave, the dissipated energy due to fatigue (DE_f) is obtained by substituting the sinusoidal stress ($\sigma_s = \sigma_i \sin \omega t$) and strain ($\varepsilon_s = \varepsilon_i \sin(\omega t - \varphi_i)$) signals into Equation 1 and integrating (σ_i , ε_i , ω and φ_i – stress amplitude, strain amplitude, angular frequency, and phase angle measured at cycle, i).

$$DE_f = 2\pi\sigma_i\varepsilon_i \sin(\varphi_i) \quad (2)$$

The dissipated energy ratio (DER) criterion is used (Ghuzlan and Carpenter, 2000) as a damage indicator.

$$DER = n \times \frac{DE_1}{DE_n} \quad (3)$$

Where DE_1 –dissipated energy at initial cycle, DE_n – dissipated energy at n^{th} load cycle. For a sinusoidal loading, the DER can be expressed as,

$$DER = n \times \frac{\pi E^*_1 \varepsilon_1^2 \sin \varphi_1}{\pi E^*_n \varepsilon_n^2 \sin \varphi_n} \quad (4)$$

For a test in controlled-strain mode, $\varepsilon_1 = \varepsilon_n$ and with approximation $\frac{\sin \varphi_1}{\sin \varphi_n} \approx \frac{\varphi_1}{\varphi_n}$, then DER is found as;

$$DER = \left(\frac{n}{E^*_n} \right) \left(\frac{E^*_1 \sin \varphi_1}{\sin \varphi_n} \right) = n \left(\frac{E^*_1}{E^*_n} \right) \left(\frac{\varphi_1}{\varphi_n} \right) \quad (5)$$

2.2 Permanent deformation failure criterion

The flow number (FN) has been used as a general failure criterion for permanent deformation (Biligiri et al., 2007). Flow number is a cycle where the viscoplastic strain rate start ascending (or the second derivative of the strain function changes from negative to a positive value, i.e., $\varepsilon_{vp}'' > 0$). The well-known Francken model (Francken and Clauwaert, 1987) is used to fit the permanent deformation test data (where A, B, C, D – are model coefficients, N – number of cycles).

$$\varepsilon_{vp} = AN^B + C(e^{DN} - 1) \quad (6)$$

$$\dot{\varepsilon}_{vp} = ABN^{B-1} + CDe^{DN} \quad (7)$$

The dissipated energy due to permanent deformation (DE_{pd}) is obtained by substituting a haversine stress pulse $\sigma_h = \sigma_0 \sin^2\left(\frac{\omega t}{2}\right)$ where σ_0 is stress amplitude and strain rate (Equation 7) into Equation 1.

$$DE_{PD} = \frac{\pi \sigma_0}{\omega} \frac{\dot{\varepsilon}_{vp}}{2} \quad (8)$$

The permanent deformation failure criterion using DER takes the following form.

$$DER_{PD} = n \frac{DE_{PD1}}{DE_{PDN}} = n \frac{AB + CDe^D}{ABN^{B-1} + CDe^{DN}} \quad (9)$$

n is current cycle number, DE_{PD1} is dissipated energy at the first cycle. The quantity $AB + CDe^D$ is a material constant dependent on compressive stress level, temperature, and initial damage of the material. The exponent component (CDe^D) is found very small compared to the first part and can be approximated as $K \cong AB$. The denominator ($ABN^{B-1} + CDe^{DN}$) is the strain rate ($\dot{\varepsilon}_{vp}$). Thus, the DER (for $0 < K < 1$) is expressed as;

$$DER_{PD} = n \left(\frac{k}{\dot{\varepsilon}_{vp}} \right) \quad (10)$$

3 TEST METHOD

3.1 Materials

Two different asphalt mixtures (AB11 and SKA11) sampled from asphalt mixing plants were used for tests in this research. The cylindrical specimens (150 mm by 180 mm height) were produced using a gyratory compactor, and the final specimens (100 mm diameter by 150 mm height) were produced by coring and cutting. In Table 1, the aggregate gradation of the mixtures is given where AB11 mixture contains a polymer-modified binder (PMB 65/105-60) and SKA11 is made of a 70/100 neat binder.

Table 1. Aggregate gradation.

Mix	Sieve size [mm]						Content [%]	
	16	11.2	8	4	2	0.25		0.063
	Percent Passing [%]							
AB11	100	95	70	48	36	15.5	10	5.6
SKA11	100	91.2	53.6	35.7	21.7	12.8	8.4	5.83

3.2 Test procedure

A Sequential Test (ST) procedure is suggested in this paper. In this procedure, fatigue and permanent deformation tests were conducted sequentially on the same specimen. The sequences are referred as PD-F and F-PD sequences (F – for fatigue, PD – for permanent deformation), as shown in Figure 2. In the PD-F sequence, permanent deformation test is conducted first with in the steady-state region and the same sample is tested in Tension-compression fatigue test. Similarly, for F-PD sequence, the new sample is tested in Tension-compression fatigue first and then under-vent permanent deformation test. The test parameters are summarized in Table 2.

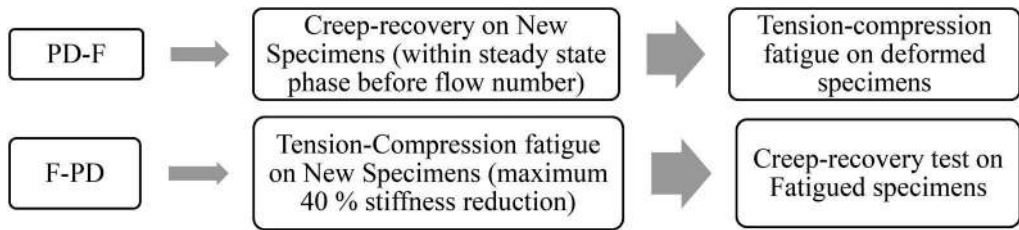


Figure 2. Sequential Test Procedure.

Table 2. Main characterization tests, parameters, and conditions.

Test	Temperature (°C)	Load waveform	Mode	Frequency/Time
T-C fatigue	10, 15, 21, 30	Sinusoidal	Control-strain (at 100, 150, 200, 300, 400 $\mu\epsilon$)	10 Hz
Creep-recovery	21, 30, 40	Haversine	Control-stress (0.5 to 2 MPa)	Loading/rest time: 0.4 / 1.6 sec

4 RESULTS AND DISCUSSION

Several asphalt concrete specimens were tested in tension-compression fatigue and cyclic creep-recovery to investigate the interaction of fatigue and permanent deformation damages according to the sequential test procedure. The first part of the tests in the sequential procedure was conducted to induce the respective pre-damage on the specimen. For example, in the F-PD procedure, the fatigue part of the test is performed to induce a certain level of fatigue cracking (maximum of 40 % stiffness reduction) on the specimen. Then fatigued specimens are tested for permanent deformation until failure. The same is true for the PD-F procedure, where the first part of the test (i.e., PD) is conducted to induce a sufficient level of strain hardening to the specimen before the flow number (within the steady-state region not to failure). Then PD specimens were tested in T-C fatigue until failure.

4.1 The F-PD procedure

In the F-PD sequence, the specimens were tested in T-C fatigue in a controlled-strain mode at temperatures of 10, 15, 21, and 30 °C and at different on-specimen target strains (150, 200, 300, 400 $\mu\epsilon$). The maximum percentage of stiffness reduction during fatigue was no more than 40 %. Then the fatigued specimens were conditioned and tested at 30 and 40 °C in a controlled-stress creep-recovery test. Examples of test results in the F-PD sequence are shown in Figure 3. As can be seen (Figure 3 a and b), samples with high fatigue damage (high on-specimen strain like 400 $\mu\epsilon$) at 10 °C have a rapid rate of permanent deformation and a small flow number (FN). However, samples fatigued at 21 and 30 °C have little effect on the permanent deformation growth. This property is related to the need of high energy to initial fatigue cracking at elevated temperatures due to viscosity.

The flow number (FN) is a classic permanent deformation failure criterion for asphalt concrete. It marks the commencement of the tertiary stage, which is characterized by a high rate of deformation and micro-crack formation. The proposed DER criterion (Equation 10) gives an additional inflection point using the DER curve. It is referred to as the peak value (PV). As shown in Figure 4, four distinct creep stages can be visualized using the DER criterion; (I) An increasing rate in the first stage, (II) a steady-state

increase in the secondary stage, (III) increment at a decreasing rate in the third stage, and (IV) descending phase after the peak point in the fourth stage. The tertiary (III) phase is dominated by micro-crack formation and propagation, resulting in macro-crack formation at PV. It is believed that the PV indicates the formation of macro-cracks and unstable deformation. The DER starts descending rapidly in the fourth stage due to excessive deformation or high energy dissipation. For the F-PD sequence (samples with pre-existing cracks due to fatigue), wing cracks can grow parallel to the load direction. At PV, the accumulated wing cracks and micro-cracks coalesce and form macro-cracks. Therefore, the FN in the DER curve corresponds to a cycle where the steady-state DER start decreasing or the dissipated energy starts increasing. Moreover, Figure 5 shows that fatigued samples have higher DE or lower DER value than new samples. Since the fatigue test is conducted at lower temperatures, healing can occur during the rest period and during conditioning at a higher temperature (40 °C) for permanent deformation.

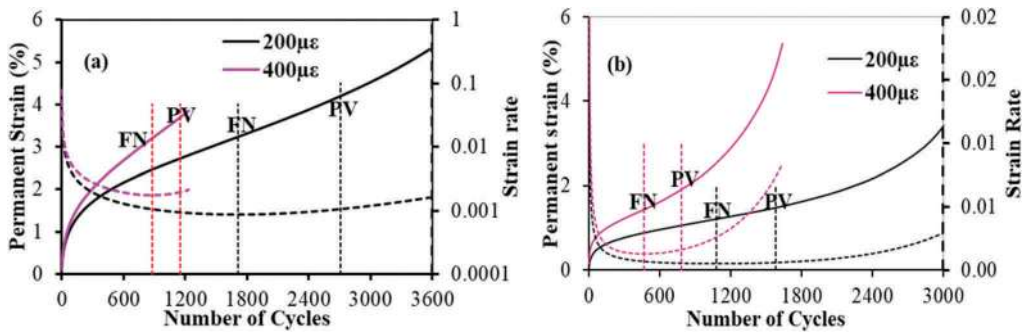


Figure 3. Permanent deformation of fatigued samples (F-PD) at 10°C and 200 and 400 µε target strain (a) AB11 – PD at 30°C, $\sigma = 2\text{MPa}$ (b) SKA11 – PD at 40°C, $\sigma = 0.65\text{MPa}$.

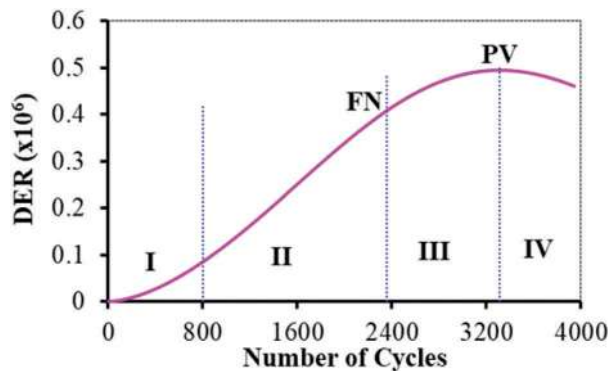


Figure 4. The typical four phases of DER Curve (F-PD - Fatigued at 10°C and 300µε, PD - 30°C and $\sigma = 2\text{MPa}$).

Furthermore, the proposed failure criterion is verified using test data on a new specimen with confinement and a longer recovery period of 16 sec (Figure 6). Confinement played a role in the energy dissipation evolution, and DE is directly proportional to axial stress and temperature. The DER shows the level of damage (viscoplastic) of the sample more clearly than the DE quantity. Large DER means the material is less damaged, and the decreasing rate of DER indicates micro-crack is initiated and flow number identified.

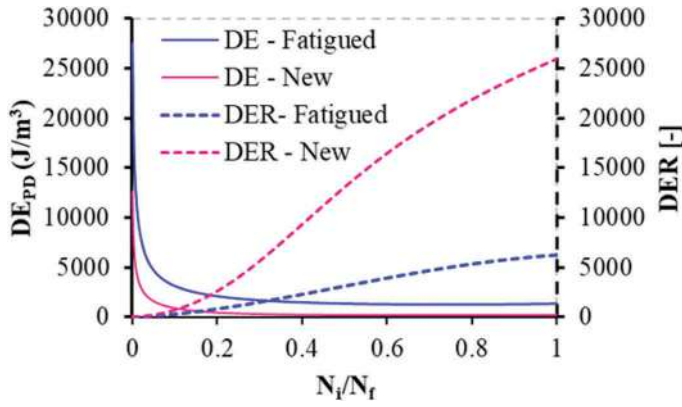


Figure 5. DE and DER for Permanent deformation (at $\sigma = 0.5\text{MPa}$, 40°C) on new and fatigued (10°C and $150\mu\epsilon$) samples.

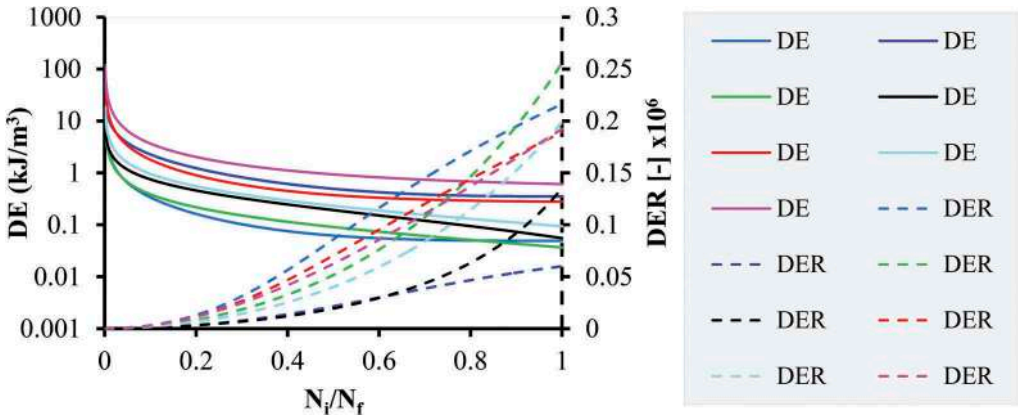


Figure 6. DE and DER due to permanent deformation with confinement on new specimens (at different axial stresses and temperatures) – AB11.

4.2 The PD-F procedure

In the PD-F procedure, permanent deformation is induced on new specimens and the deformed specimen undergoes tension-compression fatigue. Figure 7 (a and b) shows that strain hardening due to permanent deformation increases asphalt concrete's apparent dynamic modulus (stiffness). This increase in stiffness makes the mixtures prone to rapid fatigue damage rate (D).

$$D = 1 - \frac{E_i^*}{E_o^*} \quad (11)$$

where E_i^* is dynamic modulus at cycle i , and E_o^* is the initial dynamic modulus. Hence, the effect of strain hardening has a crucial role in the fatigue damage evolution. In most cases, permanent deformation can accumulate before visible fatigue cracks are seen during pavement service life. In such conditions, the PD-F sequence is a realistic and accurate way to investigate the fatigue life of asphalt concrete mixtures experimentally. However, fatigue cracks can also develop before permanent deformation, especially in cold climates, due to thermal cracking as well as fatigue cracking at intermediate temperatures.

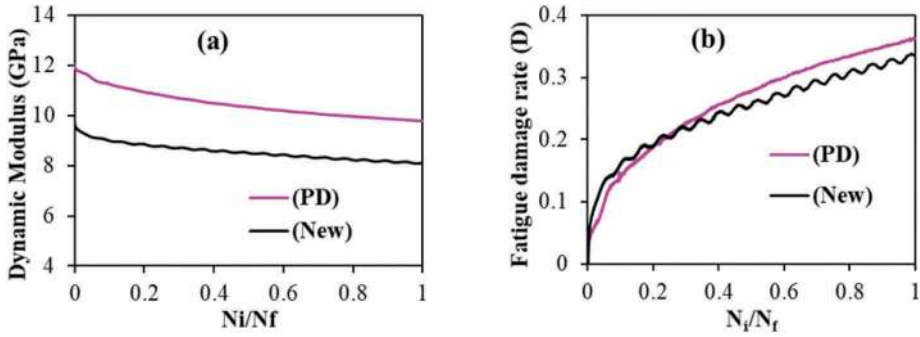


Figure 7. T-C fatigue at 10 °C and 150 $\mu\epsilon$ on new and deformed SKA11 samples (PD at 40°C, $\sigma = 0.65\text{MPa}$) (a) apparent dynamic modulus (b) damage rate, D.

4.3 Coupling the dissipated energy

The total dissipated energy (DE_T) on a specimen tested according to the sequential tests (F-PD and PD-F) can be approximated by the linear sum of dissipated energy. Thus, DE_T is expressed by adding Equation 2 and Equation 8 as follows.

$$DE_T = 2\pi\sigma_i\epsilon_i\sin(\varphi_i) + \frac{\pi\sigma_0}{\omega} \epsilon_{vp}^g \quad (12)$$

It is also important to underline that some creep deformation can be accumulated during fatigue tests that contribute to the hardening of the specimen. However, the amount of creep energy dissipation during cyclic fatigue tests is insignificant compared to that of cyclic.

Examples of dissipated energies during fatigue (DE_F), permanent deformation (DE_{PD}) and total dissipated energy (DE_T) are shown in Figure 8. The DEs in permanent deformation damage are cumulative sum upto the flow number $DE_{PD} = \sum_i^{FN} DE_i$. The fatigue dissipated energy (DE_F) is dependent on the target strain, temperature and initial level of hardening (deformation) as shown in Table 3. Generally, DE_F decreases as temperature increases due to viscoplastic heat loss instead of viscoplastic flow (deformation) at higher temperatures.

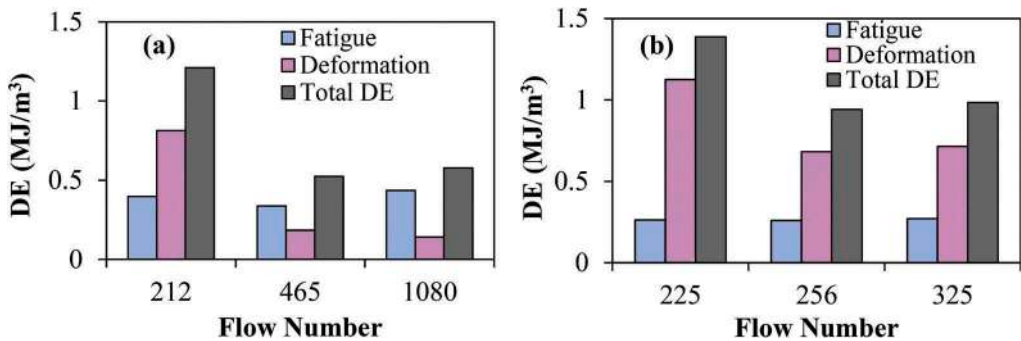


Figure 8. Dissipated energies (DE_F , DE_{PD} , DE_{Tot}) for fatigued SKA11 samples (PD at 40°C, $\sigma = 0.65\text{MPa}$) (a) 10 °C (b) 15 °C .

Table 3. Cumulative Dissipated Eenergy [J/m³] during fatigue test on new SKA11 samples.

Strain [μϵ]	Fatigue test Temperature [°C]		
	10	15	21
150	1.97E+05	-	1.7E+05
200	3.68E+05	6.74E+05	2.4E+05
300	7.91E+05	5.54E+05	2.3E+05
400	8.00E+05	1.65E+06	-

4.4 Summary

Permanent deformation and fatigue cracking are the most dominant pavement damages. These damages have been studied independently. There is also an assumption that permanent deformation occurs before fatigue cracking develops. However, such an assumption depends on the climatic condition and mixture properties. For instance, top-down cracks can develop in stiff and thick pavements due to tire compression before permanent deformation accumulates and the pre-existing crack can accelerate permanent deformation in later life of the pavement. The study presented in this paper indicates that fatigue and permanent deformation pre-damages have a significant role in the evolution of permanent deformation and fatigue cracking, respectively. Moreover, the sequential test procedure can be standardized to investigate the interaction between the two damages for a more realistic performance prediction. The F-PD procedure is more deterministic and easy to control the desired level of fatigue damage. However, the PD-F sequence should be conducted with care in order not to break the sample beyond the steady-state zone. The energy approach applied in this paper is simple and convenient to analyze the interaction of fatigue and permanent deformation.

5 CONCLUSION

The interaction of fatigue and permanent deformation is a very complex phenomenon and little attempt is made on asphalt concrete. In this paper, an investigation is made on the effect of fatigue on permanent deformation and vice versa in a sequential test procedure using an energy approach. The main findings are summarized as follows.

- The energy approach is convenient to analyze the interaction between permanent deformation and fatigue cracking.
- New failure criterion based on the dissipated energy ratio (DER) is proposed. The criterion is more comprehensive than the classic flow number (strain rate) for permanent deformation damage.
- The post flow number micro-crack growth rate can be visualized easily, and the macro-crack formation can be seen at the peak point of DER curve.
- It is observed that permanently deformed samples are more susceptible to fatigue cracking than new samples because of strain hardening. Fatigue damage at high temperatures (21 and 30°C) has a marginal effect on permanent deformation.
- The proposed sequential test method can make significant saving for both testing and material production.

REFERENCES

- Anderson, D. A., Le Hir, Y. M., Marasteanu, M. O., Planche, J.-P., Martin, D. & Gauthier, G. 2001. Evaluation Of Fatigue Criteria For Asphalt Binders. *Transportation Research Record: Journal Of The Transportation Research Board*, 1766, 48–56.

- Bahadori, A., Mansourkhaki, A. & Ameri, M. 2015. A Phenomenological Fatigue Performance Model Of Asphalt Mixtures Based On Fracture Energy Density. *Journal Of Testing And Evaluation*, 43, 133–139.
- Biligiri, K. P., Kaloush, K. E., Mamlouk, M. S. & Witzczak, M. W. 2007. Rational Modeling Of Tertiary Flow For Asphalt Mixtures. *Transportation Research Record: Journal Of The Transportation Research Board*, 2001, 63–72.
- Di Benedetto, H., Nguyen, Q. T. & Sauzéat, C. 2011. Nonlinearity, Heating, Fatigue And Thixotropy During Cyclic Loading Of Asphalt Mixtures. *Road Materials And Pavement Design*, 12, 129–158.
- Dyskin, A. V., Sahouryeh, E., Jewell, R. J., Joer, H. & Ustinov, K. B. 2003. Influence Of Shape And Locations Of Initial 3-D Cracks On Their Growth In Uniaxial Compression. *Engineering Fracture Mechanics*, 70, 2115–2136.
- Francken, L. & Clauwaert, C. Characterization And Structural Assessment Of Bound Materials For Flexible Road Structures. Sixth International Conference, Structural Design Of Asphalt Pavements, 1987 Ann Arbor, Michigan University. Michigan University.
- Ghuzlan, K. A. & Carpenter, S. H. 2000. Energy-Derived, Damage-Based Failure Criterion For Fatigue Testing. *Transportation Research Record: Journal Of The Transportation Research Board*, 1723, 141–149.
- Gupta, R. & Atul Narayan, S. P. 2019. Tensile Creep Of Asphalt Concrete In Repeated Loading Tests And Its Effect On Energy Dissipation. *International Journal Of Pavement Engineering*, 1–13.
- Korsunsky, A. M., Dini, D., Dunne, F. P. E. & Walsh, M. J. 2007. Comparative Assessment Of Dissipated Energy And Other Fatigue Criteria. *International Journal Of Fatigue*, 29, 1990–1995.
- Liu, H., Yang, X., Jiang, L., Lv, S., Huang, T. & Yang, Y. 2020. Fatigue-Creep Damage Interaction Model Of Asphalt Mixture Under The Semi-Sine Cycle Loading. *Construction And Building Materials*, 251, 119070.
- Lundstrom, R., Ekblad, J., Isacson, U. & Karlsson, R. 2007. Fatigue Modeling As Related To Flexible Pavement Design. *Road Materials And Pavement Design*, 8, 165–205.
- Onifade, I., Birgisson, B. & Balieu, R. 2015. Energy-Based Damage And Fracture Framework For Visco-elastic Asphalt Concrete. *Engineering Fracture Mechanics*, 145, 67–85.
- Pellinen, T. K., Christensen, D. W., Rowe, G. M. & Sharrock, M. 2004. Fatigue-Transfer Functions: How Do They Compare? *Transportation Research Record: Journal Of The Transportation Research Board*, 1896, 77–87.
- Roque, R., Birgisson, B., Drakos, C. & Dietrich, B. 2004. Development And Field Evaluation Of Energy-Based Criteria For Top-Down Cracking Performance Of Hot Mix Asphalt (With Discussion). *Journal Of The Association Of Asphalt Paving Technologists*, 73.
- Sangpetngam, B., Birgisson, B. & Roque, R. 2003. Development Of Efficient Crack Growth Simulator Based On Hot-Mix Asphalt Fracture Mechanics. *Transportation Research Record: Journal Of The Transportation Research Board*, 1832, 105–112.
- Shen, S., Airey, G. D., Carpenter, S. H. & Huang, H. 2006. A Dissipated Energy Approach To Fatigue Evaluation. *Road Materials And Pavement Design*, 7, 47–69.
- Widyatmoko, I., Ellis, C. & Read, J. M. 1999. Energy Dissipation And The Deformation Resistance Of Bituminous Mixtures. *Materials And Structures*, 32, 218–223.

Impact of the bearing capacity and settlement ratio of track bed on the structural performance and fatigue life of bituminous tracks

M. Sol-Sánchez, F. Moreno-Navarro, J.M. Castillo-Mingorance & M.C. Rubio-Gámez
Laboratory of Construction Engineering, University of Granada, Granada, Spain

E. Tomás-Fortún
Ciesm-Intevia, Madrid, Spain

V. Pérez-Mena
CEPSA, Madrid, Spain

ABSTRACT: The use of bituminous layers in railway tracks contribute to improve the mechanical performance and durability of superstructure as long as this structural layer preserves its properties. However, the bearing capacity and settlement ratio of the track bed under such bituminous layers can play an essential role on its structural performance and fatigue life, and therefore, this fact must be considered when designing the track section. In this sense, this paper focuses on the evaluation of the mechanical performance and fatigue life prediction of different types of bituminous materials for railway over simulated track beds with diverse strength. Particularly, it was used an innovative laboratory device that allows for reproducing various conditions of bearing capacity and settlement ratio for the support of the bituminous layers during fatigue tests reproducing traffic efforts through repetitive loads over the asphalt. Results show the correlation between the stiffness of the track bed and the durability of the bituminous layers, determining the type of asphalt more appropriate depending on bed performance. Similarly, it was seen that the higher the ratio of track bed settlement, the shorter the fatigue life of the bituminous material, leading to the cracking of fragile materials while ductile bituminous layers showed higher capacity to absorb the deformation of track beds.

Keywords: Railways, bituminous tracks, structural performance, fatigue life

1 INTRODUCTION

Railway transportation play a key role on sustainable mobility where train speed and loading capacity are fundamental to attract passenger and freight from other less environmental-friendly means of communication. However, these factors could lead to an important increase in dynamic overloads which, joined to the raising safety and comfort requirements, demands for higher vertical strength of the infrastructure to avoid the acceleration of track degradation. In this regard, the inclusion of asphalt mixtures is conceived to respond to such demand for higher bearing capacity and geometrical requirements (Teixeira et al., 2009; Rose et al., 2011). Particularly, bituminous sub-ballast is considered to allow for improving the track performance by increasing the strength of the sub-structure and reducing the trend to settlement as well as the stress and permeability over the foundation (Sol-Sánchez et al., 2016; Yu et al.,

2019). Moreover, there are other technical benefits such as reducing acceleration peaks in ballast layer (Asphalt Institute, 1998; Fang et al., 2011; Khairallah et al., 2019).

Additionally, the use of advanced materials like polymer modified binders could be of interest due to their potential for improving the mechanical performance and durability of the bituminous sub-ballast (Asgharzadeh et al., 2018). Similarly, the use of high modulus asphalt mixtures (HMAM) could be an effective solution to increase the bearing capacity of the sub-structure while improving its mechanical behaviour (Yu et al., 2019), as seen in road sector. However, the high economic and environmental costs associated with these bituminous solutions demand for proving their benefits under diverse conditions to justify their widespread application, particularly in the case of HMAM whose higher stiffness could be considered as a negative point associated with cracking under certain circumstances (Yu et al., 2020).

Thus, the development of new materials and designs for the asphalt mixtures to be used as sub-ballast in railway tracks, requires for specific analysis of their behaviour under diverse in-service conditions that can take place along material life since the durability is a key factor for bituminous sub-ballast due to the complexity of its maintenance and repair. In this sense, variations in the strength of the support for the mixture can be common and remarkable due to railway lines passing through diverse geological and ground formations. Key parameters like bearing capacity and settlement ratio of the support could influence the mechanical performance and durability of the mixtures, demanding therefore for further studies considering this issue.

However, most of laboratory tests focuses on assessing the properties and mechanical response of the bituminous sub-ballast as an isolated material (Sol-Sánchez et al., 2015), with limited consideration of the conditions or state of the surrounding components. In this context, the present article focuses on assessing the mechanical performance and durability of three different asphalt mixtures under various support conditions, while also evaluating the interaction between both bituminous sub-ballast and base supports. For this purpose, an innovative laboratory device was used to reproduce different conditions of strength and trend to settlement of the support for the asphalt specimens, subjected also to traffic loads also simulated through the laboratory test.

2 METHODOLOGY

2.1 *Materials*

This paper evaluated the performance of three asphalt mixtures with similar designing factors, but with different type of bitumen. All mixtures corresponded to an asphalt concrete, dense-graded type with a maximum aggregate size of 22 mm.

The mixtures were manufactured with a bitumen content of 5.5% over total mixture weight, but using the following three types of binder: (i) a conventional bitumen (named in this article as B) that presented a penetration value between 50-70 dmm and a softening point within 46-54°C, according with UNE-EN 1426:2015 and UNE-EN 1427:2015 standards, respectively; (ii) a crumb rubber and SBS modified bitumen named in this study as MB1, which had a penetration value between 45-80 dmm and a softening point around 65°C; (iii) the third bitumen was named as MB2, corresponding to a hard bitumen modified with SBS polymers to provide penetration values close to 10-40 dmm and softening point around 70°C.

These binders were selected to provide: a reference one (B) commonly used in the manufacturing of this type of mixtures for the application as bituminous sub-ballast (Teixeira et al., 2009; Rose et al., 2011); the MB1 allowed for evaluating the impact of using a modified bitumen (with similar penetration to the reference, but including polymers) as an alternative to conventional binders; and the MB2 was used to assess the effect of using a hard bitumen to provide high modulus asphalt, but including polymers since it has been seen to improve the mechanical performance of this type of mixtures (Akisetty et al., 2009; Sol-Sánchez et al., 2020), and then, being comparable with MB1 case, but assessing the influence of hard bitumen.

The mixtures manufactured with these bitumens presented the physical and mechanical properties listed in Table 1, which can be considered as appropriate for this type of materials for the application as sub-ballast layers in ballasted railway tracks.

Table 1. Main physical and mechanical properties of the mixtures with different bitumen.

Properties	Standard	Units	B	MB1	MB2
Bulk density	EN 12697-6	Mg/m ³	2.40	2.41	2.38
Air void content	EN 12697-8	%	4.2	3.2	4.7
Indirect Tensile Strength (dry)	EN 12697-23	kPa	2014.2	3200.9	3659.7
Indirect Tensile Strength Ratio	EN 12697-12	%	85.1	90.2	91.8
Stiffness modulus at 20°C	EN 12697-26 (C)	MPa	6896.6	9699.3	14284.2

2.2 Testing plan and methods

The testing plan focused on evaluating the mechanical performance and durability of the three types of mixture under diverse testing conditions, simulating (through an innovative laboratory device) various support states with different bearing capacity and trend to settlement.

For this purpose, Figure 1 shows the visual appearance of the device used, composed of three pairs of supports over which the asphalt specimen is fixed. Each support consists of a metallic bar over two springs with gradual length, while the distance between the extreme supports and the central one can be also modified, allowing therefore to reproduce different strength conditions for the supports, simulating railway platform with various levels of strength.

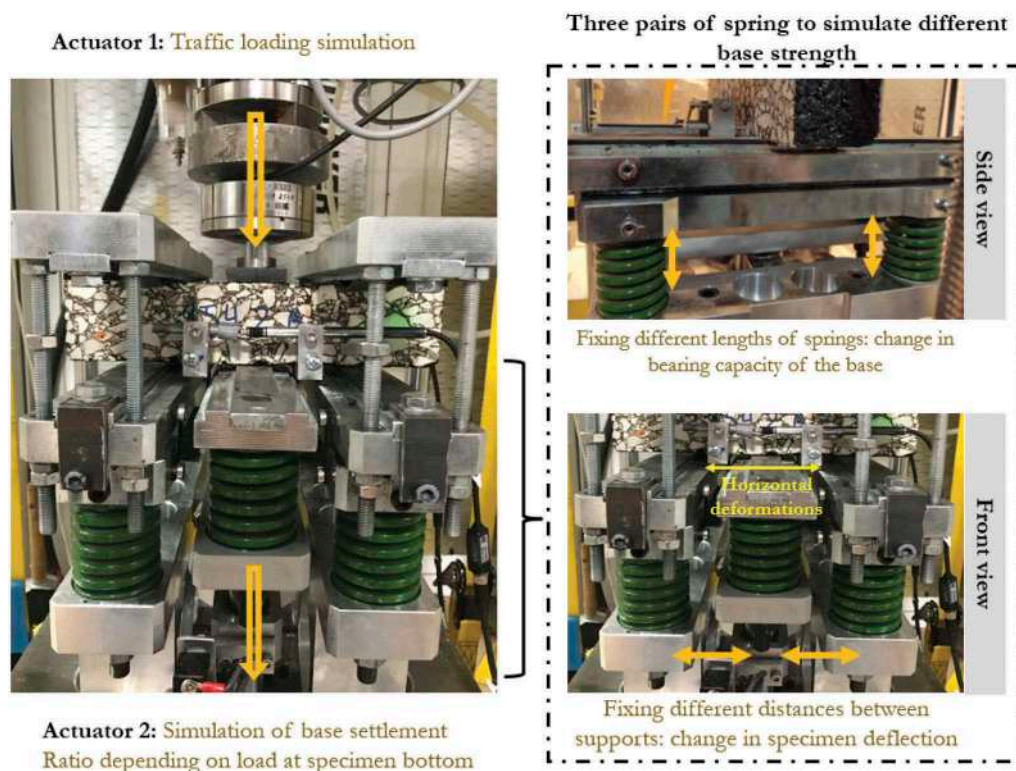


Figure 1. Visual appearance of the laboratory device used for specimen testing.

Besides, the central support is controlled by an electrical actuator that allows for reproducing different settlement ratios through the actuator going down in displacement control to vary the settlement speed, depending on the level of load received (according to the stress transmitted by the specimen). Also, the test includes two LVDTs fixed at the bottom of the specimen to control the elastic and plastic deformations due to traffic loads over specimens supported by different base conditions.

In this study, it was simulated three support conditions allowing for reproducing, in the central support, a vertical deflection of 0.25 mm (D1), 0.50 mm (D2) and 1.25 mm (D3) under dynamic loads with amplitude of 1.5 kN. This level of load was applied through a second vertical actuator sited at the top of the device to simulate traffic loads, aiming to reproduce a press close to 250 kPa in the central area (between supports) of the specimen. These level of stress was calculated by considering an area with length of around 10 cm (obtained as 2.5 cm of the width of central support, plus two half of the mean distance between supports – 7.5 cm) and a width of 6 cm, since the asphalt specimens used in this study had a size of 25 cm of length, 6 cm of width and 6 cm of height.

The three conditions of vertical deflection (D1, D2 and D3), simulating different levels of bearing capacity for mixture support, were considered as appropriate according to previous field measurements of this parameter in sections composed of granular layers and bituminous asphalt (Tonkin and Taylor, 1998). The level of stress on specimen (250 kPa) corresponded to that expected for sub-ballast layer in railway tracks, according to previous experiences (Rose, 2011). The load frequency was fixed in 5 Hz (as expected when considering bogie distance as predominant loads for speeds around 200-300 km/h) (Fu et al., 2020), and the fatigue process was carried out up to the failure of the specimens, detected when drastically increasing horizontal displacements, measured (by two LVDTs) at the bottom of the specimen.

To reproduce differential track settlement, Table 2 lists three laws of speed of vertical settlement for the central support, depending on the level of stress transmitted by the specimens. Each settlement law was associated with each support condition.

Indeed, the first law (L1, with the lowest settlement ratio) corresponded to the case with 0.25 mm of vertical deflection (D1), the second one (L2) was used in combination with D2 (0.50 mm of deflection), and L3 (such with higher displacement speed) corresponded to the case with 1.25 mm (D3). These combinations aimed to provide a strong support (case of L1 and D1) reproducing a good quality platform with high bearing capacity, and lower trend to settlement than the others (combination L3-D3 being the most unfavourable).

Table 2. Laws of vertical displacement reproduced in central support to simulate states of soil settlement, depending on level of stress received from the specimen.

Maximum stress step (kPa)	Settlement speed (mm/cycle)		
	L1	L2	L3
25	4,0E-06	7,0E-06	3,5E-05
50	1,0E-05	2,0E-05	1,0E-04
75	1,6E-05	5,0E-05	1,8E-04
100	2,2E-05	8,0E-05	2,5E-04
125	2,8E-05	1,1E-04	3,3E-04
150	3,4E-05	1,4E-04	4,0E-04
175	4,0E-05	1,7E-04	4,8E-04
200	4,6E-05	2,0E-04	5,5E-04

3 ANALYSIS OF RESULTS

Figure 2 displays the mean values of the stress transmitted by each type of mixture (with different binder) to the central support when receiving a stress of 250 kPa, depending on the support condition. Results state the importance of the bearing capacity of the bituminous

mixtures, allowing for considerable reduction in stress transmitted to bases when using stiffer materials. This could allow for higher durability of the substructure, being accentuated when using the MB2 due to the increase in stiffness associated with the combination of polymers and a hard bitumen, leading to high modulus asphalt manufactured with modified binder (Table 1).

Results also denotes the relevance of the bearing capacity of the supports since considerable differences on stress dissipation were recorded for the different testing conditions, but in all of them presenting lower values of stress when using the modified binders (MB1 and MB2).

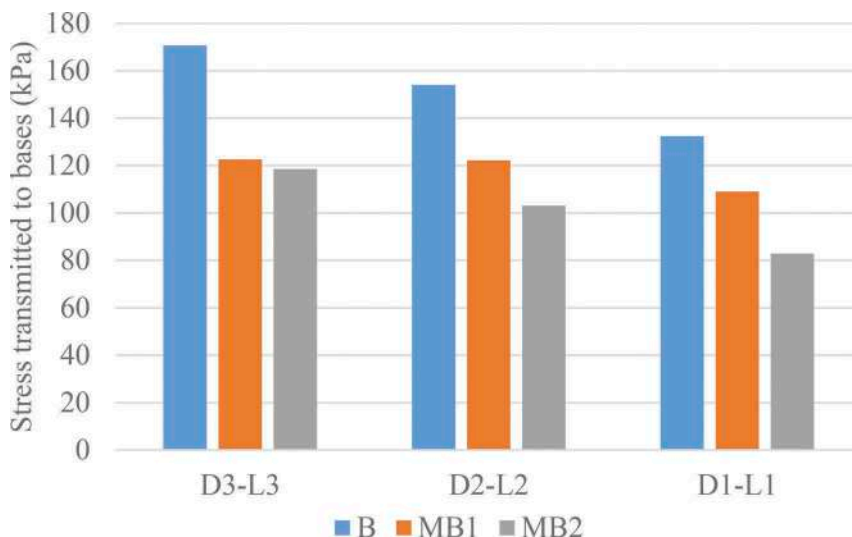


Figure 2. Mean values of stress transmitted by each mixture under various support conditions.

The increase in bearing capacity associated with higher material stiffness is also seen in Figure 3 that represented the mean values of horizontal deflection at the bottom of the specimen during the first 1,000 loading cycles of the fatigue test. Results state the importance of the bearing capacity of the base for the bituminous sub-ballast due to the increase in horizontal deflections when using softer soils under sub-ballast, where the property of the bituminous layer showed to have a key role.

In fact, for such support conditions (D3-L3 reproducing soft soil), the modified bitumen showed higher benefit to reduce the material deflection (due to higher bearing capacity) in comparison to the conventional bitumen. Therefore, these advanced binders could not only increase the strength of the sub-structure, but also reducing the susceptibility to base quality (strength). This was more remarkable in the case of applying a modified hard bitumen, which could allow for noticeable rise in the strength of the track substructure, and therefore, according to previous studies (Sol-Sánchez et al., 2016), reducing need for maintenance associated with settlement.

Besides, from results in Figure 4 (displaying the mean values of total number of cycles to materials failure depending on testing condition), it can be confirmed that the support condition plays a key role on the behaviour of bituminous sub-ballast, seeing that, regardless of the type of mixture, the use of good quality platform could exponentially increase the durability of the bituminous sub-ballast (up to 68 times according to this test).

Results also indicates that the mixtures with higher bearing capacity showed the longer material durability. Nonetheless, in contrast to the previous results, the stiffer materials (such mixtures with modified bitumen) showed higher improvement when applied over good quality platform. In this case, the fatigue life increased up to around 10 and 25 times in reference to

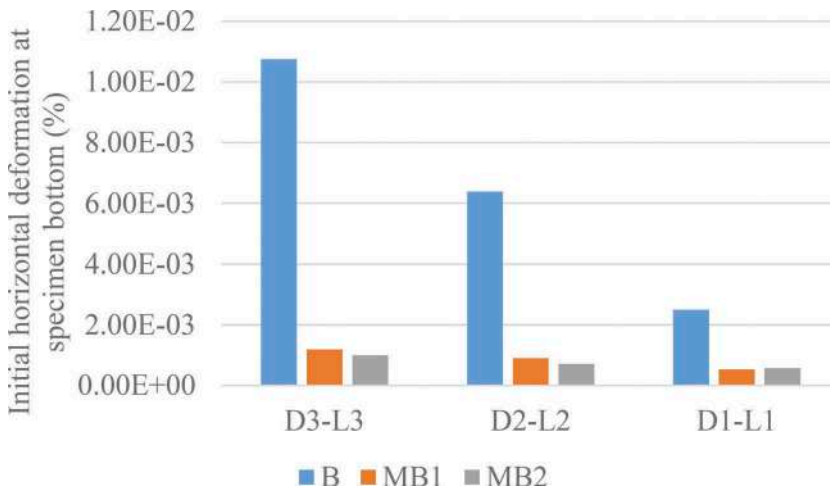


Figure 3. Mean results of initial horizontal deflection for each mixture depending on support.

the conventional bituminous sub-ballast (for the MB1 and MB2, respectively), while such increase was more limited under unfavourable conditions (D3-L3) where the increases were around 3 and 6 times.

This fact, joined to results from Figure 3, could indicate that the properties of the mixtures play a key role on the bearing capacity of the track when using a soft sub-structure (the higher the material stiffness, the higher the improvement in track strength), but limiting the benefits associated with durability when combining soft soils with higher settlement speed (which can be expected to take place in this type of sub-structures). However, when using the stiffer materials over strong supports, the benefits of polymer modified binders was highlighted since the improvement in bearing capacity remained (although reducing the level of increase), while obtaining higher increase in material durability. This could be related to the lower speed of base settlement expected in this type of bases, accentuated with the lower levels of stress transmitted by the stiffer mixtures (leading to lower settlement ratio than those for conventional bitumen).

Therefore, these results denote the relevance of considering the mechanical properties of the support for the bituminous layers in order to prove the benefits of using innovative materials, since their performance and durability vary considerably depending on key parameters like bearing capacity of the base and the settlement ratio. Thus, their benefits in increasing material life and strength will depend on soil conditions.

On the other hand, to analyse the capacity of deformation of the materials to deform before breaking, Figure 5 displays the mean values of final horizontal deformation at the bottom of asphalt specimens. Results state that this parameter is a key factor on the performance and durability of the bituminous materials since it allows for evaluating the capacity of adaption of each mixture to the sub-structure deformation without breaking (which could lead to the acceleration of structure degradation).

Results show that the modified binders led to a considerable increase in the final deformation of the mixture before failure under the most favourable conditions (D1-L1), which could be associated with the use of polymer modified binders, joined to the lower settlement ratio obtained when using these stiffer materials (by reducing the stress level transmitted to supports). Also, it was seen that these mixtures presented comparable deformation values to those from the conventional mixture when applied over soft support where premature failure of the stiffer materials could be expected. Therefore, these results could indicate that the use of polymers to modify the bitumen allow for increasing the material stiffness, but also the capacity to deform before breaking, even under high deformation ratios.

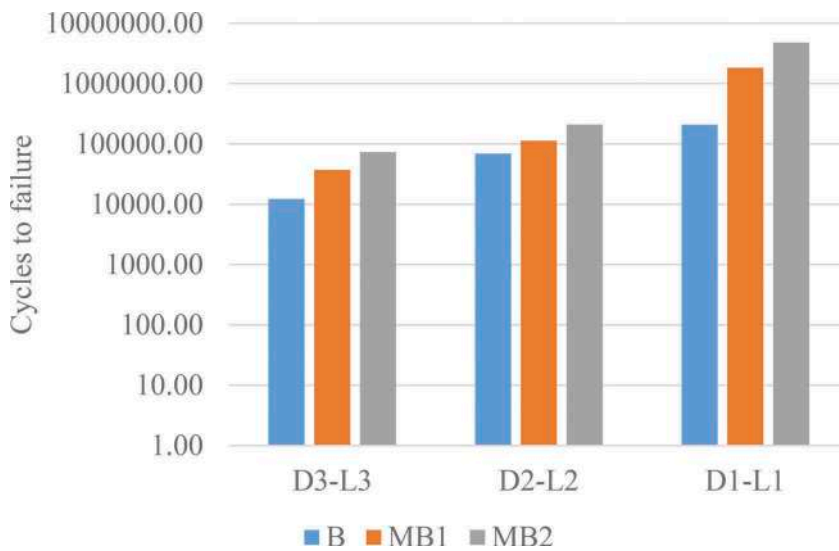


Figure 4. Number of cycles to specimen failure under simulated traffic loads over different support conditions.

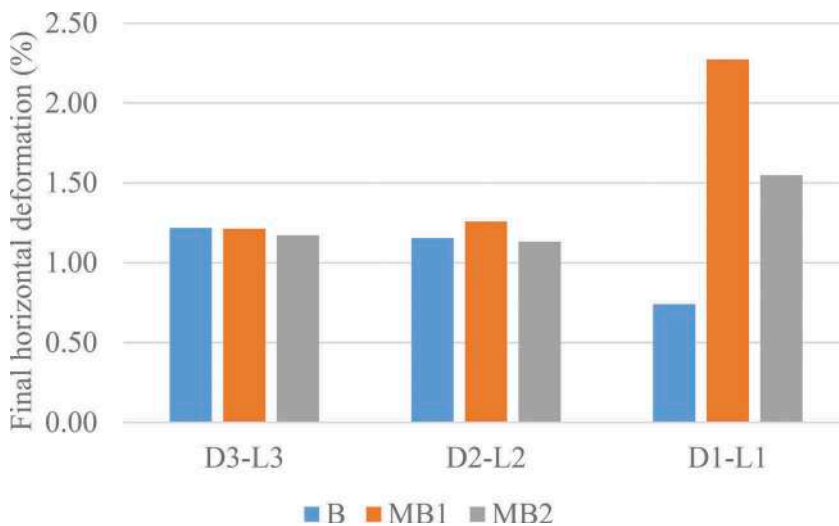


Figure 5. Mean values of final horizontal deformation at the bottom of the specimens at the end of the test under various testing conditions.

This fact could be confirmed in Figure 6, which represents the mean values of material ductility, calculated as the product of cumulative horizontal deformation and the total load applied through the multiplication of total number of cycles and level of cycle load. These results demonstrate that the support conditions have relevant importance on the type of breaking of the material, obtaining more ductile failure when using strong supports. This was accentuated when using the modified bitumen where the use of polymers led to a more ductile material, allowing for longer durability of the mixtures, particularly when applied over good quality base.

Therefore, these results denote the importance of assessing the performance of the mixtures under diverse in-service conditions expected for the bituminous sub-ballast, allowing for

understanding the potential benefits of using innovative materials and binders while identifying the optimal application of them.

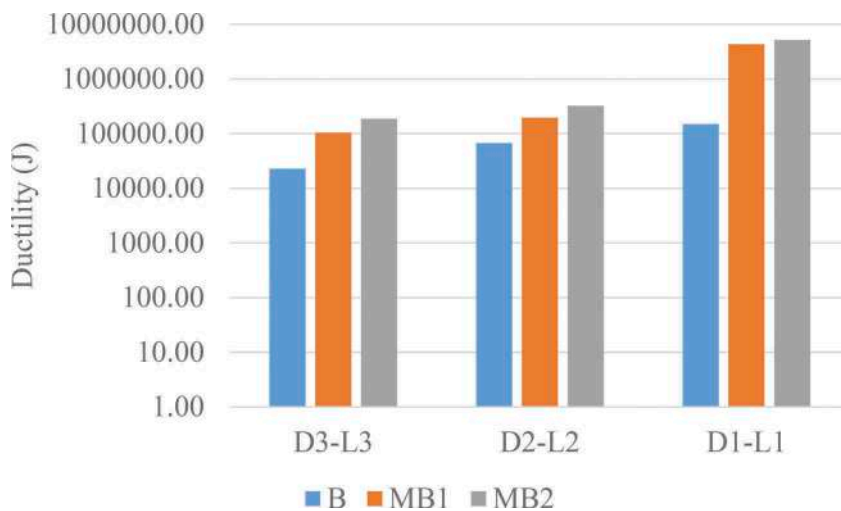


Figure 6. Results of material ductility depending on type of bitumen and testing conditions.

4 CONCLUSIONS

This paper focused on assessing the impact of the bearing capacity and settlement ratio of the support for bituminous sub-ballast on its mechanical behaviour and fatigue life. For this purpose, it was evaluated the performance of an asphalt mixture manufactured with three different bitumen, using an innovative laboratory device able to reproduce various conditions of strength and trend to settlement of the support for the asphalt specimens, assessing the influence of type of binder under diverse testing conditions. From results, the following conclusions can be drawn:

- The bearing capacity of the support for the bituminous sub-ballast plays a key role on the capacity of the asphalt layers to dissipate the stress transmitted to sublayers. This makes relevant to consider this property when evaluating the performance of these bituminous materials.
- In this sense, for the mixtures assessed in this study, the higher rate of stress dissipation where for the cases with polymer modified bitumen, particularly when using a modified hard bitumen.
- Similarly, the bearing capacity and trend to settlement of the support showed to be a key factor on the horizontal deflection for the asphalt mixtures, while also affecting clearly the durability of the material.
- In particular, results stated that, in the case of reproducing soft sub-structures, the higher the stiffness of the asphalt mixture, the higher the improvement in track strength. However, the benefits of using modified bitumen are limited in terms of durability for this type of structures when combining soft soils with higher settlement speed.
- Nonetheless, when using the stiffer materials over strong supports, the mixtures with polymer modified bitumen still reduced the stress transmitted and deflection at layer bottom, while obtaining noticeable increase in material durability.
- This fact could be associated with the higher ductility and capacity to deform of the mixtures using polymer modified bitumen, even that with a hard bitumen as base.

Therefore, based on these laboratory results, it can be said that the bearing capacity and settlement ratio of support for bituminous sub-ballast play a key role on the material

performance and durability, varying their impact depending on the design and properties of the asphalt mixtures. Thus, it could be of interest to consider these factors when proving the potential benefits of innovative asphalt mixtures to be applied as bituminous sub-ballast. Nonetheless, further studies are required to evaluate the impact of these factors on other types of asphalt mixtures, while correlation with real track performance could be of interest.

ACKNOWLEDGMENT

The present study has been conducted within the framework of the HP-RAIL (Smart technologies & high performance materials for the next railway generation, RTC-2017-6510-4) research project, funded by the Ministry of Science, Innovation and University of Spain and the Ministry of Economy and Competitiveness of Spain, respectively.

REFERENCES

- Akisetty, CK., Lee, SJ., Amirkhaniyan, SN., 2009. *High temperature properties of rubberized binders containing warm asphalt additives*. *Constr Build Mater* 23:565–573
- Asgharzadeh, S., Sadeghi, J., Peivast, P., Pedram, M., 2018. *Fatigue properties of crumb rubber asphalt mixtures used in railways*. *Constr Build Mater* 184:248–257
- Asphalt Institute, 1998. *HMA Trackbeds—Hot Mix Asphalt for Quality Railroad and Transit Trackbeds*, Informational Series 137, 10 p.
- Fang M., Rose J.G., West R.C., Qiu, Y., 2011. *Comparative analysis on dynamic behavior of two HMA railway substructures*. *J Transp Res Board*; 19(1):26–34; doi: 10.3969/j.issn.2095-087X.2011.01.005.
- Fu, Q., Chen, X., Cai, D., Lou, L., 2020 *Mechanical Characteristics and Failure Mode of Asphalt Concrete for Ballastless Track Substructure Based on In Situ Tests*. *Appl. Sci* 10: 3457
- Khairallah, D., Blanc, J., Couttineau, L., Hornych, P., et al., 2019. *Monitoring of railway structures of the high speed line BPL with bituminous and granular sublayers*. *Constr Build Mater* 211:337–348.
- Rose, J., 2011. *Design, Evaluation, and Performance of Asphalt Trackbeds – U.S. Experience*, International Seminar on Optimization of Railway Design using Bituminous Sub-Ballast. *BITU-RAIL*. Lisboa, Portugal
- Rose, J.G., Teixeira, P.F., Veit P., 2011. *International Design Practices, Applications, and Performances of Asphalt /Bituminous Railway Trackbeds*. GEORAIL, Paris, France.
- Sol-Sánchez M., Moreno-Navarro F., Hidalgo, M.E.; Pérez, V.; Rubio-Gómez M.C., 2020. *Laboratory study on asphalt mixtures for application in port pavements*. *Construction and Building Materials*, 235, 117513
- Sol-Sánchez M., Pirozzolo L., Moreno-Navarro F., Rubio-Gómez M.C., 2016. *A study into the mechanical performance of different configurations for the railway track section: A laboratory approach*. *Engineering Structures*, Volume 119, 15 July 2016, pp. 13–23
- Sol-Sánchez M., Pirozzolo L., Moreno-Navarro F., Rubio-Gómez M.C., 2015. *Advanced characterisation of bituminous sub-ballast for its application in railway tracks: The influence of temperature*. *Construction and Building Materials*, 101, pp. 338–346.
- Teixeira P.F., Ferreira P.A., López Pita A., Casas C., Bachiller A., 2009. *The use of bituminous sub-ballast on future high-speed lines in Spain: Structural design and economical impact*. *IJR International Journal of Railway*, 2, 1–7.
- Tonkin & Taylor Ltd. 1998. *Pavement deflection measurement and interpretation for the design and rehabilitation treatments*. Transfund New Zealand Research Report No. 117. 70pp.
- UNE-EN 12697-12, 2009. *Bituminous mixtures - Test methods for hot mix asphalt - Part 12: Determination of the water sensitivity of bituminous specimens*. Asociación Española de Normalización y Certificación.
- UNE-EN 12697-23, 2018. *Bituminous mixtures - Test methods for hot mix asphalt - Part 23: Determination of the indirect tensile strength of bituminous specimens*. Asociación Española de Normalización y Certificación.
- UNE-EN 12697-26, Annex C, 2009. *Bituminous mixtures - Test methods for hot mix asphalt - Part 26: Stiffness*. Asociación Española de Normalización y Certificación.
- UNE-EN 12697-6, 2012. *Bituminous mixtures - Test methods for hot mix asphalt - Part 6: Determination of bulk density of bituminous specimens*. Asociación Española de Normalización y Certificación.

- UNE-EN 12697-8, 2003. *Bituminous mixtures - Test methods for hot mix asphalt - Part 8: Determination of void characteristics of bituminous specimens*. Asociación Española de Normalización y Certificación.
- UNE-EN 1426, 2015. *Bitumen and bituminous binders - Determination of needle penetration*. Asociación Española de Normalización y Certificación.
- UNE-EN 1427, 2015. *Bitumen and bituminous binders - Determination of the softening point - Ring and Ball method*. Asociación Española de Normalización y Certificación.
- Yu, Z., Connolly, DP., Woodwar, PK., Laghrouche, O., 2019. *Settlement behaviour of hybrid asphalt-ballast railway tracks*. *Constr Build Mater* 208:808–817
- Yu, C., Wang, H., Xu, S., You, Z., 2020. *High modulus asphalt concrete: a state-of-the-art review*. *Construction and Building Materials*, 237, 117653.

Proposed damage risk assessment of pavement subsurface cavities using the rolling dynamic deflectometer

J.M.V. Flores, T.S. Tran, W.S. Lee & K.D. Kim

IRIS Technology, Seoul, South Korea

C.A. Elipse & A.O. Madlangsakay

Department of Civil and Environmental Engineering, Sejong University, Seoul, South Korea

H.J. Lee

Professor, Department of Civil and Environmental Engineering, Sejong University, Seoul, South Korea

ABSTRACT: Undetected pavement subsurface cavity can cause pavement's premature failure leading to road accidents eventually risking consumer safety. Therefore, early detection of this is essential to prevent damage accumulation resulting to pavement failure and collapse. In the past years, the ground penetrating radar (GPR) has been commonly used in finding cavities due to its performance and practicality in detection. However, GPR detection alone may not be sufficient in preventing damages that these cavities may cause. Further assessment of these cavities must be done in order to provide proper rehabilitation method based on the current condition of the pavement structure. In this study, a damage risk assessment method is proposed considering the change in the pavement's modulus and natural frequency using the rolling dynamic deflectometer (RDD). From the field analysis, it was found that the RDD backcalculated modulus is affected by the occurrence of a cavity. It was also observed that there is a decrease on the natural frequency of a pavement with cavity compared with the intact condition. Because of this, the pavement modulus and natural frequency were used as essential parameters in evaluating the current risk condition of the pavement with subsurface cavity. A damage factor is then proposed considering these parameters quantifying the deviation of the real (with cavity) from the ideal (without cavity) pavement condition. Furthermore, the damage factor also characterizes the pavement condition for proper rehabilitation method recommendation depending on the risk assessment based on its damage factor. Using the proposed approach in evaluating and assessing pavement condition based on subsurface cavity condition, a more concise and comprehensive evaluation of risk due to subsurface cavity is presented.

Keywords: Rolling dynamic deflectometer, Natural frequency, Disaster risk reduction, Cavity detection, Pavement rehabilitation

1 INTRODUCTION

Disaster risk assessment in pavement engineering is important in preventing possible accidents in the future. Several types of risk assessment have been used in different civil engineering applications such as flood mapping, earthquake mitigation, urban planning, structural health monitoring and more. In addition, disaster risk assessment methodologies have been conducted to pavements avoiding premature failure and preventing possible risks that may cause accidents.

A study by the California State University in Los Angeles, Department of Civil Engineering evaluated the resilience of pavements with respect to natural disasters by presenting scenarios and probable intensity of damage (Valenzuela 2017). Furthermore, disaster risk assessment was also then applied in analyzing pavement flooding risks (Lu 2019). In the study, different risk assessment methods were evaluated and is incorporated with pavement management. Pre-event pavement flooding risk assessment and post-event pavement management were proposed to be implemented incase such disaster arise. Another study also developed a risk assessment method for depression and cave-ins caused by subsurface cavity which is based on the Japanese Road Authority's risk rank system (Choi 2018). The established risk assessment procedure utilizes the cavity dimensions of depth and length together with the thickness of the asphalt layer in recommending necessary rehabilitation methods. However, this study is more of a reactive approach than being proactive. There is a need to develop a procedure that will assess the pavement's underground condition to prevent the occurrence of the cavity.

The ground penetrating radar (GPR) has been used in several subsurface explorations since it can profile the pavement's subsurface using reflected signals. It is used in profiling the soil to locate underground objects such as utility pipes, buried objects and cavities. In South Korea, the use of the GPR was highly recommended to be conducted before any construction due to the emerging risks caused by the presence of cavities, with an enacted law (KMGL 2016). However, determining cavity occurrence may not be enough in preventing potential disasters to happen. With this, several researchers also tried to determine the exact location and the size of the cavity to properly recommend appropriate rehabilitation methods. In one of those studies, the GPR scanned image was used in estimating the cavity dimensions by correlating actual cavity dimension with the geometric information of the GPR scanned image of the cavity (Park 2019). However, the use of the GPR is still limited when it comes to pavement cavity detection.

The rolling dynamic deflectometer (RDD), on the other hand, was originally developed to profile pavements while moving (Bay 1998). It was also used in detecting weak pavement and mapping cracks. Furthermore, it was used in the evaluation of airport pavements by determining the strength of the pavement and the joint conditions (Nam 2011, Anderson et al 2015). The RDD has a high potential in detecting underground anomalies on road sections since it can conduct testing while moving, this was presented in a study wherein field testing was done using both the GPR and the RDD (Scullion 2006, Nam 2011). In the study of Scullion (2006), the RDD and the GPR were used in testing jointed concrete pavements. It was concluded that GPR survey and visual inspection followed by the RDD survey must be conducted to properly evaluate the condition of jointed concrete pavements. Meanwhile in the study of Nam (2011), evaluation of the load transfer efficiency of airport pavements were found to be more accurate using both RDD and GPR. Also recently, a study conducted by Nam (2019), used the RDD to detect potential sink-hole occurrence. The GPR and the RDD was used together in field investigations to determine the cavity occurrence by analyzing the measured RDD deflections and the acquired GPR signals. However, there were no quantitative assessment made to properly evaluate the risk of the cavity.

In this study, a damage risk assessment procedure is proposed evaluating the occurrence of a pavement subsurface cavity. Using the GPR and the RDD, a more accurate and highly reliable disaster risk assessment method is established. The GPR was used initially in detecting potential cavity candidates using the survey's scanned images. After, the RDD backcalculated asphalt modulus and natural frequency were evaluated to determine the pavement's condition indices. Using these indices, the damage factor is calculated to determine the most probably cavity sections.

2 BACKGROUND OF THE STUDY

2.1 *Ground penetrating radar*

Several algorithms detecting subsurface objects such as utility pipes, anomalies such as air and cavity and probable sinkholes are already developed. These algorithms utilizes machine

learning in detecting and classifying subsurface objects from GPR surveyed images. In the study of Kang (2019), a deep learning-based detection tool was established in which the A, B and C scanned images of the GPR were used in evaluating the underground object. However, further evaluation is needed since acquired images of rocks or gravel are similar with the GPR surveyed cavity images. Another study evaluated the difference of signals acquired from an asphalt and concrete pavement using the GPR (Rhee 2021). Based on the type of GPR and setting, interpretation of the acquired signals maybe different hence it was recommended to evaluate first the type of GPR to be used before testing. However, this is time consuming considering different length of road sections to be surveyed.

The theoretical background and evaluation methods of the GPR is already established, it only matters on the application. In this study, the GPR used was a ground coupled GPR as shown in Figure 1a. It also used the 3D scanned images as shown in Figure 1b in the detection of potential cavity. Based on previous studies, a hyperbolic curve appearing in the B-scan image of a GPR survey suggests a high probability of cavity occurrence. In addition, considering and evaluating the other scanned images of C and D scan, potential cavity occurrence may further be confirmed which was applied in this study.

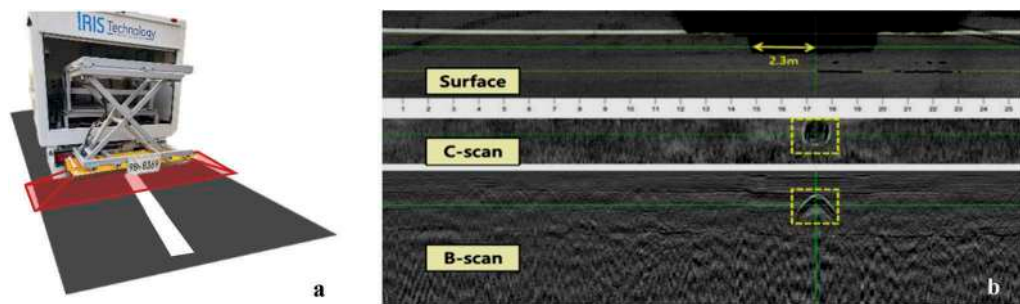


Figure 1. (a) Ground penetrating radar and its (b) surveyed scanned image.

2.2 Rolling dynamic deflectometer

The rolling dynamic deflectometer was developed in the late 1990s at the University of Texas in Austin. It was initially developed to profile the pavement continuously (Bay 1998) and eventually it evolves to as a pavement evaluation method for joints, surface cracks, and sub-grade condition as introduced. The RDD is conventionally used while moving, acquiring continuous pavement deflection. Meanwhile, a study by Flores et al (2021a), presented that the RDD can conduct stopping and moving tests. Using the acquired RDD stopping signal, the natural frequency of the pavement can be evaluated by curve fitting using the free vibration part of the signal while the loading frequency can be determined from the forced vibration part of the signal. Moreover, based on that same study, it was found that the natural frequency, ω_n , is necessary to be determined since it is essential when analyzing the acquired deflections from a vibratory loading. Theoretically, deflections, x , from an external loading is affected by the force, F , loading frequency, ω , spring constant, k , and the amplification factor, β , as shown in equations 1 and 2. This amplification factor is a function of the loading and natural frequency.

$$x(t) = \frac{F \sin(\omega t)}{k} \beta \quad (1)$$

where:

$$\beta = \frac{1}{\left\{ \left(1 - \frac{\omega^2}{\omega_n^2} \right)^2 + \left(\frac{2\zeta\omega}{\omega_n} \right)^2 \right\}^{\frac{1}{2}}} \quad (2)$$

In Figure 2a, the RDD applies a steady state vibratory loading while the sensors acquire sinusoidal deflections. The vibratory loading is caused by an actuator located between the front and back wheel of the RDD while the geophones are located behind the loading with the other sensor directly between the loading wheels. An analysis program in getting the deflections, natural frequency and the loading frequency was developed as shown in Figure 2b. Using the acquired raw signals in terms of velocity, the program converts it to peak to peak deflections which creates a deflection basin from the four geophones. The natural frequency, loading frequency, and the RDD deflections are used in the backcalculation of the pavement modulus for the asphalt, subbase and subgrade layer which is the typical pavement layer system in Korea (Flores et al 2021b).

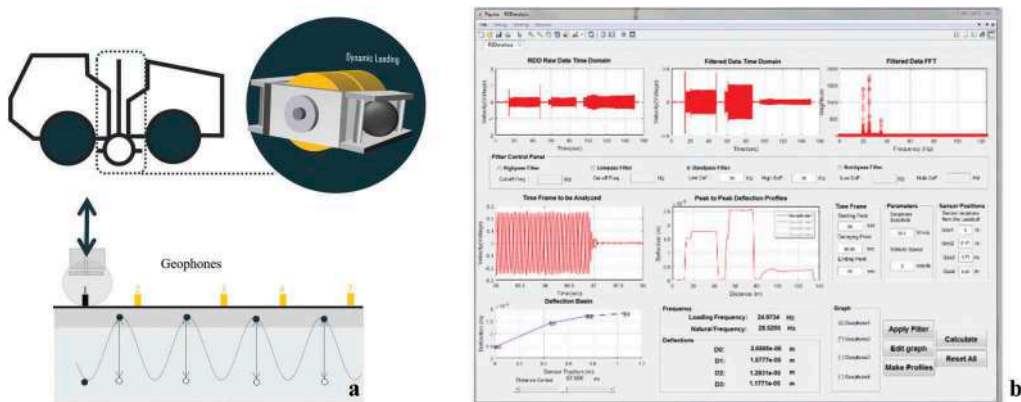


Figure 2. (a) Schematic diagram of a rolling dynamic deflectometer and the (b) program for RDD analysis.

3 FIELD TESTING METHODOLOGY

Several road locations were surveyed using the GPR and the RDD. The GPR survey was first conducted using the ground coupled GPR. The scanned images were then evaluated to determine the probable cavity candidate locations among the road locations using the 3D scanned images as discussed earlier. Next, the RDD was used to profile the pavement deflection using the moving test. Furthermore, those candidate locations for cavity occurrence were evaluated further by dividing each location into sections for RDD stopping test to determine the pavement's natural frequency. The RDD stopping test is conducted wherein the loading is directly above the potential cavity location. In addition, RDD stopping test was conducted also in intact conditions (near the cavity) to determine the intact asphalt modulus and intact natural frequency. Using the backcalculated asphalt modulus and the natural frequency, the potential occurrence of the cavity was evaluated. Field coring was then conducted to verify if the proposed method can accurately determine potential cavity locations. The summary of the field testing and analysis conducted is shown in Figure 3.

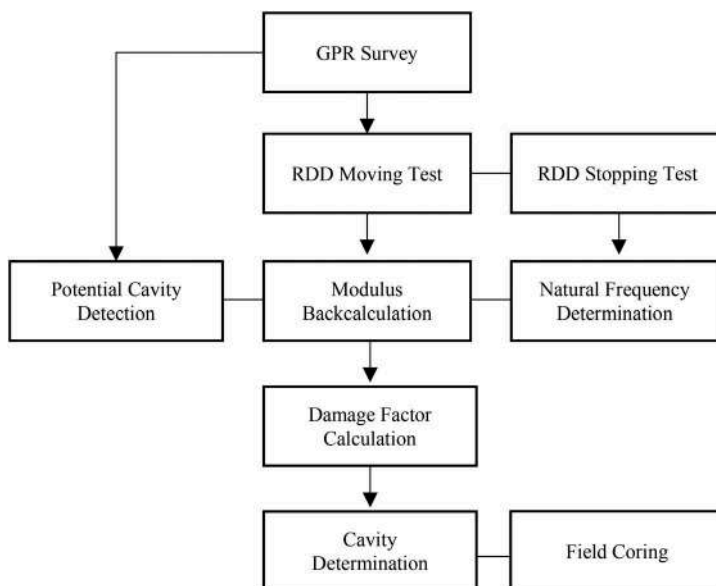


Figure 3. Field testing and experimental method for cavity detection.

4 RESULTS

Ten locations were surveyed and evaluated using the GPR and the RDD. The summary of the test results is shown in Table 1. As seen, the actual RDD loading frequency, ω , applied during testing was 25Hz and was reflected also during the calculation. Each location has also a corresponding natural frequency, ω_n , measured from the RDD stopping test. Using the acquired RDD deflections measured by the sensors, modulus values of the asphalt layer, sub-base and subgrade were backcalculated. Testing was conducted in December where the maximum temperature is averaging from 5° to 10°. The effect of the testing temperature is seen in the backcalculated asphalt modulus which is ranging from 10,000 to 12,000 MPa.

4.1 Asphalt modulus condition index

It is necessary to note that each location may have different average asphalt modulus since it depends on the age, traffic volume, environmental conditions and more. In this study, the asphalt modulus values were compared only within the test sections to consider this variability. As seen in Figure 4, most cavity section's asphalt modulus were lower than the average road section asphalt modulus. Since the cavity is directly under the RDD loading during the testing, the measured deflection is high for the geophone under the loading, D0. Because of this, even though the cavity is not located at the asphalt layer, the backcalculation algorithm assumes that it is the asphalt layer that is weak causing the low backcalculated asphalt modulus. However, it can also be seen that some sections with potential cavity have higher modulus than the average asphalt modulus. Because of this, it is proposed to quantify the asphalt modulus effect of an intact and with cavity condition which will be used further in the study.

The asphalt modulus condition index, ACMI, is developed and is calculated using equation 3 where AC_i is the asphalt modulus value of a section. It is expected that a lower ACMI means a potential cavity while an ACMI value higher than 1 means the pavement is in intact condition.

Table 1. Backcalculated modulus and natural frequency of the test locations.

Loc	Section	ω	Ave ω	ω_n	Ave ω_n	RDD Deflection						Modulus			Average AC Modulus
						D0	D1	D2	D3	AC	Subbase	Subgrade			
1	1	25.00	25	31.87	30.68	2.71E-05	3.56E-05	2.94E-05	2.29E-05	12973.56	198.44219	126.7234	11936.47		
	2	25.00		31.87		1.52E-05	2.06E-05	1.48E-05	1.14E-05	12573.79	189.2864	128.9821			
	3	24.99		23.90		1.80E-05	1.63E-05	1.06E-05	7.46E-06	10470.11	215.13075	129.8653			
	4	25.00		31.87		1.47E-05	1.70E-05	1.17E-05	9.36E-06	12549.6	217.37412	113.1007			
2	5	25.00		33.86		1.42E-05	1.56E-05	1.19E-05	8.73E-06	11115.3	211.07924	93.70446	11456.16		
	1	25.01		33.86	32.27	1.23E-05	1.94E-05	1.62E-05	1.25E-05	11597.86	190.28271	109.2925			
	2	24.99		31.87		1.32E-05	2.04E-05	1.64E-05	1.29E-05	10318.29	197.8112	93.04432			
	3	25.00		33.86		1.41E-05	1.50E-05	1.50E-05	1.21E-05	12288.49	209.92605	124.2969			
3	4	25.00		23.90		2.52E-05	1.72E-05	1.26E-05	9.25E-06	10517.35	205.13271	97.24659	11903.48		
	5	25.00		37.85		1.36E-05	1.57E-05	1.27E-05	1.01E-05	12558.83	203.19592	124.2368			
	1	25.00		39.84	35.86	3.66E-05	2.73E-05	1.53E-05	1.27E-05	12402.24	190.43721	105.9123			
	2	24.99		25.90		5.66E-05	4.55E-05	3.60E-05	2.78E-05	10842.71	195.05655	130.4343			
4	3	25.00		39.84		1.58E-05	6.61E-06	3.04E-06	1.64E-06	12045.97	197.43153	97.19174	11160.30		
	4	25.00		37.85		2.56E-05	1.61E-05	5.99E-06	3.44E-06	12322.99	206.91501	82.38781			
	1	25.00		33.86	34.36	3.39E-04	3.48E-05	1.30E-05	2.71E-05	11314.99	197.4893	82.44617			
	2	25.00		33.86		1.95E-05	1.71E-05	6.34E-06	1.13E-05	10069	208.65449	84.18073			
5	3	25.00		35.86		2.17E-05	1.57E-05	5.85E-06	1.15E-05	11508.65	200.82116	86.96063	11252.93		
	4	25.00		33.86		3.60E-05	2.89E-05	1.09E-05	1.64E-05	11748.57	205.77086	83.95917			
	1	25.00		37.85	37.44	2.90E-05	2.45E-05	1.70E-06	1.49E-05	11124.61	190.96811	127.9631			
	2	25.00		39.84		2.84E-05	2.47E-05	1.78E-06	1.59E-05	12077.21	180.46362	83.86036			
6	3	25.00		36.59		2.72E-05	2.28E-05	1.70E-06	1.42E-05	10895.98	202.65441	87.25264	11525.01		
	4	25.00		35.71		2.23E-05	2.11E-05	1.62E-06	1.51E-05	10032.33	203.48128	107.6391			
	5	25.00		37.23		2.81E-05	2.97E-05	2.02E-06	1.61E-05	12134.54	206.9088	103.452			
	1	25.00		36.08	34.60	1.48E-05	1.09E-05	6.85E-06	6.04E-07	12851.94	205.37664	121.213			
7	2	24.99		34.09		2.43E-05	1.50E-05	9.77E-06	7.33E-07	10747.94	220.22525	122.5427	11099.85		
	3	24.98		30.77		1.86E-05	1.28E-05	8.50E-06	6.55E-07	10057.71	192.91702	127.7863			
	4	25.00		35.71		1.87E-05	1.16E-05	8.37E-06	6.47E-07	12874.07	216.30704	97.03135			
	5	24.99		32.05		3.46E-05	2.02E-05	1.46E-05	1.02E-06	10653.62	189.33509	98.40334			
7	6	25.00		38.89		3.32E-05	1.57E-05	1.12E-05	8.34E-07	11964.76	193.68038	101.1695	11099.85		
	1	24.98		36.76	36.30	1.85E-05	1.30E-05	9.33E-06	7.38E-07	10250.15	190.11255	109.1367			
	2	24.98		36.08		1.94E-05	1.36E-05	9.45E-06	7.09E-07	11057.44	183.24541	97.26724			

(Continued)

Table 1. (Continued)

Loc	Section	ω	Ave ω	ω_h	Ave ω_h	RDD Deflection						Modulus			Average AC Modulus
						D0	D1	D2	D3	AC	Subbase	Subgrade			
8	3	24.99		33.33		7.35E-05	5.11E-05	3.28E-05	1.99E-06	10174.5	194.76211	108.2374	12306.07		
	4	24.99		38.46		2.26E-05	1.51E-05	1.20E-05	8.10E-07	12369.19	207.46211	124.2239			
	5	24.99		36.84		3.91E-05	2.53E-05	2.08E-05	1.32E-06	11647.96	183.9059	89.9225			
	1	25.00		36.46	33.75	2.50E-05	2.56E-05	1.95E-05	2.10E-06	12192.36	214.7994	123.5316			
	2	25.00		36.76		3.77E-05	2.40E-05	1.80E-05	1.98E-06	12101.33	223.42035	93.5942			
9	3	25.00		31.91		5.26E-05	5.34E-05	3.82E-05	3.96E-06	12403.6	218.70674	85.18523	11708.26		
	4	25.00		33.33		4.00E-05	4.09E-05	2.96E-05	3.12E-06	12692.22	209.45558	129.0432			
	5	25.01		29.41		6.88E-05	6.19E-05	5.33E-05	5.36E-06	11658.45	207.20628	91.31631			
	6	25.00		31.25		5.27E-05	4.60E-05	3.05E-05	3.14E-06	12897.66	205.83097	80.93398			
	7	24.99		33.33		5.12E-05	4.66E-05	3.21E-05	3.28E-06	11335.16	217.70418	89.79095			
	8	25.01		36.23		3.28E-05	2.43E-05	1.83E-05	2.00E-06	12841.53	203.9022	111.5866			
	9	25.00		35.09		4.19E-05	3.11E-05	1.99E-05	2.18E-06	12632.33	219.45805	95.26553			
	1	25.01		34.48	33.30	4.29E-05	3.25E-05	2.37E-05	2.46E-06	11846.95	200.58587	84.6813			
10	2	25.02		33.33		3.67E-05	2.49E-05	1.85E-05	2.03E-06	12035.12	199.68677	121.6802	11483.09		
	3	24.98		31.91		3.69E-05	3.23E-05	2.75E-05	2.83E-06	10340.43	196.30391	117.4961			
	4	25.01		33.33		3.88E-05	1.99E-05	1.58E-05	1.71E-06	12855.48	184.52348	129.6949			
	5	25.03		35.09		3.88E-05	1.99E-05	1.58E-05	1.71E-06	12136.96	195.46219	79.26069			
	6	25.02		28.09		5.16E-05	4.04E-05	2.71E-05	2.83E-06	10403.27	197.46606	89.70811			
	7	25.01		36.84		4.91E-05	3.32E-05	2.96E-05	3.05E-06	12339.64	181.38073	110.9215			
	1	25.01		36.84	36.87	4.91E-05	3.32E-05	2.96E-05	3.05E-06	11115.18	188.29775	123.127			
	2	24.99		38.46		5.25E-05	2.52E-05	1.13E-05	5.42E-06	12700.45	192.29477	86.93651			
	3	25.00		34.31		4.12E-05	2.30E-05	1.03E-05	4.94E-06	10065.79	194.50507	127.4138			
	4	24.97		37.88		3.08E-05	1.73E-05	7.76E-06	3.73E-06	12050.92	209.57718	121.3801			

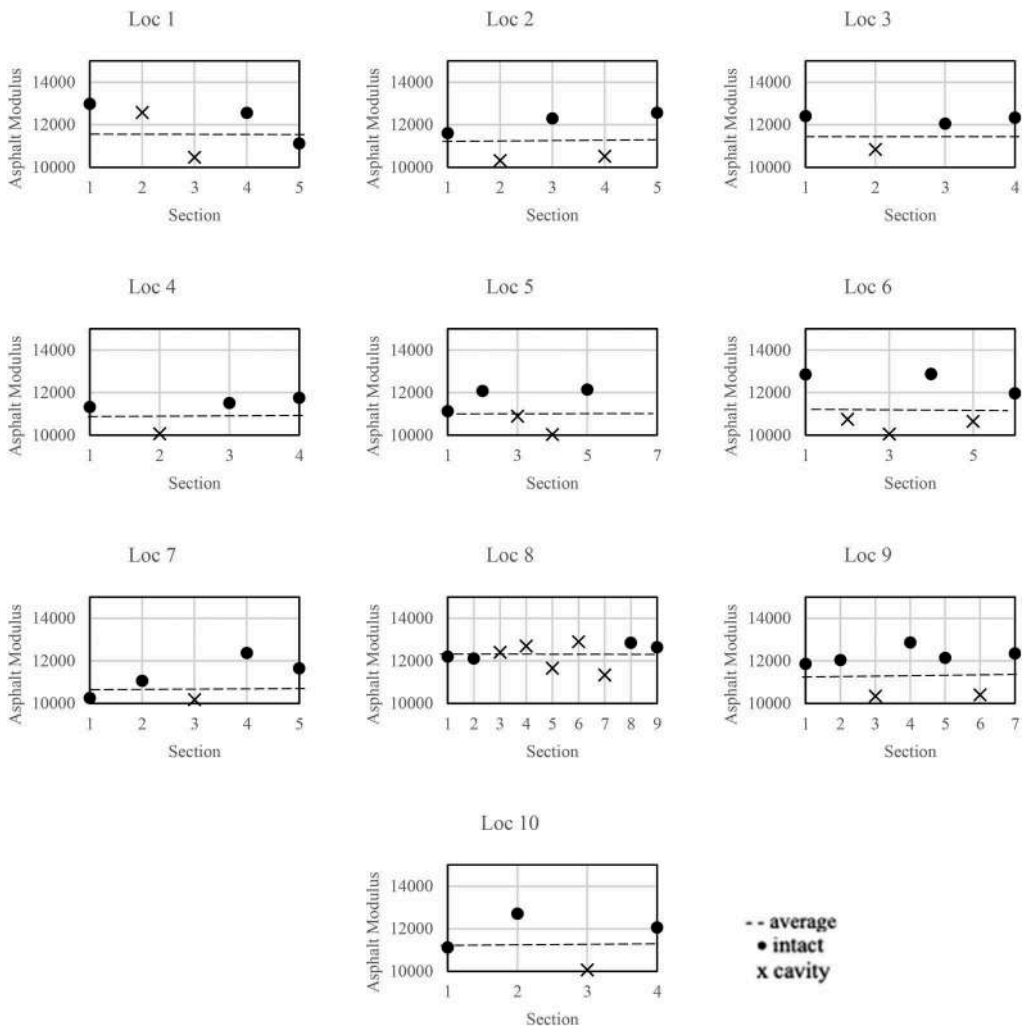


Figure 4. Comparison of the backcalculated modulus from the cavity and non-cavity locations.

$$AC \text{ Modulus Condition Index, } ACMI = \frac{AC_i}{AC_{average}} \quad (3)$$

4.2 Natural frequency condition index

The natural frequency of the cavity and intact condition is also summarized as shown in Figure 5. It was found that the behavior of the natural frequency is similar with the asphalt modulus wherein those with potential cavity have lower values than the average natural frequency. Meanwhile, those intact conditions have higher natural frequency compared with the average natural frequency.

It was also found that similar with the backcalculated asphalt modulus, some sections have higher natural frequency with the average even though it is a potential cavity location. Therefore, a natural frequency condition index, NFCI, is also developed and is calculated using in equation 4 where NF_i is the natural frequency of a road section. It is also expected that a lower NFCI means a potential cavity while a NFCI value higher than 1 means the pavement is in intact condition.

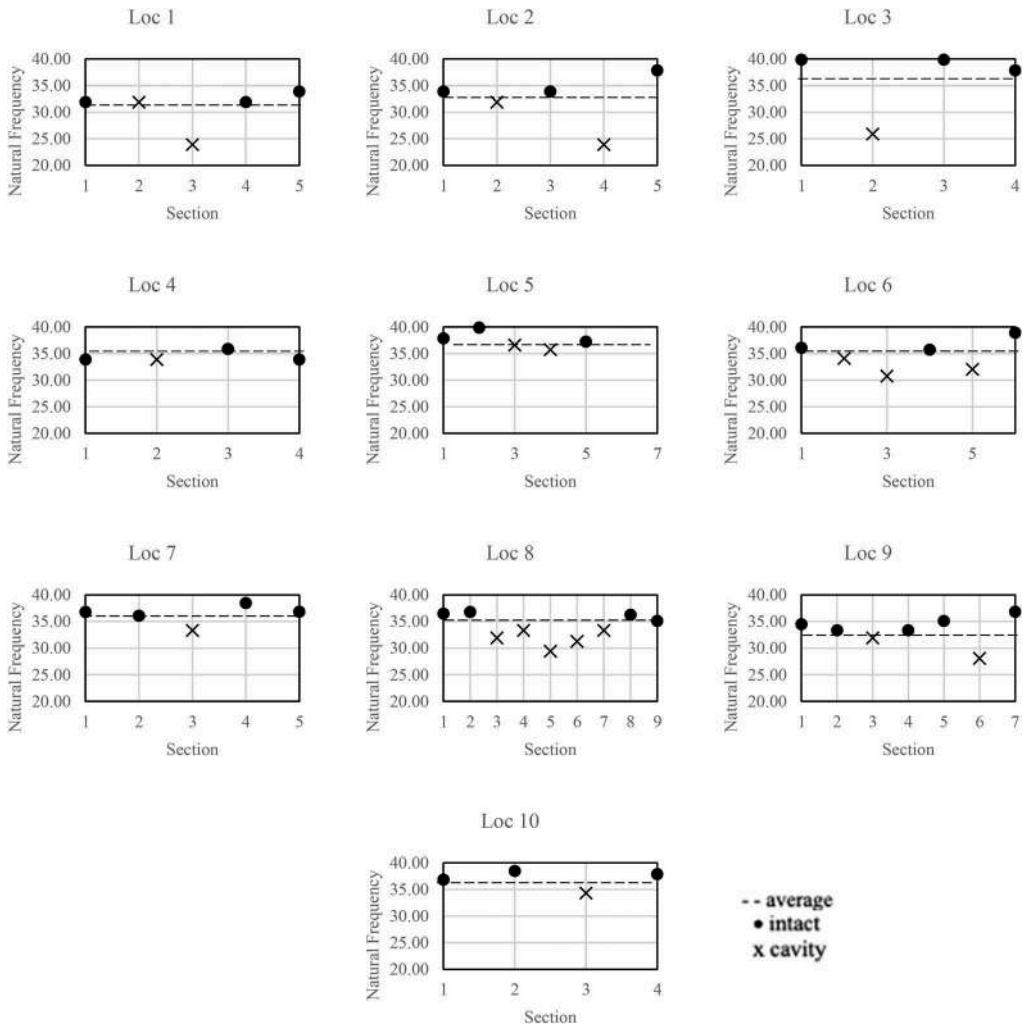


Figure 5. Comparison of the calculated natural frequency from the cavity and non-cavity locations.

$$\text{Natural Frequency Condition Index, } NF_{CI} = \frac{NF_i}{NF_{average}} \quad (4)$$

4.3 Damage factor

Determining the ACMI and the NFCI alone may not be sufficient in determining a potential cavity occurrence as discussed earlier. Some cavity sections have either the ACMI or the NFCI being higher than 1. It is expected that the potential cavity can be properly evaluated using the combined effect of the asphalt modulus and the natural frequency. Because of this, a damage factor, DF, was established. The damage factor, DF, is calculated using equation 5.

$$\text{Damage Factor, } DF = \frac{1}{(ACMI * NFCI)} \quad (5)$$

Table 2. Cavity detection final decision using the total damage factor.

Location	Section	AC mod Condi- tion Index	Nat freq Condi- tion Index	Damage Factor	True Condition	Location	Section	AC mod Condi- tion Index	Nat freq Condi- tion Index	Damage Factor	True Condition
1	1	1.09	1.04	0.89	NC	7	5	0.92	0.93	1.17	C
	2	1.05	1.04	0.91	C		6	1.04	1.12	0.86	NC
	3	0.88	0.78	1.46	C		1	0.92	1.01	1.07	C
	4	1.05	1.04	0.92	NC		2	1.00	0.99	1.01	NC
	5	0.93	1.10	0.97	NC		3	0.92	0.92	1.19	C
2	1	1.01	1.05	0.94	NC	8	4	1.11	1.06	0.85	NC
	2	0.90	0.99	1.12	C		5	1.05	1.01	0.94	NC
	3	1.07	1.05	0.89	NC		1	0.99	1.08	0.93	NC
	4	0.92	0.74	1.47	C		2	0.98	1.09	0.93	NC
	5	1.10	1.17	0.78	NC		3	1.01	0.95	1.05	C
3	1	1.04	1.11	0.86	NC	9	4	1.03	0.99	0.98	C
	2	0.91	0.72	1.52	C		5	0.95	0.87	1.21	C
	3	1.01	1.11	0.89	NC		6	1.05	0.93	1.03	C
	4	1.04	1.06	0.92	NC		7	0.92	0.99	1.10	C
	1	1.01	0.99	1.00	NC		8	1.04	1.07	0.89	NC
4	2	0.90	0.99	1.12	C	10	9	1.03	1.04	0.94	NC
	3	1.03	1.04	0.93	NC		1	1.01	1.04	0.95	NC
	4	1.05	0.99	0.96	NC		2	1.03	1.00	0.97	NC
	1	0.99	1.01	1.00	NC		3	0.88	0.96	1.18	C
	2	1.07	1.06	0.88	NC		4	1.10	1.00	0.91	NC
5	3	0.97	0.98	1.06	C	10	5	1.04	1.05	0.92	NC
	4	0.89	0.95	1.18	C		6	0.89	0.84	1.33	C
	5	1.08	0.99	0.93	NC		7	1.05	1.11	0.86	NC
	1	1.12	1.04	0.86	NC		1	0.97	1.00	1.03	NC
	2	0.93	0.99	1.09	C		2	1.11	1.04	0.87	NC
6	3	0.87	0.89	1.29	C	4	3	0.88	0.93	1.22	C
	4	1.12	1.03	0.87	NC		4	1.05	1.03	0.93	NC

Field coring was conducted to determine if the pavement is intact or has a cavity as presented in Table 2 in the “true condition” column. As seen in the table, the damage factor calculated can accurately determine a potential cavity with an accuracy of more than 90% considering all locations in the field test. It was also observed that in order to be determined as a cavity, the DF should be greater than 1.05 with the exception of one (1) location.

Moreover, using the calculated damage factor, the agency or the engineer can estimate the type of rehabilitation to be conducted. If the ideal condition is assumed to have a damage value of 1, those sections which deviates more will have more extensive rehabilitation method. Since the damage factor presented is the combined effect of the asphalt modulus and the natural frequency, it is reasonable and practical to determine rehabilitation methods based on the calculated damage factor. In addition, those sections with damage factor or 0.95 to 1 can be considered as future risk and may have the probability to be a potential cavity. These sections are recommended to be monitored occasionally to prevent it from becoming a cavity.

5 CONCLUSIONS AND RECOMMENDATIONS

In this study, a method that can evaluate potential cavity occurrence is proposed. The proposed method uses both the GPR and the RDD in evaluating the pavement condition. In addition, the pavement condition is evaluated considering the backcalculated asphalt modulus and the natural frequency of the pavement using the RDD. It was found that the proposed method for disaster risk assessment of potential cavity occurrence is reasonable, practical, and applicable with an accuracy of more than 90% in terms of potential cavity detection.

Road sections with calculated damage factor of greater than 1.05 must be rehabilitated as it is a confirmed cavity location. The rehabilitation method will then be dependent on the damage factor, on how it deviates from the ideal condition of 1. Furthermore, a damage factor of 0.95 to 1 may suggests potential risks in the future hence, monitoring is highly recommended.

However, the proposed method can be improved still. Future study will be conducted by correlating the calculated damage factor with the cavity size. In this way, a more concise and more reliable disaster risk assessment tool for potential cavity occurrence will be developed.

ACKNOWLEDGEMENT

The authors would like to acknowledge the support given by the Korea Agency for Infrastructure Technology Advancement (KAIA) grant funded by the Ministry of Land, Infrastructure and Transport (Grant 22POQW-C152690-04) and Sejong University.

REFERENCES

- Anderson, N., L. Sneed, B. Rosenblad, and Luna, R., 2015. *MoDOT pavement preservation research program volume V: Site-specific condition assessment*. Rep. No. CMR 16-004. Jefferson City, MO: Missouri DOT
- Bay, J. A., and Stokoe II, K. H., 1998. *Development of a rolling dynamic deflectometer for continuous deflection testing of pavements*. Project Summary Rep. No. 1422-3F. Austin, TX: Center for Transportation Research, Bureau of Engineering Research, University of Texas at Austin.
- Choi, Y. W., Park, H. M., Kim, Y. T., Lee, W., and Lee, H. J., 2018. *A risk assessment of asphalt for depression and cave-in by subsurface cavity*. International Journal of Pavement Engineering. <https://doi.org/10.1080/10298436.2018.1520231>.
- Flores, J. M., Lee, H. J., Elipse, C., Lee, W., Kim, K. D. and Baek, J., 2021a. *Dynamic backcalculation approach of deflections obtained from the rolling dynamic deflectometer: fundamental theory*. Journal of Transportation Engineering, Part B: Pavements, American Society of Civil Engineers. 10.1061/JPEODX.0000249.

- Flores, J. M., Lee, S. Y., Lee, H. J., Elipse, C., and Lee, W., 2021b. *Dynamic backcalculation approach of deflections obtained from the rolling dynamic deflectometer: Application and Validation*. Manuscript submitted for publication.
- Kang, M. S., Kim, N., Lee, J. J., and An, Y. K., 2020. *Deep learning-based automated underground cavity detection using three-dimensional ground penetrating radar*. *Structural Health Monitoring*, Vol 19(1) 173–185.
- Korea Ministry of Government Legislation (KMGL), 2016. *The Special Law on Underground Safety Act*. Law No. 13749; KMGL: Seoul, Korea.
- Lu, D., 2019. *Pavement Flooding Risk Assessment and Management in the Changing Climate*. University of Waterloo, Doctoral Dissertation.
- Nam, B.H., 2011. *Transition of the Rolling Dynamic Deflectometer Device from a Screening Tool to an Evaluation Tool for Rigid Airfield Pavement Projects*. Transportation Research Record. Journal of the Transportation Research Record. Washington D.C. DOI:10.3141/2206-06.
- Nam B.H., K. Stokoe II, B. Cho, Y. Kim, and Youn, H., 2019. *A Potential Technology for Road Sinkhole Assessment: The Rolling Dynamic Deflectometer*. *Journal of Testing and Evaluation* 47, no. 3: 1658–1676. <https://doi.org/10.1520/JTE20180003>.
- Park, J. J. and Hong, G., 2019. *A method for cavity scale estimation based on ground-penetrating radar (GPR) explorations: An experimental study*. *Advances in Civil Engineering*, Volume 2019. <https://doi.org/10.1155/2019/1365759>
- Rhee, J. Y., Park, K. T., Cho, J. W. and Lee, S. Y., 2021. *A study of the application and the limitations of GPR investigation on Underground survey of the Korean Expressways*. *Remote Sensing*, 13, 1805. <https://doi.org/10.3390/rs13091805>.
- Scullion, T. 2006. *Using rolling deflectometer and ground penetrating radar technologies for full coverage testing of jointed concrete pavements*. Rep. No. FHWA/TX-05/0-4517-2. Austin, TX: Texas DOT
- Valenzuela, Y., Rosas, R., Mazari, M., Rodriguez-Nikl, and Risse, M., 2017. *Resilience of Road Infrastructure in Response to Extreme Weather Events*. International Conference on Sustainable Infrastructure.
- Yamashita, Y., Kamoshita, T., Akiyama, Y., Hattori, H., Kakishita, Y., Sadaki, T., and Okazaki, H., 2018. The 13th SEGJ International Symposium. <https://doi.org/10.1190/SEGJ2018-136.1>.

Flexible pavement performance with lime treated bases

Mena I. Souliman & Nitish R. Bastola

Department of Civil Engineering and Construction Management, The University of Texas at Tyler, Tyler, USA

Mohamed H. Elshaer

US Army Corps of Engineers Engineering Research and Development Center (ERDC), Hanover, USA

ABSTRACT: The performance of the pavement is influenced by several factors, such as the pavement structure, materials, traffic, and climate conditions. These factors affect the pavement response, mainly the compressive strain developed at the top of each layer and the tensile strain developed at the bottom of the asphalt concrete layer, resulting in various forms of distresses, such as fatigue cracking. The materials used in the construction of these layers are equally important for the long-term performance of the pavements as well as its structural stability. Aggregates are the most used materials in the construction of base layers in a flexible pavement structure. Moreover, the aggregate used in the base layer provides the foundation for the overlying layers and needs to have enough strength, but due to the scarcity of quality materials and the rising demand, base layers are often treated with different types of stabilizing agents. In this study, various mechanistic analyses are performed using the 3-D Move Analysis software to study the effects of lime as a stabilizing agent on fatigue resistance performance. These analyses showed that the use of lime as a stabilizing agent increased the pavement performance up to 48 % for fatigue cracking resistance when compared to untreated base layers. The cost-effectiveness analysis also showed that the use of stabilizing agents would reduce the long-term cost of pavement as compared to untreated bases. The overall cost efficiency of the lime treated base is found to be around 1.60-1.75 times the untreated base.

Keywords: Base treatments, fatigue cracking, mechanistic analysis, lime, cost-efficiency

1 INTRODUCTION

Hot mixed asphalt (HMA) pavement consists typically of 3-layers: HMA surface layer, base layer, and subgrade. The base layer composed of aggregates is important in terms of structural performance. The load transferred from the surface of the pavement ultimately goes to the base; therefore, there is a great need for the base layer to be strong to handle the variable traffic loads and various climatic conditions (Francois, 2016). Different methods are being utilized for enhancing the strength of the base layer against traffic loading and climate conditions. The multiple layers in the pavement structure are required to withstand the traffic loads and various distress generated. A base layer should be strong and have the rigidity to not allow distortion, lateral flow, and consolidation. The base course layer is designed to have adequate thickness to reduce the traffic damage over time (Little et al. 1995). A base layer can be made either bounded or unbounded. A bounded layer refers to a base layer where stabilizing agent or treatments agents is utilized to make the layer more robust and stable. In contrast to the bound layer, an unbounded layer does not utilize any kind of external agent, and the strength of the base layer solely depends on the

strength of the aggregates. Various types of stabilizing agents are being used in bounded bases such as lime, cement, and asphalt. The use of these additives is very beneficial in constructing HMA pavement as they reduce distresses in the pavement structure. Pavement performances are also affected by environmental conditions. Therefore, a proper study regarding the utilization of these kinds of stabilizers must be made through various mechanistic and cost-effectiveness analyses.

2 LITERATURE REVIEW

Stabilization is the process of adding a cementing agent to the soil or crushed rock to produce materials that have greater strength than the original, not stabilized ones (Jaritngam et al. 2014, Wu et al. 2011). There are two types of base layers generally used in the construction of flexible asphalt pavements. These include unbound aggregate bases, which consist of untreated granular materials, and bound aggregate bases consist of granular material bounded physically or chemically by a stabilizing agent (e.g., cement, asphalt emulsion, or foamed asphalt (Jaritngam et al. 2014, Francois et al. 2019, Faysal et al. 2017)). The use of stabilized base results in an increased performance of the base layer with greater stability and proper aggregate interlock. Granular base layers have low elastic modulus values, which requires both asphalt and base layers with higher flexible pavement thickness to avoid premature failure due to rutting or fatigue cracking. The construction cost of the asphalt layer is higher than the construction cost of other pavement layers (Bodhgire et al. 2019). Using treated base layers with higher elastic moduli will reduce the thickness of the pavement layers, decrease construction costs, and conserve natural resources. Various researchers have used different stabilizing agents in HMA pavement; however, the fundamental purpose of using the stabilizing agent remains the same.

Wang investigated the performance of flexible pavements with stabilized bases. The performance of experimental pavement was observed at the Pennsylvania Transportation Research Facility. Crushed stone, aggregate bituminous concrete, aggregate cement, and aggregate lime- pozzolana were used as a base course for the pavement structures with the loading conditions of 2.4 million 18-kip equivalent axle load. The data were analyzed concerning the pavement serviceability index and distress conditions of roughness, rutting, and cracking, and superior performance was observed (Wang, 1996).

Also, Johanneck and Dai used stabilized full depth reclaimed pavement (SFDR) for judging the responses and performance at Minnesota Road Research Facility. Three stabilized sections were made with different ratios of pulverized asphalt concrete to granular base. Engineering emulsions were used as a stabilizing agent, but the emulsion content was varied between the sections. Responses were measured with strain gauges embedded in the HMA and SFDR layers under the wheel loads. The study concluded that the rutting, cracking, and international roughness index were lower, and the stabilized layer provided greater structural performance (Johanneck and Dai 2013).

Johnson studied the use of lime on bases and subgrades to increase its performance. The study found that poor subgrade and base materials can be modified to a significant level if appropriate quantities of the lime were used. The finished base was also found to be waterproof if lime was used (Johnson, 1949). Similar to Johanson's study, Saride et al. used fly ash for the stabilization of the RAP. Saride et al. found that 80 % RAP replacing virgin aggregates can be stabilized with 40% fly ash to meet both the resilient modulus and unconfined strength requirements of base material for low volume roads (Saride et al. 2015). Mohammad et al. also compared the resilient modulus of the limestone aggregate base with different base treated materials. Blended calcium sulfate (BCS) treated with steel slag and BCS treated with fly ash showed higher resilient modulus values among the investigated materials (Mohammad et al. 2016). Incinerator bottom ash (IBA) is a by-product residual produced by incinerating municipal solid waste. Ahmed et al. found that IBA treatment of crushed limestone had a better performance as a road base layer than the untreated limestone regarding their resilient moduli (Ahmed and Khalid 2011).

In addition to the structural benefits of the treated base layers of the pavement, various economic savings are also obtained. Francois et al. conducted a study on five field sections located

on Route 165 in Rhode Island (RI), which were evaluated as part of a controlled study conducted by the RI Department of Transportation (RIDOT) to assess long-term field performance using a stabilized base. It was found that it is cost-effective to use bases stabilized with Portland cement, geogrids, asphalt emulsions, or CaCl₂ over non-stabilized RAP base since the life cycle cost of the untreated RAP base section appeared to be the lowest of all the pavement sections analyzed in the study in terms of predicted performance (Francois et al. 2019).

In a recent study, Bodhgire et al. compared the cement-treated base layer with an untreated virgin aggregate layer. They found that the estimated cost for flexible pavement designed with a cement-treated base layer is 52% lower than that designed using granular aggregates base layer (Bodhgire et al. 2019). Similarly, Koroma studied the life cycle cost analysis of pavement sections containing treated open-graded bases and compared them to traditional dense-graded untreated bases using the predicted performance of the MEPDG (Koroma, 2011). Treated open-graded bases were found to have higher life cycle costs. He concluded that pavement sections with the treated layer would go extra 30 years without maintenance to have identical life cycle costs as those with untreated dense-graded bases.

The various studies presented above showed that adding additive or using base treatments significantly impacted the pavement structural capacity and life. These studies have provided analysis related to the strength, but the long-term effect on the cost and benefit is rarely described. This paper quantifies the recurring cost using mechanistic-empirical analysis based on bottom-up fatigue cracking.

3 STUDY OBJECTIVE

Base treatments are one of the most crucial construction practices to increase the overall pavement performance in addition to potential long-term cost-effectiveness benefits. Various stabilizing materials are used for base treatments. This study focuses on the use of lime as a stabilizing agent. Lime treated base is considered in determining the pavement performance using mechanistic analysis, which then was utilized to investigate the cost-effectiveness for two different asphalt mixes at four different traffic speeds.

4 3D MOVE MECHANISTIC ANALYSIS

One of the most powerful software packages in the design of flexible pavements is referred to as 3-D Move Analysis. It was developed at the University of Nevada Reno under the cooperative agreement with Federal Highway Administrative Agency. Complex surface loading such as multiple loads and non-uniform tire pavement contact stress is handled by the program with the continuum finite layer approach (Siddharthan et al. 1998). Advanced applications of the software include estimation of damage under off-road farm vehicles and assessment of pavement performance at the intersection. Some of the salient features of the 3-D Move Analysis software are adjustable loading configuration and tire, modeling of 3-D surface stresses, and analyzing non-generic tire and axle configuration. This study utilized the 3-D Move Analysis software to the utmost level to find the performance of the flexible pavement base when it accounts for the bottom-up fatigue cracking for two different asphalt mixes and three different speeds for untreated and lime treated sections. Figure 1 shows the typical section of the flexible pavement considered in this study.



Figure 1. Pavement structure considered in the study.

This research used the HMA properties determined in the National Cooperative Highway Research Program (NCHRP) 9-44 A (Witczak et al. 2013). The test results used in this study are the results presented in the project report NCHRP Report 762. The values required in the 3-D Move Analysis, such as dynamic modulus $|E^*|$, phase angle (ϕ), and fatigue regression coefficient, are derived from the same research project. NCHRP 9-44 A had two Superpave asphalt mixes considering PG 64-22 and PG 76-16 binder grades with a nominal aggregate of 19mm.

Table 1 shows the dynamic modulus values and phase angle of the asphalt mix with PG 64-22 at different temperatures and frequencies. The corresponding regression coefficient k_1 , k_2 , and k_3 of the generalized fatigue model for the asphalt mix of PG 64-22 are 0.000558, 3.876197, and 0.875271, respectively.

Table 1. Dynamic modulus (E^*) and phase angle values for asphalt mix with PG 64-22 binder (Witczak et al. 2013).

Temp (F)	Dynamic Modulus (psi)					
	Frequency (Hz)					
	0.1	0.5	1	5	10	25
14	2,501,000	2,830,000	2,946,000	3,188,000	3,328,000	3,514,000
40	1,498,000	1,894,000	2,056,000	2,479,000	2,674,000	2,917,000
70	385,000	561,000	650,000	902,000	1,017,000	1,176,000
100	98,000	148,000	180,000	291,000	360,000	496,000
130	28,000	45,000	56,000	94,000	113,000	151,000
	Phase Angle (ϕ) (degree)					
14	9	8	8	8	8	6
40	19	16	15	14	14	11
70	34	30	27	22	20	17
100	24	25	27	28	28	30
130	13	15	18	22	25	28

Similarly, for asphalt mix with PG 76-16 binder, the fatigue regression coefficients k_1 , k_2 , and k_3 are 0.000558, 3.876197, and 0.875271, respectively. Table 2 shows the dynamic modulus and phase angles values of the mix with PG 76-16 binder.

Table 2. Dynamic modulus (E^*) and phase angle values for asphalt mix with PG 76-16 binder (Witczak et al. 2013).

Temp (F)	Dynamic Modulus (Psi)					
	Frequency (Hz)					
	0.1	0.5	1	5	10	25
14	2,963,000	3,328,000	3,483,000	3,900,000	4,028,000	4,277,000
40	1,805,000	2,137,000	2,303,000	2,710,000	2,844,000	3,067,000
70	786,000	1,103,000	1,249,000	1,696,000	1,905,000	2,035,000
100	181,000	258,000	305,000	503,000	600,000	777,000
130	48,000	81,000	100,000	161,000	195,000	257,000
	Phase Angle (ϕ) (degree)					
14	7.1	9.7	10.8	11.6	11.8	12.8
40	9.5	12.9	14.4	15.0	16.0	16.3
70	14.5	17.7	20.3	24.7	26.2	29.9
100	28.2	31.3	31.4	34.7	34.5	34.0
130	31.2	27.2	26.7	22.4	20.1	19.9

Furthermore, the utilization of lime as an additive agent is made in this study. The addition of lime in the base layer is supposed to significantly enhance the performance of the pavement structure concerning the strength and cost. In general, the elastic modulus of the lime treated base layer can go as high as 100000 psi, which is significantly higher than the untreated base layer (Azadegan et al. 2016). In this study, lime is added at 2% by the volume of aggregates, and eventually, mechanistic analyses were carried under various speeds and binder grades.

5 MECHANISTIC ANALYSIS OF BOTTOM-UP FATIGUE CRACKING

Among the various types of distress conditions in flexible pavements, bottom-up fatigue cracking is one of the significant forms of distress. Bottom-up fatigue cracking is a series of interconnected cracks developed in the HMA surface or base under repeated traffic loading. Crack initiates at the bottom of the asphalt layer and propagates towards the surface of the pavement. The mechanistic performance of the base layer under various treatments, such as lime, is expected to perform better. Figure 2 shows the bottom-up fatigue cracking performance of two different types of mixtures: one with binder grade PG 64-22 and the other one with PG 76-16 under three different speeds of 25, 45, and 65 miles per hour.

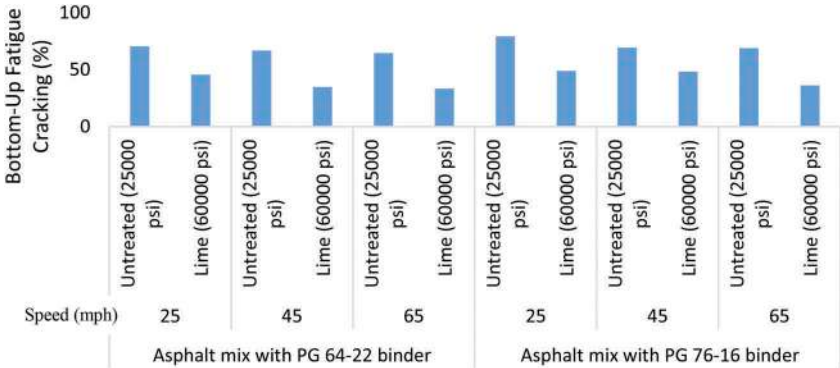


Figure 2. Bottom-up fatigue performance of pavement with lime treatment.

It can be observed from Figure 2 that lime treated base layers had superior fatigue cracking resistance as compared to untreated sections. It can also be noticed that pavement structures with stiffer asphalt binder grade (PG 76-16) are more susceptible to fatigue cracking than softer asphalt binder grade (PG 64-22). The fatigue cracking of both PG 64-22 and PG 76-16 asphalt binders decreases as the traffic speed increases due to the viscoelastic nature of asphalt pavements where pavement structures act as a strong material under high-frequency loading (high traffic speed). In contrast, it acts as a weak material under low-frequency loading (low traffic speed).

In order to mathematically quantify the performance of base treatment concerning its improved fatigue cracking resistance, a Fatigue Cracking Reduction Percentage (FCRP) was calculated as follows:

$$FCRP = \frac{\text{Fatigue cracking for untreated base section} - \text{fatigue cracking of treated base section}}{\text{Fatigue cracking for the untreated base section}} * 100\% \tag{1}$$

Table 3 shows the calculated FCRP for all structures illustrated in Figure 2. All presented lime treated bases at different traffic speeds, and asphalt mixes had an average FCRP of 41.3%. This indicates that lime base treatment has superior performances than untreated sections.

Table 3. Bottom-up fatigue cracking performance of various base treatments.

Asphalt Mix	Speed Limit (mph)	Base treatment	Bottom-Up Fatigue Cracking (%)	Fatigue Cracking Reduction Percentage (FCRP)
With PG 64-22 binder	25	Untreated (25000 psi)	70.38	N/A
		Lime (60000 psi)	45.54	35.3
	45	Untreated (25000 psi)	66.82	N/A
		Lime (60000 psi)	34.84	47.9
	65	Untreated (25000 psi)	64.56	N/A
		Lime (60000 psi)	33.32	48.4
With PG 76-16 binder	25	Untreated (25000 psi)	79.27	N/A
		Lime (60000 psi)	48.99	38.2
	45	Untreated (25000 psi)	69.37	N/A
		Lime (60000 psi)	48.29	30.4
	65	Untreated (25000 psi)	68.88	N/A
		Lime (60000 psi)	36.19	47.5

*N/A relates to the original, untreated base layer

6 COST-EFFECTIVENESS ANALYSIS OF BASE TREATMENTS

Cost-effectiveness analysis plays an essential role in determining the performance versus the cost of using different base treatment applications. In this study, a cost-effectiveness analysis was conducted for lime treated bases in terms of their improved fatigue resistance compared to untreated bases. The following is the mathematical representation of the estimated cost-effectiveness of base treatments in terms of bottom-up fatigue cracking and rutting:

$$\text{Cost – effectiveness} = \frac{\text{Undamaged Area of Pavement due to Bottom – up fatigue cracking}}{\text{cost per mile of the pavement}} \quad (2)$$

Upon determining the cost-effectiveness of each base treatment, the cost-effectiveness ratio can also be defined as follows:

$$\text{Cost – Effectiveness Ratio} = \frac{\text{Treated Cost Effectiveness}}{\text{Untreated Cost Effectiveness}} \quad (3)$$

In order to calculate the cost-effectiveness illustrated above, the following two subheadings (6.1 and 6.2) present the required calculations of both remaining undamaged pavement and the cost per mile of pavement.

6.1 Remaining undamaged pavement condition

By the end of the design life of 20 years, the remaining undamaged surface area of 1 mile of pavement section due to bottom-up fatigue cracking can be estimated as the total surface area



Figure 3. Pavement structure considered for the study.

(5280 ft*12 ft) illustrated in Figure 3 minus the predicted bottom-up fatigue cracking as shown in Table 3.

6.2 Cost per mile of pavement

To estimate the cost of each base treatment and compare it to the untreated base, the cost of one ton of each of the base treated layer was calculated given the fact the unit price for aggregates and lime \$22, \$220.71 per ton, respectively (TXDOT, 2019). In this analysis, lime was added to the base aggregates at a rate of 2% by weight of the aggregates. This leads to the cost of the base layer calculated as the following (assuming that the cost of plant and equipment is the same for all types of bases).

- 1 Ton of Untreated Base Layer: \$22/ton
- 1 Ton of Lime Treated Base: 2% of \$220.71/ton+ 98% of \$22/ton=\$25.98/ton

For 8 inches of base layer thickness, as shown in Figure 3, the required quantity is calculated as the width (12ft) × length (5280ft) × thickness (0.667 ft) × density (137.037 lb/ft3) = 2895.7 tons. Therefore, the cost required for paving with the given base and treatments can be calculated as:

- Cost to pave 1 mile of untreated base case= \$ 63,705
- Cost to pave 1 mile of lime treated base case= \$ 75,229

6.3 Cost-effectiveness of lime treatment in terms of bottom-up fatigue cracking

Based on the calculated remaining undamaged area of the pavement due to bottom-up fatigue cracking and the cost per one mile of each base-treatment, cost-effectiveness for lime

Table 4. Cost-effectiveness of lime treatment for bottom-up fatigue cracking.

Asphalt Mix	Speed Limit (mph)	Base Treatment	Remaining undamaged surface area (ft ²)	Cost to pave one mile (\$)	Cost-Effectiveness (using equation 2)	Cost-Effectiveness Ratio (using equation 3)
With PG 64-22 binder	25	Untreated (25000 psi)	18767.23	63,705	0.29	N/A
		Lime (60000 psi)	34505.86	75,229	0.46	1.56
	45	Untreated (25000 psi)	21022.85	63,705	0.33	N/A
		Lime (60000 psi)	41285.38	75,229	0.55	1.66
	65	Untreated (25000 psi)	22454.78	63,705	0.35	N/A
		Lime (60000 psi)	42248.45	75,229	0.56	1.59
With PG 76-16 binder	25	Untreated (25000 psi)	13134.53	63,705	0.21	N/A
		Lime (60000 psi)	32319.94	75,229	0.43	2.08
	45	Untreated (25000 psi)	19407.17	63,705	0.3	N/A
		Lime (60000 psi)	32763.46	75,229	0.44	1.43
	65	Untreated (25000 psi)	19717.63	63,705	0.31	N/A
		Lime (60000 psi)	40430.02	75,229	0.54	1.74
Overall Cost-Effectiveness Ratio with the use of lime on base having asphalt mix of PG 64-22 binder						1.60
Overall Cost-Effectiveness Ratio with the use of lime on base having asphalt mix of PG 76-16 binder						1.75

*N/A relates to the original, untreated base layer

treatment in terms of bottom-up fatigue cracking was calculated based on equation 2. The overall results are shown in Table 4.

The cost-effectiveness analysis of all lime treatment in terms of bottom-up fatigue cracking shows that the use of lime treatment is more economical compared to untreated bases. It can be noticed that the use of lime treatment has increased cost-effectiveness when compared to untreated pavement sections at different traffic speeds utilizing two asphalt mixes. The cost-effectiveness ratio of lime treatment is found to be higher using stiffer asphalt binder and for higher traffic speed cases (Table 4). Furthermore, the overall cost-effectiveness of the lime treated base is 1.60-1.75 times untreated base section.

7 CONCLUSIONS

The purpose of this study was to conduct a mechanistic comparative analysis between treated and untreated bases to evaluate bottom-up fatigue cracking resistance. Lime treatment was utilized for pavement sections in this study. In addition, a cost-effectiveness analysis was performed to investigate if lime treatment is worthwhile, considering given the fact their cost versus their improved field performance. Based on both mechanistic and cost-effectiveness analyses, the following conclusions can be drawn:

- In terms of bottom-up fatigue cracking performance, treated base layers had superior fatigue cracking resistance compared to untreated sections. Lime treatment had an average FCRP of 41.3%. This indicates that the lime treated base can resist the fatigue cracking more than the untreated base.
- It can also be concluded that pavement structures with stiffer asphalt binder grade (PG 76-16) were more susceptible to fatigue cracking than softer asphalt binder grade (PG 64-22).
- Fatigue cracking decreased as the traffic speed increased due to the viscoelastic nature of asphalt pavements, where pavement structures act as strong material under high-frequency loading (high traffic speed). In contrast, it acts as a weak material under low-frequency loading (low traffic speed).
- Cost-effectiveness analysis showed that base treatment resulted in the cost-efficiency in bottom-up fatigue cracking resistance. The overall cost-effectiveness ratio of lime treated bases was 1-60-1.75 times the untreated base for the bottom-up fatigue cracking.

Therefore, it can be concluded that the use of base treatments could potentially contribute to overall improved fatigue cracking resistant pavement structures. Also, lime treatment presents improved cost-efficiency in base construction practices.

REFERENCES

- Ahmed, A. and Khalid, H.A., 2011. *Quantification of the properties of enzyme-treated and untreated incinerator bottom ash waste used as road foundation*. International Journal of Pavement Engineering. **12** (03): 253–261.
- Azadegan, O., Ehgaoubi, E., & Lie, J., 2013. *Evaluation of the performance of lime and cement treated base layers in Unpaved Roads*. Electronic Journal of Geotechnical Engineering
- Bodhgire, R., Shinde, A., and Kakade, V., 2019. *Cost Comparison of Flexible Pavement Designed with Cement Treated Base and Granular Base*.
- Faysal, M., Hossain, M.S., Salah, S.B., Bhattacharjee, S., Thian, B., Khan., 2017. *Characterization of the Geo-Environmental Properties of Untreated or Cement Treated Recycled Base Materials in Pavement Base Layer Applications*. Geotechnical Frontiers 415–423.
- Francois, A. A., 2016. *Evaluating the impact of different types of stabilized bases on the overall performance of Flexible Pavement*, Rowan University.
- Francois, A., Ali, A., and Mehta, Y., 2019. *Evaluating the impact of different types of stabilized bases on the overall performance of flexible pavements*.20(8):938–946.

- Jaritngam, S., Somchainuek, O., and Neerananon, P. T., 2014. *Feasibility of laterite-cement mixture as pavement base coarse aggregate*. Iranian Journal of Science Technology, Transactions of Civil Engineering, 38(C1+): 275.
- Johanneck L. and Dai. S., 2013. *Responses and Performance of Stabilized Full-Depth Reclaimed Pavements at the Minnesota Road Research Facility*. Journal of Transportation Research Board, 2368:114–125.
- Johnson, A. M., 1949. Use of Limes in Improving Bases and Subgrades. Joint Highway Research Project.
- Koroma, A.A., 2011. Evaluation of the performance and cost-effectiveness of pavement sections containing open-graded base courses.
- Little, D. N., Scullion, T., Kota, P. B. V. S., and Bhuiyan, J., 2006. *Identification of the Structural Benefits of Base and Subgrade Stabilization*. No. FHWA/TX-94/1287-2. 1995.
- M Faysal, MS Hossain, SB Salah, S. B Thian, MS Khan, Mohammad, L.N., et al. Laboratory evaluation of untreated and treated pavement base materials: Repeated load permanent deformation test. Transportation Research Record, 1967(1): 78–88.
- Saride, S., Avirneni, D., Javvadi, S. C. P., Puppala, A., and Hoyos, L. R., 2015. Evaluation of fly ash treated reclaimed asphalt pavement for base/subbase applications, 45(4): 401–411.
- Siddharthan, R.V., Yao, J., and Sebaaly. P.E., 1998. *Pavement Strain from Moving Dynamic 3-D Load Distribution*, Journal of Transportation Eng., ASCE, 124(6):557–566.
- Texas Department of Transportation, *Average Low Bid Unit Prices*, May 2019. [Online]. Available: <https://www.txdot.gov/business/letting-bids/average-low-bid-unit-prices.html>. Accessed 12 June 2019.
- Wang M. C., 1996. *Performance Analysis for Flexible Pavement with Stabilized Base*. Transportation Research Board. 888:70–76.
- Witczak, M., Mamlouk, M., Souliman, M., and Zeiada, W., 2013. *NCHRP REPORT 762: Laboratory Validation of an Endurance Limit of Asphalt Pavement*, Transportation Research Board, Washington D.C.
- Wu, Z., Chen, X., and Yang, X., 2011. *Finite element simulation of structural performance on flexible pavements with stabilized base/treated subbase materials under accelerated loading*.

Machine learning solutions for development of performance deterioration models of flexible airfield pavements

A.Z. Ashtiani, S. Murrell & R. Speir

Applied Research Associates, Inc., Maryland, USA

D.R. Brill

*Federal Aviation Administration, Airport Technology R&D Branch, William J. Hughes Technical Center,
ANG-E262, Atlantic City International Airport, NJ, USA*

ABSTRACT: The United States Federal Aviation Administration (FAA) has initiated research to develop robust methodologies for airfield extended-life pavement design. Pavement life in this context refers to the functional life that is not considered directly in the FAA thickness design models. Under the extended life study, data were gathered for a selection of runways at large- and medium-hub U.S. airports, including construction, performance, material property, traffic, and environmental data. The FAA has proposed a performance index, called Serviceability Level (SL), which is a comprehensive index quantifying the suitability of a pavement for use by aircraft. A previous FAA study used the collected data to develop prediction models for pavement performance indexes for functional conditions including potential to develop foreign object damage (FOD), roughness and loss of friction. That study proposed a framework for development of the SL index based on logistic regression models that incorporated various performance indicators, including pavement condition index (PCI), roughness index and friction index. In the initial SL model, pavement age was considered the only predictor. This paper presents the results of using machine learning to improve the performance index anti-SCI, which is a component of SL index, by taking into account the contribution of environmental variables as predictors. The developed model is based on an autoregressive approach and used random forest as the learning algorithm. This study is an initial step toward enhancement of the SL model.

Keywords: Pavement Performance, Machine Learning, Serviceability, Airfield Pavement, Climate, Environmental Factors

1 INTRODUCTION

A goal of the FAA airport technology research program is to develop robust airfield pavement performance models which can be incorporated into a methodology for extended-life pavement design (Brill et al. 2017). In this context, pavement life refers to the functional life that is not directly considered in the FAA thickness design models. Pavements designed to meet the current 20-year standard are likely to require intervention to restore serviceability before reaching their expected design life. Since 2012, under the Extended Airport Pavement Life (EAPL) program, the FAA has gathered a variety of airfield pavement data and stored them in a dedicated EAPL database, designated PA40. The collected data include pavement performance measures, such as surface friction, profile roughness and surface distresses, as

well as maintenance work histories, runway usage and weather data. Data were collected for 28 runways at 22 major airports in the continental U.S. Of these runways, 12 are flexible and 16 rigid. The FAA has proposed a performance index, called Serviceability Level (SL), which is a combined index of various performance-related pavement indices. A preliminary study by the FAA (Ashtiani et al. 2019) proposed a framework for the development of SL as a function of the PCI, roughness indices, and groove depth. The SL model is based on a logistic regression method and predicts the probability of a pavement section being serviceable given the performance indicators. The model considered pavement age the only independent variable, assuming the age is a surrogate for traffic and weather events. That study developed regression models to predict each underlying component of SL as a function of pavement age using the data collected as part of the EAPL study.

A major challenge in developing the SL solely based on pavement age is that the effects of other factors such as climate conditions and traffic levels are not directly incorporated. Age-based models may predict the same service life for two pavement sections experiencing different levels of traffic and located in different climatic regions.

The FAA continued the research to enhance the SL model by taking into account the contribution of additional design factors such as climate and traffic in an attempt to improve the prediction accuracy. The conventional approach in pavement management is to develop separate regression models for related families of pavements. However, models based on conventional regression analysis are inadequate for predicting long-term pavement performance as a function of multiple features. This paper investigates methods based on machine learning (ML) techniques for predicting long-term pavement performance by contributing multiple predictors such as the environmental factors and pavement age.

2 MACHINE LEARNING FOR PAVEMENT PERFORMANCE MODELING

Pavement performance is influenced by various features such as climate, traffic, material properties, pavement structure, drainage condition, preventive maintenance programming, and the quality and type of pavement construction and rehabilitation. The goal of pavement performance modeling based on data-driven approaches is to identify and characterize relationships between a series of features in the data and a target which is performance measure.

Pavement performance models can be categorized into two broad approaches: continuous function approximation with regression, or discrete time-series prediction. The regression approach is the most commonly adopted method for describing the deterioration of pavement condition. In this approach the condition at age t is estimated for a set of predictors or input variables at age t (Yang et al. 2003). In the time-series approach, the preceding values of a performance index are used in addition to other variables to predict future performance. In this approach it is required that the input variables be available at preceding intervals. This approach is also called *autoregressive*. The pavement performance data are categorized as *longitudinal* autoregressive when the same samples are repeatedly measured at different time points (Tsagris et al., 2018). There is growing interest in using ML techniques for pavement performance prediction modeling. At this time, most of the developed ML models are highway pavement applications; there are very few studies of airport pavements.

ML methods operate in two types: supervised and unsupervised. In a supervised learning process, the tagged input and output training data are mapped to learn the functions that approximate the relationship between them. Supervised learning methods are often used for regression, classification and forecasting analysis. The unsupervised methods are used to investigate the clusters, patterns and correlations among input data.

The goal of an ML model is to increase the learning accuracy while maintaining low variance and avoiding overfitting to noise. The process of building ML models for data-driven applications is an iterative process and has three components: feature engineering, algorithm selection and parameter tuning (Kumar et al. 2016). Feature engineering is the process of converting raw data into sets of feature vectors (input variables) that provide the best prediction of model performance. Reducing the number of variables to a subset of useful features is

desired for an effective ML prediction. The problem with high-dimensional features is that having more dimensions increases the difficulty of gauging the influence of each feature on the prediction. In addition, models with high numbers of features relative to the number of data samples tend to be prone to overfitting. Determining the best candidate ML algorithm depends on the size and type of the data (e.g. time dependent) and sparsity of the data (infrequent, missing, irregular data). Parameter tuning is the process of determining the value of the hyper-parameters of ML algorithms. For each ML model there are unique hyper-parameter configurations (e.g. loss functions, search strategies) that affect performance. Hyper-parameters are fine-tuned iteratively to create a trade-off between the performance accuracy (bias) and variance of the ML models.

3 PREDICTIVE MODELS FOR AIRFIELD PAVEMENT PERFORMANCE INDICES

3.1 *Runway performance indices*

Key to improving the SL model is to develop accurate predictive models for its component indices. The FAA PA40 database contains various performance-related indices such as PCI and its load-related component, referred to as SCI, and complementary non-load related component, referred to as anti-SCI. One or more of the performance indices can be used as components of a SL index. This paper focuses on predictive models for anti-SCI using ML methods. Anti-SCI is scaled from zero to 100, and for flexible pavements is calculated using all distresses defined in ASTM D5340, except for alligator cracking and rutting.

Data from the FAA PA40 database were used from the following 10 runways with flexible pavements for developing the predictive models: Runway 4L-22R at Boston Logan Airport (BOS), Runways 10L-28R and 10R-28L at Columbus International Airport (CMH), Runway 5L-23R at Greensboro International Airport (GSO), Runway 4-22 at LaGuardia Airport (LGA), Runway 9-27 at Kansas City International Airport (MCI), Runway 12-30 at Miami International Airport (MIA), Runway 10R-28L at San Francisco International Airport (SFO), Runways 11L-29R and 3-21 at Tucson International Airport (TUS). Each runway is typically divided into sections with identical width but different lengths along the runway. Multiple performance data, collected over the years, are typically available for each pavement section. Since anti-SCI contains distresses that are not directly caused by aircraft loads, material aging and weather events are the most probable causes of deterioration.

3.2 *Environmental data in FAA PA40 database*

The historical environmental/climate data are the most comprehensive feature in the PA40 database. Researchers initially identified thirteen (13) environmental variables that may influence the pavement performance (Table 1). Environmental variables were calculated as average values between the last rehabilitation/construction date and inspection, or between two inspections, for each pavement section in the database. Environmental variables exhibited temporal behavior, i.e., their values were not constant over the years the performance data were collected. This indicates that in some years the pavements were exposed to more severe weather conditions than other years, which could accelerate pavement deterioration. Given that flexible pavement performance data were available for only 10 runways at 8 airports, there were more independent variables than the number of climate locations. This may pose challenges in developing reasonable predictive models. Therefore, it is desired to select or construct a subset of environmental parameters that are useful to build a good prediction model. A common problem in ML model development is predictors that are highly correlated. In this case one or more of the highly correlated predictors can be omitted because no additional information is gained by including them (Guyon and Elisseeff, 2003). High collinearity may negatively affect the prediction performance of the model. However, the major problem with high collinearity is that it makes it difficult for the predictive model to assess the relative importance of the predictors with respect to the target. To this end, researchers examined the temporal dependency among the environmental variables

based on yearly fluctuations. In addition, researchers performed various collinearity tests to explore the correlation between the environmental variables. One collinearity test was to create Pearson correlation matrices to examine the strength of pairwise linear relationships. Correlations exceeding a threshold of 0.7 were considered “high collinearity.” Based on this threshold, “Days Precipitation”, “Total Precipitation” and “Thorntwaite Index” are highly positively correlated to one another. Also, “Freeze-Thaw Cycles” is highly negatively correlated to “Average Daily Temperature” and positively to “Freezing Degree Days.”

The airports in the PA40 database are not distributed randomly across the states. Since the locations of asphalt surfaced airports do not cover all the geographic and climatic regions, a complete range of potential climate situations may not exist. Therefore, some correlations should not be eliminated without using engineering judgment. Collinearity patterns are likely to change from one data set to another dataset. For example, precipitation and moisture could be highly correlated in some climate regions, but not in other regions. Also, the correlation may change over the decades.

Table 1. Environmental variables considered in this study.

Environmental Variables	Units
Freezing Degree Days (FDD)	°F-days
Freeze Thaw Cycles (FThC)	cycles
Days Temp Over 90 (Temp90)	days
Days Precipitation (DPrec)	days
Total Precipitation (TPrec)	inches
Freeze Precipitation Days (FPD)	days
Hydration Days	days
Avg Daily Temperature (Avg Temp)	°F
Avg Daily Temperature Difference (Temp Diff)	°F
RHumidity Avg	%
Avg Wind Speed	mph
Thorntwaite Index	%
Sky Cover	oktas

4 MACHINE LEARNING FRAMEWORK FOR PAVEMENT PERFORMANCE PREDICTION

4.1 *Autoregressive machine learning approach*

Researchers used an autoregressive approach to develop the anti-SCI predictive model. This approach considered the pavement age at the time of anti-SCI measurement, the previous anti-SCI, the time lapse between the two anti-SCI measurements, and a number of environmental parameters as predictors. The model used random forest (RF) as the learning algorithm. RF is an ensemble of regression and classification techniques that makes predictions by combining the results from many individual decision trees. RF uses bagging, also known as bootstrap aggression, for combining the outputs of multiple decision trees (Breiman, 2001, Dietterich, 2000 and Svetnik et al. 2003). Researchers implemented three modeling approaches for creating the anti-SCI prediction model. All approaches were based on a similar autoregressive RF algorithm, but they used different strategies for incorporating environmental variables. The “Weka” suite was used for model implementations. Weka is a free and open-source software program for data mining and ML (Witten, 2002).

4.2 *Modeling approach 1: Subset of environmental variables*

This approach removed the environmental variables that showed high collinearity or low variance from the input space and considered six environmental variables for model development

(FThC, FDD, Temp90, Temp Diff, TPrec and Thornthwaite Index). Environmental variables were calculated as average values since the previous anti-SCI measurement or since the last rehabilitation/reconstruction.

4.3 Modeling approach 2: Principal Component Analysis (PCA)

Principal Component Analysis is an unsupervised technique for dimensionality reduction of the multivariate feature (input) space. This reduction is achieved by mapping the data onto a set of dominant variables known as principal components (PC). The PC are new uncorrelated variables constructed via linear combinations of all input variables (Jolliffe, 2002). A major disadvantage of the PCA is that the principal components do not possess any physical meaning, making it difficult to interpret the effect of a specific input variable on the target. This approach included pavement age, previous anti-SCI, time since previous anti-SCI, asphalt thickness and 11 environmental variables (as listed in Table 1, except for “Avg Temp” and “FPD” variables) in the input domain and then transformed them into PC. Analysis identified four PC that explained more than 95% of the variance of the input domain. Researchers used these four PC as input variables for predicting anti-SCI.

4.4 Modeling approach 3: Features from cluster analysis

This approach grouped data records with similar climate characteristics into clusters using *k*-means cluster analysis. Cluster analysis is an unsupervised learning technique used primarily to explore homogeneous subsets of data objects within a dataset. The *k*-means algorithm is an iterative partitioning algorithm that assigns subsets of data objects to exactly one of the *k* clusters defined by their centroids (David and Vassilvitskii, 2007). For each data record, researchers considered the time since the last performance measurement as a sliding window and calculated the average of each environmental variable over that window. Researchers then grouped the data records into clusters based on similarities of two or three of their average environmental variables. After examining different combinations of environmental variables for cluster analysis, researchers determined that clustering based on FDD, Temp90 and TPrec yielded the best model performance. Researchers grouped the performance data records into four clusters based on their environmental characteristics. The environmental variables at the clusters were similar within a group but different among groups. Table 2 lists the average environmental variables at the centroid of each cluster.

Table 2. Average environmental variables at the centroid of each cluster.

Environmental Variables	Cluster 1	Cluster 2	Cluster 3	Cluster 4
Freeze Degree Days	108	330	549	2
Days Temp above 90	21	12	22	149
Total Precipitation	35	40	30	9
Instances	117 (36%)	126 (39%)	31 (10%)	51 (16%)

Table 3 summarizes the input variables to the RF model for each modeling approach. The output (target) is anti-SCI (t).

5 MODEL IMPLEMENTATION

5.1 Data preprocessing

Before ML training, researchers applied various data preprocessing methods to both the input and output data to make sure that the database is comprehensive (having adequate predictors or data sample), complete (free of missing data) and free of outliers. The performance data

Table 3. Input variables to RF model in each modeling approach.

Modeling Approach	Input Variables	Descriptions
Model 1	Age (t)	Time since last major rehabilitation
	Anti-SCI (t-1)	Previous anti-SCI measurement
	Delta-Time	Time since previous anti-SCI measurement
	Asphalt Thickness	Thickness of asphalt at the time of anti-SCI
	Freeze-Thaw Cycles	Average environmental variables between two anti-SCI measurements
	Freeze Degree Days	
	Days Temp Over 90	
	Daily Temperature Difference	
	Precipitation Total	
	Thornthwaite Index	
Model 2	PC1, PC2, PC3 and PC4	Principal Components
Model 3	Age (t)	Time since last major rehabilitation
	Anti-SCI (t-1)	Previous anti-SCI measurement
	Delta-Time	Time since previous anti-SCI measurement
	Asphalt Thickness	Thickness of asphalt at the time of anti-SCI
	Climate Group	Cluster 1, 2, 3 or 4

had an inherent spatial variability and errors that needed to be identified and removed prior to performing ML modeling. For example, records with improved anti-SCI between two consecutive inspections, without the pavement having undergone rehabilitation, needed to be examined before using for ML prediction modeling.

5.2 Model evaluation

Researchers used cross validation to confirm the stability of the trained models. Cross validation uses multiple training and test sets to ensure the model does not overfit, meaning that accurate performance estimates can be obtained when deploying models to new data. The study used a 10-fold cross-validation to tune the regression tree hyper-parameters and to improve the predictive performance. Researchers selected the best performing model based on various criteria including accuracy of prediction (using root mean square error (RMSE), relative root mean square error (RRMSE) and coefficient of determination (R^2)), generalization (similar performance on new data) and qualitative criteria. “Qualitative” refers to methods that employ the judgment of experienced pavement engineering practitioners to verify whether the developed models conform to conventional engineering logic. RMSE and RRMSE are defined in equations 1 and 2:

$$RMSE = \sqrt{\frac{1}{n} \sum_{i=1}^n (Y_{m,i} - \hat{Y}_{p,i})^2} \quad (1)$$

$$RRMSE(\%) = 100 \times \sqrt{\frac{1}{n} \sum_{i=1}^n \left(\frac{Y_{m,i} - Y_{p,i}}{Y_{m,i}} \right)^2} \quad (2)$$

where, Y_m is the measured target and Y_p is the predicted target. RMSE is the standard deviation of prediction error. It indicates how concentrated the data are around the prediction fitted curve. Compared to mean average error, RMSE gives higher weights to larger errors. It is not a bounded metric, i. e., its value can be from zero to infinity.

5.3 Predictive models

Researchers used a total of 278 data records from 10 runways for training the RF models. One section from each runway was set aside for independent testing (38 data points). Figures 1 through 3 show the comparison of RF-predicted and measured anti-SCI, for both training and testing subsets, using three modeling approaches. Table 4 summarizes the prediction errors for both training and testing subsets. Results indicate that all three models that incorporated environmental variables are capable of predicting anti-SCI with relatively high accuracy. The third modeling approach showed lower errors on testing subsets compared to other approaches. The RMSE is less than 6 in all three models. This number indicates that the average anti-SCI prediction error is less than 6 units (on the 0-100 scale) from the prediction curve. From Table 4, the model accuracy at 10% error is above 90% on the testing subset for all three approaches (i.e., the prediction error was less than 10% for 90 percent of the data). Accuracy values in Table 4 refer to the average performance of the prediction model, but do not imply uniform accuracy across the input domain. The error analysis shows that the

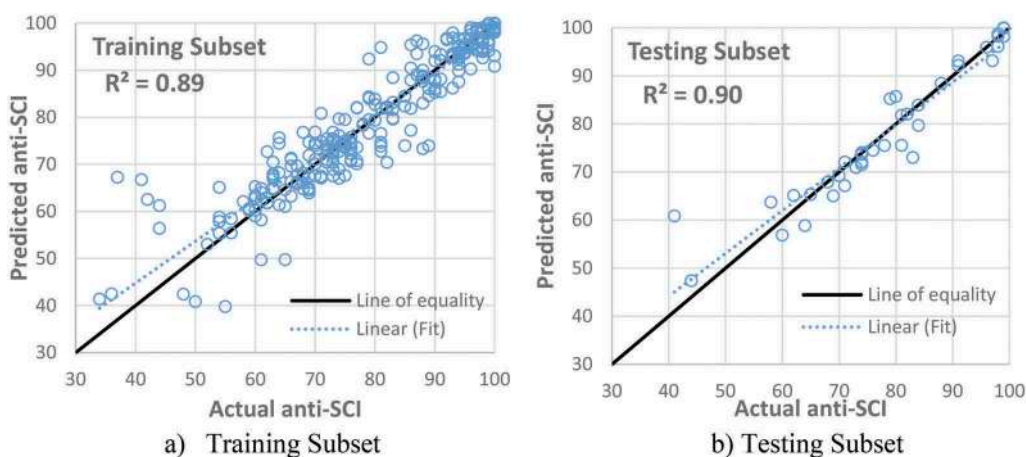


Figure 1. Comparison of predicted and actual anti-SCI for a) training and b) testing dataset - Modeling Approach 1: Subset of Environmental Variables.

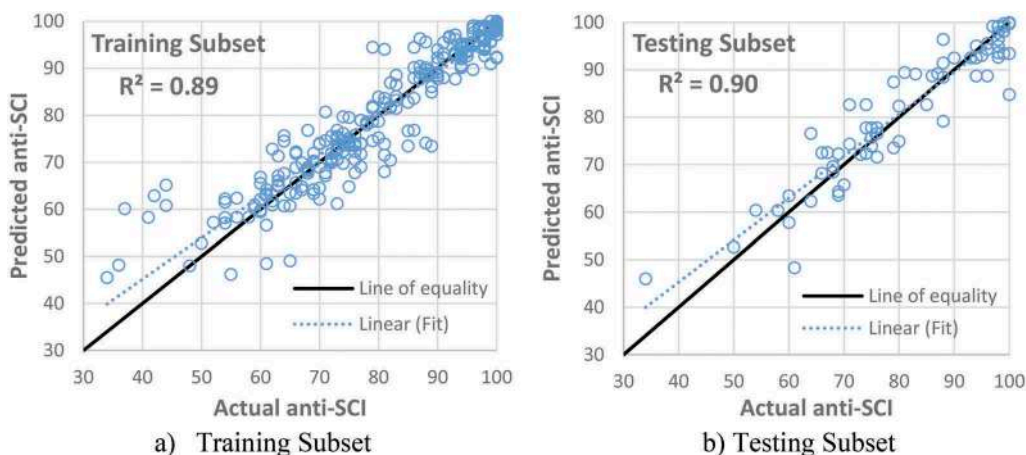


Figure 2. Comparison of predicted and actual anti-SCI for a) training and b) testing dataset - Modeling Approach 2: PCA.

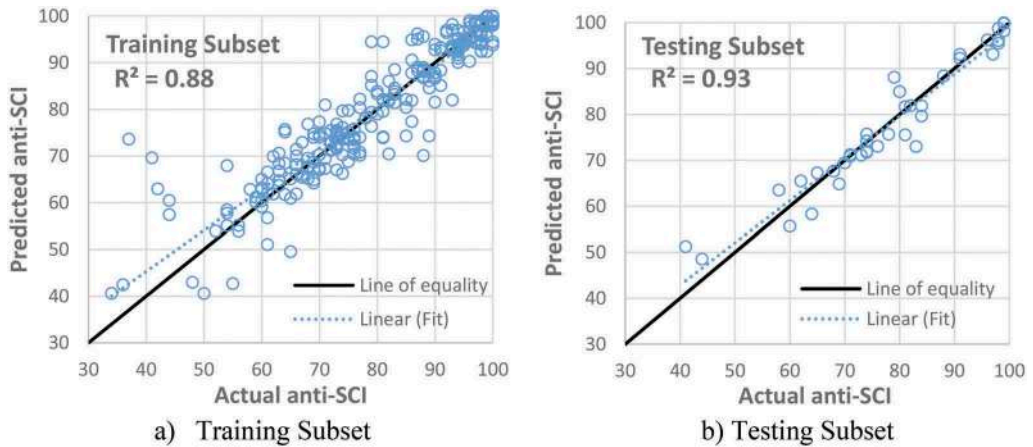


Figure 3. Comparison of predicted and actual anti-SCI for a) training and b) testing dataset - Modeling Approach 3: Features from Cluster Analysis.

Table 4. Performance of the trained RF model.

Performance Measure	Modeling Approach 1		Modeling Approach 2		Modeling Approach 3		No Climate	
	Training Subset	Testing Subset	Training Subset	Testing Subset	Training Subset	Testing Subset	Training Subset	Testing Subset
R ²	0.89	0.9	0.89	0.9	0.88	0.93	0.8	0.84
RMSE	5.16	4.55	5.11	4.81	5.41	3.86	6.8	5.9
RRSE	9.5%	9.0%	9.0%	7.3%	10.2%	6.3%	13.4%	8.1%
Accuracy (5% error)	69%	68%	74%	67%	69%	68%	67%	68%
Accuracy (10% error)	90%	95%	88%	90%	90%	92%	87%	89%

prediction errors are highest for the anti-SCI values below 50. One reason for this higher error is that limited data exist for pavements with anti-SCI less than 50, which makes the prediction in that region less reliable. This data scarcity is likely because airport owners tend to prevent a runway's pavement condition index from falling below 50 by replacing or rehabilitating the pavement. The developed ML models show promising generalization potential, as the model performance on testing subsets exceeded the performance on training subsets.

For comparison, Table 4 also includes the performance of a fourth autoregressive model that does not consider the effect of climate ("No Climate"). Taking into account the contribution of environmental/climate variables improved the prediction performance versus the "no climate" model; however, the improvement was not significant. This suggests that pavement age and previous anti-SCI remain the most significant predictors for anti-SCI.

6 CONCLUSIONS

This paper presents findings from the initial effort to enhance the SL index model beyond pavement age by taking into account additional design features. This study used data from the FAA EAPL database to develop predictive models for anti-SCI pavement performance index, which is a component of SL. Researchers developed models using performance data from ten asphalt-surfaced runways within the US. Since anti-SCI contains distresses that are

not caused directly by aircraft loading, researchers did not consider traffic in the models and used pavement age and environmental factors as primary predictors. Models incorporated an autoregressive approach and used random forest as the learner. The study considered three different modeling approaches for incorporating the environmental variables. The developed autoregressive models showed reasonable performance that can be used for incremental prediction of anti-SCI. The anti-SCI predictive model can be implemented in development of the SL index. Future research will apply ML techniques to the development of predictive models for other components of the SL index, including fundamental performance-related indexes tied to FOD potential, roughness and loss of friction.

ACKNOWLEDGMENTS/DISCLAIMER

The work described in this paper was supported by the FAA Airport Technology R&D Branch, Dr. Michel J. Hovan, Manager. The contributions of Mr. Timothy Parsons of Applied Research Associates (ARA) are gratefully acknowledged by the authors. The contents of the paper reflect the views of the authors, who are responsible for the facts and accuracy of the data presented within. The contents do not necessarily reflect the official views and policies of the FAA. The paper does not constitute a standard, specification, or regulation.

REFERENCES

- Ashtiani, A.Z., Shirazi, H., Murrell, S., Speir, R. and Brill, D.R., 2019. *Performance Model Development for Extended Airport Pavement Life*. International Airfield and Highway Pavements Conference, Chicago, IL, USA.
- Breiman, L., 2001. *Random forests*. Machine Learning, 45(1), pp. 5–32.
- Brill, D.R. and Parsons, T.A., 2017. *Development of new FAA design procedures for extended airport pavement life*. Proceedings of the Tenth International Conference on the Bearing Capacity of Roads, Railways, and Airfields, Athens, Greece.
- David, A. and Vassilvitskii, S., 2007. *K-means: The Advantages of Careful Seeding*. *SODA '07: Proceedings of the Eighteenth Annual ACM-SIAM Symposium on Discrete Algorithms*. pp. 1027–1035.
- Dietterich, T.G., 2000. *Ensemble methods in machine learning*. In: *International workshop on multiple Classifier systems*. Berlin: Springer, pp. 1–15.
- Guyon, I. and Elisseeff, A., 2003. *An Introduction to Variable and Feature Selection*. *Journal of Machine Learning Research*, 3, pp. 1157–1182.
- Jolliffe, I.T., 2002. *Principal Component Analysis*. Second Edition, Springer Series in Statistics.
- Kumar, A., McCann, R., Naughton, J. and Pate, J.M., 2016. *Model Selection Management Systems: The Next Frontier of Advanced Analytics*. *ACM SIGMOD Rec.*, vol. 44, no. 4, pp. 17–22.
- Svetnik, V., Liaw, A., Tong, C., Culberson, J.C., Sheridan, R.P. and Feuston, B.P., 2003. *Random forest: a classification and regression tool for compound classification and QSAR Modeling*. *Journal of chemical information and computer sciences*, 43(6), 1947–1958.
- Tsagris, M., Lagani, V., and Ioannis T., 2018. *Feature selection for high-dimensional temporal data*. *BMC Bioinformatics* 19, 17.
- Witten, I. H. and Frank, E., 2002. *Data mining: practical machine learning tools and techniques with Java implementations*. *Acm Sigmod Record* 31 (1), 76–77.
- Yang, J., Lu, J.J., and Gunaratne, M., 2003. *Application of neural network models for forecasting pavement crack index and pavement condition rating*. Final Report. University of South Florida.

Evaluation of subgrade mechanistic-empirical permanent deformation models in the response of a railway slab track

A. Ramos & A. Gomes Correia

University of Minho, ISISE, Department of Civil Engineering, Guimarães, Portugal

R. Calçada & P. Alves Costa

Department of Civil Engineering, Faculty of Engineering of University of Porto, Porto, Portugal

ABSTRACT: The cyclic loading submitted by the passage of trains on railway structures, induce a resilient (recoverable) deformation and/or permanent/plastic deformation on the subgrade materials. Indeed, the geomaterials when submitted to this type of loading tend to exhibit an elastoplastic behaviour. The modelling of the materials' performance can be a challenge due to their complex behaviour, influenced by the 3D character of the problem, the rotation of the principal stresses, etc. Thus, this paper is focused on the study of the permanent deformation phenomena, particularly on mechanistic-empirical approaches since they are able to simulate the response of the materials, are easy to implement, and are less time consuming when compared to the elastoplastic models. Throughout this work, a comparison between several empirical models is presented (identifying the main similarities and differences between them), considering a practical case of a passage of the *Alfa Pendular* train in a slab track (*Rheda* system) at 200 km/h in order to evaluate the influence of the subgrade in the response of the railway structure. The obtained results are analysed, discussed and compared.

Keywords: Cyclic loading, mechanistic-empirical approach, permanent deformation, subgrade, slab track

1 INTRODUCTION

The railways are usually under an excessive amount of cumulative permanent deformation due to rail traffic. The permanent deformation arises in the geomaterials and can lead to surface rutting and passenger discomfort (Puppala et al., 2009). Thus, it is important to understand this phenomenon and predict the permanent deformation of the geomaterials to avoid poor performance and reduce the respective operations and costs (Puppala et al., 1999).

Throughout the past years, researchers have been focused to find the most accurate method to predict permanent deformation. Thus, laboratory tests, such as the cyclic triaxial tests, have been used to investigate this phenomenon.

The main objective of the paper is to review the main causes and factors that influence the development of the permanent deformations on the geomaterials. Moreover, this work presents several models that can be implemented to predict permanent deformations. In this case, despite the importance of the shakedown theory or even the elastoplastic models,

this work is focused on the mechanistic-empirical models. These models are based on laboratory testing results used to correctly simulate the response of the materials when submitted to cyclic loads. These models, when compared to the elastoplastic ones, are easier to implement numerically and are also easier to characterise or parameterise since are dependent on fewer parameters. This paper reviews the existing empirical permanent deformation models. Furthermore, a case study is presented where the influence of the short- and long-term performance of the subgrade in the response of the slab track are evaluated considering the passage of the *Alfa Pendular* train at 200 km/h. This case study is based on a hybrid methodology where the stress levels are determined by the 2.5D FEM-PML approach and the long-term performance is characterised through the implementation of an empirical permanent deformation model dependent on the stress levels obtained previously.

2 CAUSES AND FACTORS INFLUENCE PERMANENT DEFORMATION

The permanent deformation can be defined and characterized by the accumulation of small increments of deformation during N load cycles. The permanent deformation usually occurs in railway lines due to repeated traffic loading (cyclic loads). In cases where there is a significant high volume of traffic, it may lead, in the limit, to structural failure. Therefore, it is very important to prevent permanent deformation and adopt proper measures even during the design process.

Another cause of the permanent deformation is associated with the induced complex stress conditions on the geomaterials. Indeed, these materials are subject to shear, vertical, and horizontal stresses during the passage of the vehicles as well as the effects of the moving loads, which is related to the rotation of the principal stresses. Indeed, Chan (1990) showed an increase in permanent deformation with the inclusion of the rotation of principal stresses in the simulations. Moreover, the self-weight of the embankment can be also an important cause in the post-settlement in railway structures allied with the traffic loading. The permanent deformation includes the settlement of the roadbed beneath the track and the subgrade.

Indeed, permanent deformation depends on several factors besides the number of load cycles and stress levels. Regarding the stresses, several studies show that permanent deformation depends mostly on the mean and deviator stresses (p and q , respectively) (Lekarp et al., 2000). However, there are other factors equally important such as the strength properties of the material, loading history, and rotation of the principal stresses. The permanent deformation is also influenced by the moisture content, matric suction, fine content, density, aggregate type, particle size distribution and the amount and type of fines (Lekarp, 1999, Xiao et al., 2015). Furthermore, Gidel et al. (2001) found that for unbound granular materials, the mineralogical nature of the material (including aggregate mineralogy and particle morphology) also influences the development of permanent deformation.

3 MODELLING APPROACHES – MECHANISTIC-EMPIRICAL PERMANENT DEFORMATION MODELS

The permanent deformation can be determined either through numerical simulation using elastoplastic models, shakedown theory, or applying the mechanistic-empirical deformation models developed based on the results obtained from laboratory tests such as the cyclic triaxial tests or hollow cylinder apparatus. The mechanistic-empirical permanent deformation models describe a relationship between the number of load cycles and the accumulated settlements. They are very easy to implement, and the numerical results can be obtained expeditiously. These models can be divided according to the approach used during the tests, the materials tested and the complexity that is related to the variables included in the model (Figure 1).

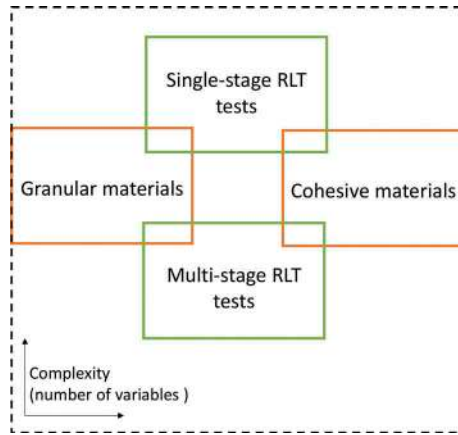


Figure 1. Division of the mechanistic-empirical permanent deformation model (adapted from Ramos et al. (2020)).

3.1 Approach

Regarding the approach, the tests and respective models can be divided into single-stage (SS) and multi-stage (MS) models. The first one implies that the load tests are carried out at one stress level in one test, which means that multiple specimens are tested at different stress levels. Otherwise, the multi-stage models can test multiple levels of stress in one test on one specimen. This approach allows considering the stress level and stress history on the development of permanent deformation. Furthermore, the MS-RLT represents better the real field conditions of the soils when subject to cyclic loads. Gidel et al. (2001) introduced this concept and Erlingsson and Rahman (2013) developed their work based on the time-hardening concept, which incorporates the stress history on the development of the permanent deformation. However, despite the reduction in time during the performance of the test, most of the models presented in the bibliography are developed under the single-stage RLT such as the Korkiala-Tanttu (2005) model described in the following expression:

$$\varepsilon_p(N) = CN^b \frac{R}{A - R} \quad (1)$$

where C is a parameter dependent on the stress, compaction degree and water content, N is the number of load cycles, b is a parameter dependent on the stress level, the ratio of failure, compaction degree and water content, A corresponds to the maximum value of the ratio and R is the ratio between the deviatoric stress (q) and failure deviatoric stress (q_f).

3.2 Complexity

The empirical permanent deformation models have been increasing their complexity with the inclusions of more variables in the models. Indeed, the first models only established a relationship between the permanent deformation and the number of load cycles and the stress levels. In fact, some of the first studies only included the number of load cycles (Barksdale, 1972). Posteriorly, the models included the direct influence of the mean and deviatoric stress (Lekarp and Dawson, 1998). Parallely, some models start to evaluate the length and slope of the stress path through the relationship between p and q , such as the model developed by Rahman and Erlingsson (2015). This model is dependent on the factor S_f that tries to quantify the slope of the stress path.

$$\varepsilon_p(N) = \alpha N^{bS_f} S_f \quad (2)$$

$$S_f = \frac{\left(\frac{q}{p_a}\right)}{\left(\frac{p}{p_a}\right)^a}$$

where N is the number of load cycles, a , b and α are the regression parameters, p is the mean stress, q is the deviatoric stress and p_a is the atmospheric pressure.

The model developed by Gidel et al. (2001) and posteriorly improved by Chen et al. (2014) is more complex than the previous ones because it is dependent on several important parameters such as the number of load cycles, stress state, initial stress state, and *yielding criterion*. The influence of the *yielding criterion* is evaluated through the strength parameters m and s of the *Mohr-Coulomb* yielding criterion. The inclusion of the initial stress state of the material is also important since it has a significant influence on the permanent deformation (Chai and Miura, 2002, Chen et al., 2014, Ling et al., 2017, Wei et al., 2017). Despite the complexity, the model is very easy to implement. Chen's model is described in the following expression:

$$\varepsilon_1^p(N) = \varepsilon_1^{p0} [1 - e^{-BN}] \left(\frac{\sqrt{p_{am}^2 + q_{am}^2}}{p_a} \right)^a \cdot \frac{1}{m \left(1 + \frac{p_{ini}}{p_{am}} \right) + \frac{s}{p_{am}} - \frac{(q_{ini} + q_{am})}{p_{am}}} \quad (3)$$

where, N is the number of load cycles, ε_1 , B and a are constants of the model, p_{am} and q_{am} are the amplitude of the mean stress and deviator stress for train loadings, p_{ini} and q_{ini} are the mean and deviator stress in the initial state of the material and m and s are defined by the *yielding criterion* $q = s + mp$

Moreover, there are some models that include the octahedral normal and shear stresses instead of the p and q stresses (Puppala et al., 1999, Puppala et al., 2009). Furthermore, there are also more complex models that include more variables related to, for example, the physical state of the material. But since these parameters are hard to obtain, this kind of model tends to be very difficult to implement and characterise. The model developed by Xiao et al. (2015) is an example.

3.3 Materials

The empirical permanent deformation models can also be divided by the nature of the materials tested: cohesive and granular materials. The response of the materials when subject to cyclic loads is different. Indeed, the models developed based on the tests performed on cohesive materials should consider the stress state, the type of soil, the physical state of the material, and variables related to moisture content and dry density (Ramos et al., 2020). Some examples of models developed with these materials are included in the work developed by Puppala et al. (1999), Puppala et al. (2009) and Chen et al. (2014).

Regarding the granular materials, there have been substantial studies about the development of permanent deformation models because of their common use in railway structures. The performance of the granular materials when subject to cyclic loading is complex. When the cyclic load is applied, there is a gradual accumulation of permanent deformation, a decrease in the number of voids, and an increment in stiffness (Erlingsson and Rahman, 2013, Ba, 2018). Moreover, the key characteristics of the materials such as the granulometry can also influence the response, as well as their physical state (Gomes Correia, 2000). Some examples of models developed with these materials are included in the work developed by Hyde (1974), Huurman (1997), Sweere (1990), Lekarp and Dawson (1998), Puppala et al. (1999), Gidel et al. (2001), Korkiala-Tanttu (2005), Puppala et al. (2009), Chen et al. (2014), Xiao et al. (2015), Rahman and Erlingsson (2015), Cai et al. (2015) and Salour and Erlingsson (2016) and Ling et al. (2017).

The review of the available mechanistic-empirical permanent deformation models shows that to simulate this behaviour, the model should be selected considering the materials tested (as well as the physical state) and the available parameters used as inputs of the model. This is important since a simpler model can easily represent better the *in situ* conditions rather than complex ones that are dependent on various variables that required the performance of specific laboratory tests. Thus, in the case study presented further, three different models are tested: Korkiala-Tanttu (2005), Salour and Erlingsson (2015) and the model developed by Chen et al. (2014).

4 CASE STUDY – PASSAGE OF THE ALFA PENDULAR TRAIN AT 200 KM/H OVER A SLAB TRACK

The evaluation of the long-term performance of the subgrade in the response of a railway slab track was performed using the stresses obtained numerically through the 2.5D FEM-PML approach (considering the passage of the *Alfa Pendular* train) that were used as inputs in the empirical permanent deformation model. This is the first step of extensive work regarding the prediction of permanent deformation. This prediction is an academic numerical exercise, whose methodology will be implemented, and the results validated in the scope of the full-scale physical modelling (Ramos et al., 2021b) and in a technical demonstrator, regarding the stress levels (obtained in the finite element model) and permanent deformation (obtained considered the implementation of the empirical permanent deformation model).

4.1 Numerical model and material properties

In this study, the train-track-ground system was modelled using the 2.5D approach. This methodology combines the 3D nature of the problem with the reduced computational effort (Yang and Hung, 2001, Alves Costa et al., 2010). The methodology of the train-track-ground system is described in more detail in the work developed by Alves Costa et al. (2010). To avoid spurious reflections, *Perfectly Matched Layers (PMLs)* were used. This methodology is described in more detail in the work developed by Lopes et al. (2014).

In this methodology, the numerical model is divided into two moduli: the train (which is modelled through a multi-body approach and only vertical movements were considered) and the track-ground structure (modelled by the 2.5D-FEM approach). The models are coupled following a compliance formulation. The wheel-rail contact is simulated by the linearized *Hertzian* stiffness. Alves Costa et al. (2012) present in more detail this methodology.

To evaluate the performance of the subgrade of a slab track (*Rheda* system), a numerical model was developed, as depicted in Figure 2. The structure was modelled by finite elements with 8 nodes, and it is composed of the rails, railpads, concrete slab, support layer (HBL), the frost protection layer (FPL) and the subgrade. The HBL (hydraulically bonded layer) is a family of cement bounded layers. This method uses binders made from cement, lime, gypsum, granulated blast-furnace slag, air-cooled steel slag, or coal fly ash. These binders are known as hydraulic binders since they set and harden in the presence of water. The rails (UIC 60) were modelled as beam elements and the railpads as a set of spring and damper (with a stiffness of 40 kN/mm and damping of 8 kNs/m). The remaining materials were modelled with linear elastic models. The assumption of a linear elastic model to represent soil behaviour (in this case representing the FPL but also the subgrade) is a simplification to the real constitutive soil behaviour and it is only acceptable when dealing with small-strains. The adopted properties are described in Table 1. The initial stresses were obtained assuming an isotropic stress state, i.e., $K_0=1$. The model takes into account the symmetric conditions of the problem in order to reduce the computation effort. By simplification, from a numerical point of view, the FPL was integrated into the subgrade layer in the determination of the cumulative permanent deformation since both materials shared the same stiffness (Table 1). Thus, in this work, the FPL has not distinguished itself from the subgrade in terms of terminology.

Regarding the vehicle, the *Alfa Pendular* train is composed of 6 car bodies and presents a symmetry plane. The average axle load is close to 135 kN. In this case, the train was modelled by a simplified model (only the mass of the wheelsets was considered). To take into account the dynamic mechanism and its influence on the response of the subgrade, an unevenness profile was generated based on the *Power Spectral Density* function defined by the *FRA* (*Federal Railroad Administration*). More details about this methodology can be found in Ramos et al. (2021a).

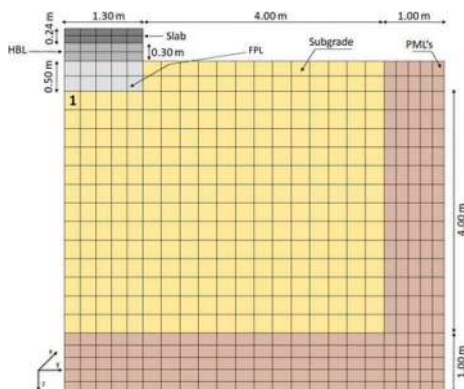


Figure 2. Numerical model of the slab track – *Rheda* system (adapted from Ramos et al. (2018)).

Table 1. Characteristics of the materials.

Elements	M_r (MPa)	ν	ξ	ρ (kg/m ³)
Concrete slab	34000	0.20	0.030	2500
HBL	10000	0.20	0.030	2500
FPL*	120	0.20	0.030	2500
Subgrade Soil*	120	0.30	0.030	2040.0

M_r = Resilient modulus, ν =Poisson's ratio, ξ =damping and ρ =density

*The subgrade soil and FPL are characterised by a $\phi=30^\circ$ and $c=0$ kPa

4.2 Results

The primary stage of this analysis is the determination of the stress levels and stress paths. In this case, the representation of the *yielding criterion* is merely indicative since only allows understanding the proximity of the stress path to the failure line.

In this analysis, the dynamic mechanism was considered, which is induced by the vehicle-track interaction (this is due to the unevenness profile). The stresses were analysed in terms of effective stresses, which means that the initial stresses and the increments induced by the passage of trains were considered.

The analysis is focused on element 1 (Figure 2) (in terms of stresses to demonstrate the typical stress paths) and its alignment to show the cumulative permanent deformation. Element 1 was selected due to its proximity to the symmetry plane, simplifying the analysis of the stress results.

In this study, a train speed equal to 200 km/h was adopted. The stress results are depicted in Figure 3. Figure 3 a) shows the variation of the vertical stress along with the depth. The maximum and minimum values are close to 12 kPa (top FPL) and 5 kPa (bottom of subgrade), respectively. Moreover, the results show that the initial mean stress is close to 17 kPa. The results also show that the stress peak is far from the failure line, which indicates low values of the permanent deformation.

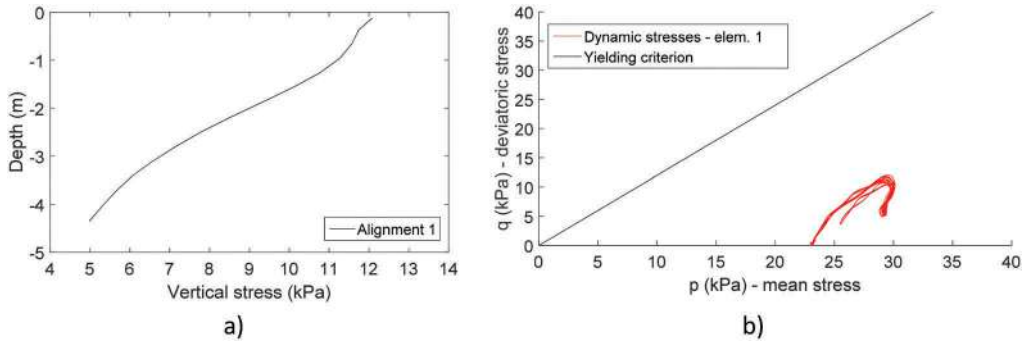


Figure 3. a) Vertical stress along with depth in the alignment 1; b) stress path of element 1.

The permanent deformation was obtained in the FPL and subgrade, which are the only elements that are contributing to its development due to its nature as geomaterials. Despite the similarities, these elements differ in terms of density and *Poisson* ratio. The cumulative permanent deformation was determined applying three different models described in expressions 1, 2 and 3. These models were selected since they present different formulations. The model developed by Korkiala-Tanttu (2005) was developed using the single-stage approach, while the two remaining models were developed based on the multi-stage approach. Furthermore, although the models considered the mean and/or deviatoric stresses as the main inputs, the way these parameters are included in the model is different.

Moreover, the shakedown approach/classification is introduced in this study through the methodology presented by Werkmeister (2003):

- Range A: $(\varepsilon_p^{5000} - \varepsilon_p^{3000}) < 0.045 \times 10^{-3}$
- Range B: $0.045 \times 10^{-3} < (\varepsilon_p^{5000} - \varepsilon_p^{3000}) < 0.4 \times 10^{-3}$
- Range C: $(\varepsilon_p^{5000} - \varepsilon_p^{3000}) > 0.4 \times 10^{-3}$

In this case, the material is divided/classified into three categories, based on the limits that represent the deformation that accumulates between the 3000th and 5000th number of load cycles. From the permanent deformation, the permanent deformation of material 1 is classified.

The obtained results regarding the long-term performance are depicted in Figure 4. Thus, three models were tested (based on the stress levels represented in Figure 3). These models are also dependent on different material parameters. These parameters were obtained in the work developed by Salour and Erlingsson (2015) considering a non-plastic silty sand according to the unified soil classification. The following values were adopted: Chen et al. model - $\varepsilon_1^{p0} = 0.00093$, $B = 0.2$ and $a = 0.65$; Korkiala-Tanttu model - $C = 0.00057$ and $b = 0.09122$; Rahman and Erlingsson model - $a = 0.135 \times 10^{-3}$, $\alpha = 0.75$ and $b = 0.307$.

The permanent deformation results show that, for these properties, the cumulative permanent deformation varies according to the empirical model selected (from 0.07 to 1.7 mm). This may be due to the adopted materials parameters but also due to the formulation of the model. The main differences between the tested models are described in Table 2. This comparison includes the direct influence of the initial stress state (both initial mean and deviatoric stresses), stress path induced by the passage of the train (evaluated through the slope/length of the stress path) and the distance between the stress path and the *yielding* criterion. Indeed, Table 2 shows that the more complete model is the model developed by Chen et al. (2014) since includes all the parameters described in Table 2. The results considering the Chen model show that the cumulative permanent deformation of this subgrade is close to 0.07 mm, which is not significantly higher.

From the results depicted in Figure 4 a), the permanent deformation of element 1 was classified according to its shakedown value/range based on the limits defined by Werkmeister (2003) and taking into account the model tested. Thus, the permanent deformation of element 1 was classified as range A (plastic shakedown) since the permanent deformation of element 1 is inferior to 0.045×10^{-3} between the 3000th and 5000th number of load cycles. This also includes the results obtained considering the model developed by Korkiala-Tanttu (2005) where the material does not show a perfect stabilisation after 1 million load cycles. Moreover, the Korkiala-Tanttu model shows high initial permanent deformations when N is close to 0. However, the number of load cycles is not zero and, due to the high values of the ratio $\frac{R}{A-R}$, the permanent deformation is significantly amplified for reduced number of load cycles.

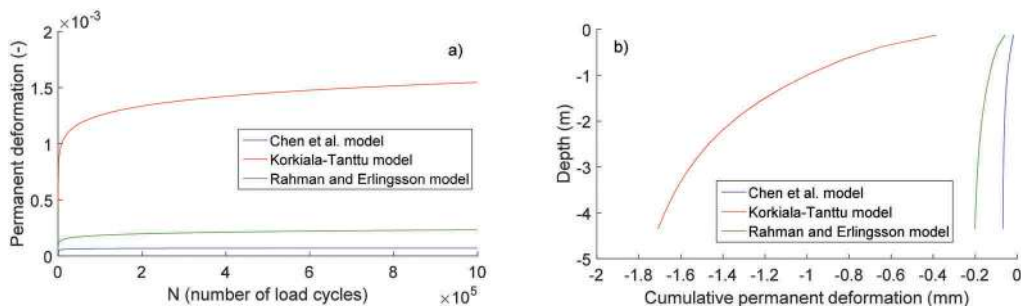


Figure 4. a) Permanent deformation induced in element 1 of the model; b) cumulative permanent deformation of the alignment of element 1 comparing different models.

Table 2. Main differences between the tested empirical permanent deformation models.

Models/Parameters	Initial stress state	Length/slope of the stress path	Yielding criterion
Chen et al. model	✓	✓	✓
Korkiala-Tanttu model	-	-	✓
Rahman and Erlingsson model	-	✓	-

5 CONCLUSIONS

This study reviews the main causes and factors that can lead to the development of permanent deformation on railway structures. With this study, it is possible to conclude that this is a complex topic since the response of the geomaterials materials when submitted to cyclic loading depends on several variables such as the type of material, physical state, stress state, initial stress state, and other properties.

The review was based on extensive research about the mechanistic-empirical permanent deformation models. In this analysis, the models were divided according to the type of materials, approach, and the complexity of the models. Based on this research, three different models were selected to study the response of the subgrade in a slab track. The methodology applied in this analysis combines the 2.5D FEM-PML approach with the implementation of an empirical permanent deformation model, which allows obtaining expeditiously the long-term performance of the track.

The obtained results show the importance of the initial stress state. If the values of the initial stress state were higher, there would be a greater distance between the stress path and the *yielding criterion*, which would imply a lower value of permanent deformation. The results also

show that the empirical permanent deformation models may include the same variables, but the final results may differ from each other due to the formulation and complexity of the model. In this analysis, three models were tested and the model developed by Chen et al. (2014) was adopted. This model is easy to implement and characterise. However, it is also complex enough to include the main variables that influence the development of permanent deformation. The value obtained from the cumulative permanent deformation in the alignment of element 1 is 0.7 mm, which is an acceptable value for a slab track system.

REFERENCES

- Alves Costa, P., Calçada, R. & Silva Cardoso, A. 2012. *Track-ground vibrations induced by railway traffic: In-situ measurements and validation of a 2.5D FEM-BEM model*. Soil Dynamics and Earthquake Engineering, 32, 111–128.
- Alves Costa, P., Calçada, R., Silva Cardoso, A. & Bodare, A. 2010. *Influence of soil non-linearity on the dynamic response of high-speed railway tracks*. Soil Dynamics and Earthquake Engineering, 30, 221–235.
- Ba, M. 2018. *Correlation between resilient modulus and permanent deformation during a large scale model experiment of unbound base course*. Lecture Notes in Civil Engineering.
- Barksdale, R. D. *Laboratory evaluation of rutting in base course materials*. Proc. 3rd Int. Conf on the Structural Design of Asphalt Pavements, 1972 London.
- Cai, Y., Sun, Q., Guo, L., Juang, C. H. & Wang, J. 2015. *Permanent deformation characteristics of saturated sand under cyclic loading*. Canadian Geotechnical Journal, 52, 795–807.
- Chai, J.-C. & Miura, N. 2002. *Traffic-load-induced permanent deformation of road on soft soil*. Journal of Geotechnical and Geoenvironmental Engineering, 128, 907–916.
- Chan, A. H. 1990. *Permanent deformation resistance of granular layers in pavements*. PhD thesis, University of Nottingham, England.
- Chen, R., Chena, J., Zhaob, X., Bian, X. & Chen, Y. 2014. *Cumulative settlement of track subgrade in high-speed railway under varying water levels*. International Journal of Rail Transportation, 2, 205–220.
- Erlingsson, S. & Rahman, M. S. 2013. *Evaluation of permanent deformation characteristics of unbound granular materials by means of multistage repeated-load triaxial tests*. Transport Research Record: Journal of the Transportation Research Board, 2369, 11–19.
- Gidel, G., Hornych, P., Chauvin, J.-J., Breysse, D. & Denis, A. 2001. *A new approach for investigating the permanent deformation behaviour of unbound granular material using the repeated load triaxial apparatus*. Bulletin des Laboratoires des Pont et Chaussées, 233, 5–21.
- Gomes Correia, A. 2000. *Influence of compaction conditions on resilient and permanent deformations of aggregates mixtures of granite*. Gomes Correia and Quibel (Editors), Compaction of soils and granular materials. Paris: Presse Nationale des Ports et des Chaussées.
- Huurman, M. 1997. *Permanent deformation in concrete block pavement*. PhD Thesis, Delft University of Technology, Netherlands.
- Hyde, A. F. L. 1974. *Repeated load triaxial testing of soils*. PhD thesis, University of Nottingham, Nottingham.
- Korkiala-Tanttu, L. *A new material model for permanent deformations in pavements*. Proc. of the Seventh Conference on Bearing Capacity of Roads and Airfields, 2005 Trondheim, Norway. 10.
- Lekarp, F. 1999. *Resilient and permanent deformation behavior of unbound aggregates under repeated loading*. PhD Thesis, The Royal Institute of Technology, KTH, Stockholm, Sweden.
- Lekarp, F. & Dawson, A. 1998. *Modelling permanent deformation behaviour of unbound granular materials*. Construction and Building Materials, 12, 9–18.
- Lekarp, F., Isacsson, U. & Dawson, A. 2000. *Permanent strain response of unbound aggregates*. Journal of Transportation Engineering, 126, 76–83.
- Ling, X., Li, P., Zhang, F., Zhao, Y., Li, Y. & An, L. 2017. *Permanent deformation characteristics of coarse grained subgrade soils under train-induced repeated load*. Advances in Materials Science and Engineering, 2017 15.
- Lopes, P., Alves Costa, P., Ferraz, M., Calçada, R. & Silva Cardoso, A. 2014. *Numerical modeling of vibrations induced by railway traffic in tunnels: From the source to the nearby buildings*. Soil Dynamics and Earthquake Engineering, Volumes 61–62, 269–285.
- Puppala, A. J., Mohammad, L. N. & Allen, A. 1999. *Permanent deformation characterization of subgrade soils from RLT test*. Journal of Materials in Civil Engineering, 11, 274–282.

- Puppala, A. J., Saride, S. & Chomtid, S. 2009. *Experimental and modeling studies of permanent strains of subgrade soils*. Journal of Geotechnical and Geoenvironmental Engineering, 135, 1379–1389.
- Rahman, M. S. & Erlingsson, S. 2015. *A model for predicting permanent deformation of unbound granular materials*. Road Materials and Pavement Design, 16, 653–673.
- Ramos, A., Gomes Correia, A., Calçada, R. & Alves Costa, P. 2021a. *Stress and permanent deformation amplification factors in subgrade induced by dynamic mechanisms in track structures*. International Journal of Rail Transportation, 1–33.
- Ramos, A., Gomes Correia, A., Calçada, R., Alves Costa, P., Esen, A., Woodward, P. K., Connolly, D. P. & Laghrouche, O. 2021b. *Influence of track foundation on the performance of ballast and concrete slab tracks under cyclic loading: Physical modelling and numerical model calibration*. Construction and Building Materials, 277, 122245.
- Ramos, A., Gomes Correia, A., Indraratna, B., Ngo, T., Calçada, R. & Costa, P. A. 2020. *Mechanistic-empirical permanent deformation models: Laboratory testing, modelling and ranking*. Transportation Geotechnics, 23, 100326.
- Ramos, A. L., Correia, A. G., Calçada, R. & Costa, P. A. 2018. *Influence of permanent deformations of substructure on ballasted and ballastless tracks performance*. Proceedings of 7th Transport Research Arena TRA 2018, April 16-19, 2018 Vienna, Austria. Zenodo.
- Salour, F. & Erlingsson, S. 2015. *Permanent deformation characteristics of silty sand subgrades from multi-stage RLT tests*. International Journal of Pavement Engineering, 18, 236–246.
- Salour, F. & Erlingsson, S. *Characterization of permanent deformation of silty sand subgrades from multi-stage RLT tests*. The 3rd International Conference on Transportation Geotechnics (ICTG 2016), 2016 Guimarães, Portugal. 300–307.
- Sweere, G. T. H. 1990. *Unbound granular bases for roads*. PhD Thesis, Delft University of Technology, Netherlands.
- Wei, X., Wang, G. & Wu, R. 2017. *Prediction of traffic loading-induced settlement of low-embankment road on soft subsoil*. International Journal of Geomechanics, 17.
- Werkmeister, S. 2003. *Permanent deformation behavior of unbound granular materials*. PhD Thesis, University of Technology, Dresden, Germany.
- Xiao, Y., Tutumluer, E. & Mishra, D. 2015. *Performance evaluation of unbound aggregate permanent deformation models for different aggregate physical properties*. Transport Research Record: Journal of the Transportation Research Board, 2525, 20–30.
- Yang, Y. & Hung, H. 2001. *A 2.5D finite/infinite element approach for modelling visco-elastic body subjected to moving loads* International Journal for Numerical Methods in Engineering 51, 1317–1336.

Follow up on reduced thickness of asphalt concrete layers on a performance specifications contract

C.A. Lenngren

AFRY Infrastructure, Västerås, Sweden

ABSTRACT: A five km long road section, a bypass in the vicinity of Gislaved in southern Sweden, was opened for traffic in 2013. The pavement design was based on performance specifications, primarily for rutting and roughness. There were also safety aspects like specified friction criteria. The structural rutting was related to a subgrade strain criterion, and a classic fatigue criterion for asphalt concrete. In addition to quality control/quality assurance, the construction was also monitored by Falling Weight Deflectometer (FWD) testing on the subgrade, subbase, and bound base layers. After the construction, FWD testing was performed on a yearly basis. Surface characteristics data were also sampled at intervals according to the contract. For the first five years the pavement deterioration proved to be normal and followed the theoretical expected values for a mechanistic design process. Then, some sections showed an accelerated deterioration, with cracks appearing in the wheel paths. Thorough investigations followed to disclose the reason for the premature failures. Possible reasons sought were unexpected overloads, climate change, and underground water movements. While coring the road, it was observed that the cooling water would not drain through the unbound base material. Thus, the top millimeter or so consisted of very fine material with low permeability, almost like clay. Obviously, traffic had acted on the material as to crush and wear it down into smaller fractions. The further mineral investigation also showed a high mica content. The present paper discusses how this process could increase the strain on the pavement, but also opens to debate whether more mechanistic procedures should be added to the Mechanistic-Empirical (ME) model. The mica content and other specifications are usually based on empirical data. With higher legal loads and load factors on trucks, the empirical data may not suffice for predicting pavement performance.

Keywords: Performance contracting, pavement life expectancy, premature failure

1 INTRODUCTION

About fifteen years ago the Swedish Transport Administration (STA) introduced contracting based on performance specifications rather than relying on traditional construction code and regulations. This gives the contractor the opportunity to come up with ideas with new methods and materials as well, to be used without having them tested and approved; a process that might take years to accomplish. The main idea is to provide incentives to new thinking and innovation to an industry that is otherwise known to be rather conservative than progressive. The result at the end, should be better and cheaper products for the transportation sector.

There are many ways to address performance specifications. It could be very detailed, including all parts in a system e.g., the shock absorbers for a car. Or it could be the entire car

working during a long time with an extended warranty program. A road should provide a safe and reliable way to move people and goods between any points along it. So, we need to define a measurable way to express this in functional and even monetary terms. Luckily, there is already an index, that correlates rather good with ride comfort, vehicle wear, road deterioration over time, and travel time, namely the International Roughness Index, (IRI). Road surface characteristics have been monitored since the late 1980:ies on a network scale, so there are plenty of data, and lot of statistics on how roads behave over time. Thus, the IRI is a given when it comes to performance specifications for roads. In addition, rutting is also monitored simultaneously, so it is also included in the performance specifications. Friction is usually tested by a mechanical device, but since it is so critical for safe travel, it is also included in the specs.

The present paper presents and discuss a five km long project from the beginning of construction, in 2011, up to about seven years in operation. The contract is based on performance requirements for rutting and roughness for a ten year long period. It addresses the strengths with such contracting, but also brings up some issues that must be solved, when regulating the outcome. The conclusions are based on this specific case, rather than generic for all performance specification contracting.

2 CONSTRUCTION PLANNING

The project in question is a bypass of National Highway 27 near Gislaved, about 120 km southeast of Gothenburg in southern Sweden. The road was designed as a divided highway, with three lanes, the odd one alternating as passing lane between the two directions.

2.1 *Pavement design parameters*

The design traffic was 5.5 million equivalent standard axle loads (ESALs). The load being ten metric tons, resting on dual wheels on each side. The alignment passes a bridge over a meandering river, which has changed its direction several times in the past leaving alluvial deposits in its way. The road also passes thru some open farmland and over an area with peat. The frost penetration depth based on actual temperatures is in a range from 230 to 740 mm over a ten-year period. The maximum frost heave is assumed to be about 30 mm, way below the 60 mm tolerance level for this road category. Thus, the STA specifications (TRVK Väg 2011) called for 500 mm of unbound materials and 150 mm of bound layers.

2.2 *Performance specifications*

The mechanistic-empirical design as used traditionally, consists of two strain criteria. The modified Kingham fatigue criterion for bound materials, and a regressed criterion for rutting. The empirical parts relate to specifications of material properties like mica content, gradation curves, grain angularity et cetera. Further there are construction control parameters to consider, like number of roller passes, weather conditions et cetera. All this infer rigorous control measures. The performance specifications are more relaxed in this sense. Except for environmental and health restrictions on use of hazardous materials, the contractor is free to build as he pleases as long as the performance requirements are fulfilled. In the present case, the contract is active for ten years, so roughness and rutting criteria must be tested, at opening, and after year one, four seven and ten. Rutting may progress according to 3 mm initial plus 0.8 mm per annum. Thus, during year ten it may not exceed 11 mm. Rutting is caused by traffic, so the calculations are quite straightforward. The correlation with top of the subgrade strain is based on regression, so the contractor needs to derive this strain somehow.

Roughness progression is harder to predict. The process is stochastic, depending on winter conditions and the following thaw period. The criteria are established based on a huge data base, and a plausible development can be decided for any category of road. Thus, the

contractor must be careful in assessing the soil type, which has a large impact on roughness. As a rule of thumb, the thicker the pavement, the better the evenness will be.

3 THE PERFORMANCE TOOLBOX

Now, as a contractor, what are the options? The obvious is to identify and utilize your own strengths. Mix design could be one specialty. Having good supplies another. Having excellent aggregate still another. High end equipment with precision capabilities yet another advantage perhaps. However, it is necessary to have a thorough understanding of the implications of altering the design.

For instance, according to the ordinary STA specifications by the modified Kingham criterion, the horizontal strain in the bottom of asphalt concrete layer should not exceed 197 micro-strain. So, if the existing support is improved, it is possible to reduce the asphalt concrete thickness, as long as the maximum strain is not exceeded. As a matter of fact, that is exactly the strategy that was used in the present case. By improving the unbound layer’s stiffness, the idea was to reduce the asphalt layer thickness from 150 mm to 85 mm, or as much as possible and still meet the strain criteria.

Table 1. AC Layer thickness.

	STA Design	Active Design	Minimum AC
Wearing Course	50 mm	35-40 mm	40 mm
Binder Layer	55 mm	40-45 mm	45 mm
Bound Base	50 mm	40-45 mm	Omitted
Unbound Base	80 mm	80-110 mm	125 mm
Subbase	420 mm	420 mm	420 mm

4 ACTIVE DESIGN

Active design is not a new concept. When ME design was being introduced in the 1980:ies and FWD was introduced as a tool to assess strain anywhere in the pavement, several agencies started research projects to follow-up construction layer by layer, with FWD testing. Under this design approach, based on the readings and strength of the newly constructed pavement layers, the following layers are adjusted to correct the performance and/or reduce costs. The tests could also replace cumbersome construction control methods like the static plate bearing test.

Anyway, it is understood that sometimes the subgrade is better than its classification, and one should be able to derive some benefits with the active design concept. The opposite also applies in that premature failure can be detected and avoided when conditions are less favorable.

Further, if the unbound layers are compacted to a stiff response, the more expensive bound layer thickness can be reduced for substantial savings on the construction costs. As it were, this strategy was chosen for the present project.

5 CONSTRUCTION

5.1 Phase One, FWD testing on the subgrade

The first FWD test was performed on the subgrade. This occurred in December 2011 and the testing conditions were far from ideal. Assessing the surfaces, sometimes below the surrounding access roads proved to be difficult with steep inclines. The surface was far from even and quite a few sensor readings had to be skipped in the following analysis. As was expected the subgrade stiffness improved much as other layers were added.

5.2 Phase Two, FWD testing on the subbase

The second FWD test was performed on the 420 mm thick subbase, the following spring, see Figure 1. After an extraordinary effort of compaction, it became evident, that the strength of the subbase was good enough for reducing the asphalt thickness for about 33% of the section length. Testing on this layer allows for altering the unbound base, and the bound base, so that the total thickness remains constant. Sections with a lower modulus, were subjected to even more compaction, and were tested once again, for a third time. Indeed, the sections stiff enough allowing for a thinner bound layer were now close to 50% of the total length. Thus the “interactive design” was beneficial.



Figure 1. Testing on the subbase in April 2012.

5.3 Phase Three, FWD testing on the bound base

The fourth FWD test was performed on the binder course, during the following summer. This served as a final test for the design of the asphalt layer thickness. Either 130 mm or 85 mm total asphalt concrete thickness was suggested. According to the test about 2/3 of the total slow lanes could be designed with the 85 mm thickness. An assumption was that the overburden of new layers contributed to an improved stiffness of the unbound layers. Hence, more sections would pass with the thinner design. A decision was made to finish all lanes, about 15 km total, with the thinner design. As a precaution, a strategy to resurface sections, which did not meet the rutting criteria in year seven or nine was recognized.

5.4 Phase Four, FWD testing on the wearing course

Thus, the fifth FWD test was carried out when the road opened for traffic in October 2012. Now about 85% should meet the performance criteria within the ten-year warranty period. Assuming, that 90-percentile is considered for the ordinary design specifications, this may be an under-design, but still reasonable considering the need for a partial overlay within the warranty period.

Table 2. FWD testing over time.

When (Month/Year)	Purpose	Note
12/2011	Subgrade	Before and after extended compaction
4/2012	Subbase	
6/2012	Bound Base	
10/2012	Finished Surface	15% under design
10/2012	(no testing)	Road opening to traffic
4/2013	1 st Follow-up	18% under design
10/2014	2 nd Follow-up	12% under design
6/2016	3 rd Follow-up	No under design
10/2018	4 th Follow-up	First Failure noted
4/2019	5 th Follow-up	Severe wheel-track cracking

6 FOLLOW-UP PROGRAM

A plan for carefully monitoring the sections was established. The surface characteristics tests according to the contract, and FWD tests on an annual basis, or as decided necessary depending on previous tests. Some sections, about 100 meters long, were designated as special test sections. They were tested with a tight spacing, several repeated tests at three drop heights. All tests were sampled and saved as time histories. Tests are listed in Table 1.

As it were, the first four years there was no change observed regarding the remaining design life, except a slight improvement, as the design traffic was written off, see Figure 2 from 2014. One could observe a stiffening of the asphalt concrete which was expected due to ageing. There was also noted only a slight influence by seasonal variation.



Figure 2. Photo from 2014, where samples were taken in 2019. Courtesy of STA survey.

In 2018 a few shorter sections with wheel-track fatigue cracking was noted. However, in 2019 several ten-meter-long sections were found with crack in the wheel-paths. This was quite unexpected, and it was decided to do some further investigations. There were some hypotheses about the cause. Severe overloads at less desirable conditions, water moving in the subgrade;

a nearby business area had been established, causing a ground water table change, and faulty construction material.

Regarding the traffic and alleged overloads, a bridge had been instrumented with strain gauges, so that each passing axle load could be assessed, i.e., the bridge serves as a weigh in motion scale. The data show some hefty overloads now and then, which could have contributed to the premature failure. Those were not considered as the primary reason though.

6.1 Backcalculation

It is interesting to study the progress of the stiffness of the backcalculated layers. For the asphalt a rather stiff binder was chosen as can be seen in Table 3. The northbound lanes also get stiffer until 2018, but during the following year cracks appears, which consequently lowers the stiffness. For reasons unknown the southbound lanes are stiffer from the beginning, and the stiffness drops, earlier due to cracking. A stiffer binder is more prone to cracking, and cracked sections were repaired and overlaid in late 2018, so in the following year the median stiffness is back to its higher value.

Table 3. Median backcalculated stiffness for bound layers [MPa].

Year	Northbound	Southbound
2014	13200	15700
2016	14000	15000
2018	17400	10400
2019	15200	15500

The unbound layers, i.e., the subbase and base combined to 500 mm show a rather consistent stiffness over time. After the first year in traffic there is a slight increase, most likely due to compaction by traffic.

The subgrade is rather stiff. There is some variability, likely due to the amount of saturation in the sections with peat. In 2019 the tests were done in the spring, after the thaw. Thus, the lower stiffness reflects the seasonal variation as the test in 2018 occurred in October.

Table 4. Median backcalculated stiffness for unbound layers [MPa].

Year	Northbound	Southbound
2014	197	214
2016	221	225
2018	226	227
2019	241	224

Up until the tests in 2016, there were no indication of an overlay needed before the end of the warranty period in 2023. But in 2018 the FWD test showed that a 30 mm overlay was needed, based on the 90-percentile strain value.

Sections with fatigue cracking, a total of 180 meters needed to be replaced entirely, which was also carried out in the wheel paths. The surface was then tack coated and subjected to a surface treatment. As mentioned above, that action raised the bound layer stiffness median notably in the southbound lanes.

The sudden demise was not fully understood, so a plan was made to investigate further. The previous annual FWD tests were all done during the fall, as that season is closest to mean

Table 5. Median backcalculated stiffness for subgrade [MPa].

Year	Northbound	Southbound
2014	193	188
2016	239	227
2018	245	265
2019	198	192

conditions for the entire year. If spring thaw and the following recovering period could shift stiffnesses considerably it could be a plausible explanation. Thus, another FWD test was planned for the spring in April 2019. The southbound direction also deteriorated faster, an industrial area established on the adjacent side could have shifted ground water levels, so there was some speculation about a shift in subgrade and possibly unbound layer decrease in stiffness. As can be seen in Tables 4 and 5, there is a larger difference between fall and spring in those layers on the southbound side. Access to the industrial area is from a different road and does not affect the present project.

7 CORING FOR LABORATORY ANALYSES

After a quick analysis of the FWD data assessed in the spring of 2019 it was still not clear why there were so many sections with wheel-track cracking. It did not make any sense as the strain levels backcalculated in 2016 were far from the then accumulated number of equivalent standard axle loads. Analyzing the traffic data showed several overloads. In a period during spring thaw 2019 there were 260 vehicles over the legal limit of 62 tons. Eleven of those were more than 80 tons. The heaviest was 125 tons on ten axles. The heaviest axle loads were 16 and 17 tons respectively. Still, it did not explain the damages observed, as there was more traffic in the less damaged northbound lanes. So, it was decided to take some field samples and have them analyzed. In June that year cores were bored at three damaged sections, see Figure 3 from site 1. In



Figure 3. Coring the pavement took place one night in June 2019. Note repaired areas.

addition, one bore hole from an undamaged reference section. The material samples were sent to a laboratory to check the usual compositions, like binder content, and recovered binder stiffness for the bound materials as well as gradation curves and mica content. For unbound materials, gradation curves, mica content and other test regarding aggregate hardness, if necessary.

However, one interesting observation was made during the actual coring. The water used for cooling the drill did not drain through the granular base at all. It was like a waterproof layer tucked on top of it. The experienced operators claimed that they never saw such behavior before, see Figure 4.

If that is the case, trapped water in the layer interface has no way to go, and pressure might be built up in front of a tire.



Figure 4. After drilling the cooling water did not drain through the unbound base.

7.1 *Lab results*

The bound layers did not show any abnormal results, other than the rather stiff binder. The gradation curves from the lab showed a high fines content in the unbound layer though. Figure 5 shows the gradation curve for the unbound base in bore hole 1. The blue line is outside the limit shown with the red lines. Apparently, there are too much fine materials up to the sand fraction. This is likely due to the traffic crushing the materials. The aggregate did obviously not resist the forces acting upon it. Gradation curves from the construction were according to specifications, inside the limiting curves.

There are also tests for mica content. The test is performed on aggregate sizes from 0.125 to 0.250 mm. The amount mica mineral should not exceed 30%, which was tested for during construction. However, all tests failed, showing mica contents above 30%, including the reference hole #4.

Thus, it looks like coarser aggregate containing mica was crushed into finer particles, so that the amount increased in the present tests. Tests at the placing of the layers did not exceed 30 %, and micro deval and gradation curves also passed the tests at construction.

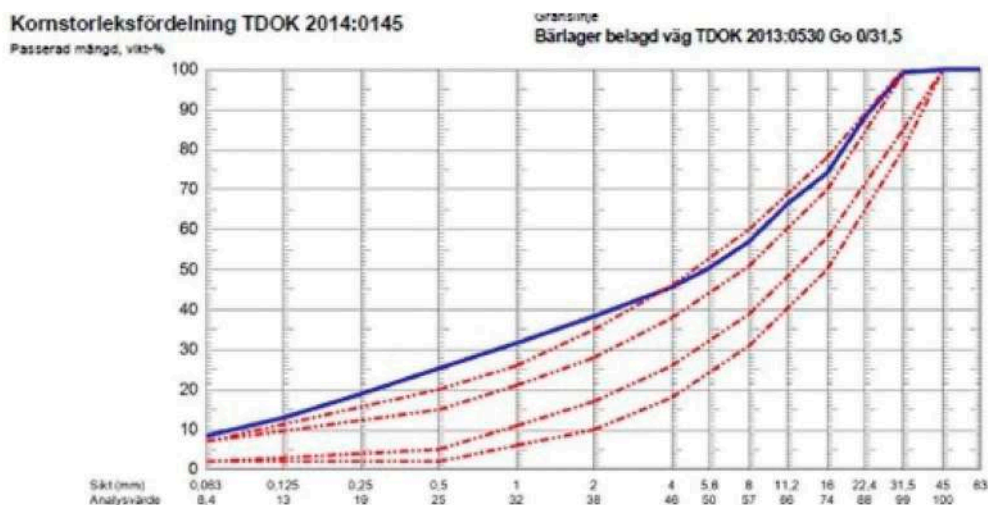


Figure 5. Gradation Curve from Bore Hole #1.

Table 6. Mica content on recovered material.

Hole	ID	Free Mica	Other Minerals
		Number of particles [%]	
1	190819-1	46.4	53.6
2	190819-2	39.1	60.9
3	190819-3	51.5	48.5
4	190819-4	41.3	58.7

8 DISCUSSION

Mica does provide a good bearing capacity when dry, but when wet is easily disintegrates into smaller particles. This might even have occurred during construction, as an extra effort was made during compaction. As many as twenty passes with roller was reported. Certainly, the compaction was good enough, but the surface might have turned into a very tight interface. The rather thin 85 mm pavement did not help either as the compression from overloaded truck could have driven this process further.

As it turned out, the material with the high mica content was provided and designated by the Transport Administration from a burrow nearby, so it was not the choice of the contractor. As stipulated by the empirical part of the ME design, tests must be done for high mica contents. It could be that the tests were not representative for the actual outcome, or that the highly specific test itself is not valid under certain circumstances. Only one fraction of the gradation curve is tested, but in this case larger aggregate with a higher content could have increased the content in fines considerably when crushed by the substantial roller passes during construction and overloads during the years in operation.

Now, the surface becomes very tight. Free water may accumulate through condensation on the underside of the asphalt concrete layer. When a load is moving the water accumulates in front of the tire, and pressure is increasing, until the material breaks, see Figure 6. The open crack relieves the pressure, and it takes maybe ten to 15 meters for the pressure to build up again to break the pavement. The only way to break the pattern is to remove the bound layers and the unbound base, and replace the latter with an open-graded material.

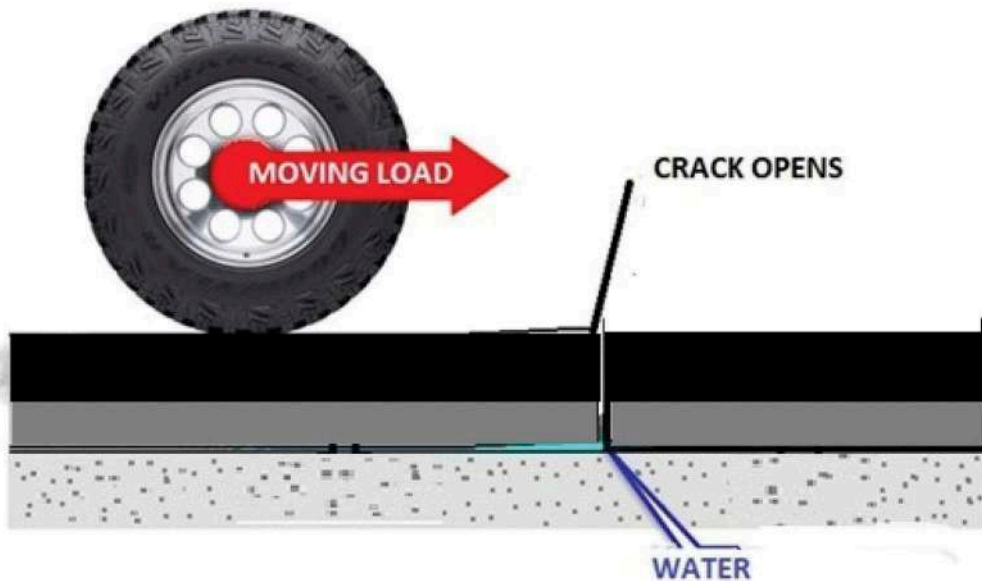


Figure 6. Cracking explained.

9 CONCLUSIONS AND RECOMMENDATIONS

The present strategy can in many ways be regarded as a perfect example for a performance specification driven project. The FWD and layer stiffness back-analyses was done for each new layer prepared, from the subgrade and up. A slight under-design left about 15% of the lane length to fail before the end of the warranty period, but that regarded rutting and not the fatigue criterion. Nevertheless, cracks appeared after four years, and more so the following year.

When writing up the performance specifications, roughness, rutting, and friction are primary parameters, easy to test at any time during the warranty period. Note, that if the warranty period is less than the usual design period, the design must be made for the usual design period of 20 to 30 years. Thus, if rutting failure is 19 mm after 20 years, the rutting after ten years should not exceed 11 mm, when 3 mm initial rutting is accepted.

A structural evaluation with a FWD and back-analyses of stiffness and strain should be done on the subbase, and bound base. The design life strain based on any criterion should be fulfilled to a least 90% of the section length.

With dynamic analysis of the FWD, it is possible to investigate strain energy as an alternative to the fatigue relationship. It is also possible to measure the dissipation of energy in the unbound layers for assessing the compaction.

Last, but not least, it is time to establish mechanistic criteria for the unbound material.

REFERENCE

TRVK Väg 2011. *Trafikverkets tekniska krav Vägkonstruktion*. TRV2011:072 TDOK:2011: 264

New backcalculation method to obtain viscoelastic properties of asphalt pavement from HWD tests

J.-M. Roussel* & M. Broutin

French Civil Aviation Technical Centre (STAC), Bonneuil-sur-Marne, France

**Formerly University of Lyon/ENTPE/LTDS*

H. Di Benedetto & C. Sauzéat

University of Lyon / ENTPE / LTDS, Vaulx-en-Velin, France

ABSTRACT: This study presents a new method to determine linear viscoelastic properties of asphalt concrete from HWD tests. The forward approach involves Spectral Element Method (SEM) to compute multi-layered pavement response under impact loading, including approximated viscoelastic behaviour for bituminous materials and dynamic effects. The optimisation is addressed in the frequency domain, taking advantage of the numerical efficiency of the SEM. This backcalculation method has been applied to several HWD tests on the flexible pavement of the STAC's test facility for several temperatures in the bituminous course.

Keywords: Heavy Weight Deflectometer, Dynamic analysis, Spectral Element Method, Linear Viscoelasticity

1 INTRODUCTION

Pavement assessment is a fundamental feature for asset management. Deflection measurement is a non-destructive evaluation method and can be achieved by several devices. Among them, the Heavy Weight Deflectometer (HWD) is widely used for airfield pavements. The HWD test consists in applying a wheel-representative load, generated by a falling mass, at the pavement surface. Deflections time histories are recorded by geophones located at several distances from the applied load. Inverse analysis procedures are needed to estimate layers mechanical properties, such as Young's modulus for Linear Elastic (LE) materials or complex modulus for Linear Viscoelastic (LVE) materials. Backcalculation methods are often based on iterative optimisation procedures which involve, at each iteration, several calls to a forward simulation. Most of backcalculation methods consider i) LE behaviour for pavement layers and ii) static HWD loading. However, it has been shown that these hypotheses are leading to misestimate bituminous layers modulus and, in most cases, to non-optimised maintenance. In order to better consider bituminous layers behaviour, it is required to use LVE constitutive model and adapted numerical methods.

In this article, a new backcalculation method is introduced. The latter considers dynamic effects and linear viscoelastic behaviour of bituminous mixtures in order to provide a more accurate characterization of pavement materials. It is based on the Spectral Element Method as a forward simulation, already used by several authors (Al-Khoury et al., 2001; Grenier & Konrad, 2009; Zhao et al., 2015). The study also includes 25 HWD tests carried out on the

STAC experimental facility at several temperatures (Broutin & Duprey, 2017). Finally, the dynamic viscoelastic backcalculation method is applied to each HWD test.

2 HWD TESTS ON STAC TEST FACILITY

The STAC test facility, located in Bonneuil-sur-Marne (Paris suburbs), is a full-scale airfield pavement dedicated to experiments (Broutin et al., 2013). It has been designed for ten jumbo jet passes per day during ten years. The four-layered flexible pavement structure is of two bituminous mixtures (base and surface asphalt concretes) laid on a layer of Untreated Graded Aggregate (UGA). The two bituminous layers are bonded together by a pure bitumen tack coat. Prior to this work, layers thicknesses had been determined by geo-radar (GPR) study. Geotechnical surveys have also shown that the bedrock is deeper than 6 m.

The STAC test facility is equipped with a variety of sensor types. In particular, the temperature profile is continuously measured in the bituminous mixtures. In the temperature measurement area (see Figure 1), three locations are instrumented with each seven PT100 probes located at several depths (surface, 30, 50, 70, 130, 190 and 250 mm). This allows to accurately characterize the thermomechanical behaviour of bituminous materials.

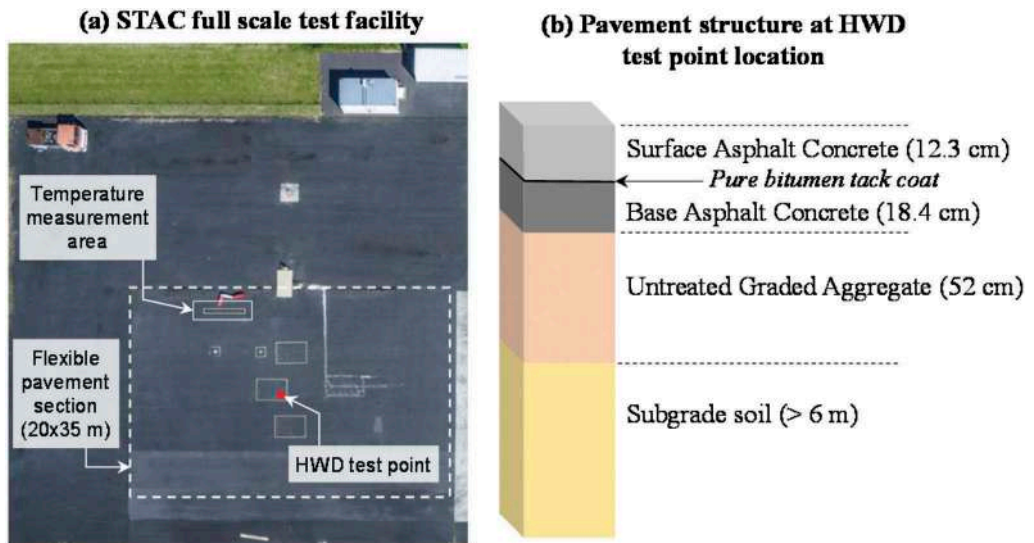


Figure 1. STAC test facility: (a) aerial view (photography DGAC/STAC); (b) pavement structure.

For the experimental campaign, 25 HWD tests have been carried out at several period of the year on the flexible structure overmentioned. 25 distinct temperature profiles have been measured during these tests. Mean temperatures, calculated over the entire bituminous mixtures thickness, are between 0°C and 30°C. All experiments are done on the same location, depicted on Figure 1. Thus, all HWD tests will be analysed by considering the same pavement structure.

For all HWD tests, the target load was 280 kN. The repeatability has been carefully checked by performing three drops. Deflections are measured by 13 geophones, located at radial distances from centre until 2.40 m. The recording time is set to 120 ms and no filter is used. In order to access to the frequency content, deflections have to be at a zero value at the end of signal. However, in reason of the poor precision of geophones sensors at low frequencies, residual deflections are observed at the end of the recording time. A parabolic correction is applied between the maximum time and the end (120ms) in

order to set the final deflection to zero. This correction is only applied on the decreasing part of each deflection and does not affect the maximum value. The pavement Frequency Response Function (FRF) is then computed at each geophone location. It is calculated according to Equation 1 by using the frequency content (obtained by FFT) of deflections $\hat{d}_i(\omega)$ and load $\hat{l}(\omega)$. FRFs allows to observe the pavement response under unit harmonic load. An example of FRF computed from HWD load and deflection histories, in terms of norm and phase angle, is presented in Figure 2. It can be noted that, due to dynamic and viscous effects, FRF norms are decreasing as a function of the loading frequency. It means that deflections are smaller for fast loadings.

$$FRF(d_i, \omega) = \frac{\overline{\hat{d}_i(\omega)\hat{l}(\omega)}}{\hat{l}(\omega)\overline{\hat{l}(\omega)}} \quad (1)$$

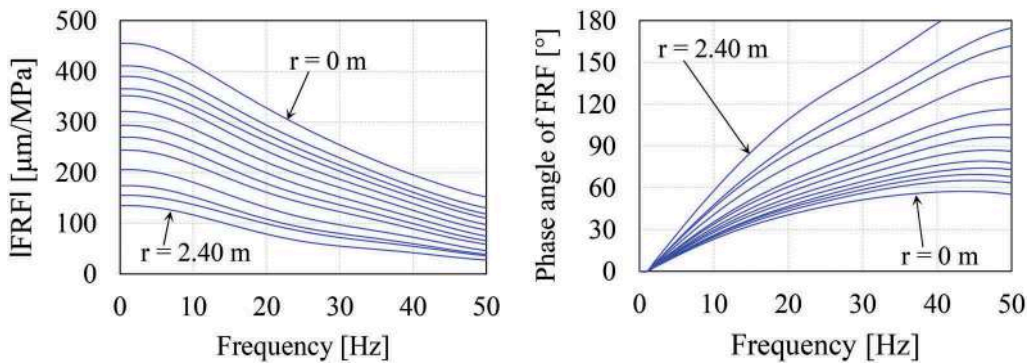


Figure 2. Frequency Response Functions example computed from an HWD test.

3 FORWARD SIMULATION OF HWD TEST USING THE SPECTRAL ELEMENT METHOD

The forward simulation is the most critical step of HWD analysis. A realistic forward simulation method guarantees the physical realism of backcalculated mechanical properties. Simulation hypotheses have to be carefully chosen. As seen before, it is important to consider the linear viscoelastic behaviour for bituminous mixtures and dynamic effects. Since it is run numerous times during the backcalculation process, the forward simulation method also has to be computationally efficient. The Spectral Element Method, described below, meets all these criteria.

3.1 Geometry, boundary conditions and equilibrium equation

In reason of the circular shape of the HWD load plate, numerical simulations for flexible pavements can be done using an axisymmetric geometry depicted in Figure 3. Pavement layers are therefore considered as perfectly plane and, as a first approximation, perfectly bonded together. The HWD loading is applied as an evenly distributed surface load. As a consequence of the short duration of the transient load signal, dynamic effects have to be considered. The equilibrium Equation 2 therefore includes an acceleration term $\gamma = (\gamma_r \ \gamma_z)^t$ weighted by the bulk density ρ .

$$\text{div}(\sigma) = \rho\gamma \Rightarrow \begin{cases} \frac{\partial \sigma_{rr}}{\partial r} + \frac{\partial \sigma_{rz}}{\partial z} + \frac{\sigma_{rr} - \sigma_{\theta\theta}}{r} = \rho\gamma_r \\ \frac{\partial \sigma_{rz}}{\partial z} + \frac{\partial \sigma_{rr}}{\partial r} + \frac{\sigma_{rz}}{r} = \rho\gamma_z \end{cases} \quad (2)$$

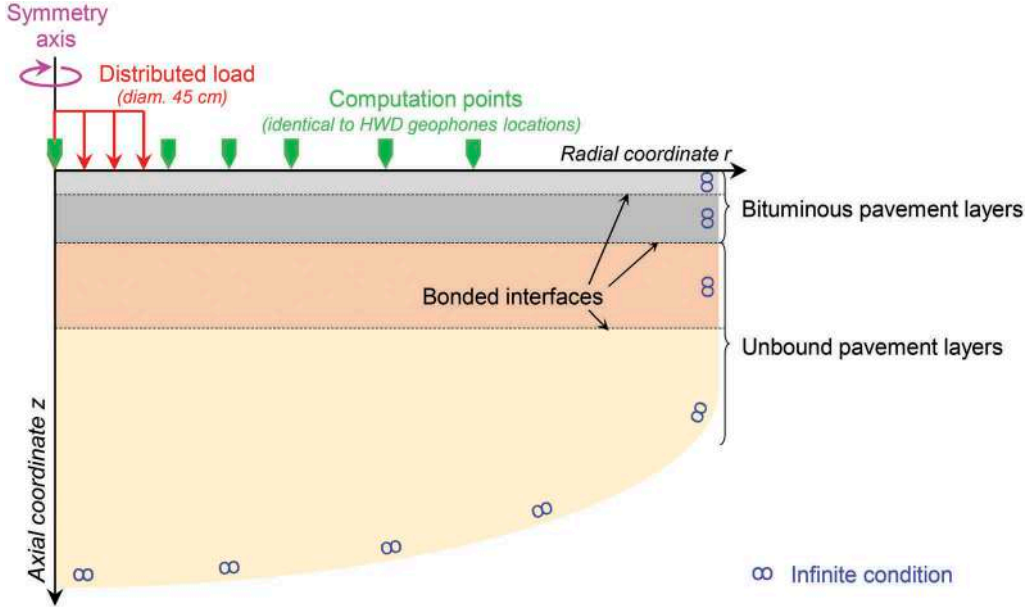


Figure 3. HWD test simulation geometry and boundary conditions.

3.2 Spectral Element Method main principle

The Spectral Element Method (SEM) is a semi-analytical and frequency-domain method. Linear viscoelasticity of bituminous materials and dynamic effects can be considered with the SEM. Moreover, it is well-adapted to the HWD test simulation since only one spectral element is required to describe one pavement layer.

The SEM main principle is schematized in Figure 4. Expressions of displacements, stresses and strains under a unit harmonic load (at a given frequency) are analytically known in one spectral element. Specified bonding conditions are then considered by ensuring the continuity of displacement (radial and axial) and stresses (normal and shear) between two adjacent spectral elements. The deflections under a unit harmonic load (also called Frequency Response Function) are obtained at surface points corresponding to geophone locations. The total frequency response of the pavement under a given HWD load is finally computed by weighting the FRF with the load frequency content, at each frequency. Time domain signals can then be calculated with the use of an inverse FFT.

Linear viscoelasticity can be considered with the direct use of a complex modulus, for any rheological model, with no additional computation time regarding to the linear elastic approach. The SEM has been implemented in the Matlab commercial software. The HWD test can be fully simulated on a four-layered pavement in 40" by using a regular laptop. The SEM code used here has been validated by comparing forward results with finite element method computations (Roussel et al., 2019, 2020).

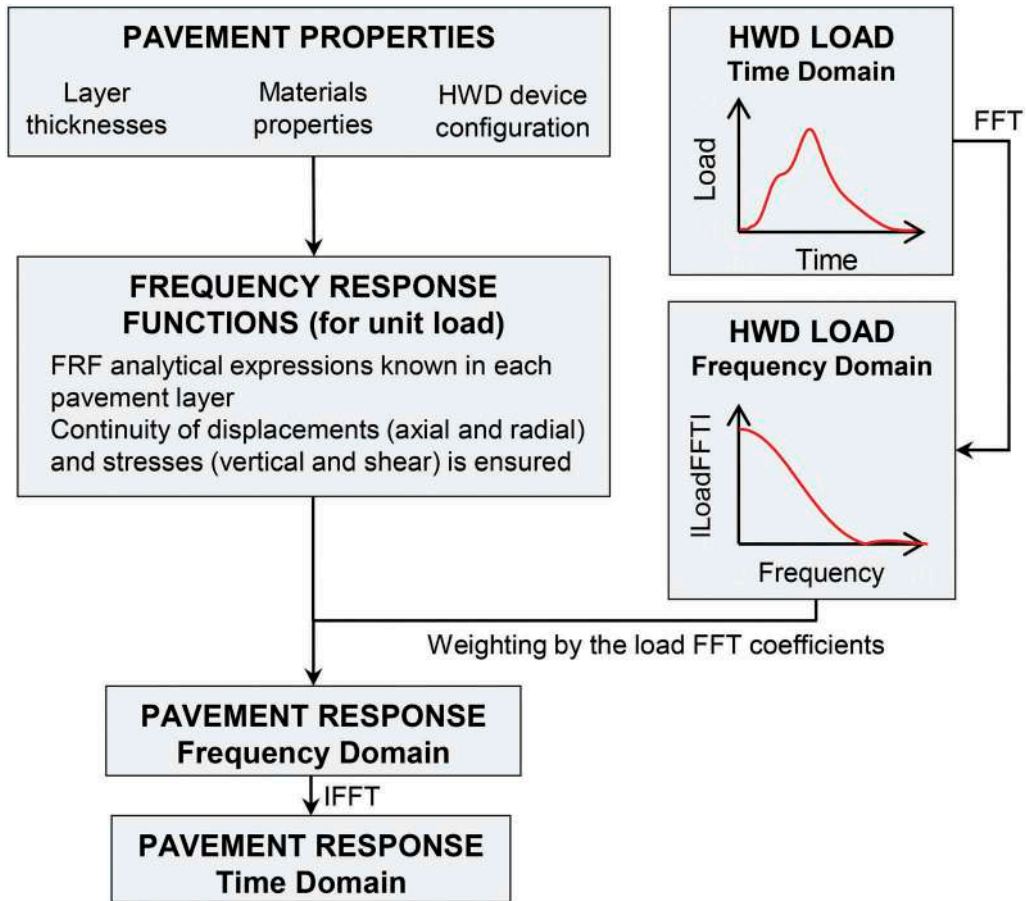


Figure 4. Spectral Element Method main principle.

4 BACKCALCULATION OF HWD TEST DATA

The proposed backcalculation is an innovative method able to accurately backcalculate mechanical properties of pavement materials. In particular, linear viscoelastic behaviour of bituminous materials can be characterized. This method is applied to the above-mentioned experimental data collected by HWD tests on the STAC test facility.

4.1 Viscoelastic dynamic backcalculation method

The backcalculation procedure aims to minimise the difference between measured and computed data. The optimisation is done in the Frequency Response Functions domain. Experimental FRF are computed from HWD signals as explained in section 2. Since FRF are complex number, the objective function is calculated in terms of norm and in terms of argument (Equation 3). The objective function is calculated on five frequencies: 10, 15, 20, 25 and 30 Hz. Indeed, on the one hand it has been noted that for frequencies lower than 10 Hz instabilities can occur in the Spectral Element Method and on the other hand the HWD load pulse does not provide enough energy for frequencies higher than 30 Hz (Fu et al., 2020). This method is very efficient because it only requires the computation of the pavement response at five frequencies. The optimisation is performed by the *Fminsearch* function, implemented in

Matlab and based on the downhill simplex method. The backcalculation is stopped when both the objective function and parameters evolution are lower than 0.01 % between two iterations.

$$F = \frac{1}{2} \frac{1}{N_{geo} N_f} \sum_{k=1}^{N_{geo}} \sum_{m=1}^{N_f} \left(\frac{\left| \frac{|FRF(d_{k,meas})| - |FRF(d_{k,comp})|}{|FRF(d_{k,meas})|} \right|}{\left| \frac{\arg(FRF(d_{k,meas})) - \arg(FRF(d_{k,comp}))}{\arg(FRF(d_{k,meas}))} \right|} \right) \quad (3)$$

$$with \left\{ \begin{array}{l} N_{geo} \text{ Number of geophones} \\ N_f \text{ Number of optimisation frequencies} \\ D_{k,meas} \text{ Maximum deflection measured at geophone } k \\ D_{k,comp} \text{ Maximum deflection computed at geophone } k \\ FRF(d_{k,meas}) \text{ Measured Frequency Response Function at geophone } k \\ FRF(d_{k,comp}) \text{ Computed Frequency Response Function at geophone } k \end{array} \right.$$

Usual linear viscoelastic models have many constants (seven for the 2S2P1D model, six for the Huet-Sayegh model). Due to this high number of constants and to the lack of sensitivity of some of them at frequencies and temperatures reached by the HWD test, the use of a classical linear viscoelastic model does not guarantee the convergence of the backcalculation procedure. Hence, an approximated viscoelastic model is used for the proposed method. The norm of the complex modulus E^* is assumed to evolve linearly as a function of the logarithm of the frequency f . Its expression is given in Equation 4. Two parameters have then to be determined: $|E^*(30Hz)|$ and α . This linearization is only valid on a limited frequency range. The phase angle of the complex modulus φ , in Equation 6, is calculated thanks to the Booi & Thoenes (1982) approximation in Equation 5, based on the Kramers-Kronig causality relationships.

$$|E^*|(f) = \alpha \log_{10} \left(\frac{f}{30[Hz]} \right) + |E^*(30Hz)| \quad (4)$$

$$\varphi(f) \approx \frac{\pi}{2} \frac{d \ln |E^*(2\pi f)|}{d \ln (2\pi f)} \quad (5)$$

$$\varphi(f) = \frac{\pi}{2} \frac{\alpha}{\alpha \log_{10} \left(\frac{f}{30[Hz]} \right) + |E^*(30Hz)|} \quad (6)$$

Granular materials are assumed to be linear elastic, following the Hooke's law. A hysteretic damping is considered. As experimentally observed, this value is independent from the loading frequency. The damping coefficient D is applied on Lamé's coefficients (λ and μ) as expressed in Equation 7. Its value is expected to be small, between 0 % and 10 %. In order to limit the number of parameters, the damping coefficient is the same for all pavement granular materials.

$$\begin{cases} \lambda^* = (1 + 2jD)\lambda \\ \mu^* = (1 + 2jD)\mu \end{cases} \quad (j^2 = -1) \quad (7)$$

4.2 Considered pavement structure and fixed parameters

For the backcalculation, layers thicknesses, Poisson's ratios and bulk densities are assumed to be known at values in Table 1. Although the top part of the pavement is made of two bituminous layers, only one asphalt concrete layer is considered here. Its thickness is equivalent to the sum of the two bituminous layers thicknesses. Therefore,

five parameters (two for asphalt concrete layer and three for granular materials layers) have to be backcalculated. For the first iteration of the backcalculation, initial values have been estimated in Table 2.

An example of backcalculation is shown in Figure 5. For this example, the final error (last value of the objective function) is 2.3 %. For all of the 25 HWD tests backcalculation, the final error is lower than 4 %.

Table 1. Considered pavement structure and fixed parameters for backcalculation.

Layer type	Thickness	Poisson's ratio	Bulk density
Asphalt Concrete (AC)	12.3 + 18.4 = 30.7 cm	0.30	2500 kg/m ³
Untreated Graded Aggregate (UGA)	52 cm	0.35	2000 kg/m ³
Subgrade Soil (SS)	∞	0.35	2000 kg/m ³

Table 2. Initial values for backcalculation.

Layer type	Parameter	Initial value
Asphalt concrete	$ E^*(30Hz) $	15000 MPa
	α	6000 MPa
Granular layers	E-modulus	600 MPa for UGA 200 MPa for SS
	Same damping coeff.	3 %

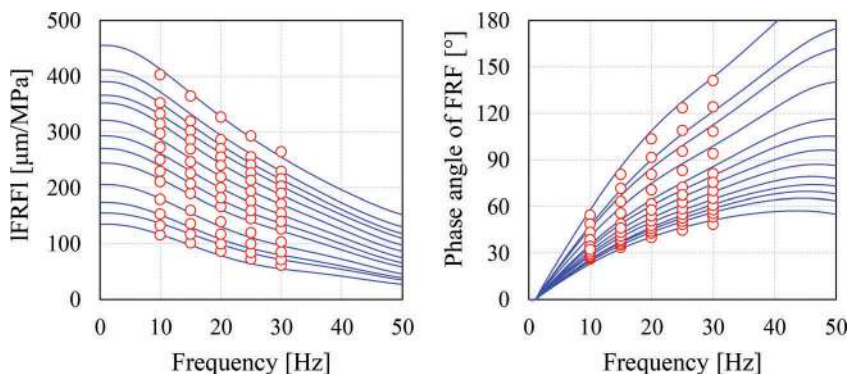


Figure 5. Backcalculation example.

4.3 Backcalculation results

The dynamic viscoelastic backcalculation method, presented above, has been applied to all HWD tests carried out on the STAC test facility (described in section 2). This database includes HWD signals time histories and temperature measurements in the bituminous materials. The main interest of this work is to accurately characterize the viscoelastic temperature-dependent behaviour of bituminous mixtures. Backcalculation results are presented as a function of the pavement mean temperature over the bituminous mixtures thickness in Figures 6 and 7.

It is clearly seen on Figure 6 that asphalt concrete properties are temperature-dependent. The $|E^*(30Hz)|$ values are decreasing with the temperature, with a decrease rate higher than 600 MPa/°C. Thus, $|E^*(30Hz)|$ values are approximately 22000 MPa at low temperatures (around 0°C) and 7000 MPa at high temperatures (around 30°C). The α coefficient seems to follow a parabolic curve. The lowest values are obtained for very low and very high temperatures. The maximum value is reached for intermediate temperature around 11°C. This means that the frequency evolution of the norm of the complex modulus is higher at intermediate temperatures.

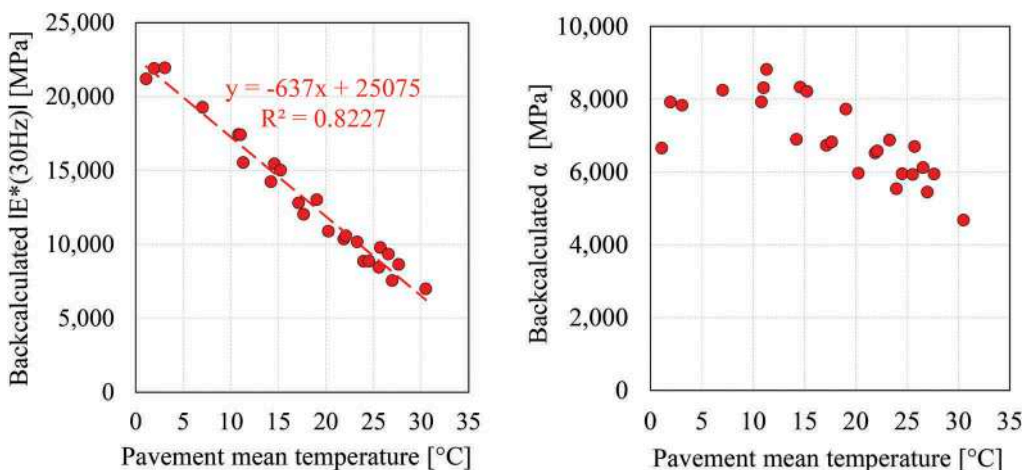


Figure 6. Backcalculated asphalt concrete mechanical properties (Equation 4).

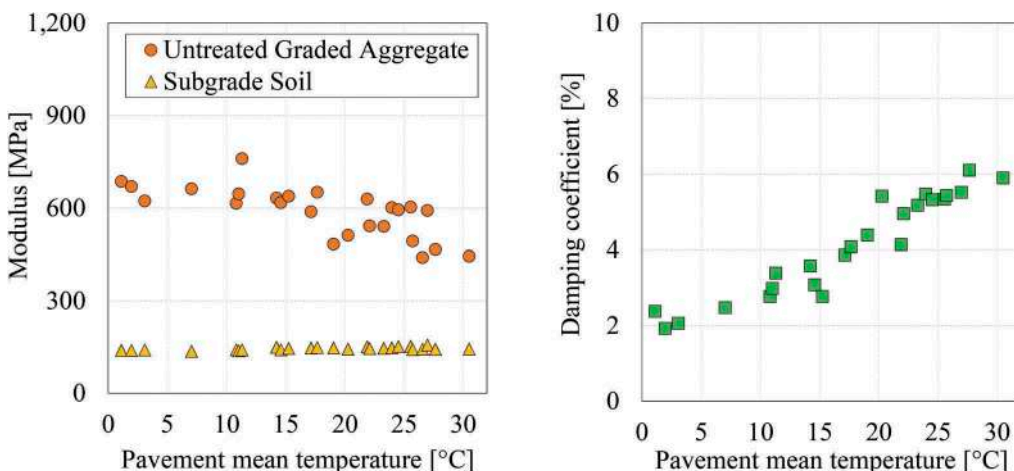


Figure 7. Backcalculated granular materials mechanical properties.

Backcalculated granular materials properties are shown in Figure 7. Mean values of 589 MPa and 145 MPa have been obtained over the 25 backcalculations for UGA and SS materials. These values are consistent with materials types and compaction levels. Damping coefficient (common to both materials UGA and SS) average value is 4.1 %. Granular materials mechanical properties are expected to be independent of the

temperature. However, trends can be observed for UGA modulus and damping ratio. These evolutions could be related either to a compensation phenomenon, or to a non-simulated phenomenon.

Most of classical backcalculation tools (including those provided by HWD manufacturers) are based on a Burmister pavement model. In such methods all pavement materials are assumed to be linear elastic. In addition, a static loading is considered, at the maximum value of the dynamic load time history, and only maximum deflections (also called deflection basin) are taken into account. In contrast, the proposed dynamic viscoelastic method considers both inertial effects and frequency-dependent behaviour for bituminous mixtures. Therefore, the backcalculated values are directly associated to a loading frequency.

Figure 8 provides a comparison between results from the classical elastostatic method and from the abovementioned dynamic viscoelastic method. Backcalculations have been performed on the same HWD data. Significant differences are observed. For the asphalt concrete, backcalculated moduli are taken as the norm of the complex modulus at two frequencies (10 Hz and 30 Hz). As an example, it is observed that the backcalculated modulus at 15°C with the elastostatic method is almost 50 % higher than the $|E^*(10\text{Hz})|$ given by the dynamic viscoelastic method. Important differences are also observed for the granular materials. This last observation may be linked with the lack of damping coefficient in the classical elastostatic method.

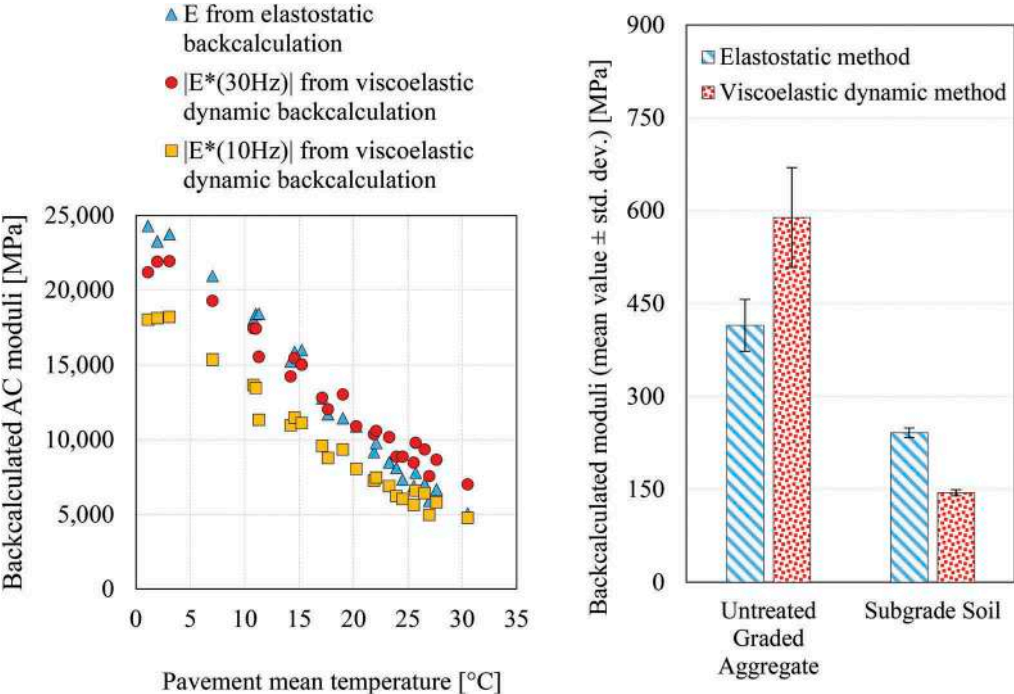


Figure 8. Comparison of backcalculated moduli of asphalt concrete (left) and granular materials (right) with elastostatic and viscoelastic dynamic methods.

5 CONCLUSION AND OUTLOOKS

In this paper, a new backcalculation method has been presented. This method, in contrast to classical elastostatic analyses, considers dynamic effects and linear viscoelasticity of bituminous materials. Therefore, it can accommodate both the frequency- and the temperature-

dependency of bituminous materials behaviour. In parallel, an experimental campaign, including HWD tests and temperature measurements, has been carried out on the STAC test facility. 25 data sets have been collected at temperatures between 0°C and 30°C. All data were analysed with the dynamic viscoelastic backcalculation method. Results show consistent mechanical properties. Comparisons with results from classical elastostatic method underline that backcalculation results highly depends upon the considered physical hypothesis. The developed dynamic viscoelastic method takes in consideration the frequency-dependent behaviour of bituminous mixtures and is therefore more accurate.

Even if good results have been obtained with the developed backcalculation method, improvements are still needed. For further work, HWD data will be analysed with the consideration of two bituminous layers (instead of one here). Then, master curve will be built and compared with those obtained by laboratory complex modulus testing for the bituminous materials.

REFERENCES

- Al-Khoury, R., Scarpas, A., Kasbergen, C., & Blaauwendraad, J. (2001). *Spectral element technique for efficient parameter identification of layered media. Part II: Inverse calculation*. International Journal of Solids and Structures, 38(9),1605–1623.
- Booij, H. C., & Thoone, G. P. J. M. (1982). *Generalization of Kramers-Kronig transforms and some approximations of relations between viscoelastic quantities*. Rheologica Acta, 21(1),15–24.
- Broutin, M., & Duprey, A. (2017). *Towards Improved Temperature Correction for NDT Data Analyses*. Proceedings of the International Conference on Highway Pavements and Airfield Technology 2017, 244–255.
- Broutin, M., Fauchet, S., & Mounier, D. (2013). *A full-scale instrumented test-facility for airport pavement modeling improvements*. Proceedings of the International Airfield and Highway Pavements Conference.
- Fu, G., Zhao, Y., Zhou, C., & Liu, W. (2020). *Determination of effective frequency range excited by falling weight deflectometer loading history for asphalt pavement*. Construction and Building Materials, 235, 9.
- Grénier, S., & Konrad, J.-M. (2009). *Dynamic interpretation of falling weight deflectometer tests on flexible pavements using the spectral element method: backcalculation*. Canadian Journal of Civil Engineering, 36(6),957–968.
- Roussel, J.-M., Di Benedetto, H., Sauzéat, C., & Broutin, M. (2020). *Simulation of Heavy Weight Deflectometer Test: Spectral Element Method vs Finite Element Method*. In Lecture Notes in Civil Engineering (Vol. 76, pp. 699–708).
- Roussel, J.-M., Sauzéat, C., Di Benedetto, H., & Broutin, M. (2019). *Numerical simulation of falling heavy weight deflectometer test considering linear viscoelastic behaviour in bituminous layers and inertia effects*. Road Materials and Pavement Design, 20(sup1), S64–S78.
- Zhao, Y., Cao, D., & Chen, P. (2015). *Dynamic backcalculation of asphalt pavement layer properties using spectral element method*. Road Materials and Pavement Design, 16(4),870–888.

Microwave deep healing of road pavements: Preliminary numerical results

F.G. Praticò, S. Zumbo, M.T. Bevacqua & T. Isernia

*DIIES, Department of Information Engineering, Infrastructures and Sustainable Energy, Università
Mediterranea di Reggio Calabria, Reggio di Calabria, Italy*

ABSTRACT: Nowadays the self-healing process is a new frontier in material engineering, which allows changing the approach to the maintenance of aged road pavements. As is well known, top-down cracking and bottom-up cracking are major damage phenomena in pavement structures. Unfortunately, self-healing properties are currently difficult to apply in case of bottom-up propagation. In this context, the aim of the presented study is to set up an innovative and non-destructive method to carry out the rehabilitation of damaged road structures, made up of materials wherein the self-healing process is induced by microwave deep healing. The method uses electromagnetic fields in the microwave frequency range in order to induce a selective and deep heating in the damaged structure and, hence, trigger the self-healing process of the material. Healing properties of the asphalt mixtures are enhanced doping the target pavement layers through conductive particles. Simulations demonstrate that the method allows achieving a deep, selective, adaptive, and not invasive healing without significantly modifying the mechanical properties of materials.

Keywords: Bottom-up cracking, doping, hot mix asphalt, microwave, road pavement, self-healing

1 INTRODUCTION

Fatigue cracks, plastic deformations (rutting), and thermal cracking imply the failure of road pavements, safety concerns, and economic burdens. One goal to achieve is the reduction of the damages as well as their repair [1]. Timeliness maintenance allows significant savings in terms of management and maintenance costs and considerably increases the expected life of the monitored road structure. The fatigue cracking generally starts at the bottom of the hot mix asphalt layer due to repeated and excessive tensile stresses, and gradually propagates up to the surface. Notably, the detection of deep cracks is more difficult than the one that refers to surface cracks and, consequently, repairing the first deep cracks before they propagate would improve the expected life and maintenance costs.

In literature there are different methods to treat damages repair, at a maintenance or rehabilitation level. Some of them, known as thermal approaches, exploit the interesting properties of the bitumen, which is the main constituent of the pavement mixture [1], to be heat sensitive. Then, when its internal temperature increases and reaches a critical threshold, this can self-repair bituminous mixture damages. Temperature increase can be achieved through different technologies. Garcia et al, [2] use the electromagnetic induction and, in order to improve the electrical conductivity of the pavement and enhance its self-healing capacity, add electrically conductive particles to the asphalt mixture. Similar methods are

presented in [10]-[14]. With respect to methods in [3]-[9], the electromagnetic induction-based approach is less invasive, but it seems the only advantage. However, the above thermal approaches allow repairing just the surface damages without implying a deep level of restoration, so they are neither selective nor governable.

In this paper, a new, innovative, and non-destructive thermal method to carry out the rehabilitation of the pavement structure via selective and not invasive microwave heating is introduced and discussed. In particular, the recovery of both internal and superficial damages is addressed for the re-establishment of the normal conditions of use of the road (rehabilitation/maintenance), as well as its continuous maintenance during pavement life. Moreover, the healing is induced by means of an electromagnetic applicator, i.e., an antenna. The selection of the fundamental parameters for the antenna (e.g., frequency, dimension and power) and for doping the target pavement layer (e.g., the length and the volume of the fibres), in order to reach the healing temperature and the optimum in term of performance of the treatment, is discussed. Note that, as mentioned for several thermal methods, this method involves the use of conductive fibres to enhance the electrical conductivity of the materials. Importantly, this method has a great potential because of its capability to rehabilitate deep layers without impacting friction courses and namely premium surfaces. Indeed, these latter have additional functional properties. To this end, note that the EU-funded project LIFE SNEAK (“optimized Surfaces against Noise And vibrations produced by tramway track and road traffic” – LIFE20 ENV/IT/000181) deals with premium road surfaces and the implementation of such a surface is scheduled in 22 in the near future.

The remainder of the paper is organized as follows. In Section 2, the general description of the proposed strategy is given. In section 3, a numerical analysis in 3-D realistic scenarios of the proposed technique is illustrated. Finally, conclusions and final remarks follow.

2 ADAPTIVE MICROWAVE HEALING

The procedure aims at healing the considered pavement at a given depth in a non-invasive way. It takes advantage from the interaction between an electromagnetic field (EMF) in the range of microwave frequency and the asphalt mixture constituting the road, which results in currents induced within the interested materials, as well as in energy absorption. This latter is converted into thermal energy, thus increasing material temperature and triggering the healing process. More in details, the procedure is composed of the following steps:

- a) doping of the layer of material at the depth wherein the deterioration phenomenon is estimated to occur;
- b) planning of the restored treatment by selecting the fundamental parameters of the antenna;
- c) supply of the restored treatment through the antenna whose characteristics are defined in step b).

The first step is related to the fact that the electromagnetic energy absorption is directly proportional to the electrical conductivity of the medium, while the pavement is made up with insulating materials. A way to make an insulating material conductive is to contaminate it with conductive materials. Then, the method includes an appropriate doping, during the construction of the pavement, of the layer wherein the anomalies are expected to start with conductive particles or fillers add to mixtures as in [2],[10]-[12],[15]-[17],[19]. The procedure due to the doping is selective and adaptive with respect to the depth wherein the deterioration phenomenon is expected to start.

Many studies were conducted using different types of additives (carbon fibres, graphite, steel wool, slags, etc.) and many of these consider steel fibers as the best choice for asphalt concrete. Steel wool with an initial length of 9.5 mm and 8% volume percentage was chosen as a possible solution, accordingly [11],[13],[17]. Based on the results obtain in the preview cited studies, in the numerical simulations the deep layer is supposed to be doped with this type and percentage of fibers.

As far as the second step, it aims at selecting the characteristics of the antenna (or eventually of an antenna system) such to obtain a maximum efficiency of the healing, that is the maximum homogeneity of the treatment, minimum time needed for the layer to reach the self-healing temperature of the structure and maximum extension of the restored area. The planning is performed by means of multi-physical simulations, according to the following sub-phases:

- modelling of the road through the identification of its structural, electromagnetic and thermal characteristics, taking also into account the depth of the doped layer, the weather season in which the treatment is carried out;
- modelling of the antenna (or the antenna system), which includes the type, working frequency, dimensions, power supply, number and position of the antennas;
- calculation of the electromagnetic field distribution and the temperature distribution over time produced in the structure being restored, by varying the characteristics of the antenna or antenna system.

The time needed for the healing procedure is selected as the time need to reach the healing temperature [18]. Healing temperatures usually range from 30 °C to 70 °C [20],[21]. They depend on materials and particularly on bitumen type and ageing. For example, for porous asphalt concretes an optimum temperature of 85°C was suggested to obtain the best healing effect with a good stiffness recovery, while higher temperatures could induce swelling and asphalt binder drainage problems [11]. Xiang et al [23] and Tang et al [24] highlighted that the optimal healing temperature is close to the softening point. This latter varies as a function of bitumen type, ranging from 53/65 (for a bitumen 20/30) to 39/47 for a bitumen 100/150). Importantly, the choice of the type of bitumen mainly depends on weather, layer and traffic. The warmer the climate is, the higher the temperature is, the severer the traffic spectrum is, the harder the bitumen should be, the lower its penetration should be (e.g., Bitumen penetration grade 50/70) and vice-versa (e.g., Bitumen penetration grade 70/100). The softening point of the majority of the asphalt binders used in bottom layers of pavements is close to 50°C [20]-[22],[23],[25]. Accordingly, the self-healing temperature has been set at 50°C. By referring to optimal healing times, 31-48 minutes were obtained by Xiang et al [23].

3 TREATMENT PLANNING VIA MULTI-PHYSICAL SIMULATIONS

The results of an extensive multi-physical numerical analysis are described in this section. This analysis is aimed at validating the proposed approach as a non-destructive, selective and deep method to carry out the restoration of a damaged road pavement. All results have been achieved by using a full wave finite element solver. In order to reduce the computation burden, the symmetry of the model has been exploited by simulating only a quarter of the pavement-antenna structure, as shown in Figure 1.

This section is divided as follows. In the first part (Subsection 3.1) a description of the electromagnetic and thermal model of the road pavement is given, with a particular characterization of the doped layer (pavement layer where the cracks originate). The modelling of the performed antenna is presented in Subsection 3.2. Finally, Subsection 3.3 shows the results in terms of absorbed power density and reached temperature in the interested internal layer of the pavement system.

3.1 Modelling of the road

Figure 1 (a), shows the considered realistic 3-D scenario, where thickness Δ_{z_i} (m) and relative permittivity ϵ_i (dimensionless) are shown. Each layer has been characterized in terms of geometry, electromagnetic and thermodynamic properties (cf. Figure 1a). From the top to the bottom, layers include: the bituminous layers (e.g., wearing course which is modelled with a thickness $\Delta_{z_1} = 0.05m$, binder course and base course, total thickness $\Delta_{z_2} = 0.19m$), non-bituminous layers (e.g., granular base course and subgrade). The method here presented,

which can be applicable to both surface and deep layers, includes a stress absorbing layer (with thickness $\Delta_{z3} = 0.03m$) doped in the pursuit of exploiting the EMF heating as described in Section 2.

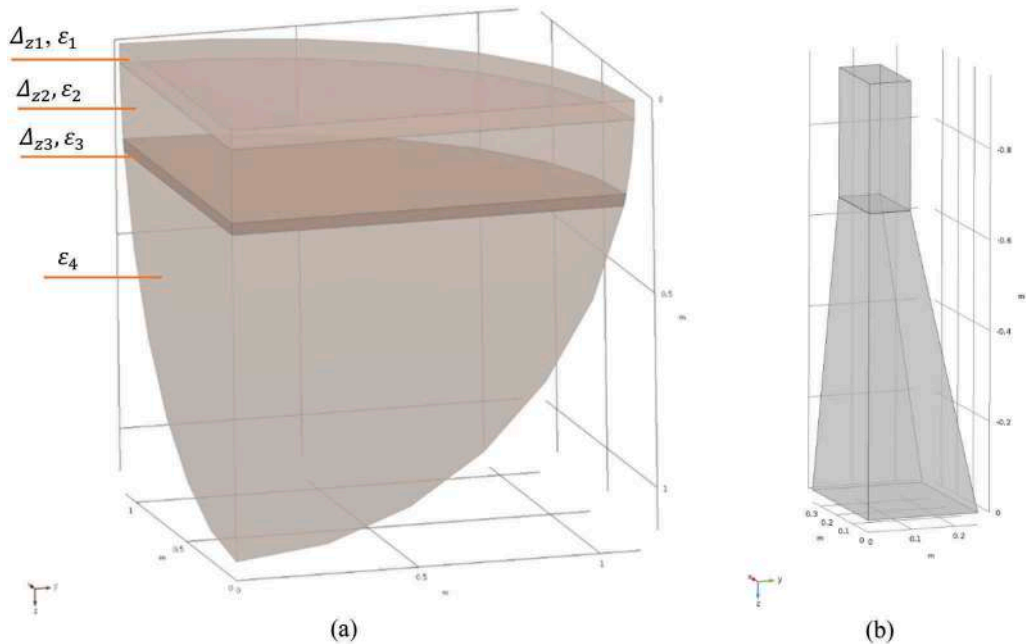


Figure 1. 3-D models of (a) a flexible road pavement; (b) pyramidal horn antenna.

The model of the road structure was built by considering that the relative permittivity and conductivity of all layers change with respect to the scenario under testing (e.g., air void content, presence of water, EM frequency, and temperature [26],[27], as well as the meteorological conditions). In order to take into account this dependence in the numerical analysis, the city of Reggio Calabria (Italy) and the parameters of the coolest months of winter were considered [28]. Temperatures were derived through the formulation given in [29] and the initial temperature of the different layers of the pavement has been set at approximately 10°C.

Asphalt concrete is essentially an insulator and its electric conductivity is quite low. Conversely, the stress absorbing layer (wherein cracks are supposed to start), according to [9], [12], [17],[22], when doped with 8% fibres (by total volume of bitumen), has a conductivity, σ , of about 0.12S/m. The relative permittivity ϵ_r of each layer has been chosen according to [27] and it has been set $\epsilon_1=\epsilon_2=\epsilon_4=5$ except for the doped layer in which $\epsilon_3=8.2$ was set.

3.2 Modelling of antenna

The increase of temperature and, in turn, the healing of the road cracks is achieved by a horn antenna, which is particularly used in the microwaves range (i.e., with frequencies between 300 MHz, corresponding to wavelengths of about 1 m, and 300 GHz, corresponding to about 1 mm).

Figure 1(b) shows the considered pyramidal horn antenna. The geometrical antenna parameters are selected according to [30]. The pyramidal horn antenna has geometrical dimensions (larger base) of a (larger base edge) and b (smaller base edge), with $a>b$. In the following numerical analysis, the length l of the horn (truncated pyramid height) is 0.677 m, $a=0.698$, and $b=0.574$ m, with a working frequency of 0.433GHz.

Another important issue for the considered antenna is the power handling capability of the entire system. In general, these types of antennas are capable of handling continuous power up to 10^4 to 10^7 W [31],[32]. However, the considered coax-to-waveguide adapter mainly limits the maximum continuous power supported by horn antennas. In the following, the input power in every case considered was set to 1kW. Moreover, in the example, the horn antenna is placed directly on the road (neglecting the interposed air).

3.3 Numerical results

Figures 2 and 3 show the absorbed power (2a, 2b, 3a, 3b) and the temperatures (2c, 2d, 3c, and 3d) for two different case-studies.

Figure 2 Shows the absorbed power density distribution in the different layers of the scenario previously described in Section 3.1, but without the doping of the interested layer. The vertical section at $y=0$ m (i.e., the cross section that contains the axis of symmetry of the truncated pyramid) is shown in Figure 2-a, while Figure 2-b corresponds to a horizontal section at $z=0.255$ m (i.e., 0.255 m below the upper surface of the pavement).

It is clear from the results that, since the starting conductivity of the pavement is very low, there is no deposited power and consequently no temperature increase. If no doping is performed, it is not possible to increase the temperature, which is always equal to the starting temperature, around 10°C in every layer.

The second example (cf. Figure 3) involves the same scenario with the same applicator, but with a doped pavement layer. In Figure 3, both the obtained power density and temperature

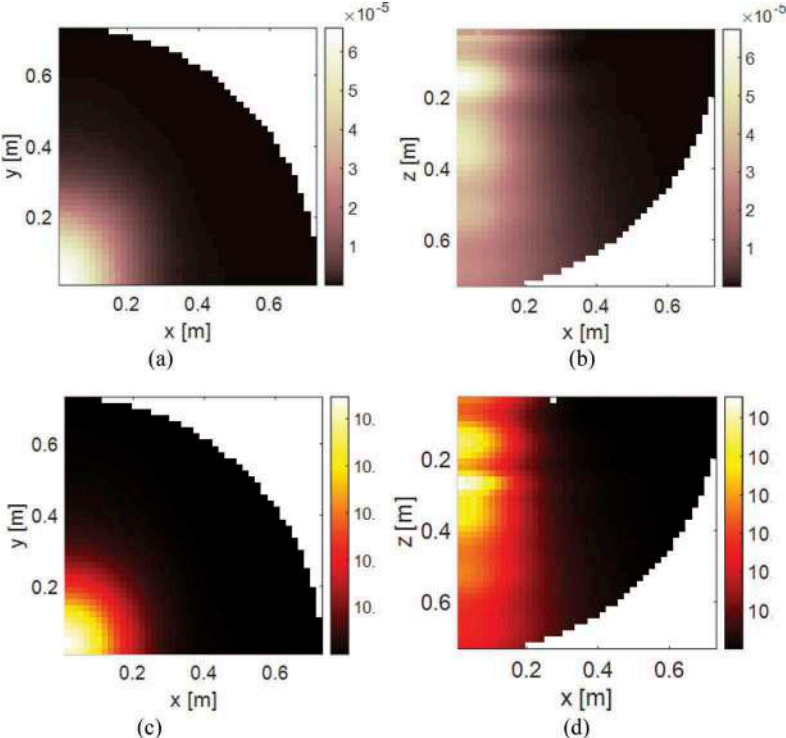


Figure 2. Microwave heating via 0.433 GHz horn antenna. Deposited power density [W/m^3] along a cut view on (a) x-y plane at $z=0.255$ m and (b) x-z plane at $y=0$ m. Temperature distributions [$^\circ\text{C}$] along a cut view on (c) x-y plane at $z=0.255$ m and (d) x-z plane at $y=0$ m. Note that in (c) and (d) all the points of the investigated scenario are at 10°C .

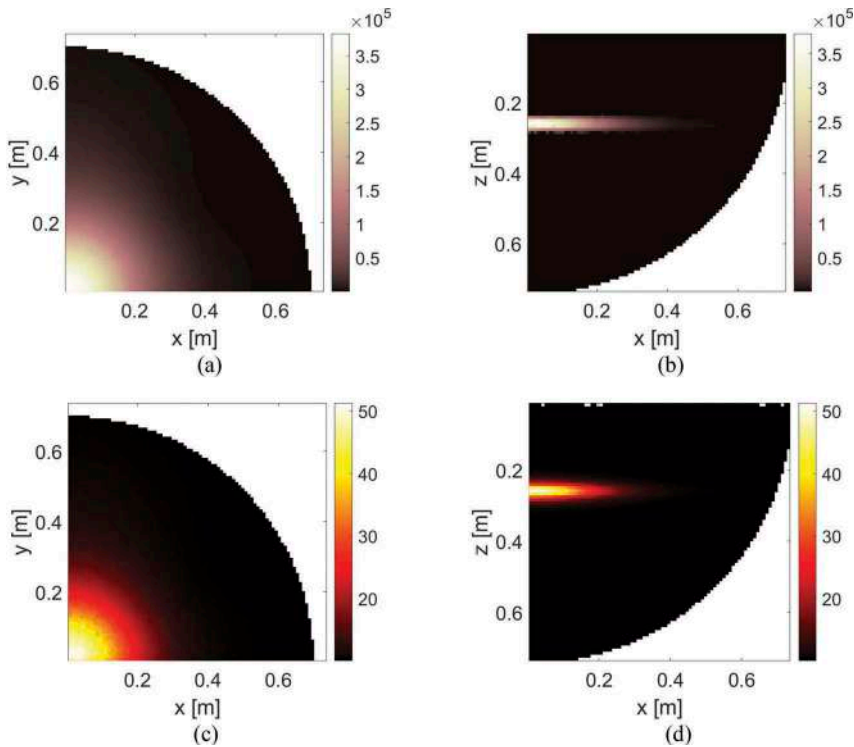


Figure 3. Microwave heating via 0.433 GHz horn antenna. Deposited power density [W/m^3] along a cut view on (a) x-y plane at $z=0.255\text{m}$ and (b) x-z plane at $y=0\text{m}$. Temperature distributions [$^{\circ}\text{C}$] along a cut view on (c) x-y plane at $z=0.255\text{m}$ and (d) x-z plane at $y=0\text{m}$.

distributions are shown. These results underline that the doping of pavement layer plays a relevant role in the proposed healing treatment.

As expected, the absorbed power density is focused only into the doped layer, according to its higher conductivity. As synthesized in Section 2, the absorbed power is converted in heat and a temperature increase is induced on the conductive structure. In Figure 3-c e Figure 3-d the temperature values distributions are shown. These results confirm that the EM field can induce the road pavement overheat, in a selective way. The healing temperature of 50°C is reached after 198s (about 3 minutes, thus improving the performance with respect to [24]).

For the extension of the healing section of the pavement, with respect to the x-axis, the healing region is expected to be extended $\approx 0.4\text{ m}$. This is an important aspect that take into account the average passage area of the wheels. Figures 3 shows that the considered applicator is able to bring the temperature to about 50°C in a region of about 0.20 m .

This example validates the proposed approach, confirms its selectivity, and underlines that the procedure is also adaptive in depth.

4 CONCLUSIONS AND SUMMARY

In this paper, a new method for healing the cracks of damaged road pavements has been proposed. Unlike the other existing ones, this procedure allows obtaining a selective, not invasive, and fast healing. Interestingly, it is also adaptive, as it can induce the healing also in the deeper layers of the road pavement. In order to achieve an adaptive and selective treatment, an adequate doping of the layers to treat (typically in the interface between granular base and

bituminous base course) is needed. The doping is required in order to increase the electrical conductivity of the asphalt and it takes place through the insertion of metallic particles (e.g., fibres) in the structure matrix. Importantly, a synergistic impact on the expected life of the concerned layer (increase) is expected based on just the fibre addition. Furthermore, this selective induction heating allows healing different layers at different heights by dynamically adjusting antenna working parameters, in the pursuit of an additional increase of the expected life *per* induction heating treatment.

The results show that the proposed approach allows reaching in few minutes the healing temperatures, which for the case under investigation have been set up at 50°C. Moreover, the numerical tests have been performed by considering as microwave applicator a pyramidal horn antenna, working at 0.433 GHz. With respect to other healing methods proposed in the literature, such as the one proposed in [24], the proposed procedure allows drastically reducing the overall treatment time.

Further methods to improve the performance of the treatment and to have a better control of the antenna radiation pattern are the optimization of the applicator, the insertion of appropriate dielectric materials inside the antenna [33], and to set up a specific control system (cf., e.g., [34]).

Finally, it seems important to highlight that in this case a frequency of 0.433 GHz (reserved for industrial, scientific and medical purposes other than telecommunications, ISM) has been used (cf. [35]). Future investigations are going to address the validation of this method capability to preserve pavement surface properties (cf. [36]) for premium friction courses (cf. [37]).

ACKNOWLEDGMENTS

The authors would like to thank all who supported them with this research, including the European Commission (LIFE SNEAK – “optimized Surfaces against Noise And vibrations produced by tramway track and road traffic” – LIFE20 ENV/IT/000181). This work was also supported by the European Commission, Fondo Sociale Europeo and Regione Calabria, POR-Calabria FSE 2014/2020.

REFERENCES

- A. Tabakovic, E. Schlangen, Self-healing technology for asphalt pavements, *Advances in Polymer Science* 273 (2016) pp. 285–306. DOI:10.1007/12_2015_335
- A. Garcia, M. Bueno, J.N. Contreras and M.N. Partl, Induction healing of dense asphalt concrete, *Construction and Building Materials* 49 (2013) pp. 1–7. DOI:10.1016/j.conbuildmat.2013.07.105
- N. Tabatabaee, M. H. Shafee, Effect of organoclay modified binders on fatigue performance, In 7th RILEM International Conference on Cracking in Pavements (2012)pp. 869–878. DOI:10.1007/978-94-007-4566-7_84
- J.Y. Lee, G.A. Buxton, A.C Balazs, Using nanoparticles to create self-healing composites. *The Journal of Chemical Physics* 121 (2004) pp. 5531–5540. DOI:10.1063/1.1784432
- Z. You, J. Mills, J. Foley, S. Roy, G. Odegard, Q. Dai, S. Goh, Nano-clay modified asphalt materials: Preparation and characterization. *Construction and Building Materials* 25 (2011) pp. 1072–1078. DOI:10.1016/j.conbuildmat.2010.06.070
- A.G. Tabakovic, A. Gibney, C. McNally, M.D. Gilchrist Influence of Recycled Asphalt Pavement on Fatigue Performance of Asphalt Concrete Base Courses *ASCE Journal of Materials in Civil Engineering* 22(6) (2010) pp. 643–650. DOI: 10.1061/(ASCE)MT.1943-5533.0000093
- C. Fang et al., Nanomaterials Applied in Asphalt Modification: A Review. *Journal of Material Science and Technology* 29(7) (2013) pp. 589–594. DOI: 10.1016/j.jmst.2013.04.008
- J.F. Su et al., Investigation the possibility of a new approach of using microcapsules containing waste cooking oil; in-situ rejuvenation. *Construction and Building Materials* 74 (2015), pp. 83–92. DOI: 10.1016/j.conbuildmat.2014.10.018
- A. Garcia, E. Schlangen, M. Van de Ven, Properties of capsules containing rejuvenators for their use in asphalt concrete. *Fuel* 90 (2011) pp. 583–91. DOI: 10.1016/j.fuel.2010.09.033
- A. Garcia, E. Schlangen, M. van de Ven, D. van Vliet, Crack repair of asphalt concrete with induction energy, *HERON* 56 (2011) pp. 33–43. ISSN 0046-7316, <http://heronjournal.nl/56-12/3.pdf>

- Q. Liu, A. Garcia, E. Schlangen, M. van de Ven, Induction healing of asphalt mastic and porous asphalt concrete, *Construction and Building Materials* 25(9) 2011 pp. 3746–3752. DOI:10.1016/j.conbuildmat.2011.04.016
- A. Menozzi, A. Garcia, M. N. Partl, G. Tebaldi, P. Schuetz., Induction healing of fatigue damage in asphalt test samples, *Construction and Building Materials* 74 (2015) pp. 162–168. DOI:10.1016/j.conbuildmat.2014.10.034
- K. Liu, C. Fu, D. Dai, C. Jin, W. Li, S. Li, X. Xu, Induction heating performance of asphalt pavements incorporating electrically conductive and magnetically absorbing layers, *Construction and Building Material* 229 (2019). DOI:10.1016/j.conbuildmat.2019.116805
- H. V. Vo, D-W. Park, J. W. Seo, T. H. M. Le, Effects of asphalt types and aging on healing performance of asphalt mixtures using induction heating method. *Journal of Traffic and Transportation Engineering* Volume 7, Issue 2 (2020) pp. 227–236. DOI:10.1016/j.jtte.2018.10.009
- Á. García, E. Schlangen, M. van de Ven, Q. Liu, Electrical conductivity of asphalt mortar containing conductive fibers and fillers, *Construction and building materials* 23 (10) (2009) pp. 3175–3181. DOI:10.1016/j.conbuildmat.2009.06.014
- S. P. Wu, X. M. Liu, Q. S. Ye, L. I. Ning, Self-monitoring electrically conductive asphalt-based composite containing carbon fillers, *Transactions of Nonferrous Metals Society of China* 16 (2006) pp. 512–516. DOI:10.1016/S1003-6326(06)60246-X
- Liu, Q., Schlangen, E., & van de Ven, M., Induction Healing of Porous Asphalt. *Transportation Research Record*, *Journal of the Transportation Research Board*, 2305(1) (2012) pp. 95–101. DOI:10.3141/2305-10
- G. Franceschetti, *Electromagnetics: theory, techniques, and engineering paradigms*, Springer Science & Business Media (2013). ISBN 978-1-4899-0259-7
- H. Wang, J. Yang, G. Lu, X. Liu. Accelerated Healing in Asphalt Concrete via Laboratory Microwave Heating, *Journal of Testing and Evaluation* 48(2) (2018). DOI:10.1520/JTE20170621
- D. Sun, G. Sun, X. Zhu, F. Ye, J. Xu, Intrinsic temperature sensitive self-healing character of asphalt binders based on molecular dynamics simulations, *Fuel* 211 (2018) pp. 609–620. DOI:10.1016/j.fuel.2017.09.089
- J. Qiu, M F. C. Van de Ven, S. Wu, J. Yu, A. A. A. Molenaar, Investigating the self healing capability of bituminous binders, *Road Materials and Pavement Design*, 10(sup1) (2009) pp. 81–94. DOI:10.1080/14680629.2009.9690237
- A. Garcia. Self-healing of open cracks in asphalt mastic. *Fuel* 93 (2012) pp. 264–72. DOI:10.1016/j.fuel.2011.09.009
- H. Xiang, Z. He, L. Chen, H. Zhu, Z. Wang, Key Factors and Optimal Conditions for Self-Healing of Bituminous Binder, *Journal of Materials in Civil Engineering* 31(9) (2019). DOI:10.1061/(ASCE)MT.1943-5533.0002760
- J. Tang, Q. Liu, S. Wu, Q. Ye, Y. Sun, E. Schlangen, Investigation of the optimal self-healing temperatures and healing time of asphalt binders, *Construction and Building Materials* 113 (2016) pp. 1029–1033. DOI:10.1016/j.conbuildmat.2016.03.145
- <http://rahabitumen.com/bitumen-penetration-grade-100-150/> (data di ultimo accesso?). 10-04-2020
- E. J. Jaselskis, J. Grigas, A. Brilingas. Dielectric properties of asphalt pavement, *Journal of materials in civil engineering* 15(5) (2003) pp. 427–434. DOI:10.1061/(ASCE)0899-1561(2003)15:5(427)T. Saarenketo, T. Scullion, Road evaluation with ground penetrating radar, *Journal of applied geophysics*, 43 (2-4)(2000), pp. 119-138. DOI:10.1016/S0926-9851(99)00052-X
- T. Saarenketo, T. Scullion, Road evaluation with ground penetrating radar, *Journal of applied geophysics*, 43(2-4) (2000), pp. 119–138. DOI:10.1016/S0926-9851(99)00052-X
- <http://www.solaritaly.enea.it/>. 10/04/2020
- B. K. Diefenderfer, I. L. Al-Qadi, S. D. Diefenderfer, Model to predict pavement temperature profile: development and validation. *Journal of Transportation Engineering* 132(2) (2006) pp. 162–167. DOI:10.1061/(ASCE)0733-947X(2006)132:2(162)
- http://www.ainfoinc.com/en/p_ant_h_std.asp 10-04-2020
- <http://www.ets-lindgren.com/products/antennas/pyramidal-standard-gain>. 10-04-2020
- R. K. Cooper and R. G. Carter, High power RF transmission, CERN, Geneva, Switzerland, Tech. Rep. CERN-2005-003 (2000). 10-04-2020
- C. Balanis, *Antenna Theory, Analysis, and Design*, 2nd ed. Wiley, 1997. New York. ISBN 978-1-118-64206-1
- P. Kilpeläinen, M. Jaakkola, P. Alanaatu, Development of a control system for a multipurpose road repairing machine, *Automation in Construction*, Volume 20, Issue 6, 2011, pp. 662–668. DOI:10.1016/j.autcon.2011.04.017.

- Bevacqua, M.T., Isernia, T., Praticò, F.G., Zumbo, S., A method for bottom-up cracks healing via selective and deep microwave heating (2021) *Automation in Construction*, 121, art. no. 103426. DOI: 10.1016/j.autcon.2020.103426.
- Praticò, F.G., Astolfi, A., A new and simplified approach to assess the pavement surface micro- and macrotexture (2017) *Construction and Building Materials*, 148, pp. 476–483. DOI: 10.1016/j.conbuildmat.2017.05.050.
- Praticò F.G., Vaiana R., Improving infrastructure sustainability in suburban and urban areas: Is porous asphalt the right answer? And how? (2012) *WIT Transactions on the Built Environment*, 128, pp. 673–684. DOI: 10.2495/UT120571

Investigation of local rail track deterioration due to sleeper support condition variation

N. Lillin, D. Rudisch & S. Freudenstein

Chair and Institute of Road, Railway and Airfield Construction, Technical University of Munich, Munich, Germany

F. Mitlmeier, F. Kotter & C. Moormann

Institute of Geotechnical Engineering, University of Stuttgart, Stuttgart, Germany

ABSTRACT: Varying sleeper support (e.g. seat stiffness) influences the load distribution of the track. Consequently, this might result in locally accelerated ballast and substructure deterioration, including mud spot development.

A vehicle-track-subgrade modelling workflow has been developed to investigate the interaction between its elements. The comprehensive approach incorporates track irregularities, vehicle dynamics, varying sleeper support and complex ballast and soil modeling, including ballast contamination.

Measurements have been conducted at two track sections with known subgrade problems, including a former and possibly reoccurring mud spot. Based on these measurements, calibration and validation parameters for the models are derived, as a case study. Individual rail seat stiffness values could be identified with an iterative approach, using strain and deflection measurement data and a finite element model.

The presented study demonstrates that the identified high variation in rail seat stiffness at the former mud spot leads to individual sleepers with significantly increased load transmission to the ballast. It also highlights the limitation of the loaded geometry, as measured by track recording cars, to reflect the rail seat stiffness variation.

Keywords: Vehicle-track-subgrade interaction, trackside measurements, rail support stiffness variation, mud spot

1 INTRODUCTION

Immaculately built and maintained ballasted rail tracks distribute the vehicle loads evenly across the track through the ballast to the substructure. In practice, railroad tracks can have imperfections like varying support conditions of the sleepers in the ballast bed.

Varying sleeper support (e.g. seat stiffness) influences the local rail deflections and can result in significant local increases of the forces transmitted from particular sleepers to the ballast. Consequently, the locally increased dynamic interactions can lead to locally accelerated ballast and substructure deterioration.

Locally increased dynamic forces and cohesive and saturated soils (e.g. due to lack of drainage performance) may induce mud spots (Rapp, 2017). A mud spot can lead to a rapid track deterioration, including the development of track geometry faults, which supersede safety thresholds and compromise safe train passages (Hudson et al., 2016).

A comprehensive numerical simulation workflow has been established to analyze the interaction between vehicle, track and subgrade during train passages over tracks with support layer problems. Those include varying rail seat support and ballast contamination, which can occur at mud spots.

A measurement site with known subgrade problems has been selected as a case study, at a former mud spot and a reference site. Different measurements have been conducted to provide realistic input values for the developed methodology and to evaluate the results.

The presented study focuses on the investigation of the effects of varying rail seat stiffness.

2 MEASUREMENTS & SUPPORT STIFFNESS IDENTIFICATION

2.1 Measurement site

To investigate the track behavior in a case study at a single-track railway line with known subgrade problems, an in-service track section has been selected where mud spots have developed in the past. Track geometry measurements have been carried out and geotechnical information has been gathered. Two 14.5m sections in close proximity have been selected to carry out track deformation measurements during train passages.

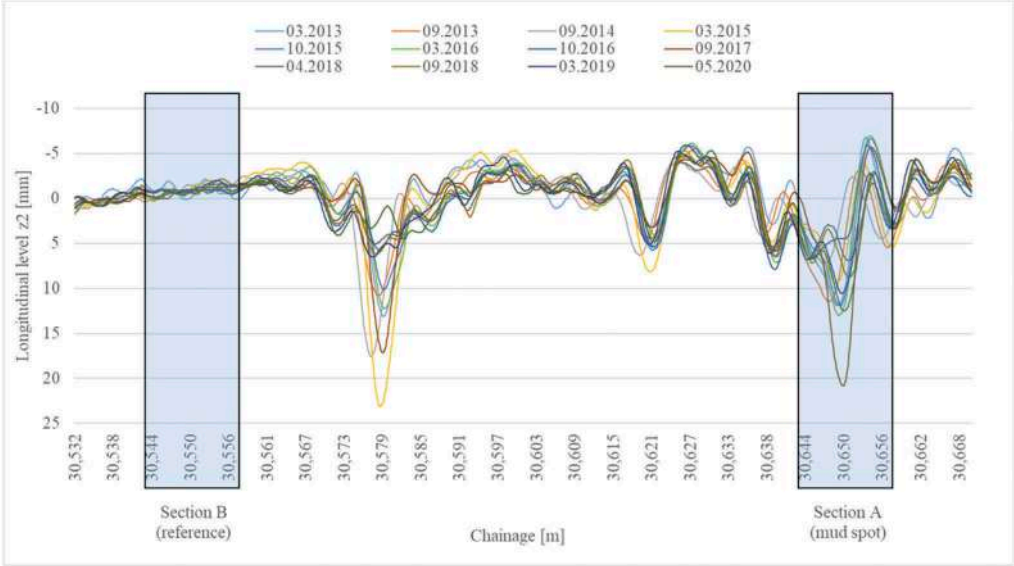


Figure 1. Loaded vertical geometry of right rail – RAILab measurements 2013-2020 – selected measurement sites.

Section A represents a former mud spot, which has been maintained locally two years prior to the track deformation measurements of the presented study. The development of the mud spot can be observed in the analysis of the loaded geometry, represented by track measurement data by a RAILab measurement train by Deutsche Bahn (see Figure 1). The maintenance measure included replacing ballast, sleepers and fastening systems and introducing a geotextile layer between subgrade and the replaced ballast. Two years after maintenance, fine particles can be observed in the ballast (see Figure 2), indicating the reappearance of a mud spot.



Figure 2. Ballast cross section at (former) mud spot – Measurement section A.

Section B is at a distance of 100m to the first section. It has the same track characteristics and geotechnical boundary conditions, but did not show any progression in the analysis of the loaded geometry (see Figure 1). Hence, section B was selected as a reference section.

2.2 Unloaded and loaded track geometry

Track recording cars measure the track geometry under their vehicle load usually under the permissible track operating speed (DB Netz AG, 2016). This *loaded track geometry* is supposed to represent the safety critical track defects. On the other hand, the *unloaded track geometry*, recorded by hand-driven measurement carts, represents the track geometry without the influence of vehicle mass and vehicle speed.

The vertical loaded track geometry, recorded by RAILab measurement vehicles, were used to analyze the track section and for selection of the measurement site (see chapter 2.1).

The unloaded track geometry was measured on a 1000m section with an inertial measurement unit AMU 1030, mounted on a hand driven measurement cart GRP 3000 IMS, both by the company Amberg Technologies. For the purpose of the presented study, only the vertical geometry of the two rails was considered. To reduce the influence of the track layout (here: longitudinal inclination changes) a band pass filter has been applied to the dataset. The used Butterworth filter has a low cutoff wavelength of 3m and a high cutoff wavelength of 70m, comparable to the filter characteristics used by RAILab data filter (Sandner et al., 2020). The measured vertical track geometry of both rails was used to calculate rail-wheel forces (see chapter 3.1). Due to the measurement system and the filter characteristics short-wavelength track defects are not included in the determination of rail-wheel forces.

By processing both loaded and unloaded vertical track geometry equivalently, and eliminating the influence of the track layout, the resulting difference between both signals can be attributed to the load-dependent deflection of the rails under the dynamic load of the measurement vehicle. This difference might vary along the track due to variations in track stiffness.

Figure 3 shows a fictitious example, where for illustration purposes the absolute track geometry is displayed by introducing a difference between loaded and unloaded vertical track geometry, representing the rail deflection under load. The blue line describes the unloaded vertical track geometry, while the green line, assuming a constant deflection under the vehicle load of 1.5mm, represents the loaded track geometry. The red line illustrates a section with reduced stiffness, as one might expect at a developed mud spot. In this imaginary example, the reduced stiffness at the mud spot causes a deviation of the loaded from the unloaded vertical

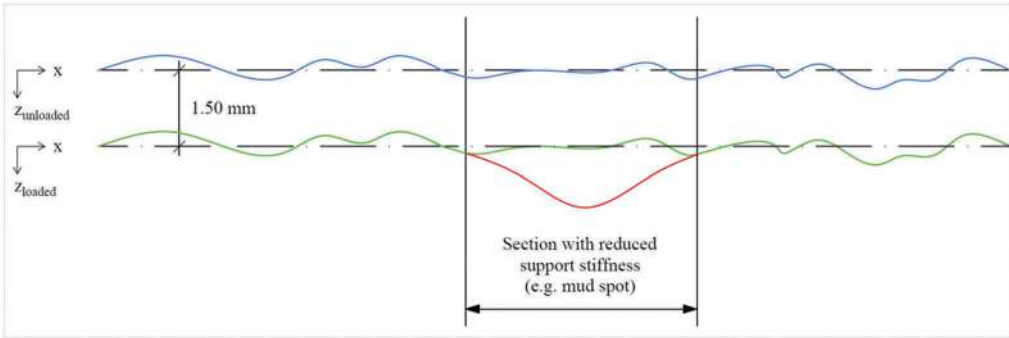


Figure 3. Concept of unloaded (blue line) and loaded (green line) vertical geometry – example of locally reduced stiffness, as would be expected at mud spot (red line).

track geometry. The resulting loaded track geometry signal contains both the influence of the unloaded geometry and the varying stiffness. With appropriate signal processing, possibly under the additional use of unloaded track geometry measurements, the stiffness variation can be identified.

2.3 Track deformation measurements

To provide input for the numerical models as a case study and to validate the results, high frequency track deformation measurements have been carried out representatively on the right rail at the two mentioned 14.5m sections, with identical instrumentation. All sensors of both sites were collected at one computer to obtain simultaneous results with a common time signal.

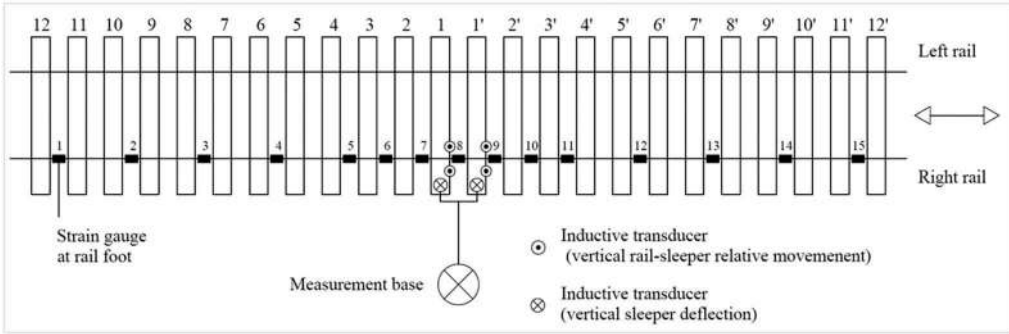


Figure 4. Identical instrumentation of both measurement sites.

Per measurement site, fifteen strain gauges have been attached each to the rail foot in the center of the sleeper compartment to measure the rail foot strain and to obtain information about the bending moment of the rail during train passage. In the center of each section, strain gauges were fitted in every sleeper compartment. Towards the edges of each section, every second compartment has been equipped with a sensor, to obtain information about the bending behavior of a longer section (see Figure 4).

Inductive transducers connected to the two centered sleepers of each sections recorded the vertical deflection of the sleepers during train passage. The inductive transducers have been attached to a measurement base mounted on a drainage shaft, to reduce the influence of soil vibration. Additionally two inductive transducers per sleeper measured the relative vertical movement between rail and sleeper (see Figure 4).

Multiple train runs, of both passenger trains and freight trains, have been recorded and analyzed. The train run of two BR218 locomotives, without additional wagons, was selected for the purpose of the present study.

2.4 Identification of rail seat stiffness

As uneven sleeper support might have an important impact on vehicle-track-subgrade interaction (Dahlberg, 2010) it is also incorporated in the proposed coupled workflow (see chapter 4) and thus had to be identified at the measurement site.

Although varying sleeper support might have various reasons, like changing subgrade properties, crushed or contaminated ballast or voided sleepers, they result in uneven rail deflection under a specific load along a track (see chapter 2.2). Measuring only rail deflections under a specific load along a track, e.g. with Benkelman measurements (Leykauf et al., 1997) does not allow the determination of sleeper-specific stiffnesses. Since the deflection of a specific point along the rail is not only influenced by the sleeper below this section of rail, but also by neighboring sleepers, due to the bending stiffness of the rail.

To identify sleeper-specific seat stiffnesses a procedure using measurement data and a finite element model has been developed, inspired by (Chen et al. 2018). In this procedure specific load positions of the measurements are replicated in the finite element model created in ANSYS, simplifying seat stiffness as linear-elastic support of the rail. The 20m long 2D finite element model represents the bending stiffness of the measured right rail as a beam and the vertical stiffness of the rail support by discrete supports, assumed as linear-elastic, in the distance of sleeper spacing. Individual load positions of the measurement have been reproduced in the model by placing single loads on the rail, primarily the first axle of the locomotive BR218 on each sleeper compartment. By iteratively adjusting the seat stiffnesses at each load position, a combination of seat stiffness values could be identified, so that the rail foot strain in the model corresponds to the strain under the equivalent rail foot position in the measurement. Subsequently, load cases with the first two axles of the BR 218 locomotives have been tested on the model (see Figure 5) and showed only minor deviations. The same procedure with different train runs each resulted in similar stiffness ratios, therefore the identified stiffness ratio is realistic and can be used for purposes of the here presented case study. Additionally, the measured sleeper deflections at the two sleepers have been used to calibrate the final rail seat stiffness values, since the initial valued did not result in the correct rail deflection as measured. This is necessary, because some input values of the seat stiffness identification process might not have been accurate. Input values with possible errors include the unknown dynamic wheel forces, the actual value of the bending stiffness of the rail or the fact, that the effective distance between two sleepers is not equal to the distance of the sleeper centers.

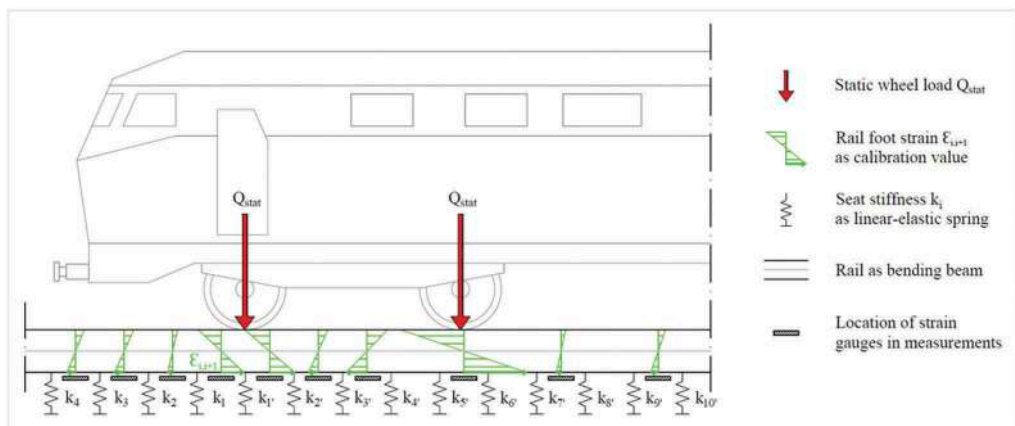


Figure 5. Model to identify rail seat stiffness variation (locomotive for illustration purposes).

Hence, the identified and for the case study selected seat stiffnesses result in sleeper deflections, which are in agreement with the measurements. Additionally, the ratio of stiffnesses per section results in rail foot strain values, which are in agreement with the ratio of stiffnesses in the measurements (see Figure 6).

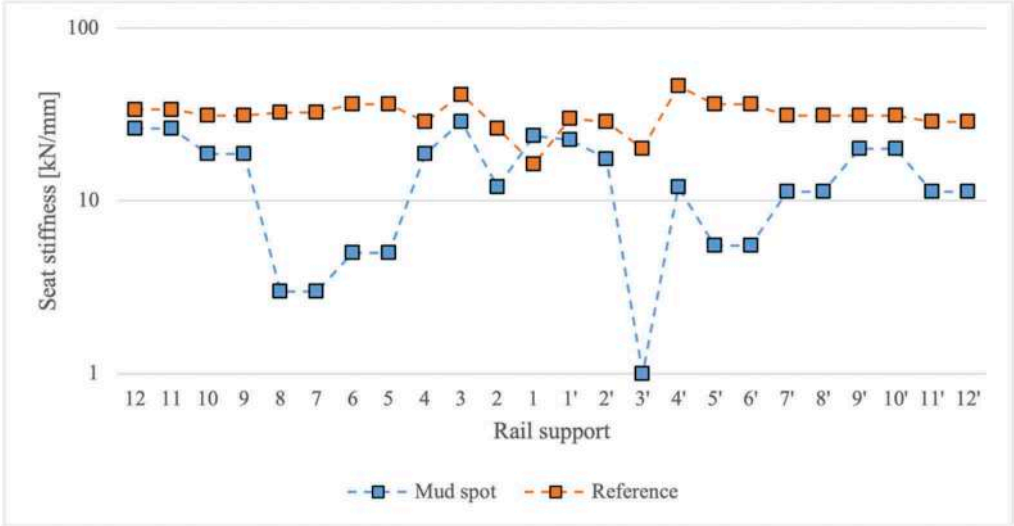


Figure 6. Identified rail seat stiffnesses at the two measurement sections.

One can observe that section A, the former mud spot, has a high variation of stiffness, and section B has a significantly lower variation. Even if the exact values might differ somewhat, and are influenced by nonlinearities, like voided sleepers, the variation from sleeper to sleeper is still large. Variations up to factor 17.5 can be observed from one sleeper to the next, approximating the rail support as linear-elastic. It is noteworthy, that the identified seat stiffnesses at the former mud spot (measurement section A), although displaying high variation, show no reduction in stiffness towards a conceivable center of the mud spot, as it could have been expected (see Figure 3).

This leads to the conclusion that varying rail seat stiffness has to be included in the analysis of the vehicle-track-subgrade interaction of this track. The resulting stiffnesses were used as a close-to-reality example in the presented case study for the coupled vehicle-track-subgrade interaction model (chapter 3.1).

3 SIMULATIONS

3.1 Coupled vehicle-track-subgrade interaction modelling

The goal of the presented methodology for coupled vehicle-track-subgrade interaction modeling is to create a tool to investigate the interaction between vehicle, track and subgrade comprehensively in an integral approach. It combines the effects of 3D vehicle-track interaction, the vertical load distribution of a flexible track with varying support stiffness and the ballast and subgrade reaction with complex soil models and soil properties. Thereby, the influence of each parameter and the resulting interdependencies can be analyzed. In the presented study, the focus lies on the influence of varying support conditions. Firstly the resulting impact on the ballast and possible deterioration of the track components and secondly the resulting vehicle reaction, and possible vehicle-side detectability of support stiffness variations.

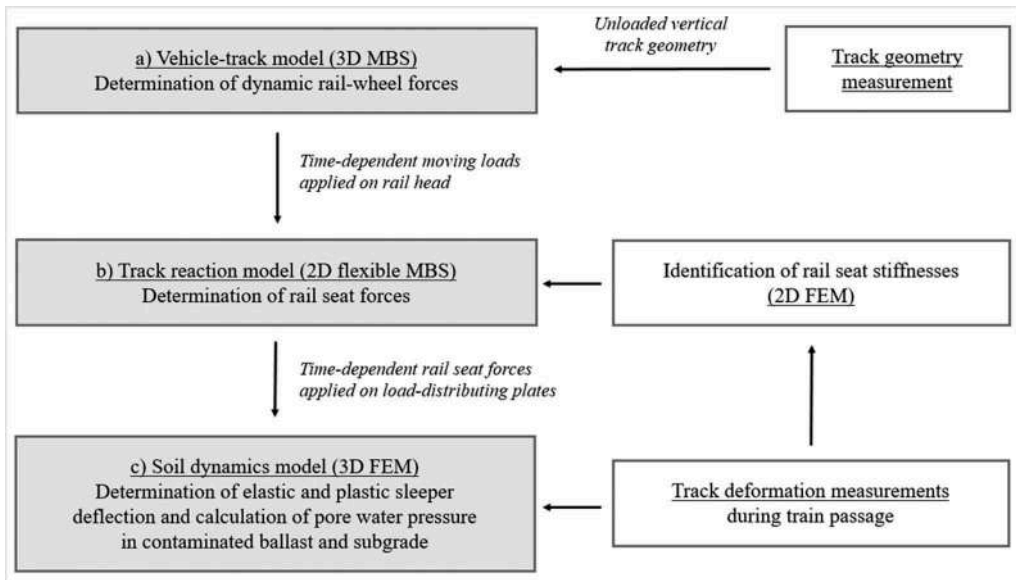


Figure 7. Workflow of the presented methodology.

Figure 7 shows the elements of the methodology and the workflow and dataflow between the steps of the procedure. Figure 8 illustrates the modelling steps.

Model step a) is a 3D multi body simulation model, created in the software SIMPACK. It comprises a bogie model, in this case representing a bogie of the BR218 locomotive, running on a 500m long three-dimensional track, with the measured unloaded track geometry as track-side excitations. It comprises a complex rail-wheel contact model, taking into account the rail-head and wheel profile. The running behavior of the bogie, or alternatively a whole railway vehicle, can be investigated in this model, but is not the focus of this study. The main purpose of *model step a)* is the calculation of rail-wheel-forces, due to the interaction between vehicle and track, with the measured geometry. A vehicle velocity of 30m/s was chosen for the simulation corresponding to the velocity of the locomotives during the measurement run (ca. 32m/s).

Exemplarily Figure 9 shows the calculated rail-wheel-forces for the first wheelset of the locomotive BR 218.

Model step b) is a flexible 2D multi body simulation model created in the software SIMPACK. It represents the bending and load distributing behavior of one rail on discrete support points. A flexible Timoshenko beam represents the stiffness of the rail. The support points are modeled as linear-elastic springs. The stiffness values of the rail seat stiffnesses determined in chapter 2.4 were assigned to the springs in the center of the 86 m long model. Moving time-dependent loads are applied on the rail to represent the train run of the two BR 218 locomotives. Separately the rail-wheel forces of the right and the left wheels of *model step a)* are used, with the same progress speed (30m/s) as in that model. *Model step b)* is able to calculate the deflection and the rail seat forces of the rail under the moving loads. The latter represent the loads transmitted through half sleepers in the ballast. Consequently the partial sleeper mass is added to the rail seat forces.

Figure 10 shows an exemplary section of rail seat forces of seven consecutive sleepers subjected to the passage of one bogie of the locomotive BR 218. In this example sleeper 3, sleeper 4 and sleeper 9 are surrounding less supported sleepers 5 to 8. Thus a large part of the load is transferred through the well supported sleepers, represented by high (positive) compression forces. The linear-elastic assumption of the support points causes an overestimation of the (negative) tensional forces. The tensional rail seat forces do not affect the subsequent simulations, as tension forces are not applied on the 3D continuum model of *model step c)*.

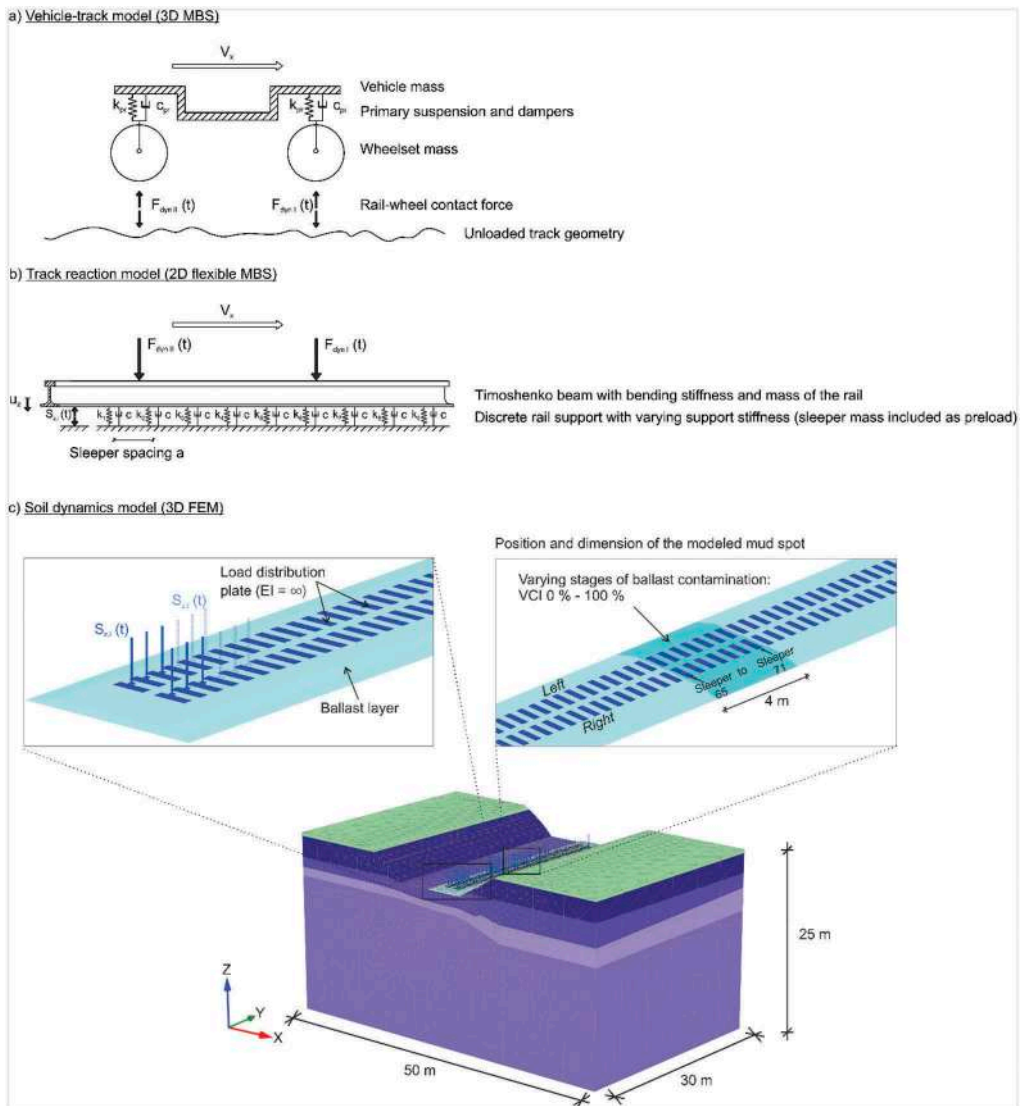


Figure 8. Illustrations of the simulation steps of the workflow.

Model step c) is a 3D finite element model, created in the software PLAXIS. The dynamic 3D continuum model represents the ballast body and the surrounding soil and embankment. A hypoplastic soil model is used to calculate plausible elastic and plastic deformations as well as pore water pressure throughout the continuum. The properties of the model have been calibrated by provided geotechnical exploration data from the measurement section. Stiff load plates, representing each a half sleeper sole minus a support-free center section, apply the time-dependent rail seat forces calculated in *model step b)*. The resulting elastic deflections under the sleeper sole have been validated by the sleeper deflection measurements (see chapter 2.3).

As an example for the generated output, Figure 11 shows plastic deformations under the sleepers for various ballast contamination levels, representing the accumulation of fine particles in the ballast body after track operation. The used Void Contaminant Index (VCI) was proposed in (Tennakoon, 2012) and corresponds to different levels of ballast contamination, which can be expected during mud spot development.

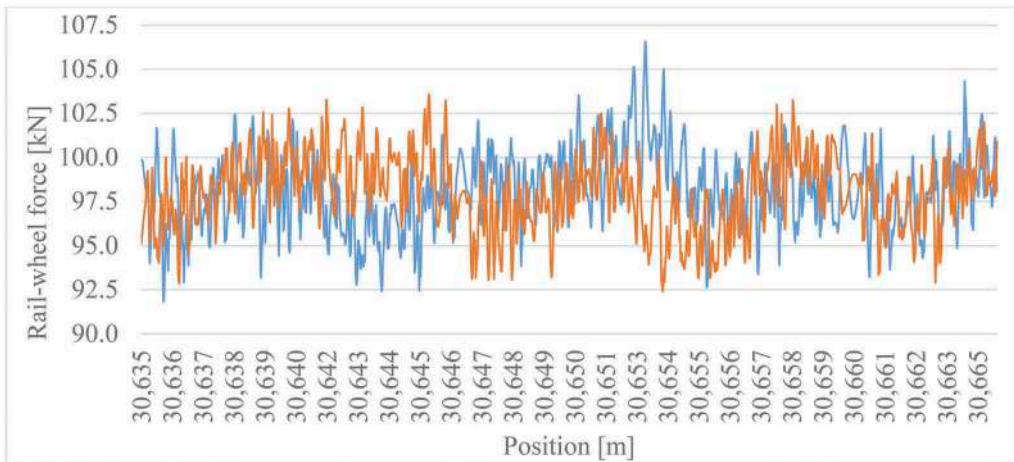


Figure 9. Sample of rail-wheel-forces calculated by *model step a*) – front left wheel (orange line); front right wheel (blue line).

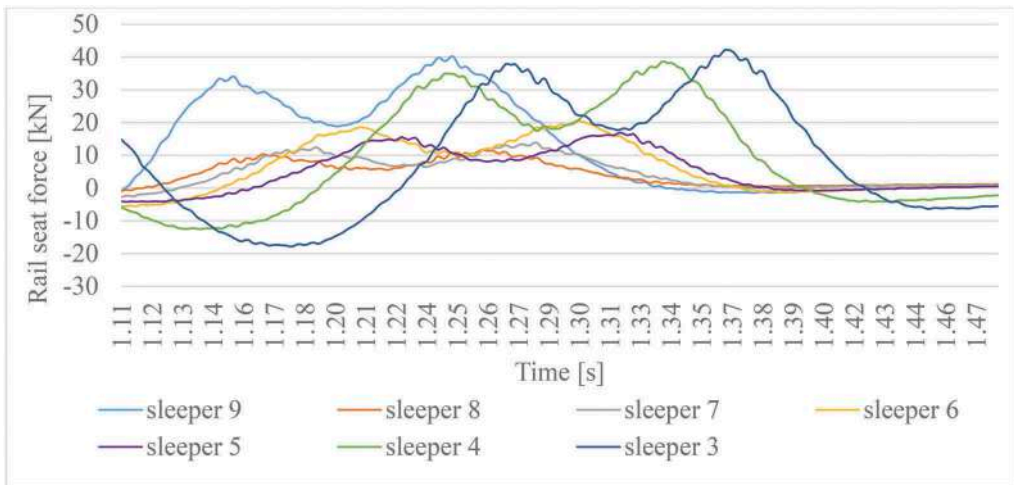


Figure 10. Sample of sleeper support forces calculated by *model step b*).

3.2 Results and discussion

Figure 12 contains results of *model step b*) for both sections of the case study. It shows the vertical rail deflection and the corresponding rail seat forces, in case the first wheel of the locomotive BR 218 is at the respective sleeper position.

At section A, representing the former mud spot, a large variation in rail seat force can be observed. From one sleeper to the next one variations up to factor eight occur. This is less than the determined variation of rail seat stiffness at this track section (see chapter 2.4) but still significant. The variation leads to the fact that individual sleepers transmit significantly more load to the ballast, than others do. Figure 10 also illustrates the highly changed load distribution of the track. It can be expected that ballast deterioration increases locally under the sleepers with high load transmission, during thousands of axle transitions in the course of train operations on the investigated track. Possibly, there is also a locally increased impact on the soil.

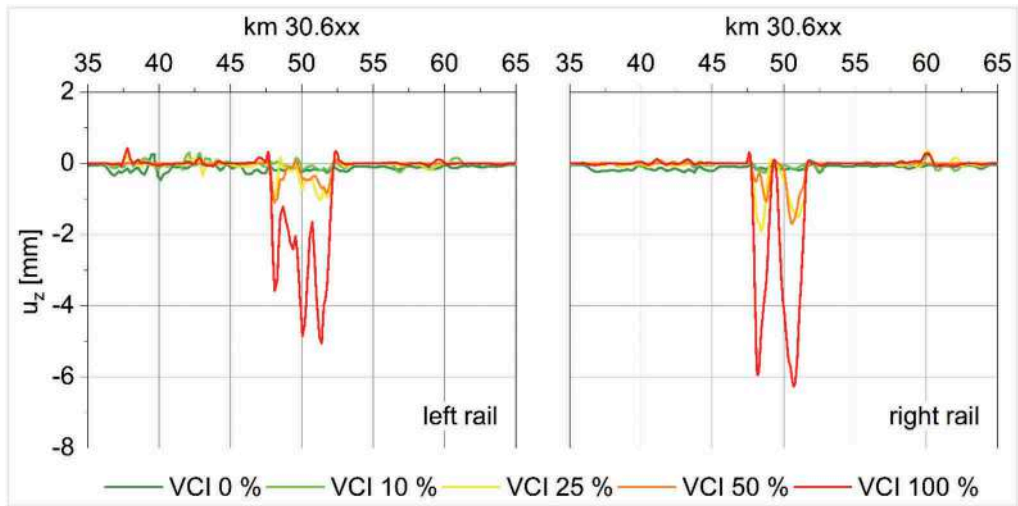


Figure 11. Sample of plastic deformations u_z under the sleepers calculated by *model step c*).

At section B, representing the reference site, the maximum rail seat forces are much more homogeneous and only small variations are observed.

Figure 13 illustrates that the variation in rail seat force can be attributed primarily to the rail seat stiffness variation. Although it is not possible to draw a clear causal line from the stiffness variation at the former mud spot to mud spot development in general, it is noticeable, that the identified seat stiffness varies much more at the mud spot section, than at the reference section (see also Figure 12). In addition, the reference section did not show any signs of major changes in track geometry in the past, unlike the former mud spot (see Figure 1). Moreover, two years after the maintenance the accumulation of fine particles in the ballast indicates that the mud spot may be reappearing (see Figure 2).

In conclusion, a correlation between the reappearing mud spot and the observed rail seat stiffness variation is present. Together with the presented results that sleeper support variation leads to a changed load distribution of the track and to individual sleepers with high load transmissions, the significance of rail seat stiffness variation to the deterioration of the track becomes evident.

Further investigation needs to be done, to determine the causal relationships during mud spot development and other track deterioration phenomena. The present study highlights that seat stiffness variation should be considered.

3.1.1 Identification of seat stiffness variation in track inspection

As demonstrated, sleeper support condition variation leads to changed load distribution, higher local deterioration and subsequently to possible track defects. The necessity for a well-maintained and consequently homogeneous track structure is obvious. However, as most tracks are subject of continuous train operations and maintenance resources are limited, the need arises to identify sections with varying support stiffness during track inspection, to facilitate timely and effective measures.

Track inspection uses mainly loaded geometry measurements (e.g. RAILab). The vertical loaded geometry signals can contain some information about the stiffness along the track, as illustrated in Figure 3. With suitable signal processing, this information can possibly be extracted and used.

On the other hand Figure 12 shows, that seat stiffness variation between individual sleepers do not always manifest in the rail deflections under the wheel load (e.g. sleeper number 4'), especially evaluated only at the sleeper positions. Hereby, the evaluation of rail deflections under a wheel load corresponds to the stiffness component of the loaded track geometry. Even if it is evaluated continuously (see Figure 13) individual rail seat stiffnesses hardly

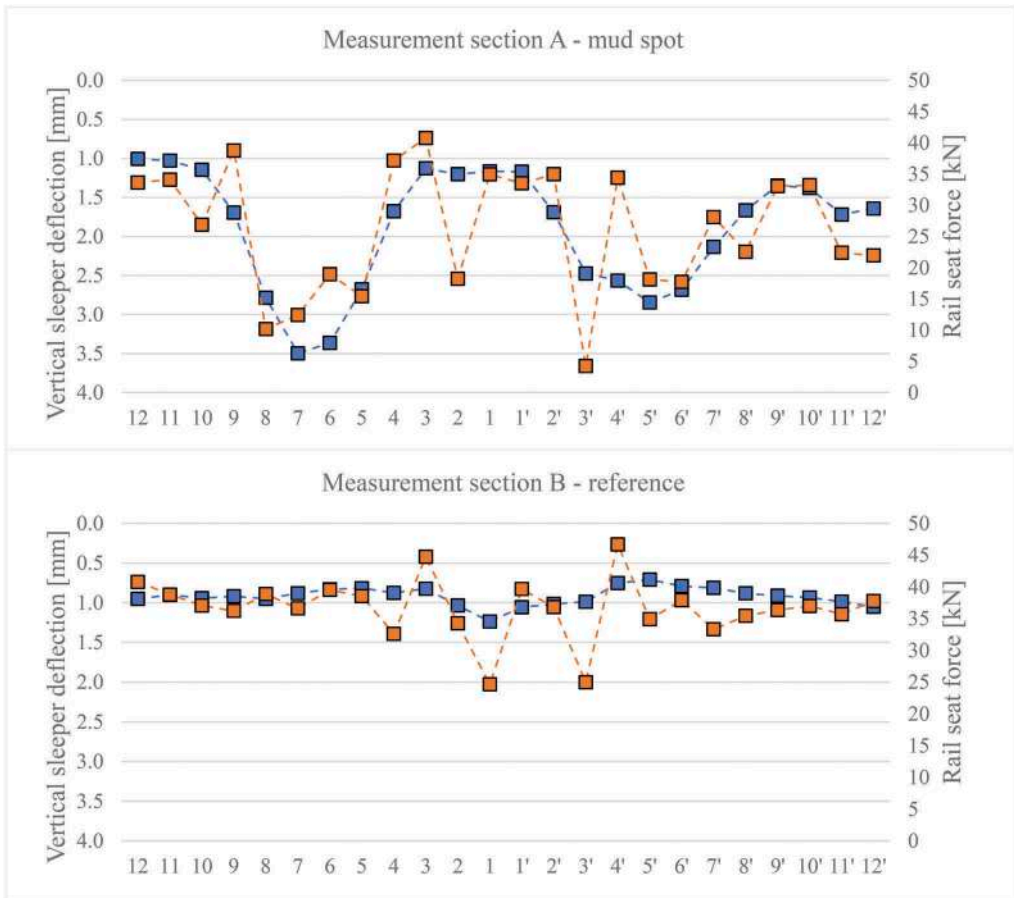


Figure 12. Rail deflection in case the first wheel of the locomotive is over a specific sleeper (blue markers) and corresponding rail seat forces (orange markers).

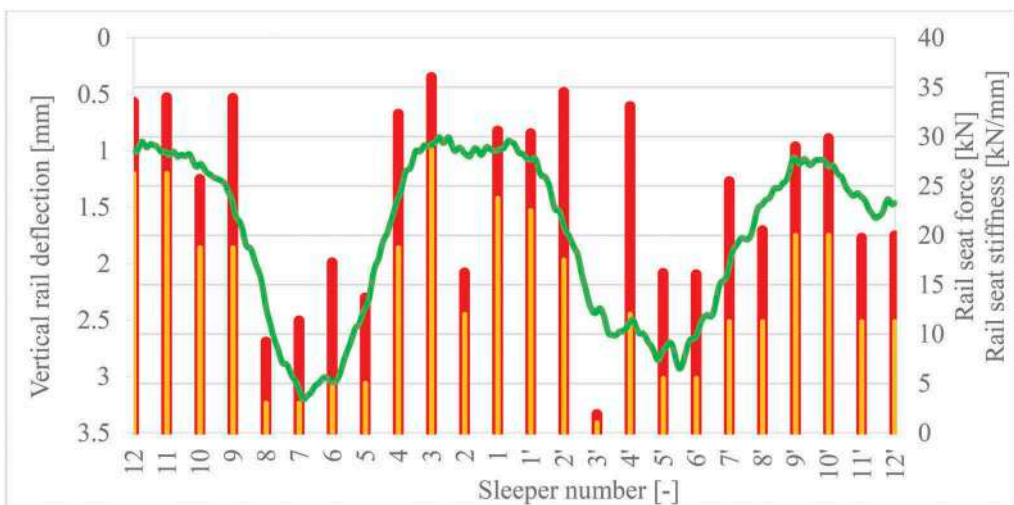


Figure 13. Results along measurement site A "mud spot": Rail deflection under the first wheel of the locomotive (green line); rail seat force of specific sleeper in case the first wheel of the locomotive is over that rail seat (red bars); rail seat stiffness for corresponding sleeper (orange bars).

manifest in the loaded track geometry. The underlying reason is that the load distributing capability of the track grid always influences the stiffness evaluation performed by using rail deflection measurements. Consequently, other systems that are based on rail deflection measurement, like the Benkelman beam or stiffness measurement vehicles, do not allow a sleeper specific evaluation of the seat stiffness. Therefore, possible problematic sleepers (e.g. sleeper 4' in this case study) might not be identified.

Further investigations on the correlation between stiffness variation at the individual sleeper level and vehicle reaction (e.g. axle box accelerations) are promising to enable signal evaluation methods that can be applied to track inspection.

4 CONCLUSIONS & OUTLOOK

The developed vehicle-track-subgrade coupling methodology allows the investigation of the interaction between vehicle, track and subgrade, taking into account track irregularities, vehicle dynamics, varying sleeper support and complex ballast and soil reactions, including ballast contamination.

Additionally, an iterative approach to identify individual rail seat stiffness at a measurement site was presented here. With the use of a finite element model and rail foot strain and sleeper and rail deflection measurements, rail seat stiffnesses was identified.

The presented study, focused on the effects of rail seat stiffness variation, showed that a stiffness variation, as identified in the measurement section, can lead to a changed load distribution and that individual sleepers transmitting significantly more load to the ballast than others. Ultimately, this leads to locally increased ballast deterioration and a locally increased impact on the subsoil, which might facilitate mud spot development. On the other hand, the cause of the increased sleeper load, the rail seat stiffness variation, can hardly be identified on an individual sleeper level by using loaded geometry data.

Open questions, like the causal relationships during mud spot development and other deterioration phenomena, still have to be investigated. The developed vehicle-track-subgrade coupling methodology presented here can provide a basis for future studies. Additionally, an integral coupling approach allows the detailed analysis of the vehicle reaction. Further investigations of the correlation between individual sleeper support variations and vehicle reactions may allow providing characteristic patterns for track inspection.

ACKNOWLEDGEMENTS

The authors would like to thank the German Research Foundation (DFG). The research was supported under the grants MO 2246/3-1 („Simulation punktueller Instabilitäten infolge plastischer Verformungen im Unterbau/Untergrund unter dynamischer Belastung durch Eisenbahnverkehr (EPIB 1.2)“) and FR 2910/2-1 („Detektieren von punktuellen Instabilitäten anhand typischer Rad-Schiene-Kräfte (EPIB 2)“).

REFERENCES

- Chen, K., Lechner, B. and Freudenstein, S., 2018. *Investigation of track stiffness quality based on rail foot bending strain utilizing structure optimization methods*. Proceedings of 7th Transport Research Arena TRA 2018, April 16-19, 2018, Vienna, Austria.
- Dahlberg, T., 2010. *Railway Track Stiffness Variations – Consequences and Countermeasures*. International Journal of Civil Engineering 8.
- DB Netz AG, 2016. *Richtlinie 821 “Oberbau inspizieren”*. Munich, Germany.
- Hudson, A., Watson, G., Le Pen, L. and Powrie, W., 2016. *Remediation of Mud Pumping on a Ballasted Railway Track*. Procedia Engineering, 143, 1043–1050.

- Leykauf, G. and Mattner, L., 1997. *Untersuchung von Feste Fahrbahn-Konstruktionen durch eine anerkannte Prüfstelle*. Eisenbahntechnische Rundschau ETR, Edition Feste Fahrbahn (Sonderveröffentlichung), 48–55, Hestra-Verlag, Darmstadt.
- Rapp, S., 2017. *Modell zur Identifizierung von punktuellen Instabilitäten am Bahnkörper in konventioneller Schotterbauweise*. Dissertation, Institute of Railway and Transportation Engineering, Faculty Civil and Environmental Engineering, University of Stuttgart, Stuttgart, Germany.
- Sandner, C., Ripke, B. and Wunderlich, T., 2020. *Monitoring and evaluation of railway infrastructure*. Ingenieurvermessung 20. Beiträge zum 19. Internationalen Ingenieurvermessungskurs München, 325–338, Herbert Wichmann Verlag, Berlin, Germany.
- Tennakoon, N., 2012. *Geotechnical study of engineering behaviour of fouled ballast*. Doctor of Philosophy thesis, Department of Civil, Mining and Environmental Engineering, University of Wollongong.

Sleeper contact modelling in asphalt overlayment trackbeds

P. Jørgensen, R.N.H. Perslev & E. Levenberg*

Department of Civil Engineering, Section for Geotechnics and Geology, The Technical University of Denmark, Kongens Lyngby, Denmark

ABSTRACT: This study targeted the mechanics of asphalt overlayment trackbeds – a ballastless track type that mandates special wide-base sleepers equipped with a geotextile at the bottom. The objective was to develop an analytical model for quantifying how a geotextile and its compressibility properties influence the contact stress distribution at the sleeper-geotextile-asphalt interface. A nonlinear-hardening Winkler spring-bed was utilised to represent a geotextile, a rigid beam was utilised to represent a sleeper, and the pavement system was treated as an elastic half-space. Based on a parametric investigation of the new model it is concluded that the insertion of a geotextile at the sleeper-asphalt interface considerably affects the vertical stress distribution. The presence of a geotextile is shown to produce a more uniform stress distribution and eliminate excessively high contact stresses that would have developed near the sleeper perimeter. It is also shown that geotextile compression adds extra vertical flexibility to the track system with an order of magnitude similar to that of common rail pads. The developed model can handle realistic geotextile compressibility properties as well as any sleeper geometry; its analytical nature provides relative ease of replication for subsequent design and analysis.

Keywords: Ballastless asphalt tracks, Geotextile, Nonlinear Winkler spring-bed, Analytical modelling

1 INTRODUCTION

Conventional ballasted tracks are the most common trackbed type worldwide (Esveld, 2001). With the demand for faster, heavier, and more train passes, this standard track solution mandates increased frequency of repair activities, e.g., track realignment, ballast replacement, and sleeper replacement (Köllo, Puskás, & Köllö, 2015). The elevated maintenance effort led to the development of ballastless tracks based on Portland cement concrete – commonly known as slab track – offering improved track stability and reduced maintenance needs (Freudenstein, Geisler, Mölter, & Missler, 2018). Slab track is an established and accepted trackbed alternative in Germany, China, Japan, and South Korea, accommodating (especially) high-speed trains.

Another ballastless track alternative is asphalt overlayment. In this trackbed type, the sleepers with rails on top are supported over an asphalt pavement system, commonly composed of (top to bottom): several lifts of asphalt concrete, unbound aggregate base and subbase, and subgrade soil (or rock). In the absence of crib and shoulder ballast, and to safeguard track stability, asphalt overlayment involves special sleepers that are twice as wide and therefore twice as heavy compared to standard sleepers (Bose,

*Corresponding author
DOI: 10.1201/9781003222910-22

Levenberg, & Zania, 2018). Also, these special wide sleepers include a geotextile attached to their bottom; the geotextile is added to increase the contact area with the asphalt concrete surface, compensating for geometric unevenness at their interface. Potential advantages of this ballastless trackbed type include lower initial construction costs compared to a slab track solution, reduced noise and ground vibrations compared to both slab track and ballasted track, and reduced maintenance effort compared to a conventional track. Another advantage of using asphalt is environmental friendliness, given that the material is fully recyclable (NAPA, 2020).

Despite the above-mentioned merits, the asphalt overlayment idea is not widely accepted, with only a few full-scale applications – mostly inside tunnels within the German railway network (RailOne, 2011). Also, the mechanics of such a track solution is not deeply researched compared to ballasted tracks and slab tracks. Noteworthy studies in this context include the work of Lee et al. (2016) which experimentally evaluated an asphalt overlayment track with three different asphalt concrete thicknesses. The stated aim of the study was to identify an optimal structural cross-section; this was sought based on static loads applied to a full-scale mockup pavement, and subsequent observations of stress and strain responses within the structure. The study concluded that a 30 cm thick asphalt layer is optimal. Another relevant investigation was performed by Bose et al. (2018). The purpose of this work was to analyse track responses due to train braking. The analysis was purely analytic and focused on estimating the friction demand at a sleeper base that is required to resist longitudinal slippage during an emergency train braking event. For an asphalt overlayment solution, where the sliding resistance of the sleepers is solely supplied by a frictional mechanism at the base, it was shown that special heavy sleepers are needed to ensure lateral stability. In a recent investigation, Bose et al. (2018) experimentally analysed asphalt overlayment trackbeds based on full-scale instrumented sections loaded by a passing train. A numerical investigation accompanied the study focusing on horizontal strains and vertical stresses at the bottom of the asphalt concrete. However, the modelling did not consider a geotextile at the bottom of the sleepers. Lastly, Bose et al. (2021) reported on the development of a finite element model for asphalt overlayment tracks considering wide-base sleepers equipped with a geotextile at the bottom. The asphalt layer was modelled as linear viscoelastic, and the underlying unbound granular layer was treated as stress-dependent nonlinear-elastic; all other track layers and elements were treated as linear elastic. The model was calibrated and validated against measurements from a full-scale instrumented mockup excited by vertical loads: it was able to reproduce and predict a wide range of measured response traces due to different loading situations. Specifically, it was shown – both numerically and experimentally – that peak vertical deformations in the track structure were roughly composed of: 77% in the rail pad, 15% in the geotextile, and 6% in the unbound granular layer. The model of Bose et al. was elaborate and computationally heavy, requiring a large number of input parameters to execute.

The current study is motivated by the desire to further promote the asphalt overlayment solution; this is sought by contributing to an improved understanding of the system mechanics. Specifically, this paper aims to investigate the contact interaction between a single sleeper exposed to vertical loads (coming from the rails) and a supporting asphalt pavement system – when a geotextile is introduced at the interface. The objective is to develop a mechanistic model for quantifying how a geotextile and its compressibility properties influence the contact stress distribution at the sleeper-geotextile-asphalt interface. This development will be based on closed-form analytic formulations, and the paper aims to offer a step-by-step reproducible approach to all underlying equations. Unlike purely numerical methods, the reliance on analytical solutions is chosen to promote engineering utilisation and broaden the spectrum of applicability. Analytical solutions enable model parameters to accept a wide range of values without convergence concerns. The work also includes a narrow-scope parametric investigation, showcasing selected results and demonstrating some of the model capabilities.

2 CONTACT MODELLING

The problem considered hereafter deals with a single loaded sleeper, having a geotextile at the bottom, and resting on the surface of an asphalt pavement system. A plan view of this arrangement is shown in Figure 1a, and a cross-sectional view is shown in Figure 1b. As can be seen, the sleeper is a rectangular cuboid hosting a pair of rail pads. Train axle loads applied to the rails are transferred to the sleeper via these rail pads. The pavement system has three layers: asphalt concrete, aggregate base, and subgrade soil (or rock) extending to a large depth. The geotextile is a thin layer with an area that identically covers the sleeper's bottom.

The corresponding model is graphically presented in Figure 1c (plan view) and in Figure 1d (cross-sectional view). The sleeper is modelled as a weightless Euler-Bernoulli beam having infinite bending rigidity. Two identical point loads, each with intensity P , are applied at the position of the rail pads to represent the effects of a train axle. The pavement system is modelled as a half-space that is linear elastic, isotropic, homogeneous, and weightless. The geotextile is treated as a weightless nonlinear-hardening Winkler spring-bed residing in-between the beam and the half-space.

The aim of the modelling is to resolve the vertical stress distribution in the nonlinear Winkler spring-bed. This is sought through an iterative calculation-correction procedure wherein the stress distribution across the springs is first assumed uniform (iteration 0), and then applied to deform the half-space. This stress distribution is also, in a parallel calculation, applied to compress the springs from their initial length into a shorter (compressed) length. Next, the surface deflection of the half-space is added to the shortening of the springs, and the result of this addition is compared against a flat surface corresponding to the bottom of a rigid beam. Finally, the initial stress distribution assumption is refined such that the discrepancy with a perfectly flat surface is minimised. The refinement procedure is iterated until achieving satisfactory convergence.

To facilitate the calculations, the Winkler spring-bed, which covers the entire contact zone, is split into a large number of identical square areas numbered $n = 1 \dots N$. The deflection (or vertical surface displacement) of the half-space during iteration i ($i = 0, 1, 2, \dots$) at the centre of any square area n is $\delta_n^{(i)}$; it is based on superposition:

$$\delta_n^{(i)} = \delta_{1,n}^{(i)} + \sum_{m=1}^N \delta_{2,m}^{(i)} \quad (m \neq n) \quad (1)$$

where $\delta_{1,n}^{(i)}$ and $\delta_{2,n}^{(i)}$ are based on Boussinesq's solution for a vertical force applied to the surface of a linear elastic half-space:

$$\delta_{1,n}^{(i)} = \frac{4q_n^{(i)} a(1 - \nu^2) \ln(1 + \sqrt{2})}{E\pi} \quad (2)$$

$$\delta_{2,n}^{(i)} = \frac{q_m^{(i)} a^2(1 - \nu^2)}{E\pi r_{n,m}} \quad (m \neq n) \quad (3)$$

in which $\delta_{1,n}^{(i)}$ describes the half-space deflection at the centre of the n^{th} square (during iteration i) when it is loaded by a stress intensity $q_n^{(i)}$ while all other squares are not loaded, $\delta_{2,n}^{(i)}$ describes the half-space deflection (during iteration i) at the centre of the n^{th} square due to loading with stress intensity $q_m^{(i)}$ applied over the m^{th} square. Given the assumption of loading via a rigid beam, both $q_n^{(i)}$ and $\delta_n^{(i)}$ are always non-negative. The parameter $r_{n,m}$ denotes the distance between square n and square m whenever $m \neq n$. Both $q_n^{(i)}$ and $q_m^{(i)}$ differ from location to location depending on the stress distribution in the spring bed. The parameter a denotes the side-length of a square area, ν is Poisson's ratio of the half-space, and E is Young's modulus of the half-space. By repeating the above calculations for the entire contact area (i.e., for $n = 1 \dots N$), the half-space deflection below the Winkler spring-bed is determined.

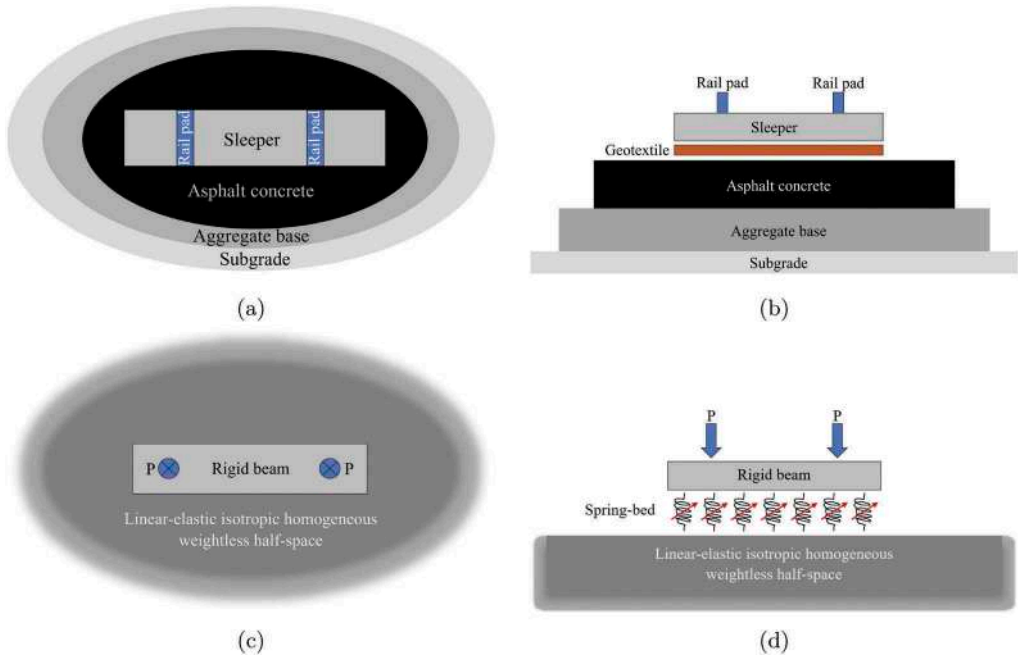


Figure 1. Sleeper-geotextile-pavement contact problem: (a) plan view of a sleeper resting on an asphalt pavement system, (b) cross-sectional view of a sleeper resting on an asphalt pavement system, (c) plan view of model, (d) cross-sectional view of model.

The next calculation step (during iteration i) targets the shortening of the spring-bed covering the n^{th} square. This shortening is also a non-negative entity; it is denoted by $\Delta_n^{(i)}$, and calculated based on Hooke's Law:

$$\Delta_n^{(i)} = \frac{q_n^{(i)}}{k_n^{(i)}} \quad (4)$$

wherein $k_n^{(i)}$ expresses the nonlinear stiffness of the Winkler spring-bed associated with the n^{th} square:

$$k_n^{(i)} = k_0 \left(1 + \frac{c \Delta_n^{(i)}}{t - \Delta_n^{(i)}} \right) \quad (t > \Delta_n^{(i)}) \quad (5)$$

where k_0 is the initial spring-bed stiffness (units of force per volume), t denotes the initial length of the spring-bed – analogous to the thickness of the geotextile when no train loads are applied to the rails, and c is a non-negative unitless parameter that governs the nonlinear-hardening behaviour of the spring-bed. As can be seen, if $c = 0$ then the spring-bed is linear, characterised by a constant stiffness k_0 . For $c > 0$ this expression produces an ever increasing spring-bed stiffness as the shortening approaches the initial length t . In actuality, both the sleeper bottom and the asphalt surface are not perfectly flat. This means that the geotextile thickness (both initial and under train loading) will vary from location to location – bridging the irregularities in the contact area. Hence, all above-listed spring-bed properties represent average effective properties.

A graphical representation of Equation (5) is offered by Figure 2. The chart depicts the dependence of $k_n^{(i)}$ on the shorting $\Delta_n^{(i)}$ for four different values of k_0 . As can be seen, for very

small shortening levels the spring-bed stiffness increases approximately linearly with respect to the shortening level. As the shortening gets closer to the initial length t , the spring-bed stiffness increases sharply and rapidly towards infinity. This model is deemed realistic, as it is practically impossible to compress a geotextile to zero thickness.

The iterative solution procedure of the contact problem advances with the aim of refining the stress intensity operating over each of the square areas, i.e., determining $q_n^{(i+1)}$. This is pursued by requiring that the upper-end of the Winkler spring-bed makes a perfectly flat surface – corresponding to the bottom of a rigid sleeper. In this context, the spring-bed upper-end surface elevation above the n^{th} square area is obtained by summing the half-space deflection $\delta_n^{(i)}$ with the spring-bed shortening $\Delta_n^{(i)}$. A perfectly flat upper surface means that all individual summations (i.e., for any n) yield the exact same result. In other words, that each individual summation is identical to the average over all summations. Based on this observation, it is possible to iteratively refine the stress intensity at the n^{th} square as follows:

$$q_n^{(i+1)} = q_n^{(i)} + \Delta q_n^{(i)} \quad (6)$$

where

$$\Delta q_n^{(i)} = \left(\underbrace{\left(\frac{1}{N} \sum_{n=1}^N (\Delta_n^{(i)} + \delta_n^{(i)}) \right)}_A - \underbrace{\beta (\Delta_n^{(i)} + \delta_n^{(i)})}_B \right) k_n^{(i)} \quad (7)$$

in which the A term denotes the average over all summations, the B term is the individual summation, and their difference at the n^{th} square is multiplied by the spring-bed stiffness – corresponding to the n^{th} square – to provide the stress intensity refinement $\Delta q_n^{(i)}$. As all the springs approach a flat surface at the upper end, the difference between the A term and the B term decreases to zero. The outcome is that $\Delta q_n^{(i)}$ decreases to zero leading to $q_n^{(i)}$ approaching $q_n^{(i+1)}$. Iterations are stopped once convergence is attained, e.g., when $|\Delta q_n^{(i)}|$ is smaller than some predefined stress value (for all n 's); another option is to stop the iterations when the absolute difference between the A and B terms is smaller than some predefined value (across all n 's). The β parameter is a positive unitless multiplier introduced to facilitate the iteration procedure, either accelerate it ($\beta > 1$) or decelerate it ($\beta < 1$).

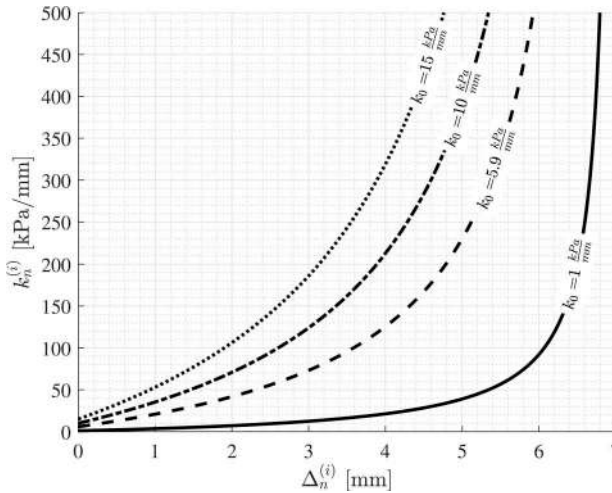


Figure 2. Graphical representation of the nonlinear-hardening Winkler spring-bed stiffness represented by Equation (5) with $t = 7$ mm and $c = 15$ for different k_0 values.

3 MODEL DEMONSTRATION

The aim here is to apply and demonstrate the proposed sleeper-geotextile-asphalt contact model. In this context, a narrow-scope parametric investigation is carried out involving a wide range of half-space moduli combined with a range of spring-bed properties covering several k_0 values with $c = 15$ and $t = 7$ mm. The later two parameters were chosen based on a laboratory characterisation of the geotextile currently utilised in the GETRAC A3 sleepers (RailOne, 2011).

The case considered hereafter deals with a wide sleeper that is 2.5 m long and 0.6 m wide; the overall loading intensity over this sleeper is 71 kN, i.e., $P=35.5$ kN (see Figure 1d). This intensity was chosen based on a separate analysis which included an infinitely long beam representing a UIC60 rail supported on a linear spring-bed or track modulus, and loaded by a point force of 100 kN representing one side of a single-axle carrying a total of 200 kN. With a track modulus of 50 MPa combined with a centre-to-centre sleeper spacing of 0.6 m (Bose & Levenberg, 2020), the maximal sleeper load is 35.5% of the axle load (hence 71 kN). Assumption of a track modulus, even though it considers a linear rail support, does not invalidate the analysis herein; it is merely a structured manner to arrive at a loading intensity applied to a single sleeper.

Figure 3 presents the contact conditions at the bottom of the sleeper for $E=200$ MPa and $k_0=5.9$ kPa/mm (and also $c = 15$ and $t = 7$ mm). The figure was prepared with $a=10$ mm (i.e., $N=15000$), $\beta = 0.5$, and 30 calculation iterations. The resulting maximal $|\Delta q_n^{(29)}|$ in Equation (6) was 0.3 kPa and the peak absolute difference between the A and B terms in Equation (7) was 9.7 microns. Shown in Figure 3a is a heat map of the stress distribution in the spring bed, i.e., $q_n^{(30)}$ in Equation (6). Contour lines of points experiencing identical stress level are included to facilitate the presentation. As can be seen, the overall distribution pattern is such that higher stresses concentrate around the sleeper edges. The contact stresses span a relatively narrow range, from 46 kPa to about 52 kPa with a mean stress value of 47.3 kPa and a standard deviation of 1.5 kPa. Shown in Figure 3b is a heat map of the spring-bed shortening (or geotextile compression), i.e., $\Delta_n^{(30)}$ in Equation (4). Contour lines are included – indicating points experiencing identical shortening. Overall, the shortening values span a relatively narrow range, from 1.50 mm to about 1.60 mm with a mean value of 1.55 mm and a standard deviation of 0.02 mm. As can be seen, the overall distribution pattern is such that slightly higher shortening concentrates near the sleeper edges.

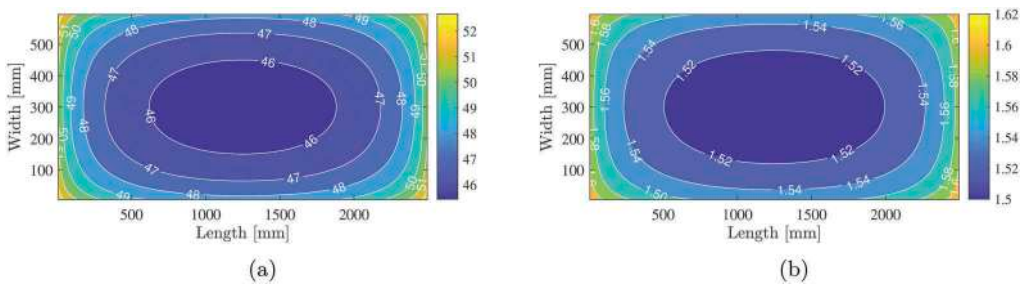


Figure 3. Contact conditions at the bottom of a wide sleeper with $E = 200$ MPa and $k_0=5.9$ kPa/mm: (a) vertical stress [kPa], and (b) geotextile compression [mm].

Investigated next is the standard deviation of the contact stress distribution, i.e., the standard deviation of $q_n^{(30)}$ for $n = 1 \dots N$. This entity is hereafter denoted by σ ; it encapsulates in a single parameter the influence of the geotextile on the prevailing contact conditions. Without introducing a geotextile at the sleeper-pavement interface, the vertical stress distribution is expected to be highly non-uniform – as model stresses would tend to infinity at the sleeper edges. On the other hand, insertion of a geotextile at the sleeper-pavement interface eliminates

the infinite stresses at the edges and produces a more even stress distribution – associated with a smaller σ .

Figure 4a offers a semi-log plot of σ against E for three levels of the initial spring-bed stiffness k_0 . The half-space modulus (depicted on the abscissa) spans the range 100 MPa to 40000 MPa. This range was chosen to encapsulate the two extreme moduli values that asphalt concrete may experience. The low-end is associated with the material’s equilibrium modulus approached at very high temperatures while the high-end value is associated with the material’s instantaneous modulus approached at very low temperatures Levenberg, 2020). As can be seen in the chart, there is a monotonous decrease in σ as the half-space modulus increases, indicating an improvement in contact stress uniformity and therefore an increase in the geotextile’s effectiveness. The chart also shows that for a given half-space modulus, smaller k_0 values improve the contact stress uniformity.

Figure 4b offers a semi-log plot of σ against k_0 for three levels of the half-space modulus: 200 MPa, 2000 MPa, and 20000 MPa. The initial spring-bed coefficient (depicted on the abscissa) spans the range 0.01 kPa/mm to 20 kPa/mm. As can be seen in the chart, as k_0 increases in value for a given E , σ first decreases slightly, and then increases monotonically towards some horizontal asymptote. The chart also shows that for a given k_0 value, a larger half-space modulus improves the contact stress uniformity (drop in σ); this effect is very pronounced, exhibiting high dependence upon the modulus level.

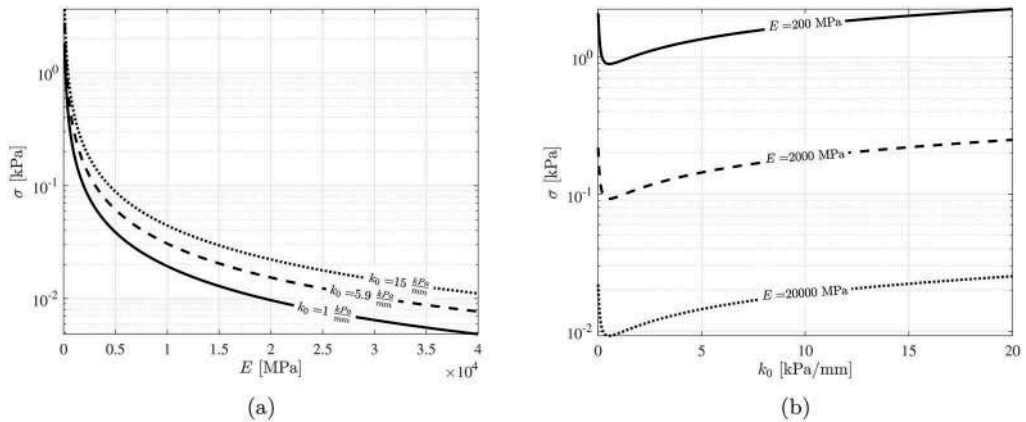


Figure 4. Dependence of σ , the standard deviation of the contact stress distribution, upon: (a) the half-space modulus for different k_0 values, and (b) the initial spring-bed stiffness for different E values.

4 CONCLUSION

This study targeted the mechanics of asphalt overlayment trackbeds, focusing on the sleeper-geotextile-asphalt contact interaction under quasi-static train loading conditions. An iterative analytical model was proposed (see Section 2) to estimate the geotextile compression (see Equation (4)) and the associated vertical stress distribution (see Equation (6)). The work also included a narrow-scope parametric investigation in which the model was applied to generate some results with realistic input parameters (see Section 3). A nonlinear-hardening Winkler spring-bed was utilised to represent the geotextile (see Equation (5)); treatment of the sleeper and pavement system involved more radical modelling simplifications: sleeper as a rigid beam and pavement system as an elastic half-space (see Figure 1).

It is concluded that the insertion of a geotextile at the sleeper-asphalt interface considerably affects the vertical stress distribution. The presence of a geotextile produces a more uniform stress distribution, and eliminates excessively high contact stresses that would have developed

near the sleeper perimeter. The significance of this is that the presence of a geotextile limits sleeper spalling damage along the edges, and also limits mechanical indentation of the asphalt surface.

Given that the geotextile is compressed (i.e., thickness is shortened) under train loadings, extra vertical flexibility of the rail support is introduced into the track system. The shortening is expected to be of the same order of magnitude as the compression of common rail pads. This result coincides with the behaviour exhibited in full-scale tests, as reported by Bose et al. (2021). Nonetheless, the proposed model mandates a more direct and targeted experimental validation. One approach to achieve this is measuring the geotextile compression at the sleeper perimeter – as was done Bose et al. (2020). Another model validation approach is placing a pressure sensitive film (Liggins et al. (1995)) in contact with the geotextile.

Ultimately, the model proposed herein can accept and handle realistic geotextile compressibility properties; as such, it can support the choice of geotextile properties in a given situation. In effect, the model is material agnostic, which means that it can potentially apply to under sleeper pads (which are becoming common in ballasted tracks). Also, the model can accept and handle any sleeper geometry, i.e., the formulation is not restricted to a rectangular contact area. Lastly, the utilisation of closed-form analytic solutions ensures superior numerical stability and ease of replication for subsequent engineering application.

REFERENCES

- Bose, T., & Levenberg, E. (2020). A priori determination of track modulus based on elastic solutions. *KSCE Journal of Civil Engineering*, 24(10), 2939–2948.
- Bose, T., Levenberg, E., & Zania, V. (2018). Analyzing track responses to train braking. *Proceedings of the Institution of Mechanical Engineers, Part F: Journal of Rail and Rapid Transit*, 232 (7), 1984–1993.
- Bose, T., Levenberg, E., & Zania, V. (2021). Numerical modeling of a ballastless track mockup based on asphalt. *Construction and Building Materials*, 274(121852), 1–18.
- Bose, T., Zania, V., & Levenberg, E. (2020). Experimental investigation of a ballastless asphalt track mockup under vertical loads. *Construction and Building Materials*, 261, 119711.
- Esveld, C. (2001). *Modern railway track*. MRT–Productions.
- Freudenstein, S., Geisler, K., Mölter, T., & Missler, M. (2018). *Ballastless tracks*. John Wiley & Sons.
- Köllo, S. A., Puskás, A., & Köllö, G. (2015). Ballasted track versus ballastless track. In *Key engineering materials* (Vol. 660, pp. 219–224).
- Lee, S.-H., Choi, Y.-T., Lee, H.-M., & Park, D.-W. (2016). Performance evaluation of directly fastened asphalt track using a full-scale test. *Construction and Building Materials*, 113, 404–414
- Lee, S.-H., Park, D.-W., Vo, H. V., & Fang, M. (2019). Analysis of asphalt concrete track based on service line test results. *Construction and Building Materials*, 203, 558–566.
- Levenberg, E. (2020). *Pavement mechanics – lecture notes*. Eyal Levenberg - Danish Publisher 972317. doi: 10.11581/dtu:00000088
- Liggins, A., Hardie, W., & Finlay, J. (1995). The spatial and pressure resolution of fuji pressuresensitive film. *Experimental Mechanics*, 35(2), 166–173.
- NAPA. (2020). *Asphalt for recycling and energy reduction*. Retrieved 3-15-2020, from https://www.asphaltpavement.org/index.php?option=com_content&view=article&id=201&Itemid=774
- RailOne. (2011). *Getrac, the ballastless track system on asphalt*. Rail.One. Retrieved from https://www.railone.com/fileadmin/daten/05-presse-medien/downloads/broschueren/en/Getrac_EN2012_ebook.pdf

Analytical study on structural remaining life of airfield pavement using FWD

F. Varela Soto & R. Pacheco-Torres

Department of Civil Engineering: Construction, Infrastructure and Transport, Universidad Politécnica de Madrid, Madrid, Spain

ABSTRACT: This paper aims to develop a life remaining model for airfield pavement, from the deflection data obtained using a falling weight deflectometer (FWD) over the years. The case study is an existing airport with more than one half million passengers every year. Data obtained from a testing campaign with FWD conducted in 2014 are used as input data in a “back-calculation” program to obtain the modulus of elasticity for the pavement layers. Bearing capacity is evaluated according to the method described by the ICAO. Remaining life is analysed in terms of cumulative damage factor (CDF) using the freeware computer software FAARFIELD. An impairment model is obtained for each of the zones of the pavement based on its bearing capacity. The sensitivity of the model to influence parameters, such as landing gear and takeoff frequency, is evaluated. After several FWD test campaigns in 2016 and 2018, the model is calibrated and results are compared. The results obtained show that the proposed methodology, which combines non-destructive testing with analytical methods, is useful for airport pavement structural evaluation. The analysis also shows the sensitivity of FAARFIELD to key input parameters.

Keywords: airport pavement, FWD, CDF

1 INTRODUCTION

Aviation is one of the main sectors driving globalization, moving thousands of millions of passengers each year in its two main areas: tourism and business. To date, around 42,000 airports have been built. Management of the assets making up each of these airports is necessary work which requires full coordination between the air (pavement, warning lights, ancillary resources, etc.) and ground (terminal building, luggage transport and distribution, etc.) sides.

Proper management of upkeep, through planned inspection and maintenance, means a considerable improvement in safety for travellers and savings for the managing entity. Structural evaluation of the pavement encompasses a group of techniques intended to determine the remaining capacity of the pavement and is a preliminary step to taking action. Among these techniques, monitoring is essential to detect possible failures in the pavement, also facilitating possible maintenance plans for the future. Additionally, calculating the remaining life of the pavement using progression curves or models will contribute to the aim of determining the capacity of the pavement based on traffic, and thus make it possible to optimize the section in construction design.

2 OBJECTIVES

The main aim of this paper is to develop a service life model applicable to airport pavements, based on deflection data measured using a Falling Weight Deflectometer (FWD). Additionally, the purpose is to calibrate the proposed model with real data obtained on successive measurement campaigns.

3 METHODOLOGY

The thickness of all pavements at modern airports is established using mechanistic-empirical software. These tools offer a significant advantage over the purely empirical methods used in the past, such as the capacity to consider almost any composition or materials in a pavement, recording all the aircraft that make up the design traffic spectrum, and the ability to quickly change one or more values related to the sensitivity of the thicknesses calculated.

The Federal Aviation Administration (FAA) method is the most commonly used to design flexible pavements at airports (Federal Aviation Administration, 2016). This presents a series of graphs which are used to determine thicknesses in what are identified as critical areas, over which the aircraft with the maximum load travel.

3.1 Calculation factors

Traffic is among the factors with the greatest influence on the service life of the pavement, largely due to increasingly more excessive aircraft measurements and wingspans, which in turn involve enormous tonnages that require ongoing runway maintenance. In addition, the number of takeoffs and landings of these aircraft entail considering them all the more when designing the type of pavement.

Based on the standards formulated by the FAA, the equivalent impact of traffic is taken into consideration as the Cumulative Damage Factor (CDF). This is defined as the amount of structural fatigue used up by the pavement during its service life. It is expressed as the ratio of applied load repetitions to allowable load repetitions to failure. As soon as the CDF has a value of 1, it is understood that the pavement has exhausted all its allowable fatigue. If the number of applied load repetitions is less than the maximum allowed, the failure will not occur but a fraction of damage that accumulates (Ruiz Calvo, 2003)

$$CDF = \frac{APPLIED\ LOAD\ REPETITIONS}{NUMBER\ OF\ ALLOWABLE\ LOAD\ REPETITIONS\ TO\ FAILURE}$$

According to the FAA 150/5320-6F standard, when an aircraft travels along a runway, it seldom moves in a straight path or along the same path as the previous wheel. It will move along the runways with a statistically normal distribution. Coverage occurs when the wheel of an aircraft landing gear passes along a unit area. The number of passes required for coverage of said unit area is expressed as the pass-to-coverage (P/C) ratio.

The configuration of the landing gear and the total weight of the aircraft are also determining factors of pavement design. As aircraft have become heavier, the number of wheels in the landing gear has increased to better distribute the load. The basic configurations with single, dual, triple and quadruple, all of which can be combined in tandem (International Civil Aviation Organization, 2009)

The effective elastic modulus of a material characterizes the relationship between stresses and the deformation of the pavement as a whole. This must be analogous to the existing conditions of the non-destructive tests conducted, obtained using the back-calculation process. The set of moduli for each layer will provide, more or less accurately, the same deflection surface measured from various distances from the centre of the load, that is, when elastic pavements similar to that used in the back-calculation process are entered in the software.

The properties of the subgrade layer are indicated using the CBR rate. This is the method most commonly used to evaluate the resistance of the materials in the subgrade, subbase and base, including the recycled materials used in road and runway pavements. The CBR value obtained in this test makes up an integral part of various design models for flexible pavements.

3.2 *Software used*

In this research, the FAARFIELD 1.42 software was used to evaluate the service life of the pavement. The software uses an iterative method for the design, following a procedure developed by the Federal Aviation Administration (FAA)(Federal Aviation Administration, 2017).

Once the values are known for the elastic moduli and the composition of the traffic, these are entered in the FAARFIELD software in order to obtain the CDF for the pavement and subsequently be able to locate the most affected areas. All these values will make it possible to reflect in a graph the service life and damage to the pavement due to the action of traffic during the years of the study.

Additionally, a parallel study will be conducted concerning the way in which the configuration of the aircraft landing gear affects the CDF of the pavement, and consequently, helps to decrease or increase the service life of said pavement.

4 CASE STUDY

The aim of this case study is to confirm and demonstrate the service life model for the pavement on the runway of an international airport in Mexico. The airport has a 2700-metre main runway, and other supplementary runways: alpha, delta and echo. All the taxiways have flexible pavement, primarily made up of a 31-cm asphalt layer, a 16-cm hydraulic base, a 16-cm subbase, and finally a subgrade.

4.1 *Initial data*

4.1.1 *Traffic*

The traffic traveling on the runway consists of 36 aircraft with different tonnages and number of annual departures. The following graph summarizes the aircraft type, weight and annual departures. For the purposes of calculation, a 4% increase in departure operations is estimated.

The aircraft with the highest number of departures is the S-20, whose weight is low in comparison with the others. The following aircraft with higher frequency are B737-800, A320-100 and EMB-170.

4.1.2 *Elastic moduli from deflections*

For this study, the elastic moduli for the current condition of the pavement are used as initial data. These moduli were obtained from a back-calculation process from the deflections obtained using the FWD during the years 2016 and 2018, as part of the airport's upkeep and maintenance plan. It was decided to divide the runway into three delimited zones, denominated Zone A, Zone B and Zone C, to facilitate recognition of the points where the highest deflections have been detected. Take-off and landing operations can occur in both directions.

On the runway, data were taken with the FWD on four imaginary lanes separated from each other and from the central axis by a distance of 7 m. The deflection measurement was taken every 25 m. For a runway 2,350 m long, this results in a total of 376 deflection values. The runway is made up of a 31 cm asphalt layer and a 32 cm stabilized granular base. The initial CBR is 6.5.

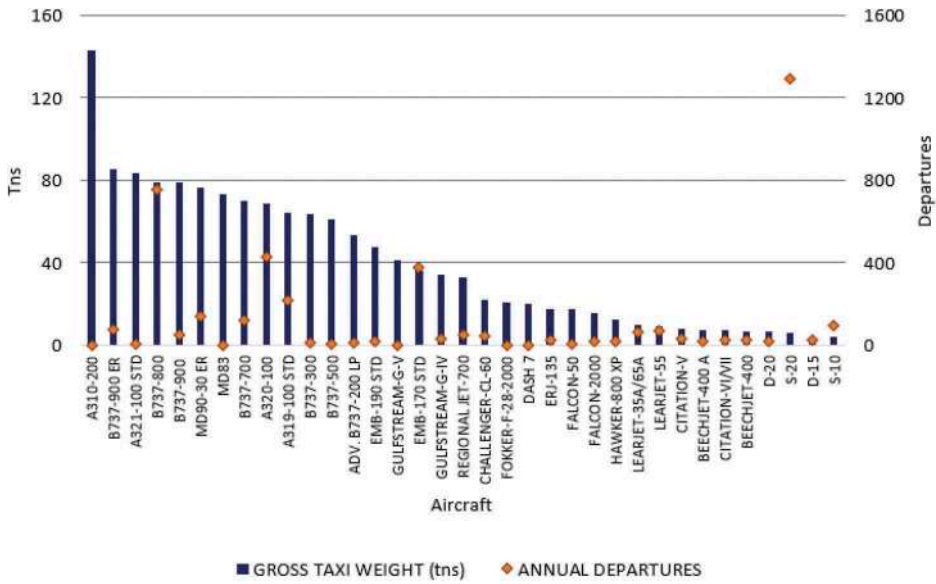


Figure 1. Aircraft, weight and number of annual departures.

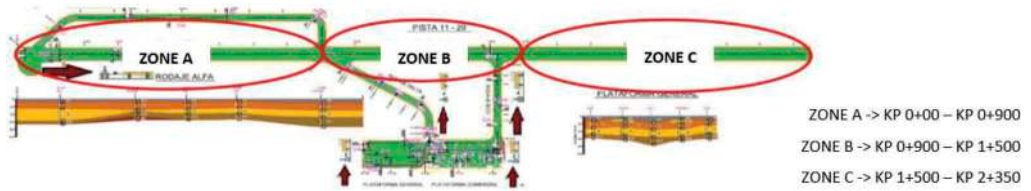


Figure 2. Zones identified on the takeoff/landing runway.

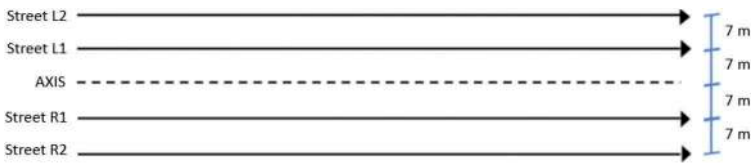


Figure 3. Measurement lanes with FWD.

5 RESULTS

5.1 Elastic moduli

Due to the measurement process itself, there is variability in the elastic modulus value (in MPa) and the CBR value along each runway zone. The data obtained were analysed and filtered. In order to be able to work with the elastic moduli as input data in the calculation program, the value of the average modulus per zone was obtained. Table 1 summarizes the elastic moduli and CBR for each zone in the two years measured (2016 and 2018).

Table 1. Elastic moduli and CBR.

	ZONE A		ZONE B		ZONE C	
	YEAR		YEAR		YEAR	
	2016	2018	2016	2018	2016	2018
Asphalt layer (MPa)	2472	2149	1940	1831	1874	1717
Granular layer (MPa)	358	300	387	288	328	272
Subbase (CBR)	6.05	5.81	6.35	5.92	6.08	5.58

5.2 CDF contribution

The traffic and pavement condition being known for the two study years, the data were entered in FAARFIELD to obtain the contribution of each aircraft to the damage caused, in this case, to the CDF rate. The service life of the pavement is estimated to be 30 years.

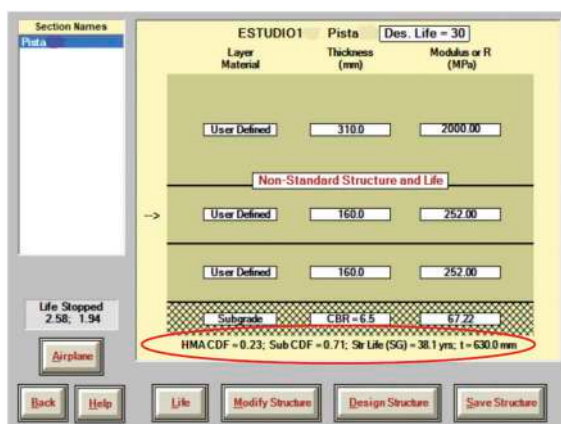


Figure 4. FAARFIELD Software.

The aircraft and number of departures data were entered in the calculation program. The pavement structure was then defined in its initial state. FAARFIELD calculates the CDF of the most damaging aircraft and traffic as a whole. Table 2 summarized the CDF obtained in each of the zones identified on the takeoff/landing runway for years 2016 and 2018.

Table 2. CDF results obtained with FAARFIELD.

	CDF total	
	Year	
	2016	2018
Zone A	0.10	1.17
Zone B	0.21	2.03
Zone C	0.89	4.74

The calculations with the modulus of elasticity obtained for 2018 indicate that all areas of the runway have exceeded the allowable fatigue. It can be seen that area C is the most

damaged, due to the fact that a large part of the take-offs takes place in this area, as could be observed on the inspection “in-situ”. The CDF graph for each aircraft is shown below, corresponding to zone C in year 2016. The B737-800, MD90-30 ER and B737-900 are the aircraft that cause the most cumulative damage to the subgrade.

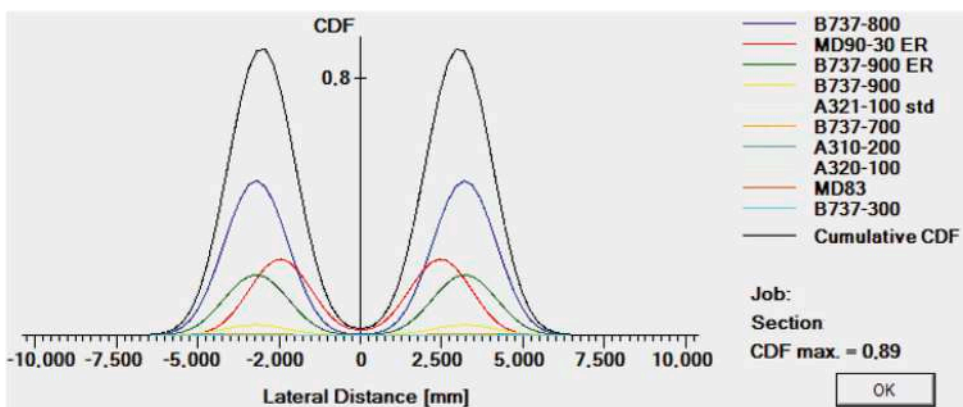


Figure 5. CDF of each aeroplane for zone C/year 2016.

The CDF not only depends on the weight of the airplane, but also on the number of operations and the configuration of the aircraft itself. A more detailed sensitivity analysis was thus conducted.

5.3 Sensitivity analysis

This section will study the impact of the configuration of the landing gear on the damage caused by the most damaging aircraft in the case study. The arrangement of the wheels on a large-tonnage aircraft entails a greater distribution of loads on a higher level of the subgrade. This will be reflected in the spacing between configurations. In other words, the greater the separation among the wheel configuration, the lower the CDF produced by the aircraft, and vice versa (Gholam Ali Shafabakhsh, 2015). In addition, the gross weight of the aircraft does not in itself constitute an effective factor for calculating the CDF, as this value must be combined with the weight borne by each wheel, based on the configuration of the landing gear.

To investigate the interaction between wheel loads and the pavement, in the FAARFIELD software, a traffic mix was created, made up of four aircraft: firstly, B747-400 ER and B777-300 ER; and secondly, A380 and A340-600. To facilitate subsequent calculations, the same number was entered for both annual take-offs (500) and annual growth (4%). The pavement structure for this study will be the same as the case study airport. These aircraft were chosen because they have different landing gear configurations, as shown in the following figure:

The Figure 7 shows the comparison of weight per wheel and CDF caused by each aircraft considered.

We can see that the B747-400 ER aircraft weighs more than the B777-300 ER. However, its CDF on the pavement is lower. This is due to the fact that its entire weight is better distributed on its 16 wheels, in comparison with the 12 of the B777-300 ER aircraft. In addition, it should be pointed out that the 12 wheels on the landing gear of the B777-300 ER aircraft are distributed over only four strips of the pavement, while the 16 wheels of the B747-400 ER are distributed over eight. This results in increased damage on a special section of the pavement surface.

Similarly to the previous case, the A380 aircraft weighs more than the A340-500. However, its CDF on the pavement is lower. Again, this is due to the fact that the weight of the A380 is

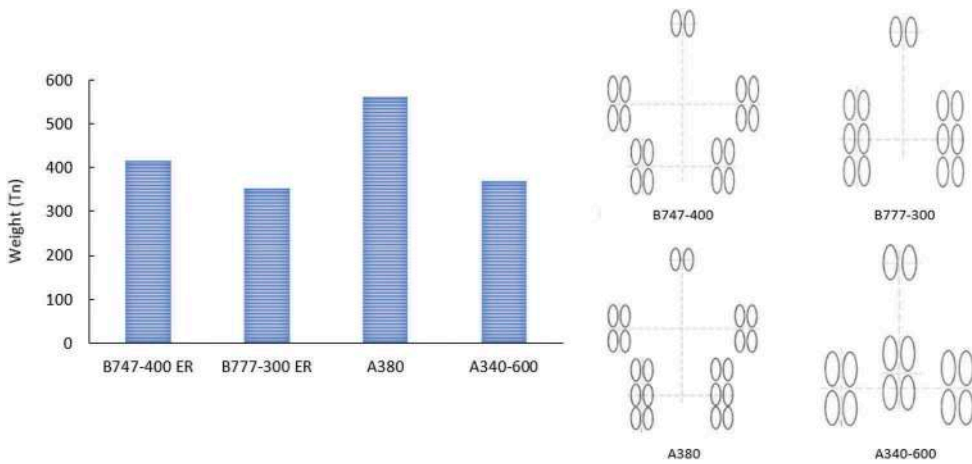


Figure 6. Total weight and landing gear configuration of the aircraft studied.

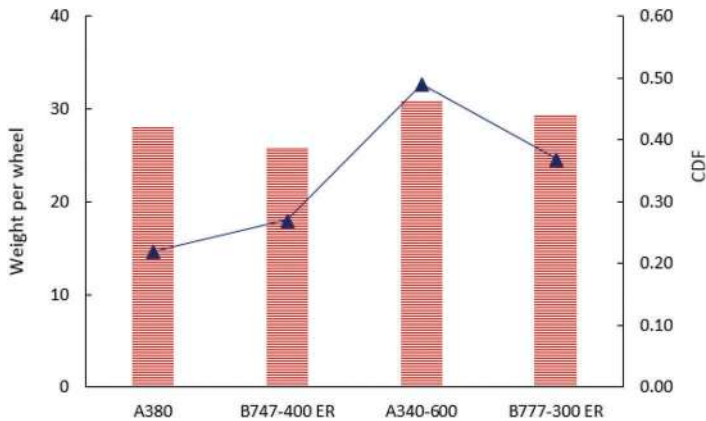


Figure 7. Weight per wheel and associated CDF.

better distributed on its 20 wheels, in comparison with the 12 of the A340-600. Lastly, the 12 wheels of the landing gear of the A340-500/600 aircraft are also distributed over only six strips of pavement, while the 20 wheels of the A380 are distributed over eight, causing less damage on a special section of the pavement surface.

6 CONCLUSIONS

The results of the study, based on non-destructive test with FWD and the analysis of the accumulate damage, indicate that the pavement has suffered damage and an improvement intervention is urgently needed. This methodology, which combines in situ tests with damage calculations, is of interest for airport pavement management and conservation models.

The subsequent analysis demonstrates the sensitivity of the FAARFIELD program to variations in the elastic modulus. This translates into a sharper reduction in the CDF when the bearing capacity of the asphalt layer is improved (higher modulus), due primarily to the absorption of the vertical and horizontal loads, distributing them to lower layers to a lesser extent. The results also highlight the need to conduct a study of the CDF based on the aircraft landing gear and weight per wheel, rather than just the total weight of the aircraft.

REFERENCES

- Federal Aviation Administration. (2016). Airport Pavement Design and Evaluation, AC 150/5320-6F. Washington, DC.
- Federal Aviation Administration. (2017). FAARFIELD 1.42.
- Gholam Ali Shafabakhsh, E. K. (2015). Effect of Aircraft Wheel Load and Configuration on Runway Damages. *Periodica Polytechnica Civil Engineering*, 85–94.
- International Civil Aviation Organization. (2009). ICAO AC 150/5320-6E Airport pavement design and evaluation.
- Ruiz Calvo, J. (2003). Teorías de Daño Acumulativo en la Fatiga. *Técnica Industrial*, 38.

Analysis of evaluation and assessment procedures for the application of the TSD on asphalt pavements

M. Čičković

HELLER Ingenieurgesellschaft mbH, Darmstadt, Germany

ABSTRACT: The aim of the present research project was to find suitable approaches for the assessment and evaluation of bearing capacity measurements with the TSD.

In a first step, the state of the art regarding bearing capacity measurements with the TSD were established. A further area of research is the empirical data available of TSD deployment. This was used as a transition to the introduction of possible bearing capacity parameters. A total of 26 bearing capacity parameters were identified, which are used as characteristic values of the structural substance of pavements.

Additionally, the influence of environmental circumstances on the measurement was analysed. It can be stated that the measuring speed has hardly any influence within the usual speed window ($v > 20$ km/h). Wheel load has an influence, but the scattering can be compensated by a linear correction approach. The temperature has a decisive influence, the correction approaches presented can also limit the influence to some extent, but these must be refined for the TSD measurement procedure.

At the same time, the deformation bowl calculation methods were also analysed. The area-under-the-curve method (AUTC) and the PEDERSEN method (2013) were compared by using 3D-Move simulation. The result was that the AUTC method shows deviations due to the tailtaming approach for stiff pavements, whereas the PEDERSEN (2013) approach shows very good agreement throughout.

In 3D-Move, a large number of simulations were carried out in which a lot of parameters were varied. For this purpose, all corresponding bearing capacity parameters were calculated, resulting in a sensitivity analysis that allowed statements about their respective significance. This makes it clear that the parameters of the SCI family are very reliable parameters for describing the stiffness of the layer under consideration. The same applies to the characteristic values of the stiffness backcalculation method (SBM).

Keywords: TSD, Bearing capacity, Pavement, Non-destructive testing, Asphalt

1 INTRODUCTION

The Traffic Speed Deflectometer (TSD) was developed in Denmark at the end of the last century with the aim of detecting deformations at high speed (Rasmussen 2002). The measuring system is installed on a truck (incl. all associated instrumentation, see Figure 1). Thus, the recording of the bearing capacity at a speed of approx. 80 km/h is possible. The measuring beam must be resistant to bending and torsion, and its temperature profile must be as uniform as possible in order to ensure equal conditions for the correction of the individual Doppler laser data (Forschungsgesellschaft für Straßen- und Verkehrswesen (FGSV) 2015).

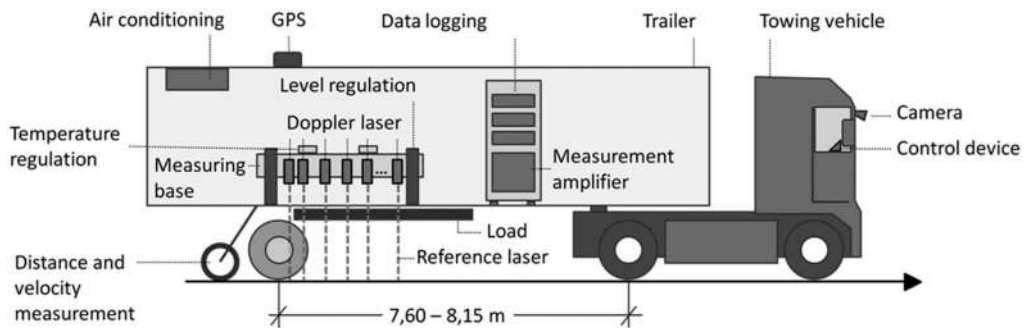


Figure 1. Principle sketch of the TSD (Forschungsgesellschaft für Straßen- und Verkehrswesen (FGSV) 2015).

The principle of data acquisition of the TSD is based on the Doppler effect, i.e. the wavelength of the emitted light beam is different than the wavelength of the imitted (reflected) light beam. Thus the oblique speed of the deformation can be recorded. In order to measure only the deformation speed, exact knowledge of the inclined position of the Doppler laser and the horizontal speed is necessary. The inclined position is measured with the aid of a reference laser. In addition, acceleration sensors and gyroscopes are used to record the movements during data acquisition. The horizontal speed of the vehicle is recorded by a hodometer and is used to calculate the vertical speed (i.e. the deformation speed) (Hildebrand et al. 2000).

2 APPROACH

As a first step, the current state of knowledge regarding bearing capacity measurements was compiled via an extensive, international literature study. A further focus was on existing experiences with the TSD. Starting with investigations on repeatability and comparability up to first application cases. This was used as a transition to the introduction of possible bearing capacity parameters which can be recorded or calculated with TSD measurements. From international technical literature a total of 26 bearing capacity parameters could be identified (see Table 1), as characteristic values of the structural integrity of pavements.

At the same time, post-processing was also examined, especially the effects of measurement conditions on the measurement results. On the one hand, the measuring speed, which represents a new component compared to FWD measurements, is to be mentioned, but also the prevailing temperatures and the actual stress. For this purpose, first correction approaches were compiled. A further point of post-processing is the calculation of deformation bowls from the slope values of the TSD. Two competing approaches exist here that are being used right now and that need a thorough investigation on possible differences.

The next step is to verify the previous findings with data. Two approaches were pursued here: On the one hand, a parameter study is carried out with the aid of the calculation program 3D-Move from the University of Nevada, in which a wide range of boundary conditions (temperature, wheel load, Young's modulus of the bound and unbound layers, thickness of the bound layers, speed, load class) are varied. The advantage of this program is that a calculation of deformations and deformation velocities is possible and thus also slope values (since the horizontal velocity is always known) are available. On the other hand, the German Federal Highway Research Institute (BASt) and the Bavarian State Ministry of Housing, Construction and Transport (StMB) have provided TSD measurement data for evaluation. These data sets were used to examine the reliability.

Table 1. Bearing capacity parameters.

Geometric parameter	Mechanics-based parameters
Slope P_i	Phase shift angle δ
Deflections D_i	Layer modulus of the half-space M_0
Radii of curvature R_i	Resilient modulus of the unbound layers M_r
Area A	Elastic length l
Shape factors F_i	Characteristic stiffness of the load-distributing layers $M_1 h^3$
Surface curvature index SCI_i	Impact stiffness modulus ISM
Surface curvature index SCI_{SUB}	Effective structural number SN_{eff}
Base curvature index BCI	Backcalculation of Young's moduli E_i
Base damage index BDI	Determination of equivalent reinforcement thickness d_{eq}
Area under the pavement profile $AUPP$	
Tangential slope TS_i	
Deformation slope SD_i	
Deformation slope index DSI_i	
Spreadability S	
Tragfähigkeitzahl Tz	
RWD index RI	
RWD zone index ZRI	
Skewness of the deformation bowl γ	

2.1 3D move

In order to be able to simulate overrolling of vehicles and thus perform parameter studies with varying reference conditions in terms of environment and material properties, the continuum-based finite layer analysis program 3D-Move (Asphalt Research Consortium 2013) was used. The program can simulate the response of a multilayer system to an overrolling vehicle at constant velocity through the approach of Fourier transforms, and can also represent the visco-elastic material properties of asphalt layers (Siddharthan et al. 1998; Zafir et al. 1994). Due to the fact that both visco-elastic material behaviour and a constant velocity can be simulated, a simulation of a TSD passing and the resulting deformation is possible (Nasimifar et al. 2015).

For the present research work a very simple load configuration was chosen. Here, a load of 50 kN is applied to the fixture, with a pressure of 0.862 MPa. 3D-Move outputs the stress and strain state as well as the resulting deformations in all coordinate directions for a point under consideration. It should be noted that the output deformation is in the time domain, i.e. it is an Euler representation of the deformation. In order to change to the Lagrangian representation, a conversion must take place with the help of the travel speed and the information concerning the distance of the starting point with respect to the distinguished point.

The unbound layers are represented using a linear-elastic material behavior, while asphalt layers can also be calculated visco-elastically. When defining the material properties of the unbound layers, it is possible to select from a catalog of predefined materials or to directly enter the Young's modulus E , the transverse contraction coefficient μ , the damping factor D , the density ρ and the thickness d . The density ρ and the thickness d are calculated using the linear-elastic method. The density ρ and the thickness d are also one of the input values when defining the material parameters of the asphalt. When defining the visco-elastic properties, there are two different possibilities: Either laboratory parameters are used, which come from the split tensile swell test (Master Curve) and the Dynamic Shear Rheometer (DSR). The second option is to use the Witczak model, which functionally describes the dynamic elastic modulus $|E^*|$ of the asphalt based on material properties of the bitumen used and volumetric properties of the asphalt mixture. During the simulation, the following parameters were varied in order to identify their influence on the characteristics of individual load-bearing capacity parameters:

- driving speed
- wheel load
- asphalt core temperature
- Young's modulus of the unbound layers
- thickness of the asphalt layer
- Young's modulus of the asphalt layer

2.2 Existing TSD data sets

The BAST provided TSD data sets of two test routes. The first type of data sets were data sets of the “Königsforster Runde” (see Figure 2), which is located in the immediate vicinity of the BAST and comprises a large number of different road categories. Here, a total of 14 data sets were made available, i.e. the repeatability of the measurements can be investigated, but also the influence of the ambient temperature on the measured values (as a comparison to the theoretical calculations in 3D-Move). In addition, the fact that different road categories are available offered the possibility to check whether and to what extent individual bearing capacity values show fluctuations in real measurements due to this.



Figure 2. Route of the “Königsforster Runde (Jansen 2019).

3 NORMALISATION TO REFERENCE CONDITIONS

3.1 Vehicle speed

Further investigations by PODOLSKI (2020) showed that the vehicle speed in the range of 20 km/h - 90 km/h has a very small influence on the deformations and the bearing capacity parameters derived from them. For this purpose, the bearing capacity in the straight section was recorded at the Aldenhoven Testing Center (ATC) in 10 km/h increments (from 20 km/h - 90 km/h) with the aid of the TSD. The straight section used for the investigation had a length of approx. 400 m. The mean values were analysed. The mean and median values of the SCI_{300} were analysed as a function of speed. No dependence was discernible. It should be noted, however, that the overall deformations were very low: $D_0 < 100 \mu\text{m}$, $SCI_{300} < 300 \mu\text{m}$ (Podolski 2020).

A parameter study was also performed using 3D Move. The different superstructures were selected, whereby these superstructures were selected in accordance with the German regulations. A very stiff and a very weak superstructure were chosen.

It is clear that the horizontal velocity of the TSD has an influence on the expression of the deflection bowl, but this influence decreases with increasing velocity. At very low velocities, the area near the load center shows a clear dependence on the horizontal velocity. In the outer region of the deflection bowl, no such dependence can be observed. In addition, it is clear that the velocity influence increases with decreasing stiffness of the unbound layers - significantly larger deformations occur. From the parameter study it is evident that the horizontal speed of the TSD does have an influence on the quantitative expression of the bearing capacity quantities, but only from a speed range below 20 km/h. This is due to the fact that the horizontal speed of the TSD has a significant influence on the quantitative expression of the bearing capacity quantities. If the driving speed of the TSD is within the speed window specified by the manufacturer (40 km/h to 80 km/h), the influence of the speed on the load-bearing capacity quantities is negligible – at least for the given temperature range and a rather stiff pavement. The stiffness of the unbound layers has no influence in the relative consideration of the change in the bearing capacity quantities.

Based on the investigations of PODOLSKI (2020) and the parameter study in 3D-Move, a velocity normalisation therefore does not appear necessary.

3.2 Load

The problem of load normalisation is due to the fact that the amount of dynamic wheel load has two origins: Mass and mass distribution of the TSD, unevenness of the road surface. While the mass and mass distribution of the TSD are still variable (on a small scale), the unevenness of the road surface and the resulting reaction of the chassis and mechanical stress on the road structure are hardly controllable, so that parameter studies can only be applied here to a limited extent. For this reason, the influence of the dynamic axle load on load-bearing capacity variables was investigated with the aid of simulations.

For this purpose, a wheel rollover at 80 km/h and different wheel loads were simulated in 3D-Move. In 3D-Move, the following can also be varied: Wheel load, tire pressure, geometry of the wheel contact area, wheel and axle distances. In this parameter study, the tire pressure was selected to be constant ($p = 125 \text{ psi} = 8.6 \text{ bar}$), the wheel and axle spacings (L_1 , L_2 and S_1) were selected so that only one wheel is present, and the wheel load was varied.

It is clear that the actual applied wheel load has a significant effect on the calculated bearing capacity parameters, i.e., the variations in dynamic wheel load are not negligible. However, a linear correction of the deflection bowl can reproduce or absorb the effects of the fluctuations well (if the actual wheel load is known).

3.3 Core temperature

For many bearing capacity measurement methods, procedures exist that take into account the influence of temperature (and moisture content in the unbound layers). However, these methods have mostly been developed for the FWD, so that experience backgrounds for standardisation methods for the TSD do not yet exist. There is still a need for research in this area in order to develop a usable procedure.

4 CALCULATION OF DEFLECTION BOWLS

Since the deflection bowl is often calculated first when evaluating bearing capacity measurement data by means of TSD in order to determine characteristic values, the calculation of the deflection bowl on the basis of the original TSD measurement data is of great importance. For this purpose, three methods are presented which are currently in use. In addition to

a theoretical explanation of the procedure, an exemplary calculation of deflection bowls and characteristic values will be carried out in order to shed more light on the differences. The following methods are commonly used to calculate deflection bowls:

- use of Winkler’s subgrade reaction function
- asymmetric model according to PEDERSEN (2013) (Pedersen 2013)
- Area-under-the-curve method (AUTC) (Muller and Roberts 2013)

For the evaluation and analysis of the deflection bowl calculation methods, all simulations carried out in 3D-Move and the resulting deflection bowls (143 deflection bowls) were used and reduced to possible sensor positions. The selected positions are (related to the load center): -450 mm, -300 mm, -200 mm, 110 mm, 210 mm, 310 mm, 460 mm, 610 mm, 910 mm, 1,510 mm, 3,010 mm. The 3D-Move program is able to calculate and output deformation velocities and deformations. Using the information of the horizontal velocity (known as input variable), slope values can also be calculated. These were sent to Greenwood A/S on the one hand, and also to ARRB on the other hand, in order to calculate deformation curves from this and the respective procedure. In addition, the AUTC method was programmed and applied by ourselves, since it is comparatively easy to reconstruct. The method of Winkler’s bedding function was not considered, since this method is obsolete. Since “actual” deformation curves are available, the two methods can thus be compared and evaluated with the “actual” curves.

Both deflection bowl calculation methods show very good agreement with the “real” deformations from 3D-Move. The good agreement with the “real” values, calculated by means of the deformation values from 3D-Move, is also evident at the level of the ultimate limit state variables. Figure 3, for example, shows the comparison of the two methods with the “real” data from 3D-Move at the level of SCI_{300} . The deviations are comparatively small, especially for the method according to PEDERSEN (2013).

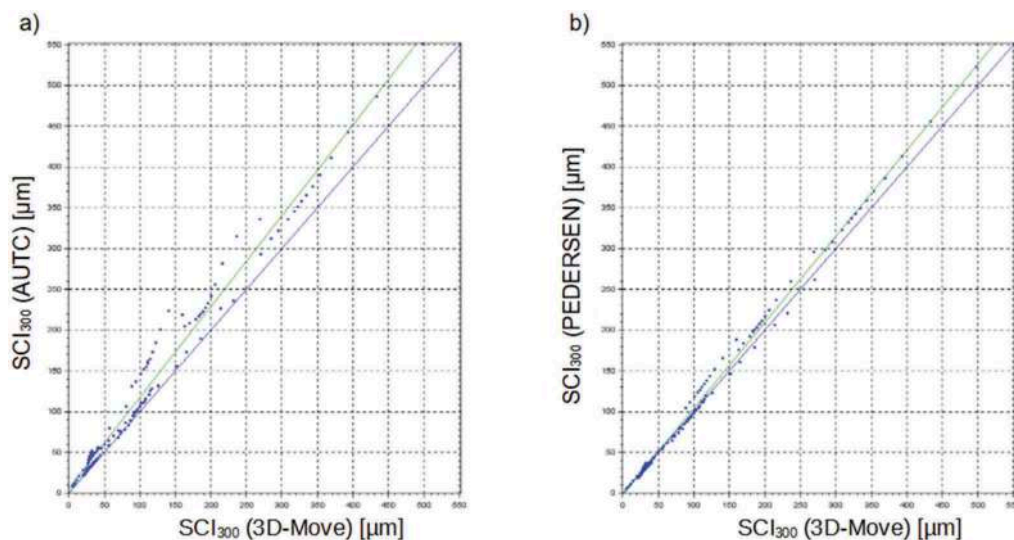


Figure 3. Comparison of the surface curvature index SCI_{300} according to the type of deflection bowl calculation approach a) according to AUTC method; b) according to PEDERSEN (2013).

Only the “tail taming” of the AUTC method can lead to problems in the deflection bowl calculation for certain stiffness constellations of the pavement. In the procedure according to PEDERSEN (2013), such systematic errors have not been noticed. Therefore, taking into account the problems with tail taming, both procedures can be used to determine bearing capacity parameters based on deformation values. However, NASIMIFAR et al. (2018) point out that for more advanced back-calculations, for example, to calculate elastic moduli according

to multilayer theory, using the AUTC approach to calculate deformations can be problematic, especially in the presence of slope anomalies (Nasimifar et al. 2018).

5 CHARACTERISTIC BEARING CAPACITY PARAMETERS

There are two common approaches to defining characteristic values. On the one hand, conclusions about the load-bearing capacity of the fastening can be drawn from the original TSD data, i.e. from the slope values. On the other hand, the deformation trough can be determined from the original TSD data, from which characteristic values for evaluating the bearing capacity can then be calculated. A large number of research papers have demonstrated the link between back-calculation parameters from bearing capacity measurements and mechanical properties of pavements (Park et al. 2005; Xu et al. 2002a, 2002b). Table 1 shows the bearing capacity parameters discussed:

When considering the characteristic bearing capacity parameters, the results from the 3D move simulations and the real measured data were used. When analysing the results of the 3D move simulations, the primary aim is to find out how the characteristic parameters react to the varying parameter, i.e. a bearing capacity parameter would then stand out positively if changes in the varying reference condition parameter were reflected very strongly in the value of the bearing capacity parameter. For this purpose, the bearing capacity parameter is always set as 1 at the lowest level of the reference condition parameter to be varied. The further bearing capacity parameter values were then formed as a quotient to the mentioned bearing capacity parameter value at the lowest reference condition level. If the bearing capacity parameter value becomes lower due to the parameter variation (e.g. when the asphalt body temperature is increased), the reciprocal of this quotient is chosen as the index of sensitivity. An example of such an individual graphs of the sensitivity analysis (depending on the parameter varied) is shown below in Figure 4. A more detailed analysis of the dependencies is given in the research report (Čičković et al. 2020).

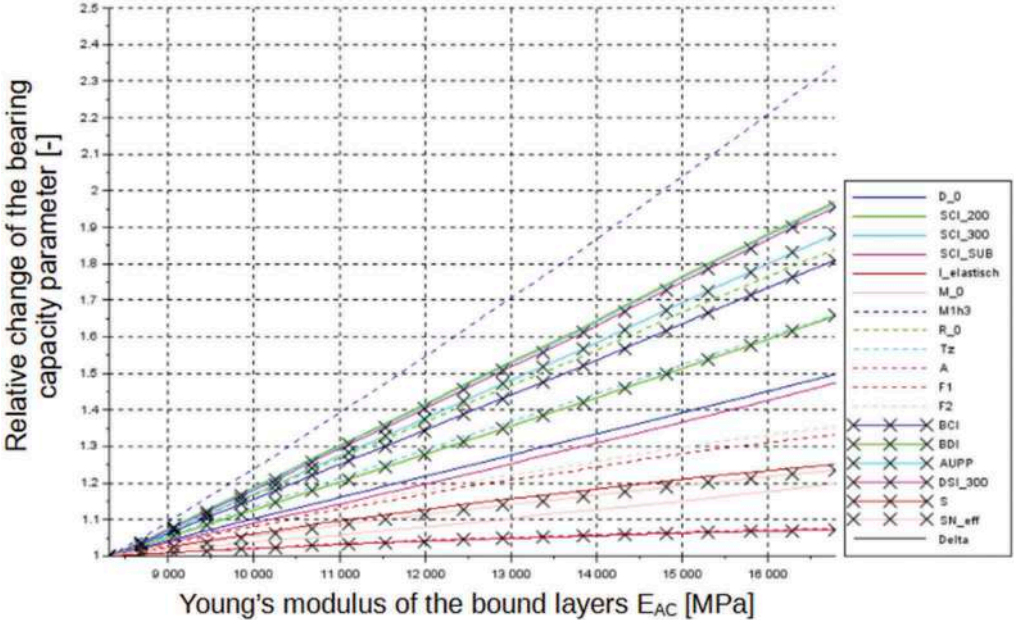


Figure 4. Sensitivity analysis for the parameter variation of the Young's modulus of the bound layers.

For the consideration of the real measurement data, mainly the data sets of the Königsforster Runde were used, since a large number of measurement campaigns are available here. This has the advantage that the repeatability and the temperature dependence of the respective bearing capacity parameter can also be investigated. For this purpose, the characteristics of individual bearing capacity parameters per measurement campaign were plotted in a network diagram in order to be able to visually represent conspicuous features. It is important to note that a measurement campaign consists of ten sections. Analogous to the procedure described above for the sensitivity analysis in 3D-Move, the lowest value of a bearing capacity parameter was set to 1 for each measurement campaign and the quotient of the section value and the lowest value was formed for the remaining sections (see Figure 5, the section mean value was always used). A quality feature here would be if the courses of the individual measurement campaigns were similar to each other. The characteristic value in the radar chart was also always selected in relation to the lowest value of the respective measurement campaign in order to exclude possible non-linear temperature dependencies. In a second step, the bearing capacity parameter values of the individual measurement campaigns were compared with each other. On the one hand, the 10 m individual and 100 m section values were used to determine the effect of averaging on the correlation. This includes a tabulation of the repeatability in the form of a cross-correlation of the individual measurement campaigns. It should be noted that only the correlations of the 100 m section values were used, since these consistently showed a higher correlation.

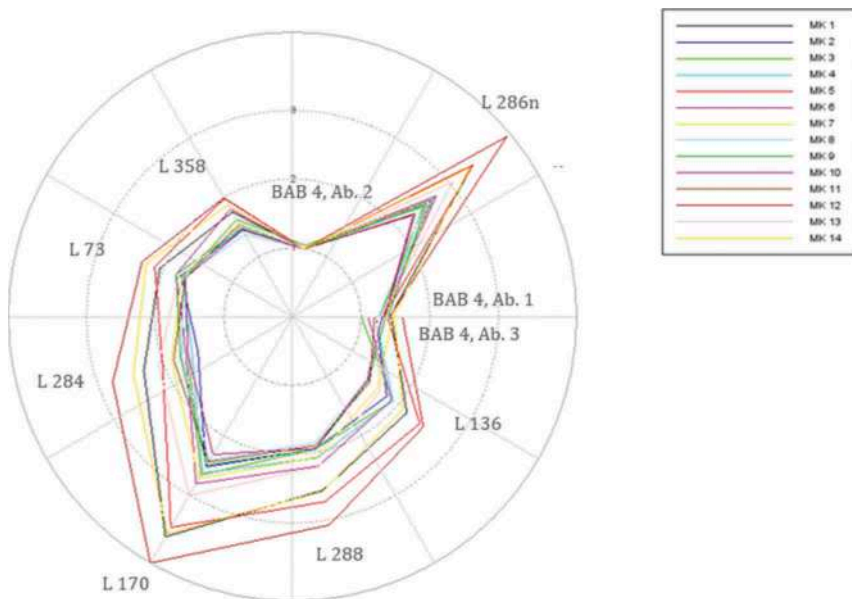


Figure 5. Exemplary radar chart for 14 measurement campaigns (MK) of the Königsforster Runde.

From these two investigations, it can be concluded that characteristic values of the SCI family provide good results in terms of significance and reliability both in the 3D move simulation and when applied to real measurement data. Characteristic values of the stiffness back calculation method show very high sensitivities in the 3D move simulation, i.e. they are able to signal changes in the stiffness of the respective layer under consideration. For the application on real measured data, the number of usable Doppler lasers is too small to determine the characteristic values reliably. There is a need for research to determine the extent to which additional Doppler lasers can increase reliability in the area remote from the load (more

information about the stiffness back calculation method (SBM) and its respective parameters can be found in ČIČKOVIĆ & BALD (2017).

6 CONCLUSION

The aim of the research project was to compile, evaluate and finally evaluate evaluation procedures for bearing capacity measurements with the TSD. In the course of the project, a large number of different evaluation and assessment procedures were developed, which originated primarily from bearing capacity measurements with the FWD. With the help of evaluations based on real measurement data and a parameter study in 3D-Move, advantages and disadvantages of individual methods could be presented and requirements for quality assurance during measurement data acquisition could be worked out.

There is a need for research with regard to temperature normalisation. Up to now, approaches from FWD bearing capacity measurements have been used almost exclusively. However, these carry out the temperature normalisation on the deformation side, which may result in inadmissible or inconclusive characteristic parameters. It must at least be discussed whether temperature normalisation on the resistance side or normalisation on the level of the bearing capacity parameters or values represent the more sensible alternative.

If the deflection bowl is known, all evaluation methods can in principle be applied that are known from the currently already established bearing capacity measurement systems and for which extensive evaluation backgrounds are available. However, it must be taken into account that the shape of the deflection bowl is systematically distorted by the specific, highly dynamic loading due to the measuring principle and the inertia and viscosity effects activated by it: The deflection bowl is generally steeper near the load centre (i.e. in front of the wheel) than in the area further away from the load centre (i.e. behind the wheel) and its low point is shifted backwards relative to the load center (the loading wheel).

Depending on the application purpose, different evaluations are useful. Simple bearing capacity parameters, for example, are suitable for quick evaluations:

- recognition of developments
- qualitative comparison of bearing capacity levels

Simple load capacity characteristic values to be mentioned here are:

- Deformation at the load center D_0
- Surface curvature indices

In this context, the British TSD-specific evaluation option should at least be briefly touched upon. There, the slope values 30 cm in front of the loading wheel are used as load capacity indices. This is the point at which the deflection bowls of soft pavements have their inflection point, i.e. the point at which the slope within the deflection bowl is at its greatest. For softer pavements, this value therefore differentiates very well. For stiffer structures, the inflection point is further away from the load point - the slope at the evaluation point therefore decreases disproportionately. The evaluation method is therefore suitable for recognising soft pavements and allows within this group a good differentiation into good/bad or the recognition of deteriorations.

For more specific evaluations, it makes sense to perform evaluations that allow conclusions to be drawn about the effect of the load-distributing layer and the influence of the base. It can be roughly said that the level of curvature of the deflection bowl indicates the stiffness of the load-distributing layer (higher curvature $\hat{=}$ softer layer), and the level of deformation (also outside the load zone) indicates the stiffness of the base. However, there are mutual (weaker) dependencies between these two factors of influence, which are taken into account in the more sophisticated evaluation methods.

In this respect, the evaluation parameters describing the two characteristic values “curvature of the deflection bowl” (e.g. $SCI_{300} = D_0 - D_{300}$) and “level of deflection” (e.g. $SCI_{SUB} = D_{900} - D_{1.500}$) are helpful.

Finally, the requirements for quality assurance need to be discussed. It was shown that even small temperature differences within the cross-section of the measuring beam lead to significant deviations at the level of the bearing capacity parameter values. Here, great attention must be paid to the temperature control system within the measuring trailer during the measurements - and also during post-processing.

ACKNOWLEDGMENT

This report is based on parts of the research project carried out at the request of the Federal Ministry of Transport and Digital Infrastructure, represented by the Federal Highway Research Institute, under research project No. 04.0318/2018/MRB. The author is solely responsible for the content.”

REFERENCES

- Asphalt Research Consortium (2013): 3D-Move. Version 2.1. Reno.
- Čičković, Marko; Bald, J. Stefan (2017): Rückrechnung der charakteristischen mechanischen Parameter von Verkehrsbefestigungen aus FWD-Messungen. In *Straße und Autobahn* 68 (12), pp. 950–957.
- Čičković, Marko; Bald, J. Stefan; Middendorf, Moritz (2020): Analyse von Auswertungs- und Bewertungsverfahren für die Anwendung des Traffic-Speed-Deflectometers auf Asphaltbefestigungen. Schlussbericht zum Forschungsvorhaben FE-Nr. 04.0318/2018/MRB. Darmstadt.
- Forschungsgesellschaft für Straßen- und Verkehrswesen (FGSV) (2015): Arbeitspapier. Tragfähigkeit von Verkehrsflächenbefestigungen. Teil B 5: Schnell fahrendes Messsystem Traffic Speed Deflectometer (TSD). Gerätebeschreibung, Messdurchführung (AP Trag Teil B 5). Köln: FGSV-Verlag.
- Hildebrand, Gregers; Rasmussen, Søren; Andrés, R. (2000): Development of a laser-based high speed deflectograph. In Shiraz D. Tayabji, Erland O. Lukanen (Eds.): *Nondestructive testing of pavements and backcalculation of moduli*. Proceedings of the “Third International Symposium Nondestructive Testing of Pavements and Backcalculation of Moduli”, held Seattle, Washington, 30 June - 1 July 1999. Fredericksberg: American Society for Testing and Materials (ASTM) (ASTM STP, 1375), pp. 457–469.
- Jansen, Dirk (2019): Multifunctional assessment tool for the structural evaluation and the design of pavements (MESAS). Update from BASt. 11th DaRTS-Meeting. Deflection at Road Traffic Speed (DaRTS) Group. Roanoke, 2019.
- Muller, Wayne B.; Roberts, Jon (2013): Revised approach to assessing Traffic Speed Deflectometer data and field validation of deflection bowl predictions. In *International Journal of Pavement Engineering* 14 (4), pp. 388–402.
- Nasimifar, Mahdi; Siddharthan, Raj V.; Rada, Gonzalo R.; Nazarian, Soheil (2015): Dynamic analyses of traffic speed deflection devices. In *International Journal of Pavement Engineering* 18 (5), pp. 381–390.
- Nasimifar, Mahdi; Thyagarajan, Senthilmurugan; Sivaneswaran, Nadarajah (2018): Computation of pavement vertical surface deflections from Traffic Speed Deflectometer data: evaluation of current methods. In *Journal of Transportation Engineering, Part B: Pavements* 144 (1), p. 4018001.
- Pedersen, Louis (2013): Viscoelastic modelling of road deflections for use with the Traffic Speed Deflectometer. Dissertation. Technical University of Denmark (DTU), Lyngby.
- Podolski, Claudia (2020): TSD measurements. Effect of driving speed on deflections. 12th DaRTS-Meeting. Deflection at Road Traffic Speed (DaRTS) Group. Washington D.C., 2020.
- Rasmussen, Søren (2002): Development of a high speed deflectograph. Danish Road Institute. Roskilde (Report 117).
- Siddharthan, Raj V.; Yao, Jian; Sebaaly, Peter E. (1998): Pavement strain from moving dynamic 3D load distribution. In *Journal of Transportation Engineering* 124, pp. 557–566.
- Zafir, Zia; Siddharthan, Raj V.; Sebaaly, Peter E. (1994): Dynamic pavement-strain histories from moving traffic load. In *Journal of Transportation Engineering* 120, pp. 821–842.

International roughness index model for jointed reinforced concrete highway pavements: An artificial neural network application

S. Sultana, Y. Najjar, H. Yasarer, W. Uddin & R. Barros

Department of Civil Engineering, University of Mississippi, Oxford, Mississippi, USA

ABSTRACT: The pavement management system is of utmost importance for state agencies. Pavement performance prediction is an important component of the pavement management system. This paper aims to develop pavement performance prediction models with the least number of explanatory (independent) variables to predict the pavement performance for future planning of maintenance and rehabilitation (M&R). The artificial Neural Networks (ANNs) approach is utilized to develop the Jointed Reinforced Concrete Pavement (JRCP) performance prediction models. The study was carried out with the database collected from Long Term Pavement Performance (LTPP) program. The International Roughness Index (IRI), in meter per kilometer, was mainly used for dependent variables while initial IRI, pavement age, concrete pavement thickness, base/subbase thickness, average contraction spacing of pavement, cumulative equivalent single axle load (CESAL), base/subbase type (granular, stabilized), climatic region (wet-freeze, wet non-freeze), and construction number (CN) were used in the search of best models. There were several models with constructive statistical measures with a good fit of observed and predicted data. However, the best performing ANN model resulted in promising statistical measures (i.e., $R^2 = 0.93$) which can be used to successfully estimate the IRI values considering the M&R history of the pavements.

Keywords: International Roughness Index (IRI), Artificial Neural Network (ANN), Long-Term Pavement Performance (LTPP), Jointed Reinforced Concrete Pavement (JRCP)

1 INTRODUCTION

According to the 2019 report of the U.S. Department of Transportation (USDOT), the U.S. has a total 54, 632 miles of concrete pavement all over the country. Texas and Iowa have more than 5,000 miles of concrete pavement. The cumulative vehicle miles traveled (VMT) through these roads was about 3,269.1 billion in 2019. These statistics show that the road infrastructure is imperative to sustain the road user's movement. Road and highway infrastructures performance is impacted by load repetitions and it is further compromised by climate attributes. The combination of climate and traffic-induced distresses are measured to identify the present road condition of the pavements. The Long Term Pavement Performance (LTPP) database contains the most comprehensive information on road conditions for more than 2,500 test sections throughout the U.S and Canada. The LTPP data is collected at different spatial locations that exhibit values that are different across the LTPP climatic regions.

Pavement smoothness is one of the foremost important measures of pavement performance. Within the Mechanistic-Empirical Pavement Design Guide (MEPDG) study of NCHRP 1-37 A (MEPDG 2002), pavement smoothness is defined by the International Roughness Index (IRI). The IRI statistic is generally used as an internationally recognized pavement conditioning

rating system. The IRI is calculated from the measured longitudinal profile of a pavement. A higher IRI number indicates a rough pavement profile and, a lower number indicates a smooth pavement profile (Sayers 1986). An extensive literature review revealed that several performance prediction models were developed using multiple linear regression (MLR) modeling techniques for rigid pavements (MEPDG 2002, El-Hakim et al. 2013, Oh et al 2019). These models showed a range of accuracy but the models are difficult to implement. The variables used in the models were distresses (i.e., faulting, transverse cracking, spalling, etc.) and these distresses had to be measured in the field before using the model equations for future predictions. Several artificial neural network (ANN) models were developed using the same variables that showed better accuracy (El-Hakim et al. 2013, Bayrak et al. 2004, Tennant Duckworth 2019, Yasarer et al 2020). There is not much research done to study the pavement performance specifically for jointed reinforced concrete pavement.

The main objective of this paper is to analyze the roughness data collected from the LTPP database for jointed reinforced concrete pavement (JRCP) and develop roughness prediction models employing the ANN modeling technique. Furthermore, this study evaluates the accuracy of the developed ANN model using statistical measurements by performing a sensitivity analysis.

2 LITERATURE REVIEW

Relatively few smoothness (IRI) models were developed for JRCP pavements. Some models were developed only for specific states of a specific area. The FHWA RPPR study (MEPDG 2002) investigated the effect of distress on both serviceability (PSR) and smoothness (IRI) for JRCP. The model developed for IRI as part of the RPPR study is shown in Equation 1:

$$IRI^2 = 99.59 + 2.6098 * FaultTT + 2.2802 * T - crack^3 + 1.8407 * Spall \quad (1)$$

$R^2 = 0.61$, $SEE = 64.11$ in/mile, $N = 1441$ Where, IRI = International Roughness Index, in/mile; Fault TT = total accumulated joint faulting, in/mile; T-crack = amount of transverse cracking, number of cracks per mile; Spall = percentage of joints spalled. There were several models developed for concrete and flexible pavements using different modeling techniques. Ziari et al. (2016) developed a model predicting IRI using data collected from the LTPP database employing ANN and group method of data handling (GMDH) techniques. The study modeled IRI for both flexible and rigid highway pavements employing a large 9-100-50-30-1 ANN model in addition to other ANN models. The study used the ANN model for both short- and long-term IRI predictions. Jaafar (2019) developed models for predicting IRI for asphalt pavements using ANN modeling techniques employing data extracted from the LTPP database. The ANN model (7-5-1 structure; 7 inputs, 5 hidden nodes, 1 output) had a high coefficient of correlation (R) of 0.72. This study of pavement performance models of asphalt pavement is the first study that embedded M&R intervention compared to the above literature review. The literature review indicates that the M&R history was not considered in the concrete pavement condition deterioration progression modeling. Therefore, this paper considered M&R history for developing performance models for the jointed reinforced concrete pavements. The independent variables used in the previously developed models are mostly distress, age, and environmental data. However, for future prediction of IRI, these distresses need to be predicted as well. The performance models developed in this paper will predict the IRI values using easily available variables that will help the local and state agencies to prepare M&R programs and budgets without estimating distresses in future years.

3 MODEL DEVELOPMENT

3.1 Data collection

The LTPP program was established during 1987-1991 under the Strategic Highway Research Program (SHRP) of the National Academy of Science. The program monitor and collect pavement performance data and have the most comprehensive pavement performance database. The LTPP program has two vital classes: General Pavement Study (GPS) and Specific Pavement Studies (SPS).

The LTPP data is collected at different spatial locations that exhibit values that are different across the LTPP regions. The LTPP climate zone classification map was created during the initial recruitment phases of the LTPP test sections (Jaafar 2019), which indicates spatial and temporal variability that applied to the collected pavement attributes. Four different climates zones were identified namely wet, freeze, wet, non-freeze, dry, freeze, and dry, non-freeze zones.

The data were collected from the LTPP database of JRCP, which is GPS-4. A total of 49 GPS-4 JRCP pavement sections are included in the LTPP that are located throughout the United States. The IRI measurements are from 1989 to 2017. By averaging the IRI value from one run, a dataset was created which has 577 data points. Figure 1 shows the spatial map of JRCP sections included in the LTPP database. JRCP sections included in the LTPP database are located in two climatic regions (Wet, Non-Freeze, and Wet, Freeze). 36.37% (18 of 49) sections are in the wet, non-freeze climatic region and 63.27% (31 of 49) sections are in the wet, freeze climatic region.

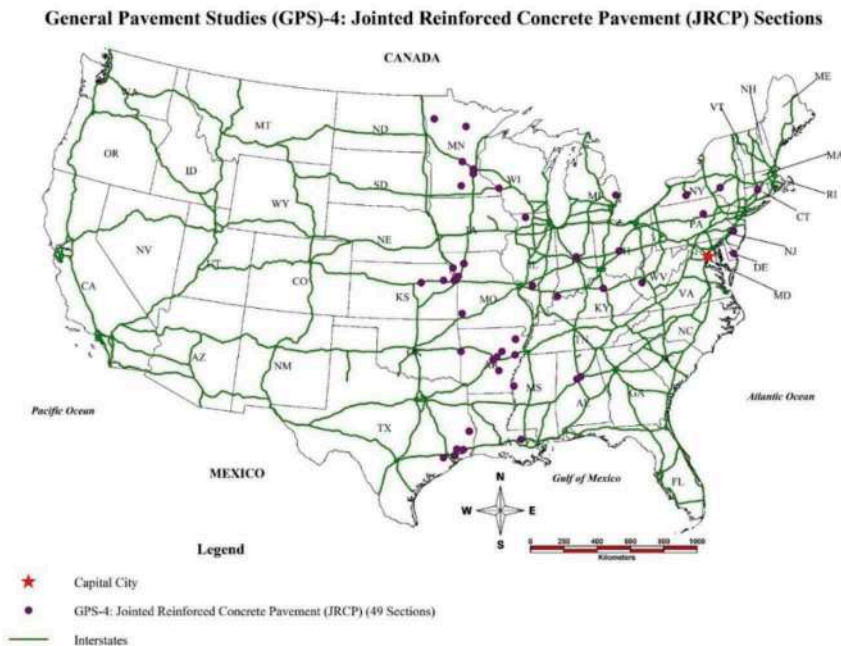


Figure 1. Spatial map of JRCP sections in the USA.

3.2 Database development

The database was developed by collecting data from the LTPP database. The output variable, IRI measurements were collected first and all input variables were collected corresponding to the IRI measurement data. The output and input variables are discussed in this section.

3.2.1 Output variables

International Roughness Index (IRI) is considered as the output variable in the pavement performance modeling process for this research. IRI measurements included IRI measured at left (inside) wheel path and IRI measured at right (outside) wheel path. Jaafar (2019), Sultana et al. (2021), and Barros et al. (2021) found that the IRI outside wheel path (m/km) is significantly higher than IRI inside wheel path (m/km) for highway pavements. Hence, IRI outside wheel path (m/km) was used as the output variable for JRCP performance model development. Figure 2 shows the IRI measurements for outside wheel path.

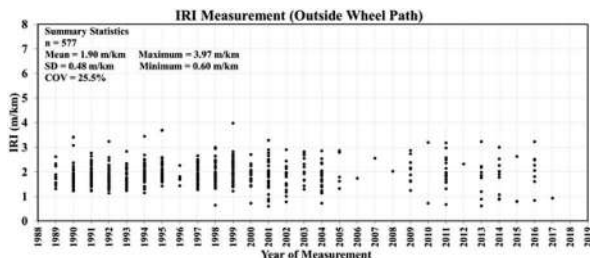


Figure 2. IRI measurement (Outside Wheel Path) of JRCP sections.

3.2.2 Input variables

An input or independent variable is also known as a predictor variable is used to predict the output variable. Pavement performance is affected by several factors such as pavement structure, climate, traffic, and maintenance over the years. An extensive literature review was done to identify the key input variables that influence pavement performance. Sultana et al. (2021) found that the input variables related to pavement structure, traffic, and M&R history can successfully predict performance (i.e., IRI) for jointed plain concrete pavement (JPCP). This study used the same variables to develop the pavement performance model for JRCP. The input variables were collected from the LTPP database corresponded to the output variable (IRI outside wheel path) measurement taken date (visit date). The relationship between each input variable and output variable (IRI outside wheel path) was studied by creating several plots. Figure 3 shows several plots of IRI (outside wheel path) (m/km) and major input variables.

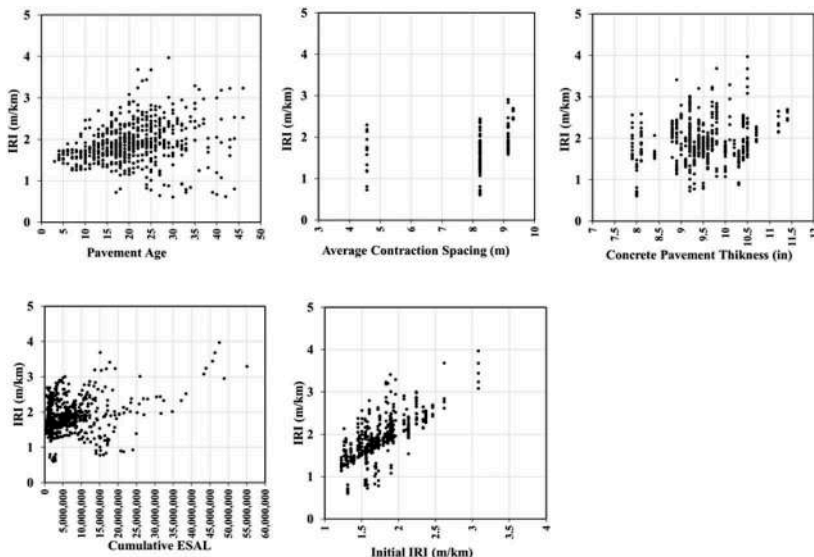


Figure 3. Independent variables versus IRI (Outside Wheel Path).

In the LTPP database, the Maintenance and Rehabilitation (M&R) sequence is denoted by the construction number (CN). In the LTPP study, a test section on the road network was assigned CN1 when it was opened to the traffic. When the first M&R treatment was conducted, the construction number changed to CN2. The CN values increase as a result of more frequent M&R treatments. Generally, the M&R treatment intervention improves the pavement condition. This study considered CN for developing performance models of concrete pavements.

Table 1. Descriptive statistics of input variables.

Statistics	Mean	SD	COV	Maximum	Minimum	Correlation with IRI (outside wheel path), r
Initial IRI (Outside Wheel Path) (m/km)	1.743	0.330	18.95%	3.083	1.226	0.728
Age	20	8	40.89%	46	3	0.251
Concrete Pavement Thickness (in.)	9.5	0.733	7.72%	11.4	7.9	0.249
Base/Subbase Thickness (in)	5.6	2.777	49.66%	15	0	0.017
Average Contraction Spacing (m)	13.80	4.483	32.49%	23.84	4.57	0.187
Cumulative ESAL	7148272	7686590	107.53%	55100663	256750	0.285

Notes: Coefficient of Variation (COV);

A correlation analysis was performed to obtain the Pearson correlation coefficient (r) between input and output variables. The correlation matrix summarizes the correlation coefficient (r) values and it is easy to observe if the variables are linearly associated with the output variable, IRI (outside wheel path). It is important to note that this correlation coefficient (r) only provides a linear association between variables, if the data is not linearly correlated it will have a low correlation value. Table 1 summarizes the descriptive statistics of input variables used in this study and the correlation between each input variable and the output variable (IRI outside wheel path). The three highest correlations between input variables and IRI outside wheel path (m/km) were observed with the variable initial IRI (outside wheel path) (m/km) (0.728) followed by cumulative ESAL (0.285), and age (0.251). Other variables show low correlation coefficient (r) values, which means they are not linearly correlated with the output variable. However, these variables might follow a non-linear correlation with IRI outside wheel path (m/km) that cannot be identified by the correlational analysis. Therefore, even though some correlation coefficient values were low, all input variables were used in this study for the development of ANN models.

Some variables were dummy coded as 0 and 1 for modeling purposes and they are noted as categorical variables. The base/ subbase materials, climatic regions, and CN_Code were categorical variables used in this study. The base/subbase materials represent the type of base/subbase materials used in the pavement section which consists of two types, unbound (granular) or bound (stabilized). The climatic region represents the climate zones defined by the LTPP which consists of two different regions for JRCP: wet non-freeze and wet freeze. The CN_Code used in this model is based on the original CN collected from the LTPP database. No M&R action was assigned as 0 and M&R actions were assigned as 1.

4 ANN MODEL DEVELOPMENT

4.1 Overview of ANN

The artificial neural network is a powerful computational tool, in which highly interconnected processing neurons work together to investigate and solve a complex problem in a nontraditional

manner (Lin 2003). The architecture of a typical ANN consists of some nodes that are usually arranged in layers such as an input layer, hidden layers, and an output layer. Multilayered neural networks have more than one hidden layer. ANNs are a proven alternative to conventional function approximation methods, which are very often limited by strict assumptions of normality, linearity, and variable independence (Hossain 2019). ANNs offer some advantages such as they can implicitly detect complex nonlinear relationships between dependent and independent variables and all possible interactions between predictor variables.

The comparison among developed ANN networks is done using three statistical accuracy measures. The three measures are the Coefficient of Determination (R^2), the Mean Absolute Relative Error (MARE), and the Average Square Error (ASE). The statistical measures of the network producing the minimum values of ASE and MARE and the highest R^2 indicate a level of agreement between predicted and actual output values. The ASE and MARE value is computed by Equations 2 and 3, respectively (Yasarer 2020):

$$ASE = \frac{\sum_{i=1}^N \sum_{j=1}^n (Y_{ij}^P - Y_{ij}^O)^2}{N.n} \quad (2)$$

$$MARE = \frac{\sum_{i=1}^N \sum_{j=1}^n \left| \frac{Y_{ij}^P - Y_{ij}^O}{Y_{ij}^O} \right|}{N.n} \quad (3)$$

Where, Y_{ij}^P = Predicted output; Y_{ij}^O = Actual output; N = number of datasets; and n = number of outputs.

4.2 ANN methodology

The development of the ANN model includes four sequential stages. The ANN architecture is determined based on parameter characteristics and ANN knowledge in the first stage. In this step, the datasets are divided into three different sub-datasets: training, testing, and validation. The datasets that include minimum and maximum values of each variable were included in the training phase for the network to represent the characteristics of the response. The maximum and minimum ranges of each input/output variable for ANN model development were chosen on purpose to be wider than their actual ranges for better mathematical mapping (Yasarer and Najjar 2011). In Yasarer's study, the network was trained and tested, in the second stage using the optimum number of hidden nodes and iteration, attained from the first stage (Yasarer 2010). The best performing networks are determined in this stage based on the lowest ASE, lowest MARE, and highest R^2 values. The best performing network obtained from the second stage was validated using validation sub-datasets in the third stage. The best performing network attained from the second stage was retrained using all the data, in the fourth stage (Yasarer 2010). Normally, retraining the network with all experimental data is expected to provide reliable predictions and overall better accuracy measures. However, it has been shown through several research studies (Yasarer 2010, Yasarer and Najjar 2011, Najjar 1999) that stage four is recommended to arrive at a better performing network model. In this research, the development of ANN models was carried out using the ANN TRSEQ1 computer program (Najjar 1999).

4.3 ANN model network selection

The inputs for the model are initial IRI, age, concrete pavement thickness, base/subbase thickness, average contraction spacing, CESAL, base/subbase materials type, climatic region, and construction number and the output is IRI (outside wheel path) (m/km). Four model networks were chosen after training and testing to compare the accuracy of the models after validation and all data. Table 2 shows the statistical accuracy of the four chosen networks. Based on the ASE, MARE, and R^2 , the chosen best model network is 11-19-20000 (Input Variables-FinalHN-Iteration). The best network's ASE values for training, testing, validation, and all data are

0.00395, 0.00465, 0.00413, and 0.00089, respectively. Though three other model networks have lower ASE in the validation dataset, the chosen best model network has the lowest ASE in testing, training, and all data. R^2 values for this model are as follows: 0.953 for the training, 0.695 for the testing, 0.720 for the validation, and 0.934 for all data. The chosen model network's R^2 value is highest for training, testing, and all data. The final architecture of this model is 11-19-1, where 11 is the number of inputs, 19 is the number of hidden nodes and 1 is the number of output.

Table 2. Statistical accuracy measures of four chosen model networks.

InitialHN-FinalHN-Iteration		Best Model 11-19-20000	3-19-20000	6-17-20000	7-15-20000
Training	MARE	4.871	5.464	5.569	6.039
	R^2	0.953	0.943	0.938	0.935
	ASE	0.00395	0.00450	0.00614	0.00520
Testing	MARE	8.226	8.304	10.444	10.365
	R^2	0.695	0.673	0.562	0.630
	ASE	0.00465	0.00536	0.00705	0.00620
Validation	MARE	8.501	8.084	9.188	9.039
	R^2	0.720	0.771	0.738	0.761
	ASE	0.00413	0.00333	0.00404	0.00344
All Data	MARE	4.841	5.221	5.930	5.769
	R^2	0.934	0.927	0.910	0.909
	ASE	0.00089	0.00098	0.00120	0.00122
Final Structure (Input Variables-FinalHN- Output Variable)		11-19-1	11-19-1	11-17-1	11-15-1

Note: HN = Hidden Nodes

4.4 ANN model results

The discussion in the previous section demonstrates that 11-19-20000 (InitialHN-FinalHN-Iteration) is the best performing network based on all statistical measures (ASE, MARE, and R^2 value). The final model structure has 11 inputs of independent variables, 19 hidden nodes, and 1 output (11-19-1). The comparison of the prediction accuracy measures for the best ANN model is graphically presented in Figure 4. The predicted IRI has apprehended most of the variability in the IRI observed values.

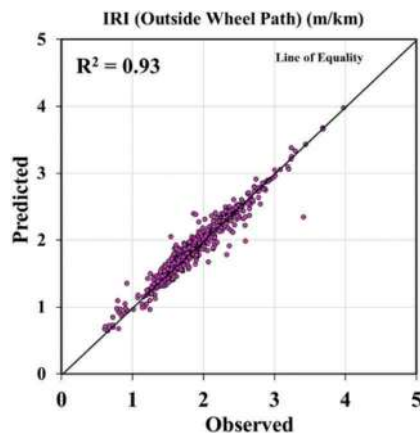


Figure 4. Observed IRI (Outside Wheel Path) (m/km) vs. predicted IRI (Outside Wheel Path) (m/km).

Figure 5 shows the observed and predicted IRI for section 20-4052, in Kansas and section 29-5081, in Missouri. The predicted values follow the observed values closely. The difference in the mean values of observed and predicted is 1.1% in section 20-4052 and 0.12% in section 29-5081.

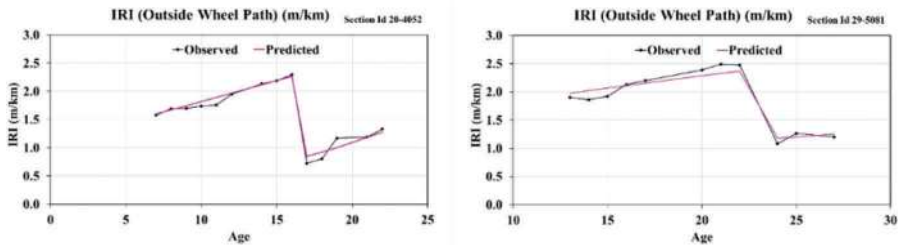


Figure 5. Observed and predicted plots of IRI (Outside Wheel Path) (m/km) for section 20-4052 in Kansas and section 29-5081 in Missouri.

5 SENSITIVITY ANALYSIS

A sensitivity analysis was carried out to evaluate the significance of the inputs on the output. A Graphical User Interface (GUI) was developed by importing all the final ANN model parameters into an excel spreadsheet. To examine the models, some input was changed while keeping the other inputs constant. In this paper, the sensitivity analysis of the developed model is presented. All inputs were kept constant except age and CESAL that were changed to generate future predictions of IRI. The future year's CESAL values were calculated using the previous year's data. Two randomly selected sections (Section 20-4052 in Kansas and Section 29-5081 in Missouri) with one M&R action done was used to show the sensitivity analysis. Figure 6 and Figure 7 show that the IRI prediction model follows the trend of the observed values. Additionally, it can estimate the increase of IRI values with time and decrease of IRI value after M&R action. Usually, without any rehabilitation, pavement deteriorates over time, therefore, predicted IRI increases as CESAL increases.

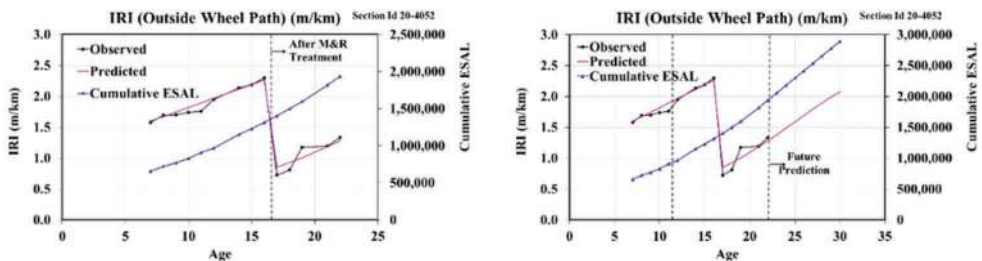


Figure 6. ANN future prediction plot of IRI (Outside Wheel Path) (m/km) for section 20-4052 in Kansas.

6 CONCLUSIONS

The concluding remarks are summarized below:

- (1) The LTPP database contained 49 JRCP sections under the GPS-4 study. All the pavements are in the wet, freeze and wet, non-freeze climatic regions.
- (2) The best performing ANN model has a network structure of 11-19-1 (i.e., 11 inputs, 19 hidden nodes, and 1 output). The ANN model to predict IRI has an R^2 value of 0.93. The total data points used to develop the IRI prediction ANN model were 577.

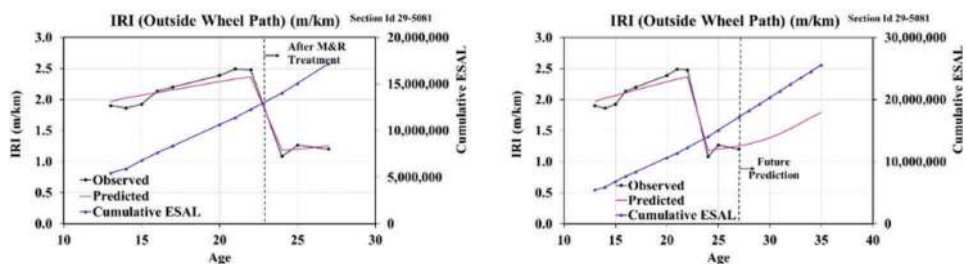


Figure 7. ANN future prediction plot of IRI (Outside Wheel Path) (m/km) for section 29-5081 in Missouri.

- (3) The developed IRI prediction model can successfully characterize the behavior (i.e., the increase of IRI values with time as CESAL increases and decrease of IRI value after maintenance and rehabilitation).
- (4) The ANN model developed in this research used easily available independent variables. The developed model can predict the IRI values without using distress data that will help the local and state agencies to prepare M&R programs and budgets without estimating distresses in future years. The only variable needing to be estimated is CESAL data. The agency can use the historical traffic data for a particular pavement and project the future traffic data based on the annual traffic growth rate for the highway to provide this input.

REFERENCES

- Barros, R., Yasarer, H. I., Uddin, W., Sultana, S. (2021). Roughness Modeling for Composite Pavements using Machine Learning. will be published at 6th World Multidisciplinary Civil Engineering-Architecture-Urban Planning Symposium - WMCAUS 2021, Prague (Czech Republic), 30 August - 3 September 2021.
- Bayrak, M. B., Teomete, E., and Agrawal, M. (2004). Use of Artificial Neural Networks for Predicting Rigid Pavement Roughness, Midwest Transportation Consortium Fall Student Conference, Ames, Iowa.
- El-Hakim, R.A. El-Badawy, S. (2013). "International Roughness Index Prediction for Rigid Pavements: An Artificial Neural Network Application", *Advanced Materials Research*, Vol 723, pp. 854–860.
- Jaafar, Z. F. M. (2019). "Computational Modeling and Simulations of Condition Deterioration to Enhance Asphalt Highway Pavement Design and Asset Management." *Ph.D. Dissertation*, University of Mississippi.
- Lin, J., Yau, J.-T., and Hsiao, L.-H. (2003). "Correlation Analysis Between International Roughness Index (IRI) By." *Transportation Research Board 82th Annual Meeting*, (January), 1–21.
- Najjar, Y. M. and Mryyan, S. (2009). "ANN-Based Profiling: Data Importance," *Intelligent Engineering Systems through Artificial Neural Networks*, Vol. 19, pp. 155–162.
- Najjar, Y. (1999). *Quick Manual for the Use of ANN program TRSEQ1*. Manhattan, Kansas.
- Oh, Han Jin, Young Park, J., Bae Kim, H. Kyong Jung, W., and Hun Lee, J. (2019) Performance Evaluation of JPCP with Changes of Pavement Mix Design Using Pavement Management Data. *Advances in Civil Engineering*, Volume 2019, Article ID 8763679, 10.1155/2019/8763679.
- Sayers, M. W., Gillespie, T. D., and Queiroz, C. A. V. (1986). "International Road Roughness Experiment: a Basis for Establishing a Standard Scale for Road Roughness Measurements." *Transportation Research Record*, 76–85.
- Sultana, S., Yasarer, H. I., Uddin, W., Barros, R. (2021). International Roughness Index Modeling for Jointed Plain Concrete Pavement using Artificial Neural Network. will be published at 6th World Multidisciplinary Civil Engineering-Architecture-Urban Planning Symposium- WMCAUS 2021, Prague (Czech Republic), 30 August- 3 September 2021.
- TRB. (2002). "Development of the 2002Guide for the Design of New and Rehabilitated Pavement Structures: Phase II." NCHRP 01-37A, *Transportation Research Board (TRB)*. <http://apps.trb.org/cmsfeed/TRBNetProjectDisplay.asp?ProjectID=218> Accessed 9 September 2015.

- Yasarer, H. and Najjar, Y. (2011). Development of a Mix-Design Based Rapid Chloride Permeability Assessment Model Using Neuronets. Proceedings of *International Joint Conference on Neural Networks*, San Jose, California, USA.
- Yasarer, H. I. (2010). Characterizing the Permeability of Concrete Mixes Used in Transportation Applications: A Neuronet Approach, Master's Thesis, Kansas State University, Manhattan, KS, 2010. 105 pp.
- Yasarer, H., Oyan, M. N. S., and Najjar, Y. (2020). "A Performance Prediction Model for Continuously Reinforced Concrete Pavement Using Artificial Neural Network." Proceedings of the 9th International Conference on Maintenance and Rehabilitation of Pavements—Mairepav9, 771–782.
- Ziari, H., Sobhani, J., Ayoubinejad, J., and Hartmann, T. (2016). "Prediction of IRI In Short and Long Terms for Flexible Pavements: ANN and GMDH Methods." *Int. J. Pavement Eng.* 17 (9): 776–788. <https://doi.org/10.1080/10298436.2015.1019498>.

Composite pavement roughness modeling for LTPP wet freeze climate region using machine learning

R. Barros, H. Yasarer, W. Uddin, S. Sultana & Y. Najjar

Department of Civil Engineering, University of Mississippi, Oxford, Mississippi, USA

ABSTRACT: Objective decisions related to the management of road networks are based on important measures of pavement performance. The International Roughness Index (IRI) is a critical indicator of pavement performance, and it is considered the standard for pavement roughness. A reliable pavement performance prediction model is needed to predict future pavement conditions and identify maintenance and rehabilitation (M&R) needs. This study intends to develop pavement roughness models using the Artificial Neural Networks (ANNs) approach for composite (asphalt overlay on concrete) pavements using the Long-Term Performance Pavement (LTPP) program database for the Wet-Freeze climate region. A total of 186 pavement sections with 1,930 data points were analyzed. Five models were developed using different independent variables (i.e., Initial IRI_{Right}, Age, Seasons, Asphalt Thickness, Concrete Thickness, Subbase Thickness, Subbase Type, Construction Number (CN), Cumulative Equivalent Single Axle Load (CESAL), Air Temperature, Freeze Index, Freeze-Thaw, and Precipitation) and one dependent variable (i.e., IRI_{Right}). The best-performing model was selected based on the lowest average square error (ASE), lowest mean absolute relative error (MARE), and highest coefficient of determination (R^2). Results showed that the developed models had satisfactory results with a good fit of observed and predicted data. Therefore, local and state agencies can use the developed ANN roughness models as a tool for better condition assessment and effective M&R scheduling. Furthermore, the use of available climatological and historical traffic data to predict IRI changes will also eliminate time-consuming data collection and processing, accordingly, reducing costs.

Keywords: International Roughness Index (IRI), Artificial Neural Network (ANN), Long-Term Pavement Performance (LTPP), composite pavement, wet freeze

1 INTRODUCTION

A large portion of the paved highways in the U.S. comprises composite pavements. This type of pavement is commonly a result of concrete pavement rehabilitation, where an asphalt layer is overlaid on a concrete surface (Chen et al. 2015). In the U.S., pavement performance models are required for state highway agencies to assist in their pavement management decision-making processes (Kaya et al. 2020). Performance models bring key features to a successful pavement management system (PMS) (Elhadidy et al. 2021) providing an estimation of pavement conditions and rehabilitation needs and allowing agencies to prioritize road sections that are in the worst conditions. Performance models are easy to understand and can provide deeper insights converting performance indices into operational measures to inform how long and how well the road will continue to serve the users (Kaya et al. 2020). Numerous pavement performance indices have been developed in the last three decades; however, the international roughness index (IRI)

is the most well-recognized performance index (Bashar and Torres-Machi 2021; Zeiada et al. 2020). The IRI expresses the irregularities in the pavement surfaces that affect the ride quality, and it is useful for making objective decisions related to the management of road networks (Jaafar 2019a; Sayers et al. 1986).

Pavement performance modeling is a challenging task due to the complexity of the pavement structure and its responses under traffic loading, dynamic weather and climate changes, variability in construction activities, and the interaction among all these elements (Gupta, Ankit; Kumar, Praveen; Rastogi 2012). Advanced modeling techniques such as artificial neural networks (ANNs) have been used successfully in several studies offering significant improvements over traditional techniques (i.e., linear regression) by processing large volumes of data with excellent accuracy. However, several performance models in the literature use the Long-Term Performance Pavement (LTPP) database to develop models without considering specific conditions of local climate and geography, which makes the model less accurate.

Therefore, this paper proposes the development of pavement roughness prediction models to study the performance of composite pavements using the ANN approach according to the specific climate and geographical conditions (wet freeze climate zone), pavement structure, and traffic data using the LTPP database.

1.1 Objectives

The major objectives of this paper are to:

- (1) Analyze roughness data for composite pavement sections in the wet freeze region using the LTPP database.
- (2) Use the ANN approach to develop roughness models for composite pavements in the wet freeze region of the LTPP database using different independent variables.
- (3) Evaluate the accuracy of the ANN models using statistical measurements to identify the most accurate model.
- (4) Perform a model comparison among the developed models using two random sections of the database to identify the best-performing model.

2 LITERATURE REVIEW

The literature review shows that a remarkable number of researchers have used ANN to predict pavement roughness. Tennant Duckworth (2020) and Yasarer et al. (2020) developed pavement performance prediction models for flexible and continuously reinforced concrete pavement (CRCP) sections, respectively, using the ANNs approach based on the Mississippi Department of Transportation (MDOT) database. Both papers concluded the ANN model successfully predicted roughness values and could be used for pavement performance prediction.

Hossain et al. (2019) and Hossain et al. (2020) also developed ANN roughness prediction models for flexible and concrete pavements, respectively, but using climate and traffic data collected from the LTPP database. The studies used data from the wet freeze climate zone for flexible pavements and wet non-freeze for rigid pavements. An RMSE of 0.027 and 0.01 were found for the flexible and rigid ANN models, respectively, indicating that the IRI prediction was reasonable for both short-term and long-term predictions.

Jaafar (2019a) and Jaafar (2019b) developed IRI prediction models for asphalt pavements using multiple linear regression and ANN modeling approaches using all the LTPP database and the Western region of the LTPP database, respectively. The ANN model showed a high coefficient of correlation (R) of 0.72 and 0.85, respectively, showing promising results for IRI predictions in asphalt pavements. For flexible and composite pavements, Kaya et al. (2020) used the Iowa database to develop ANN-based models that were found to be good tools for

predicting pavement deterioration when there were many pavement sections with various traffic, thickness, and other various deterioration trends.

The literature shows ANN models successfully predicted IRI values for asphalt, concrete, and composite pavements. However, composite pavements have not been well investigated, especially the effects of traffic and climate variables for a specific climate region of the LTPP database. Since each location has its local climate and specific characteristics, it is necessary to use data from an individual region to assist the performance models to be more accurate. Hence, this paper develops a pavement roughness prediction model using the ANNs approach for composite pavement sections using data from the wet freeze climate zone of the LTPP database.

3 MODEL DEVELOPMENT

3.1 Data collection

The LTPP program created in 1987 to collect and store performance data over several years was used as the database for the data analysis in this study. The LTPP program was developed to support analysis and product development, analyze the collected data to describe pavement performance, and translate these insights into usable engineering products related to pavement design, construction, rehabilitation, maintenance, preservation, and management. The data collection started in 1989, and 2,509 pavement test sections from 51 U.S. states and ten Canadian provinces were selected or constructed for the program. The LTPP developed a climate zone classification that included four different zones identified as wet freeze, wet non-freeze, dry-freeze, and dry non-freeze zones (FHWA 2019; Jaafar 2019a). The LTPP used the precipitation per year to identify wet (higher than 508 mm) and dry (lower than 508mm) climate zones. For freeze and non-freeze climate zones, the LTPP used a threshold based on an annual average freezing index of 83 °C (150 °F) days. Locations with an index over this threshold were classified in the freeze zone and those under the threshold in a non-freeze climate zone (FHWA 2019).

A total of 264 composite sections where the asphalt layer thickness over the concrete layer is equal to or greater than three inches were found using the LTPP database. For this study, only composite pavement sections located in the wet freeze climate zone were used. A total of 186 pavement sections with 1,930 data points were used for the analysis.

3.2 Data processing

To construct the database used in this study, all the variables were retrieved from the LTPP database. The data processing for output and input variables is described in this section.

3.2.1 Output variables

The IRI is accepted as one of the most important indicators of pavement performance and used as the standard for pavement roughness, and it was used as the output variable for modeling. Each section in the database had two types of IRI measurements: IRI inside wheel path (IRI_{Left}) and IRI outside wheel path (IRI_{Right}). Several IRI measurements were done on each visit date for each section. By averaging the IRI measurement runs, a single IRI measurement was obtained for IRI_{Left} and IRI_{Right} for each visit date. By doing this, a total of 1,930 IRI measurements from 1989 to 2018 were found for the 186 sections.

IRI measurements for IRI_{Right} (1.27 m/km or 80.5 in./mile) were 8% greater than the IRI_{Left} (1.18 m/km or 74.8 in./mile), which agreed with previous research (Barros et al. 2021a; b; Jaafar 2019a; Sultana et al. 2021a; b). An independent samples t-test was used to determine whether IRI_{Right} and IRI_{Left} differ on average from each other. The t-test result shows that the difference in the means of IRI_{Right} and IRI_{Left} is statistically significant at α 0.05 probability of chance error implying that both samples are from different populations. Therefore, this study used IRI_{Right} as a dependent variable since it shows the highest value for pavement roughness.

3.2.2 Input variables

For the input variables, the literature shows that pavement structure, climate, traffic, and maintenance are key variables to account for pavement deterioration. This research used some variables that were already studied in the literature but introduced new variables that were found to help the model to achieve better results. An important step of modeling is to identify how the input variables relate to the output variable. Figure 1 shows plots of each input variable versus IRI_{Right} . Two variables used in this study are categorical variables (CN_{Code} , subbase type), which have fixed values of 0 or 1 for modeling purposes and were not included in Figure 1.

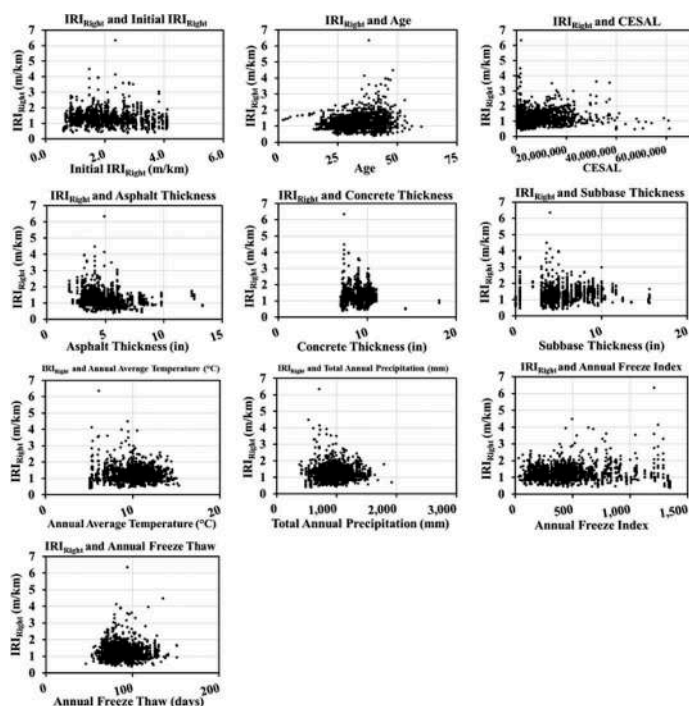


Figure 1. Independent variables versus IRI_{Right} .

Table 1 shows a summary of the descriptive statistics of input variables and the correlation between each input variable and the output variable (IRI_{Right}). A correlation test was performed to obtain the Pearson correlation coefficient (r) among all variables. The correlation analysis provides the linear association between the output and the proposed input variables. Hence, if the data analyzed do not have a good linear correlation, the coefficient will show low values.

The three highest correlations were observed with the variable “ CN_{Code} ” (0.21) followed by a negative correlation with “surface asphalt thickness” (-0.21), and “age” (0.20). Other variables indicate low linear correlation values, implying they are not linearly correlated with IRI_{Right} . However, these variables might follow a non-linear correlation that cannot be identified by the correlational analysis. Therefore, even though the correlation was low in some cases, all independent variables were used for the development of ANN models.

Table 1. Descriptive statistics of input variables.

Input Variable	Mean	Standard Deviation	COV (%)	Max.	Min.	r (IRI _{Right})
IRI ₀ , Initial IRI Right (m/km)	1.90	0.83	43.7%	4.1	0.60	0.058
Age	32.63	7.77	23.8%	60.0	2.00	0.199
CESAL	7649125	8113176	1.06	61276201	35566.00	0.059
Surface Asphalt Thickness (in)	5.13	1.88	36.6%	13.3	1.90	-0.214
Concrete Thickness (in)	9.25	1.05	11.4%	18.1	7.00	-0.079
Subbase Thickness (in)	5.18	2.67	51.5%	15.6	0.00	0.058
Annual Average Temperature (°C)	10.07	1.93	19.2%	15.3	5.10	-0.008
Total Annual Precipitation (mm)	966.58	218.80	22.6%	1919.5	377.40	-0.015
Annual Freeze Index	458.10	270.40	59.0%	1345.0	28.00	0.067
Annual Freeze-Thaw (days)	87.33	15.00	17.2%	151.0	46.00	0.006
IRI Right (m/km)	1.25	0.45	35.6%	6.4	0.39	1.000

Notes: Coefficient of Variation (COV); Pearson Correlation with IRI_{Right} (r (IRI_{Right}))

4 ANN DEVELOPMENT

ANNs are a predictive modeling technique based on mathematical models built to simulate the neural structure of a human brain using the concept of human cognition and neural biology (Najjar and Huang 2007). The neural networks can successfully represent complex relationships that are difficult to be identified using traditional sequential, logic-based modeling, and computational techniques (Najjar and Huang 2007).

A feedforward neural network with a back-propagation training algorithm was used for the development of the roughness prediction model in this study. A one hidden layer network was considered in the model development since the use of more than one hidden layer may cause the network to memorize the data in the training phase (Yasarer 2010). A sigmoidal function was used for data generalization purposes and the TR-SEQ1 computer program (Najjar 1999) was used to develop the ANN models.

4.1 ANN model architecture

For this paper, five models were developed using different independent variables and IRI_{Right} as the dependent variable. Table 2 shows the independent variables used for each ANN model.

Model 1 used 8 input variables; however, the “granular subbase,” “treated seasons,” and “CN_{Code}” are categorical variables. The “CN_{Code}” is a categorical variable that represents M&R interventions in the pavement structure. A value of 1 is assigned when an M&R intervention was performed. If there was no M&R intervention, a 0 value was assigned. Model 2 used 9 input variables, including an input variable responsible for traffic loads, CESAL. Model 3 used 13 input variables including four more variables that represent the season in which each test was performed in the section. It consists of four seasons spring (March, April, May), summer (June, July, August), autumn (September, October, November), and winter (December, January, February), and represents the effect of climate and season on pavement deterioration. Model 4 used 11 input variables including “air temperature” and “precipitation” to account for the climate effects on the pavement. Model 5 used 13 input variables and included “freeze index” and “freeze-thaw” to account for the effect of lower temperatures on pavement performance. All variables used in this study are not related to distress data and are easily available for federal and state transportation agencies.

Table 2. Input variables configuration for five ANN models.

No.	Model 1	Model 2	Model 3	Model 4	Model 5
1	IRI ₀	IRI ₀	IRI ₀	IRI ₀	IRI ₀
2	Age	Age	Age	Age	Age
	-	-	Winter (Dec-Feb)		
3	-	-	Spring (Mar-May)		
	-	-	Summer (June-Aug)		
	-	-	Autumn (Sept-Nov)		
4	Granular Subbase	Granular Subbase	Granular Subbase	Granular Subbase	Granular Subbase
5	Treated Subbase	Treated Subbase	Treated Subbase	Treated Subbase	Treated Subbase
6	CN _{Code}	CN _{Code}	CN _{Code}	CN _{Code}	CN _{Code}
7	-	CESAL	CESAL	CESAL	CESAL
8	$h_{asphalt}$	$h_{asphalt}$	$h_{asphalt}$	$h_{asphalt}$	$h_{asphalt}$
9	$h_{concrete}$	$h_{concrete}$	$h_{concrete}$	$h_{concrete}$	$h_{concrete}$
10	$h_{subbase}$	$h_{subbase}$	$h_{subbase}$	$h_{subbase}$	$h_{subbase}$
11	-	-	-	Air Temp.	Air Temp.
12	-	-	-	Precipitation	Precipitation
13	-	-	-	-	Freeze Index
14	-	-	-	-	Freeze-Thaw

4.2 ANN model selection

The best ANN model was chosen based on the lowest average square error (ASE), lowest mean absolute relative error (MARE), and highest coefficient of determination (R^2). Table 3 demonstrates the statistical measures of each ANN model development stage (i.e., training, testing, validation, and all data) for all developed models.

Table 3. ANN Model Results.

Model		1	2	3	4	5
Structure		4-19-20000	6-18-20000	4-19-20000	7-19-20000	8-19-20000
Training	MARE	20.09	20.19	17.39	17.03	18.11
	R^2	0.58	0.58	0.69	0.69	0.71
	ASE	0.00097	0.0010	0.0007	0.00068	0.00070
Testing	MARE	23.81	19.85	22.73	20.22	20.84
	R^2	0.34	0.51	0.32	0.53	0.44
	ASE	0.00140	0.0011	0.0016	0.00099	0.00136
Validation	MARE	26.65	20.90	25.00	19.21	22.29
	R^2	0.27	0.45	0.22	0.50	0.37
	ASE	0.00195	0.0012	0.0023	0.00099	0.00157
All Data	MARE	17.94	17.94	17.29	17.14	15.77
	R^2	0.57	0.59	0.62	0.68	0.71
	ASE	0.00087	0.00082	0.00076	0.00066	0.00059

Training, testing, and validation stages used 972, 479, and 479 data points, respectively. After developing the possible networks for each model, the all-data stage used all 1,930 data points from the database to retrain the network at its optimal structure and iteration. Therefore, the all-data stage statistics were used as the main comparison between each model. The all-data stage for model 5 outperformed the other models with more accurate measures. Hence, model 5 was chosen as the best-performing ANN model. The final model structure includes 13 input variables, one hidden layer with 19 hidden nodes, 20,000 iterations, and one output.

5 DISCUSSION

Figure 2 shows a graphical comparison of the accuracy measurements for the all-data stage among all developed models.

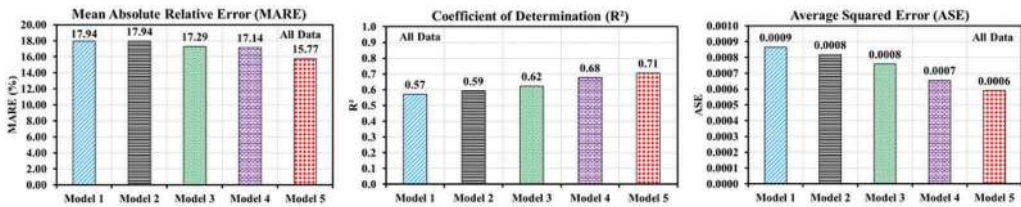


Figure 2. Graphical comparison of accuracy measures between Developed ANN models.

The accuracy measures show reliable results for all models developed. However, model 5 outperformed all other models developed in this study. Compared to models 1, 2, 3, and 4, the all-data stage of model 5 showed an ASE 32%, 28%, 22%, and 10% lower, a MARE 12%, 12%, 9%, and 8% lower, and an R² 24%, 19%, 13%, and 4% higher, respectively. Figure 3 illustrates the observed IRI_{Right} values collected from the LTPP database and the predicted values using model 5. The ANN model was capable of imitating the pavement deterioration behavior. However, some higher IRI values were not captured by the model, which predicted lower values compared to the observed IRI. Predicted values tried to cluster around the line of equality but some values were underpredicted, especially when the observed IRI_{Right} values were higher than 3 m/km; however, all values were used in the model. Nevertheless, a good R² of 0.71 was obtained for the ANN model 5.

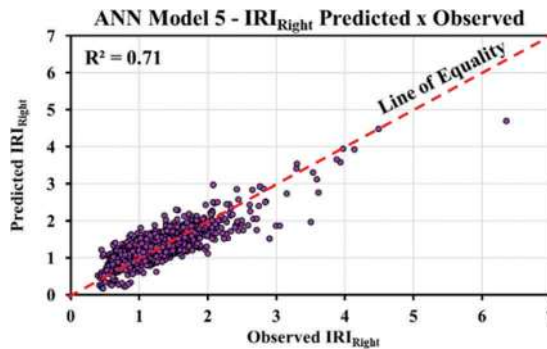


Figure 3. Observed versus predicted IRI_{Right} for ANN model 5.

6 MODEL COMPARISON

Model comparison was conducted to evaluate the performance of the developed models in two random sections of the database. IRI prediction values were generated using all models and compared with observed values. Figure 4 shows the observed versus predicted plots of IRI_{Right} for section 29-0661 in Missouri and section 46-7049 in South Dakota.

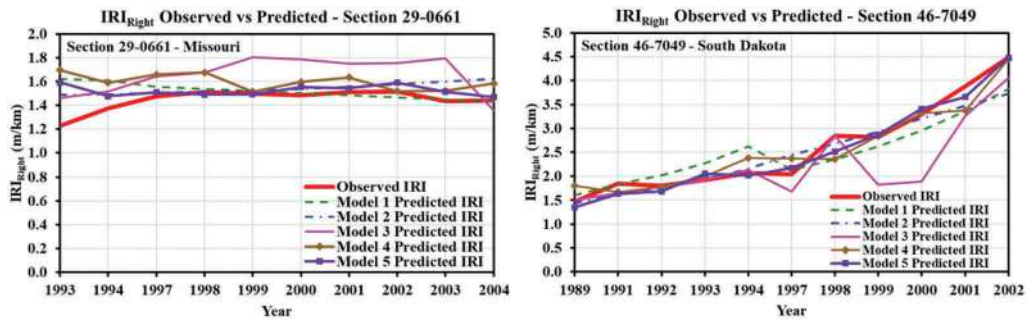


Figure 4. Observed and predicted plots of IRI_{Right} for section 29-0661 and section 46-7049.

Predicted values were close to observed values for almost all models in both sections. Model 3 was the only one to not closely follow the observed IRI_{Right} values. This might happen because model 3 was the only model to use the input variable “season,” which could cause the model to predict less accurate values. Model 5 showed the most accurate results for both sections, being the best to explain the variability in the model and capture the pavement deterioration behavior. The use of variables that represents the pavement initial condition (IRI_0), effects of pavement exposure time (age), pavement structure (thickness of asphalt, concrete, subbase, and type of subbase), the effect of maintenance and rehabilitation (CN_{Code}), the effect of traffic loads (CESAL), and climatological effects of temperature, moisture, and freeze (air temperature, precipitation, freeze index, freeze-thaw) in the same model might be the reason why model 5 had a better performance than other models that did not use all variables at the same time.

Therefore, the model comparison showed that all developed models were reasonably accurate and reliable for both analyzed sections and can be used to predict pavement roughness. Furthermore, the analysis showed that by combining all input variables in the same model, the predictions were more accurate since the model had a better understanding of the pavement deterioration behavior and translated this into more precise IRI_{Right} values. Therefore, the developed models in this study can be used as a powerful tool to predict pavement’s future condition and better M&R planning.

7 CONCLUSIONS

The concluding remarks are summarized, as follows:

- (1) The pavement roughness models for composite pavements were developed using the artificial neural networks modeling technique. The models used data collected from the LTPP database for the wet freeze climate zone.
- (2) The best-performing ANN model was selected based on the accuracy measures presented in Table 3. Model 5 outperformed all other models accounting for 71% of the variability with an R^2 of 0.71 with 13 input variables, one hidden layer with 19 hidden nodes, 20,000 iterations, and one output.
- (3) Compared to models 1, 2, 3, and 4, the all-data stage of model 5 showed an ASE 32%, 28%, 22%, and 10% lower, a MARE 12%, 12%, 9%, and 8% lower, and an R^2 24%, 19%, 13%, and 4% higher, respectively.
- (4) The ANN model could replicate the pavement deterioration behavior with reasonable accuracy. Predicted values cluster around the line of equality but some values were under-predicted, especially when the observed IRI_{Right} values were higher than 3 m/km.
- (5) Model comparison was performed for sections 29-0661 and 46-7049. Predicted values were close to observed values for almost all models in both sections. Model 5 showed to be the most accurate.

- (6) The study showed that the use of a specific climate zone combined with input variables that represent the pavement's initial condition, effects of pavement exposure time, pavement structure, effects of maintenance and rehabilitation, effects of traffic loads, and climatological effects of temperature, moisture, and freeze in the same model increased the model accuracy.
- (7) Therefore, the developed ANN model efficiently characterized the pavement roughness behavior on composite pavements and can be used by agencies as a prediction tool for IRI values and guide decision-makers to develop a better M&R plan. Furthermore, the developed model can predict IRI values without using distress data, which will result in cost reductions and more effective M&R scheduling.

REFERENCES

- Barros, R., Yasarer, H., Uddin, W., and Sultana, S. (2021a). "Roughness Modeling for Composite Pavements using Machine Learning." *IOP Conference Series: Material Science and Engineering*, 6th WMCAUS 2021.
- Barros, R., Yasarer, H., Uddin, W., and Sultana, S. (2021b). "Roughness Modeling for Asphalt Overlay on Concrete Pavements Using Neural Networks." *Transportation Research Board*.
- Bashar, M. Z., and Torres-Machi, C. (2021). "Performance of Machine Learning Algorithms in Predicting the Pavement International Roughness Index." *Transportation Research Record: Journal of the Transportation Research Board*, 036119812098617.
- Chen, C., Williams, R. C., Marasinghe, M. G., Ashlock, J. C., Smadi, O., Schram, S., and Buss, A. (2015). "Assessment of composite pavement performance by survival analysis." *Journal of Transportation Engineering*, 141(9),1–9.
- Elhadidy, A. A., El-Badawy, S. M., and Elbeltagi, E. E. (2021). "A simplified pavement condition index regression model for pavement evaluation." *International Journal of Pavement Engineering*, 22(5),643–652.
- FHWA, F. H. A. (2019). *LONG-TERM PAVEMENT PERFORMANCE Information Management System User Guide. Information Management System User Guide*.
- Gupta, Ankit; Kumar, Praveen; Rastogi, R. (2012). "A critical review of flexible pavement performance models developed for indian perspective." *Indian Highway*, 40(3),41–60.
- Hossain, M., Gopiseti, L. S. P., and Miah, M. S. (2020). "Artificial neural network modelling to predict international roughness index of rigid pavements." *International Journal of Pavement Research and Technology*, 13(3),229–239.
- Hossain, M. I., Gopiseti, L. S. P., and Miah, M. S. (2019). "International roughness index prediction of flexible pavements using neural networks." *Journal of Stomatology*, 145(1),1–10.
- Jaafar, Z. F. M. (2019a). "Computational Modeling and Simulations of Condition Deterioration to Enhance Asphalt Highway Pavement Design and Asset Management." *Ph.D. Dissertation*, University of Mississippi.
- Jaafar, Z. F. M. (2019b). "Pavement Roughness Modeling Using Regression And Ann Methods For LTPP Western Region." (June), 536–548.
- Kaya, O., Ceylan, H., Kim, S., Waid, D., and Moore, B. P. (2020). "Statistics and Artificial Intelligence-Based Pavement Performance and Remaining Service Life Prediction Models for Flexible and Composite Pavement Systems." *Transportation Research Record*, 2674(10),448–460.
- Najjar, Y. (1999). *Quick Manual for the Use of ANN program TRSEQ1*. Manhattan, Kansas.
- Najjar, Y. M., and Huang, C. (2007). "Simulating the stress-strain behavior of Georgia kaolin via recurrent neuronet approach." *Computers and Geotechnics*, 34(5),346–361.
- Sayers, M. W., Gillespie, T. D., and Queiroz, C. A. V. (1986). "International Road Roughness Experiment: a Basis for Establishing a Standard Scale for Road Roughness Measurements." *Transportation Research Record*, 76–85.
- Sultana, S., Yasarer, H. I., Uddin, W., and Barros, R. (2021a). "International Roughness Index Model for Jointed Plain Concrete Highway Pavements: An Artificial Neural Network Application." *Transportation Research Board*.
- Sultana, S., Yasarer, H., Uddin, W., and Barros, R. (2021b). "International Roughness Index Modeling For Jointed Plain Concrete Pavement Using Artificial Neural Network." *IOP Conference Series: Material Science and Engineering*, 6th WMCAUS 2021.

- Tennant Duckworth, P. (2020). "Evaluation of Flexible Pavement Performance Models in Mississippi: a Neural Network Approach." *Master Thesis*.
- Yasarer, H. (2010). "Characterizing the Permeability of Concrete Mixes Used in." *Master Thesis*, Kansas State University.
- Yasarer, H., Oyan, M. N. S., and Najjar, Y. (2020). "A Performance Prediction Model for Continuously Reinforced Concrete Pavement Using Artificial Neural Network." *Proceedings of the 9th International Conference on Maintenance and Rehabilitation of Pavements—Mairepav9*, 771–782.
- Zeida, W., Dabous, S. A., Hamad, K., Al-Ruzouq, R., and Khalil, M. A. (2020). "Machine Learning for Pavement Performance Modelling in Warm Climate Regions." *Arabian Journal for Science and Engineering*, Springer Berlin Heidelberg, 45(5),4091–4109.

Prediction of asphalt pavement responses under moving loads with non-uniform tire footprints using the Fourier finite layer method

Gustavo Canon Falla, Christiane Weise & Sabine Leischner

Institute of pavement and urban engineering, Technische Universität Dresden, Dresden, Germany

Markus Oeser

Institute of Highway Engineering, RWTH Aachen, Aachen, Germany

Frohmut Wellner

Institute of pavement and urban engineering, Technische Universität Dresden, Dresden, Germany

ABSTRACT: Multilayer theory (MLT) is one of the most widely used numerical methods for determining pavement responses. The main advantage of MLT compared to other numerical solutions is its efficiency in computational time. From the mathematical point of view, the solution of the continuum mechanics equations using MLT can be obtained by two different approaches: using Hankel transforms and using Fourier transforms. The first approach is based on the solution of an axisymmetric problem with a constant circular load expressed in the form of Hankel functions. The second approach consists of taking a two-dimensional Fourier transform of the traffic load and solving the equilibrium equation for each Fourier term. The advantage of the Fourier method over the Hankel method is that it can simulate non-circular loads, including dynamic and viscoelastic effects. The Fourier method was programmed in a software, called DynaPave, which includes state-of-the-art viscoelastic material models, such as the Olard-Di Benedetto model and the Huet-Sayegh model. In this paper, DynaPave is used to determine the viscoelastic responses of asphalt pavements under the action of moving loads. Two design cases were conducted to evaluate how the viscoelastic behavior of asphalt materials and the irregular shape of the traffic load affect the pavement responses.

Keywords: Mechanistic pavement design, pavement responses, fatigue, multilayer theory, Fourier finite layer method

1 INTRODUCTION

One of the most important elements of any mechanistic empirical (ME) methodology for pavement design is the numerical model used to predict the mechanical responses within the pavement. Existing response models differ in terms of assumptions/simplifications about material properties, tire-pavement interaction and interlayer contact conditions. Multilayer theory (MLT) is one of the most widely used numerical methods for determining pavement responses. The main advantage of MLT compared to other numerical solutions, such as the finite element method (FEM), is its efficiency in computation time. The fact that MLT provides results in tenths of a second makes this numerical technique very useful for ME pavement design, where hundreds/thousands of separate calculations are needed. In addition, it is also essential to keep

in mind that the next generation of ME methodologies will include big datasets of traffic and environmental measurements that may require millions of calculations.

From the mathematical point of view, the solution of the continuum mechanics equations through the MLT is usually obtained by means of Hankel transformations. This approach is based on the solution of an axisymmetric problem with a constant circular load expressed in the form of Hankel functions. The MLT with Hankel transformations is formulated based on several simplifying assumptions: linear elastic materials, uniform circular loading, weightless layers and static loading conditions. These intrinsic assumptions are a disadvantage of the method. Therefore, a need has arisen to develop new software that implement more accurate numerical solutions to realistically simulate tire-pavement interaction and material properties.

This paper presents a new pavement response software, DynaPave, developed in cooperation between the institute of pavement engineering of TU Dresden and the Institute of Highway Engineering of RWTH Aachen. DynaPave uses Fourier transforms to solve the multilayer problem. The advantage of the Fourier method over the Hankel method is that it can simulate non-circular loads, including dynamic and viscoelastic effects. The paper starts with a brief description of the software. Then, two case studies are presented to evaluate how the viscoelastic behavior of asphalt materials and the irregular shape of the traffic load affect the pavement responses.

2 DYNAPAVE: A FOURIER FINITE LAYER SOFTWARE FOR THE SIMULATION OF MOVING LOADS ON FLEXIBLE PAVEMENTS

The German guideline for ME asphalt pavement design, RDO-Asphalt [6], uses PaDesTo [10] and Ad2Pave [1] software as the numerical kernel for determining pavement responses. These computer programs are based on axisymmetric multilayer elastic theory with Hankel transformations (MLTH). To overcome the limitation of the MLTH, a software called DynaPve was introduced. DynaPave uses the multilayer theory with Fourier transforms (MLTF). The procedure consists of taking a two-dimensional Fourier transform of the surface load and solving the equilibrium and continuum equations in the frequency domain for each Fourier harmonic used to describe the load. With the MLTF it is possible to handle complex surface loads, different vehicle velocities and dynamic and viscoelastic effects.

In DynaPave the pavement structure is considered as a semi-infinite multilayered system composed of n horizontal layers stacked in the vertical direction. In a stationary coordinate system the x coordinate corresponds to the longitudinal/traffic direction, the y coordinate is used for the transverse direction, and the z coordinate for the vertical/depth direction, as seen in Figure 1.

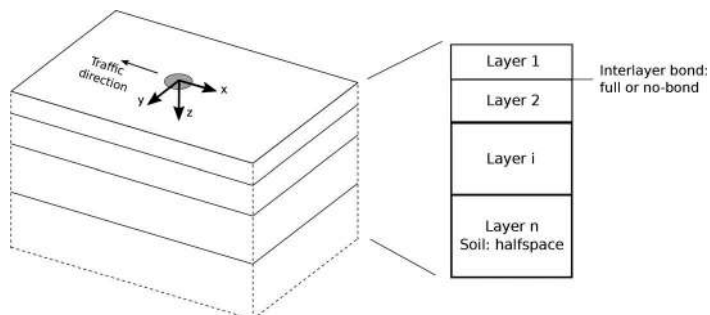


Figure 1. Schematic representation of pavement structure in DynaPave.

The computational model is based on the assumption that the traffic load moves at constant velocity, V , towards the x direction. With this assumption, the stationary coordinate system (x, y, z) can be transformed into a moving coordinate system (X, Y, Z) , as follows:

when the thickness of the viscoelastic layers increases. To investigate further the assumption of the German method, the responses of seven pavement structures were compared between static elastic simulations (10 Hz rule: material properties determined at 20°C and 10 Hz) and viscoelastic simulations (material properties determined at 20 °C and 80 km/h).

Table 1 shows the identification and thicknesses of the pavement structures investigated. The thicknesses of the asphalt layers were selected from the German empirical pavement design guide, RSTO [7]. The thickness of the subbase was varied to keep the overall frost protection depth (i.e. asphalt layers + granular base + subbase) constant. Following the guidelines of RDO-Asphalt, the asphalt layers were modelled full bond between them and the interfaces between asphalt base course - granular base, granular base - subbase, and subbase - subgrade were defined as no-bounded.

Table 1. Pavement structures investigated: identification and thickness (in mm).

Layer	Pavement structures						
	BK100	Bk32	Bk10	B3,2	Bk1,8	Bk1,0	Bk0,3
Wearing course	40	40	40	40	40	40	40
Binder course	80	80	80	60	0	0	0
Base course	220	180	140	120	160	140	100
Granular base	200	200	200	200	200	200	200
Subbase	300	340	380	420	440	460	500
Subgrade	∞	∞	∞	∞	∞	∞	∞

For all the seven structures, comparisons between a viscoelastic and an elastic case were made. In the viscoelastic case the asphalt materials were modeled using the Olard - Di Benedetto model [9], or 2S2P1D model. The 2S2P1D model is a rheological model made of two springs, two parabolic elements and one dashpot, as seen in Figure 3. In the frequency domain, the complex modulus (E^*) of the 2S2P1D model is defined per Equation (3).

$$E^*(\omega) = E_{00} + \frac{E_0 - E_{00}}{1 + \delta(j\omega\tau)^{-k} + (j\omega\tau)^{-h} + (j\omega\tau\beta)^{-1}} \quad (3)$$

where E_{00} is the static modulus, E_0 is the glassy modulus, j is the complex number, ω is the angular frequency ($\omega = k_1 V$), h and k are exponents of the parabolic elements ($1 > h > k > 0$), δ is a positive non-dimensional constant, τ is a time parameter and β is a dimensionless constant related to Newtonian viscosity η .

In the linear elastic case, an equivalent modulus of the asphalt layers was determined with Equation (3) using a constant frequency of 10 Hz. Table 2 shows the material properties/parameters of all layers. It can be observed that in both cases (elastic and viscoelastic) the unbound layers were assumed as linear elastic.

The traffic load was represented by a single load exerting a uniform distributed pressure of 700 kPa on a circular patch of 300 mm diameter, which corresponds to the values used in the German ME design of pavements. For the viscoelastic design case, the velocity of the load was 80 km/h. Four coefficients of the load were obtained with Equation (4).

$$\hat{f}_z = \frac{f_0 J_1 \left(r [k_1^2 + k_2^2]^{\frac{1}{2}} \right)}{r [k_1^2 + k_2^2]^{\frac{1}{2}}} \quad (4)$$

Layer	Pavement structures						
	BK100	Bk32	Bk10	B3,2	Bk1,8	Bk1,0	Bk0,3
Wearing course	40	40	40	40	40	40	40
Binder course	80	80	80	60	0	0	0
Base course	220	180	140	120	160	140	100
Granular base	200	200	200	200	200	200	200
Subbase	300	340	380	420	440	460	500
Subgrade	∞	∞	∞	∞	∞	∞	∞

Figure 3. Schematic representation of the Olard - Di Benedetto viscoelastic model.

Table 2. Material parameters.

Layer	Material properties	
	Linear elastic case (20°C and 10 Hz)	Linear viscoelastic case (2S2P1D model at 20°C)
Wearing course	$E=9158 \text{ MPa}$, $\nu=0.35$, $\rho=2200 \text{ kg/m}^3$	$E_{00}=48 \text{ MPa}$, $E_0=37827 \text{ MPa}$, $\beta=2608$, $\tau=0.0091$, $h=0.494$, $k=0.187$, $\delta=1.810$, $\nu=0.35$, $\rho=2200 \text{ kg/m}^3$
Binder course	$E=17175 \text{ MPa}$, $\nu=0.35$, $\rho=2200 \text{ kg/m}^3$	$E_{00}=22 \text{ MPa}$, $E_0=43414 \text{ MPa}$, $\beta=944$, $\tau=0.202$, $h=0.522$, $k=0.174$, $\delta=2.09$, $\nu=0.35$, $\rho=2200 \text{ kg/m}^3$
Base course	$E=8016 \text{ MPa}$, $\nu=0.35$, $\rho=2200 \text{ kg/m}^3$	$E_{00}=23 \text{ MPa}$, $E_0=30812 \text{ MPa}$, $\beta=619$, $\tau=0.017$, $h=0.588$, $k=0.21$, $\delta=2.15$, $\nu=0.35$, $\rho=2200 \text{ kg/m}^3$
Granular base	$E=400 \text{ MPa}$, $\nu=0.4$, $\rho=2300 \text{ kg/m}^3$	$E=400 \text{ MPa}$, $\nu=0.4$, $\rho=2300 \text{ kg/m}^3$
Subbase	$E=150 \text{ MPa}$, $\nu=0.4$, $\rho=2300 \text{ kg/m}^3$	$E=150 \text{ MPa}$, $\nu=0.4$, $\rho=2300 \text{ kg/m}^3$
Subgrade	$E=80 \text{ MPa}$, $\nu=0.4$, $\rho=2000 \text{ kg/m}^3$	$E=80 \text{ MPa}$, $\nu=0.4$, $\rho=2000 \text{ kg/m}^3$

where f_0 and r are the magnitude and radius of the load, respectively. And J_1 is a Bessel function of the first kind.

Of particular interest are the critical response variables required as input to common pavement performance models. For the selected pavement structures, and considering the German conditions, the most critical response variable is the maximum horizontal tensile strain at the bottom of the asphalt base as indicator of fatigue cracking. Figure 4 shows the results of DynaPave for the simulations on Structure BK100. It is observed a difference in the maximum horizontal strains of almost 19% between the linear elastic case (10 Hz rule) and the viscoelastic case at 80 km/h. Additionally, the viscoelastic calculations show the delay of the strain that the elastic simulations cannot predict.

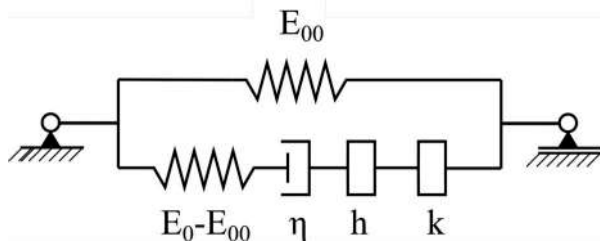


Figure 4. Horizontal tensile strains at the bottom of the asphalt base. Comparison between linear elastic case and viscoelastic case.

Figure 5 shows the maximum horizontal tensile strains at the bottom of the base course for the seven pavement structures. The results confirmed the findings of earlier studies [5] about the importance of considering viscoelasticity when calculating responses of thick asphalt pavements.

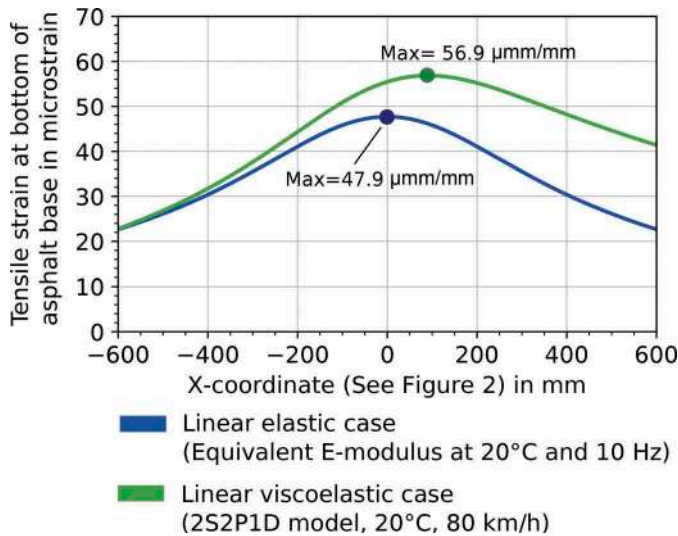


Figure 5. Maximum horizontal strains at the bottom of the asphalt base for the seven pavement structures. Comparison between linear elastic case and viscoelastic case.

The discrepancy between elastic and viscoelastic calculations is more evident when using transfer functions to obtain the allowed number of load cycles. In the German ME design guideline, the fatigue transfer function is given by Equation (5) where the horizontal strain at the bottom of the asphalt base, ϵ_h , is elevated to the power of f_2 , which is a material parameter that ranges between -2 and -3. Thus, a difference of 19% in ϵ_h (as the one found for BK100) results in a difference of more than 30% in the calculated number of load cycles.

$$N_f = \frac{SF}{F} f_1 \epsilon_h^{f_2} \quad (5)$$

where N_f is the maximum load cycles before fatigue failure, SF is a transfer constant ($SF = 1500$), F is a safety factor, and f_1 and f_2 are material parameters determined from indirect tensile test.

4 PAVEMENT RESPONSES UNDER MOVING NON-UNIFORM TIRE FOOTPRINTS

Most ME pavement design methodologies assume that the tire load is applied evenly over a circular contact area, which size depends on the contact pressure of the tire. However, the tire contact pressure is actually not evenly distributed over a circular area [4]. Measurements of the contact pressure between road surface and moving tires has shown that the distribution of stresses depends mainly on the load of the tire, the inflation pressure, and the characteristics of the materials from which the tire is made [11]. On this context, this section presents the numerical modeling of a pavement structure under a representative tire load. The objective was to identify the impact of the non-uniform tire contact stresses on the pavement responses. With this aim, the results of two design cases were compared: Footprint case, a design case in which the tire load was modeled using a non-uniform stress distribution, and Circular case, a case in which the load was simplified using an equivalent uniform circular stress distribution.

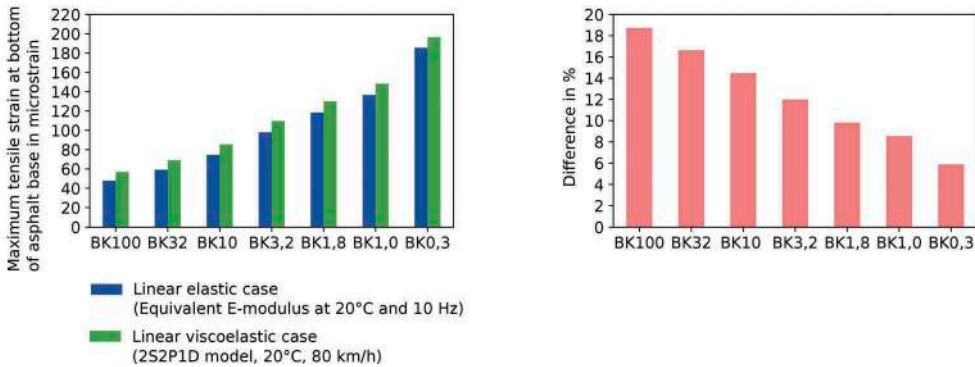
Previous studies [5] showed the importance of considering non-uniform tire footprints in ME design of thin asphalt pavements. Therefore, the thinnest pavement structure of Germany (acc. to RSTO [7]) was chosen. The pavement corresponds to structure Bk0,3 of Table 1. The materials were modelled using the viscoelastic parameters (i.e. 2S2P2D model for asphalt materials and linear elastic model for granular materials) indicated in Table 2.

The traffic load corresponds to the vertical stress distribution measured under a wide base radial tire 385/65R22.5 with a tire inflation pressure of 900 kPa. The tire was subjected to a static load of 35 kN. The chosen tire corresponds to an European articulated truck with super-single trailer tires (equivalent axle load of approx. 7 tonnes). This is a highly probable traffic load that can be expected on a low volume road of Germany.

DynaPave cannot simulate directly non-uniform tire footprints. Therefore, the principle of superposition was employed using 196 rectangular areas ($[-a, a] \times [-b, b]$), as seen in Figure 6. The Fourier coefficients of each rectangular load was determined with the following formula:

$$\hat{f}_Z = f_0 \frac{4\sin(k_1 a)\sin(k_2 b)}{k_1 k_2} \quad (6)$$

where f_0 is the magnitude of the load of each rectangular area, obtained by subdivision of the tire footprint measurements.



a) Comparison between linear elastic case and linear viscoelastic case.

b) Difference between linear elastic case and linear viscoelastic case.

Figure 6. Simplification of tire footprint measurements by using 196 rectangular subdivisions.

The actual tire footprint was compared with an equivalent uniform load under a circular patch. The measured footprint contact area (45908 mm^2) and the applied tire load (35 kN) were used to obtain an equivalent circular load of 762 kPa over a circular patch of 121 mm radius.

As in Section 3, the parameter used for fatigue cracking analysis was the longitudinal tensile stress at the bottom of the asphalt base. Figure 7a shows the results of both design cases. It can be seen that the magnitude of the horizontal strain at the bottom of the asphalt base is not greatly affected by the non-uniformity of the load (7 percent difference between the two cases). It is important to note that this conclusion has been obtained using the pavement structure (Bk0.3) of a low volume road in Germany, which has a 140 mm thick asphalt layer. It is expected that for thinner pavements, with asphalt layers less than 50 mm thick, the difference between the footprint case and the circular case will be more pronounced. Figure 7b shows the vertical strain distribution at the pavement surface for the footprint case. It is observed high localized strains which may result in the development of permanent deformation areas near the load.

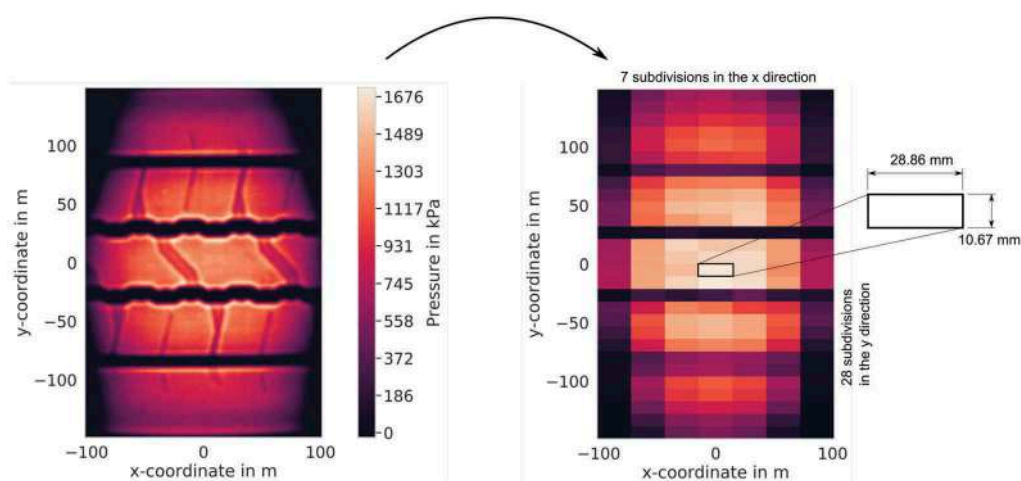


Figure 7. DynaPave results: comparison between the results of the footprint case and the circular case.

5 CONCLUSIONS

A new pavement response software, known as DynaPave, was introduced. DynaPave was conceived as an alternative to the existing numerical kernels of the German mechanistic pavement design guide. DynaPave uses multilayer theory with Fourier transforms. The procedure consists of taking a two-dimensional Fourier transform of the surface loading and solving the equilibrium and continuum equations in the frequency domain for each Fourier harmonic used to describe the loading. With DynaPave it is possible to handle complex surface loads, different vehicle speeds, and dynamic and viscoelastic effects, with state-of-the-art viscoelastic models such as the Olard-Di Benedetto model and the Huet-Sayegh model. DynaPave was used to determine the viscoelastic responses of asphalt pavements under the action of moving loads. Two design cases were investigated to evaluate how the viscoelastic behavior of asphalt materials and the irregular shape of the traffic load affect the pavement responses. The results highlighted the importance of taking viscoelasticity into account when calculating fatigue response points for thick asphalt pavements. The uneven tire contact pressure was simulated in DynaPave with a series of uniform rectangular loads considering the superposition principle. The simulations showed the importance of considering the actual footprint when evaluating the development of localized ruts near the pavement surface.

ACKNOWLEDGMENTS

Funded by the Deutsche Forschungsgemeinschaft (DFG, German Research Foundation) – SFB/TRR 339, Project-ID 453596084.

REFERENCES

- [1] *AdToPave: Analysing and Design Tool for Pavements*. Accessed: 2021-10-01: <https://www.adtopave.de/deutsch/adtopave/adtopave.html>.
- [2] Armelle Chabot et al. “Visco-elastic modeling for asphalt pavements – software ViscoRoute”. In: *Conference: R. Lytton Symposium on Mechanics of Flexible Pavements*. 2006.
- [3] O. Chupin et al. “Influence of sliding interfaces on the response of a layered viscoelastic medium under a moving load”. In: *International Journal of Solids and Structures* 47.25 (2010), pp. 3435–3446.
- [4] M. De Beer et al. “Toward using tire-road contact stresses in pavement design and analysis”. In: *Tire Science and Technology* 40 (Oct. 2012), pp. 246–271.
- [5] G. Canon Falla. “Characterization and modeling of asphalt concrete from micro-to-macro scale”. PhD thesis. Technische Universität Dresden, 2002.
- [6] FGSV. *RDO: Richtlinie für die rechnerische Dimensionierung des Oberbaues von Verkehrsflächen mit Asphaltdeckschicht (Mechanistic German pavement design guideline– in German)*. 2009.
- [7] FGSV. *RSTO: Richtlinie für die Standardisierung des Oberbaues von Verkehrsflächen (Empirical German pavement design guideline– in German)*. 2012.
- [8] V.H. Nguyen. “Comportement dynamique de structures non-linéaires soumises à des charges mobiles”. PhD thesis. Ecole Nationale des Ponts et Chaussées, France, 2021.
- [9] F. O. and H. Di Benedetto. “General “2S2P1D” Model and Relation Between the Linear Viscoelastic Behaviours of Bituminous Binders and Mixes”. In: *Road Materials and Pavement Design* 4.2 (2003), pp. 185–224.
- [10] *PaDesTo: Pavement Design Tool*. Accessed: 2021-10-01: <https://www.primia.de/en/padestooverview/>.
- [11] F. Wang. “Mechanistic-empirical study of effects of truck tire pressure on asphalt pavement performance.” PhD thesis. University of Texas at Austin., 2005.

Compressive strength of concrete using different field-curing methods

P. Solanki & H. Xie

Construction Management Program, Department of Technology, Illinois State University, Normal, IL, USA

ABSTRACT: This study was conducted to develop a cost-effective field-curing method of concrete specimens that can accurately represent the strength of an in-place concrete item. The results from this study can help concrete construction companies to improve service and assist decision-makers to determine falsework/formwork removal and road opening times. Specifically, a total of four slabs representing in-place concrete items and 52 cylindrical specimens were prepared and cured using four different curing methods. Selected specimens were also embedded with sensors for monitoring the internal temperature of concrete with time. Results showed that curing specimens in a power-operated box provided the early 1-Day strength closest to in-place concrete slabs compared to the curing methods of ambient air, insulated coolers, and insulated cylinders. The data from both the power-operated boxes and insulated coolers showed satisfactory estimations of early strengths of the in-place concrete slabs up to a 3-Day duration. Beyond the 3-Day duration, all four methods used in this study overestimated the compressive strength of in-place concrete slabs. Therefore, concrete construction can use power-operated box for decision-making on early strength because of its cost-effectiveness.

Keywords: Concrete, field-curing, compressive strength, pavement, construction

1 INTRODUCTION

The selection of concrete field-curing methods affects the strength and quality of concrete structures. Prior work on the decision-making of curing methods has focused on federal or local material standards for concrete construction. This is different from knowing constantly changing site conditions and various concrete mix designs well enough to choose an appropriate curing method for the specific requirements of concrete construction. During a concrete construction process, aggregate, cement, small stones, sand, gravel, and water are mixed bond together to create a stone-like material with a designed strength. Concrete strength relies on multiple factors, such as water-cement ratio, compaction, weather, and curing conditions. Just as a sample is an analytic subset of a population in statistics, a concrete test specimen can be used to examine the slump, air content, temperature, density, and most importantly, strength. Therefore, it is critical to precisely measure concrete moisture, temperature, and strength during the curing process. As a result of the structural integrity of in-situ concrete, concrete testing must rely on cylinders or beams, thereby verifying whether the in-situ concrete has enough strength and is acceptable for the job (Tseng and Wang 2004). The selection of curing methods, in this case, can affect the estimate of the in-situ concrete strengths.

Most agencies of the Department of Transportation (DOT) in the US comply with the AASHTO T 23 test method to construct and cure concrete test specimens in the field.

The AASHTO T 23 method recommends using field-cure strength specimens to determine when to put concrete structure into service or remove formwork/falsework. However, when cured in the field, smaller cylindrical specimens tend to take a longer time to develop strengths than beams. Therefore, researchers developed maturity modeling in which concrete strength is estimated based on concrete time-strength curves or charts (Allen & Iano, 2011). In this case, developing time-strength maturity curves for each and every mix containing aggregates from different sources is not a cost-effective method for DOTs. Further, site temperatures and real-world conditions are under constant changes, which can influence concrete strengths and quality levels considerably (Breysse & Martínez-Fernández, 2014; Juenger & Siddique, 2015). Therefore, the primary objective of this study was to develop a cost-effective field-curing method of concrete specimens that can accurately represent the strength of an in-place concrete item. The results can help concrete construction companies to improve service and assist decision-makers to determine falsework/formwork removal and road opening times.

To achieve the aforementioned objective, a total of four – 600 mm × 600 mm × 200 mm (24 in. × 24 in. × 8 in.) cast-in-place test slabs and 52 – 100 mm x 200 mm (4 in. × 8 in.) were constructed in this study. Each slab had four pre-installed, metal sleeves for cast-in-place concrete cylinders. Because of the slab thickness, the cylinders from the slabs were all 100 mm x 200 mm (4 in. × 8 in.) cylindrical specimens. The cylinders from these slabs were tested after 1, 3, 7, and 14 days of curing and represented in-place concrete item strength. A total of 52 cylindrical specimens were cured using four different curing methods. The cylindrical specimens cured using four curing methods were also tested after 1, 3, 7, and 14 days. Selected specimens were embedded with sensors for monitoring internal concrete temperatures with time. The research contributes to concrete studies by comparing the assorted field-curing methods and correlating the strength of cylindrical specimens with the field-curing conditions.

2 BACKGROUND

Researchers have devoted their work to study the factors causing variability in concrete strength. For example, Légeron and Paultre (2000) studied the effect of curing of concrete members on flexural tensile strength when cured under standard testing conditions and cured under site conditions. Their results indicated that significant differences existed between the modulus of rupture of concrete specimens, which varied from 35% to 100%. Bazant and Novak (2001) proposed the standard test method for the flexural tensile strength of concrete regarding its size dependence. Furthermore, Safiuddin, et al. (2007) studied the effects of different curing methods on concrete properties by casting cylinder and cube specimens and curing them under three methods such as water curing, wrapped curing, and dry-air curing with the controlled temperature of $20 \pm 2^\circ\text{C}$. They concluded that water curing as well as wrapped curing provided much better results than dry-air curing; whereas, specimens under dry-air curing had the most significant rate of moisture movement. Later, Graybeal and Davis (2008) investigated six different types of cube and cylinder specimens, including 51, 76, and 102 mm (2, 3, and 4 in.) and 51, 70.7 and 100 mm (2, 2.78, and 4 in.) cube specimens. They found that the compressive strength of the concrete tested ranged from 80 to 200 MPa (11.6 to 29 ksi). Their test results also showed that 102 mm (4 in.) diameter cylinders, 76 mm (3 in.) diameter cylinders, and 100 mm (4 in.) cubes are acceptable and interchangeable test specimens for the determination of the compressive strength of ultra-high-performance fiber-reinforced concrete.

Recently, Lee et al. (2015) investigated the effects of cylinder size (150 by 300 mm and 100 by 200 mm) on static elastic moduli and compressive strength, as well as static and dynamic elastic moduli of concrete. They tested two sets of 120 concrete cylinders, 150 by 300 mm and 100 by 200 mm, prepared from three different mixtures with the designed compressive strengths of 30, 35, and 40 MPa. Their results indicated that cylinder sizes had an insignificant influence on experimental variability, compressive strength, and static and dynamic elastic moduli for normal strength concrete (≤ 40 MPa). However, the cylinder size affected high-strength concrete substantially. Additionally, Ahmed et al. (2014) examined the effect of the size of the specimen on the flexural tensile strength of concrete. They concluded that the concrete member size has a significant effect and

proposed an equation incorporating the effect of the size of concrete for predicting the flexural tensile strength of concrete. Therefore, there lacks a consistent guideline for decision-making on the strengths of field-curing test specimens for an in-place concrete item.

3 MATERIALS AND METHODS

3.1 Concrete mixes

For this study, the IDOT Class PV (pavements) mix for pavement was used. The main reason for selecting the Class PV mix was that the results from the this study could be beneficial for a contractor who desires to open the pavement to traffic prior to 14 days from the time of concrete placement. Specifically, the mix design had a water to cement ratio (w/c) of 0.40, cement content of 255 kg/m³ (430 lb/yd³), fly ash content of 86 kg/m³ (145 lb/yd³), coarse aggregate content of 1102 kg/m³ (1858 lb/yd³), and fine aggregate content of 739 kg/m³ (1245 lb/yd³). The slump of the fresh mixture was between 89 mm and 114 mm (3.5 and 4.5 in.). The entrained air was required with an air content between 5.0% and 8.0%. The design requirements of 14-day compressive and flexural strengths were at least 24 MPa (3500 psi) and 4.5 MPa (650 psi), respectively. Due to the relatively large volume of concrete used in this study (approximately 2.4 kg/m³, i.e., 4.0 cubic yards of each mix), central-mixed concrete was ordered from a local ready-mix concrete supplier, Stark Materials Inc. (located in Normal, Illinois), which was approximately 4 miles (6.44 km) in distance from the concrete experiment site.

3.2 Casting and curing of concrete slab and cylinders

Overall, a total of four – 600 mm x 600 mm x 200 mm (24 in. x 24 in. x 8 in.) cast-in-place test slabs and 52 – 100 mm x 200 mm (4 in. x 8 in.) cylinders were prepared in this study. To mimic field conditions, all slabs and specimens were cured outside in the parking lot area (the concrete experiment site) of the Turner Hall building at Illinois State University. Further casting procedure is described below:

Cast-in-place Test Slabs: The four – 600 mm x 600 mm x 200 mm (24 in. x 24 in. x 8 in.) slabs were poured using the concrete mix design. Each slab consisted of four 100 mm x 200 mm (4 in. x 8 in.) cast-in-place cylinder molds inside the slab formwork in accordance with modified ASTM C873 (Popovics et al., 2014) (Figure 1a). Each special mold consisted of an outer cylindrical, an adjustable steel sleeve with straps tied to the slab, and an inner standard plastic cylinder mold. Each slab was poured in two lifts and compacted with a battery-operated vibrating rod in two equal lifts. The cylinders were consolidated outside the slab by rodding in two lifts. Specifically, each lift was rodded 25 times using a 10 mm (0.375 in.) diameter rod in accordance with the ASTM C 192 test method. After slab consolidation, the cast-in-place cylinders were placed inside the metal sleeves. There were four 100 mm x 200 mm (4 in. x 8 in.) cylindrical specimens from each slab (Slab#1, #2, #3, and #4), which were tested after 1, 3, 7, and 14 days of curing, respectively. After pouring the slabs and placing the cast-in-place cylinders, each slab was covered with polyethylene sheeting for curing until the day of testing. Additionally, the slab was sealed with an insulated layer cover on the top to ensure better (i.e., less gradient) heat distribution within the cast-in-place specimens (Popovics et al., 2016). A photographic view of a slab before and after casting is shown in Figure 1 (a) and (b), respectively.

Test Cylinders: The cylinders were cast for concrete mix in accordance with ASTM C 192 test method. Specifically, they were compacted by rodding in two lifts and each lift was rodded 25 times using a 10 mm (0.375 inches) diameter rod. After casting, concrete cylinders were cured using the following four different types of cost-effective methods:

- Method#1: Cured in ambient air and stripped on the day of the test (\$1.64 per plastic cylinder mold);

- Method#2: Gang-cured in an insulated cooler on the lab loading dock of the outdoor experiment site and stripped on the day of the test (\$1.64 per plastic cylinder mold + \$70 cooler which is reusable);
- Method#3: Gang-cured in a thermostatically controlled curing box (power-operated) and stripped on the day of the test (\$1.64 per plastic cylinder mold + \$1,185 box + power supply);
- Method#4: Cured inside an insulated concrete cylinder mold and taken out of the insulated mold on the day of the test (\$5.67 per insulated cylinder mold).

Each curing method consisted of a total of 13 specimens. Out of the 13 specimens, 12 specimens were tested for compressive strengths after 1, 3, 7, and 14 days of curing (three replicates tested on each day). The remaining one specimen was embedded with a sensor for monitoring temperature with time.



Figure 1. Photographic view of slab with four cast-in-place cylinders (a) before casting, and (b) after casting.

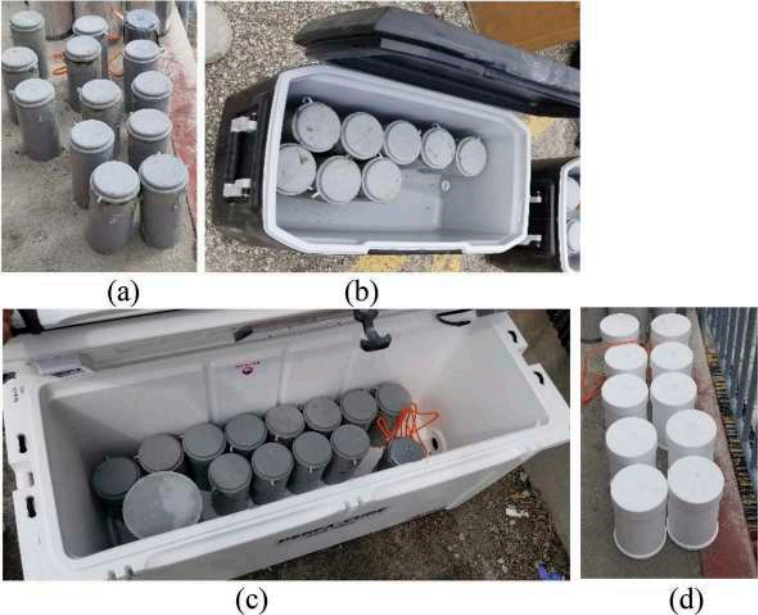


Figure 2. Specimens under curing for (a) Method#1, (b) Method#2, (c) Method#3, and (d) Method#4.

3.3 Properties of concrete mixes

Both fresh properties and hardened properties of concrete were evaluated in this study. The workability of the fresh concrete mix was evaluated by conducting slump tests in accordance with the ASTM C143 test procedure. Then, the unit weight was obtained by pouring concrete into the container in three layers of equal volume in accordance with the ASTM C138 test procedure. Further, the same container was used for measuring the air content of the concrete mix by using the pressure in accordance with the ASTM C231 test method. The hardened concrete cylinders were tested for compressive strengths. The cured specimens were first measured for their volumes and then weighed to calculate the density of each cylinder. This was done for ensuring consistent quality of the specimens, specifically with regard to the density and entrained air of each specimen to obtain accurate strength results. Then, these cylinders were tested for compressive strengths in accordance with the AASHTO T122 test method by using a Universal testing machine.

4 RESULTS

The average slump and air content of concrete mix were 114 mm (4.5 in.) and 5.1%, respectively. Further, the average ambient air temperature and relative humidity monitored using sensors during the concrete pouring time were 10.4°C (50.7°F) and 33.1%, respectively. Additional discussion of the compressive strengths and internal temperatures of concrete results is described below.

Figure 3 shows the compressive strength comparison of cast-in-place cylinders slabs and 4” cylinders cured using various curing methods. Also, Figure 4 shows the temperature variations with time inside the cylinders under curing using the four different methods along with the conditions of ambient air. It is evident from Figure 3 that curing of cylinders using Method#1 resulted in the lowest 1-Day compressive strength. Further, Method#3 provided the closest 1-Day strength results to corresponding 1-Day cast-in-place cylinders (within 6.2%). On the contrary, the 3-Day compressive strength results showed that Method#1 generated the closest results to the cast-in-place concrete strengths (within 3.3%). On the 7th and 14th days, all four curing methods overestimated the compressive strengths of the slabs, as indicated by cast-in-place cylinders.

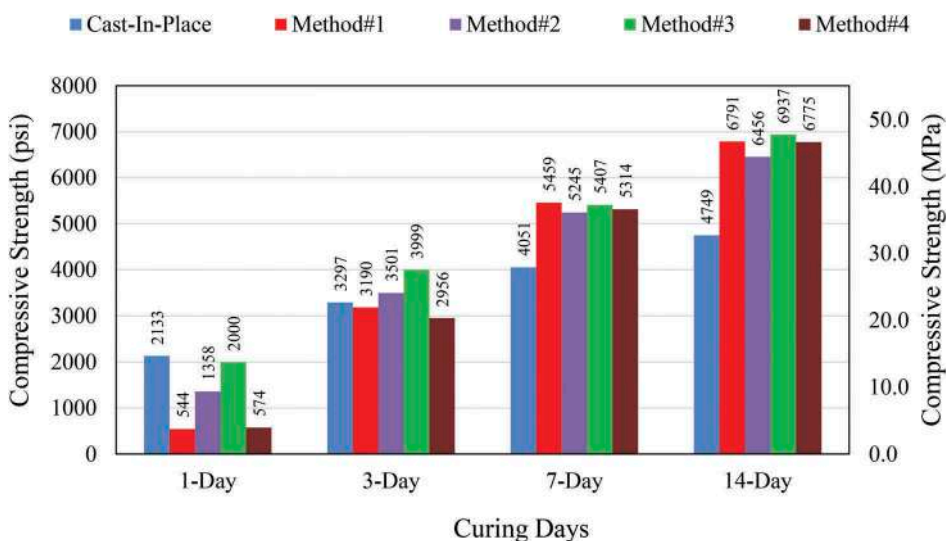


Figure 3. Compressive strength of specimens cured using different methods versus number of curing days.

Moreover, Method#3 provided the highest 14th-day compressive strengths compared to the rest methods. One possible reason for this result is because of the consistent warmer temperature (70°F, i.e., 21.1°C or higher) inside the power-operated boxes than the other methods, as shown by the green line in Figure 4. The insulated coolers (Method#2) also provided relatively consistent and warmer temperatures to cylinders, but the average difference between the power-operated boxes (Method#3) and the insulated coolers (Method#2) over the 14-day period was 4.11°C (7.4°F). Specifically, the average difference between the insulated coolers (Method#2) and the ambient air temperatures over the 14-day period was 3.67°C (6.6°F). The average difference between the power-operated boxes (Method#3) and the ambient air temperatures over the 14-day period was 7.78°C (14.0°F).

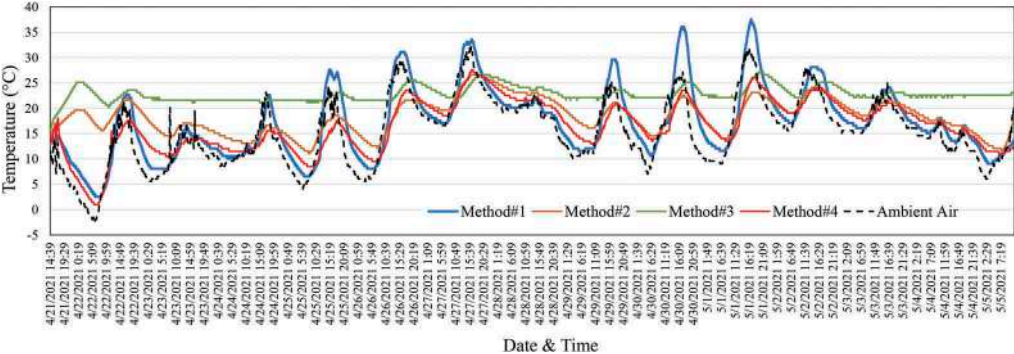


Figure 4. Internal temperature of concrete of specimens cured using different methods versus time.

5 CONCLUSIONS

In this study, the influence of field-curing conditions on the compressive strength of concrete test specimens was investigated. Both concrete slabs and cylinders were prepared and cured using a total of four different field-curing methods. Results showed that curing of specimens in a power-operated box provided early 1-Day strength closest to an in-place concrete slab. Both power-operated boxes and insulated coolers showed satisfactory estimations of the early strength of in-place concrete slabs up to 3-Day. Beyond 3-Day, all the four methods used in this study overestimated the compressive strength of the in-place concrete slabs. This behavior could be attributed to warmer internal concrete temperatures provided by all four curing methods. Hence, construction managers should pay close attention to the curing method selection of concrete items. For the Class PV mix and similar designs, contractors can consider using a power-operated box for field-cured concrete cylinder specimens for decision-making on early strength because of its cost-effectiveness. Concrete contractors can also choose insulated coolers because they are more cost-effective and consume less energy than power-operated boxes and can achieve the second-to-best results.

This research compares various curing methods and finds the correlation between temperature variations of different curing methods and compressive strengths. The experiment results can help the construction industry to improve the reliability of decision-making on concrete work. The technical suggestions of this research also contemplate the cost-effectiveness and energy consumption of the available options. Future research should focus on the features of fresh concrete under different mix designs, such as early-strength concrete or extra-high strength concrete.

ACKNOWLEDGEMENTS

The support for this study was provided by the Illinois DOT as part of the Illinois Center for Transportation (ICT) R27-219 project. The authors would like to acknowledge several graduate and undergraduate students (Harsh Chauhan, Juhi Patil, Tejaswi Reddy, Shahab Rajput, Russell Smallwood, Brendon Philips, Jake Vickers, Levi Brooks) for assisting in specimen preparation and testing. The authors would also like to acknowledge the members of IDOT Technical Review Panel (TRP) for their useful advice at different stages of this research.

REFERENCES

- Ahmed, M., Hadi, K. M. E., Hasan, M. A., Mallick, J., & Ahmed, A. (2014). Evaluating the co-relationship between concrete flexural tensile strength and compressive strength. *International Journal of Structural Engineering*, 5(2), 115–131.
- Allen, E., & Iano, J. (2011). *Fundamentals of building construction: materials and methods*. John Wiley & Sons. Pages. 515–551.
- Bazant, Z. P., & Novak, D. (2001). Proposal for the standard test of modulus of rupture of concrete with its size dependence. *ACI Materials Journal*, 98(1), 79–87.
- Breysse, D., & Martínez-Fernández, J. L. (2014). Assessing concrete strength with rebound hammer: review of key issues and ideas for more reliable conclusions. *Materials and Structures*, 47(9), 1589–1604.
- Đurišić, M. P., Tafa, Z., Dimić, G., & Milutinović, V. (2012, June). A survey of military applications of wireless sensor networks. In *Embedded Computing (MECO), 2012 Mediterranean Conference on* (pp. 196–199). IEEE.
- Graybeal, B., & Davis, M. (2008). Cylinder or cube: strength testing of 80 to 200 MPa (11.6 to 29 ksi) ultra-high-performance fiber-reinforced concrete. *ACI Materials Journal*, 105(6), 603.
- Juenger, M. C., & Siddique, R. (2015). Recent advances in understanding the role of supplementary cementitious materials in concrete. *Cement and Concrete Research*, 78, 71–80.
- Lee, B. J., Kee, S. H., Oh, T., & Kim, Y. Y. (2015). Effect of cylinder size on the modulus of elasticity and compressive strength of concrete from static and dynamic tests. *Advances in materials science and engineering*, 2015.
- Legeron, F., & Paultre, P. (2000). Prediction of modulus of rupture of concrete. *Materials Journal*, 97(2), 193–200.
- Popovics, J. S., Ham, S., and Garrett, S. (2014), *State of Practice for Concrete Cylinder Match Curing and Effect of Test Cylinder Size*, Report No. ICT-14-003, Illinois Department of Transportation, Springfield, IL.
- Riding, K. A., Poole, J. L., Schindler, A. K., Juenger, M. C., & Folliard, K. J. (2006). Evaluation of temperature prediction methods for mass concrete members. *ACI Materials Journal*, 103(5), 357–365.
- Safiuddin, M., Raman, S. N., & Zain, M. F. M. (2007). Effect of different curing methods on the properties of microsilica concrete. *Australian Journal of Basic and Applied Sciences*, 1(2), 87–95.
- Tahersima, M., & Tikalsky, P. (2017). Finite element modeling of hydration heat in a concrete slab-on-grade floor with limestone blended cement. *Construction and Building Materials*, 154, 44–50.
- Tseng, K. K., & Wang, L. (2004). Smart piezoelectric transducers for in situ health monitoring of concrete. *Smart Materials and Structures*, 13(5), 1017.

Pavement structural performance: Predicting remaining life using rapid non-destructive testing

G. Salt & L. Grimshaw

Pavement Analytics Group, GeoSolve Ltd, New Zealand

A. Marradi

Department of Civil and Industrial Engineering, Università di Pisa, Italy

ABSTRACT: Non-destructive testing of pavements has progressed, from widely spaced pseudo-static methods, namely Falling Weight Deflectometer (with typically 300 tests per day), to Traffic Speed Deflectometer (40-70 km/hr), and now Multi-Speed Deflectometer (5-65 km/hr) testing both wheelpaths at 1m centres with 300,000 tests per day on urban roads. Analysis methods have also advanced so that interpretation can now be a matter of hours at most or close to real time in some instances. The technology has advanced, but has the interpretation and prediction of pavement performance? Deflection test studies of “Hit Rate” (defined as the success of predicting whether a given treatment length would reach a terminal structural condition within a prescribed time period) have been attempted previously, but well documented case histories are rare. This article presents the establishment of a study involving sites where different deflection methods have been applied, including some for which data were collected many years ago, with a long record of subsequent performance under known traffic loading. As well as documenting the necessary data for determination of Hit Rate, alternative methods of analysis and interpretation are used to compare the old and newer technologies as well as the outcomes using both traditional analysis methods and more recent developments, so that network managers, designers and contractors can evaluate the reliability of different techniques now available for predicting the remaining structural life of pavements.

Keywords: Pavement, life, prediction, traffic, speed

1 BACKGROUND

Prediction of pavement performance is a key issue where a medium- or long-term forward work programme for structural rehabilitation and its associated cost is a statutory obligation of roading authorities. Using surface condition data and visual observations, many experienced pavement practitioners can predict the lengths and extents of their roads which will reach a terminal structural condition in the next year, and maybe the next two years.

However, where the demand is for a Forward Work Programme for structural rehabilitation that predicts the timing of terminal structural condition out for more than 30 months (and out to 30 years), reliable methodology to produce a dependable annual budget over even a moderate time is a challenge.

This article addresses the success (or otherwise) of specific methods of pavement life prediction focusing on structural rehabilitation rather than resurfacing (as the former is usually the more uncertain cost per lane kilometre for any given network in any given future year).

2 TERMINAL CONDITION & HIT RATE

Highway authorities with good subsurface (structural) information may define the terminal condition of a given treatment length as being when the net present value (NPV) of long term ongoing structural maintenance exceeds the value of structural rehabilitation. However, that necessitates what is often a highly subjective speculation on what type and extent of maintenance will be required to effectively calculate costs in every subsequent future year for the duration of the planned Forward Work Programme.

On the other hand, authorities for local roads tend to have less budget per kilometre, and for lesser trafficked roads they may have only surface condition (rather than any structural) information, hence there may be a tendency to place more weighting on visual inspections of the surfacing and surface condition indices (such as PCI, PSR or SCI). The visual Level of Service (LOS) approach usually adopts trend analysis and prescribes trigger criteria for individual distress modes (rutting, roughness, cracking etc) primarily to make decisions on timing of re-surfacing.

Whether structural rehabilitation is required at the same time or later is a separate issue necessitating structural information without which the approach is likely to be adequate only for the short term (1-2 years). The assignment of terminal condition may therefore be consistent within a network but could vary considerably between networks where different definitions (e.g., LOS vs NPV or other criteria) apply.

Historically, the industry's ability to predict pavement structural life in the range of say 30 months to 30 years has been at best questionable with some studies showing orders of magnitude error (Arnold et al, 2009). The terminal structural condition of a treatment length can be simply defined as its condition in the year in which the controlling authority (or others affected by the funding consequences) for that road finally confirms that rehabilitation is to commence (i.e., using reality of the situation rather than any calculations or assumptions made in NPV or LOS approaches).

To have a measure of the reliability of predicting pavement life, the Hit Rate could be defined as the success of predicting whether a given treatment length would reach a terminal structural condition within a prescribed period. Because that definition is qualitative, then for the purposes of this study, Hit/Miss outcomes will be assigned by assuming "useful prediction" to be when the number of years to terminal condition is within 1 year +/- 10% from the time of prediction. This allows for the necessary marginal cases whereby at least one treatment length may be either brought forward or deferred a year by the controlling authority for administrative or budget reasons regardless of the engineering evaluation.

For example, if 10 years is the originally predicted life, a Hit would be assigned if the actual year in which rehabilitation is confirmed by the authority eventuates between 8 and 12 years while any other time estimate would constitute a Miss. Alternatively, rather than be constrained to a binary measure, a Hit Rate% could be defined as the minimum ratio of the two durations after allowing for the accepted margin, but expressed as a percentage. In the above case, if the actual rehabilitation is done after 6 years and the initial prediction of 10 years (considered acceptable at $10 - (10 \times 10\%) = 8$ years), then the ratio becomes $6/8$, i.e., the Hit Rate% is 75%, (relative to an ideal of 100%). For this study, the objective is to establish a quantitative (yet practical) performance measure for comparison of different methodologies for life prediction.

While the Hit Rate concept has been discussed for the last 20 years, since 2010 there have been no formally published local case histories, even though 6 years of Traffic Speed Deflectometer (TSD) data have been collected regularly throughout New Zealand's national state highways.

Some documentation exists for a case that arose after the Kaikoura Earthquake due to the re-routing of traffic from a heavily loaded primary highway onto 800 lane km of secondary highways. This presented an effective opportunity to observe accelerated trafficking of highways with inadequate structural capacity for the loads imposed, (Stevens et al, 2016). Over the following year, effectively 15 years of the customary heavy traffic was experienced. Predictions of the effects of such overloading were made from TSD structural data at 10m intervals: the model was prepared using generalised mechanistic procedures for the analysis but limiting the necessary site calibrations by adopting an "80/20" approach for expedience. The intention was to target 80% reliability for predictions while limiting site validation time to 20% of that desirable for a thoroughly calibrated model.

The calibration of the model used an approach termed Regional Precedent Performance (RPP, discussed below) which uses the historic performance of a wide selection of mature pavements from the local road network using field observations and monitoring under the actual traffic (rather than nominal fatigue criteria from laboratory or overseas studies). The findings were presented to the project engineer responsible for remediating the effects of overloading who remarked that the targeted 80% reliability for RPP life predictions from the 10m TSD data was achieved, and in his view was closer to 90%.

A second RPP case history was carried out at the same time for all highways in the Waikato region of New Zealand. This highway network also had full coverage with TSD Gen. II at 10m centres in each lane. Before visual site calibration was carried out, the GIS image showing the RPP remaining life throughout the network was presented to the roading authority's Regional Engineer, who considered the duration and spatial distribution entirely consistent with his substantial field experience and expectation.

These two specific cases indicated that TSD data and its interpretation can be highly effective for prediction. The findings were passed on at the following Deflection at Road Traffic Speed meeting (DaRTS, a forum of specialist TSD users and researchers led by TRL/Highways England) but met the response from one TSD user that 80% reliability was not considered achievable. Evidently, documentation of prediction versus reality for a more comprehensive range of cases histories is warranted.

3 ALTERNATIVE METHODS OF PAVEMENT LIFE PREDICTION

Many methods of pavement life prediction have been considered (most being empirical only), but with increasing ease of adopting highly efficient processing of large datasets from traffic speed structural data collection, mechanistic-empirical models can provide much greater insight. The bases of some of the models that have been (or are being) used locally, are given below.

Table 1. Predictive Methods.

METHOD	BASIS
Benkelman Beam	Central deflection
Shell - Asphalt Institute	Vertical strain at top of subgrade and horizontal strain at base of asphalt layer. General fatigue criteria.
NRB, Austroads	Subgrade CBR and pavement thickness
HDM III, IV, RIMS	Structural number (SN, SNC, SNP)
AASHTO '86	Structural number
AASHTO '93	Structural number
Austroads Simplified	Central deflection if unbound. Curvature function added for surface bound layer.
Austroads GMP	Vertical strain at top of subgrade and pavement layer thicknesses if unbound. Include horizontal strain for any bound layer. General fatigue criteria.
APT-LTPP (Accelerated Pavement Testing and Long-Term Pavement Performance Sites)	Vertical strains in all unbound layers and pavement layer thicknesses with horizontal strains in bound layers. General rutting fatigue criteria from FWD nationally. (Arnold et al, 2009; Salt et al 2010)
RPP (Regional Precedent Performance)	Vertical, horizontal and shear strains (and other parameters) determined in all layers (bound or unbound). Calibrated mechanistic fatigue criteria for all distress modes for each large network or region. Based on FWD (including full time histories) on terminal sites in the same region with extension to TSD and/or Multi-Speed Deflectometer (MSD). Extended to small network datasets using meta-analyses of nearby larger (external) datasets.

Up until about 2010, pavement life prediction was relatively uncertain with moderate or long term predictions often being out by an order of magnitude in log time or more. Using the nominal definition of reliability in Section 2 above, predictions of either 1 year or 100 years compared to actual life of 14 years would translate to hit rate of 15%. Issues include the intrinsic natural variation of subgrade consistency and the variability (Ullidtz, 1987) of particulate materials whose properties vary both spatially and with time along any given treatment length. However, the primary issues until about 2010 were (1) usually only widely spaced FWD data were available and (2) preoccupation with empirical parameters such as deflection and Structural Number which effectively ignore much of the data recorded by each FWD test.

The near continuous, accurate measurement now available from TSD has transformed pavement engineering capability in this respect. The Kaikoura Earthquake study in 2016 provided the first occasion nationally for an ultimate reality check on TSD interpretation giving due recognition to Regional Precedent Performance (RPP).

Pavement engineering inherently provides an ideal environment to validate any new theory or innovative prediction as each treatment length provides for its own “experiment” - subject only to some delay as ongoing traffic loading progressively takes each to the terminal condition necessary to compare prediction with reality. However, the immediate limitation is that true independence is best ensured by enabling interested parties to unequivocally distinguish and compare predictions from the actual outcome. For this reason, raw data is being collated from multiple sites where either FWD and/or TSD has been carried out to establish a GIS database. Fields include the surveyed structural parameters at 10 or 20 m centres in each lane, and the predicted outcome(s) using one or more of the above methods in Table 1.

Using the widely accessible Google Street View (which now has historical imagery on road-networks in many locations, sometimes every few months), any reviewer can regularly inspect a suitable quality photograph and track whether the surface condition deterioration reflects the parameters and/or expectations of any of the predictive methods used.

A key objective is to validate and expand the database with all available alternative predictions using the same source data but interpreted with any other methodology, however simple or complex. At this stage, how the outcome is achieved is less important than to address the primary question “How reliable can predictions of remaining structural life be in practice?” Previous studies suggest that methods that do not include all elements of Table 2 (below) will have low reliability. However, the objective is to achieve the greatest reliability, regardless of the means, and establish a quantifiable measure to compare different techniques.

Establishing a baseline database enables any predictions to be subject to independent verification at any later date. On the weaker sections of the more heavily trafficked roads, either deterioration or repairs may well be visible within a year, and as more substantial distress becomes evident in the medium and longer term, the ongoing study will provide a sound basis for subsequent improvements of predictive models.

4 CONSTITUENTS OF A RELIABLE LIFE PREDICTION MODEL

Significant progress has been made from basic empirical models towards mechanistic-empirical procedures with much more facility for incorporating rational, evidence-based parameters for characterisation of pavement materials. In thick AC pavements, the number of visually recognisable distress modes can be relatively limited but with cement stabilised or unbound granular pavement with thin surfacings, a myriad of different modes of distress can be experienced in just one region.

The essential features of a suitable mechanistic model were the subject of study by Dawson (2002 Mechanistic Design Workshop) where he proposed over 20 distress modes. His briefing notes, along with those notes produced as a set of outcomes, have provided the basis for the effective advances made with unbound (and some bound) pavement performance predictions for local networks. Five critical elements for a reliable predictive model were nominated at the workshop to bring together a truly mechanistic procedure. Establishing and adhering to such

Table 2. Reliable Mechanistic Prediction of Pavement Structural Life.

1: Distress Modes	<p>It is necessary to identify the myriad ways (up to 23 or more) in which individual treatment lengths deteriorate to a terminal condition for the specific network. Multiple terminal conditions may be defined based on NPV and/or LOS but ideally both. Allocate any necessary adjustments according to each road classification or situation.</p> <p>Then identify a key mechanical measure for each, usually a vertical, horizontal or shear strain (or stress) at a specific depth and plan location relative to the contact patch of the design load, which will act as an indicator of the performance.</p>
2: Loading	<p>Reliable measurement and systematic classification of heavy traffic vertical loading spectra for each road. Speed of loading, longitudinal shear (braking and acceleration), geometrics and transverse shear (roundabouts) can be critical in specific cases.</p>
3: Load Equivalency	<p>Evaluation and assignment of load equivalency for the traffic spectrum for each individual distress mode/layer. Load damage exponents (LDEs) used to be considered to be constants. This came from short term studies of very dry pavements where strains were low (about half their critical fatigue limits). However, in recent years it has been widely acknowledged that is not the case: longer term in situ testing of in-service pavements demonstrates each distress mode has its own characteristic LDE and that each LDE increases exponentially over the life of the pavement (manifested by accelerated deterioration towards the terminal state). An alternative to LDE is to follow procedures for systematically calculating cumulative damage for each applicable axle group separately for each distress mode.</p>
4: Rooding Database	<p>A comprehensive roading database is required for modelling reliability. Surface condition and distress severity may in some cases be adequate for short term trends, but relevant structural data subjected to detailed quality assurance (including correction for seasonal bias) are necessary for moderate term and long-term analysis.</p>
5: Computational Analysis	<p>A technique which reproduces all relevant deformation that develops in the in situ loaded state is needed and it should accommodate the properties of the range of materials encountered in each region.</p>
6: Material Characterisation	<p>The validity of the computational technique rests, to a large extent, on the veracity of the constituent materials' stress-strain relationships. Modulus non-linearity with applied stress (or with ambient stress) needs to be addressed. The measurement techniques need to be accurate, and the correct parameters need to be evaluated.</p>
7: Sampling	<p>Given the inherent variation of both subgrades and imported materials, test spacing needs to be commensurate with spatial variability and the application: network level, project level and maintenance level evaluations benefit from successively smaller averaging intervals, and local experience is that test sampling at 20m or closer in each lane is essential for adequate reliability (80% target).</p> <p>Intervals of 20, 10 & 2m are feasible with TSD now that there is little difference in cost. Simultaneous testing of both wheelpaths is advantageous in mature networks where maintenance has been carried out.</p>
8: Treatment Length Designation	<p>Systematic sub-sectioning procedures for identification and delineation of homogeneous structural treatment lengths (STL's) are fundamental to an optimised, cost-efficient Forward Work Programme. Incremental recursive techniques are required, with re-assignment of STL's each year. This is essential where material properties such as layer moduli undergo loading or environmental changes and where spatial changes are induced by patching, dig-outs or other inevitable maintenance requirements, particularly for thin-surfaced or mature pavements.</p>
9: Design Criteria	<p>Each key mechanistic measure must be computable, and relevant terminal values (fatigue criteria) characterised. These need to be defined for each</p>

(Continued)

Table 2. (Cont.)

10: Reality Checks and Calibration	<p>region or sub-region to accommodate what are now recognised as highly significant local effects, namely subgrade types, aggregate sources, construction practices, level of quality assurance, customary specifications, maintenance style/frequency and most importantly, climate (temperature, rainfall ingress, groundwater fluctuation and the impact of humidity on the equilibrium water content of unbound aggregates).</p> <p>Site inspection is essential, to ensure adequate characterisation of the wide variety of distress modes exhibited by treatment lengths which have reached or are close to terminal condition (programmed for the rehabilitation in the current year). These provide the ideal candidates for calibration. The transitions from consistently distressed to consistently non-distressed treatment lengths provide ideal points for fine tuning of distress modes and their limiting fatigue criteria.</p>
------------------------------------	--

a basis has been found to be imperative in local practice since that time, hence those elements with some additional points are summarised below.

The local (RPP) methodology, based on Dawson’s initiative as expanded above in Table 2, was established in view of the extensive national database containing 3 decades of systematically recorded full time histories of several million FWD points. FWD data were later used to transform the 6 years of repeated TSD dynamic tests into pseudo-static FWD equivalent deflection bowls providing millions more test points on the same highways (mostly at 10m intervals with some at 2m intervals).

Every database entry is scrutinised by a series of QA algorithms for any inconsistencies or anomalies within each bowl and along each road. Because this specific database includes many points on unbound pavements with thin surfacings, multi-layer non-linear elastic analysis reveals much greater insight into pavement performance than is obtained with thick structural AC roads where the subtle strains from lower layers are difficult to differentiate because they are effectively masked by the surface stiffness (deflections are an order less).

The highly fortuitous outcome from this database was that detailed models of stresses, strains and moduli of every layer were able to be more readily modelled and a wide spectrum of innovative fatigue criteria explored. A Forward Work Programme is generated after including the relevant non-structural data (traffic, surface condition progression, maintenance history etc). Reality checks ensued on the numerous instances of advanced terminal distress that characterise mature thin surfaced highway pavements.

RPP uses mechanistic analysis rather than solely pseudo-mechanistic or empirical parameters such as structural number or deflection for the reasons detailed and promoted by Ullidtz (1987). The “regional” aspect of RPP refers to the importance of developing individually tailored models of pavement performance to best reflect the various local characteristics such as systems for traffic spectra measurements, assigning load equivalency, back-analysis software, subgrade types, aggregate sources, construction and QA practices, customary specifications, maintenance style/frequency and, most importantly, climate. The “precedent performance” refers to the traditional use of this practice since its promotion by Major (1980), NRB (1989), for rehabilitation design, as well as the extension for network evaluation (Geo-Solve, 2021).

The RPP methodology was reviewed and commended by Ullidtz (2015) who also proposed that it should be upgraded with recursive functionality to model the progressive change in layer moduli with both load repetitions and time (environmental ageing). This has been partially implemented with implicit recursive modelling of changes in Load Damage Exponents, but in relation to other bound and unbound layers remains a work in progress that is expected will further improve current capability for performance prediction of bituminous and unbound layers.

5 COLLECTION OF PAVEMENT STRUCTURAL DATA

Falling Weight Deflectometer (FWD) and Traffic Speed Deflectometer (TSD) testing have been carried out using customary methods on all national state highways in New Zealand. The FWD data have been supplemented with full time histories for each geophone providing additional characteristics for modelling.

TSD data have been collected consistently by using a specific Generation II device. The latter does not measure both wheel-paths or bowl asymmetry, nor precision in the manner now achievable with later generations, but locally calibrated methods have been developed to enable effective conversion to equivalent FWD bowls. This technique does not provide definition of subgrade modulus non-linearity as well as that obtained directly with FWD, but this is compensated to some degree by the closer sampling frequency.

Unfortunately, for unknown reasons, all local TSD data in New Zealand has been collected in peak summer. This may provide consistency, but requires considerable “rationalisation” of the data to reflect the more adverse conditions throughout the rest of the year, and it soon became evident that specific intervals of highways need to be entirely rejected (depending on the terrain).

The Multi Speed Deflectometer (MSD) is an emerging technology initially developed as a rapid structural screening tool for low volume roads. The MSD simply comprises a tyre with embedded sensors that is mounted to a short wheel-based truck. The simplicity and portability of the system offers the advantage of being able to test roads all over the world at all times of the year. The utilisation of a shorter truck facilitates testing in locations that the longer TSD cannot access so that large urban networks can be collected at minimal cost.

Full network level testing of cities is best achieved with the MSD allowing the remaining budget to be allocated to closer spacing FWD testing confined to only the critical (weaker) sections of the road identified by the MSD. Additionally, being able to test on wet or unsurfaced materials, enables the MSD to be a highly effective tool for rapid screening of earthworks including surveys on each layer during construction to determine areas of weaker support or lesser compaction.

MSD surveys in New Zealand initially used single (outer) wheel-path data collection, but this has now been largely replaced with dual wheel-path surveys with readings at 1m centres, averaged to 10 or 20m intervals for presentation. Focus to date has been on conversion to equivalent FWD parameters so that all methods can be related to the widely recognised standard.

Future developments of the MSD include using the principles of RPP and big datasets to predict pavement life, develop structurally homogenous treatment lengths, and ultimately generate Forward Works Programmes for overall asset management.

6 CASE STUDIES

Summaries of the sites tested and monitored with the various types of deflection equipment are given by GeoSolve (2021).

6.1 *Falling Weight Deflectometer (FWD)*

All surveys used standard Dynatest FWD equipment with 9 geophones located out to 1500mm with full time histories recorded. The categories of sites do not include Portland Cement Concrete (PCC) but do include thick structural asphaltic concrete and foamed bitumen stabilisation as well as cement stabilised, cement modified and unbound granular with thin bituminous surfacing. Most sites are New Zealand (NZ) state highways, with reliable traffic counts.

6.2 *Traffic Speed Deflectometer (TSD)*

All surveys used the same TSD Gen II, but over the years, slightly faster speed was used which led to a steady decrease in deflection for many roads. All testing was done in mid-summer requiring consideration of seasonal effects. All sites are NZ state highways with reliable traffic counts.

6.3 Multi-Speed Deflectometer (MSD)

The MSD has less accuracy than the TSD, providing relative parameters suitable for benchmarking, but has the advantage of manoeuvrability on winding roads and intersections, as well as the advantage of sampling at traffic speed at 1m centres in both wheel tracks. Most surveys are on NZ local roads, with some comparisons on NZ state highways where TSD and/or FWD were also available. An MSD study of thick structural asphalt pavement, with distress ranging from minimal (new) to severe (near terminal condition) is included, on the main arterials of Rome (300 lane km).

7 CONCLUSIONS

Since the development of the Benkelman Beam in 1953, pavement engineers have been making some form of prediction of pavement life, but only in the last few years has technology provided the potential for useful estimates of structural life in the moderate or long term. The combination of TSD with near continuous sampling supplemented with the accuracy of the FWD and subject to appropriate mechanistic procedures (Table 2) has proved effective on national and local roads, while MSD provides an additional tool for inclusion of urban streets and at more critical climactic conditions (i.e., wet season).

The reliability of predicting pavement life prior to 2010 has been questionable with studies indicating Hit Rates of seldom as high as 10%. Such a result is considered inevitable if any one of the 10 key criteria initiated by Dawson (Table 2) is ignored. To date, approaches based on empirical parameters alone or attempts to use sample intervals greater than 20m have been problematic. The database now established, provides for an ongoing study of Hit Rates for alternative approaches to predicting pavement life.

A Hit Rate of 80% for pavement life prediction is a reasonable expectation for large networks where currently available technology is used for systematic data collection of the relevant pavement characteristics, followed by state-of-the-art mechanistic evaluation, for generation of a reliable Forward Work Programme extending well beyond the current short-term models. Once the Forward Work Programme is generated, it provides the opportunity to quantitatively assess the “Hit Rate” from ongoing observation and monitoring. Reliability can hence be tracked over time, and the effectiveness of alternative prediction techniques can be evaluated independently by practitioners and potential users.

REFERENCES

- Arnold, G. Salt, D. Stevens, D. Werkmeister, S. Alabaster, D. and Van Blerk, G. 2009 *Compliance testing using the Falling Weight Deflectometer for pavement construction, rehabilitation and area-wide treatments*. NZ Transport Agency Research Report 381.
- ARRB, 2003. *Controlling moisture in pavements*. Technical note 13. www.austroads.com.au/pdf/TechNotes/aprgTN13.pdf.
- Austroads, 2012. *Guide to Pavement Technology, Part 2: Pavement Structural Design*. AGPT02-12. Traffic Load Distribution and calculation of Load Equivalence Factors.
- Dawson, A., 2002. *The mechanistic design and evaluation of unsealed & chip-sealed pavements*. University of Canterbury workshop briefing paper. www.pavementanalysis.com/papers/documents/pavements_workshop02/briefing.pdf.
- Dawson, A., 2003. *Workshop outcomes*. Paper prepared following the Workshop on Mechanistic Design and Evaluation, University of Canterbury.
- GeoSolve, 2021. Basis of Regional Precedent Performance Analysis and Case Histories.
- Main Roads Western Australia (MRWA), 1993. *Controlling moisture in pavements*. Technical Note 7. The State Government of Queensland.
- Major, N.G., 1980. *Pavement Evaluation for Rehabilitation*. Presentation to Institution of Professional Engineers, New Zealand.
- National Roads Board (NRB), 1989. *State Highway Pavement Design and Rehabilitation Manual*.

- Stevens, D. and Schmitz, G., 2016. *Traffic Speed Deflection Data Applied to Asset Management: The Kairourua Bypass reality check*. Presentation to RIMS Forum.
- Ullidtz, P., 1987. *Pavement Analysis*. The Technical University of Denmark. *Developments in Civil Engineering*, 19. Elsevier.
- Ullidtz, P., 1998. *Modelling Flexible Pavement Response and Performance*. Narayana Press.

Numerical modelling of the evolution of differential settlement of railway tracks

C. Charoenwong, D.P. Connolly & P.K. Woodward

Institute for High Speed Rail and Systems Integration, School of Civil Engineering, University of Leeds, UK

P. Galvín

Escuela Técnica Superior de Ingeniería, Universidad de Sevilla, Sevilla, Spain

Laboratory of Engineering for Energy and Environmental Sustainability, Universidad de Sevilla, Sevilla, Spain

P. Alves Costa

Faculty of Engineering, University of Porto, Portugal

ABSTRACT: Railway tracks experience different settlement over time due to repeated train passages. Typically, when the standard deviation of this vertical profile exceeds a threshold limit, maintenance (often tamping) is required to correct the profile. Therefore, when planning future maintenance and attempting to optimise track life-cycle cost, it is important to know when future maintenance will be required. To predict this, this paper presents a novel numerical approach to calculate track irregularity evolution. It is particularly useful for scenarios where it is difficult to extrapolate historical standard deviation changes into the future, such as new track constructions or increased freight tonnage. The model combines empirical settlement laws with finite elements for the track and ground. Perfectly matched layers are used to absorb outgoing wave energy, and a multi-body rolling-stock model is used for train-track interaction. The model is solved using a combination of frequency-wavenumber and time-space domains, to give a highly efficient solution approach. This optimised solution procedure allows for the track profile to be updated after every axle passage, before applying the next load, meaning the train-track interaction is constantly evolving like on a real track. This is highly novel considering the model's ability to also calculate 3D stress fields. After showing model development, it is used to perform a parametric study that shows track subgrade material properties have a marked effect on track differential settlement.

Keywords: Railway track geometry, railway track-ground settlement, differential settlement, train-track interaction, railway track-ground non-linearity

1 INTRODUCTION

Railway tracks experience long-term differential settlement due to repeated dynamic loading and varying conditions of track support in longitudinal direction. These changes in track geometry induces higher dynamic forces due to train-track interaction, causing an increase in track settlement and poorer track geometry quality. The indicator, which is widely used to

describe the track geometric quality, is the standard deviation (SD) of vertical track geometry over a defined track length (Neuhold et al., 2020). When the track geometry SD indicator is higher than a threshold limit value, it means the track geometry becomes low quality and requires maintenance action. The most common method to predict the future maintenance interval extrapolates the future value from historical changes in track geometry at a given location (Lee et al., 2020). However, in the situations where changes are made to the rolling stock or the track, the historical geometry data can no longer be used for extrapolating the future track deterioration.

Two main modelling approaches to estimate settlement include constitutive and empirical. The constitutive approach often requires high computation effort and several input parameters that are difficult to measure, thus challenging for the prediction of long-term differential settlement (Chen and McDowell, 2016). In contrast, the empirical approach only requires a few number of input parameters and provides similar accuracy compared to the constitutive approach (Ramos et al., 2020). However, the existing form of empirical settlement models predict settlement based upon equivalent magnitudes, thus non-realistic when considering the evolution of train-track dynamic interaction force.

To predict future differential track settlement accounting for the evolution of train-track interaction force due to changes in track geometry, some methodologies has been presented by (Guo and Zhai, 2018; Kumar et al., 2021; Nielsen and Li, 2018). An iterative approach is used together with an empirical modelling method to compute differential settlement considering train-track interaction. However, the distribution of stresses in the track and ground is not modelled explicitly. Most of the works in the literature simulate the track using a series of springs and dashpots solving in the time domain, thus unsuitable for calculating the 3D dynamic stress fields in the track and ground (Connolly et al., 2020; Connolly and Costa, 2020; P.Chumyen et al., 2022). These stresses are used to calculate the deviatoric stress which is one of the most influential parameters on settlement (Li and Selig, 1996). Therefore, when computing differential settlement over a large number of load cycles, these inaccuracies can considerably affect the final predicted result.

In this paper, a novel numerical algorithm based on several recommended characteristics to accurately compute differential railway track settlements is proposed. The model is based on a FEM-PML (Finite Element Method with Perfectly Matched Layers (Connolly et al., 2014)) approach coupled with empirical settlement laws, solved across frequency-wavenumber and time-space domains. The characteristics of stiffness nonlinearity in the track and ground materials due to heavy and high speed moving loads are taken into account. The 3D stress field propagation are modelled explicitly using solid elements. Train-track interaction and vehicle dynamics are modelled using a multi-body rolling-stock model. After every axle passage, the irregularities in track geometry along the given distance are updated, and the corresponding train-track dynamic interaction force and the distribution of deviatoric stress are recalculated as a consequence. Solving across the frequency-wavenumber and time-space domains obtains an optimal computational requirement of the implementation, and allows an update of the differential settlement every load passage (Charoenwong et al., 2022).

2 CHARACTERISTICS OF A DIFFERENTIAL SETTLEMENT PREDICTION MODEL

To estimate future maintenance schedules, particularly automated tamping, it is important that any numerical model should allow for predicting differential settlement over the wavelength which tamping is effective. The estimation of long-term track deformation is challenging as several variables are involved such as track-ground non-linear behaviour (Dong et al., 2019), train-track dynamic interaction and an evolving track geometry profile. Therefore, four main characteristics are recommended for any numerical models that attempt to predict differential settlement.

The first characteristic is that full 3D stress fields in the track and the subgrade are calculated. This is vital because deviatoric stress is the most influential parameter on settlement. The second characteristic involves calculating train-track dynamic interaction forces. The dynamic forces due to the interaction between rolling stock and irregularities in track geometry are a main source of differential settlement. The third recommendation is that the evolution of train-track interaction forces is simulated, allowing deviatoric stresses to be recalculated after load passages. This is particularly important when operating different types of rolling stock on a line. The last characteristic is the evolution of track-subgrade settlement laws. The increment of track settlement depends upon both ballast and subgrade settlements induced by previous load passages. Considering the train-track dynamic interaction forces exerted on evolving track profile, the settlement formulations should account for this.

Even though these recommended characteristics can be achieved using a direct approach where non-linear behaviour of soil is modelled directly, expensive computational costs (Lamprea-Pineda et al., 2022) and the estimation of several input parameters for simulating non-linear behaviour in track and soils are required for its application. Therefore, an indirect approach which is more practical for engineering purposes is preferred. This approach uses an equivalent linear approach to estimate the track-ground stress fields and then empirical laws to compute settlement.

3 NUMERICAL MODELLING DEVELOPMENT

To meet the criteria mentioned above, this paper introduces a novel modelling strategy, dividing into two primary steps, solved in a combination of frequency-wavenumber and time-space domains. The two steps include Step A pre-calculation and Step B iterative process, as shown in Figure 1:

Step A involves computing the 3D elastodynamic response in the track and ground, solved in the frequency-wavenumber domain. The geo-static stresses are calculated in this step. It then calculates the moving load transfer function considering non-linear effect in track-ground stiffness using an equivalent linear approach. Next, the 3D stress fields are computed in the wavenumber-frequency domain, which include quasi-static and dynamic components. The matrices for track compliance and train compliance used for train-track dynamic interaction model are computed in advance. Step A is only implemented once for each vehicle speed being considered in the simulation. These various pre-calculated parts allow Step B to be computed differential settlement for every axle passage in an efficient manner.

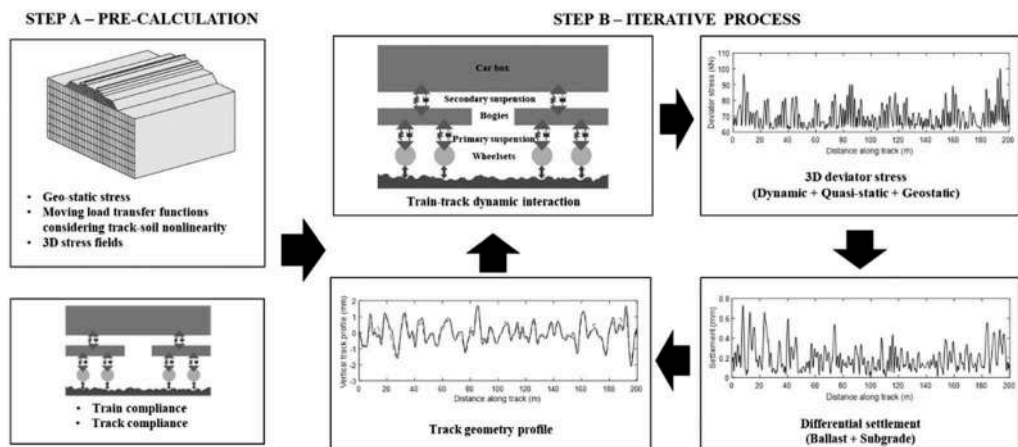


Figure 1. Model overview.

Step B involves computing the differential track settlement using a combination of wave-number-frequency and space-time domain methods. It calculates train-track dynamic interaction force based on irregularities in track geometry profile using a multi-body rolling-stock model. The corresponding deviatoric stress and settlements in the track and the soil over the entire track length are then calculated. The total deviatoric stress is based on quasi-static, dynamic and geo-static responses. The vertical track geometry profile is updated after every axle passage and thus the train-track dynamic force and deviatoric stress are recalculated. These subsequent steps are repeated until either the defined traffic or threshold limit input is reached.

4 PERMANENT STRAIN AND SETTLEMENT MODELS

4.1 Ballast settlement

The empirical settlement model for ballast is based on the ORE-type model (ORE, 1970). By performing curve fitting, the empirical constants are obtained to improve the fit with the test data from a laboratory representation of a track section provided by (Abadi et al., 2016). Figure 2 compares the proposed equation and the laboratory data in terms of settlement rate and the number of loading cycles using a semi-logarithmic plot. The ballast particles are rapidly rearranged during the initial loading, causing some errors from lab testing, thus the settlement after the first loading cycles is removed to minimise these effects. The proposed equation confirms a strong fit with the laboratory data.

A key advantage of modelling with an iterative approach is that differential settlement and irregularities in track geometry can be updated after every axle passage. However, this requires the recalculation of deviatoric stress after every load passage. Further, the equation should allow for computing settlement in different scenarios, including the case of newly constructed/renewed /tamped track and the case of existing track.

To regularly update the track irregularity profile and cover these mentioned scenarios, an alternative form of the ORE-type equation that is able to account for the previous load settlement is required. Therefore, a modified version of the equation to compute permanent strain increment at all iterative steps is proposed:

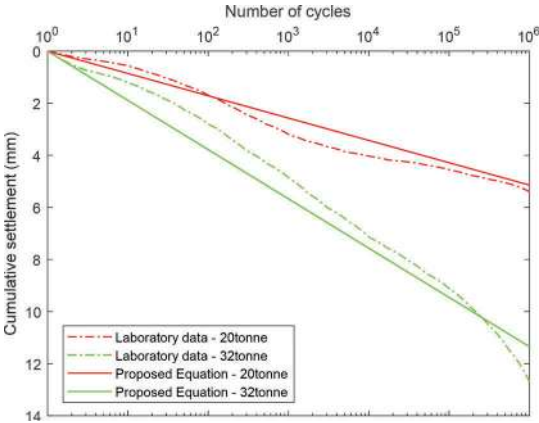


Figure 2. Comparison of proposed ballast settlement model with experimental data.

$$\Delta\varepsilon_{p-b,i} = 0.375(\sigma_{d-b,i})^2 \times [(1 + 0.4 \log_{10}((dN \cdot i) + N_{lb})) - (1 + 0.4 \log_{10}((dN \cdot (i - 1)) + N_{lb}))] \quad (1)$$

The corresponding settlement is then:

$$\Delta S_{b,i} = \sum_{j=1}^k \Delta\varepsilon_{p-b,i,j} \cdot h_j \quad (2)$$

where $\Delta\varepsilon_{p-b,i}$ = ballast permanent strain increment; $\sigma_{d-b,i}$ = ballast deviatoric stress updated every iterative step (in MPa); dN = the repeated load application for each iterative step; i = iterative step; N_{lb} = the number of load cycles after the last ballast renewal/tamping; $\Delta S_{b,i}$ = ballast settlement increment; k = number of sublayers; and h_j = the thickness of each layer.

4.2 Subgrade settlement

Considering settlement in the subgrade which depends on soil types (Ramos et al., 2021), the equation is modified from Li-Selig model (Li and Selig, 1996). Similar to the ballast settlement calculation approach, the modification is to take into account the evolving dynamic stress and to be able to simulate for the scenarios of newly constructed track and existing track/subgrade. A modified equation for calculating permanent strain increment at each iterative step is proposed:

$$\Delta\varepsilon_{p-s,i} = \frac{a}{100} \left(\frac{\sigma_{d-s,i}}{\sigma_s} \right)^m \left[((dN \cdot i) + N_{ls})^b - ((dN \cdot (i - 1)) + N_{ls})^b \right] \quad (3)$$

$$\Delta S_{s,i} = \sum_{j=1}^k \Delta\varepsilon_{p-s,i,j} \cdot h_j \quad (4)$$

where $\Delta\varepsilon_{p-s,i}$ = subgrade permanent strain increment; $\sigma_{d-s,i}$ = subgrade deviatoric stress updated every iterative step (in Pa); σ_s = soil compressive strength (in Pa); N_{ls} = the number of load cycles after the last subgrade renewal; $\Delta S_{s,i}$ = subgrade settlement increment; and a , m , and b = material parameters given in Table 1.

Table 1. Li-Selig settlement parameters a , b , and m (Li and Selig, 1996).

Li-Selig material parameter	Soil type			
	CH (fat clay)	CL (lean clay)	MH (elastic silt)	ML (silt)
a	1.20	1.10	0.84	0.64
b	0.18	0.16	0.13	0.10
m	2.40	2.00	2.00	1.70

Three example scenarios for different settlement rates that the model can simulate are illustrated in Figure 3. The first scenario is the case of newly constructed track (newly installed ballast and soft subgrade), where the settlement in subgrade layer is higher than ballast layer during the years after construction, as shown in Figure 3(a). Alternatively, the second scenario is the case where the track has been in place for several years, but the ballast layer has recently been tamped or renewed. The settlement in ballast layer, for this case, exceeds the subgrade, particularly during the initial years after tamping or renewal, as shown in Figure 3(b).

The third scenario is the case where both ballast and subgrade have been in place for many years without any maintenance action. The settlement rates of both ballast and subgrade accumulate slowly over the number of loading cycles, as shown in Figure 3(c).

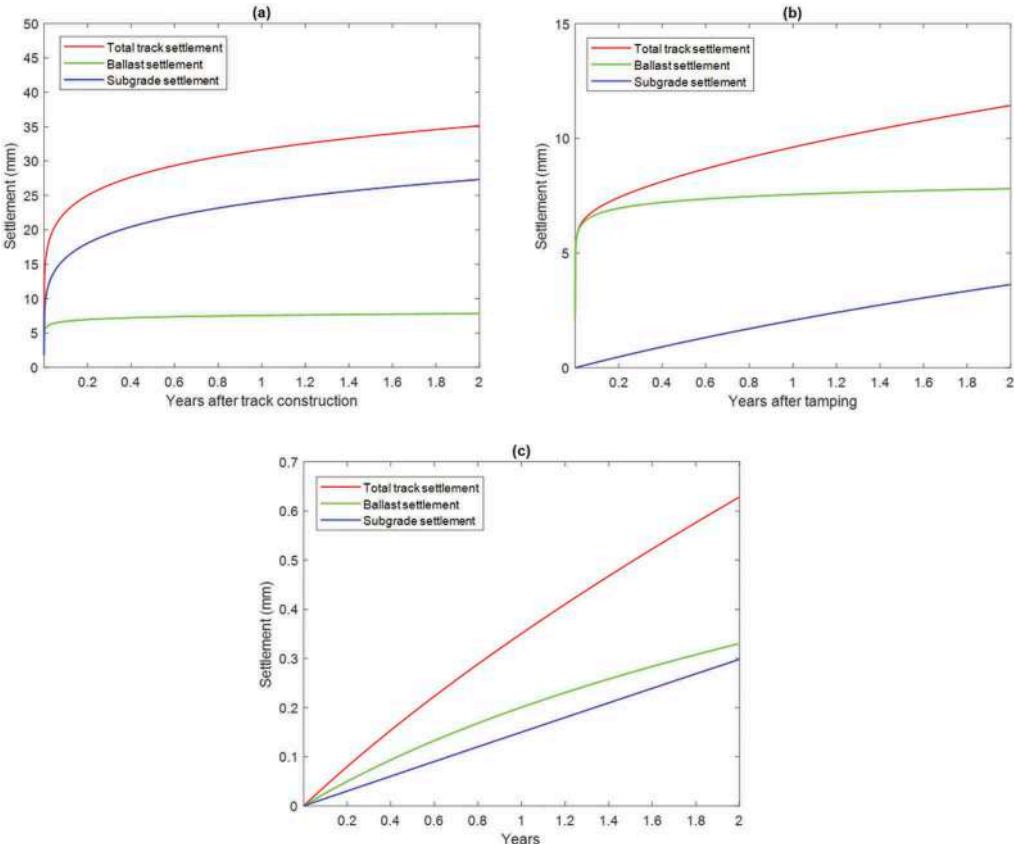


Figure 3. Ballast, subgrade, and total track settlement: (a) a newly constructed track (b) an existing track following tamping and (c) an existing track that has not recently been tamped.

5 VALIDATION OF DIFFERENTIAL SETTLEMENT

To validate the model’s ability to predict the vertical track geometry evolution with increasing load passages, historical track geometry data collected by a track recording vehicle is used for comparison. The data is from a selected track section on the UK’s West Coast Main Line. The quality of the track is defined by calculating standard deviation of the vertical track geometry data over a 200m track length. Only the wavelength range between 3m and 25m are considered as the model aims to predict tamping intervals.

The properties of the track and subgrade on this site are shown in Table 2. The subgrade soil type is silt (ML) with a shear strength of 25 kPa. The parameters a, b and m for the Li-Selig subgrade settlement model are 0.64, 0.10, and 1.7 respectively. To reduce the variation in vehicle types, the site was specifically chosen to have minimal freight traffic. Table 3 shows the properties of the dominant vehicle which is based upon the British Rail Class 390 (Pendolino). Regarding the traffic information, the operational line speed is 125 mph with annual tonnage of 37 MGT (million gross tonnes), 98% of which is passenger traffic. Over a year period, track

geometry data was recorded on 04-Jan-2017, 26-Apr-2017, 16-Aug-2017, and 16-Dec-2017, without tamping between these dates.

Table 2. Ballasted track properties.

Component	Value	Description
UIC 60 Rail (single rail)	0.172	Height (m)
	0.015	Length in transversal direction (m)
	7.677×10^3	Section area (m ²)
	3.038×10^{-5}	Moment of Inertia y-y (m ⁴)
	0.512×10^{-5}	Moment of Inertia z-z (m ⁴)
	2.11×10^{11}	Young's modulus (Pa)
	7850	Density (kg/m ³)
	0.3	Poisson's ratio
	0.01	Hysteric damping coefficient
	Railpad (spring element)	255×10^6
22.5×10^3		Viscous damping (Ns ² /m)
Sleeper (G44)	0.2	Height (m)
	2.5	Length in transversal direction (m)
	0.65	Sleeper spacing (m)
	3×10^{10}	Young's modulus (Pa)
	2500	Density (kg/m ³)
	0.2	Poisson's ratio
Ballast	0.01	Hysteric damping coefficient
	0.3	Height (m)
	2.8	Length in transversal direction (m)
	197×10^6	Young's modulus (Pa)
	1591	Density (kg/m ³)
	0.12	Poisson's ratio
Sub-ballast	0.061	Hysteric damping coefficient
	0.5	Height (m)
	3.5	Length in transversal direction (m)
	212×10^6	Young's modulus (Pa)
	1913	Density (kg/m ³)
Subgrade	0.3	Poisson's ratio
	0.054	Hysteric damping coefficient
	60×10^6	Young's modulus (Pa)
	2000	Density (kg/m ³)
	0.35	Poisson's ratio
	0.03	Hysteric damping coefficient

The track geometry data measured on 04-Jan-2017 was used as the initial track irregularity profile in the simulation. The model simulated and updated the track irregularity profile after every individual axle passage until reaching the defined MGT. The predicted geometry SD evolution from the model is compared against the real historical data, as shown in Figure 4. The triangle markers represent the recording geometry SD data from the site, and the black marker is the SD of the starting vertical track geometry profile. The black solid line represents the geometry SD predicted in simulation after every load cycle. This result shows a strong match between the predicted geometry SD curve and the real data. Combined with the vertical track geometry profile results, it is confirmed that the model is capable of accurately predicting differential settlement and the evolution of geometry SD.

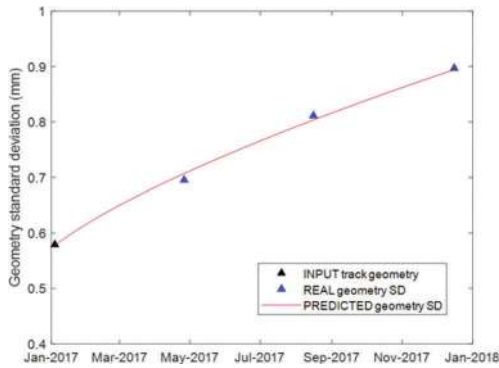


Figure 4. Evolution of geometry SD with time: predicted values vs field data.

6 A PARAMETRIC STUDY OF SUBGRADE MATERIAL PROPERTIES

The model of subgrade material is characterised by elastodynamic properties and settlement properties. The elastodynamic properties describe the propagation of stress fields, while the settlement properties describe how the stress fields result in settlement. A sensitivity analysis is performed to understand the relation between these properties. The Young's modulus and the Li-Selig settlement parameters (a, b and m) were chosen to vary. The two different Young's modulus properties, representing a stiff and soft soil, are shown in Table 3. The four different settlement parameters, depending on soil types, are shown in Table 1. It should be noted that this analysis does not focus on the simulation of any particular soil types, instead, it is to understand the influence of each subgrade parameter.

Figure 5 shows the finite element mesh of the simulation which the properties of the rails, rail pads, sleepers, ballast and sub-ballast are the same as described in Table 2. The vehicle is a Class 390 train (Pendolino) travelling at 125mph. The starting track geometry profile is artificially generated to represent a new track, constructed to tight tolerances and prior to significant train loading.

Figure 6 shows the change in geometry SD versus number of load cycles, for changing the Li-Selig settlement parameters: CH, CL, MH, ML, and for the stiff (Soil 1) and soft soils (Soil 2). Considering Soil 1 shown in Figure 6(a), the geometry SD for a ML soil is 0.149mm, while the SD increases by 4.09% for MH, 7.84% for CL and 16.49% for CH. For Soil 2 shown in Figure 6(b), in similar manner, the same soil parameters cause increases of 4.74% for MH, 8.38% for CL and 20.66% for CH. Therefore, it can be concluded that an increase of clay

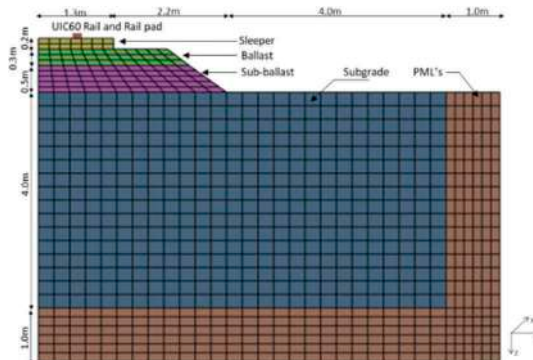


Figure 5. Finite element mesh.

content in the soil results in the larger settlement. However, although the parameters of the subgrade settlement model significantly affect track geometry deterioration, the difference between the stiff soil (Soil 1) and soft soil (Soil 2) is even greater. The soft soil results in a significantly higher geometry SD for all settlement parameters, meaning that the subgrade stiffness is important on track performance.

Table 3. Subgrade properties.

Parameter	Soil 1	Soil 2
Young's modulus (Pa)	120×10^6	60×10^6
Density (kg/m^3)	2000	2000
Poisson's ratio	0.3	0.3
Hysteric damping coefficient	0.03	0.03
Primary wave speed (m/s)	284	201
Secondary wave speed (m/s)	152	107

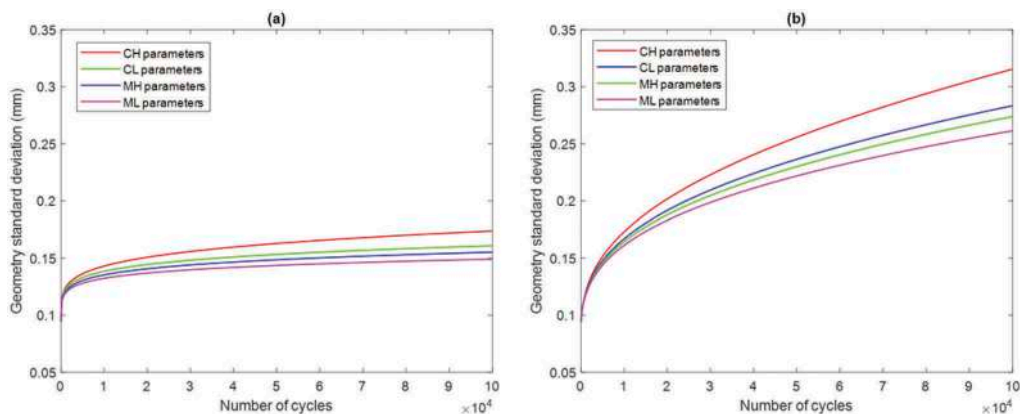


Figure 6. Track geometry evolution for varying subgrade properties: (a) Soil 1 (b) Soil 2.

7 CONCLUSIONS

This paper presents a novel numerical algorithm to predict the evolution of irregularities in track geometry and differential settlement of railway track. To maximise the computational efficiency of the implementation and allow for irregularities in track geometry to be updated after every axle passage, the model is solved using a combination of frequency-wavenumber and time-space domains. The fully coupled track and ground are modelled explicitly, allowing for 3D stress fields to be computed. The effect of nonlinearity in track and ground material properties is accounted for. The modified settlement laws are used to account for the evolving train-track interaction forces due to changes in the track irregularity profile. The model is validated against the field geometry data to confirm the ability of the model to accurately predict the future changes in track geometry profile. Finally, the validated model is used to perform a parametric study, where the elastodynamic properties and settlement parameters of the subgrade are investigated. The results show that subgrade material properties have a marked effect on track settlement. The stiffer soils can greatly reduce settlement and increase the life of track, thus the importance for well design and construction of the subgrade is highlighted.

REFERENCES

- Abadi, T., Le Pen, L., Zervos, A., Powrie, W., 2016. A Review and Evaluation of Ballast Settlement Models using Results from the Southampton Railway Testing Facility (SRTF). *Procedia Eng.* 143, 999–1006.
- Charoenwong, C., Connolly, D.P., Woodward, P.K., Galvin, P., Alves Costa, P., 2022. Analytical forecasting of long-term railway track settlement. *Comput. Geotech.* 143, 104601.
- Chen, C., McDowell, G.R., 2016. An investigation of the dynamic behaviour of track transition zones using discrete element modelling. *Proc. Inst. Mech. Eng. Part F J. Rail Rapid Transit* 230, 117–128.
- Connolly, D.P., Costa, P.A., 2020. Geodynamics of very high speed transport systems. *Soil Dyn. Earthq. Eng.* 130, 105982.
- Connolly, D.P., Dong, K., Alves Costa, P., Soares, P., Woodward, P.K., 2020. High speed railway ground dynamics: a multi-model analysis. *Int. J. Rail Transp.* 8, 324–346.
- Connolly, D.P., Giannopoulos, A., Forde, M.C., 2014. A higher order perfectly matched layer formulation for finite-difference time-domain seismic wave modeling. *Geophysics* 80, T1–T16.
- Dong, K., Connolly, D.P., Laghrouche, O., Woodward, P.K., Alves Costa, P., 2019. Non-linear soil behaviour on high speed rail lines. *Comput. Geotech.* 112, 302–318.
- Guo, Y., Zhai, W., 2018. Long-term prediction of track geometry degradation in high-speed vehicle–ballastless track system due to differential subgrade settlement. *Soil Dyn. Earthq. Eng.* 113, 1–11.
- Kumar, N., Kossmann, C., Scherriau, S., Six, K., 2021. An efficient physical-based method for predicting the long-term evolution of vertical railway track geometries. *Proc. Inst. Mech. Eng. Part F J. Rail Rapid Transit*.
- Lamprea-Pineda, A.C., Connolly, D.P., Hussein, M.F.M., 2022. Beams on elastic foundations – A review of railway applications and solutions. *Transp. Geotech.* 33, 100696.
- Lee, J.S., Hwang, S.H., Choi, I.Y., Choi, Y., 2020. Deterioration Prediction of Track Geometry Using Periodic Measurement Data and Incremental Support Vector Regression Model. *J. Transp. Eng. Part A Syst.* 146, 04019057.
- Li, D., Selig, E.T., 1996. Cumulative Plastic Deformation for Fine-Grained Subgrade Soils. *J. Geotech. Eng.* 122, 1006–1013.
- Neuhold, J., Landgraf, M., Marschnig, S., Veit, P., 2020. Measurement Data-Driven Life-Cycle Management of Railway Track. *Transp. Res. Rec.* 2674, 685–696.
- Nielsen, J.C.O., Li, X., 2018. Railway track geometry degradation due to differential settlement of ballast/subgrade – Numerical prediction by an iterative procedure. *J. Sound Vib.* 412, 441–456.
- ORE, 1970. Question D71: Stresses in the Rails, the Ballast and in the Formation Resulting from Traffic Loads. Stresses in the formation (results of the third phase; measurements under dynamic conditions). International Union of Railways, Office for Research and Experiments.
- P.Chumyten, D.P., Connolly, P.K., Woodward, V., Markine, 2022. The effect of soil improvement and auxiliary rails at railway track transition zones. *Transp. Geotech.*
- Ramos, A., Gomes Correia, A., Calçada, R., Alves Costa, P., Esen, A., Woodward, P.K., Connolly, D. P., Laghrouche, O., 2021. Influence of track foundation on the performance of ballast and concrete slab tracks under cyclic loading: Physical modelling and numerical model calibration. *Constr. Build. Mater.* 277, 122245.
- Ramos, A., Gomes Correia, A., Indraratna, B., Ngo, T., Calçada, R., Costa, P.A., 2020. Mechanistic-empirical permanent deformation models: Laboratory testing, modelling and ranking. *Transp. Geotech.* 23.

Utilization of traditional and recycled materials



Taylor & Francis

Taylor & Francis Group

<http://taylorandfrancis.com>

E* master curve parameters as indicators of cracking susceptibility of mixtures with recycled asphalt shingles

F. Leiva & A. Taylor

National Center for Asphalt Technology, Auburn University, Alabama, USA

ABSTRACT: The parameter or coefficient γ obtained from the E* master curve has been shown to relate to the width of the relaxation spectra and is related to the slope of the master curve. Incorporation of aged binders or binders with hardening modifiers to a mixture leads to an increase in γ , which corresponds to a flattening of the master curve (lower susceptibility to frequency changes) and widening of the relaxation spectra. For a standard logistic function, the inflection point modulus ($-\beta/\gamma$) is controlled by the aggregate structure and volumetric effects. At high temperatures, the aggregate structure begins to dominate the behavior of the mixture, while volumetric properties and binder stiffness control the behavior at lower temperatures. Incorporation of aged binder or hardening modifiers to a mixture leads to a shift of the inflection point to lower frequencies. In this study, 15 asphalt mixtures containing Recycled Asphalt Shingles (RAS) were tested to evaluate their cracking susceptibility in the laboratory. Besides mixture characterization under dynamic modulus test protocols, the laboratory testing program evaluated recovered binder performance grade and fatigue cracking laboratory performance tests including Bending Beam Fatigue test, Energy Ratio, Overlay Tester and Fracture Energy (Flexibility Index test). The results of this study indicated good relationships between the master curve inflection point with the flexibility index and the dissipated creep strain energy (DCSE, from Energy Ratio testing). These results suggested that as the mixtures become more susceptible to cracking (lower Flexibility Index) and become more brittle (lower DCSE) the inflection point of the master curve decreases (due to stiffening of the binder in the mixture). In addition, when all the mixtures were ranked from top to bottom cracking susceptibility, the master curve inflection point agreed well with all the other cracking test results.

Keywords: Dynamic Modulus, Asphalt Shingles, Cracking, Warm Mix

1 INTRODUCTION

New pavement technologies are continuously being developed and evaluated by highway agencies and the asphalt pavement industry to reduce the consumption of natural resources and costs of asphalt paving mixtures. Two technologies that have received substantial attention in recent years are the use of recycled asphalt shingles (RAS) and warm mix asphalt (WMA) (Williams et al. 2018). These new technologies address important issues that face the asphalt industry in different ways. RAS contains a high percentage of asphalt binder, which can reduce the amount of virgin asphalt binder needed in a mixture. Since binder is the most expensive component of an asphalt mixture, the use of RAS can significantly reduce mixture costs. WMA, on the other hand, uses additives or other means of decreasing the viscosity of asphalt binders (Mallick et al, 2008) in

order to allow lower production and compaction temperatures compared to conventional hot mix asphalt (HMA). Lowering the temperature reduces the amount of energy required for the production of asphalt paving mixtures, thereby reducing emissions, exposure risks for paving crews, and production costs (West et al. 2014).

The use of reclaimed asphalt pavement (RAP) in combination with WMA technologies had offered a solution to maintain the current state of technology that enables to utilize RAP at a relatively lower temperature than HMA mixtures. O'Sullivan and Wall (2009) indicated that the utilization of RAP with WMA technologies decreases the environmental impacts by using less virgin material and reducing CO₂ emissions. Mallick et al. (2007) and West et al. (2012) reported that it is possible to manufacture mixes with RAP with similar properties to HMA mixes through the use of WMA additives. However, manufacturing RAS-WMA mixtures with similar properties to RAS-HMA mixtures are still under investigation.

Annual surveys by the National Asphalt Pavement Association (NAPA) shows that WMA usage continues to grow, and as of 2017, it was 38.9% of the total asphalt paving mixture market (Williams et al 2018). Although RAS has had limited use in asphalt paving mixtures for several decades, its use increased significantly between 2009 and 2015 primarily due to spikes in virgin asphalt prices as well as greater interests in sustainability. In the last few years however, RAS usage has declined from the peak in 2014 (Williams et al 2018). Currently about half of the state DOTs allow the use of RAS. However some contractors use RAS in commercial projects in states where the DOT bans its use. Typical RAS contents are three to five percent of the total mix by weight, but due to the high asphalt content of RAS, the RAP binder usually constitutes about 20 percent of the mixture's total binder content.

However, the convergence of these two technologies raised some concerns. Some experts in the industry have questioned if the lower mix temperatures with WMA are sufficient to soften and activate hard RAS binders (LaPlante 2011, Williams 2013). A review of the literature found that no method has been identified to determine the degree to which RAS binder activates and becomes an integral part of the composite binder in an asphalt mixture. Some indirect evidence suggests that at least partial activation of a RAS binder increases with higher mixing temperatures and longer mixture storage time. For lower mixing temperatures associated with WMA, there is a greater chance that the very hard RAS binders may not be sufficiently softened to blend with virgin binders during the mixing process. Other factors that are likely to contribute to the degree of activation include the stiffness of the RAS binder, sizes of the RAS particles, chemical properties of the virgin binder and/or rejuvenator or other additives, and mixing time.

Rather than trying to determine the degree of activation directly, this study examined properties of mixtures containing RAS produced with and without WMA technologies and the associated decrease in mixing temperatures. This work was sponsored by the National Cooperative Highway Research Program (NCHRP) project 09-55 entitled "Recycled Asphalt Shingles in Asphalt Mixtures with Warm Mix Asphalt Technologies."

1.1 *Experimental plan*

The objective of this study was to evaluate cracking potential of asphalt mixtures incorporating WMA technologies and RAS and compare them to the companion HMA mixtures. This research was also envisioned to evaluate E* Master curve parameters as potential indicators of cracking susceptibility

The experimental plan involved identifying field projects using mixtures containing RAS where the mixtures were produced at hot mix temperatures and with a WMA technology at a reduced production temperature. Five field projects were selected for this study. The laboratory testing program evaluated recovered binder properties and results of five mixture cracking tests: Bending Beam Fatigue (AASHTO T 321-14), Energy Ratio, Overlay Tester (TxDOT 248-F), Semi-Circular Bend Test (SCB) (ASTM D8044-16), and Illinois Flexibility Index Test (AASHTO TP 124-16).

1.2 Mixtures properties

The five projects built and evaluated during this study are summarized in Table 1. For each project, a control HMA section was constructed to provide a direct comparison for field performance and materials properties to mixtures using a WMA technology. All mixtures contained RAS. Table 2 shows a summary of the volumetric properties for samples compacted on-site.

Table 1. Projects and mix information.

Project #	1	2	3	4	5
Location	Larsen, WI	Enterprise, AL	Oak Ridge, TN	Wilson, NC	LaPorte, IN
Project Date	09/2013	06/2014	10/2014	06/2015	9/2015
# of Mixtures	3	4	2	4	2
Mix Variable(s)	WMA vs. HMA	WMA vs. HMA & Design Va	WMA vs. HMA	WMA vs. HMA & PC vs. MW	WMA vs. HMA
WMA Technology	Zycotherm and Rediset	Gencor Foamer	Evotherm M1	Evotherm 3G	Foaming
Average Produc. Temp., °F	HMA: 324 WMA: 319	HMA: 351 WMA: 308	HMA: 315 WMA: 267	HMA: 300 WMA: 276	HMA: 318 WMA: 303
Design Air Voids	4.0	4.0 and 3.5	4.0	4.0	4.0
Road	STH 96	US 84	TN 170	SC 42	SR39
ESAL Range, 10 ⁶	1-3	1.5	NA	0.3 – 3	NA
Virgin Binder	58-28	67-22	64-22	58-28	64-22
NMAS, mm	12.5	12.5	12.5	9.5	9.5
% RAP	14	15	10	20	15
% MW RAS	3	0	0	5*	2
% PC RAS	0	5	3.5	5*	0
% RAP Binder	12.1	13.5	10.9	18.5	NA
% RAS Binder	11.2	19.6	11.7	16.7	NA

MW = Manufacturer Waste, PC = Post Consumer, NA = Not Available

Note: 5% PC was used in one mix while 5% MW was used in the second mix.

2 CRACKING TEST RESULTS

As previously noted, five asphalt mixture cracking tests were conducted on the mixtures from the five field projects. Mixture samples were obtained during production from haul trucks and placed in 19 liter metal cans. Later, the cans containing the mixtures were reheated to 150°C for two hours, quartered into appropriate masses for specimens, then heated to the respective compaction temperature for one hour, and finally compacted to $7 \pm 0.5\%$ air voids using a Superpave Gyrotory Compactor (SGC).

2.1 Bending beam fatigue

Bending beam fatigue tests were conducted in accordance with AASHTO T 321-14. Three beams each were tested at two strain magnitudes. For the Wisconsin project, several beams tested at $250 \mu\epsilon$ did not fail within 12 million cycles (test stopping criteria), so the strain levels were adjusted for the other projects. Table 7 shows the results of the beam fatigue tests. For the WI mixture results, failure was based on the old AASHTO criteria of a 50% reduction in beam stiffness. For the other projects, the new method for determining failure based on peak modulus \times cycles was used.

Table 2. Summary of hot-compacted volumetric mix properties.

Loc.	Mix ID	Air Voids, %	Voids in Mineral Aggregate, %	Voids Filled with Asphalt, %	Dust/Binder	Binder, %
WI	Control	4.4	15.5	71.7	0.9	5.5
	Rediset	4.4	15.0	70.8	0.9	5.3
	Zycotherm	4.4	15.8	72.0	0.8	5.4
AL	Low Va HMA	1.8	12.9	86.2	1.1	5.5
	Low Va WMA	1.3	13.5	90.6	0.9	5.1
	Adj. Va HMA	3.0	13.3	77.2	1.1	5.2
	Adj. Va WMA	2.5	13.3	81.1	1.2	4.8
TN	HMA	6.2	16.1	61.3	1.3	5.0
	WMA	5.3	16.7	68.1	1.0	5.7
NC	HMA MWRAS	6.4	16.5	61.3	1.0	5.0
	WMA MWRAS	4.9	15.8	69.2	1.0	5.2
	HMA PCRAS	4.2	15.8	73.2	1.0	5.4
	WMA PCRAS	4.2	15.6	73	1.1	5.4
IN	HMA	5.3	16.0	67.1	1.4	5.5
	WMA	4.2	15.2	72.5	1.3	5.7

Table 3. Bending beam fatigue test results.

Loc.	Mix	Micro-strain 1	Average N_f	Micro-strain 2	Average N_f	Endurance Limit, $\mu\epsilon$	Million N_f @ 400 $\mu\epsilon$
WI	Control	500	287,530	250	126,510,069	258	3.28
	Rediset	500	258,840	250	81,180,843	241	2.58
	Zycotherm	500	339,997	250	92,643,767	228	3.20
AL	Low Va HMA	600	53,803	300	4,074,857	169	0.96
	Low Va WMA	600	107,263	300	7,841,577	197	1.88
	Adj. Va HMA	600	91,153	300	1,451,193	83	0.58
	Adj. Va WMA	600	76,497	300	4,453,407	140	1.15
TN	HMA	600	66,908	300	2,842,008	149	0.81
	WMA	600	59,745	300	1,105,585	94	0.42
NC	MW HMA	700	45,565	350	1,830,803	165	1.10
	MW WMA	700	38,264	350	861,843	113	0.55
	PC HMA	700	17,427	350	954,994	139	0.54
	PC WMA	700	25,221	350	820,699	118	0.50
IN	HMA	600	59,437	300	2,245,642	143	0.67
	WMA	600	89,964	300	2,473,384	112	0.82

2.2 Energy ratio

Energy Ratio (ER) is determined using a combination of three tests: resilient modulus, creep compliance, and indirect tensile strength. Roque et al recommend a minimum dissipated creep strain energy $DSCE_{HMA}$ of 0.75 and a minimum ER of 1.95 to avoid top-down cracking (Roque et al. 2004). It is important to remember that these criteria were developed for Florida's climate and materials.

The ER results for each mixture are summarized in Table 8. All of the WI and TN mixtures met the recommended Florida $DSCE_{HMA}$ and ER criteria. For the AL mixtures, only the low air voids (Low Va) WMA mixture had a $DSCE_{HMA}$ greater than 0.75, which is considered a minimum threshold value to discriminate brittle mixtures. The AL adjusted air voids (Adj. Va) HMA mixture had the lowest $DSCE_{HMA}$ value of 0.08, and the lowest Fracture Energy of 0.2, indicating a mixture very susceptible to top-down cracking.

Table 4. Energy Ratio results.

Loc.	Mixture	m-value	Tensile Strength, MPa	Resilient Modulus, GPa	Fracture Energy (kJ/m ³)	DSCE _{HMA} , kJ/m ³	Energy Ratio
WI	Control	0.386	2.14	10.14	3.4	3.17	3.23
	Rediset	0.447	2.13	9.34	4.6	4.36	3.73
	Zycotherm	0.441	2.03	9.81	4.1	3.89	2.75
AL	Low Va HMA	0.328	2.13	13.97	0.6	0.44	1.70
	Low Va WMA	0.419	2.44	10.72	2.0	1.72	1.92
	Adj. Va HMA	0.266	1.9	14.94	0.2	0.08	0.59
	Adj. Va WMA	0.385	2.16	14.23	0.9	0.74	2.03
TN	HMA	0.420	2.75	12.12	3.4	3.09	4.48
	WMA	0.521	2.4	11.12	5.0	4.74	3.06
NC	HMA MWRAS	0.426	1.77	12.26	0.3	0.17	0.29
	WMA MWRAS	0.586	2.26	9.01	6.2	5.92	2.12
	HMA PCRAS	0.406	2.59	11.43	2.8	2.51	3.89
	WMA PCRAS	0.479	2.39	8.69	5.0	4.67	2.44
IN	HMA	0.424	2.70	13.50	3.20	2.93	4.39
	WMA	0.429	2.45	13.18	2.60	2.37	3.51

2.3 Overlay test and flexibility index

The Overlay Tests were performed using the first generation OT jig in the IPC Global AMPT in accordance with the TxDOT 248-F parameters, which specify a cyclic maximum opening displacement of 0.025" and a test temperature of 25°C. In addition to the standard procedure, samples from WI were also tested at 10°C using a smaller displacement, 0.015 inches, to represent the colder climate (Table 5). WMA mixtures tended to perform better than HMA mixtures with the top five OT performers being WMA mixtures. In addition, each WMA mixture outperformed its corresponding HMA pair. The Illinois Flexibility Index test (I-FIT) was performed in accordance with AASHTO T 324-16. A higher FI is generally indicative of a mixture with greater resistance to cracking. The Illinois DOT has set a preliminary minimum criterion for the Flexibility Index at 8.0 (Al-Qadi et al., 2015). The test results for all mixtures are given in Figure 1. None of the tested mixtures meet the preliminary IL DOT criterion. The NC WMA MWRAS mixture had the highest FI of 7.31. Three of the AL mixes had FI results below 1.0; those mixes also had very low OT cycles to failure. The WMA mixture performed better than its corresponding HMA mixture in all cases except for the WI Zycotherm mixture.

2.4 Dynamic modulus

Dynamic modulus testing was conducted to assess differences in mix stiffness between WMA and HMA. Dynamic modulus testing was performed using AASHTO TP 79-13. The samples were prepared to $7 \pm 0.5\%$ air voids and were compacted to a height of 175 mm and a diameter of 150 mm in accordance with AASHTO P 60-09 tolerances.

Dynamic modulus testing was performed using an IPC Global Asphalt Mixture Performance Tester (AMPT). Dynamic modulus testing is performed to quantify the stiffness of the asphalt mixture over a wide range of testing temperatures and frequencies. The temperatures and frequencies used for testing these mixes are those recommended in AASHTO PP 61-13. For this methodology, the high test temperature is dependent on the high PG grade of the base binder utilized in the mix being tested.

The collected data were used to generate a master curve for each individual mix. The master curve uses the principle of time-temperature superposition to horizontally shift data at multiple temperatures and frequencies to a reference temperature so that the stiffness data can be viewed without temperature as a variable. This method of analysis allows for visual relative

Table 5. Overlay Test results.

Loc.	Mix	Cycles until Failure (OT) ₂		Flexibility Index (FI)	
		Average	St. Dev.	Average	St. Dev.
WI	Control	241	83.8	3.33	0.52
	Rediset	285	51.1	5.77	1.76
	Zycotherm	436	96.4	2.90	0.47
AL	Low Va HMA	19	0.6	0.66	0.40
	Low Va WMA	214	69.1	2.93	0.65
	Adj. Va HMA	24	8.4	0.15	0.05
	Adj. Va WMA	44	5.6	0.97	0.16
TN	HMA	226	55.4	3.34	0.90
	WMA	807	148.2	4.92	0.73
NC	HMA MWRAS	125	78.6	1.77	0.56
	WMA MWRAS	619	88.4	7.31	0.56
	HMA PCRAS	215	54.9	3.69	0.81
	WMA PCRAS	333	142.2	4.67	0.52
IN	HMA	109	30.3	1.05	0.39
	WMA	158	71.1	1.72	0.17

comparisons to be made between multiple mixes. Table 6 provides a summary of the master curve regression coefficients generated using the modified MEPDG master curve model. Goodness of fit parameters are also shown.

Table 6. Master curve coefficients.

Loc.	Mix ID	Max E* (ksi)	Min E* (ksi)	Beta	Gamma	$\Delta E A$	R ²	Se/Sy
WI	Control	3,128.7	8.69	-0.749	-0.524	186,531	0.997	0.037
	Rediset	3,132.6	8.31	-0.625	-0.526	170,765	0.995	0.050
	Zycotherm	3,121.6	7.99	-0.680	-0.504	182,310	0.996	0.042
AL	Low Va HMA	3,116.6	3.59	-1.329	-0.451	203,433	0.999	0.019
	Low Va WMA	3,122.3	3.42	-1.131	-0.482	202,939	0.999	0.025
	Adj. Va HMA	3,162.9	5.85	-1.340	-0.491	197,753	0.998	0.032
	Adj. Va WMA	3,158.4	3.62	-1.351	-0.463	198,600	0.999	0.024
TN	HMA	3,220.7	5.63	-1.247	-0.528	203,066	0.998	0.028
	WMA	3,140.4	8.78	-0.860	-0.593	200,477	0.996	0.043
NC	HMA MWRAS	3,181.5	5.52	-1.074	-0.485	198,723	0.999	0.021
	WMA MWRAS	3,128.2	4.81	-0.733	-0.561	182,240	0.997	0.040
	HMA PCRAS	3,120.5	3.23	-1.182	-0.452	195,575	0.999	0.018
	WMA PCRAS	3,119.7	3.77	-0.918	-0.501	191,667	0.999	0.025
	HMA	3,250.7	8.15	-1.351	-0.526	185,979	0.999	0.019
	WMA	3,216.8	7.90	-1.358	-0.512	191,034	0.999	0.020

3 E*PARAMETERS AS INDICATORS OF CRACKING SUSCEPTIBILITY

The parameter γ (gamma) obtained from the E* master curve has been shown to relate to the width of the relaxation spectra and is related to the slope of the master curve (Bhattacharjee et al. 2012). Incorporation of aged binders or binders with hardening modifiers to a mixture leads to an increase in γ , which corresponds to a flattening of the master curve (lower susceptibility to frequency changes) and widening of the relaxation spectra. For a standard logistic function, the inflection point modulus ($-\beta/\gamma$) is controlled by the aggregate structure and volumetric effects. At high temperatures, the aggregate structure begins to dominate the behavior of the mixture, while volumetric properties and binder stiffness control the behavior at lower temperatures. Incorporation of aged binder or hardening modifiers to a mixture leads to a shift of the inflection point to lower frequencies. Figure 1 shows a plot of the relaxation

spectra parameter versus the inflection point for all mixtures from the new projects. As observed, hardening increases from WMA to HMA mixtures for all cases except the AL Low Va and the IN mixtures. This type of analysis was recently used by Mensching et al. (2016) while trying to define failure criteria for low temperature performance of asphalt mixtures.

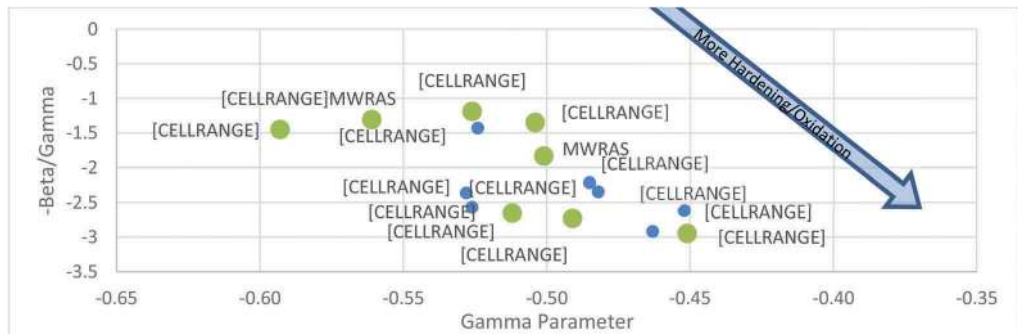


Figure 1. Relaxation spectra parameter versus inflection point.

Figure 2 shows the relationship between the inflection point and the flexibility index for all mixtures. A reasonable correlation was obtained between these parameters ($R^2 = 0.54$) and the results follow the expected trend regarding aging and cracking susceptibility. Figure 2 also shows another reasonable correlation ($R^2 = 0.57$) of the inflection point, this time with the dissipated creep strain energy at failure from the energy ratio test and indirect tensile strength test. Lower dissipated creep strain energy to failure is expected for mixtures containing aged binders, thus confirming the observed relationship between relaxation spectra shape parameters and cracking susceptibility of asphalt mixtures.

The average dynamic modulus and phase angle data were plotted in Black Space for each of the mixtures. Due to the interaction of the asphalt binder and aggregate, mixtures generally exhibit a peak phase angle at an intermediate dynamic modulus. This peak value is associated with the inflection point in the master curve ($-\beta/\gamma$). The greater the E^* inflection point (towards the right), the stiffer and/or more oxidized the mixture. The greater the phase angle inflection point, the more viscous the mixture. The phase angle represents the amount of energy a specimen can absorb, which indicates how well a specimen will resist cracking. A large peak phase angle indicates that a specimen will tend to deform before it cracks. Phase angle is one of the testing parameters for the dynamic modulus test and is inversely related to the stiffness of the asphalt specimen. If the specimen has a relatively high stiffness at one frequency, it will tend to have a low phase angle at the same frequency. Potential cracking indicators could include the peak phase angle, the peak E^* value, or the $-\beta/\gamma$ parameter. For all cases, except for IN mixtures and AL Adjusted Va mixtures, the E^* peak values of HMA mixtures were equal to or greater than the WMA mixtures and the phase angle peak values were equal or lower for HMA mixtures (Figure 3).

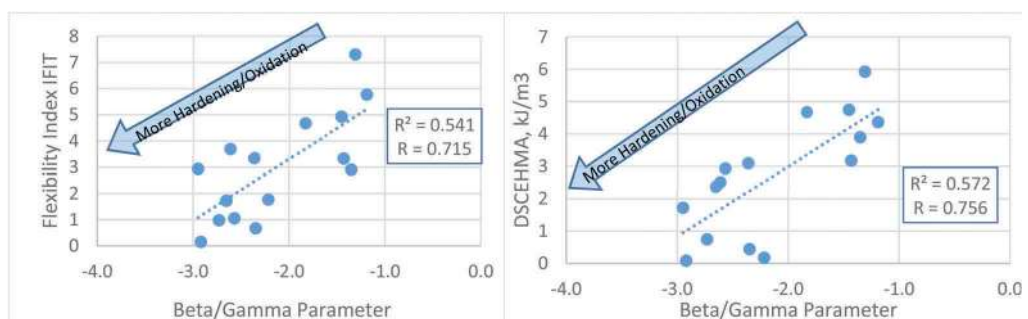


Figure 2. Inflection point vs. flexibility index and dissipated creep strain energy at failure.

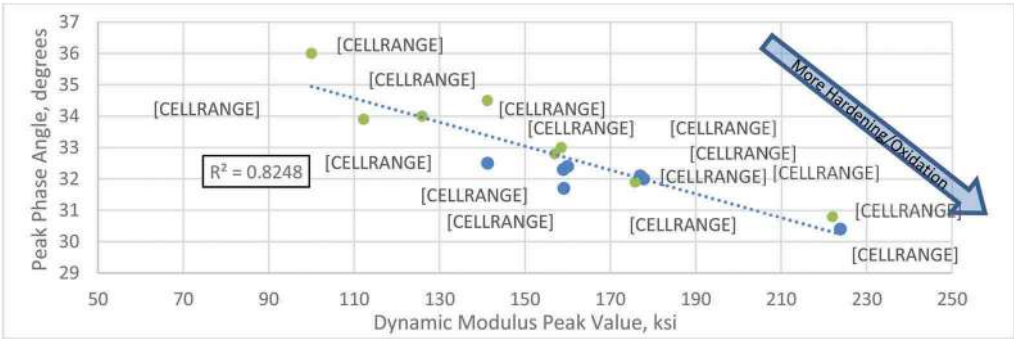


Figure 3. Black space diagram peak values.

Figure 4 shows the $-\beta/\gamma$ parameter for each mixture ranked from highest to lowest cracking susceptibility. The three mixtures with the highest values, and likely more resistant to intermediate temperature cracking, are WMA mixtures. On the other hand, most HMA mixtures tend to rank as more susceptible to cracking. Figure 5 shows the peak phase angle ranking for all mixtures. Higher phase angles are desirable to reduce cracking susceptibility. It can be seen that the six mixtures with the highest values were WMA mixtures.

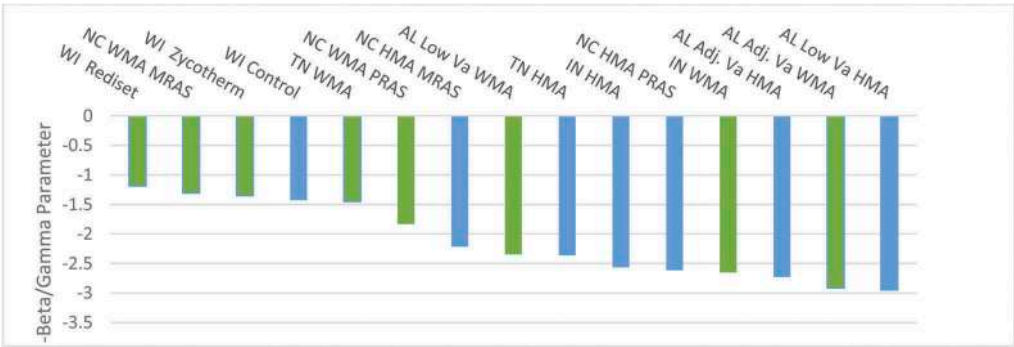


Figure 4. Ranking of mixtures by $-\beta/\gamma$ parameter.

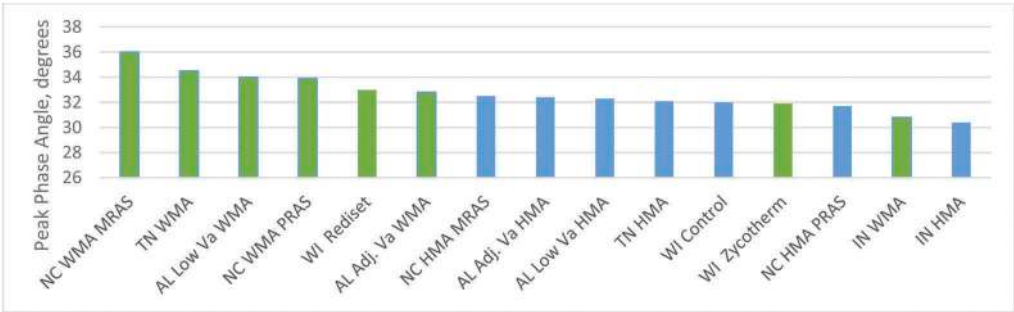


Figure 5. Ranking of mixtures by peak phase angle.

Table 7 shows a comparison of the cracking test parameters ranking results for each test from best (1) to worst (15). From the overall combined rank, the top five are all WMA mixtures, and within each project, the WMA mixtures rank higher than the HMA mixtures. Bending beam fatigue results were not included in the analysis due to the difference in procedures used to obtain the number of cycles to failure on the first project. Since the J_C parameter showed poor correlation with the other cracking test parameters and in several cases did not follow the expected trend when comparing HMA and WMA mixtures, it was not included in this analysis. As expected, all WMA mixtures outperformed their respective HMA pairs, and overall, the top six cracking-resistant mixtures were WMA mixtures.

Table 7. Comparison of rankings among cracking parameters.

Mix ID	DSCE _f	ER	OT	I-FIT	Peak E*	Peak Phase Angle	-β/ γ	Overall Combined Rank
WI Control	7	6	6	7	13	11	4	8
WI Rediset	5	4	5	2	7	5	1	3
WI Zycotherm	6	8	3	9	11	12	3	5
AL Low Va HMA	13	13	15	14	8	9	15	14
AL Low Va WMA	10	12	9	8	3	3	8	6
AL Adj. Va HMA	15	14	14	15	10	8	13	15
AL Adj. Va WMA	12	11	13	13	6	6	14	12
TN HMA	8	1	7	6	12	10	9	7
TN WMA	3	7	1	3	4	2	5	2
NC HMA MWRAS	14	15	11	10	5	7	7	11
NC WMA MWRAS	1	10	2	1	1	1	2	1
NC HMA PCRAS	9	3	8	5	9	13	11	9
NC WMA PCRAS	4	9	4	4	2	4	6	4
IN HMA	11	2	12	12	15	15	10	13
IN WMA	2	5	10	11	14	14	12	10

4 CONCLUSIONS

Analysis of E* master curve parameters indicated that the inflection point of the master curve and peak E* values and phase angles from black space diagrams generally agree with results obtained from other laboratory cracking tests. The results of this study indicated good relationships between the master curve inflection point with the flexibility index and the dissipated creep strain energy (DCSE, from Energy Ratio testing). These results suggested that as the mixtures become more susceptible to cracking (lower Flexibility Index) and become more brittle (lower DCSE) the inflection point of the master curve decreases (due to stiffening of the binder in the mixture). In addition, when all the mixtures were ranked from top to bottom cracking susceptibility, the master curve inflection point agreed well with all the other cracking test results.

REFERENCES

- Al-Qadi, I., H. Ozer, J. Lambros, A. El Khatib, P. Singhvi, T. Khan, J. R. Pérez, and B. Doll. *Testing Protocols to Ensure Performance of High Asphalt Binder Replacement Mixes using RAP and RAS*. Illinois Center for Transportation Series No. 15-017. Illinois Center for Transportation/University of Illinois at Urbana-Champaign. 2015.
- LaPlante, A. *Recycled Asphalt Shingles in HMA*. Pace Construction. Webinar. 2011.
- Mallick, R., J. Bradley, and R. Bradbury. *An Evaluation of Heated Reclaimed Asphalt Pavement (RAP) Material and Wax Modified Asphalt for Use in Recycled Hot Mix Asphalt (HMA)*. Journal of the Transportation Research Board, Volume 1998, 112–122. 2007.

- Mallick, R., P. Kandhal, and R. Bradbury. *Using Warm Mix Asphalt Technology to Incorporate High Percentage of Reclaimed Asphalt Pavement (RAP) Material in Asphalt Mixtures*. Journal of the Transportation Research Board, Volume 2051, 71–79. 2008.
- Mensing D. J., G. M. Rowe, and J. S. Daniel. *A Mixture-Based Black Space Parameter for Low Temperature Performance of Hot Mix Asphalt*. Journal of the Association of Asphalt Pavement Technologists Annual Meeting, Indianapolis, IN. 2016.
- O'Sullivan, K., and P. Wall. *The Effect of Warm Mix Asphalt Additives on Recycled Asphalt Pavement*. Worcester Polytechnic Institute. Master of Science Thesis. 2009.
- Roque, R., B. Birgisson, C. Drakos, and B. Dietrich. *Development and Field Evaluation of Energy-Based Criteria for Top-down Cracking Performance of Hot Mix Asphalt*. Journal of the Association of Asphalt Paving Technologists, Vol. 73, 229–260. 2004.
- West, R., C. Rodezno, G. Julian, and B. Prowell. *Field Performance of Warm Mix Asphalt Technologies*. NCHRP Report 779. Transportation Research Board. 2014.
- West, R.C., et al. *Phase IV NCAT Test Track Findings*. NCAT Report No. 12-10. National Center for Asphalt Technology, Auburn University. 2012.
- Williams, B.A., A. Copeland, and T.C. Ross. *Asphalt Pavement Industry Survey on Recycled Materials and Warm-Mix Asphalt Usage: 2017*. Information Series 138 (8th Edition), National Asphalt Pavement Association, Lanham, MD. 2018.
- Williams, R. C., A. Cascione, J. Yu, D. Haugen, M. Marasteanu, and J. McGraw. *Performance of Recycled Asphalt Shingles in Hot Mix Asphalt*. InTrans Project Reports. 19. 2013.

Laboratory study of soil-cement manufactured with RAP for its application as a sustainable and high-performance base in asphalt pavements

F. Moreno-Navarro, M. Sol-Sánchez, G. García-Travé, R. Tauste-Martínez & M.C. Rubio-Gámez

Laboratory of Construction Engineering, University of Granada, Granada, Spain

C. Rodriguez-López & M. Hernández-Pérez

Centro Tecnológico de la Construcción, Murcia, Spain

J. Gambín-Peñalver

Tecnología de la Construcción y Obras Públicas, S.A., TECOPSA, Murcia, Spain

ABSTRACT: With the aim of improving the structural performance of the base of asphalt pavements, the use of soil-cement can be an appropriate solution providing high bearing capacity and resistance to permanent deformations. However, these improved granular layers can present cracking problems due to the brittleness and the shrinkage produced by the hydration of the cement, reducing their capacity to absorb deformations and resulting in cracks that can be reflected in the upper layers of the pavement (which would accelerate the degradation of the whole infrastructure). In this context, the present paper focuses on the study of soil-cement manufactured with reclaimed asphalt pavements (RAP), as a substitutive of natural aggregates that would improve its ductility. This solution aims to provide a more sustainable and high-performance granular layer, reducing the consumption of raw materials while increasing the mechanical performance of the base layer. For this purpose, a laboratory study (that includes tensile and compression modulus tests, tensile and compression strength tests, and fatigue cracking test) was carried out using different RAP and cement content.

Keywords: Soil, cement, RAP, Sustainability, laboratory and field study, fatigue cracking test

1 INTRODUCTION

Bearing capacity of bases or subbases plays an essential role on the durability and mechanical performance of road, port and airport pavements. In the last decades, these infrastructures must respond to the growing trend in number of vehicles, axle loading and tire pressure, among other factors associated with the high level of mobility due to the globalization of the commerce. In this sense, from the middle of the last century, cement treated base (CTB) and subbase courses have been used as an effective solution to improve the strength of these infrastructures (Grilli et al. 2012).

This provides a stiffer support of the pavement that allows for better distribution of the traffic stresses while reducing the tensile strain at the bottom of bituminous layers in semi-rigid pavements (Xuan et al. 2012; Pérez et al. 2013). This category of structure is commonly

used on highways or heavy-traffic roads with the aim of increasing the durability and quality of the pavement while reducing the thickness of the bituminous layers (Baghini et al. 2016), searching for lower economic and environmental costs.

These benefits, joined to those associated with cement treatment improving the properties of poor-grade soils or industrial aggregates to enable use as pavement materials, are possible due to the hardening effect of CTB that takes place when defining a proper material design, manufacturing process, compaction and curing (Avirneni et al. 2016). This provides the previously cited benefits as long as the CTB maintain the strength and bearing capacity. However, the excessive stiffness and brittle behavior of the cement treated materials could affect negatively the life-span of the pavement because of premature cracking, whose propagation may result in a poor support, and therefore, accelerating the degradation process of the global pavement structure (Jitsangiam et al. 2021).

For such inconvenience, the use of additives aims to improve the tensile strength and ductility of the CTB, as done when employed in common cement concrete (Lanzoni et al. 2012). In this sense, it could be highlighted the use of fibres of different nature (steel, plastic, etc.) that could increase tensile cracking resistance, reduce brittleness and premature shrinkage cracking (Brandt, 2008). Similarly, diverse studies (Yang et al. 2009; Baghini et al. 2014; Du et al. 2016) have been recently focused on analysing the benefits of using bituminous emulsion or polymers like styrene-butadiene copolymer latex as additives in combination with the cement, aiming to enhance the durability and mechanical performance of the CTB for pavement structures.

Nonetheless, all these alternatives result in costs and consumption of raw materials increments (as well as energy during their manufacturing), joined to the negative effects of using high volume of specific natural aggregates (with particular resistance requirements, which sometimes difficult the use of available soils and increase transport distances) for the cement treated base (Ren et al. 2020). Therefore, on the base of current political and social awareness for more sustainable constructions, the application of reclaimed asphalt pavements (RAP) for the replacement of part or total of natural aggregates in CTB provides an interesting method for preserving natural resources while decreasing the accumulation of RAP from deteriorated old pavements (Taha et al. 2002). Additionally, the use of RAP could be expected to reduce the brittle behavior of CTB due to the bitumen content of the recycled aggregates. In fact, previous studies (Grilli et al. 2012) have demonstrated that the use of dosages up to 80% of RAP as replacement of natural aggregates, in combination with polypropylene fibres, could reach comparable bearing capacity to conventional CTB, while offering higher resistance to cracking, providing an efficient solution from an economic and environmental point of view.

In this context, this article aims to contribute with the development of such research line by studying high performance CTB manufactured with RAP. Particularly, this focuses on the design of high performance CTB with high dosages of RAP searching for an efficient improvement of the mechanical performance at short and long-term. For this purpose, various CTB were designed in laboratory with different RAP contents and cement dosages to provide a material with appropriate bearing capacity and resistance to cracking, in reference to conventional CTB (without RAP).

2 METHODOLOGY

2.1 *Materials*

The natural aggregates (used in this study as a reference to evaluate the effect of RAP) were selected to provide a good quality material to ensure an adequate granular structure, presenting appropriate gradation as well as physical and mechanical properties for the application as CTB.

On the other hand, the RAP was employed as “black aggregates” containing a cover of bitumen, but mixed as cold temperature, and therefore, not activating the bitumen as binder. Then, this material was characterized as aggregates with appropriate gradation for its combination at different dosages with conventional aggregates.

With these materials, the CTB studied in this research can be qualified in three groups attending to the quantity of RAP.

(1) CTA: cement-treated aggregates, where the 100% of the material consisted of natural soil. For this material, the quantity of cement varied from 2.5% (by aggregate weight), 4.5% and 9.0%. These dosages were selected to represent the range commonly used in road CTB (2.5-4.5%), in consonance with previous studies [Grilli et al. 2012; Ren et al. 2020]. In addition, from Figure 1 that represents the compression strength values at 28 curing days, this range provides appropriate resistance for the application in road structures (2.5% of cement fitting the minimum requirements, and 4.5% as high-performance material), in agreement with the Spanish Standard [Dirección General de Carreteras 2015] being also in consonance with previous researchers [Baghini et al. 2016; Zhao et al. 2021]. Also, the dosage of 9% of cement was used as a reference to analyse the effect of employing high dosages of RAP. In Figure 1 can be seen that higher quantities of cement are to be assessed to provide high mechanical performance, in reference to the compressive strength of the conventional CTB with high cement content.

(2, 3) 75RAP and 100RAP: these base materials consisted of replacing 75% and 100%, respectively, of natural aggregates (by weight) with those from reclaimed asphalt pavements. The dosage of cement studied in combination with these materials varied from 4.5 to 9.0 by aggregate weight. These limit range values were selected with the aim of assessing the impact of high RAP content on the short and long-term behavior in comparison with the reference CTB (at 2.5-4.5% of cement), when all presenting comparable (and appropriate) initial compression resistance (Figure 1). Also, the impact of RAP can be compared to the reference CTB when both types using similar cement contents (4.5-9.0% over aggregate weight).

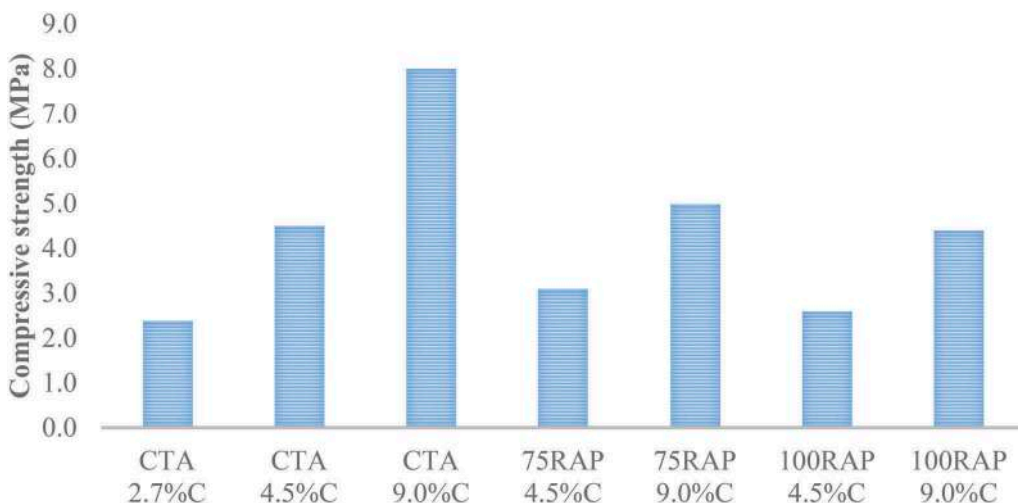


Figure 1. Compressive strength values at 28 curing days of different materials.

2.2 Testing plan and methodology

The experimental program in this research study was divided in different stages:

- (a) Design of the CTB with RAP, selecting the cement range for each case to offer appropriate performance. For this purpose, various high dosages of RAP (75% and 100% over aggregate weight) were designed at different cement stabilizations (4.5% and 9.0% by aggregate weight) in order to evaluate their resistance in comparison with standard CTB (with only

natural aggregates) at also various cement contents (2.7% as minimum requirement; 4.5% as high-performance; 9.0% to compare with RAP cases with such content).

The evaluation of the mechanical performance of the different materials was carried out through the assessment of indirect tensile and compression modulus (EN 12697-26 2019, Annex C; EN 12390-13 2014), while the resistance was evaluated also under indirect tensile and compression efforts according to (EN 12697-23 2018; EN 12390-3 2020). These tests were carried out at 20°C after the curing periods of 28, 60 and 90 days in a chamber at 23 ± 3 °C and higher than 95% of relative humidity.

- (b) Evaluation of the long-term performance of the most appropriate CTB (selected from previous step). Particularly, this step focused on evaluating the resistance to fatigue cracking for samples of CTB 4.5%C (as reference of high-performance treated base), of bases with 75% of RAP at cement dosages of 4.5%, 6.0% and 9.0%, and the cases with 100% RAP at 6.0% and 9.0% of cement. This study was done at 28 days of curing time through the University of Granada – Fatigue Cracking Test (UGR-FACT) (Moreno-Navarro and Rubio-Gómez 2013) that allows for studying the long-term performance of these materials under similar efforts to those expected during their service life. The specimens used in this test have prismatic geometry, with a length higher than 100 mm and width of 60 mm, while the height depended on the study step, analysing the influence of this parameter by using 45 mm, 65 mm and 85 mm. The loading process consisted of applying semi-sinusoidal pulses up to material cracking at 5 Hz under force mode with amplitude of 0.6 kN (500 kPa).
- (c) Study of the influence of the layer thickness, with the aim of evaluating its impact on the bearing capacity and resistance of the different CTB. The thicknesses of the samples were 45 mm, 65 mm and 85 mm, selected as a range of values susceptible to be used as treated bases in road structures. This study focused on the cases 75RAP 9.0%C and 100RAP 9.0% C as representative of the sustainable high-performance materials, in reference to the standard of CTA 4.5%C (conventional high-performance treated base). The evaluation of the thickness impact was carried out by a multi-loading procedure for the UGR-FACT test, applying increasing loading steps that allows for correlating the tensile strain at layer bottom with different loading conditions, while determining durability depending on material thickness. The failure criterion corresponded to the specimen broken in two parts (crack from bottom to top). Figure 2 displays the configuration of the test and the values of specimen thickness that were assessed.

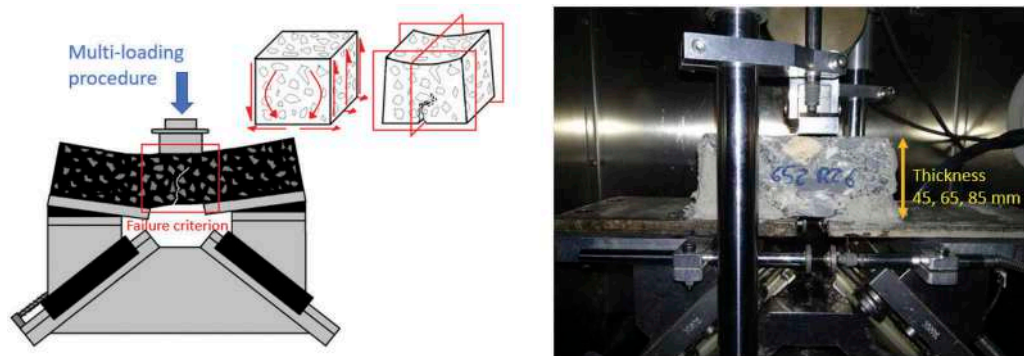


Figure 2. UGR-FACT test configuration.

3 ANALYSIS OF RESULTS

3.1 Influence of RAP content

Figure 3 represents the influence of RAP content on the indirect tensile stiffness modulus of the CTB, for the cases with 4.5% and 9.0% of cement, in reference to the minimum

requirement for this type of materials commonly used in road structures (represented by the case of CTB without RAP, at 2.5% of cement - CTA).

Results indicates that the inclusion of RAP reduces the stiffness of the material, regardless of the curing time (which stated lower influence than the RAP content), increasing therefore the flexibility of the CTB under a same load level, which is in consonance with previous experiences (Grilli et al. 2012; Lopez et al. 2018; Ren et al. 2020). In particular, 75%RAP reduced the stiffness of the material in comparison with the conventional CTB for both cement contents, while still presenting higher values than those from the reference for minimum requirements (CTA with 2.5% cement). However, when increasing the RAP content up to 100%, it was seen that cement dosage must be close to 9.0% to offer a bearing capacity similar (or higher) to the reference.

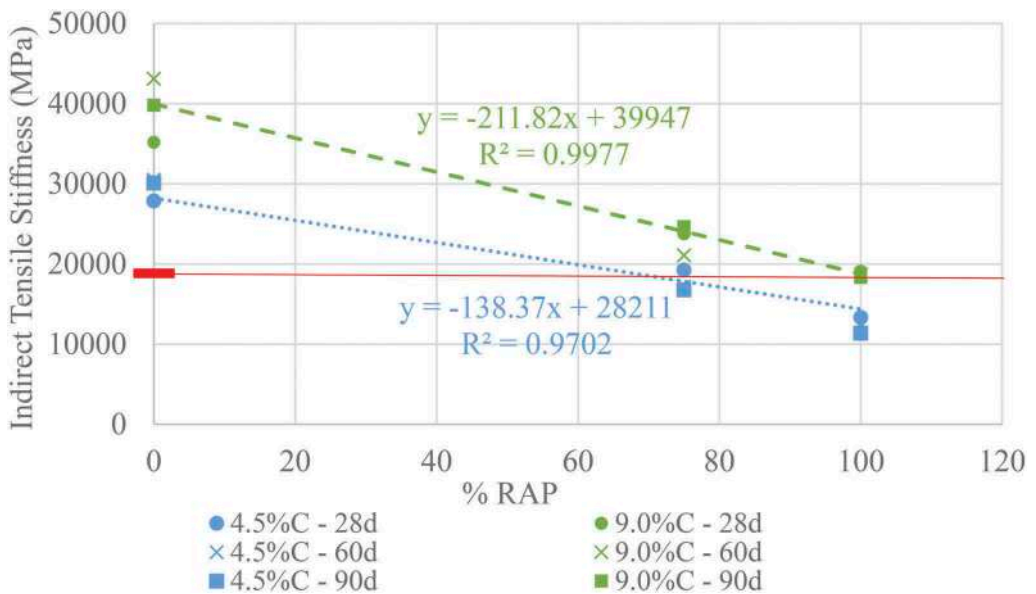


Figure 3. Indirect tensile stiffness modulus for different RAP content.

Similarly, Figure 4, that represents the influence of RAP on the compressive modulus, states that RAP led to reduce the stiffness of the material, but still presenting higher bearing capacity than those from the minimum requirement reference (CTA 2.5%C) while offering similar values to high-performance reference (CTA 4.5%C) when using cement dosages higher than 4.5% for the case with 75%RAP, and close to 9.0% for the 100%RAP. Again, the curing period showed lower impact on the results trend, where the RAP and cement contents presented higher effect. This denotes that, similar to conventional cement treated bases (Ismail et al., 2014), the cases with RAP showed stable performance from 28 curing days.

3.2 Fatigue behavior and layer thickness assessment

In view of previous results, fatigue resistance was assessed in a high-performance reference without RAP (CTA 4.5%C), the cases of 75%RAP with 4.5%, 6% and 9% of cement, and 100%RAP with 6% and 9% of cement. The cement ranges were selected from a minimum value, 4.5%C, that was seen as appropriate for 75%RAP to obtain comparable results to those from conventional high-performance CTA 4.5%C, while the 9% of cement was seen as

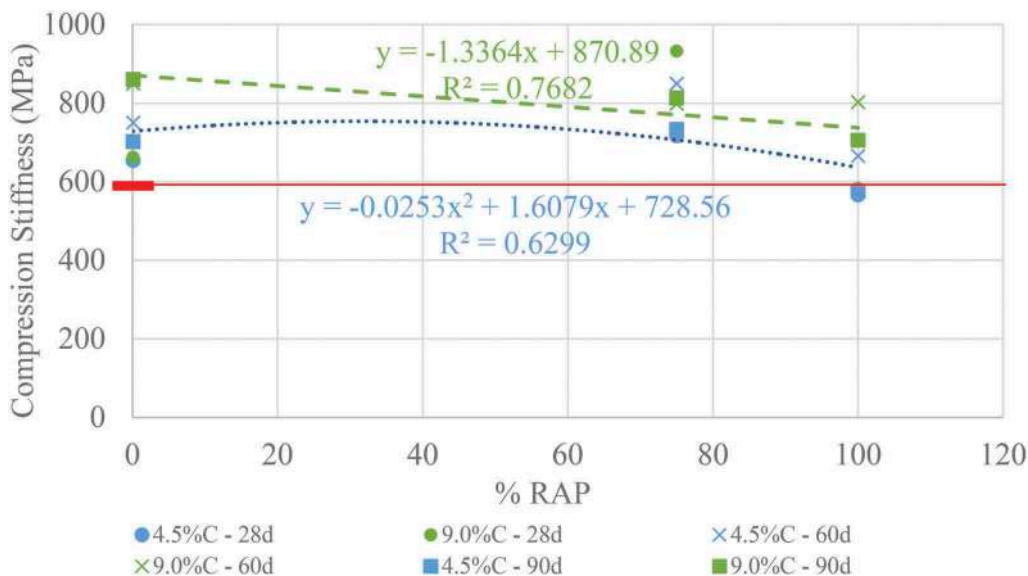


Figure 4. Compression stiffness modulus for different RAP contents.

appropriate when using 100%RAP to obtain a high-performance material. The 6% cases were studied as intermediate solutions.

Figure 5 displays the results of fatigue, stating that the use of high RAP contents, as those used in this article, could require higher cement dosages than the conventional high-performance CTA to obtain similar cohesion and durability under cyclic loads simulating the efforts expected during their life. In particular, the cases with 75%RAP offered longer life

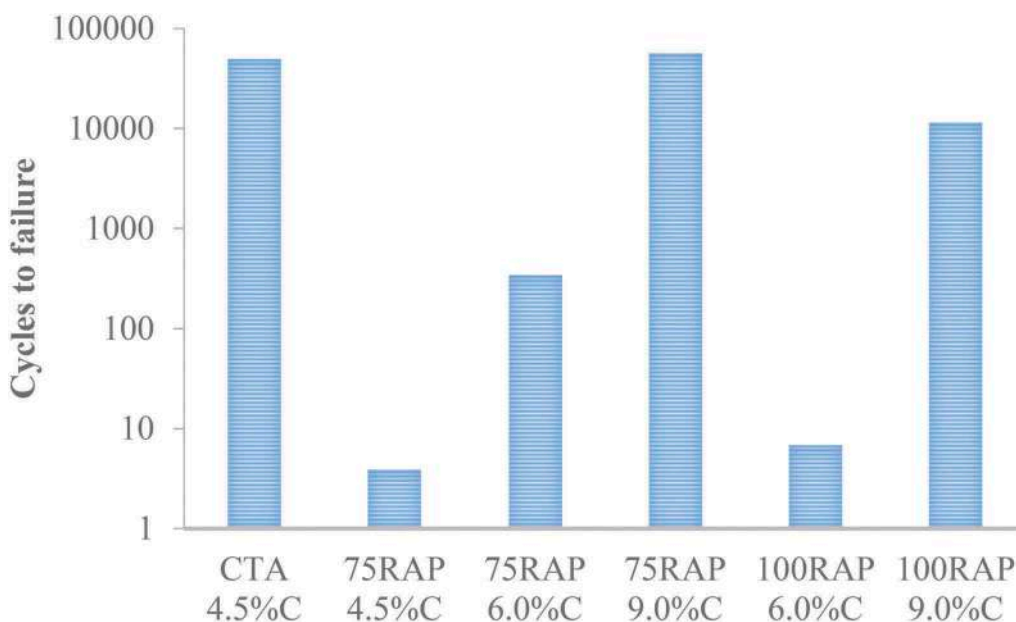


Figure 5. Cycles to failure for diverse RAP contents.

than the 100%RAP, but requiring both around 9% of cement to lead to comparable number of cycles to failure than the high-performance reference.

Therefore, the deeper analysis of results into fatigue behavior and thickness optimization is carried out for a reference (CTA 4.5%C) and the cases with 75% and 100% of RAP with a cement dosage of 9%. Figure 6 relates the different thickness values with the durability of each material. These results denote that the case with 75%RAP offered comparable (or even higher) long-term performance to the reference CTA 4.5%C, while the case with 100%RAP could require for higher layer thickness to offer similar durability to the other high-performance materials studied in this research.

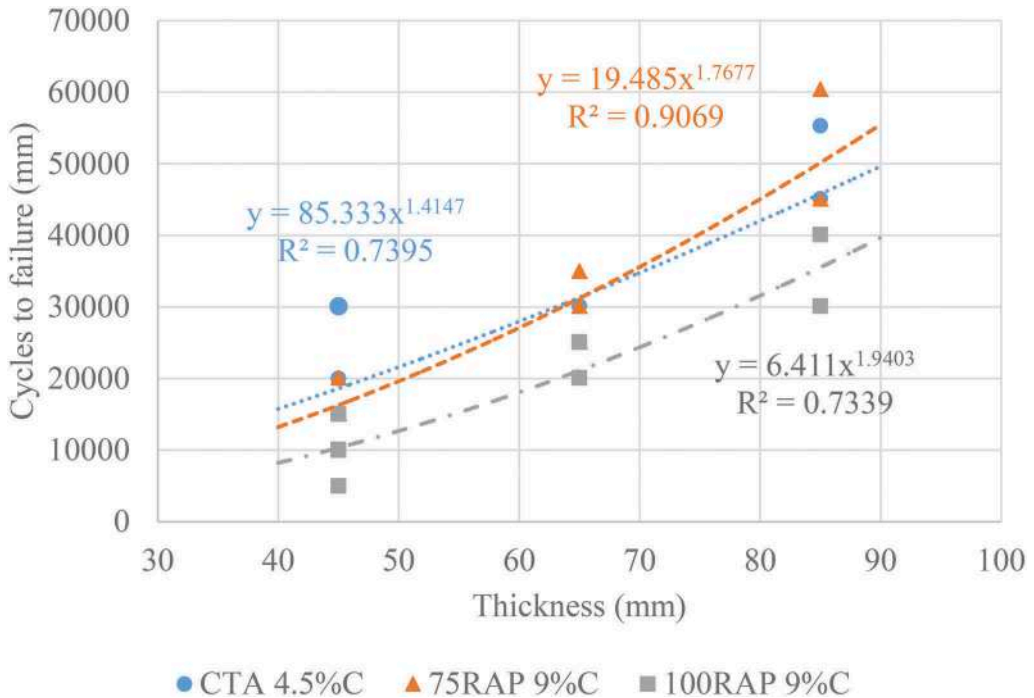


Figure 6. Cycles to failure of different thickness values of materials studied.

4 CONCLUSIONS

This paper presents the results of a laboratory study examining the effects of the design of high-performance cement treated base (CTB) with high dosages of RAP searching for an efficient improvement of the mechanical performance at short and long-term. Based on the results obtained, the following conclusion can be drawn:

- The presence of RAP leads to a decrease in the stiffness of the material, regardless of the curing time, increasing therefore the flexibility of the CTB under a same load level.
- CTB with 75% of RAP presented appropriate tensile and compressive resistance when using 4.5% of cement (in comparison with standard reference), while the case with 100% RAP required for higher cement dosages (up to 9%).
- The results of fatigue showed that the use of high RAP contents could require higher cement dosages than the conventional high-performance CTB to obtain similar durability under cyclic loads simulating the efforts expected during their life.

- Nonetheless, results stated that the case with 75%RAP offered comparable long-term performance to the reference CTB, which could be associated with the higher flexibility of the material.

According to these conclusions it was demonstrated that the use of high percentages of RAP as part of soil-cement materials can be an appropriate solution providing high bearing capacity as well as reducing the fragile behavior of these materials and, therefore, enhancing their durability.

REFERENCES

- Avirneni, D., Peddinti, P. R., Saride, S., 2016. *Durability and long-term performance of geopolymer stabilized reclaimed asphalt pavement base courses*. Construction and Building Materials, 121, 198–209.
- Baghini, M. S., Ismail, A., Karim, M. R., Shokri, F., and Firoozi, A. A., 2014. *Effect of styrene-butadiene copolymer latex on properties and durability of road base stabilized with Portland cement additive*. Construction and Building Materials, 68, 740–749.
- Baghini, M. S., Ismail, A., Naserlavi, S. S., and Firoozi, A. A., 2016. *Performance evaluation of road base stabilized with styrene-butadiene copolymer latex and Portland cement*. International Journal of Pavement Research and Technology, 9(4),321–336.
- Brandt, A. M., 2008. *Fibre reinforced cement-based (FRC) composites after over 40 years of development in building and civil engineering*. Composite structures, 86(1-3), 3–9.
- Dirección General de Carreteras. Ministerio de Fomento, 2015. *Pliego de prescripciones técnicas generales para obras de carreteras y puentes (PG-3)*. Centro de Publicaciones, Ministerio de Fomento.
- Du, S., 2016. *Influence of chemical additives on mixing procedures and performance properties of asphalt emulsion recycled mixture with reclaimed cement-stabilized macadam*. Construction and Building Materials, 118, 146–154.
- EN 12390-13, 2014. *Testing hardened concrete - Part 13: Determination of secant modulus of elasticity in compression*. European Committee for Standardization. Asociación Española de Normalización y Certificación, Spain.
- EN 12390-3, 2020. *Testing hardened concrete - Part 3: Compressive strength of test specimens*. European Committee for Standardization. Asociación Española de Normalización y Certificación, Spain.
- EN 12697-23, 2018. *Bituminous mixtures - Test methods - Part 23: Determination of the indirect tensile strength of bituminous specimens*. European Committee for Standardization. Asociación Española de Normalización y Certificación, Spain.
- EN 12697-26, 2019. *Bituminous mixtures - Test methods - Part 26: Stiffness*. European Committee for Standardization. Asociación Española de Normalización y Certificación, Spain.
- Grilli, A., Bocci, M., and Tarantino, A. M., 2013. *Experimental investigation on fibre-reinforced cement-treated materials using reclaimed asphalt*. Construction and Building Materials, 38, 491–496.
- Ismail, A., Baghini, M. S., Karim, M. R., Shokri, F., Al-Mansob, R. A., Firoozi, A. A., and Firoozi, A. A., 2014. *Laboratory investigation on the strength characteristics of cement-treated base*. In Applied mechanics and materials (Vol. 507, pp. 353–360). Trans Tech Publications Ltd.
- Lanzoni, L., Nobili, A., and Tarantino, A. M., 2012. *Performance evaluation of a polypropylene-based draw-wired fibre for concrete structures*. Construction and building materials, 28(1),798–806.
- López, M. A. C., Fedrigo, W., Kleinert, T. R., Matuella, M. F., Núñez, W. P., and Ceratti, J. A. P., 2018. *Flexural fatigue evaluation of cement-treated mixtures of reclaimed asphalt pavement and crushed aggregates*. Construction and Building Materials, 158, 320–325.
- Moreno-Navarro, F., and Rubio-Gámez, M. C., 2013. *UGR-FACT test for the study of fatigue cracking in bituminous mixes*. Construction and Building Materials, 43, 184–190.
- Pérez, P., Agrela, F., Herrador, R., and Ordoñez, J., 2013. *Application of cement-treated recycled materials in the construction of a section of road in Malaga, Spain*. Construction and Building Materials, 44, 593–599.
- Ren, J., Wang, S., and Zang, G., 2020. *Effects of recycled aggregate composition on the mechanical characteristics and material design of cement stabilized cold recycling mixtures using road milling materials*. Construction and Building Materials, 244, 118329.
- Taha, R., Al-Harthy, A., Al-Shamsi, K., and Al-Zubeidi, M., 2002. *Cement stabilization of reclaimed asphalt pavement aggregate for road bases and subbases*. Journal of materials in civil engineering, 14(3),239–245.

- Xuan, D. X., Houben, L. J. M., Molenaar, A. A. A., and Shui, Z. H., 2012. *Mechanical properties of cement-treated aggregate material—a review*. *Materials and Design*, 33, 496–502.
- Yang, Z., Shi, X., Creighton, A. T., and Peterson, M. M., 2009. *Effect of styrene–butadiene rubber latex on the chloride permeability and microstructure of Portland cement mortar*. *Construction and Building Materials*, 23(6),2283–2290.
- Zhao, Z., Wang, S., Ren, J., Wang, Y., and Wang, C., 2021. *Fatigue characteristics and prediction of cement-stabilized cold recycled mixture with road-milling materials considering recycled aggregate composition*. *Construction and Building Materials*, 301, 124122.

Fundamental study on combined aging for warm-mixed asphalt and RAP-WMA mixtures using SATS conditioning

M. Iwama & K. Hayano

Institution of Urban Innovation, Yokohama National University, Yokohama, Japan

ABSTRACT: In recent years, there is growing awareness of environmental issue such as global warming and climate change. This kind of problem becomes more pronounce, where asphalt surfaces are exposed extremely higher temperature and heavy rain during summer time. In addition, it is desirable for asphalt paving industry to accelerate recycling technology, in terms of sustainability. Therefore, there is still room for discussion about the durability of asphalt mixtures under harsh conditions, in terms of temperature and moisture sensitivity. In order to tackle this challenging issue, both warm-mix asphalt (WMA) mixture and reclaimed asphalt pavement (RAP) with WMA are assessed using the saturation aging tensile stiffness (SATS) test, then those mechanical properties are examined through laboratory experiments. This paper assesses the durability of both WMA mixture and reclaimed asphalt pavements with WMA, looking at the two factors: stiffness and fatigue, then the following conclusions are being drawn through laboratory experiments. With regard to stiffness modulus, the Indirect Tensile Stiffness Modulus (ITSM) results show that RAP-WMA mixtures tend to show increase in stiffness modulus with SATS conditioning. In terms of the retained stiffness, the RAP-WMA mixture did not indicate a reduction in retained stiffness whilst the WMA mixture demonstrated a significant drop in stiffness with the SATS conditioning. In addition, the Indirect Tensile Fatigue Tests (ITFT) demonstrated that the WMA mixture with SATS conditioning showed a large initial strain resulting in a shorter fatigue life, whereas the RAP-WMA mixtures indicated a longer fatigue life than the WMA mixture with SATS conditioning. Finally, failure pattern analysis reveals that RAP-WMA mixtures show difference in fatigue patterns among the two RAP-WMA mixtures. This might be related to the effect in rejuvenators on fatigue properties.

Keywords: Warm-mix asphalt (WMA), reclaimed asphalt mixture (RAP), moisture, aging, SATS conditioning

1 INTRODUCTION

In recent years, there is growing awareness that increases in heat wave and torrential rain are caused by serious environmental issue such as climate change. According to the report from International Panel for Climate Change (IPCC), these issues might be related significantly to global warming (Intergovernmental Panel on Climate Change 2021). In particular, asphalt pavements are exposed to harsh conditions among road structures since it was directly subjected repeated heavy traffic loading, as well as summer heat and heavy rain.

Past studies suggested the existence of moisture leads to stripping in asphalt mixture during service. This leads to the loss of adhesion related to aggregate – binder interface, resulting the premature failure of asphalt mixtures (Terrel, R.L. and Shute, J. W. 1989, Kandhal, P.S.

1994, Kennedy, T. W. 1985). In general, moisture damage will cause the loss of adhesion and cohesion among aggregate and binder in asphalt mixtures. In case of hot mix asphalt (HMA), the loss of adhesion should carefully be considered because virgin aggregates and binders are attached during service life. In order to overcome such difficulties, a various types of laboratory test methods looking at moisture sensitivity were developed and studies through research (Lottman 1982, Terrel and Al-Swailmi 1993, Airey and Choi 2002).

In terms of reduction in carbon dioxide (CO₂) and preservation of natural resource, the use of warm-mix asphalt (WMA) mixture and Reclaimed Asphalt Pavement (RAP) has been widely used in practice as the amount of RAP mixture production has been risen. Inevitably, these two technologies are combined and applied on site. However, few research efforts have been conducted for WMA and high RAP mixture with combined aging (i.e. moisture, oxidation and heat). In particular, the use of rejuvenator agent related to aging is not understood for RAP mixtures, although many research efforts have been made for rejuvenated RAP binder. Therefore, these assessments with due consideration for recent issue such as moisture are required especially focusing on stiffness, fatigue and combined aging.

This paper examines the durability assessment of WMA and RAP mixtures using the Saturation Aging Tensile Stiffness Test.

2 MATERIAL PREPARATION

2.1 Binder

In this research, five types of asphalt mixtures were studied experimentally: warm mixed asphalt mixture, warm-mixed RAP1 and RAP2. For warm-mixed asphalt straight run asphalt 60/80 pen bitumen was used as binder. The blending protocol was as per the criteria of the Japan Road Association (2010). In terms of warm-mix asphalt, a wax additive called “Sasobit®” was used as the additive agent. Sasobit is a synthetic material using Fisher-Tropsch wax. Since it is widely used in practice, the additive was blended with fresh and RA binders when the specimens were manufactured. In the case of the warm-mixed RAP mixtures, 30% and 60% RA mixtures were selected in this study.

Table 1 shows properties of virgin and reclaimed asphalt binder. The penetration grade of RA binders was restored using rejuvenators, and blended with fresh binder. Two types of rejuvenator were compared to examined warm mixing properties. The penetration grade was designed to be 70 pen grade.

Table 1. Properties of virgin and reclaimed asphalt (RA) binders.

	Penetration at 25°C	Softening point	Viscosity at	
	(1/10 mm)	(°C)	120°C (mPa.s)	150°C(mPa.s)
Virgin binder	63	48.5	835.6	186.5
RA binder	12	80.5	21300	2035

The results show the significant reduction in penetration of extracted RA binder, compared with that of virgin binder. The results also demonstrate dramatic increase in softening point and viscosity for the extracted binder as compared with virgin binder. In addition, this trend is consistent in viscosity both at 120°C and 150°C. From this result, it can be said that the extracted binder examined in this study was heavily aged during in-service conditions. Therefore, it is worth recovering the old asphalt by dosing rejuvenator agents, in case of RAP mixture productions.

For binder blending design, 70 pen grade was targeted as RA binder. The amount of rejuvenator were determined by adding it with old asphalt. The target grade (i.e. 70 pen grade) was determined by changing the rejuvenator ratio in 0%, 15% and 20% (percentage by mass of

old asphalt), then the optimum rejuvenator amount was selected through linear relationship between penetration and the added binder. In addition, two types of rejuvenator were compared to characterize the properties. The characteristics of the two rejuvenators were shown in Table 2.

Table 2. Rejuvenator properties.

	Density (g/cm ³)	Dynamic viscosity (mm ² /s)	Ratio of viscosity with thin-film oven test (TFOT) to that without TFOT	Reduction rate of mass content with TFOT to that without TFOT (%)
Rejuvenator 1	0.948	48.5	1.10	-0.28
Rejuvenator 2	0.925	80.5	1.05	-1.37

It should be noted that the RAP 1 rejuvenator indicated higher density than that of RAP 2. However, it can be seen that both agents showed similar characteristics, in terms of viscosity. In order to analyse the differences between the two rejuvenators from RAP binder perspective, the blended binders were analysed using the chromatographic method. The analysis results are show in Figure 1.

As can be seen from the result of the four groups (i.e. Saturation, Aromatic, Resins and Asphaltenes), the two rejuvenators shows differences, especially in Aromatic and Resin components. RAP 1 binder shows high in resin, whilst RAP 2 binder gives large percentage in Aromatic. However, both binders showed increase in aromatic and reduction in resin components, when compared to the extracted binder.

It can be, therefore, said that the extracted binder from the RAP source was recovered for this experiment.

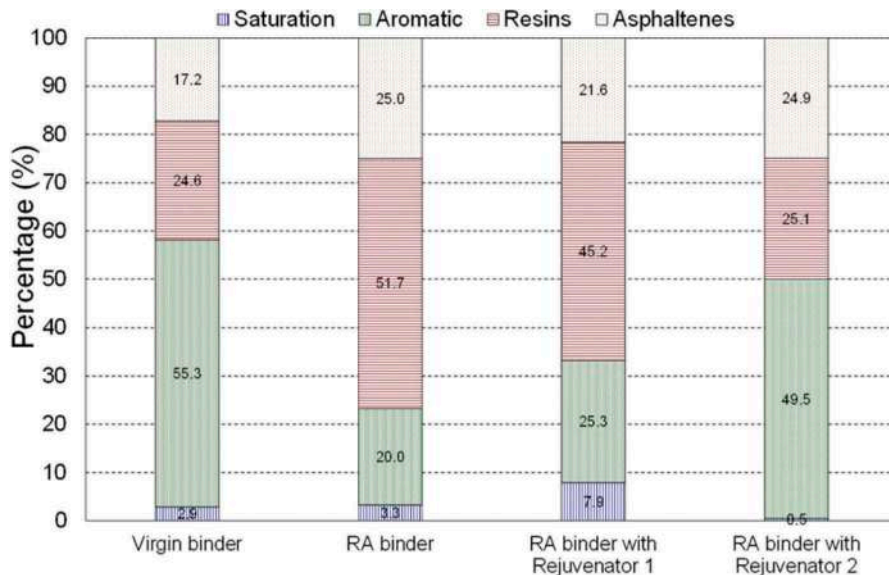


Figure 1. Chemical compositions of virgin binder, reclaimed asphalt (RA) binder, RA binder with Rejuvenator 1, and RA binder with Rejuvenator 2.

2.2 Mixture

In this study, the aggregate gradation used was continuous grading and dense asphalt mixtures (AC13) produced in the laboratory. For the RAP mixture, RA content of 30% and 60%

were selected to assess the characteristics of the RAP mixture, and those RAP aggregates were blended with fresh aggregate, adjusted as much as possible to AC 13 mixture limits (see Figure 2). The design penetration was set at 70 pen grade using both fresh binder and rejuvenator. As for the warm-mix asphalt, 3% of the additive (i.e. Sasobit) was added to the binder, then it was mixed with conventional and reclaimed size asphalt mixture at 130°C, respectively.

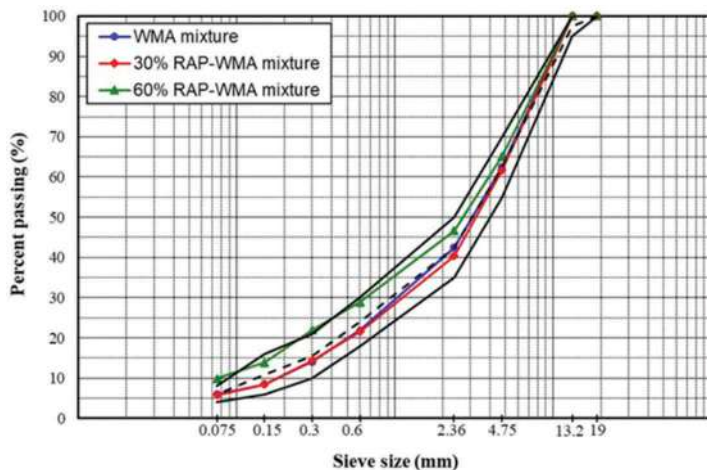


Figure 2. Gradation curves of WMA mixture and RAP-WMA mixtures with the 30% and 60% RAP contents.

Table 3 shows the properties of the five mixtures. In case of RAP mixture design, the four mixtures were designed (as close as WMA) to be approached to WMA gradation. As can be seen in the table, the density of the RAP mixtures was within one percent of WMA. In addition, air void contents of RAP mixtures were less than 0.2%. Therefore, it can be said that RAP mixtures used in this study were designed to be acceptable, when compared to that of WMA.

Table 3. Properties of mixtures prepared.

Mixture type	Density (kg/m ³)	Air void content (%)
WMA mixture	2372	5.4
30% RAP1-WMA mixture	2356	5.6
60% RAP1-WMA mixture	2368	5.5
30% RAP2-WMA mixture	2368	5.5
60% RAP2-WMA mixture	2380	5.5

3 EXPERIMENTAL PROGRAMME

Laboratory specimens (diameter: $\phi = 100$ mm, height: $h = 50$ mm) were prepared from the five types of mixtures (WMA, 30% RAP1-WMA, 60% RAP1-WMA, 30% RAP2-WMA and 60% RAP2-WMA). Then, the physical and mechanical properties of the mixtures as well as those of the binders extracted from the mixtures were assessed through various types of laboratory experiments as shown in Figure 3. In order to simulate the combined aging, Saturation Aging Tensile Stiffness (SATS) test was conducted on targeted laboratory specimens based on the EN 12697-45. The SATS test was originally developed at the University of Nottingham (Airey 2002, 2003, Collop et al. 2004a, Collop, A.C., Choi, Y.K. and Airey, G.D. 2004b, Airey et al.

2005, 2007, Nicholls et al. 2006, Grenfell et al. 2011, 2012, 2015) and the test features combined aging with moisture, temperature and pressure conditionings. The compacted specimens were placed in a pressurized vessel, and then conditioned at a predetermined moisture saturation level, temperature and pressure for 24 hours (Nicholls *et al* 2011, DeCarlo *et al.* 2020) (see Figure 4).

As in Figure 3, after the specimens were prepared, Indirect Tensile Stiffness Modulus (ITSM) tests were first performed on the specimens, in accordance with the BS EN 12697-26. Then the specimens were divided in two groups. The specimens in one group were subjected to the SATS conditioning. The detailed procedure of the SATS conditioning will be presented later. Following the SATS conditioning, ITSM tests and Indirect Tensile Fatigue Tests (ITFTs) were carried out on the specimens. ITFTs were carried out based on the BS EN 12697-24.

Meanwhile, the specimens in the other group were not subjected to the SATS conditioning. After the ITSM tests were conducted, the ITFTs were carried out on the specimens in the same way as on those with the SATS conditioning.

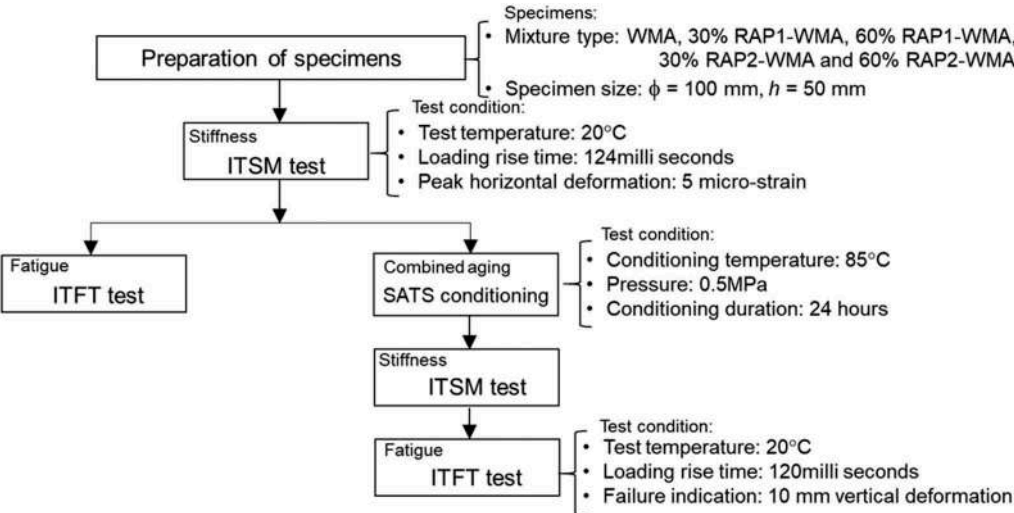


Figure 3. Overview of experimental program.

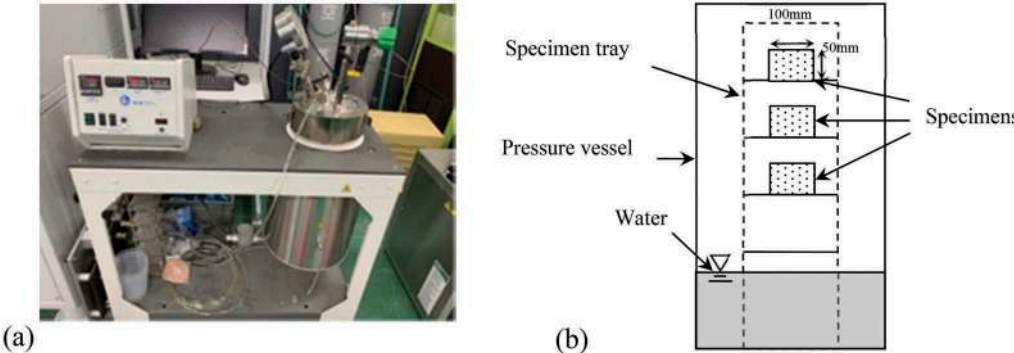


Figure 4. SATS condition vessel (a) Overview, (b) Schematic of inside of vessel.

4 CHANGES IN STIFFNESS MODULUS WITH AND WITHOUT SATS CONDITIONING

4.1 Stiffness modulus results

To examine the changes in stiffness modulus of the five mixtures with and without SATS conditioning, ITSM tests were performed, by following test procedure shown in Figure 2. Table 4 shows air voids and stiffness of the mixtures with and without SATS conditioning. As can be seen from this table, stiffness modulus of WMA and 30% RAP2 binders demonstrate reduction in stiffness whilst 30% RAP1, 60% RAP1 and 60% RAP2 mixtures indicated increase in stiffness with SATS conditioning.

Table 4. Stiffness of the mixtures with and without SATS conditioning.

WMA	30% RAP1-WMA		60% RAP1-WMA		30% RAP2-WMA		60% RAP2-WMA			
	Without	With	Without	With	Without	With	Without	With	Without	With
Average air voids (%)	4.7		5.0		5.3		4.9		4.9	
Average stiffness (MPa)	2952	2423	2469	2694	2147	2527	2551	2235	2063	2261
Std Dev. Stiffness (MPa)	298	128	146	52	120	82	35	265	75	18

This trend can be clearly seen in the form of stiffness ratio. Figure 5 shows relative stiffness ratio derived from SATS conditioning. As can be seen in the figure, both WMA and 30% RAP2-WMA mixtures indicated drop in stiffness with conditioning whereas other three mixtures demonstrated rise in stiffness with SATS condition.

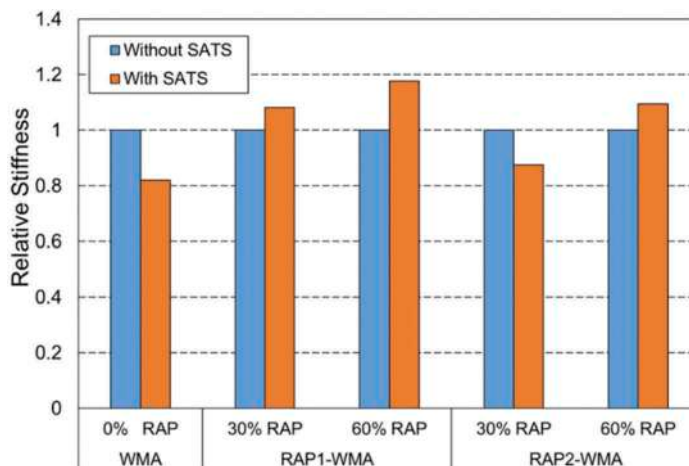


Figure 5. Relative stiffness ratio derived from SATS conditioning.

4.2 Retained stiffness ratio and saturation

Figure 6 shows the retained stiffness ratio plotted against the retained saturation for the five specimens. Retained stiffness is the ratio of stiffness with the SATS conditioning to that without the SATS. As can be seen from the figure, the result shows that the stiffness ration tends

to decrease with an increase in the retained saturation. In addition, RAP-WMA mixtures are apt to show higher ratio with lower retained saturation whereas WMA mixture indicates lower retained stiffness ratio with higher saturations. However, there is exception for 30% RAP2-WMA mixture. The result shows less stiffness ratio with higher saturation. As can be seen in Figure 1, RAP2 rejuvenator indicates similar properties with virgin binder, in terms of SARA fraction. Therefore, it is speculated that RAP2-WMA mixtures tend to demonstrate similar properties to the WMA mixture.

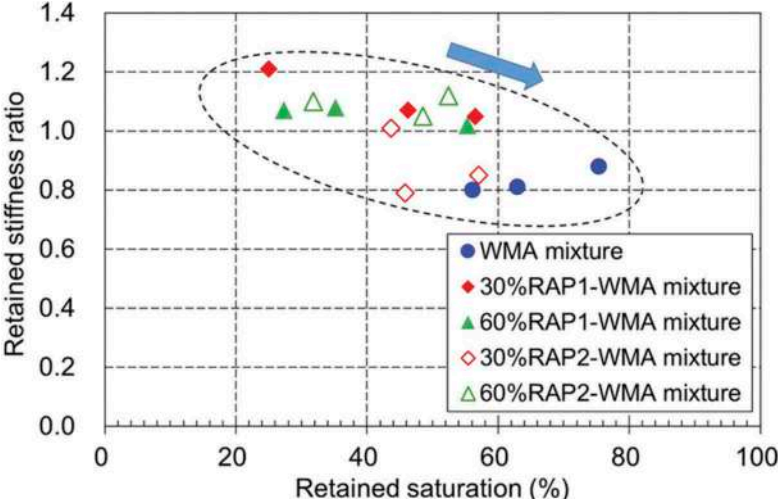


Figure 6. Relative stiffness ratio derived from SATS conditioning.

5 CHANGES IN FATIGUE FAILURE WITH AND WITHOUT SATS CONDITIONING

5.1 Fatigue test results

Fatigue characteristics of the five mixtures with and without SATS condition were evaluated through ITFTs, following the test conditions shown in Figure 2. Linear regression analysis of the ITFT results was conducted to determine the fatigue functions for the asphalt mixtures based on the following relationship:

$$N_f = a \varepsilon_0^{-b} \tag{1}$$

where N_f is the fatigue life, ε_0 is the initial tensile strain (microstrain) and a and b are experimentally determined coefficients.

Figure 7 shows the results for WMA and RAP-WMA mixtures without SATS conditioning. From this result, it was found that RAP-WMA mixtures are longer fatigue life than the WMA mixture. This trend is consistent in both RAP1 and RAP2.

However, the WMA mixture shows dramatic changes in fatigue characteristics with the SATS conditioning. Figure 8 describes the results for the WMA and RAP-WMA mixtures with the SATS conditioning. As can be seen in the figure, the WMA mixture demonstrates larger initial strain showing shorter fatigue life, when compared with that without the SATS conditioning. On the other hand, RAP-WMA mixtures indicated reduction in fatigue cycles although those mixtures does not show significant change in initial strain. This result might be related

to the Figure 6, showing the retained stiffness ratio of the RAP mixtures are close to 1.0. This suggest that RAP-WMA mixtures with the SATS conditioning are longer fatigue life due to the higher retained stiffness ration and lower retained saturation, compared with the WMA with the conditioning. This trend is more pronounced when the RAP aggregate contents are risen from 30% to 60% for both the RAP 1 and 2 mixtures.

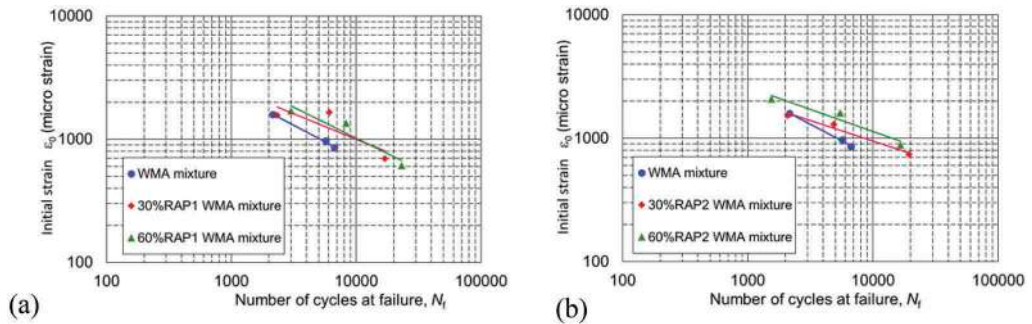


Figure 7. Relationships between the initial strain and the number of cycles at failure of the mixtures without SATS conditioning from ITFTs (a) WMA & RAP1-WMA mixtures, (b) WMA & RAP2-WMA mixtures.

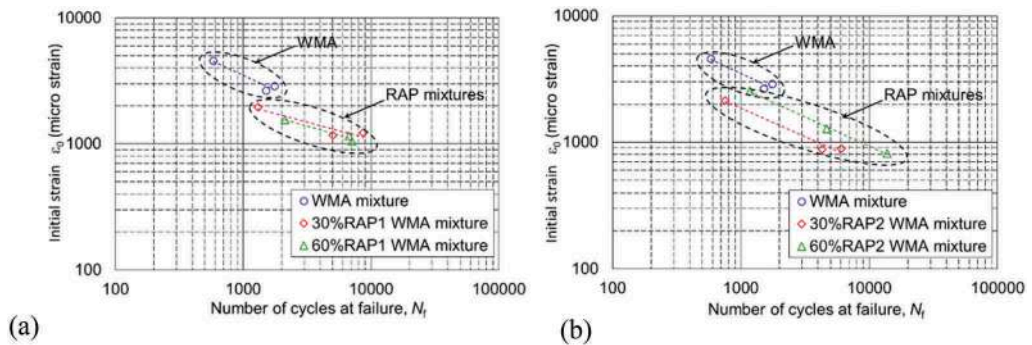


Figure 8. Relationships between the initial strain and the number of cycles at failure of the mixtures with SATS conditioning from ITFTs (a) WMA & RAP1-WMA mixtures, (b) WMA & RAP2-WMA mixtures.

5.2 Mixture failure pattern

In order to understand the fatigue characteristics of WMA and RAP-WMA mixtures in more detail, the fatigue results of the five specimens were analyzed in this study. Figure 9 shows the fatigue failure patterns for WMA and RAP-WMA mixtures with SATS conditioning, based on ITFT results conducted at 500kPa. As can be seen in the results, the differences in RAP ratio and rejuvenators were confirmed from each failure mode. RAP mixtures showed longer fatigue life, when compared with that of WMA mixtures. This result is more pronounced when RAP ratio was increased from 30% to 60%, and the same trend can be seen in RAP1-WMA and RAP2-WMA specimens.

Meanwhile, looking at differences in rejuvenators, RAP1-WMA mixtures demonstrated longer fatigue life, when compared with that of RAP2-WMA mixtures. As described in the previous section, despite the fact that RAP 1 specimen showed slight difference in air void

contents compared to RAP 2 specimens, it indicated longer fatigue life. In addition, this trend is more pronounced as RAP contents increase. This might highlight influence of rejuvenator for the mechanical properties of RAP-WMA mixtures. Therefore, it seems that this result imply the differences in rejuvenators in the fatigue life of RAP-WMA mixtures.

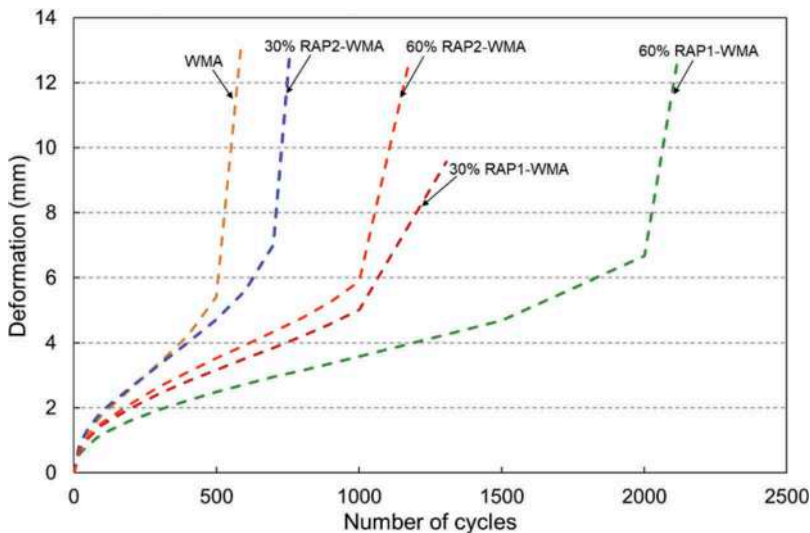


Figure 9. Fatigue relationships for WMA and RAP-WMA mixtures with SATS conditioning (Stress level: 500 kPa).

6 SUMMARY

This paper presents a durability assessment of WMA and RAP-WMA mixtures through SATS conditioning procedures. Based on the results obtained from previous sections, the following conclusions can be drawn in this study:

- In terms of stiffness modulus, RAP-WMA mixtures tend to indicate increase in stiffness with SATS conditioning, when compared with that of WMA mixtures. However, 30% RAP2-WMA mixture shows reduction in stiffness after the conditioning
- With regard to the retained stiffness, the ITSM results reveal that the RAP-WMA mixtures tend to show higher ratio with lower retained saturation whilst the WMA mixtures demonstrated a significant drop in stiffness with the SATS conditioning. This trend was also confirmed from relative stiffness ratio derived from SATS conditioning.
- Regarding fatigue properties, the ITFTs demonstrated that the WMA mixture with SATS conditioning showed a large initial strain, resulting in a shorter fatigue life. On the other hand, the RAP-WMA mixtures indicated a longer fatigue life than the WMA mixture with SATS conditioning. However, 30% and 60% RAP-WMA mixtures showed different fatigue properties in terms of fatigue life
- With respect to failure pattern with SATS conditioning, RAP-WMA mixtures shows longer fatigue life than that of WMA mixture. However, there were differences in fatigue cycle between RAP1-WMA and RAP2-WMA mixtures. Therefore, the differences in rejuvenator might be related to fatigue properties.

REFERENCES

- Airey G. D. and Choi, Y-K., 2002. State of the art report on moisture sensitivity test methods for bituminous pavement materials. *International Journal of road materials and pavement design*, 3 (4), pp. 355–372.

- Airey, G.D., *et al.*, 2005. Combined laboratory ageing/moisture sensitivity assessment of high modulus base asphalt mixture. *Journal of the Association of Asphalt Paving Technologist*, 74, 307–346.
- Airey, G.D., *et al.*, 2007. Moisture damage assessment of asphalt mixtures using the UK SATS test. *Transportation Research Board 86th Annual Meeting*. 21–25 January. Washington, D.C.
- BS EN 12697–24: 2012 Bituminous mixtures. Test methods. *Resistance to fatigue*. British Standards Institution, London.
- BS EN 12697–26: 2012 Bituminous mixtures. Test methods. *Stiffness*. British Standards Institution, London.
- Cocurullo, A., *et al.*, 2008. Indirect tensile versus two-point bending fatigue testing. *Proceedings of the Institution of the Civil Engineers*, Transport 161 Issue TR4, 207–220.
- Collop, A.C., *et al.*, 2004. Development of the saturation Ageing Tensile Stiffness (SATS) test. *Proceedings of the Institution of Civil Engineers (ICE)*, 157 (3), 163–171.
- Collop, A.C., *et al.*, 2004. Development of a Combined ageing/moisture Sensitivity Laboratory test. *Third Euraspalt and Eurobetume Congress*, Vienna, Austria, May 12–14.
- DeCarlo, C., *et al.*, 2020. Comparative Evaluation of Moisture Susceptibility Test Methods for Routine Usage in Asphalt Mixture Design. *Journal of Testing and Evaluation*, ASTM.
- Grenfell, J., *et al.* 2011. Assessment of asphalt durability tests; Part 1: Widening the applicability of the SATS test. *TRL Published Project Report PPR 535*. Crowthorn: Transport Research Laboratory.
- Grenfell, J., *et al.*, 2012. Optimising the moisture durability SATS conditioning parameters for universal asphalt mixture application. *International Journal of Pavement Engineering*, 13, 433–450.
- Highway Agency. 2007. Revised MCHW Specification 900 series, Clause 953: Durability of Bituminous Materials – Saturation Ageing Tensile Stiffness (SATS) Test. Interim Advise Note 101/07. London: The Stationery Office, London.
- Intergovernmental Panel on Climate Change, 2021. Climate Change 2021 The Physical Science Basis.
- Japan Road Association 2010 *Guide line for Reclaimed Asphalt Pavement*.
- Kandhal P.S., 1994. *Field and laboratory evaluation of stripping in asphalt pavements: state-of-the art report*. Transportation Research Record 1454, TRB.
- Kennedy T.W., 1985. *Prevention of water damage in asphalt mixtures*. STP 899, American Society for Testing and Materials, pp. 119–133.
- Lottman, R. P., 1982. Predicting moisture-induced damage to asphaltic concrete: field evaluation. National cooperative Highway Research Program 246. Washington, DC: National Academies Press.
- Nicholls, J. C., *et al.*, 2011. Assessment of asphalt durability tests; Part 3: Review of SATS Test to Evaluate Existing Base Layer. *TRL Published Project Report PPR 537*. Crowthorn: Transport Research Laboratory.
- Nicholls, J. C., *et al.* 2011. Review of Saturation Aging Tensile Stiffness (SATS) test for use in Ireland. *TRL Published Project Report PPR 547*. Crowthorn: Transport Research Laboratory.
- Terrel, R.L. and Al-Swailmi, S., 1993. The role of pessimum voids concept in understanding moisture damage to asphalt concrete mixtures. *Transportation research record: journal of the transportation research board*, 1386, pp. 31–37.
- Terrel, R. L., and Shute, J.W., 1989. Water sensitivity of asphalt-aggregate mixes: test selection, SHRP-A-403, Strategic Highway Research Program, National Research Council, Washington, D.C.

Bio-based emulsifiers for pavement material: Emulsion formulation and cold asphalt mix properties

F. Lévenard, V. Gaudefroy, C. Petiteau & E. Chailleux
Université Gustave Eiffel, Nantes, France

I. Capron
Biopolymères Interactions Assemblages, INRAE, Nantes, France

B. Bujoli
Chimie Et Interdisciplinarité: Synthèse Analyse Modélisation (CEISAM), Université de Nantes, Nantes, France

ABSTRACT: The use of two bio-based polymers, B1 and B2, as emulsifier for the preparation of bitumen emulsions, has been investigated. These emulsifiers allowed to prepare bitumen-in-water emulsions with a bitumen content of 50%. Emulsions were prepared with two different processes and were characterized using optical microscopy, laser granulometry, rheological measurements and calorimetry. Emulsions stability was monitored by following the droplets size distribution droplets over time. A comparison was made with a bitumen emulsion stabilized by a cationic surfactant usually used in the road pavement industry. Emulsions prepared with the two bio-based emulsifiers (Em-B1 and Em-B2) presented different properties. Em-B1 had larger droplets and was less stable: after 20 days, the coalescence increased and breaking occurred. Em-B2 had a droplets size distribution closer to the reference and was still stable after a month. Emulsified asphalt mixes were successfully prepared by mixing the emulsions with aggregates. Test specimens were molded in order to evaluate the water sensitivity throughout compressive strength measurement. Static compacted specimens kept in air presented a compression strength similar to the ones obtained for mixes prepared with an amine-type emulsion. For specimens immersed in water, the compression strength decreased significantly, indicating a high water sensitivity likely due to the ability of the polymers to swell with water and the poor interactions between the binder and the aggregates.

Keywords: Emulsions, bitumen, bio-based materials, mixture performances

1 INTRODUCTION

Over the last decades, to face the need to reduce our environmental impact, sustainable development policies have been implemented in many sectors, including the road construction industry. The standard practice in pavement construction, which consists in using hot mix asphalt, implies heating bitumen at high temperatures, leading to CO₂ and hazardous fumes emissions and high energy consumption (Gaudefroy et al. 2010, Jullien et al. 2010). In this context, low-temperature manufacturing process, using bitumen emulsions, is a relevant alternative to traditional processes. Indeed, it reduces energy consumption, gas production and effects on workers' health.

Bitumen emulsions consist in droplets of bitumen dispersed in an aqueous phase containing an emulsifier. Usually, these emulsions contain 50 to 70 % bitumen with droplets diameter ranging from 1 to 50 μm . Emulsifiers are amphiphilic petrochemical surfactants, with a hydrophilic head and a lipophilic tail. This particularity allows the surfactant to adsorb at the water/oil interface, thus facilitating the emulsification and stabilizing the emulsion by decreasing the interfacial tension between the two phases. The breaking process of the bitumen emulsion is initiated when the droplets are brought into contact with mineral aggregates. It is due to interactions with these aggregates and water loss. Cationic surfactants, mostly containing a nitrogen group, like amine, are the most commonly used since they can adsorb at electronegative siliceous aggregates, promoting the adhesion of bitumen (Paria & Khilar, 2004, Ziyani et al. 2014). In many cases, addition of acid is needed to protonate the cationic surfactants. (Mercado and Fuentes, 2016).

Several studies aim at developing bitumen emulsions stabilized by bio-based emulsifiers (McClements et al. 2016), including polymers (Yuliestyan et al. 2017, Mallawarachchi, et al. 2016) or particles (Anaclet et al. 2017), as an alternative to these surfactants.

In order to reduce the road industry's dependence on petrochemical emulsifiers and to limit their environmental impact, our work focuses on the use of bio-based polymers as bitumen emulsifiers and emulsion stabilizers. Firstly, this study deals with bituminous emulsion formulation and characterization. Secondly, the possibility to manufacture emulsified asphalt mixes with these emulsions is evaluated. A comparison is made with a conventional bitumen emulsion considering emulsions properties (Gutierrez et al. 2002) as well as emulsified asphalt mixes performances (Serfass et al. 2004, Serfass et al. 2011).

2 EXPERIMENTAL SECTION

2.1 *Materials*

The bio-based emulsifiers used, B1 and B2, were two polymers with close chemical structure and two different molar masses ($M_{wB1} \approx 300\,000\text{ g/mol}$ and $M_{wB2} \approx 75\,000\text{ g/mol}$). Around 80% of the polymers are derived from renewable material. These compounds present amphiphilic, emulsifying and stabilizing properties, and can be used at neutral pH. Cationic bitumen emulsifier Polyram S was purchased from Ceca Arkema, and hydrochloric acid from Sigma-Aldrich. All emulsions were prepared with a 160/220 pen-grade bitumen for pavement application.

2.2 *Emulsions preparation*

First, the different emulsifiers were solubilized in deionized water under stirring, in the presence of HCl for Polyram S. Preparation of bitumen emulsions was performed according to the following two different methods: 1) using a homogenizer-disperser IKA DI 25 basic equipped with a toothed rotor-stator S25N-8G-ST dispersion tool and 2) using a Rink Electro colloid mill.

The first method was used to produce small quantities of emulsions (100 mg). It allowed varying the water/bitumen/emulsifier ratio in order to optimize the emulsifier quantity needed to obtain an emulsion containing at least 50 wt % bitumen, stable over several days. The dispersion tool (IKA ultra-turrax) has a 0.25 mm gap between the rotor and the stator. The bitumen heated at 140°C was gradually added and mixed to the aqueous phase at 50°C. After all bitumen was added, the mixture was stirred at 11 000 rpm for 3 minutes.

For the promising compositions, the emulsions were produced in larger quantities (about 1kg) using the colloid mill. This process provides more shear energy and is closer to industrial processes. The apparatus induces an apparent shear rate of 14.10^3 s^{-1} and has a 0.3 mm gap. The mix was continuously sheared by a rotor-stator system and circulates in a closed circuit through a re-injection pipe. As well as with the first process, bitumen was heated at 140°C and aqueous phase at 50°C. After addition of all the bitumen, the shearing was kept for 5 minutes, as no reduction of the droplets size was observed for a longer shearing time.

Three emulsions were prepared with the colloid mill, their compositions are given in Table 1. After preparation, all emulsions were stored at 40°C.

Table 1. Compositions of emulsions prepared with the colloid mill.

Emulsion	Emulsifier	Emulsifier content in the water phase (wt %)	Bitumen content in the emulsion (wt %)
Em-A	Polyram S + HCl	1.14	50
Em-B1	B1	0.60	50
Em-B2	B2	1.25	50

2.3 Optical microscopy

Emulsions were observed with an optical microscope Olympus BX60 equipped with a video camera Olympus XC50. This technique enables to simply and quickly determine their type and gives a first view of the droplets size. The emulsions were always diluted in order to obtain an image with sufficient contrast and avoid the multilayers of drops present when the sample is too concentrated.

2.4 Laser diffraction analysis

The emulsions prepared with the colloid mill were analyzed to determine their droplets size distribution. Laser diffraction measurements were carried out using a Malvern mastersizer 3000 laser particle size analyzer equipped with a liquid sample dispersion module, Hydro MV (Malvern UK), which can work with particle sizes ranging from 0.01 to 3500 μm . Emulsions were diluted in deionized water in the measuring cell and stirred in order to avoid interactions between droplets and aggregation phenomena.

The volume-weighted mean diameters, $d_{4,3}$, were calculated according to:

$$d_{4,3} = \frac{\sum_i n_i d_i^4}{\sum_i n_i d_i^3}$$

With n_i the number of droplets of diameter d_i .

2.5 Viscosity of emulsions

The viscosity of emulsions was measured with an Anton Paar MCR 102 rheometer equipped with a 25 mm diameter sandblasted plane-plane geometry. The gap is 1 mm. The flow curves were obtained by imposing an increasing and then decreasing shear rate, ranging from 0.01 s^{-1} to 1000 s^{-1} and then from 1000 s^{-1} to 0.01 s^{-1} , in 10 minutes. Experiments were performed at 20°C. The rheometer was equipped with a temperature control system operating by Peltier effect and with a Peltier hood allowing to maintain the sample at a homogeneous temperature.

2.6 Differential scanning calorimetry

Differential scanning calorimetry experiments were carried out on the emulsions with a Mettler DSC 3 apparatus, in order to investigate their type: oil-in-water (o/w) or water-in-oil-in-water (w/o/w). A sample of about 14mg of emulsion was taken and placed in a crucible previously weighed and tared. The crucible was then sealed with a pre-pierced lid. Finally, the sample was placed in the DSC apparatus. For each emulsion, two samples were analyzed. A cooling from 20 to -50°C at 2.5°C/min is applied and the analysis of the crystallization peaks is done during the cooling.

2.6 Compression strength test method: Duriez test

The behavior of emulsified asphalt mixes depends on many factors: the presence of water, the aggregate and emulsion chemical reactivity, voids size, gradual cohesion build-up, etc. For this reason, specific tests methods have been introduced for bitumen emulsion cold mixes. The Duriez test which is covered by the French standard NF P 98-251-4, is designed to determine the water sensitivity of asphalt mixes. Test specimens were manufactured and their voids percentages were calculated. After seven days of conditioning in air at 18°C, with a relative hygrometry of 50%, the test specimens were separated into two series. The first one was immersed in water at 18°C for seven days while the other was stored in air at 18°C and 50% relative hygrometry. The compressive strength of the specimens kept in air (R), and the compressive strength of the specimens kept in water (r) were determined. The immersion/compression ratio r/R , that characterizes water sensitivity was calculated. The closer the ratio r/R to 1, the less water sensitive.

2.7 Emulsified asphalt mixes: Manufacturing of grave-emulsions and test specimens

Two grave-emulsions 0/10, called GE-A and GE-B2 were manufactured with emulsions Em-A and Em-B2 respectively, and diorite aggregates from La Noubleau quarry, with the granular composition given in Table 1 (NF-EN 13108-31). The mixtures were made with a water content of 5.0% and a residual binder content of 5.0%. A shaft mixer with a vertical paddle and a moving bucket was used to prepare the mixtures.

Test specimens were prepared by filling the GE into molds of 80mm diameter, before static compaction at 60 kN.

Table 2. Granular composition of GE-A and GE-B2 grave-emulsions.

Granular fractions	Percentages by weight (%)
6/10	31.5%
4/6	16.0%
2/4	17.0%
0/2	34.3%
limestone	1.2%

3 RESULTS AND DISCUSSION

3.1 Emulsions droplets size

Optical microscopy showed that Em-B1 and Em-B2 were both bitumen-in-water emulsions. Both emulsions were visually homogenous. When prepared with the first process (IKA disperser), the emulsions presented polydisperse bitumen drops with diameters up to 400 μm . As shown in Figure 1, switching from the first process (Figure 1a) to the second (colloid mill) (Figure 1b) for the same composition, led to an important reduction of the droplet size, as this process provides more energy.

As shown in Figure 2 representing droplets size distribution obtained by laser diffraction, Em-A presented a monodisperse size distribution in the range of conventional bitumen emulsions, ranging from 1 to 15 μm , with a $d_{4,3}$ of 4.33 μm . Em-B1 had significantly larger droplets diameters, ranging from 10 to 100 μm , with a $d_{4,3}$ of 49 μm . Em-B2 had a size distribution between Em-A and Em-B1, ranging from 1 to 70 μm , with a $d_{4,3}$ of 11.8 μm . This is likely due to the fact that B1 and B2 are polymers, therefore they have much higher molar masses than a surfactant, making it more difficult to obtain fine droplets. Nevertheless, B2 allowed to obtain a considerable reduction of the droplets size, as it has a lower molar mass than B1, implying that this polymer has shorter chains, leading to smaller droplets.

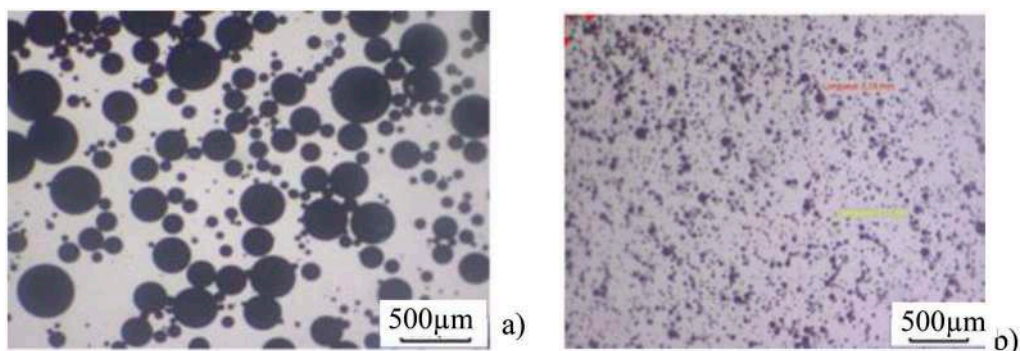


Figure 1. Optical microscopy images of the emulsion containing 50% bitumen and 0.6% emulsifier B1 in the aqueous phase, prepared with a) the IKA disperser equipped with toothed rotor/stator element and b) using the colloid mill.

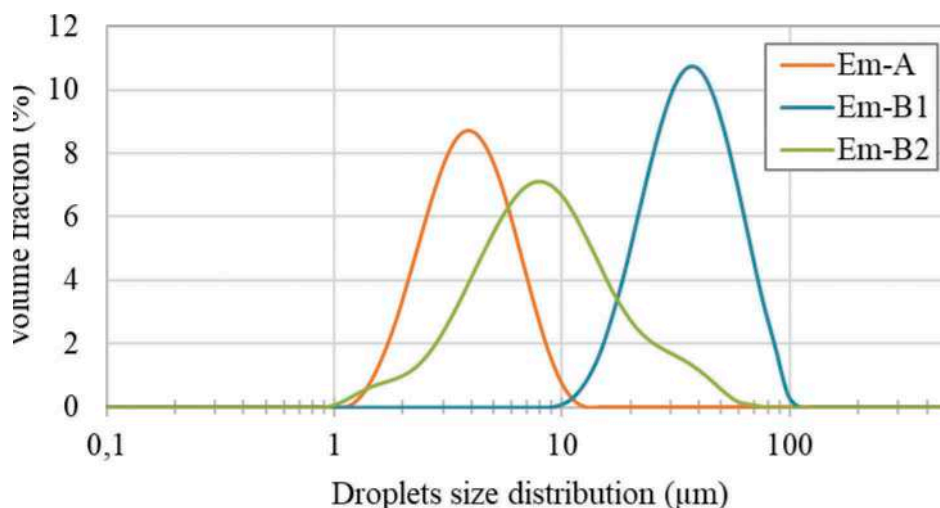


Figure 2. Droplets size distribution of Em-A, Em-B1 and Em-B2, two hours after emulsification.

3.2 Emulsion stability

Visually, after one day of storage at 40°C, it was observed that Em-B1 tends to sediment more than Em-A and Em-B2 likely due to the fact that droplets of Em-B1 are larger than those of the two other emulsions, thus limiting the repulsion between droplets.

The droplets size distributions of Em-A, Em-B1 and Em-B2 were investigated over 30 days using laser diffraction. During this time, emulsions were homogenized every two days.

The evolution of Em-B1 droplets size distribution is presented in Figure 3. The size distribution of Em-B1 remained almost identical over 12 days, with a $d_{4,3}$ around 45-50 μm. Then the whole size distribution shifted to larger sizes ($d_{4,3} = 66$ μm after 19 days), but the polydispersity barely increased: coalescence phenomenon remained limited. After 26 days, the $d_{4,3}$ had significantly increased (189 μm), as well as the dispersion: drops between 500 and 2000 μm have appeared with aggregates that can be observed visually. This indicates that an important coalescence phenomenon occurred. The emulsion had destabilized.

The droplets size distribution of Em-B2 presented in Figure 4, did not evolve for 30 days, which confirms that this emulsion is much more stable than Em-B1. As a comparison, Em-A

was still stable after 30 days, with no evolution of the size distribution (remaining as the one shown in Figure 1).

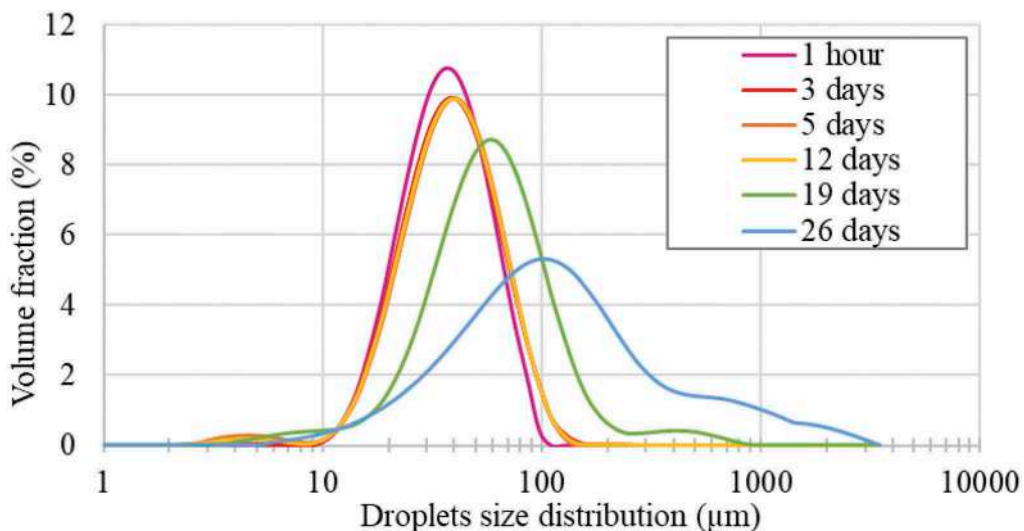


Figure 3. Evolution of the droplets size distribution of emulsion Em-B1 over time.

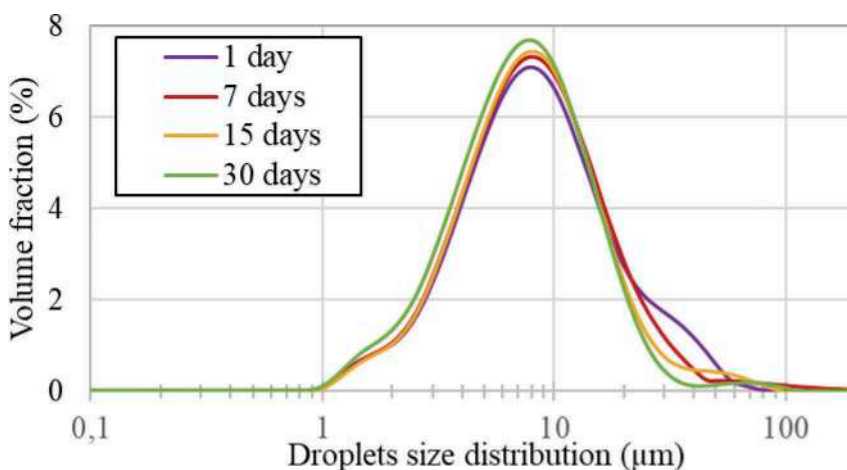


Figure 4. Evolution of the droplets size distribution of emulsion Em-B2 over time.

3.3 Emulsion viscosity

As Em-B1 was not sufficiently stable over time, Em-B2 was selected to carry on the study.

The flow curves, presented in Figure 5, were performed on Em-A and Em-B2. Both emulsions showed a shear thinning behavior as the viscosity decreases with increasing shear rate. Em-B2 had a significantly higher viscosity than Em-A. For a shear rate of 500 s^{-1} , where viscosities reached a plateau, Em-A had a viscosity of $0.01 \text{ Pa}\cdot\text{s}$, corresponding to conventional bitumen emulsions viscosities, while Em-B2 had a viscosity of $0.13 \text{ Pa}\cdot\text{s}$. Em-B2 also showed a thixotropic behavior: a lower viscosity was measured when decreasing the shear rate than

when increasing it and this phenomenon was reversible after a restructuring time. This means that the shear induces a deformation of the material which is reflected in a delayed way in time. Once at rest, the emulsion regains its original structure and mechanical properties. This behavior implies that shearing the emulsion at a constant rate for a certain time will lead to a decrease in viscosity, reaching one more suitable for pumping.

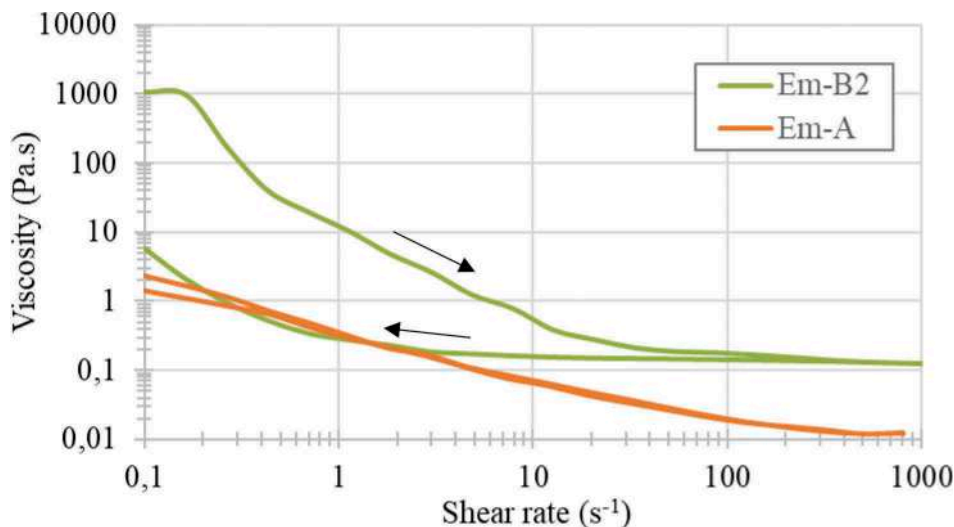


Figure 5. Flow curves obtained at 20°C for Em-A and Em-B2 with increasing and decreasing shear rate.

To be sure that the high viscosity of Em-B2 is due to the presence of polymer B2 and not to the presence of a multiple w/o/w emulsion, DSC measurements were performed. Indeed, in an emulsion, the internal water phase and the continuous water phase do not crystallize at the same temperature. In fact, it depends on the volume: the smaller the volume, the lower the crystallization temperature, due to the lack of nucleation sites. In a DSC sample, the continuous phase of an emulsion would crystallize around -20°C while the dispersed water droplets would crystallize around -40°C (Clausse et al., 2005). The DSC experiments showed a single crystallization temperature at -18°C corresponding to the continuous water phase, and no crystallization around -40°C. Em-B2 is a bitumen-in-water emulsion, so the viscosity is not due to the presence of fine water droplets dispersed in the bitumen.

3.4 Cold mixtures water resistance

During the manufacture of the two grave-emulsions GE-A and GE-B2, a good coating of the aggregates by the emulsions was observed.

The average voids content of the test specimens were close for the two GE: 10.9% for the test specimens of GE-A and 9.9% for those of GE-B2, so a low impact on the values obtained during the compression test was expected.

The compression strength values as well as the water contents are summarized in Table 2. For specimens stored in air, compression strengths were similar for both GE. However, the values for specimens stored in water differed, as the strength of the GE-B2 was much lower. This resulted in an r/R ratio of 0.85 for GE-A and 0.219 for GE-B2. As the standards require an $r/R > 0.70$, this showed a significant impact of water on GE-B2. Water contents confirm this since after 15 days in air they are similar for both GE but after 7 days in water, the one of GE-B2 specimens (4.74%) is much higher than the one of GE-A (2.87%). This water recovery led to a high bitumen

stripping phenomenon (Vinet-Cantot et al. 2019). This high sensitivity to water might be due to the nature of the emulsifier which can swell with water, and its poor interaction with the aggregates.

Table 3. Duriez test results.

	GE-A	GE-B2
r (MPa)	3.07	0.75
R (MPa)	3.62	3.90
r/R (-)	0.85	0.19
Water content after 15 days in air (%)	0.63	0.49
Water content after 7 days in air and 7 days in water (%)	2.87	4.74

4 CONCLUSIONS

The bio-based polymers tested allowed to manufacture bitumen in water emulsions with a 50 wt % bitumen content. Em-B1 presented large droplets and was less stable over time. But Em-B2 was a promising emulsion which presented a droplets size distribution close to the one of conventional bitumen emulsions and was still stable after a month. Em-B2 presented a higher viscosity than conventional bitumen emulsions. Emulsified asphalt mixes could be prepared, as the emulsions provided an initial good coating of fine and coarse aggregates. Compression strengths obtained by Duriez test were equivalent to those of conventional asphalt mixes when specimens were stored in air. However, when immersed in water, the compression strength considerably decreased, showing high water sensitivity for this material. In this study, a first step of bio-based stabilized bitumen emulsion has been established; however, water resistance will have to be improved. To do so, tuning of the bio-based emulsifier and adjustment of the emulsion formulation are currently under investigation.

ACKNOWLEDGEMENT

The authors acknowledge the French “Region des Pays de la Loire”, “Nantes Métropole” and the French program “Investing for the Future” for their financial support.

REFERENCES

- Anaclet, P., Julien, V., Mariotti, S., Backov, R., & Schmitt, V., 2017. *Development of dispersible and flowable powdered bitumen*. Journal of Cleaner Production, 141, 940–946.
- Clausse, D., Gomez, F., Pezron, I., Komunjer, L., & Dalmazzone, C., 2005. *Morphology characterization of emulsions by differential scanning calorimetry*. Advances in colloid and interface science, 117(1-3), 59–74.
- Gaufrey, V., Viranaiken, V., Paranhos, R., Jullien, A., de La Roche, C., 2010. *Laboratory Assessment of Fumes Generated by Bituminous Mixtures and Bitumen*. Road Materials and Pavement Design, 11, 83–100.
- Gutierrez, X., Silva, F., Chirinos, M., Leiva, J. & Rivas, H., 2002. *Bitumen-in-Water Emulsions: An Overview on Formation, Stability, and Rheological Properties*, Journal of Dispersion Science and Technology, 23: 1-3, 405–418.
- Jullien, A., Gaufrey, V., Ventura, A., de La Roche, C., Paranhos, R., Monéron, P., 2010. *Airborne emissions assessment of hot asphalt mixing - methods and limitations*, Road Materials and Pavement Design, 11, 149–169.
- Mallawarachchi, D. R., Amarasinghe, A. D. U. S., & Prashantha, M. A. B., 2016. *Suitability of Chitosan as an emulsifier for cationic bitumen emulsions and its behaviour as an additive to bitumen emulsion*. Construction and Building Materials, 102, 1–6.

- McClements, D. J., & Gumus, C. E., 2016. *Natural emulsifiers—Biosurfactants, phospholipids, biopolymers, and colloidal particles: Molecular and physicochemical basis of functional performance*. *Advances in Colloid and Interface Science*, 234, 3–26.
- Mercado, R., & Fuentes, L., 2016. *Asphalt emulsions formulation: State-of-the-art and dependency of formulation on emulsions properties*. *Construction and Building Materials*, 123, 162–173.
- NF P 98-251-4, *Tests relating to pavements - Static tests on bituminous mixtures - Part 4: modified DURIEZ test on bitumen emulsion based cold mix asphalts*, AFNOR, 2004.
- NF-EN 13108-31 *Bituminous mixtures - Material specifications - Part 31: asphalt Concrete with Bituminous Emulsion*, AFNOR, 2019.
- Paria, S., & Khilar, K. C., 2004. *A review on experimental studies of surfactant adsorption at the hydrophilic solid–water interface*. *Advances in colloid and interface science*, 110(3), 75–95.
- Serfass, J. P., De La Roche, C., Wendling, L., Gaudefroy, V., & Verhée, F., 2011. *Emulsified asphalt mixes: Behaviour and design of grave-emulsion*. Public private cooperation. Towards a complete design method. *European roads review*, (19), 1–4.
- Serfass, J.-P., Poirier, J., Henrat, J., Carbonneau, X., 2004. *Influence of curing on cold mix mechanical performance*, *Materials and Structures*, 37, 365–368.
- Vinet-Cantot, J., Gaudefroy, V., Delfosse, F., Chailleux, E., & Crews, E., 2019. *Stripping at the Bitumen–Aggregate Interface: A Laboratory Method to Assess the Loss of Chemical Adhesion*. *Energy & Fuels*, 33(4), 2641–2650
- Yuliestyan, A., Garcia-Morales, M., Moreno, E., Carrera, V., & Partal, P., 2017. *Assessment of modified lignin cationic emulsifier for bitumen emulsions used in road paving*. *Materials & Design*, 131, 242–251.
- Zhang, R., & Somasundaran, P., 2006. *Advances in adsorption of surfactants and their mixtures at solid solution interfaces*. *Advances in colloid and interface science*, 123, 213–229.
- Ziyani, L., Gaudefroy, V., Ferber, V., Deneele, D., & Hammoum, F., 2014. *Chemical reactivity of mineral aggregates in aqueous solution: relationship with bitumen emulsion breaking*. *Journal of Materials Science*, 49(6), 2465–2476.

Characterization of multiple recycled reclaimed asphalt incorporating polymer modified bitumen

I. Widyatmoko, A. Subhy & C. Ojum

AECOM, Nottingham, UK

A. Khojinian & R. Hudson-Griffiths

National Highways (formerly Highways England), Bedford, UK

D. Giles

Eurobitume, UK

M. Simms

Mineral Products Association, London, UK

ABSTRACT: A state of the art process has been carried out to inform and improve the assessment and efficiency of Reclaimed Asphalt (RA) containing Polymer Modified Bitumen (PMB) in multiple recycling of asphalt mixtures. The methodology developed included detailed laboratory investigation of the fundamental properties of RA containing PMBs and those of the binders recovered from various stages of sample manufacturing and after ageing processes. Laboratory manufactured asphalt mixtures were evaluated for stiffness, water sensitivity and deformation resistance. The key findings from this project show that asphalt mixtures produced using 50% PMB-RA have comparable mechanical properties to the mixtures containing 100% primary components (control). The recyclability assessment indicated that the desired rheological properties of the PMB were largely maintained after multiple recycling for asphalt mixtures incorporating highly polymer modified PMB. The findings from this work show the feasibility of improving sustainability by using high levels of RA with PMB.

Keywords: Reclaimed asphalt, rheological properties, polymer modified bitumen, multiple recycling

1 INTRODUCTION

The Strategic Road Network (SRN) in England plays a vital role in improving productivity and driving economic growth. National Highways, formerly Highways England, aims to provide a safe and serviceable network with free-flowing roads. The feasibility for increased use of Reclaimed Asphalt (RA) into future production of asphalt materials supports the 'Construction 2025' report (BIS 2013) with aspirations of 50% carbon reduction by 2025 and ultimately the United Kingdom's target for net-zero carbon by 2050.

Polymer Modified Bitumen (PMB) has been successfully and widely used in different types of asphalt for decades in the UK. PMBs have desirable rheological properties that can contribute to enhanced resistance to rutting and fatigue cracking (Kim et al. 2009; Airey 2002; Huang et al. 2005). Many PMB asphalts on the SRN are now approaching

the end of their first life, potentially offering a valuable source of RA materials containing high quality aggregates as well as bitumen with high quality rheological properties. The main concern with replacing a larger volumetric portion of asphalt mixtures with RA is the perceived risk of compromising the end performance, due to possible inconsistency of the RA properties that may vary with, for example: recovery techniques, and the maintenance and in-service history of pavements (Subhy et al. 2019). This has led many highway authorities to place restrictions to limit the total amount of RA materials that can be incorporated in new asphalt mixtures.

Despite these limitations, collaborative works between researchers, highway authorities and the asphalt industry have been progressing to develop better techniques and designs that enable higher amounts of RA to be incorporated without compromising the mechanical properties and performance of the materials and ultimately, the pavement durability. The use of high RA content in asphalt mixtures has been shown to provide multiple potential benefits, particularly when carefully controlled and monitored (Shen et al 2007; Shu et al 2008; Sunil et al 2014; Mollenhauer et al. 2011; Al-Qadi et al. 2012; Oliveira et al. 2013; Carrión et al 2015).

The research presented in this paper was an effort to further support the Highways England's Sustainable Development Strategy in delivering both economic and environmental benefits from recycling with higher RA content. Full results and details of this research are available online (Subhy and Hadri 2021).

2 SCOPE AND METHODOLOGY

The adopted methodology included an extensive suite of laboratory testing. The rheological and chemical properties of the bitumens were evaluated under different ageing conditions, namely: NA (Non-Aged), STA (Short-Term-Aged) and LTA (Long-Term-Aged). The Modified Rolling Thin Film Oven Test (MRTFOT) according to UK Specification for Highway Works Clause 955 was used to serve two purposes: (1) to age the PMBs; and, (2) a means for blending the recovered bitumen from RA with primary bitumens. More details about the blending protocol and methodology can be found in (Subhy and Hadri 2021).

The PMBs with different ageing conditions were characterized using the Dynamic Shear Rheometer (DSR); chemical properties using Fourier Transform Infrared Spectroscopy (FTIR) and derivation of the basic chemical components of bitumen, i.e., the fractions of Saturates, Aromatics, Resins, and Asphaltenes (SARA). The testing matrix also included evaluating asphalt mixtures using the Indirect Tensile Stiffness Test (ITSM), Water Sensitivity and Wheel Track Testing (WTT).

3 MATERIALS AND EXPERIMENTAL PROGRAMME

3.1 *Components for sample manufacturing*

The primary components used in this project were granite aggregates and limestone filler. Surface course asphalt planings (site-won asphalt) were collected from M42 J9-8 (Southbound direction), England and were processed as RA for use in this study. Information associated with these materials is presented below in Figure 1.

The selected classification of the primary PMB was 75/130-75 in accordance with BS EN 14023. Table 1 shows the results of the penetration and softening point test results for the selected primary PMB and under different ageing conditions. The selected PMB was considered to be a highly polymer modified bitumen, as indicated by its high softening point with a relatively high penetration value. It is worth noting that whilst increased ageing is expected to result in bitumen hardening, and thus reduced the penetration value, the tested PMB however presented a trend of lowering softening point value. The latter could have been due to PMB degradation into lower molecular weight during the prolonged ageing conditions.

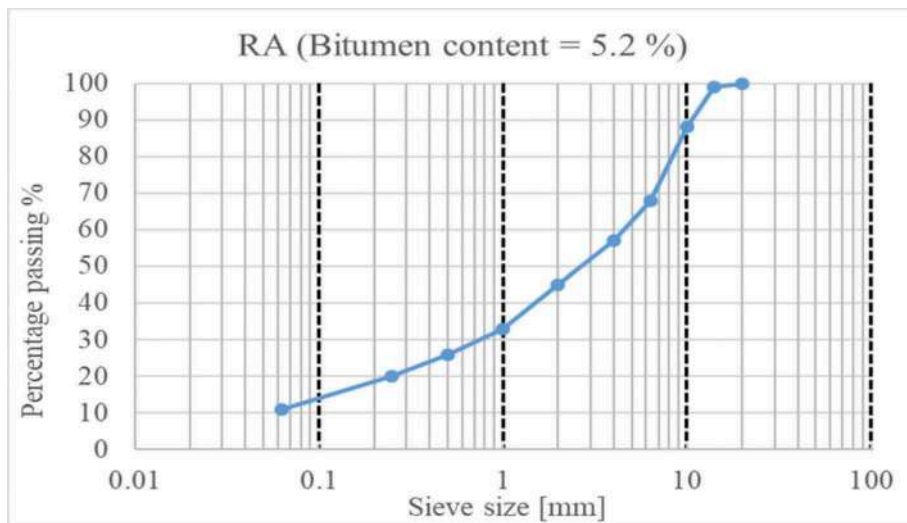


Figure 1. Reclaimed asphalt compositional analysis.

Table 1. Penetration and softening point results of the selected PMB.

Ageing condition	Penetration (dmm)	Softening Point (°C)
Non-Aged (NA)	94	90.5
Shot-Term-Aged (STA)	66	88.0
Long-Term-Aged (LTA)	40	67.6

3.2 Bitumen samples

Table 2 shows the project reference of different bitumens with a description to give information about the processing conditions and/or composition of these materials.

3.3 Asphalt mixture samples

A generic Stone Mastic Asphalt of 10mm nominal aggregate size (SMA 10) conforming to BS EN 13108-5 and BSI PD 6691:2015+A1:2016 was selected for this study. The target bitumen content was specified as 6.2% by mass of the total mixture. For asphalt mixtures incorporating RA, the active bitumen availability from the RA was assumed to be 90% and was subtracted from the design bitumen content (6.2%). Table 3 shows the project references of different asphalt mixtures with their description.

4 RESULTS AND ANALYSIS

4.1 Rheological and chemical properties of bitumens

4.1.1 Glover-Rowe parameter

Research has shown that the Glover-Rowe (G-R) parameter can effectively capture the resistance of bitumens to thermal and traffic-induced stresses (Rowe 2014). Figure 2 shows the results of the G-R parameter, where the complex modulus (G^*) and the phase angle δ were tested at 0°C and 1.59 Hz using the DSR to compute the G-R parameter.

Table 2. Bitumen samples.

Bitumen reference	Description
PMB ₀	Primary PMB classified as 75/130-75
PMB _{sta}	PMB ₀ subjected to short-term ageing (STA) using modified rolling thin film oven test (MRTFOT), i.e., conditioned in the oven for 45 mins \pm 1 min at a temperature of 163 \pm 1°C
PMB _{lta}	PMB ₀ subjected to long-term ageing (LTA) using modified rolling thin film oven test (MRTFOT), i.e., conditioned firstly for 60 mins \pm 1 min at a temperature of 163 \pm 1°C, followed by 6 hours \pm 10 minutes at 135 \pm 1°C in addition to the time for the MRTFOT to reach 135°C.
PMB _r	The recovered bitumens from asphalt mixture with 100% of primary aggregate and PMB ₀ .
RA _r	The recovered bitumens from the reclaimed asphalt (asphalt planings)
RA1 _r	The mixture made using 50% of RA, primary aggregate and PMB ₀ after further processing (crushed and lab-aged at 85°C for 120 hours) to produce laboratory aged RA1. RA1 _r is the recovered bitumens from the laboratory aged RA1
25:75(PMB+RA) _r	The recovered bitumen from the asphalt mixture made using 25% of RA, primary aggregate and PMB ₀ .
25:75(PMB+RA) _r _{sta}	The recovered bitumen from the RA blended at 25% with the PMB ₀ using the MRTFOT after short-term ageing.
25:75(PMB+RA) _r _{lta}	The recovered bitumen from the RA blended at 25% with the PMB ₀ using the MRTFOT after long-term ageing
50:50(PMB+RA) _r	The recovered bitumens from asphalt mixture made using 50% of RA, primary aggregate and PMB ₀ .
50:50(PMB+RA) _r _{sta}	The recovered bitumen from the RA was directly blended at 50% with PMB ₀ using the MRTFOT under short-term ageing.
50:50(PMB+RA) _r _{lta}	The recovered bitumen from the RA was directly blended at 50% with PMB ₀ using the MRTFOT after long-term ageing.
50:50(PMB+RA1) _r	The recovered bitumens from asphalt mixture made using 50% of lab-aged RA1, primary aggregate and PMB ₀ .

Table 3. Asphalt mixture samples.

Asphalt mixture reference	Description
Mixture 1 0% RA	Asphalt mixture made using 100% primary aggregate and PMB ₀ .
Mixture 2 25%RA	Asphalt mixture made using 75% primary aggregate, 25% reclaimed asphalt and PMB ₀ .
Mixture 3 50%RA	Asphalt mixture made using 50% primary aggregate, 50% reclaimed asphalt and PMB ₀ .
Mixture 4 50% RA1	Asphalt mixture made using 50% primary aggregate, 50% lab-aged Mixture 3 and PMB ₀ .

The lower the G-R value the better the bitumen is at resisting damage from thermal and traffic-induced cracking, without developing large stresses and regaining its original shape with minimum dissipated energy (Rowe 2014). The results showed that the G-R parameter increased with ageing indicating that the PMBs would become more susceptible to thermal and traffic-induced cracking with ageing. The G-R value of the RA_r was interestingly comparable to the primary PMB. The effect of adding the RA_r combined with the effect of MRTFOT ageing conditions led to increase in the G-R values indicating the hardening of the materials. The G-R values, as expected, increased with increases of the RA content. The addition of 25% RA resulted in only a slight increase in the G-R value. The G-R values for the bitumens

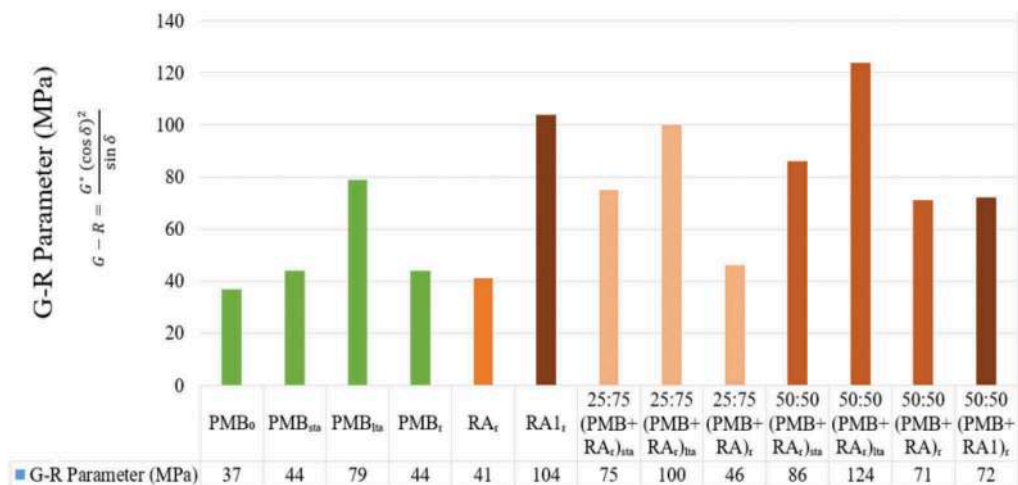


Figure 2. G-R parameter computed at 0 °C and 1.59 Hz.

recovered from asphalt mixtures containing RA were generally smaller than their corresponding values when directly blended under MRTFOT conditions. The larger amount of the primary PMB contributed to good rheological properties. The RA_r recovered from multiple recycled asphalt mixture (RA1) exhibited only a slight increase in the G-R value.

4.1.2 Multiple Stress Creep and Recovery (MSCR)

The Multiple Stress Creep Recovery (MSCR) test was conducted by applying repeated creep-recovery cycles in accordance with AASHTO TP 70-13 at isothermal temperature of 60°C applied as 1-second creep shear stress followed by a 9-second recovery period. The main parameters retrieved from MSCR are the non-recoverable creep compliance (J_{nr}) and the % Recovery.

Asphalts with bitumens that have low J_{nr} values and high recoveries may be less susceptible to rutting at high pavement temperatures. Figure 3 is used by AASHTO TP 70-13 as an indicator of the presence of an acceptable elastomeric polymer. The average percentage recovery at 3.2 kPa, versus the average non-recoverable creep compliance at 3.2 kPa was plotted on the graph. All blended bitumens of RA with the PMB at 25% and 50% as well as the recovered bitumens from asphalt mixtures incorporating RA or RA1 fell above the line indicating an “acceptable” elastomeric polymer behaviour except for the 50:50(PMB+RA_r)_{sta}. The results for the 50:50(PMB+RA1)_r had high recovery and low J_n value indicating excellent rutting performance. These results highlighted the desirable properties imparted by the PMB already available in the RA1 mixtures in addition to the added primary PMB.

4.1.3 Fourier transform infrared spectroscopy (FTIR)

The main functional groups of bitumen that are affected by oxidative ageing are Carbonyls C=O (centred around 1700 cm⁻¹) and Sulfoxides S=O (centred around 1030 cm⁻¹) as detailed in (Feng et al. 2016; Mirwald et al. 2020). Monitoring the formation of the Carbonyls and Sulfoxides can indicate the amount of oxygen intake for the different bitumens due to oxidative ageing. Bitumens that exhibit less oxygen intake during ageing and ultimately less hardening are preferred. Figure 4 shows typical results of FTIR scan spectra (bandwidth vs absorbances) for the PMB under different oxidative conditions. The S=O peaks showed a consistent trend throughout the FTIR testing. The average peaks calculated are also shown in Figure 4. These presented a quantitative indication for the effect of ageing. Figure 5 shows qualitatively the effect of ageing on the Sulfoxides S=O with peaks visible at approximately 1027 cm⁻¹. As expected, the total peaks increased with ageing for all the blends. The peak results of 25:75 blends were, as

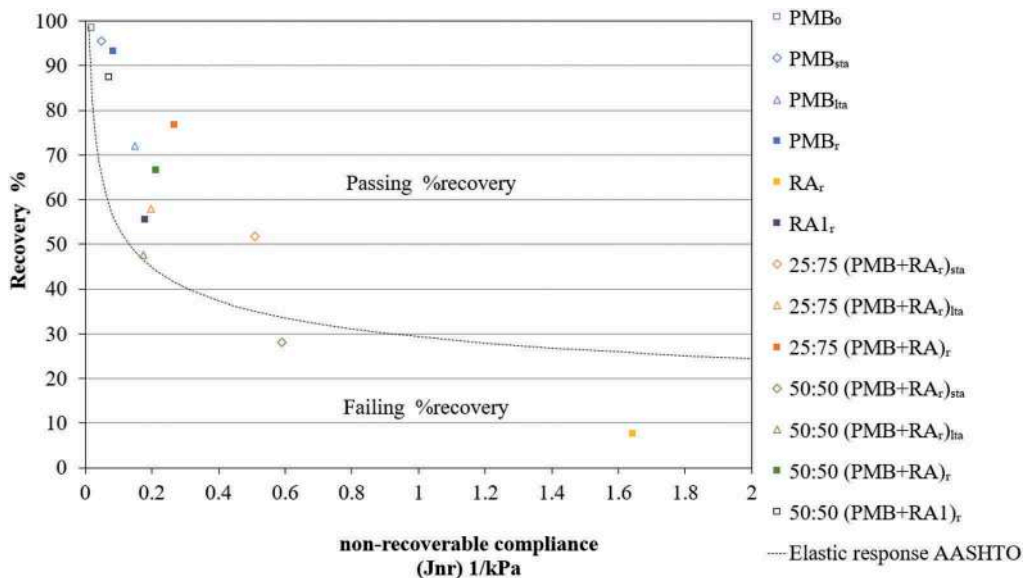


Figure 3. The elastic response of the blended and recovered bitumens.

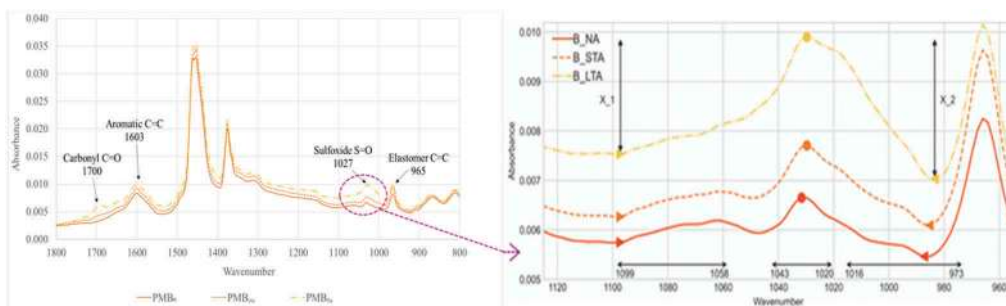


Figure 4. Typical FTIR scan for bitumen PMB and the procedure for calculating the S=O.

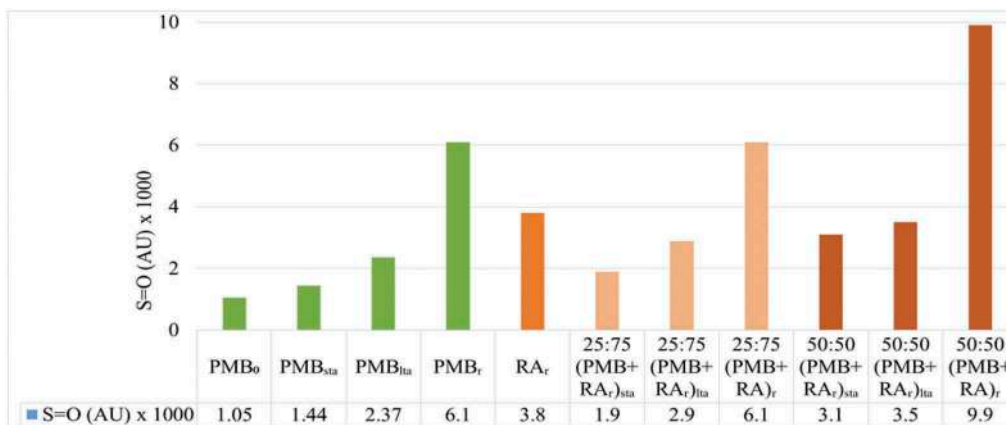


Figure 5. The sulfoxide peaks for the different bitumens.

expected, lower than for the 50:50 blends. The S=O peaks of the recovered bitumens from the asphalt mixtures were almost three times greater than those of their corresponding bitumens (directly blended using MRTFOT). It should be mentioned that the FTIR measurements are very sensitive to any trace of contamination that could have remained during the recovery process.

4.1.4 Saturates, Aromatics, Resins, and Asphaltenes (SARA)

Saturates, Aromatics, Resins, and Asphaltenes (SARA) analysis were carried out to monitor the evolution of the bitumen samples, as it relates to ageing. The hardening of bitumens during ageing is generally related to volatilization and oxidation of the light components (mainly aromatics) which convert into more chemically polar molecules or asphaltenes. The Colloidal Index (CI), calculated as the ratio between combined contents of asphaltenes and saturates (flocculent agents) and resins and aromatics (peptizing agents), was used to evaluate the stability of the colloidal structure.

The proportion of the peptising agents to asphaltenes determines whether the bitumens have sol-type behaviour or gel-type behaviour. If there are adequate peptising agents a solution (SOL) structure bitumen occurs, but a reduction forms a gelatinous (GEL) structure in the bitumen. Bitumens having a CI below 0.7 exhibits typical sol-type behaviour. Bitumens with a CI >1.2 exhibits a gel-type behaviour and bitumens with a CI between 0.7 to 1.2 are considered a sol/gel type structure. Bitumens with sol-type behaviour are considered better able to resist thermal and traffic-induced stresses (Evans et al. 2011). The results in Figure 6 showed that the 25:75 and 50:50 blends changed towards a more gel-like colloidal structure with ageing, indicating that they would be more susceptible to thermal and traffic-induced stresses. However, all the bitumens are considered to have sol-type behaviour <0.7 CI.

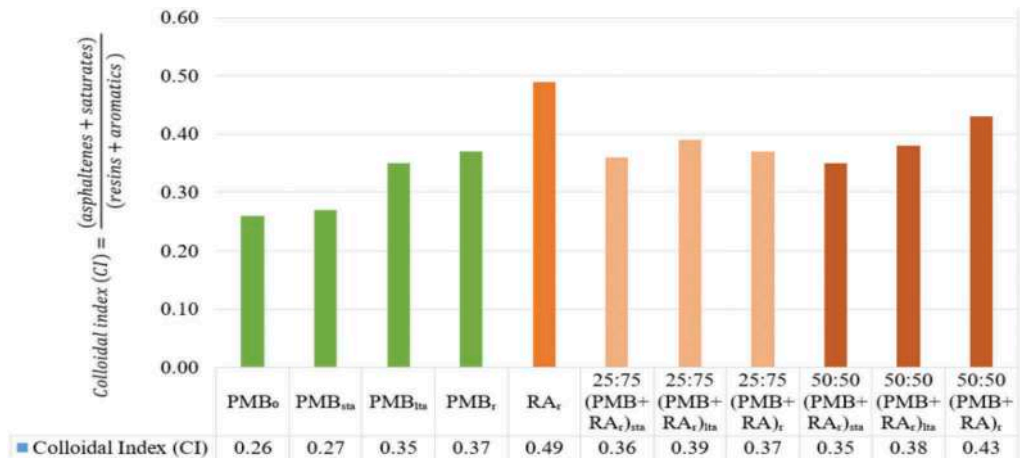


Figure 6. Colloidal index (CI) for the different bitumens.

4.2 Asphalt mixture test results

The asphalt mixture stiffness, deformation resistance and water sensitivity test results are summarized in Table 4.

4.2.1 Stiffness

Stiffness testing was conducted at 20°C in accordance with BS EN 12697-26: 2004 (Annex C), the Indirect Tensile Stiffness Modulus (ITSM). The test results, summarized in Table 4, were all in the range of 1,000 to 2,000 MPa with the stiffness values increasing with the increase of RA content. Published 20°C ITSM data for SMA thin surfacings were reported to have

Table 4. Asphalt mixture test results.

Asphalt mixture	Stiffness	Deformation resistance		Water sensitivity		
	ITSM at 20°C (MPa)	RD _{air} at 60°C, 10000 cycles (mm)	WTS _{air} at 60°C (mm/1000 cycles)	ITS _d at 25°C (kPa)	ITS _w at 25°C (kPa)	ITSR (%)
0% RA	1010	2.6	0.05	754	633	84
25%RA	1605	2.4	0.04	894	822	92
50%RA	1955	2.8	0.06	1.05 x 10 ³	908	86
50%RA1	1580	2.1	0.05	1.14 x 10 ³	1.12 x 10 ³	98

a typical stiffness value in the range of 1,000 MPa to 3,500 MPa when new (Widyatmoko et al. 2006). This can increase by a factor of 1.5 to 2.0 when aged in service.

4.2.2 Deformation resistance

Resistance to deformation was assessed using Wheel Tracking Tests (WTT) in accordance with EN 12697-22:2020 using the small device to 10,000 cycles in air at 60°C. Each result presented for WTT is the mean value of the 2 comparable samples tested. Table 4 shows that the measured rut depth (RD_{air}) ranged from 2.1 mm for the 50% RA1 to 2.8 mm for the 50% RA and the wheel track slope (WTS_{air}) were in the range of 0.04 mm/1000 cycles to 0.06 mm/1000 cycles. According to the requirements defined in PD 6691:2015+A1:2016, the WTS_{air} results indicated that all mixtures have excellent rutting resistance.

4.2.3 Water sensitivity

Resistance to moisture damage of the asphalt mixtures was measured by conducting water sensitivity testing in accordance with EN 12697-12:2018 – Method A. Table 4 shows the average Indirect Tensile Strength of the wet group (ITS_w) and the dry group (ITS_d) of samples. The values of both the ITS_w and the ITS_d increase as the percentage of RA increases. All mixtures exceeded the 80% of the Indirect Tensile Strength Ratio (ITSR), indicating mixture being not sensitive to moisture damage (Widyatmoko et al. 2006).

5 CONCLUSIONS AND RECOMMENDATIONS

The main findings and conclusions are presented below:

1. The Modified Rolling Thin Film Oven Test (MRTFOT) provided a realistic and practical protocol for blending bitumen recovered from RA with primary bitumens, whilst at the same time providing a means to accelerate ageing in the laboratory.
2. The results of bitumen characterization highlighted the importance of using more fundamental and performance related testing to characterize PMBs during asphalt recycling. The rheological protocols used provided effective tools to distinguish between the retained effectiveness of polymer modification. The addition of up to 50% of recovered PMB-RA bitumen can still result in having blended bitumen with “acceptable” elastic recovery properties, in accordance with AASHTO TP 70-13.
3. The G-R parameter and SARA analysis provided consistent results about the combined effect of ageing and RA contents on the cracking resistance of bitumens. In this context, the combined effect appeared to make materials more susceptible to thermal and induced cracking. The addition of 25% RA had, however, comparable performance to the control materials (100% primary PMB) in terms of low temperature properties.
4. The asphalt mixtures produced using 50% RA showed comparable or enhanced mechanical properties to those of the control material, when tested for stiffness, rutting resistance and water sensitivity.

5. The desirable rheological properties of the original (primary) PMB were largely maintained after multiple (second round) recycling for asphalt mixtures containing a highly modified PMB. The re-recycled asphalt mixtures showed mechanical properties at least comparable to those of the control mixtures containing 0% RA.

The following recommendations are proposed to obtain a better understanding of RA materials containing PMBs and to validate the laboratory test results:

- extending this research to full-scale asphalt plant and road trials;
- incorporating long-term durability assessments, including evaluating the low temperature cracking characteristics.

ACKNOWLEDGEMENT

This paper presents findings from Work Package 1-979 Collaborative Research on Assessment of the potential durability impacts of RA on asphalt mixtures containing aged PMB, funded by Highways England, Mineral Products Association and Eurobitume UK, and delivered by AECOM. We acknowledge the contributions from Dave Whiteoak, Omar Hadri, Neil Longstaff and Lukasz Kozicz for their input, data collection and discussions during this research.

REFERENCES

- Airey, GD. 2002. "Rheological Evaluation of Ethylene Vinyl Acetate Polymer Modified Bitumens" *Construction and Building Materials* 16 (8): 473–487.
- Al-Qadi, IL., Aurangzeb, Q., Carpenter, SH., Pine, WJ. and Trepanier, J. 2012. "Impact of High RAP Content on Structural and Performance Properties of Asphalt Mixtures".
- Carrión, AJ., Lo Presti, D. and Airey, GD. 2015. "Binder Design of High RAP Content Hot and Warm Asphalt Mixture Wearing Courses." *Road Materials and Pavement Design*.
- BIS. 2013. "Construction 2025 - Industrial Strategy: Government and Industry in Partnership."
- Evans, M., Marchildon, R. and Hesp, SAM. 2011. "Effects of Physical Hardening on Stress Relaxation in Asphalt Cements: Implications for Pavement Performance" *TRR* 2207 (1): 34–42.
- Feng, Z., Bian, H., Li, X. and Yu, J. 2016. "FTIR Analysis of UV Aging on Bitumen and Its Fractions" *Materials and Structures* 49 (4): 1381–89.
- Huang, B., Li, G., Vukosavljevic, D., Shu, X and Egan, BK. 2005. "Laboratory Investigation of Mixing Hot-Mix Asphalt with Reclaimed Asphalt Pavement" *TRR* 1929 (1): 37–45.
- Kim, S., Sholar, GA., Byron, T. and Kim, J. 2009. "Performance of Polymer-Modified Asphalt Mixture with Reclaimed Asphalt Pavement" *TRR* 2126 (1): 109–14.
- Mirwald, J., Werkovits, S., Camargo, I., Maschauer, D., Hofko, B. and Grothe, H. 2020. "Investigating Bitumen Long-Term-Ageing in the Laboratory by Spectroscopic Analysis of the SARA Fractions" *Construction and Building Materials* 258: 119577.
- Mollenhauer, K., Ipavec, A., Gaspar, L., Marsac, P., Mirski, K., Batista, F., Antunes, M., McNally, C. and Karlsson, R. 2011. "Synthesis of National and International Documents on Existing Knowledge Regarding the Recycling of Reclaimed Road Materials in Asphalt". *DIRECT-MAT Deliverable D6; EC No 218656*.
- Oliveira JRM, HMRD Silva, CMG Jesus, LPF Abreu, and SRM Fernandes. 2013. "Pushing the Asphalt Recycling Technology to the Limit." *International Journal of Pavement Research and Technology* 6 (2): 109–16.
- Rowe, GM. 2014. "Interrelationships in Rheology for Asphalt Binder Specifications". 59th Annual Conference of the Canadian Technical Asphalt Association (CTAA). Manitoba.
- Shen, J., Amirkhanian, S. and Miller, JA. 2007. "Effects of Rejuvenating Agents on Superpave Mixtures Containing Reclaimed Asphalt Pavement." *Journal of Materials in Civil Engineering* 19 (5): 376–84.
- Shu, X., Huang, B. and Vukosavljevic, D. 2008. "Laboratory Evaluation of Fatigue Characteristics of Recycled Asphalt Mixture." *Construction and Building Materials* 1330 (7): 1323–30.
- Subhy, A. and Hadri, O. 2021. "Sub-Task 1: Assessment of Reclaimed Asphalts Containing Aged Polymer Modified Bitumen." Nottingham.
- Subhy, A., Pires, GM., Jim, A., Lo Presti, D. and Airey, GD. 2019. "Binder and Mixture Fatigue Performance of Plant-Produced Road Surface Course Asphalt Mixtures with High Contents of Reclaimed Asphalt."

- Sunil, S., KM Mallesh, and Chandrasekaraiah, T. 2014. "Experimental Investigations on the Performance of Bituminous Mixes with Reclaimed Asphalt Pavement (RAP) Materials (Case Study Tumkur to Chitradurga-NH4)" *International Journal of Research in Engineering and Technology*, 297–303.
- Widyatmoko, I., Zhao, B., Elliot, RC. and Lloyd, WG. 2006. "Curing Characteristics and the Performance and Durability of Epoxy Asphalts". 10th International Conference on Asphalt Pavements. Quebec.

Selection of sand gradations and proportions for sand-bentonite mixtures of fine-grained soil

Gaurav Verma & Brind Kumar

Department of Civil and Transportation Engineering, Indian Institute of Technology (Banaras Hindu University), Varanasi, Uttar Pradesh, India

ABSTRACT: Sand-bentonite mixtures are greatly used as a liner material for covering the waste disposal sites. Naturally available sand contains the altered proportions of fine, medium and coarse sand therefore, the selection of sand gradations and proportions with bentonite is a challenging assignment for any highway material engineers. Additionally, compacted sand-bentonite mixtures used for liner must have higher maximum dry density and for that attempting various numbers of laboratory compaction tests at different proportions of various graded sand with bentonite is costly, laborious and time consuming. This study is an attempt to select the sand gradations and proportions for sand-bentonite mixtures. Results obtained through the laboratory investigation and mathematical technique (Percent Variance) reveals that by just knowing the MDD of bentonite and percentage of fine, medium and coarse sand; the maximum dry density of any sand-bentonite mixtures could be estimated within $\pm 3\%$ variation in actual and estimated values. Based on that selection of mix combination of sand-bentonite for liner can be identified as well as the quantity of soil required for any project work consequently, the cost for any earthwork project can be designed.

Keywords: Sand-bentonite, maximum dry density, optimum moisture content, fine sand, medium sand, coarse sand, fine-grained soils

1 INTRODUCTION

Compaction of soil is the process of enhancing the dry unit weight by the application of mechanical force applied either statically or dynamically. Compaction parameters are equally significant for both laboratory and field engineers (Verma and Kumar 2019) as the laboratory obtained parameters are further used for the field earthwork projects such as road embankment and sub-grade, trench backfill, solid waste liner as well as for the estimation of quantity of soil required for these project work. Compaction play an important role for covering the waste disposal sites produces noxious gases and contaminated liquids which degraded the environment as well as the ground water. So as to prevent or minimize the leakage of these contaminant a barrier of well compacted soils are utilized as a liner. Typically, sand-bentonite mixtures are significantly used as a geotechnical barriers for controlling these waste disposal sites. Hydraulic conductivity of sand-bentonite mixture is extremely influenced by the compaction parameters (Günaydın 2009) as well as the proportions of different graded sand. In order to minimize the contaminant hydraulic conductivity of compacted liner must be less than 1×10^{-9} m/s (Günaydın 2009). Therefore, compacted sand-bentonite mixtures used for liner must have higher MDD and for that different proportions of sand with bentonite are attempted which is more laborious, costly and time consuming. Previously attempted study show that compaction parameters are greatly influenced by the types of

soil, compactive effort and proportions of different particle size (Johnson and Sallberg 1960, 1962, Bodman and Constantin 1965, Pandian, Nagaraj, and Manoj 1997, Deb, Sawant, and Kiran 2010, Patra, Sivakugan, and Das 2010). Naturally available sand contains the altered proportions of fine, medium and coarse sand. Hence, knowing their exact gradation and proportions of each, which could contribute the maximum amount of MDD, is particularly a difficult task for field engineers. Researchers in the past emphasized on the estimation of compaction parameters of sand-bentonite mixtures (Wang and Huang 1984, Sinha and Wang 2008). But no such studies were directed to assess the compaction parameters along with gradation and proportion of different sand particles i.e. fine, medium and coarse. Any study leading to perform in this direction will be time saving for project design engineers. This study is focused to estimate the maximum dry density of sand-bentonite mixtures using simple mathematical technique. The obtained results shows that the present investigation could be helpful in the selection of mix gradation of sand-bentonite mixtures, serving the maximum amount of MDD used for hydraulic conductivity, as well as the quantity of soil required for any earthwork project.

2 MATERIALS AND METHODOLOGY

The soils used for the investigation were bentonite and sand. Bentonite was collected from Jodhpur, Rajasthan state in India. Locally available Sone river sand was taken and graded into fine (0.075mm-0.425mm), medium (0.425mm-2.0mm) and coarse sand (2.0mm-4.75mm) to investigate the influence of different gradations of sand. The laboratory preparation of fine sand (FS), medium sand (MS) and coarse sand (CS) was performed as per ASTM D 6913-04 (2009) in which mechanical sieving is done and material retained on 0.075mm sieve was washed through demineralized water. The physical characterization of bentonite, FS, MS and CS is presented in Table 1. FS, MS and CS were mixed severally as well as collectively to bentonite. FS, MS and CS were varied from 10 to 50% of dry weight of soil in order to achieve all the combinations for fine-grained soil thus a total of 45 artificial mixes were obtained in the laboratory.

Table 1. Geotechnical characterization of bentonite.

Properties	Bentonite
Specific gravity (G_s)	2.76
Particle size distribution	
Clay (%)	72.0
Silt (%)	28.0
Sand (%)	0.0
Atterberg's limits	
Liquid limit (%)	264.10
Plastic limit (%)	27.62
Plasticity index (%)	236.48
Compaction parameters	
MDD (g/cc)	1.525
OMC (%)	25.85

The following tests were conducted on prepared mixes according to the standard procedures:

- Particle size distribution (ASTM D 6913-04 2009, ASTM D 7928 2016)
- Atterberg limits test (BS 1377-2 1990, ASTM D 4318-17e1 2017)
- Specific gravity test (ASTM D 854 2014)
- Modified Proctor compaction test (ASTM D 1557 2012)

The grain size distribution analysis was conducted through hydrometer analysis (refer Figure 1(a)), based on the principle of sedimentation of soil particles in the water, for bentonite whereas dry sieve analysis (refer Figure 1(b)) was performed on FS, MS and CS (sun dried

sand). Liquid and plastic limit tests were performed using fall cone penetrometer method and thread rolling method, respectively ((refer Figure 1(c-d)). Density bottle (50ml capacity) was used to calculate the specific gravity of bentonite, kerosene in lieu of water was used to avoid



(a)



(b)



(c)



(d)



(e)



(f)

Figure 1. Laboratory test methods for the grain size distribution analysis (a-b), atterberg limit test (c-d), specific gravity (e) and modified proctor compaction test (f).

the swelling and any chemical reactions (refer Figure 1(e)), whereas pycnometer bottle was used for FS, MS and CS. Proctor heavy compaction test (refer Figure 1(f)) was conducted on all artificially prepared mixes.

3 RESULTS AND DISCUSSION

Table 2 presents the results of maximum dry density (MDD) and optimum moisture content (OMC) for B-FS, B-MS and B-CS. It can be observed that there is an increase in MDD with increase in sand content (10 to 50%) as well as size of sand particles (FS, MS and CS) simultaneously OMC was found to decrease (see Figure 2).

Table 2. Compaction characteristics of bentonite mixed FS/MS/CS.

Mix proportions		MDD (g/cc)			OMC (%)		
Bentonite	FS/MS/CS	B-FS	B-MS	B-CS	B-FS	B-MS	B-CS
90	10	1.590	1.615	1.620	22.10	21.60	20.90
80	20	1.685	1.702	1.705	19.60	18.25	17.90
70	30	1.765	1.755	1.783	16.00	16.90	15.70
60	40	1.814	1.835	1.865	14.85	13.30	13.80
50	50	1.845	1.905	1.915	13.90	10.50	11.70

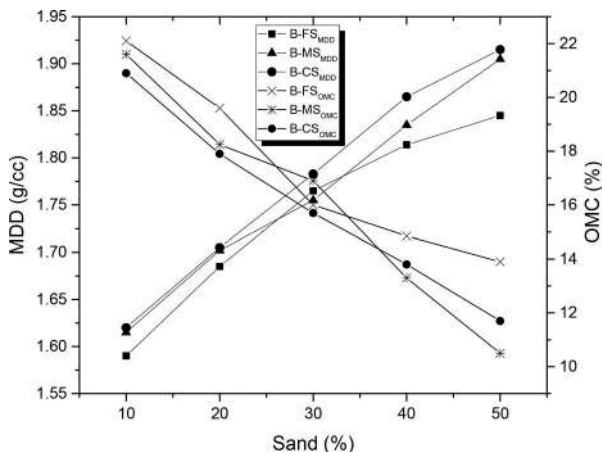


Figure 2. Behavior of compaction parameters under various percentages and gradations of sand.

Using simple mathematical calculation the percent variation in MDD and OMC were calculated at 10, 20, 30, 40 and 50% of fine, medium and coarse sand by means of compaction parameters of B-FS, B-MS, B-CS and parent soil (bentonite alone). For example, the MDD of pure bentonite is 1.525g/cc and for the mix of 90% Bentonite 10% FS is 1.590g/cc, the percent variation (increase or decrease) from parent to the addition of that 10% FS is 4.26%. Similarly, percent variations, later termed as contributed amount (%), for other percentages of fine, medium and coarse sand has also been calculated for both MDD and OMC.

The contributed amount for fine, medium and coarse sand under various percentages (10, 20, 30, 40 and 50) are presented in Figures 3 and 4 for MDD and OMC, respectively. It can clearly be seen from Figure 3 that MDD increases almost as linearly as the percentage of fine, medium and coarse sand increases and OMC decreases almost as linearly as the sand content increases (see Figure 4). The linearity obtained (in term of coefficient of determination, R^2) for MDD was of maximum order in B-MS followed by B-CS and B-FS as shown in Figure 3. While OMC was of maximum order for B-CS followed by B-MS and B-FS as presented in Figure 4. Moreover, the basic equations (1) to (6) were also developed for estimating the contributed amount at various percentage of fine, medium and coarse sand which could further be used for estimating the MDD and OMC of different graded sand-bentonite mixtures.

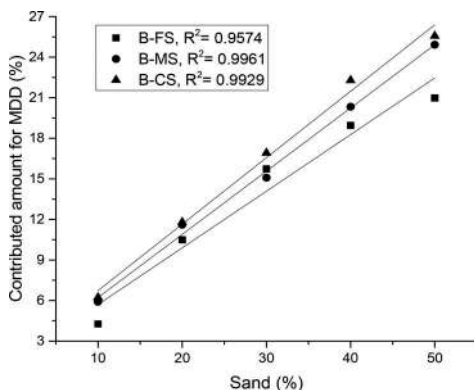


Figure 3. Contributed amount for MDD at various sand gradations.

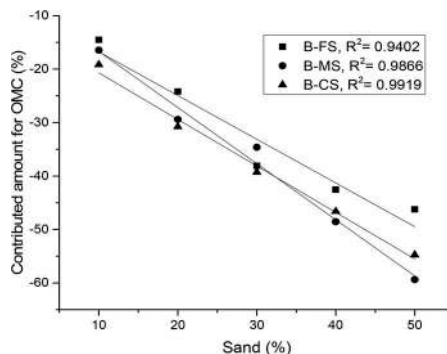


Figure 4. Contributed amount for OMC at various sand gradations.

$$\% \text{ variation due to FS} = 0.4190x + 1.5145 \quad (1)$$

For MDD $\% \text{ variation due to MS} = 0.4675y + 1.5145 \quad (2)$

$$\% \text{ variation due to CS} = 0.4918z + 1.81 \quad (3)$$

$$\% \text{ variation due to FS} = -0.8181x - 8.571 \quad (4)$$

For OMC $\% \text{ variation due to MS} = -0.0503y - 6.169 \quad (5)$

$$\% \text{ variation due to CS} = -0.8705z - 11.989 \quad (6)$$

Where, x , y and z are the percentage of fine, medium and coarse sand, respectively.

3.1 Comparison between actual and estimated values of MDD and OMC

The results obtained from compaction parameters of bentonite, B-FS, B-MS and B-CS showing a good correlation alongwith the sand content and contributed amount for both maximum dry density (see Figure 3) as well as optimum moisture content (see Figure 4) therefore, the number of equations were developed for calculating the contributed amount at various percentage of fine, medium and coarse sand for MDD and OMC. These equations were further processed for their validity and for that artificial mixes were prepared (in order to obtain fine-grained soil) at varying percentage of bentonite, FS, MS and CS, the obtained mix proportions are as shown in Table 3. The actual values of MDD and OMC for all mix combinations, a total of 30 (10 for each i.e. B-FS-MS, B-FS-CS and B-MS-CS), were calculated using laboratory modified compaction test and compared with the estimated values. The estimated values of MDD and OMC for mix combinations were calculated using their respective equations and compaction parameters of bentonite alone as illustrated by example shown below.

4 ILLUSTRATIVE EXAMPLE

Consider a mix combination of 50% (B) + 40% (FS) + 10% (CS) having the fine and coarse sand 40% and 10%, respectively and the laboratory MDD and OMC obtained was 1.886g/cc and 11.50%, respectively.

Solution:

The above mix combination containing the fine and coarse sand only, therefore, equation (1), (3) for MDD and equation (4), (6) for OMC were used and the estimated value of MDD and OMC for a given mix combination is calculated as follows

Estimation of maximum dry density

$$\begin{aligned}\% \text{ contribution for FS} &= 0.419x + 1.5145 \\ &= 0.419 * 40 + 1.5145 \\ &= 18.275\%\end{aligned}$$

$$\begin{aligned}\% \text{ contribution for CS} &= 0.4918x + 1.81 \\ &= 0.4918 * 10 + 1.81 \\ &= 6.728\%\end{aligned}$$

$$\text{Estimated MDD} = MDD_B + MDD_B \frac{(\% \text{ contribution for FS} + \% \text{ contribution for CS})}{100}$$

$$\begin{aligned}\text{Estimated MDD} &= 1.525 + 1.525 \frac{(18.275 + 6.728)}{100} \\ &= 1.906 \text{g/cc}\end{aligned}$$

$$\begin{aligned}\text{Percent variation in MDD} &= \left(\frac{1.906 - 1.886}{1.886} \right) * 100 \\ &= 1.06\%\end{aligned}$$

Estimation of optimum moisture content

$$\begin{aligned}\% \text{ contribution for FS} &= -0.8181x - 8.571 \\ &= -0.8181 * 40 - 8.571 \\ &= -41.295\%\end{aligned}$$

$$\begin{aligned}\% \text{ contribution for CS} &= -0.8705x - 11.989 \\ &= -0.8705 * 10 - 11.989 \\ &= -20.694\%\end{aligned}$$

$$\text{Estimated OMC} = OMC_B + OMC_B \frac{(\% \text{ contribution for FS} + \% \text{ contribution for CS})}{100}$$

$$\begin{aligned}\text{Estimated OMC} &= 25.85 + 25.85 \frac{(-41.295 - 20.694)}{100} \\ &= 9.83\%\end{aligned}$$

$$\begin{aligned}\text{Percent variation in OMC} &= \left(\frac{9.83 - 11.50}{11.50} \right) * 100 \\ &= -14.52\%\end{aligned}$$

Similarly, the MDD and OMC for other mix combination of B-FS-MS, B-FS-CS and B-MS-CS were also estimated as per above procedural method. Additionally, the actual values for MDD and OMC were also calculated using laboratory modified compaction test. The

comparative analysis among the actual and estimated values of MDD is presented in Figure 5- (a), (b) and (c) for B-FS-MS, B-FS-CS and B-MS-CS, respectively and OMC is shown in Figure 5(d), (e) and (f) for B-FS-MS, B-FS-CS and B-MS-CS, respectively. It is clearly seen from Figure 5(a), (b) and (c) that the stem of the estimated and actual values of MDD are almost closer to each other in all combinations. Unlike to MDD, numerous variation between the actual and estimated values were observed for OMC (see Figure 5(d), (e) and (f)) which can also be justified from Table 3 showing the percentage variation in estimated and actual value of MDD and OMC. All the percent variation for MDD are less than $\pm 3\%$ as well as the maximum numbers occur under the range of 0-1% while too much variations were reported for OMC somewhere even more then 25%. Earlier, it seems like that both MDD and OMC could be estimated using the compaction parameter of bentonite and sand content but eventually, the comparative analysis of actual and estimated values has vindicated that only MDD

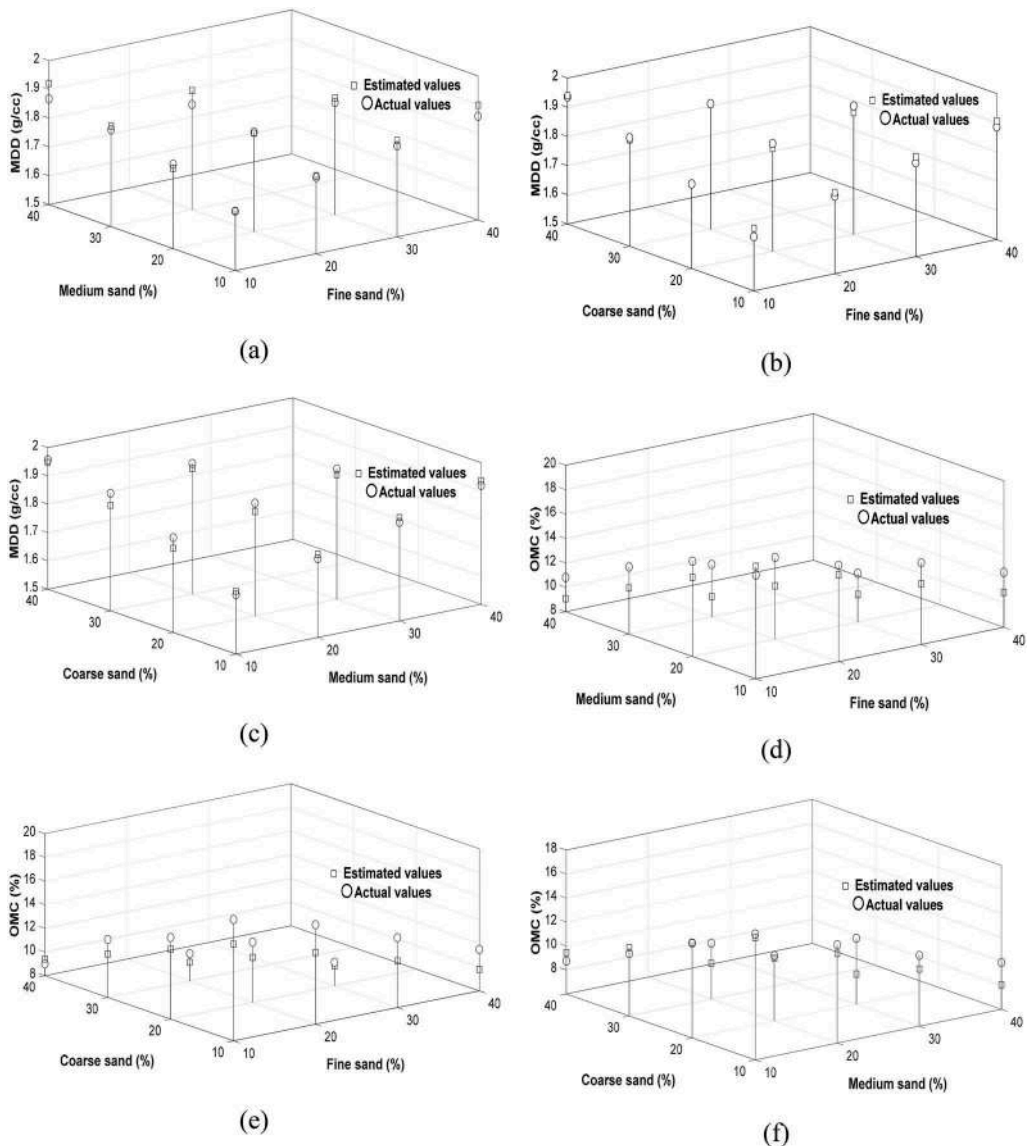


Figure 5. Actual versus predicted value for the MDD (a-c) and OMC (d-f) of various soil mixtures.

Table 3. Percent variation in compaction characteristics of B-FS-MS, B-FS-CS and B-MS-CS.

Mix proportions			% Variation in MDD			% Variation in OMC		
Bentonite	FS/MS	MS/CS	B-FS-MS	B-FS-CS	B-MS-CS	B-FS-MS	B-FS-CS	B-MS-CS
80	10	10	0.048	1.757	0.726	4.309	-11.388	-1.864
70	20	10	0.323	0.708	0.883	-5.054	-14.285	-5.101
70	10	20	-0.831	-0.022	-2.048	-8.265	-6.576	0.294
60	30	10	1.025	1.120	0.920	-11.688	-14.081	-9.568
60	20	20	-0.217	-0.882	-1.543	-15.785	-9.880	-1.973
60	10	30	0.730	-0.395	-2.224	-12.742	-9.525	4.392
50	40	10	2.070	1.076	0.849	-13.082	-14.560	-18.716
50	30	20	0.841	-1.165	-1.020	-14.458	-3.088	-26.002
50	20	30	2.590	-0.078	-0.933	-21.420	-7.216	-15.727
50	10	40	2.876	0.186	-0.490	-16.059	4.664	7.891

of sand-bentonite, for fine-grained soil, can be estimated within $\pm 3\%$ variation. Moreover, the comparative analysis of MDD also shows that the minimum number of percent variations was reported in case of B-FS-CS followed by B-MS-CS and B-FS-MS. Therefore, one can suggest that maximum dry density of sand-bentonite varies in predictable manner with the amount of different sand gradation (FS, MS and CS) and MDD of bentonite alone.

5 CONCLUSIONS

1. Maximum dry density of B-FS, B-MS and B-CS increases with increase in percentage of sand as well as size of sand particle (from FS to CS through MS) concurrently optimum moisture content reported to decreases.
2. Additionally, maximum dry density was found to increase as linearly as the percentage of fine, medium and coarse sand increases. Among the mix combinations of B-FS, B-MS and B-CS, the linearity was of maximum order for bentonite with medium sand ensued by coarse and fine sand.
3. On the contrary, optimum moisture content decreases almost as linearly as the percentage of fine, medium and coarse sand increases. Linearity for bentonite with coarse sand is of maximum order followed by medium and fine sand.
4. Actual and estimated values obtained for MDD and OMC shows that the percent variation in MDD is less than $\pm 3\%$ while for OMC reached up to 25%. Hence, it is concluded that only MDD can be estimated using this streamlined mathematical technique. Furthermore, this also indicates the important of validation for any estimating process.
5. By just knowing the MDD of bentonite alone and the percentage of fine, medium and coarse sand, the MDD for any combination of sand-bentonite mixer can be achieved. Which could be helpful in selecting the appropriate mix combination of sand-bentonite for liner purposes as well for calculating the quantity of soil required for any earthwork project.

REFERENCES

- ASTM D 854. 2014. "Standard test methods for specific gravity of soil solids by water pycnometer." *ASTM standards*.
- ASTM D 1557. 2012. "Standard test methods for laboratory compaction characteristics of soil using modified effort." *ASTM standards*.
- ASTM D 4318-17e1. 2017. "Standard test methods for Liquid Limit, Plastic Limit, and Plasticity Index of Soils." *American Society for Testing and Materials (ASTM), Philadelphia*.
- ASTM D 6913-04. 2009. "Standard Test Methods for Particle-Size Distribution (Gradation) of Soils Using Sieve Analysis." *ASTM standards*.

- ASTM D 7928. 2016. "Standard Test Method for Particle-Size Distribution (Gradation) of Fine-Grained Soils Using the Sedimentation (Hydrometer) Analysis." *ASTM standards*.
- Bodman, G, and G Constantin. 1965. "Influence of particle size distribution in soil compaction." *Hilgardia* 36 (15):567–591.
- BS 1377-2. 1990. "Methods of test for soils for civil engineering purposes-Part 2: Classification tests." London, UK: *British Standard Institution (BSI)*.
- Deb, Kousik, V Sawant, and A Kiran. 2010. "Effects of fines on compaction characteristics of poorly graded sands." *International Journal of Geotechnical Engineering* 4 (2):299–304.
- Günaydın, O. 2009. "Estimation of soil compaction parameters by using statistical analyses and artificial neural networks." *Environmental Geology* 57 (1):203.
- Johnson, Alfred Walton, and John R Sallberg. 1960. "Factors that influence field compaction of soils." *Highway Research Board Bulletin* (272).
- Johnson, Alfred Walton, and John R Sallberg. 1962. "Factors influencing compaction test results." *Highway Research Board Bulletin* (319).
- Pandian, NS, TS Nagaraj, and M Manoj. 1997. "Re-examination of compaction characteristics of fine-grained soils." *Geotechnique* 47 (2):363–366.
- Patra, C, N Sivakugan, and B Das. 2010. "Relative density and median grain-size correlation from laboratory compaction tests on granular soil." *International Journal of Geotechnical Engineering* 4 (1):55–62.
- Sinha, Sunil K, and Mian C Wang. 2008. "Artificial neural network prediction models for soil compaction and permeability." *Geotechnical and Geological Engineering* 26 (1):47–64.
- Verma, Gaurav, and Brind Kumar. 2019. "Prediction of compaction parameters for fine-grained and coarse-grained soils: a review." *International Journal of Geotechnical Engineering*:1–8. doi: 10.1080/19386362.2019.1595301.
- Wang, MC, and CC Huang. 1984. "Soil compaction and permeability prediction models." *Journal of Environmental Engineering* 110 (6):1063–1083.

Preparation of artificial aggregate to be used in the asphalt mixture

Gang Liu*, Mingwei Ding & Hongyuan Xing

State Key Laboratory of Silicate Materials for Architectures, Wuhan University of Technology, Wuhan, China

Haoliang Huang

School of Materials Science and Engineering, South China University of Technology

Guzal Anvarona Kasimova

Center for Advanced Technologies in Uzbekistan

Hao Chen

Department of Civil and Environmental Engineering, Norwegian University of Science and Technology, Trondheim, Norway

ABSTRACT: Phosphogypsum (PG) is a by-product of the fertilizer industry when producing phosphoric acid from phosphate rock. Massively consuming phosphogypsum (PG) has attracted worldwide attention. This study adopted PG to prepare the artificial aggregate by the disk granulation to be used in the asphalt mixture. Morphology, strength and internal structure of the aggregate were characterized. The result indicates artificial aggregate has higher sphericity but lower angularity and texture than natural aggregate. After the 7-day curing, the aggregate strength can reach 40.8 MPa. Later on, the strength grows slowly due to the formation of large number of pores. The water absorption ratio of the aggregate can be reduced less than 2% after treated by the silicone resin at a mass ratio of 2.68%. This study offers an economical alternative for massively consuming PG and saving natural resources.

Keywords: Phosphogypsum, artificial aggregate, strength, structure

1 INTRODUCTION

Phosphogypsum (PG) is a by-product of the fertilizer industry when producing phosphoric acid from phosphate rock. China is the largest PG producer globally, and its PG stockpile has reached 250 million tons, with an increasing rate of around 55 million tons per year. However, its annual comprehensive utilization rate is less than 20%. Stockpiled PG occupies considerable land resources and causes serious environmental problems (Cardenas-Escudero et al., 2011; Zielinski et al., 2011). Therefore, low-cost, large-scale processing technology is needed to consume such a large amount of PG.

More and more research has been performed to consume PG. At present, the utilization methods of PG include producing super-sulfated cement, cement retarder, pneumatic cementitious material, gypsum mortar, and so on (Tam et al., 2018).

Using PG as cement retarder is a significant method to consume it. Gypsum content in Portland cement is usually 3%-5%, meaning less than 50 kg of PG can be consumed for each

*Corresponding author
DOI: 10.1201/9781003222910-37

ton of Portland cement. However, PG's high water content and complex chemical composition require a complex pre-treatment, and it has a poor compatibility with other admixtures. (Nizevicene et al., 2018; Wang et al., 2019).

CaSO₄ in PG can be decomposed into CaO and SO₂ at high temperature: the former is used to produce cement, and the later used to produce sulfuric acid (Yu et al., 2016). By this way, the cement production with an annual output of 1.5 million tons can consume about 2.2 million tons of dry PG (Yang et al., 2016). However, high energy is needed, and it is difficult to ensure the high decomposition rate of PG in the production process, resulting in unstable cement quality.

Products of gypsum air-hardening materials includes gypsum block, wall plate, etc. The gypsum has to be treated by the high-temperature to become semi-aqueous gypsum. After mixing with water and some admixtures, the strength of the PG based cementitious materials can reach more than 10 MPa (Liu et al., 2015; Zheng, 2016). Different types of functional mortars, such as gypsum-based self-levelling mortars and thermal insulation mortars, are produced by mixing PG with other admixtures, (Li et al., 2018; Lu, 2014). However, the water resistance of these products is very low, and the consuming amount is limited.

The excess-sulfate gypsum slag cement (ESGSC) was firstly defined by Huang and Lin (Huang and Lin, 2010b). It consisted of 45-50% gypsum, 46-53% ground granulated blast-furnace slag (GGBFS), 2-4% clinker, with a 28-day compressive strength exceeding 40 MPa. In this cementitious system, excess PG as the core is surrounded by the ettringite and C-S-H which form a spatial network structure (Lin et al., 2015). This cement can harden in the water or in the air although a large amount of free gypsum remains after hydration. Furthermore, NaOH as an alkali activator significantly reduces the cement setting time and improves the cement early strength (Huang and Lin, 2010a). Therefore, it is theoretically feasible to prepare PG-based artificial aggregate, according to the cementing mechanism of ESGSC,

This study adopts PG to prepare the artificial aggregate by the disk granulation to be used in the asphalt mixture. Morphology, strength, internal structure and hydration products of the aggregate were characterized and compared with those of natural aggregates. This research aims to offer a new approach to massively consume PG.

2 MATERIALS AND METHODS

2.1 Materials

Three main raw materials were used to produce the artificial aggregate: phosphogypsum (PG), clinker and slag. Hubei Yangfeng Phosphate Co., Ltd provided PG. It usually contained 15-20 % water. The Portland cement clinker and ground granulated blast-furnace slag were supplied by Huaxin Cement Co., Ltd. Their SEM images are shown in Figure 1.

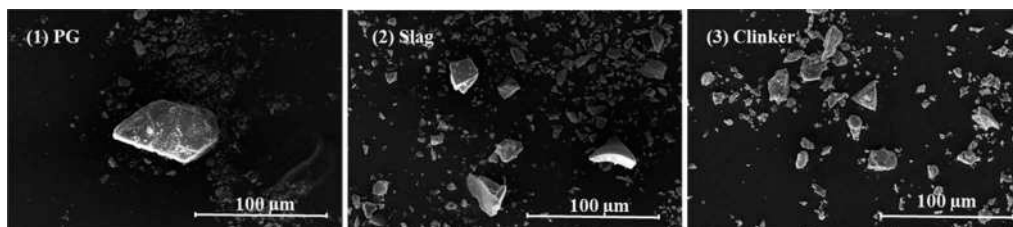


Figure 1. SEM images of PG, slag and clinker.

Figure 2 shows the thermogravimetric calorimetric curve of PG. The adsorbed water content is 0.89%, and the bound water content is 17.68%. The content of dihydrous gypsum in PG is 84.48%, calculated by Formula (1). The loss of water of crystallization starts at 109.6 °C and ends at 137.6 °C, with an endothermic peak at 131.7 °C. The PG sample is first dried in a 60 °C oven and then ground in a $\phi 500$ mm \times 600 mm laboratory ball mill for half an hour. Finally, the PG powder passed the sieve with a size of 1.18 mm.

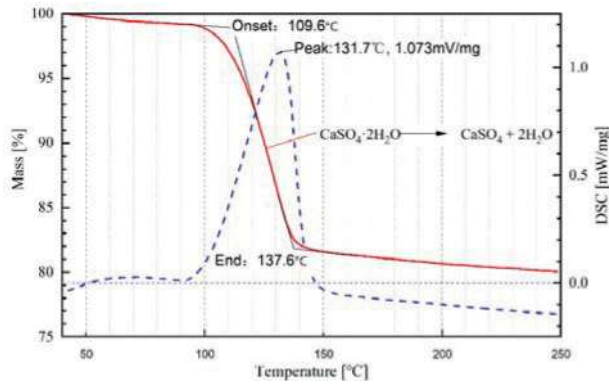


Figure 2. Thermogravimetric curve of PG.

$$G = \frac{M(\text{CaSO}_4 \cdot 2\text{H}_2\text{O})}{2 \cdot M(\text{H}_2\text{O})} \times H \quad (1)$$

where, G is the mass content of dihydrous gypsum in PG, $M(\text{CaSO}_4 \cdot 2\text{H}_2\text{O})$ is the molar mass of dihydrate gypsum, $M(\text{H}_2\text{O})$ is the molar mass of water molecule, and H is the mass content of water.

2.2 Preparation process of artificial aggregate

The artificial aggregate was prepared by the method of the disk granulation. Figure 3 is the disk granulator and its structure diagram. The disk-granulating method uses the adhesive force between wet powder particles to polymerize each other into balls to form aggregates. The rotating motion of the disk granulator makes the mixed powder particles produce centripetal force by spraying water to the powder. The surface of powder particles absorbs water to form a film, making the friction resistance between particles become larger and the fluidity of powder decreases. At the same time, the hydration reaction between powder particles produces a cementation force. Under these factors, the aggregate spheres gradually form.

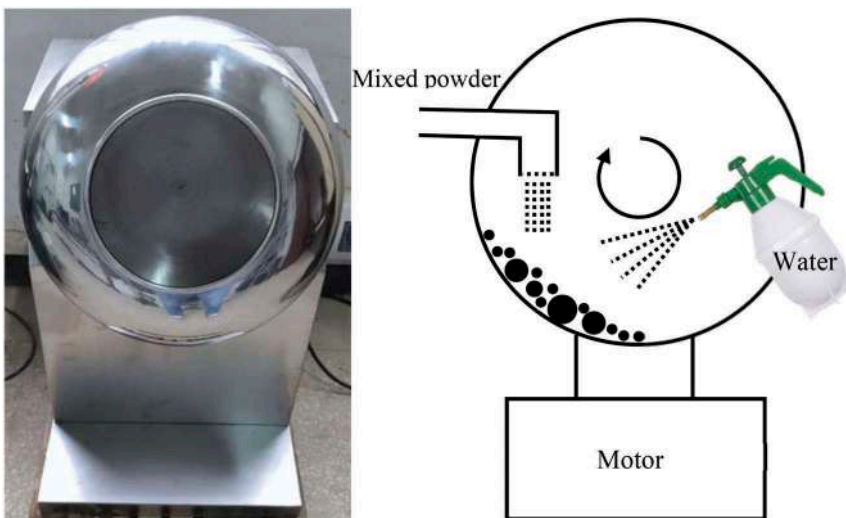


Figure 3. Disk granulator and its structure diagram.

The aggregate was immersed in water and cured at 60 °C after prepared by disk granulator. Figure 4 shows the image of the nature aggregate (limestone used in this study) and artificial aggregate with the size from 4.75 mm to 13.2 mm.



Figure 4. Images of natural aggregate and artificial aggregate with a size of 4.75-13.2 mm.

2.3 Methods

Aggregate strength was tested according to the standard JGJ 70-2009. The aggregate is cut into a cubic with a side length of 10mm by the cutting machine (SYJ150) produced in Shenyang Kejing Auto-instrument Co., LTD. The aggregate morphology analysis was characterized by the Aggregate Image Measurement System (AIMS) from Pine Test Equipment, Inc. The aggregate's angularity, texture, and sphericity were evaluated.

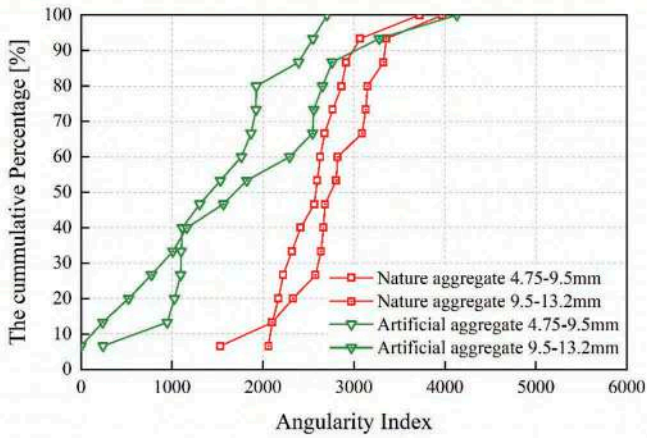
The X-Ray Computed Tomography (CT) (Xradia 510 Versa, Zeiss Gruppe) was used to characterize the internal structure with a resolution of 6 μm for the aggregate with a particle size of 4.75 mm, at different curing ages of 0 day, 3 days, 7 days and 28 days.

A scanning electron microscope (SEM/JSM-IT300) was used to characterize aggregate morphology. The comprehensive thermal analyzer (TG-DSC/STA449F3) was used to characterize the thermal stability of PG. The increase rate of temperature was 10 °C/min from 25°C to 250 °C in the atmosphere circumstance.

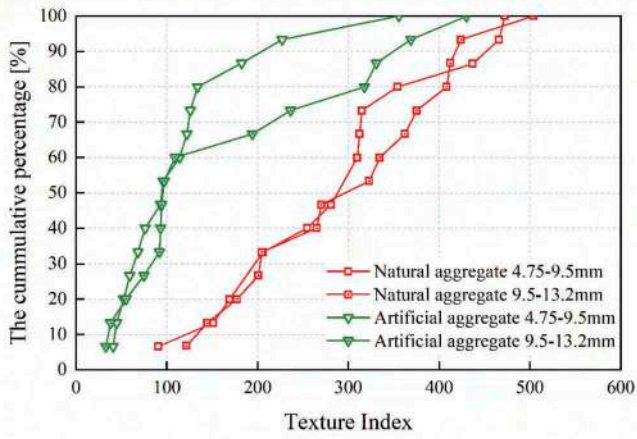
3 RESULTS AND DISCUSSION

3.1 Morphology

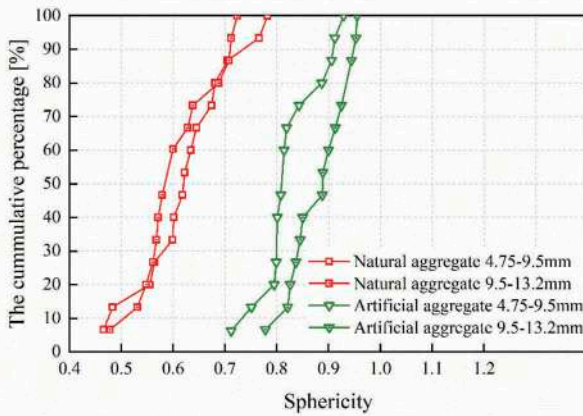
One hundred particles for natural aggregate and artificial aggregate were randomly selected and analyzed using the AIMS equipment. The morphological characteristics include angularity, texture and sphericity. Angularity index and texture index reflect the sharpness and roughness of aggregate particles, respectively. Meanwhile, sphericity reflects the approximate degree of the aggregate and standard sphere (Rezaei et al., 2011). Figure 5 shows the morphological characteristics of natural aggregate and artificial aggregate. Artificial aggregate has a lower angularity index and texture index than natural aggregate. The sphericity of artificial aggregate is higher than natural aggregate. As the particle size increases, the artificial aggregate becomes more rounded.



(a)



(b)



(c)

Figure 5. (a) Angularity (b) texture (c) sphericity of natural aggregate and artificial aggregate.

3.2 Aggregate strength

Figure 6 shows the compressive strength of aggregates at different curing periods. The aggregate strength increases as the extension of curing time. From 0 day to 7 days, aggregate strength increases by 18.3MPa. However, aggregate strength increased by only 4.2MPa from 7 days to 28 days. Figure 7 shows the SEM image of artificial aggregate at curing ages of 7days and 28days. At the beginning of curing, the dissolution of PG in the aggregate resulted in a significant increase in the concentration of Ca^{2+} and SO_4^{2-} in the liquid phase. The clinker hydrates and raises the pH of the liquid phase, causing slag particles to be activated. The slag particles reacts with Ca^{2+} and SO_4^{2-} in the liquid phase. The surface of PG particles is coated by the hydration products C-S-H gel and ettringite (Aft), which improves the aggregate strength. Figure 8 shows the BSE-SEM images of artificial aggregate at 7 days, 28 days and 300 days. The aggregate was relatively dense at 7 days with few pores. At 28 days of age, some cracks are observed along the edges of PG particles. More cracks appear along the edges of PG particles in the 300-day cured aggregate, while not along the edges of slag particles. The reason could be that excess PG got dissolved when curing in the water. Therefore, the 7-day curing period is recommended.

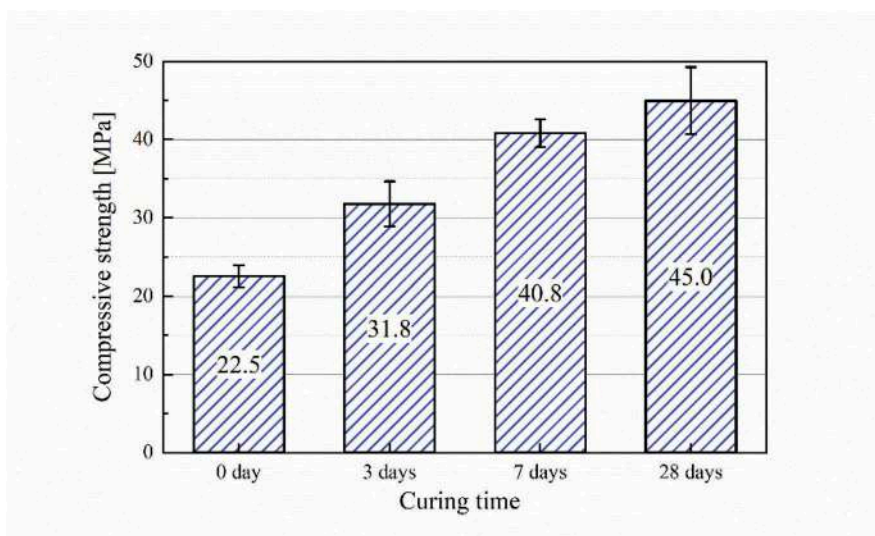


Figure 6. Compressive strength of aggregate at the curing time of 0, 3, 7 and 28 days.

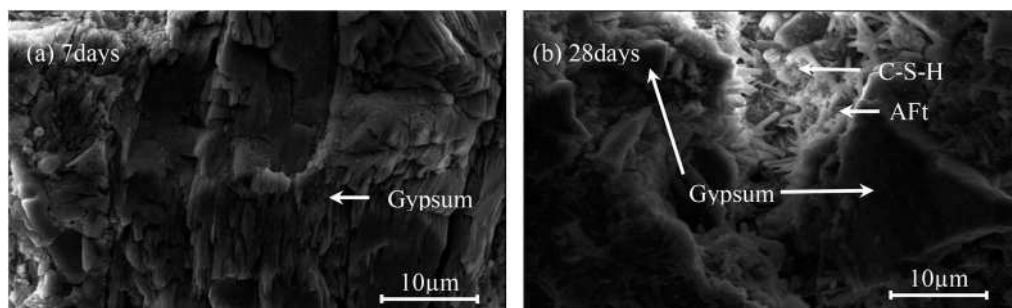


Figure 7. SEM images of artificial aggregate at the curing time of 7 and 28 days.

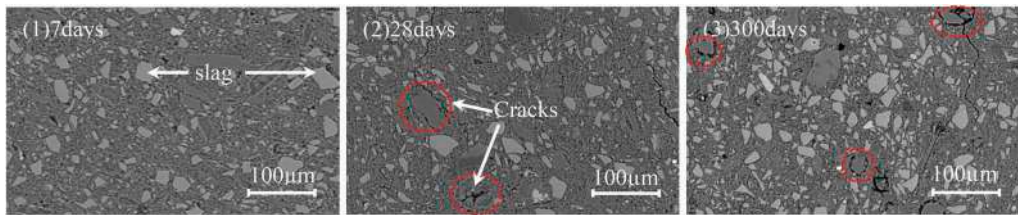


Figure 8. BSE-SEM images of artificial aggregate at the curing time of 7days, 28days and 300days.

One aggregate with a size of 4.5mm is observed by the CT scanning, and its 3D reconstruction image is shown in Figure 9. Its internal structure on the same cross section at 0 day, 3days, 7days and 28 days curing periods is shown in Figure 10. In the CT scanning image, more white the colour, more dense the material. The black part in the image means the pores. As shown in Figure 10, the pores gradually increase in the aggregate as the hydration time extends from 0 to 28 days.

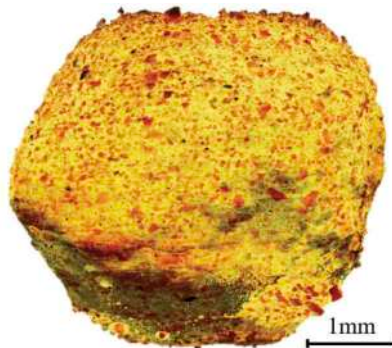


Figure 9. 3D reconstruction image of aggregate.

Pore analysis data are obtained from the 3D reconstruction images of CT scanning. Figure 11 shows the relation between pore number and pore size in the aggregate at different hydration periods, with an accuracy of 5 µm. The pore size is nearly normal distributed at a micrometre level, with a maximum value of 80 µm. The pore numbers from 0 day to 7 days are very close under the dual effect of the hydration densification and the PG dissolution. After the 28-day curing, the pore number increased by about 3 times due to the continuous solubility of PG and the decrease of hydration rate.

3.3 Surface treatment of aggregate

Figure 12 shows the BSE-SEM images of the edge and the internal part of artificial aggregate. PG particles can be easily identified due to their strip shape with a dark grey. Slag or clink particles has a light grey colour. PG strips are distributed parallelly to the surface at the edge of the aggregate (see Figure 12a). However, they are distributed randomly in the internal part of the aggregate (see Figure 12b). During the granulation process, the centripetal force of aggregates increase as the increase of aggregate mass, and the PG particles begin to adhere to the surface of the aggregate in a specific orientation.

Figure 12(a) shows that there is a transition zone with a thickness of about 60 microns on the surface of the aggregate, with a loose structure. It increases the possibility of a high water absorption of the aggregate and the stripping of fine particles during the mixing of aggregate when it is used the asphalt mixture or the base-layer material.

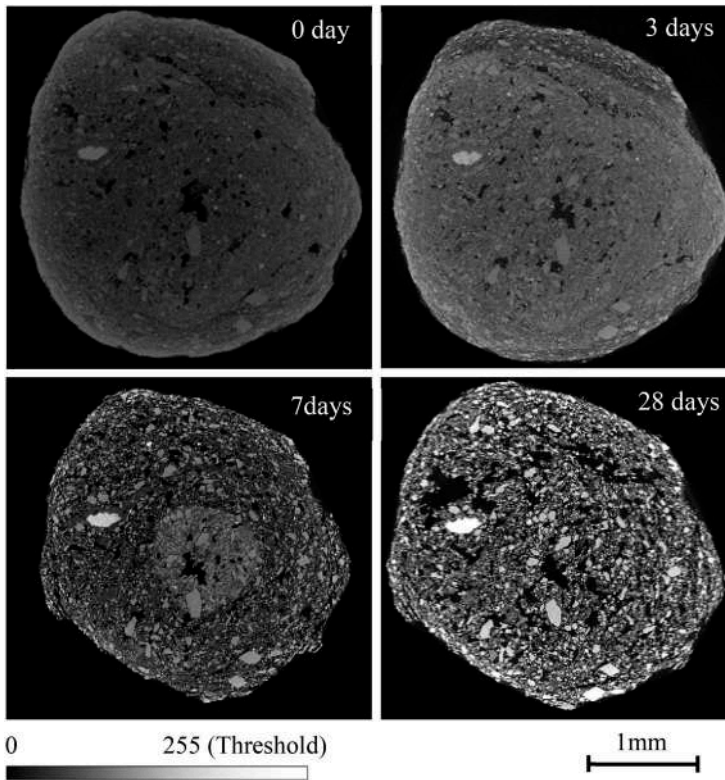


Figure 10. CT scanning image on the same cross section at 0, 3, 7 and 28 days curing periods.

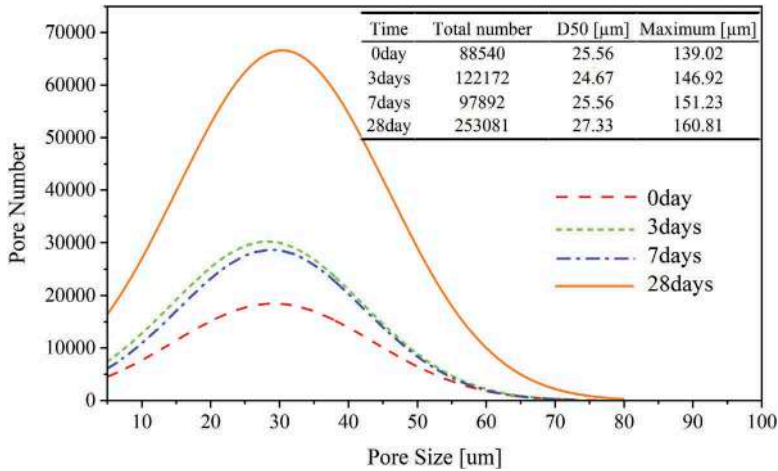


Figure 11. Relationship between pore size and pore number in the aggregate at different hydration periods.

In this study, silicone resin is used to treat the aggregates for the purpose of densification. The silicone resin is sprayed on the surface, and then kept in the oven at 60 °C for 24 h for the solidification. Figure 13 shows the relationship between the resin amount and the water

absorption rate of aggregate. The water absorption of the aggregate can be reduced to less than 2% after resin spraying at a 2.68% mass ratio, which meets the requirements of the China standard JTG F40-2004.

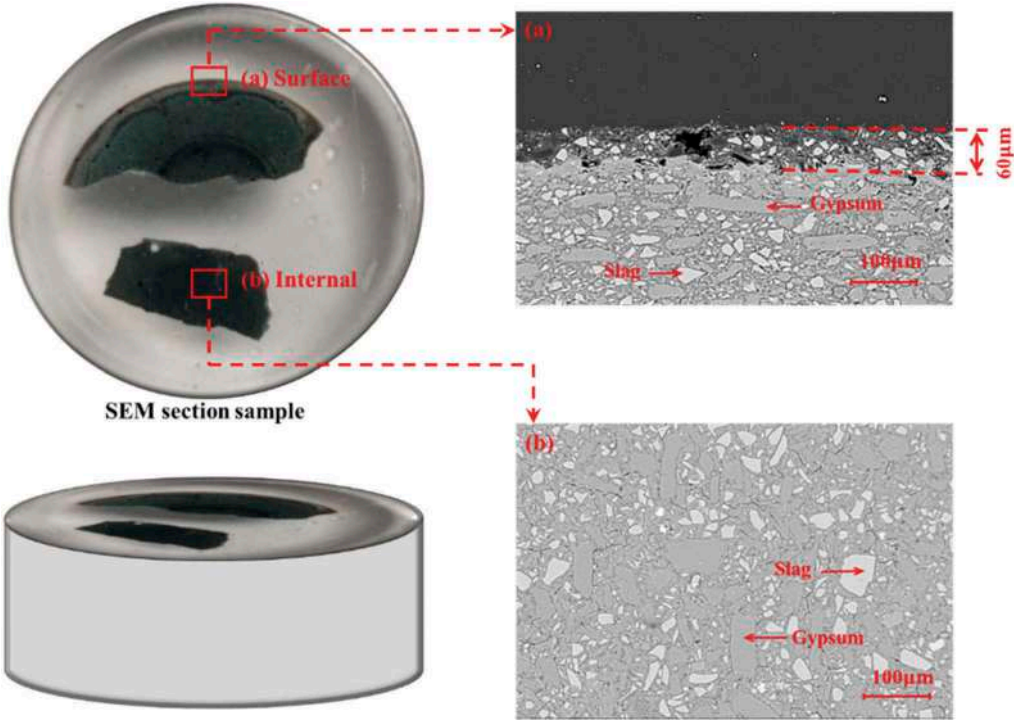


Figure 12. BSE-SEM images of (a) the edge of artificial aggregate, (b) the internal part of artificial aggregate.

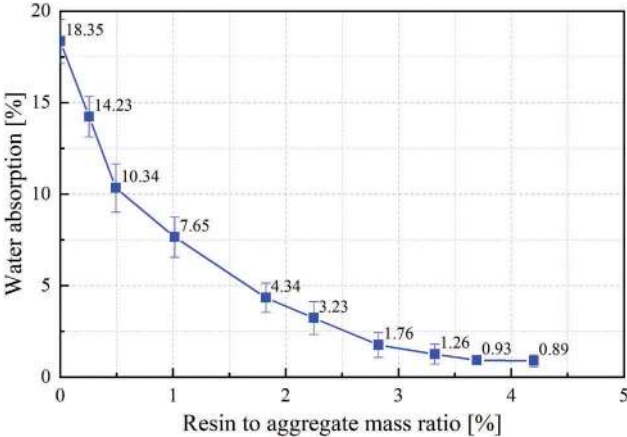


Figure 13. Resin spray mass versus water absorption.

4 CONCLUSIONS

This study used the PG to prepare the artificial aggregate. The characteristics of artificial aggregates were investigated. Based on the results, the following conclusions can be drawn:

1. Artificial aggregate prepared by disk granulation has higher sphericity but lower angularity and texture than natural aggregate.
2. After 7-day curing, the aggregate strength can reach 40.8 MPa. Later on, the strength grows slowly due to the formation of large number of pores.
3. The water absorption ratio of the aggregate can be reduced less than 2% after treated by the silicone resin at a mass ratio of 2.68%.

Its influence on the properties of asphalt mixture will be studied in the future. This technology could be an economical alternative for massively consuming PG and saving natural resources.

ACKNOWLEDGEMENTS

The research was supported by the Key R&D Program of Hubei Province (No. 20211G0098), the Nature Fund of Hainan Province Joint Fund (No: 520LH016), the National Natural Science Foundation of China, Grant No: 52068061, and the Science and Technology Project of the Tibet Autonomous Region Transportation Department (Project Number. XZJTKJ [2018]02).

REFERENCES

- Cardenas-Escudero, C., Morales-Florez, V., Perez-Lopez, R., Santos, A., Esquivias, L., 2011. Procedure to use phosphogypsum industrial waste for mineral CO₂ sequestration. *Journal of Hazardous Materials*. 196, 431–435.
- Huang, Y., Lin, Z.S., 2010a. Effect of Sodium Hydroxide on the Properties of Phosphogypsum based Cement. *Journal of Wuhan University of Technology-Materials Science Edition*. 25, 342–345.
- Huang, Y., Lin, Z.S., 2010b. Investigation on phosphogypsum-steel slag-granulated blast-furnace slag-limestone cement. *Construction and Building Materials*. 24, 1296–1301.
- Li, Y., Dai, S., Zhang, Y., Huang, J., Su, Y., Ma, B., 2018. Preparation and thermal insulation performance of cast-in-situ phosphogypsum wall. *Journal of Applied Biomaterials & Functional Materials*. 16, 81–92.
- Lin, Z., Huang, Y., Shui, Z., Liu, C., Jin, F., 2015. *Excess-Sulfate Phosphogypsum Slag Cement and Concrete*. Wuhan University of Technology Press, Wu Han.
- Liu, L., Zhang, Y., Tan, K., 2015. Cementitious binder of phosphogypsum and other materials. *Advances in Cement Research*. 27, 567–570.
- Lu, S., 2014. *Research and application of phosphogypsum - based self-leveling materials*. Wuhan University of Technology.
- Nizevicene, D., Vaiciukyniene, D., Michalik, B., Bonczyk, M., Vaitkevicius, V., Jusas, V., 2018. The treatment of phosphogypsum with zeolite to use it in binding material. *Construction and Building Materials*. 180, 134–142.
- Rezaei, A., Hoyt, D., Martin, A.E., 2011. Simple Laboratory Method for Measuring Pavement Macrotexture: Pavement Cores and Aggregate Image Measurement System. *Transportation Research Record*. 2227, 146–152.
- Tam, V.W.Y., Soomro, M., Jorge Evangelista, A.C., 2018. A review of recycled aggregate in concrete applications (2000-2017). *Construction and Building Materials*. 172, 272–292.
- Wang, J., Dong, F., Wang, Z., Yang, F., Tao, Y., Fu, K., Wang, Z., 2019. Study on new purification technology of phosphogypsum by flotation. *Non-metallic mines*. 42, 1–5.
- Yang, Z., Chen, Q., Guo, Q., Dang, Y., Li, X., Qian, J., 2016. Application status and prospect of phosphogypsum in cement production. *Bulletin of the Chinese Ceramic Society*. 35, 2860–2865.
- Yu, D., Zhou, J., Shu, Z., Wang, Y., 2016. High-Strength, Cement-Free Concrete of Flue Gas Desulfurization Gypsum-Based Non-Fired Brick. *ACI Materials Journal*. 113, 745–752.
- Zheng, S., 2016. *Study on preparation of light wall material by phosphogypsum α hemihydrate gypsum*. Kunming University of Science and Technology.
- Zielinski, R.A., Al-Hwaiti, M.S., Budahn, J.R., Ranville, J.F., 2011. Radionuclides, trace elements, and radium residence in phosphogypsum of Jordan. *Environmental geochemistry and health*. 33, 149–165.

Aspects concerning the structural evaluation of non-conventional pavements

V. Papavasiliou & A. Loizos

Laboratory of Pavement Engineering, National Technical University of Athens (NTUA), Athens, Greece

ABSTRACT: This paper includes aspects concerning the structural evaluation of heavy-duty asphalt pavements that have been constructed with non-conventional materials. The test pavement included an existing pavement, a cold in-place recycled (CIR) layer and an asphalt concrete (AC) overlay layer, considered in the whole as a non-conventional pavement. Although the use of CIR technology on locally available materials produces a new pavement base with minimized environmental impact, these non-conventional materials, also present great challenges, as far as the in-situ material behavior is concerned, as for example potential reduction of the modulus over time, which affects the bearing capacity of the entire pavement. The research is focusing on the influence of the traffic loading and the environmental impact on the structural condition of the AC layers in terms of the material stiffness, by performing non-destructive tests (NDTs) and related advanced analysis tools (back-analysis). Considering the limitations of the back-analysis procedure, the stiffness of the aged AC material was estimated from laboratory testing. Moreover, by conducting laboratory tests on AC cores at different temperatures, the influence of the temperature on the modulus of the aged AC material and consequently the accuracy of the correction algorithms of the back-analyzed moduli at the reference temperature was evaluated.

Keywords: Non-conventional pavement, cold in-place recycling (CIR), non-destructive tests (NDTs), laboratory tests

1 INTRODUCTION

This research study includes aspects concerning the structural evaluation of heavy-duty asphalt pavements that have been constructed with non-conventional materials. In particular a highway trial section was considered for the purpose of the analysis. This included an existing pavement, a cold in-place recycled (CIR) layer utilizing foamed asphalt (FA) as a stabilization treatment for base works and asphalt concrete (AC) overlay layers. The pavement was initially semi-rigid, i.e. constructed with cement bound material (CBM), overlaid with thin AC layers.

Considering the above-mentioned rehabilitation procedure with an approximately 25 cm thick FA layer based on the remaining CBM layer, the recycled pavement can be characterized as “non-conventional”.

It is well known that the use of CIR technology on locally-available materials produce a new pavement base with minimized environmental impact and therefore can deliver great economic and sustainability benefits. These non-conventional materials however, also present great challenges, as far as the in-situ material behavior is concerned, as for example potential

reduction of the modulus over time. This behavior affects the bearing capacity of the entire pavement (Thom & Dawson, 2019).

In order to assess the performance of heavily trafficked pavements, a common international practice is to conduct non-destructive tests (NDTs). Non-destructive testing uses deflection basin data generated from a loading device to quantify the response of a pavement structure to known load drops. The Falling Weight Deflectometer (FWD) is the most common system for measuring nondestructive surface deflections. Generally, surface deflections obtained from FWD testing are used to back-calculate in situ material properties (Kim & Park 2002). For the measured deflections, a back-analysis is applied in order to assess the modulus values of the pavement materials. The back-calculated moduli are considered representative of the pavement response to load and can be used to calculate stresses and strains in the pavement structure.

The present research investigates the ability of non-destructive testing (NDT) to provide accurate information about the influence of the traffic loading and the environmental impact on the structural condition of the AC layers of non-conventional pavements, in terms of the material stiffness. In order to achieve this goal, in-situ NDTs including FWD measurements were carried out at different chronological periods, up to 16 years after the rehabilitated pavement was given to traffic. Based on measured deflections, back-analysis was performed in order to assess the modulus values of the individual pavement layers.

However, the back-analysis procedure has several limitations, considering the accuracy of the back-calculated moduli in cases of non-conventional pavements, due to the existence of layers with different compositions and similar moduli (Irwin, 1994). In order to face this problem and to support/verify the back-analysis results, sample cores were extracted and tested in the laboratory in terms of the estimation of Indirect Tensile Asphalt Stiffness Modulus (ITSM) of the asphalt mixes. Moreover, by conducting ITSM laboratory tests on AC cores at different temperatures, the influence of the temperature on the modulus of the aged AC material and consequently the accuracy of the transformation functions of the back-analyzed moduli at the reference temperature was evaluated.

The present investigation demonstrates and discusses the in-situ mechanism of such non-conventional materials in terms of the performance of heavy-duty pavements, focusing on the AC material stiffness estimation over time.

2 TEST SECTION AND MATERIAL PROPERTIES

The initially constructed semi-rigid pavement, comprised of two layers of cement bound material (CBM), overlaid with an 8 cm AC layer (Figure 1a). CIR utilizing foamed asphalt as a stabilization agent was used for the rehabilitation of the severely cracked test section of the pavement.

An analytical rehabilitation design approach was used based on national and international experience to estimate the pavement structural capacity. According to the analytical design with a structural capacity requirement in excess of 10 million 13-ton axle-loads, the pavement structure is described by an AC overlay (9 cm thick) and a cold in-place recycled and stabilized with foamed asphalt (FA) 25 cm thick layer (Figure 1b).

A foamed asphalt mix design was undertaken to establish the application rates for foamed asphalt and active filler (cement), to achieve optimal strengths and to determine the strength characteristics for use in the structural design exercise, on several different blends of material recovered from the test pits. These blends were treated with foamed bitumen using the appropriate laboratory unit and several briquettes were manufactured for testing purposes to determine the indirect tensile strength (ITS), the unconfined compressive strength (UCS), the cohesion (c) and the angle of internal friction (Φ), as well as the determination of the indirect tensile stiffness modulus (ITSM). Details of the mix design blends can be found in (Loizos et al., 2004).

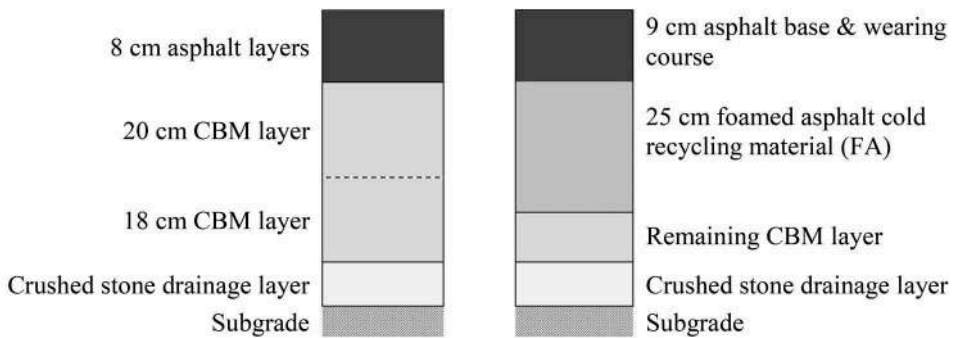


Fig. 1a: Semi-rigid pavement before rehabilitation

Fig. 1b: CIR pavement structure

Figure 1. Pavement cross-section before and after rehabilitation.

According to the mix design, 3% foamed asphalt (from 80/100 Pen grade bitumen) and 1% ordinary Portland cement was used for the composition of the FA mix. The decision to introduce 1% cement was based on the improvement in the achieved soaked strengths. Since milling machines produce few fines, it was decided to introduce 30% (by volume) natural fine sandy material to blend with the recovered material. It is noted, that the remaining layer after the CIR implementation where the FA layer is based, defined as “soil support” of the recycled layer, was initially consisting of cement bound material (CBM).

3 DATA COLLECTION AND ANALYSIS

A comprehensive FWD survey was undertaken initially up to 7 years and approximately 16 years after the pavement was placed in service. The test section was about 350 m long.

During construction, FWD measurements were conducted on the surface of the recycled layer (FA), on the AC base course and finally on the wearing course 3 weeks after the rehabilitation work. The post-construction monitoring was comprised of measurements on the wearing course approximately 6 months and 1-7 years after construction, i.e. after completion of the curing of the recycled material. FWD survey was undertaken once per year, in spring. After that, no other measurements were conducted, until the last one, i.e. approximately 16 years after construction. Before rehabilitation/reconstruction, the semi-rigid pavement was either severely damaged locally or in relatively good condition (stiff), due to the presence of the CBM layers below the AC overlay. For this reason, it was meaningless to conduct FWD measurements.

The peaks of the vertical deflections were measured at the center of the loading plate and at several radial positions (200, 300, 450, 600, 900, 1200, 1500 and 1800 mm) by a series of 9 deflection sensors. The standard load of 50 kN (pressure 700 kPa) was used for FWD measurements. The last of the three drops at each test location was utilized for further analysis.

Measurements were conducted at 10 specific points on both the outer wheel path (OWP), where the pavement was distressed by traffic loading (trafficked path), as well as the respective in between wheel path (IWP), where the pavement was essentially unloaded.

Cores from the new constructed layers were extracted at five specific test points along the test section. The extracted cores were used to estimate the different layer (AC and FA) thicknesses for the analysis. The remaining CBM layer (beneath the recycled layer) thickness was estimated through GPR geophysical analysis (Geophysical Survey Systems Inc., 2002). The testing system used is appropriate for the evaluation of the upper layers of the pavement structure since it produces reliable information up to an approximately 0.7 m penetration depth. The system follows the principles of ASTM and is supported by the appropriate software (Roadscanners, 2001).

Back-analysis was performed using the latest metric version of the MODCOMP software (Irwin, 1994), at the 5 test points (tp) where detailed thickness information (from AC and FA cores) was available. The back-calculated modulus of the asphalt overlay (AC layers) is referred to as $E(AC)$ and the modulus of the FA recycled layer as $E(FA)$. Including the subgrade below the CBM layer, the back-analysis model consisted of four layers (Figure 2), i.e. the AC layers, the FA layer (based on core thickness values), the remaining CBM layer (estimated using GPR analysis) and the subgrade.

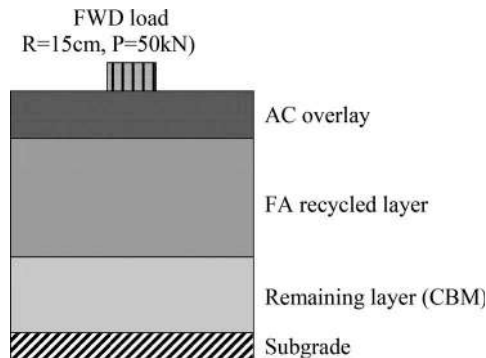


Figure 2. Pavement modeling (cross-section).

As detected from extracted cores the AC overlay, was in most cases more than 90 mm and ranged from 90 to 121 mm. According to reference Irwin (1994), the above measured thicknesses are thick enough for reliable back-analysis results. FA layers thicknesses used for back-analysis ranged from 235 to 270 mm. The layer thicknesses used for the analysis are presented graphically in Figure 3.

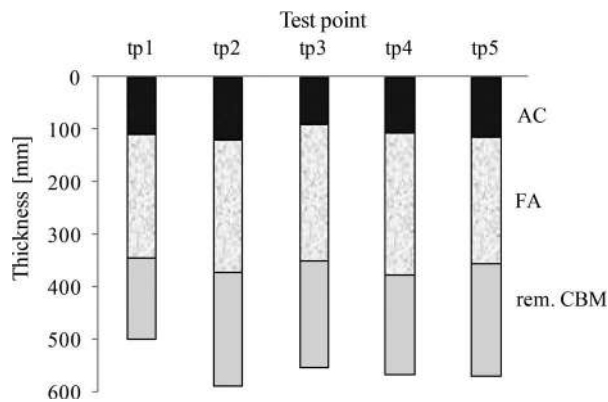


Figure 3. Layer thicknesses.

The 5 sample cores on each wheel path (OWP and IWP) were tested in the laboratory and the Indirect Tensile Stiffness Modulus (ITSM) of the AC mixes was estimated at four different temperatures, i.e. 10, 20, 32 and 40°C. Each core was cut in two specimens according to each individual asphalt layer, i.e. wearing course (wear.c.) and base course (base.c.). The ITSM values of the two specimens of each core were used for the estimation of one composite modulus (SHRP, 1993), representative for the laboratory estimated modulus of the AC overlay.

4 DATA ANALYSIS RESULTS AND DISCUSSION

4.1 *Deflection indicators*

The overall pavement condition of the recycled pavement was determined using internationally accepted indicators (COST-336, 1998), which are relevant to the measured elastic deflections. For this purpose, the center (maximum) deflection (D1) was considered, which represents the overall pavement performance at the time of the investigation (Hakim et al., 2002). The surface curvature index (SCI) based on the deflection deference was also calculated, for the evaluation of structural condition of the new constructed layers (FA and AC). The in-situ collected data were normalized to the reference temperature of 20°C (Van Gurp, 1995).

The temperature in the body of the AC overlay was 21°C during the measurements on the OWP and 25°C during the measurements on the IWP. During the measurements approximately 16 years after the pavement was given to traffic, the average D1 was 40.4 microns (standard deviation 10.3) on the OWP and 41.2 microns (standard deviation 13.1) on the IWP. The average value of the SCI was 10.9 microns (standard deviation 6.4) on the OWP and 10.4 microns (standard deviation 4.3) on the IWP.

These very low D1 and SCI values, with no significant differences between loaded (OWP) and unloaded (IWP) part of the pavement are indicative of a stiff pavement structure with no impact of the heavy traffic loading.

Another important remark is the fact that on the OWP the average D1 value during the measurements 16 years after construction (40.4 microns) was approximately 20% reduced in comparison with the average D1 value of the annually conducted measurements 1 to 7 years after construction (average 50.7 microns, ranging from 47 to 56.3 microns, standard deviation 5.6 - 10). The average SCI value (OWP) during the measurements 16 years after construction (10.9 microns) was approximately 26% reduced in comparison with the average SCI value of the measurements during 1 to 7 years after construction (average 14.7 microns, ranging from 12.2 to 18.6 microns, standard deviation 1.6 - 3). The above remarks indicate a hardening/altering of the upper pavement layers, probably due to environmental impact. Considering that the center deflection (D1) represents the overall pavement performance and the SCI the structural condition of the new constructed layers (FA and AC), it is clear that these indicators cannot provide information about the reason of the upper layers stiffening. In order to find out whether this is due to the ageing of the AC layers or due to other reasons and to assess how the individual FA and AC layers behave over time, in terms of potential moduli changes, back-analysis of the FWD deflections was conducted.

4.2 *Back-analysis results*

In order to get more information about the condition of the upper pavement layers, a back-analysis of the collected data was conducted. The back-calculated asphalt layer moduli were corrected to 20°C according to (Baltzer & Jansen, 1994).

Due to the fact that on one test point on the OWP the back-calculated E(AC) was extremely high, the aforementioned cross-section was excluded from the analysis. Nevertheless, the average back-calculated AC moduli were very high. The average AC modulus value was 21% to 196% on the OWP and 49% to 249% on the IWP higher than the related average AC moduli 1-7 years after construction. On the other hand, the average FA modulus values did not show significant differences, in comparison with the average FA moduli 1-7 years after construction.

The average back-calculated AC and FA moduli resulted from the FWD survey approximately 16 years after construction and the related moduli values 1 to 7 years after construction (for comparison reasons) are presented graphically in Figure 4.

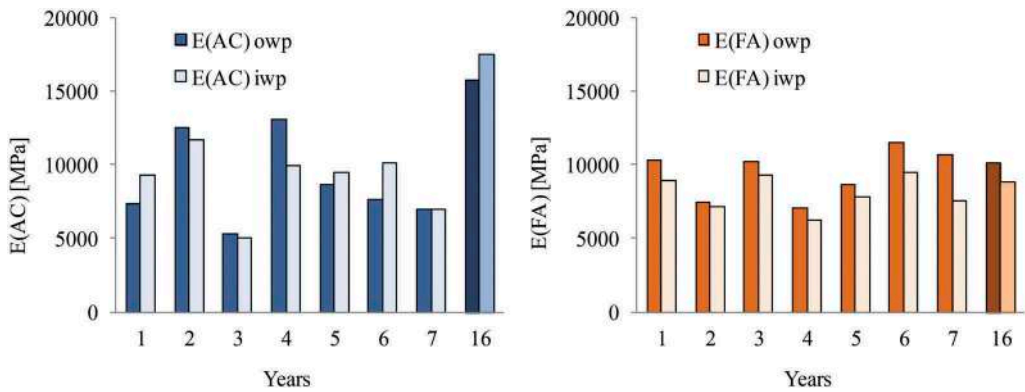


Figure 4. Average back-calculated AC and FA moduli (20°C).

From the above back-analysis results, the following conclusions can be drawn.

The heavy traffic loading did not cause any structural damage on the 16 years in service pavement. The latest confirms estimates based on previous research (Papavasiliou & Loizos, 2017).

The structural condition of FA layer seems to be stable during the 16 years of traffic loading. Moreover, the moduli on the trafficked path (OWP) are higher than the related on the in between wheel path (IWP), where the pavement was essentially unloaded. This can be due to the post-compaction from traffic during the early life of the CIR pavement.

The AC overlay found very stiff and this can be attributed to the effect of the climatic conditions, i.e. ageing of the AC material. Compaction of the AC layers from traffic may be excluded, due to the absence of rutting on the wheel paths. However, due to the very high back-calculated moduli values, there is an evidence that back-analysis may lead to overestimated AC overlay moduli. This may be due to the existence of layers with different compositions and similar moduli (Irwin, 1994), i.e. the AC and FA layers, based on a relative stiff CBM layer. In order to overcome the aforementioned limitation of the back-analysis procedure, as far as the accuracy of the back-calculated moduli is concerned and to verify the ageing effect of the AC layer, laboratory ITSM tests on AC cores were conducted.

4.3 Laboratory test results

The ITSM average values at 20°C of the wearing course (wear.c.) and base course (base.c.) on cores extracted from the OWP and IWP approximately 16 years after construction and the related moduli values 2 and 3 years after construction (for comparison reasons) are presented in Figure 5.

According to the ITSM test results, the average AC stiffness moduli approximately 16 years after construction were about 50% higher, in comparison with the related ITSM values 2 and 3 years after construction.

The average composite (i.e. the combined wearing and base course) ITSM values, in comparison with the related average back-calculated moduli approximately 16 years after construction and the related moduli values 2 and 3 years after construction (for comparison reasons) are presented in Figure 6.

On average, the ratio of the FWD based stiffness ($E_{FWD}=E_{field}$) to the related value through laboratory tests (E_{lab}) approximately 16 years after construction was: aver. $E_{field}/E_{lab}=2.3$. The related average E_{field}/E_{lab} values during the survey 2 and 3 years after construction were generally lower, i.e. aver. $E_{field}/E_{lab}=2.0$ (OWP) and aver. $E_{field}/E_{lab}=1.6$ (IWP).

From the above analysis results, the following conclusions can be drawn.

The laboratory ITSM testing confirmed the conclusions resulted from the field testing, as far as the no negative influence of the 16 years heavy traffic loading on the structural

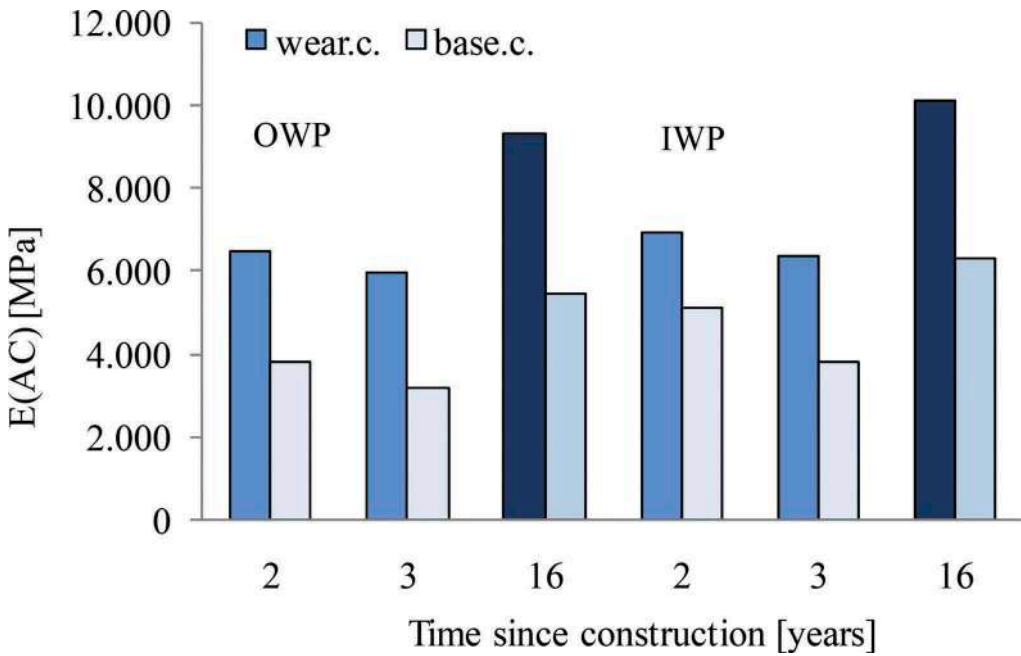


Figure 5. Average ITSM values (wearing course and base course) (20°C).

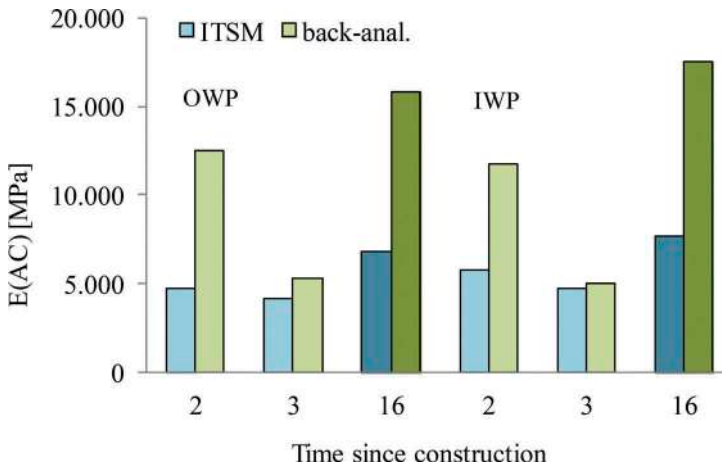


Figure 6. Average ITSM values vs. back-calculated AC moduli (20°C).

condition of the asphaltic layers overlay is concerned and the fact that the AC overlay became stiffer, due to the ageing effect of the asphalt binder.

The stiffening of the AC mixture did not only occur on the wearing course, as expected due to the effect of the climatic conditions, but also on the asphalt base course.

Comparing the ratio of the FWD based AC stiffness to the related stiffness through laboratory tests approximately 16 years after construction with the relative ratio values during the first years after construction, it can be concluded that the back-analysis procedure may produce overestimated asphalt layer moduli, in cases of aged binder of the AC overlay of such pavements.

4.4 Temperature sensitivity of AC overlay mixture

The temperature sensitivity of the 16 years old AC mixes was evaluated from ITSM tests on cores extracted from the test section and cut in two pieces, i.e. wearing course (wear.c.16y) and base course (base.c.16y). These results were compared with relative tests on laboratory produced AC specimens, i.e. modified wearing course mixes (spec.mod) and typical dense-graded bitumen mixture used for asphaltic base courses in Greece (spec.). The results (average values of ITSM) are presented graphically in Figure 7.

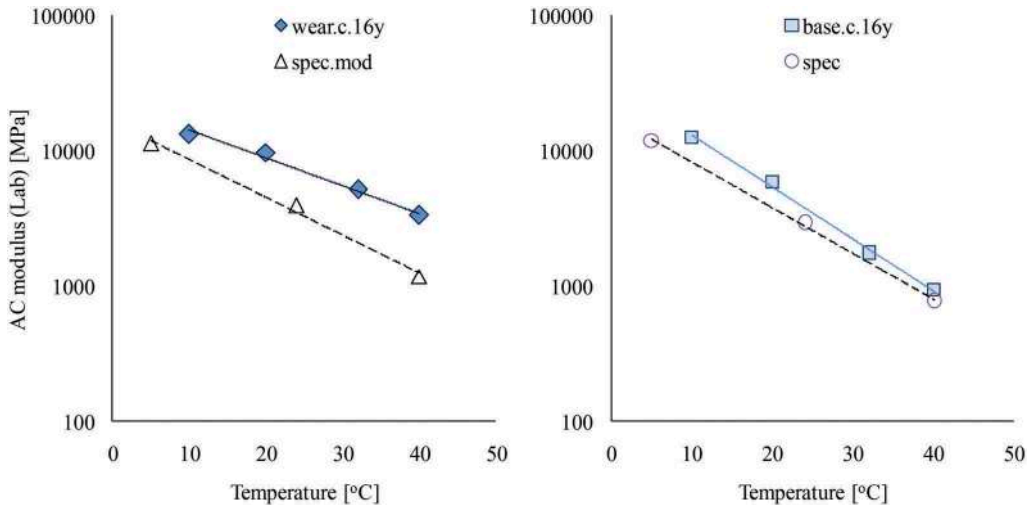


Figure 7. Average ITSM values vs. temperature.

The AC mixture of the wearing course, exposed for approximately 16 years to environmental impact, seems to be less temperature sensitive in comparison with the fresh produced AC mixture. This fact can be attributed to the aging effect of the asphalt binder. However, despite the stiffening of the AC mixture of the base course with time, no reduction of its temperature sensitivity was found.

From the laboratory conducted ITSM test results at different temperatures, the following Equation (1) was resulted. The ITSM values of the two specimens of each core were used for the estimation of one composite modulus (SHRP, 1993), representative for the laboratory estimated modulus of the AC overlay. These values with respect to the test temperature were further utilized to produce a temperature correction Equation (1).

$$E_{20}^{ITSM} = E_T e^{0.068(T-20)} \quad (1)$$

In order to estimate the effectiveness of the above equation (1) to correct the back-calculated moduli, the FWD survey was repeated on the OWP at AC temperature 32°C. The back-calculated asphalt layer moduli were corrected to 20°C according to Equation (1) and to an existing algorithm (Baltzer & Jansen, 1994) as well.

The results, i.e. the back-calculated average AC modulus from measurements at 21°C and corrected to 20°C utilizing Equation (1) (code “E(AC)20°C”), from measurements at 32°C and corrected to 20°C utilizing Equation (1) (code: “Eq. (1)”) as well as from measurements at 32°C and corrected to 20°C utilizing existing algorithm (code: “exist.alg.”), are presented in Figure 8. Test point tp3 was excluded from the analysis, due to the extremely high back-calculated AC modulus value.

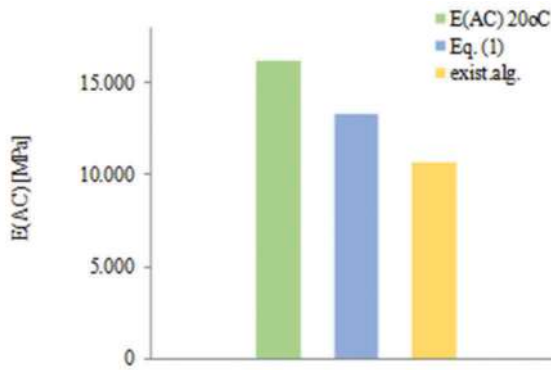


Figure 8. Average corrected back-calculated AC moduli values (20°C).

According to the analysis results, the absolute difference of the corrected (from 32°C to 20°C) back-calculated moduli values from the related back-calculated moduli values at 20°C, were lower (aver. 18%) than the related differences when using an existing algorithm (aver. 38%). This indicates the need of conducting laboratory tests for more accurate temperature correction of back-calculated moduli of aged AC mixtures.

5 CONCLUSIONS

Objective of this paper is to investigate several aspects concerning the structural evaluation of heavy-duty pavements constructed with non-conventional materials. In order to achieve this goal, in-situ NDT, including FWD survey were performed on a highway trial section. This pavement can be characterized as “non-conventional”, due to the fact that it was initially semi-rigid and has been rehabilitated using a cold in-place recycled (CIR) layer stabilized with foamed asphalt (FA) and asphalt concrete (AC) overlay layers.

The research is focusing on the influence of the traffic loading and the environmental impact on the structural condition of the AC layers in terms of the material stiffness, by performing non-destructive tests (NDTs) and related analysis tools (performance indicators, back-analysis).

Considering the limitations of the performance indicators and the back-analysis procedure, the stiffness of the aged AC material was estimated from laboratory testing.

Based on the analysis results, the following conclusions can be drawn.

Data analysis using deflection indicators, as a quick tool for performance assessment of the pavement, can provide useful information about the overall condition of the non-conventional pavement. However, these indicators cannot provide always with accurate information about the structural condition of the AC overlay.

Using back-analysis based on the field collected data, approximately 16 years after construction, the AC overlay was found through the pavement analysis very stiff. This can be attributed to the effect of the climatic conditions. Moreover, there is an evidence that the obtained high moduli values could reflect the cases of aged binder of the AC overlay.

The laboratory estimated AC moduli confirmed the fact that the AC overlay became stiffer and this can be attributed to the aging effect of the asphalt binder. Moreover, it was proven, that the stiffening of the AC mixture did not only occurred on the wearing course, as expected due to the effect of the climatic conditions, but also on the asphalt base course.

There is an indication, that the use of temperature correction equation based on laboratory data, i.e. by performing laboratory testing on cores at different temperatures, can be useful for more accurate temperature correction of back-calculated moduli of aged AC mixtures.

Further investigation is needed in order to prove whether the above outcome can be extended to other non-conventional pavements, with the similar characteristics.

REFERENCES

- Baltzer, S. and Jansen, J. M., 1994. *Temperature Correction of Asphalt-Moduli for FWD-Measurements*. Proceedings of the 4th International Conference on the Bearing Capacity of Roads and Airfields: 7–25, University of Minneapolis, Minnesota.
- COST-336., 1998. *Guidelines for Evaluation of Flexible Pavements at Project Level Using Falling Weight Deflectometer. Final Report*. European Commission. Brussels.
- Geophysical Survey Systems Inc., 2002. *RADAN for Windows NT, Version 4.0, User's Manual*. North Salem. New Hampshire.
- Hakim, B. A., Brown, S. F. and Armitage, R. J., 2002. *Pavement Evaluation and Strengthening Design: Six-teen Years Experience*. Proceedings of the 9th International Conference on Asphalt Pavements, ISAP. 3: 1–12. Copenhagen.
- Irwin, L.H., 1994. *Instructional Guide for Backcalculation and the Use of Modcomp3, Tutorial, User's Manual*. CLRP Publication No. 94-10. Cornell University.
- Kim, Y.R. and Park, H., 2002. *Use of falling weight deflectometer multi-load data for pavement strength estimation. Final Report, Research Project No HWY-00-4*. Department of Civil Engineering, North Carolina State University Raleigh, NC.
- Loizos, A., Collins, D. and Jenkins, K., 2004. *Rehabilitation of a Major Greek Highway by Recycling/Stabilizing with Foamed Bitumen*. Proceedings of the 8th Conference on Asphalt Pavements for Southern Africa (CAPSA 04): 119–126. Sun City, Southern Africa.
- Papavasiliou, V. and Loizos, A., 2017. *Assessment of the bearing capacity of pavements using fiber optic sensors*. Proceedings of the tenth International Conference on the Bearing Capacity of Roads, Railways and Airfields (BCRRA), 28-30 June, Athens.
- Roadscanners, 2001 *Road Doctor, User's Guide*.
- SHRP's Layer Moduli Backcalculation Procedure, 1993. *Strategic Highway Research Program (SHRP)*. National Research Council. Washington, DC.
- Thom, N. and Dawson, A., 2019. *Sustainable Road Design: Promoting Recycling and Non-Conventional Materials*. Sustainability 2019, 11, 6106; doi:10.3390/su11216106 <http://www.mdpi.com/journal/sustainability>.
- Van Gorp, C. 1995. *Seasonal Influence on Asphalt Pavements with the Use of Falling Weight Deflectometers*. Phd Thesis. Delft, The Netherlands.

Manufacturing and characterization of asphalt binders designed on the bases of polymer modified bitumen with cement by-pass dust and fly ash

R. Merijs-Meri, J. Zicans, T. Ivanova, R. Berzina, A. Bernava, M. Žiganova & A. Ābele
Faculty of Materials Science and Applied Chemistry, Institute of Polymer Materials, Riga Technical University, Riga, Latvia

V. Haritonovs
Faculty of Civil Engineering, Department of Roads and Bridges, Riga Technical University, Riga, Latvia

ABSTRACT: Growing environmental and social concerns demand development of environmentally friendly and resource efficient solutions in road construction sector. Consequently, the current research is devoted to valorization of two types of industrial waste – cement by-pass dust (BPD) and biomass fly ash (FA) – to develop efficient binder for construction of more durable asphalt pavements. Within the research certain amounts of BPD and FA (6, 7 and 8 wt.%) have been introduced within styrene butadiene styrene (SBS) modified 70/100 grade bitumen to develop environmentally friendly hybrid binder systems (HBS) by high shear mixing. Structure, chemical composition and thermal stability of FA and BPD fillers have been characterized. Performance of the developed HBS have been assessed by means of rheological investigations (DSR and MSCR tests). It has been observed that HBS are characterized with improved rutting resistance in comparison to neat bitumen as well as improved elastic recovery and hence low-temperature characteristics in comparison to SBS modified bituminous compositions.

Keywords: Bitumen, styrene-butadiene-styrene copolymer, cement by-pass dust, fly ash, rheology

1 INTRODUCTION

Use of bitumen as binder material for road construction has a long history. However, due to increased traffic loads the necessity of bitumen modification has arisen with the main aim of increasing durability. By considering that bitumen is produced from highly restricted fossil resources as well as its high price, there is a will to decrease the use of bitumen, concomitant ensuring that wetting of aggregates has occurred and the necessary interfacial adhesion within the bituminous system is maintained to provide the desired durability.

One of the ways to reduce consumption of bitumen and to improve its properties is modification with mineral fillers. The mineral filler is used in hot mix asphalt mixture to meet gradation requirements of the whole minerals, to stabilize the mixture, to increase the post-compaction resistance of the mixtures, to improve the bond strength between the bituminous binder and aggregate, to stiffen the asphalt. Another commonly accepted approach of increasing durability of roads is modification of bitumen with thermoplastic elastomers, particularly styrene-butadiene-styrene block co-polymer (SBS), which allows considerably

improve a number of characteristics of bituminous mixtures, including, increased softening point and decreased penetration, lessened thermal susceptibility, decreased Fraass breaking point, moderated stiffening due to the oxidation process.

By increasing durability of pavements, it would be possible to reduce impact on an environment as longer service life as well as less frequent repair of road structures are expected. In fact, construction of sustainable and durable road structures promotes implementation of principles of the Circular Economy Action Plan (SWD, 2020) in respects of improved product durability, reusability, upgradability and reparability, increased re-used and recycled content in products, while ensuring their performance and safety, as well as reduced carbon and environmental footprints. Thus, sustainable road surfacing layers may be designed by increasing the content of reclaimed asphalt pavement even up to 100% (Zaumanis et al, 2014), by replacing fossil SBS with biobased alternative binders such as lignin (Xu et al, 2021), fluxing bituminous binder with bio-oil (Hainian et al, 2020) or by introducing industrial waste for partial replacement of mineral fillers. The last approach was used also in this research, namely, biomass fly ash (FA) and cement by-pass dust (BPD) were utilized as non-toxic fillers of SBS modified bitumen thus allowing to develop environmentally friendly hybrid binder systems (HBS) for manufacturing of high-performance asphalt concrete. Novelty of the proposed solution at developing of HBS is justified by the fact that SBS and industrial waste filler both were introduced in the bituminous matrix at elevated temperature during single manufacturing phase of asphalt binder. Most of the research groups working in that area until now have been mainly focused either on investigation of polymer modified bituminous systems (Polacco et al, 2015) or discovering the possibilities of industrial waste particulate matter for modification of neat bitumen or partial replacement of traditional mineral fillers (Dimulescu and Burlacu, 2021).

Besides, it is worth of mentioning that both fillers have been obtained from sustainably managed technological processes; thus, FA is obtained from renewable biomass co-generation plant, whereas BPD is obtained from tire waste co-fired cement plant. In the case of the latter use of waste tire as fuel supplement is known to increase energy efficiency and reduce carbon dioxide emissions (Uson et al, 2013). In both cases, however, FA and BPD are produced unavoidably as solid waste. Consequently, there is a necessity to increase benefit of these waste products, leading to the idea of current research, based on purposeful utilization of BPD and FA as SBS modified bitumen fillers, thus contributing to sustainable management practice of these industrial wastes in accordance with European Green Deal.

2 MATERIALS AND METHODS

70/100 grade bitumen was mixed with SBS and two types of locally abundant industrial waste fillers (BPD and FA) to develop sustainable multicomponent HBS for use in high performance asphalt concrete. BPD was obtained from local cement plant, whereas FA was obtained from local biomass cogeneration power plant. Concentration of the fillers was changed in the range from 6 to 8 wt.% whereas the amount of SBS was kept constant (4wt.%) in respects to that of the bitumen. Various compositions of HBS were prepared as follows: the vessel with hot bitumen (140°C) was placed in a silicone oil bath and heated until temperature reached 185°C, after that the elastomer was gradually added and mixing at 6400 rpm was continued for 3 hours by using Silverson L5M-A laboratory mixer equipped with square hole high shear screen. During the last 10 minutes, inorganic fillers were introduced in the mix. After preparation HBS compositions were kept at sub-zero temperatures until measurements.

Structure of BPD and FA were characterized by means of scanning electron microscopy (SEM), surface area analysis, X-ray diffractometry, Fourier transform infrared spectroscopy (FTIR) and thermogravimetric analysis (TGA). Structure of the developed HBS compositions were characterized by means of fluorescent microscopy. Performance characteristics of the developed HBS compositions were characterized by means of rheological measurements (DSR test and MSCR test).

3 RESULTS AND DISCUSSION

Chemical composition of FA and BPD is summarized in Table 1. Main constituents of FA are CaO and SiO₂, which are responsible for forming a network of the filler (Xu and Shi, 2018). High sulfate content in FA may be explained with fertilizer traces in wood biomass. Presence of calcium carbonate in FA may be attributed to secondary reactions during combustion of biomass, use of calcium carbonate for capture of acid gases as well as composition of lignocellulosic biomass burned. Similarly to FA, BPD consists of considerable amounts of CaO and SiO₂. In addition, in the case of BPD CaCO₃ may be produced also from main production process of cement. The amount of other constituents of BPD and FA is believed to be below 10 %.

Table 1. Chemical composition of FA and BPD.

Filler	Chemical composition						
	CaO	SiO ₂	CaCO ₃	CaSO ₄	KCl	K ₂ S	Other constituents
BPD	23	13	11	n.d.	21	11	<10
FA	21	20	17	38	n.d.	n.d.	<10

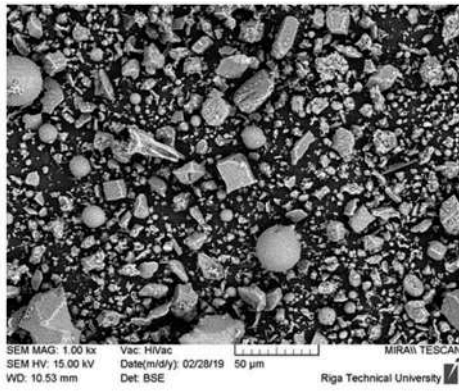
n.d. – not detected at significant amounts

Morphology of the used filler particles is depicted in Figure 1. Morphology of FA particles is much more diverse in comparison to BPD particles. In the case of FA, broad size and shape distribution of the particles may be observed. Consequently, FA particles consist of cenosphere like particles of different sizes and high sphericity, irregularly shaped particles as well as tiny fibrous structures, mainly deposited on the surface of larger particles. BPD particles, in its turn, are more roundish, besides it they represent broad size distribution with a number of larger particles as agglomerates. Nevertheless, specific surface area of both mineral fillers is similar: 2.9 m²/g for FA and 2.6 m²/g for BPD.

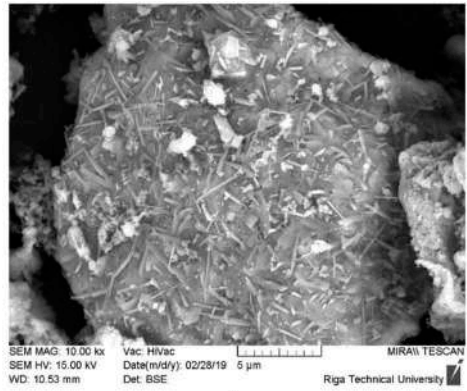
FTIR spectra and TGA thermograms of mineral fillers used in this research as well as SBS modifier and bituminous matrix are compared in Figures 2 and 3, respectively. By considering that thermal stability of all the constituents exceeds manufacturing temperature of bituminous mixtures (185°C), no considerable structural change is expected during mixing. From TGA thermograms two distinct weight loss steps may be observed. In the case of bitumen and SBS the first weight loss step is attributed to destruction of main organic part of the constituents, whereas the second weight loss step is associated with decomposition of the formed oxidation products. For the 70/100 grade bitumen the second weight loss step occurs at higher temperatures, as well as it is observed over broader temperature range, which is connected with much more complex structure of bitumen. For FA and BPD the step heights are much smaller and at the end of the test do not exceed 10% from the initial weight of the fillers.

As depicted in representative image, demonstrated in Figure 4, microstructure of the obtained HBS in accordance with EN 13632 can be characterized by the code B/H/s/r, meaning that relatively small mainly spherical modifier and filler particles (<10 μ) are homogeneously distributed within continuous bitumen matrix. This allows judging that the particles of dispersed phase have been dispersed successfully within the volume of bituminous matrix during high shear (6400 rpm) and high temperature (184°C) mixing.

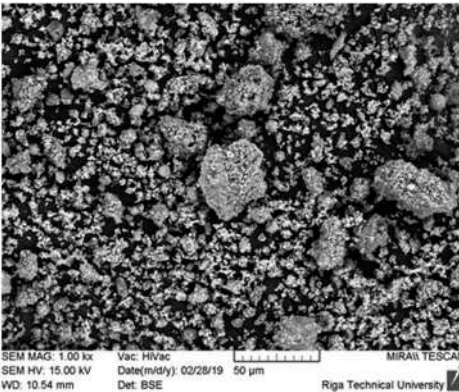
Effect of the mineral fillers on the upper critical temperature is demonstrated in Figure 5. It is shown that due to introduction of either of the mineral fillers within the bituminous matrix considerable increment (by more than 10°C at least) of higher critical temperature in respects



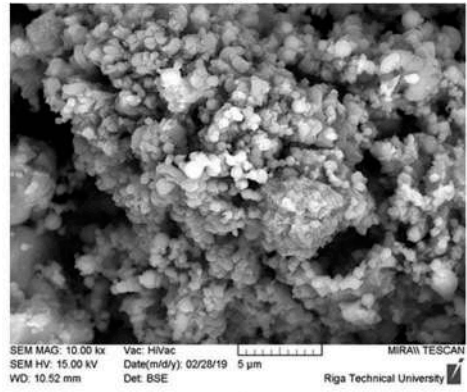
a



b



c



d

Figure 1. SEM micrographs of FA (a, b) and BPD (c, d) at different magnifications (as shown on barscale).

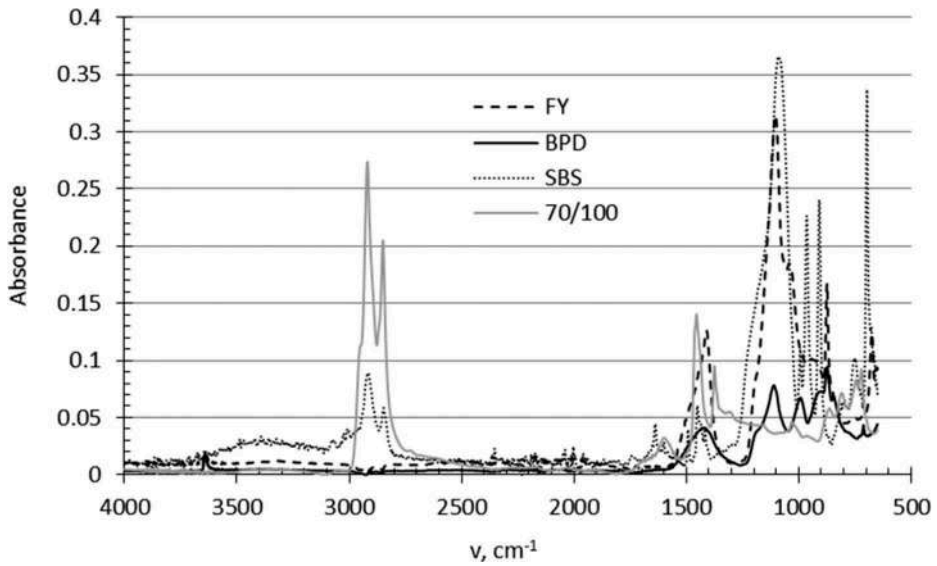


Figure 2. FTIR spectra of FA, BPD, SBS and 70/100 grade bitumen.

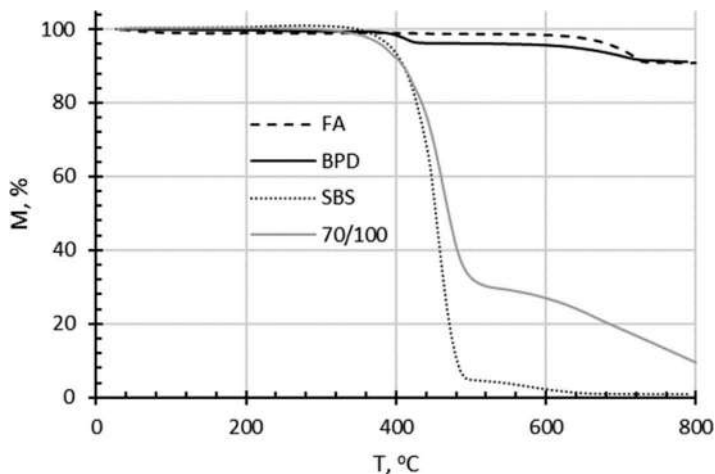


Figure 3. TGA thermograms of FA, BPD, SBS and 70/100 grade bitumen.



Figure 4. Representative image of fluorescent microscopy of HBS with 7 wt.% of BPD.

to neat 70/100 is observed. This allows predict improved rutting resistance of the developed HBS. However, minor decrement (not more than 2°C) of rut resistance of FA and BPD containing systems in comparison to SBS modified bitumen is observed. This may be related to decreased stiffness of certain HBS compositions.

Results of MSCR test of the investigated compositions of HBS at 58°C are demonstrated in Figure 6. It is confirmed that SBS modified bituminous composition demonstrates the highest rutting resistance due to the lowest value of non-recoverable creep compliance at 3.2 kPa. Concomitant, the highest value of elastic recovery is demonstrated by HBS compositions containing 8 wt.% of the mineral filler. Elastic recovery of FA containing bituminous compositions are somewhat higher in comparison to the those with BPD most probably because of the smaller surface area as well as the presence of more uniform spherical particles in the utilized FA fraction. Consequently, it is believed that HBS within the investigated FA filler range will demonstrate comparable or even superior low-temperature properties in comparison to SBS modified bitumen. Besides its successful valorization of FA waste will be ensured.

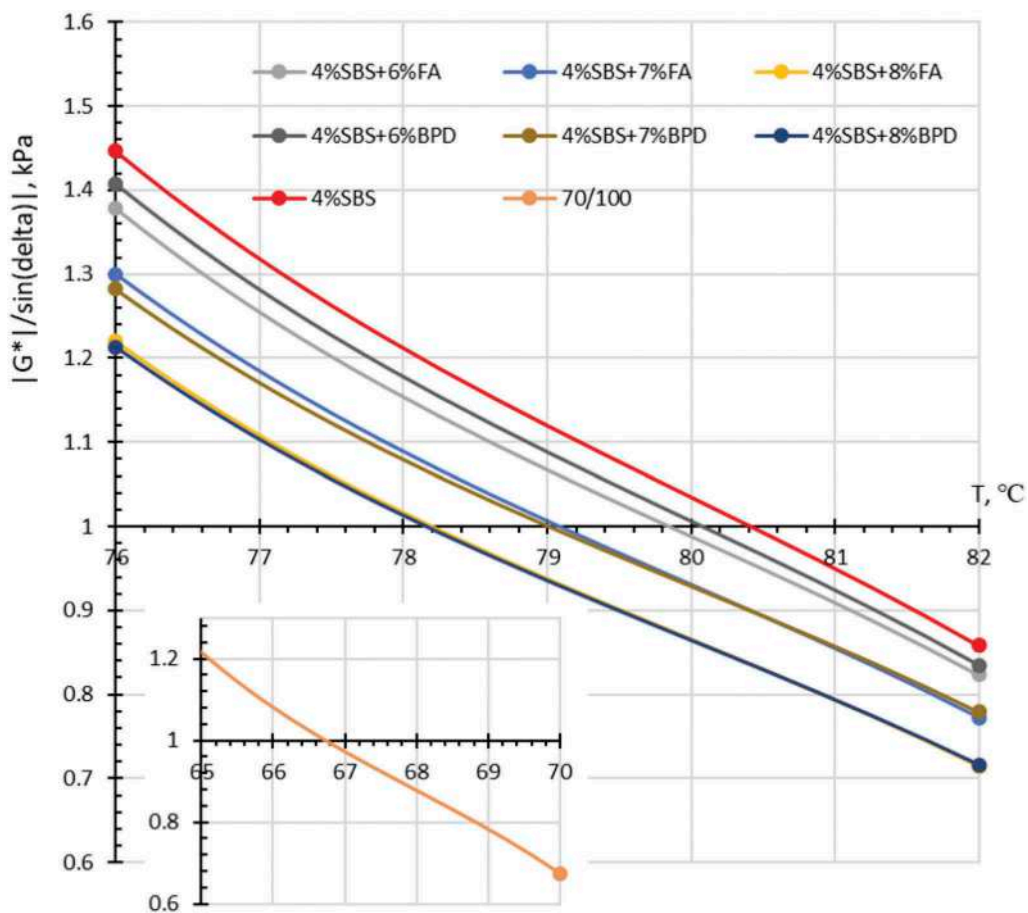


Figure 5. $|G^*/\sin(\delta)|$ temperature relationships of HBS with various contents of BPD and FA. Inset of the plot demonstrates $|G^*/\sin(\delta)|$ temperature relationship of 70/100.

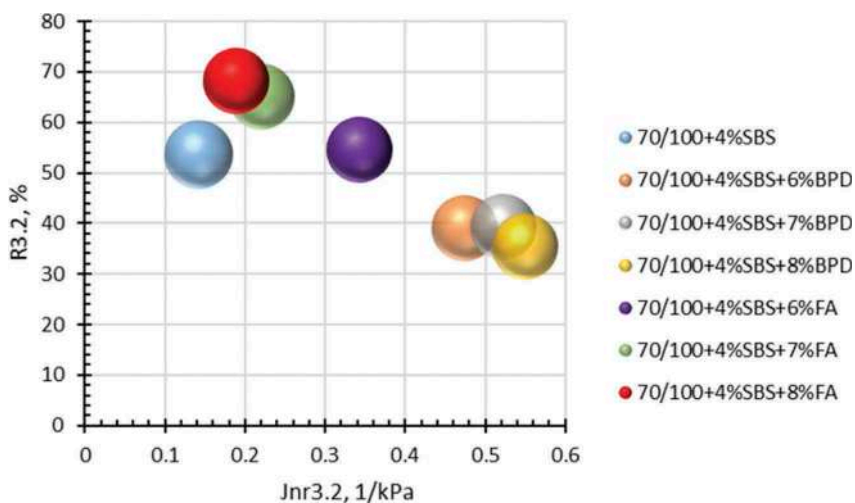


Figure 6. Percent elastic recovery at 3.2 kPa (R3.2) vs non-recoverable compliance at 3.2 kPa (Jnr3.2) of HBS with various contents of BPD and FA at 58°C.

4 CONCLUSION

The current research on the valorization of abundant biomass FA and cement BPD waste by development of environmentally friendly HBS for construction of more durable pavements allows make following conclusions:

- 1) Addition of certain amounts (6-8 wt.%) of FA or BPD filler to SBS modified bitumen decreases rutting resistance of the binder, however, not below the rutting point of neat bitumen binder;
- 2) All the tested HBS compositions demonstrate improved rutting behavior (improvement of at least 10°C) of the binder in respects to neat bitumen;
- 3) FA and BPD, both may be successfully utilized by developing HBS, demonstrating improved rutting resistance in comparison to neat bitumen;
- 4) Addition of FA also contributes for improvement of elastic recovery of SBS modified bitumen.

REFERENCES

- SWD(2020) 100, 2020. *Leading the way to a global circular economy: state of play and outlook*. Commission staff working document. Brussels, Belgium.
- Zaumanis, M., Mallick, R. and Frank, R., 2014. *100% Recycled Hot Mix Asphalt: A Review and Analysis*. Resources, Conservation & Recycling, Vol.92, pp.230–245. ISSN 0921-3449. <https://doi.org/10.1016/j.resconrec.2014.07.007>.
- Xu, C., Wang, D., Zhang, S., Guo, E., Luo, H., Zhang, Z., and Yu, H., 2021. *Effect of Lignin Modifier on Engineering Performance of Bituminous Binder and Mixture*. Polymers, 2021 13, 1083. <https://doi.org/10.3390/polym13071083> <https://www.mdpi.com/journal/polymer>.
- Hainian, W., Ziyue, M., Xi C., Mohd, R., Mohd, H., 2020. *Preparation process of bio-oil and bio-asphalt, their performance, and the application of bio-asphalt: A comprehensive review*. Journal of Traffic and Transportation Engineering (English Edition), Volume 7, Issue 2, April 2020, Pages , 137–151, <https://doi.org/10.1016/j.jtte.2020.03.002>.
- Polacco, G., Filippi, S., Merusi, F., Stastna, G., 2015. *A review of the fundamentals of polymer-modified asphalts: Asphalt/polymer interactions and principles of compatibility*. Advances in Colloid and Interface Science, Volume 224, October 2015, 72–112, <https://doi.org/10.1016/j.cis.2015.07.010>
- Dimulescu, C. and Burlacu, A., 2021. *Industrial Waste Materials as Alternative Fillers in Asphalt Mixtures*. Sustainability, 13, 8068. <https://doi.org/10.3390/su13148068> <https://www.mdpi.com/journal/sustainability>.
- Xu, G. and Shi, X., 2018. *Characteristics and applications of fly ash as a sustainable construction material: A state-of-the-art review*. Resources, Conservation & Recycling, 136, 95–109 <https://doi.org/10.1016/j.resconrec.2018.04.010>.
- Uson, A.A., Lopez-Sabiron, A.M., Ferreira, G., Sastresa, E.L., 2013. *Uses of alternative fuels and raw materials in the cement industry as sustainable waste management options*. Renewable and Sustainable Energy Reviews 23, 242–260. <http://dx.doi.org/10.1016/j.rser.2013.02.024>.

Bearing capacity behavior of base course reinforced with woven geotextile

K. Sato, T. Fujikawa & C. Koga

Department of Civil Engineering, Fukuoka University, Fukuoka, Japan

Y. Wakabayashi

Kiso-Jiban Consultants Co. Ltd, Tokyo, Japan

M. Shimazaki & K. Hirakawa

Taisei Rotec Corporation, Tokyo, Japan

J. Hironaka

Mitsuichemicals, Tokyo, Japan

Y. Isobe

IMAGEi Consultant, Tokyo, Japan

ABSTRACT: In Japan, there has been a rapid increase in the number of road pavements that have exceeded 40 years of service life. As a result, it is anticipated that the number of pavements in need of repair, including the base course, will increase. In addition, the cost of repairing the pavement including the base course will be higher than if only the asphalt pavement were repaired. Therefore, it is desirable to extend the service life of road pavements in order to reduce future maintenance costs. This study focused on reinforcing the base course of road pavements and aimed to increase the durability and extend the service life of road pavements by laying geotextiles on the base course. The effect of different types of geotextiles on the reinforcement of the base course was reported from the results of bearing capacity tests using a small soil container.

Keywords: Bearing capacity, base course, geotextile-reinforcement

1 INTRODUCTION

In Japan, modern infrastructures were intensively constructed during the high economic growth period, which will reach the end of their service life. Thus, the aging of these infrastructures is becoming a social problem. After the beginning of operation, the durability of the pavement is impaired by heavy vehicle traffic and rainwater, and the pavement surface is subject to cracking and rutting. It has been reported that the bearing capacity of base course due to the ingress of rainwater from cracks has a significant impact on the durability of asphalt pavements [1]. Thus, the base course has an important role in the service life of a road pavement. However, there are few cases in which the base course is replaced in the repair work because of maintenance cost reduction, increase in repair cost, and road closure due to construction.

In recent years, research and development has been focused on base course reinforcement, especially the reinforcement of base courses using geotextiles [2]. It is well known that geotextiles are very useful materials in the construction of soil structures, such as their function as tensile reinforcement [3, 4]. The use of geotextiles in pavement construction in Japan has been used as a countermeasure for soft base course in road pavements [5]. However, there are few examples of geotextiles being used to reinforce base courses. Thus, the research on the application of geotextiles to base courses has attracted a lot of attention. Hirakawa et al. showed that even a single layer of geogrid in the base course greatly suppressed the amount of residual subsidence in the base course. Furthermore, it was found that when used in conjunction with a high density of the base course, progressive residual settlements could be effectively restrained as well [6].

In this study, two types of loading tests, constant strain loading and cyclic loading, were conducted on a geotextile-reinforced base course. This study described the results of the investigation on the effect of geotextile type on bearing and deformation characteristics. The effect of geotextile laying depth and laying length on cyclic loading tests was also discussed.

2 TESTING PROCEDURE

2.1 Materials

A single grain size of Mikawa silica sand no.5 was used in the soil test to check the deformation of the ground by loading. The physical properties of this silica sand are shown in Table 1. Five types of geotextiles with different material properties such as stiffness and frictional force of geotextiles were used in this study: two types of woven fabrics, nonwoven fabrics and two types of geonets. Table 2 shows the geotextiles used and their physical properties. The woven fabric is a material that has a very large tensile strength compared to other geotextiles. Geonet is also a geotextile that can create an interlocking effect due to the continuity of soil particles.

Table 1. Physical property of Mikawa silica sand.






Sample	Mikawa quartz sand no.5
Photo	
Soil particle density ρ_s (g/cm^3)	2.655
Minimum void ratio e_{max}	1.139
Minimum void ratio e_{min}	0.723
Uniformity coefficient U_c	1.766
Coefficient of curvature U_c	1.052

Table 2. Geotextiles.

Reinforcement	Woven fabric A,B	Nonwoven	Geonet A	Geonet B
Photo				
Tensile strength (kN/m)	A 89.0 B 74.0	11.7	5.6	3.6
Mesh size (mm)	-	-	2.5	10

2.2 Experimental apparatus and method

Figure 1 shows an outline of the small soil container (loading device) used in this experiment, which has a height of 90 cm, width of 120 cm, and depth of 20 cm. Six steel plates and springs with a spring constant of 3.75 kN/mm were installed at the bottom of the box. This was designed to easily cause ground deformation during loading. The deformation of the model ground surface was measured by using a displacement gauge at three positions: at the loading position, 10 cm and 20 cm from the center of the loading. The relative density of the model ground was set at 80%.

The model ground was prepared by the tamping method with the moisture content of the samples adjusted to 5%. The bottom 30 cm of the model ground was made in three layers of 10 cm thickness. In particular, the upper 10 cm of the model ground was made in five layers with a thickness of 2 cm, because the geotextile was to be laid in a shallow area. After the preparation of the model ground, a 1 cm thick, 119 cm long, and 19.6 cm wide rubber plate was installed to simulate the asphalt pavement surface. Kaolin clay with a width of about 1 cm was placed at a depth of 20 and 30 cm from the top of the acrylic plate in order to visually capture the deformation of the model ground by the loading test.

Static loading was carried out at 1 mm/min, and the loading was terminated at a load stress of 5 kN/m². On the other hand, the cyclic loading was carried out under the sinusoidal stress control at a loading speed of 0.1 Hz with a maximum loading stress of 100 kN/m². In this test, the repetition rate $N=360$ cycles (1 h) was set as the end condition. In this model test, the loading speed was set slower in order to see the reinforcing effect of the geotextile and the deformation of the ground by the loading test.

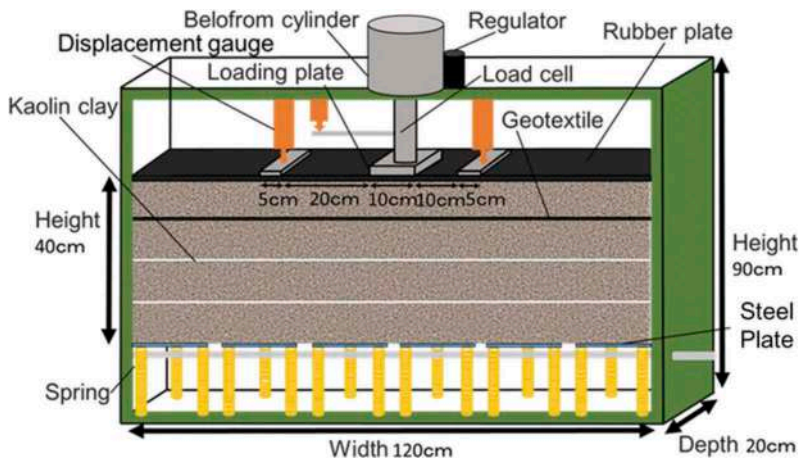


Figure 1. Small soil container.

2.3 Investigation of material friction characteristics of geotextiles

In this study, a pull-out test was conducted to understand the frictional resistance of geotextiles and soil materials. Figures 2(a) and 2(b) show schematic diagrams of the pull-out testing apparatus used in the experiment. The model ground was prepared on a soil tank 40 cm high, 100 cm wide and 40 cm deep. Two types of soil pull-out test and spring-loaded test were conducted using this soil container. The soil pull-out test machine (Figures 2(a)) was loaded with a predetermined load from the top of the soil container by air pressure, and the pull-out speed was set to 1 mm/min, and the test was completed at 100 mm pull-out displacement. On the other hand, in the spring-loaded test apparatus, a geotextile was placed on top of a soil material of similar density to the soil pull-out test, and the geotextile was weighted on a 25 x 25 cm loading plate and pulled out using a spring only, with low loading stress (Figures 2(b)).

The experimental conditions of the pull-out test are shown in Table 3. In this experiment, geotextiles with high tensile strength (two types of woven and one type of non-woven fabrics) were conducted in soil pull-out test. The geotextiles with low tensile strength and large deformation (two geonets) were tested by spring loaded test in consideration of the breakage during the soil pull-out test.

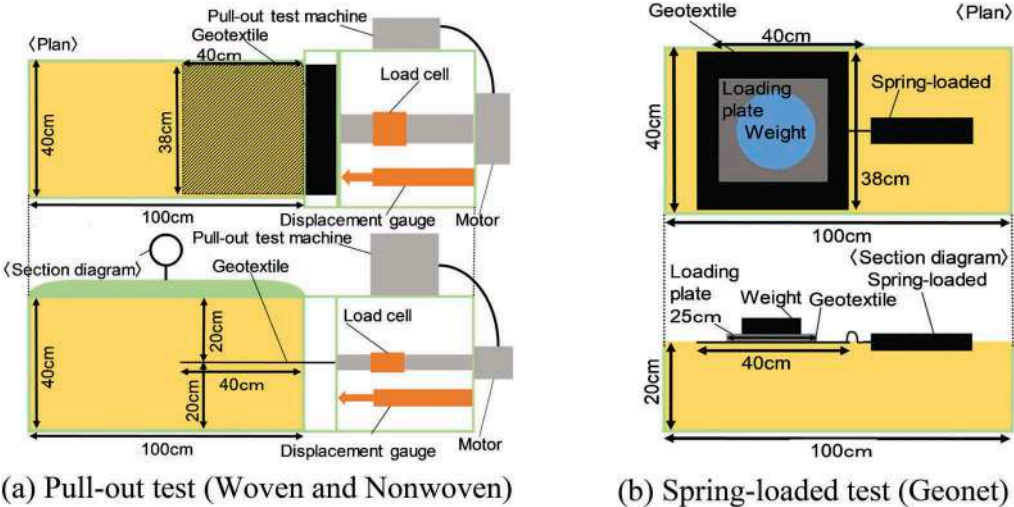


Figure 2. Schematic diagrams of the pull-out testing apparatus.

Table 3. Experimental conditions (pull-out and spring-loaded tests).

Relative density D_r (%)	Loading stress (kN/m^2)	Experimental method	Geotextile types	Size (cm) Length \times Width	Laying depth D (cm)
80	10,20,30	Pull-out test	Woven fabric A	38 \times 40	20
			Woven fabric B		
	1.6,3.1,4.7	Spring-loaded test	Nonwoven	38 \times 10	
			Geonet A	38 \times 40	-
			Geonet B		

2.4 Experimental conditions

Figure 3 shows the stress distribution when a loading stress of 100 kN/m^2 was applied to a 10 cm^2 loading plate. It is considered that the stress distribution shown in Figure 2 acts in the model ground, so the laying length L of a woven fabric A below the center of the loading plate was set to 15, 30, 60, and 120 cm. In addition, the rubber plate assumed as asphalt layer in this research was one-fifth as thick as the real asphalt layer, so the experiment this time was considered as one fifth of the real condition in the scale. The base course rolling thickness in practical construction was 10-15 cm. But regarding the scale of the experiment, the laying depth is adjusted into 2, 4, 8, and 10 cm (assumed from 10, 20, 40, and 50 cm in practical terms).

As the test condition shown in Tables 4 and 5, the influence of laying position (depth), laying length, geotextile types, and loading method on reinforcement effect was discussed on the model ground with a relative density of 80 %.

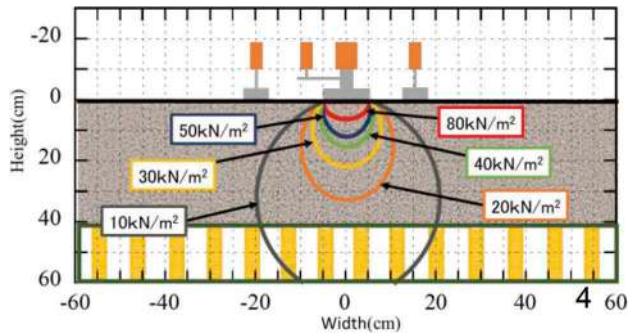


Figure 3. Stress distribution when a loading stress of 100kN/m².

Table 4. Experimental conditions (static loading tests).

Relative density <i>Dr</i> (%)	Laying depth <i>D</i> (cm)	Laying length <i>L</i> (cm)	Loading method	Geotextile types
80	10	120	Static loading Cyclic loading	Woven fabric A,B Nonwoven Geonet A,B

Table 5. Experimental conditions (cyclic loading tests).

Relative density <i>Dr</i> (%)	Laying depth <i>D</i> (cm)	Laying length <i>L</i> (cm)	Loading method	Geotextile types
80	- 2 4,6,8 10	- 15,30,60,120 60 30,60,120	Cyclic loading	No laying Woven fabric A,

3 RESULTS AND DISCUSSIONS

3.1 Pull-out test results of geotextiles

Figure 4 (a–c) shows the results of the pull-out tests for woven fabric A, B and nonwoven. In each geotextile, the maximum pull-out shear stress increases as the vertical stress increases. It can be seen that woven fabrics with high tensile strength of geotextiles have little decrease after the peak of pullout shear stress when compared to non-woven fabrics. This indicates that the geotextile has a greater frictional resistance to the soil material.

Figure 5 (a) and (b) show the relationship between the vertical stress and the maximum pull-out shear stress. The apparent shear resistance angle of each reinforcement is 43.1 for woven fabric B. This result suggests that woven fabric B is more effective than the other reinforcements in reinforcing the base course through reinforcement friction. On the other hand, the apparent shear resistance angle of geonet, as determined from the spring-loaded pull-out test, is smaller than that of the woven fabric, and the apparent cohesion is close to zero. Geonet is a material with low tensile strength and its ability to constrain the deformation of the base course is considered to be smaller than that of woven and nonwoven fabrics. However, because of its mesh structure, it does not interfere with the continuity of the base course material and can be considered as a reinforcing material with frictional effects due to the interlocking effect.

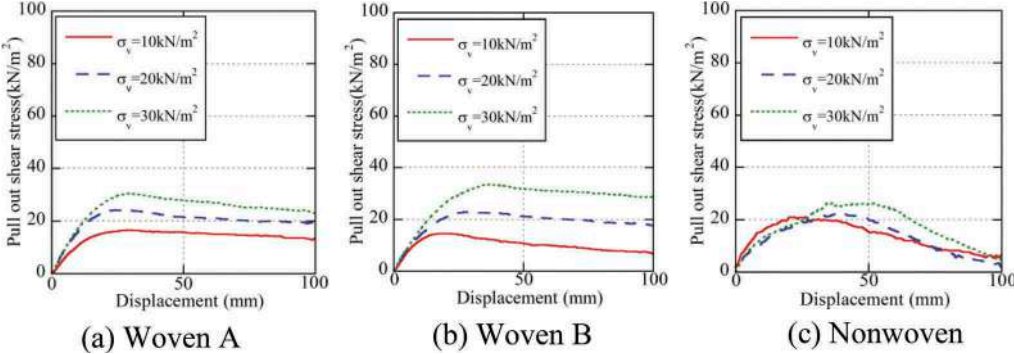


Figure 4. The results of the pull-out tests for woven A, B and nonwoven.

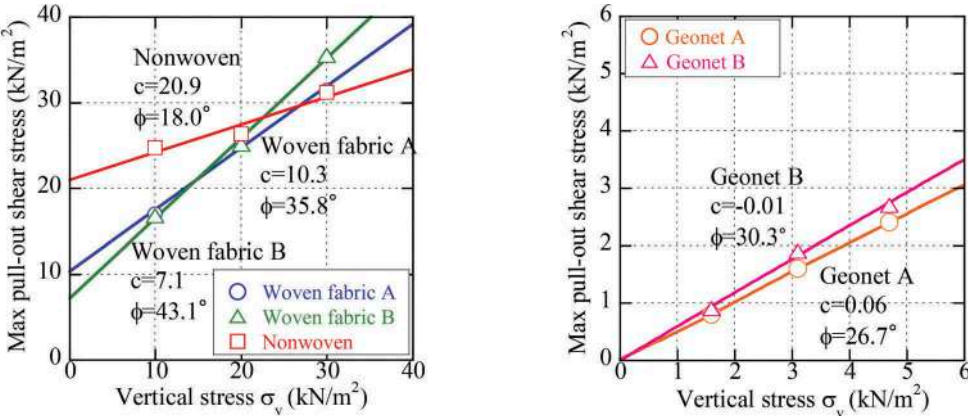


Figure 5. Vertical stress and maximum pull-out shear stress.

3.2 Effect of the type of geotextiles

Figure 6 (a) and (b) show the relationship between loading displacement and loading stress of each geotextile by static loading test. By laying various geotextiles, loading displacement was suppressed due to an increase in loading stress. Moreover, about the types of geotextiles, the woven fabric A exhibited the most effective displacement-suppression effect. It can also be seen that the suppression of load displacement depends on the tensile strength of each geotextile and the magnitude of the apparent internal friction angle and cohesion obtained by the pull-out test. In particular, the woven fabric with higher tensile strength and greater apparent internal friction angle and cohesion suppresses the load displacement compared to the two geonets.

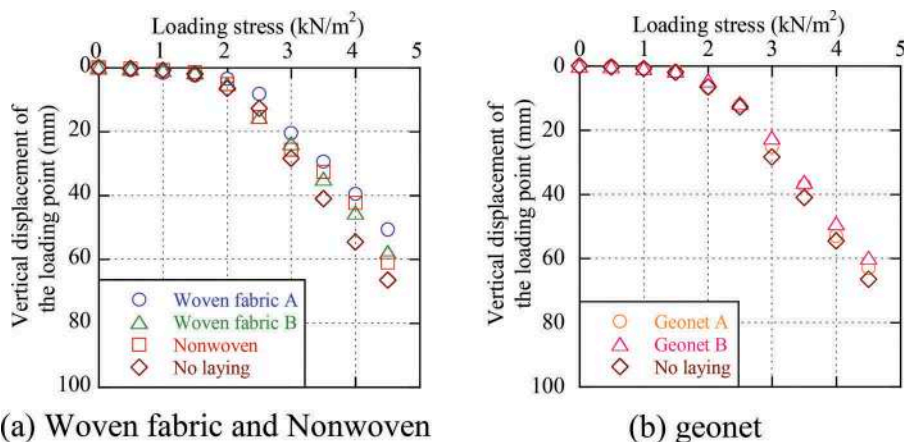


Figure 6. Vertical loading displacement of loading plate and loading stress (static loading).

Figure 7(a) shows the relationship between the number of loadings in the cyclic loading test for each geotextile and the loading displacement at the center of the loading plate, and Figure 7(b) shows the loading displacement after 360 times of repeated loading. Figure 7(a) and (b) show that all the reinforcing materials were deformed immediately after loading, and then gradually changed in loading. Moreover, loading displacement was suppressed by laying in all the reinforcing materials, and the reinforcing effect was exhibited.

In terms of the difference in the types of geotextiles, the displacement suppression effect was most exhibited in woven fabric A as in the case of static loading. In addition, when comparing the woven fabrics A and B, which are the same material, the load displacement was more suppressed in the woven fabric A which has a higher tensile strength, so. Thus, the tensile strength of each woven fabric affects the load displacement in the woven fabric. However, comparing two types of geonets with different strengths and shapes, the reinforcement effect was exerted more in geonets with larger meshes, although the strength was inferior. The reason was thought to be that the frictional force due to meshing with the ground material was more exhibited due to the large mesh. For this reason, the geonet is considered to be a reinforcing material that can be expected to have a friction effect due to the meshing effect with the base course material.

3.3 Effect of geotextile laying depths and lengths

Figure 8(a) shows the relationship between the number of loadings at each laying depth in the repeated loading test and the loading displacement at the center of the loading plate, and

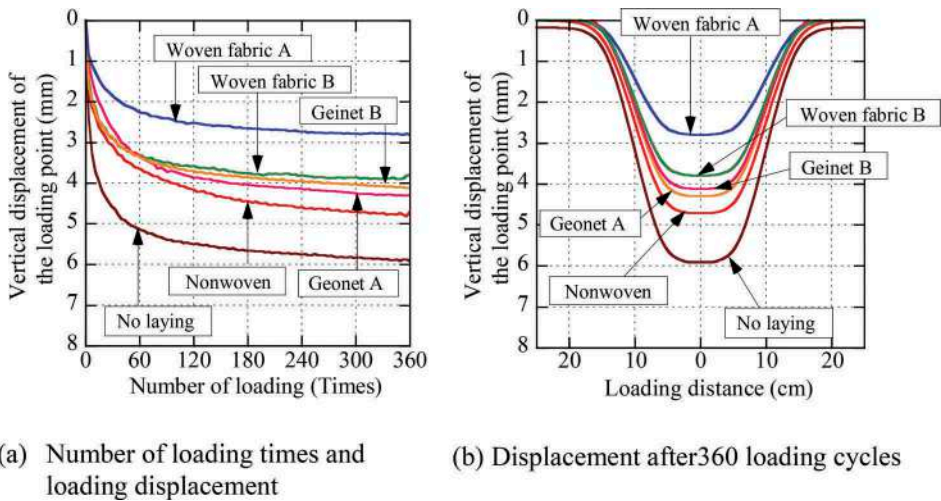


Figure 7. Effect of types of geotextiles on cyclic loading tests.

Figure 8(b) shows the loading displacement after 360 times of repeated loading for woven fabrics A with cyclic loading. Both showed the results for $L = 60$ cm. The shallower the laying depth is, the better the reinforcement effect against displacement suppression becomes. The displacement was the smallest and the reinforcement effect was greatest when $D = 2$ cm. This is considered to be due to the low geotextile laying depth, dispersion of the load, and increase of ground bearing capacity.

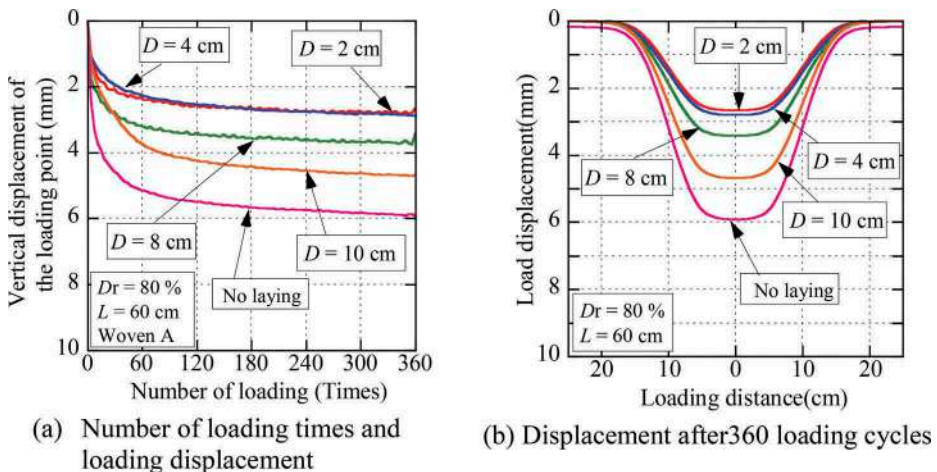


Figure 8. Effect of laying depths on cyclic loading tests.

Figures 9(a) and (b) show the effect on the reinforcement effect because of the laying length at $D = 10$ cm. The loading displacement decreased in the order of $L = 30, 60,$ and 120 cm. This showed that the longer the laying length is, the more effective the reinforcement becomes. It is because the longer the laying length is, the greater the frictional force against the geotextile

becomes through the increase of contact area between the geotextile and ground material. The frictional force will become greater with the increase of contact area and the tensile force of the reinforcing material is generated by this frictional force. However, when $L = 30$ cm, the result shows a larger displacement than the condition without laying. From the stress distribution in Figure 2, when $L = 30$ cm, the geotextile is within the range of the stress distribution, so it can be said that the tensile reinforcement effect of the geotextile is not enough in this condition. From those facts, it is shown that in practical road pavement, if the length extends beyond the range of the wheel load, the reinforcing effect can become better. Then, Figures 10 (a) and (b) show the effect on the reinforcement effect of the laying length at $D = 2$ cm. It shows the same effect as the case of $D = 10$ cm, which is that the loading displacement is becoming less with an increase of the laying length. In addition, compared with the case of $D = 10$ cm, the reinforcing effect can be good even when the laying length is short. This indicates that if the laying depth is reduced, the effect can be good even when the laying length of the geotextile is short.

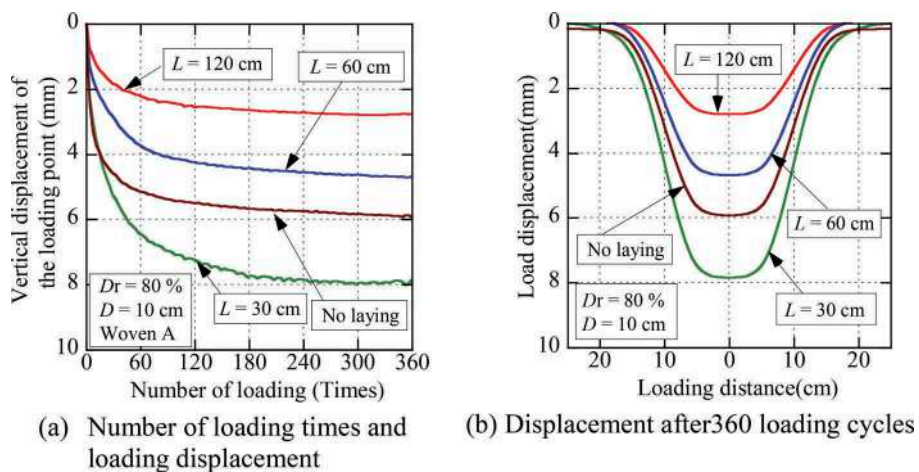


Figure 9. Effect of laying length on cyclic loading tests ($D = 10$ cm).

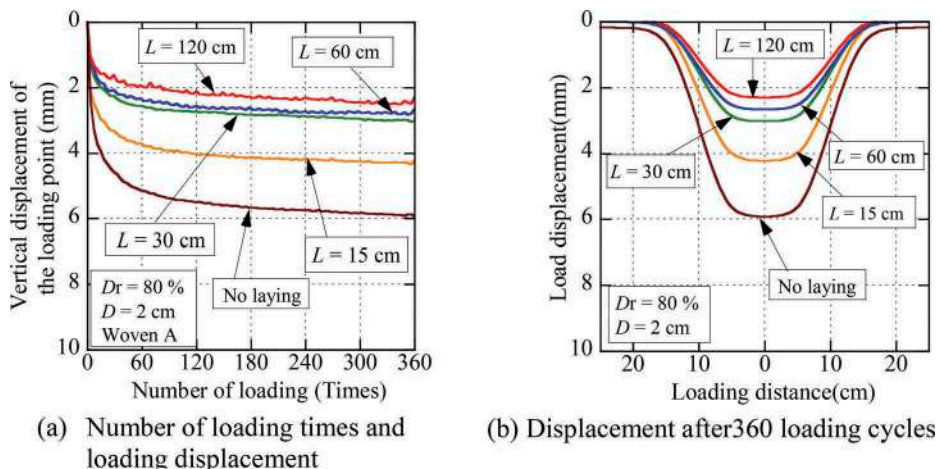


Figure 10. Effect of laying length on cyclic loading tests ($D = 2$ cm).

Photo 1 shows the state of settlement of the loaded plate after repeated loading. In the state of settlement of the loading plate, it can be seen that there is almost no deformation when $D = 2$ cm and $L = 120$ cm. This also indicates that by reducing the geotextile laying depth and increasing the laying length, all the stress acting on the ground is dispersed at a shallow position. The frictional surface with the ground material and the reinforcement effect also increases. As mentioned above, when laying geotextiles on a road, it is important to make sure a low laying depth and determine the laying length considering the wheel load.

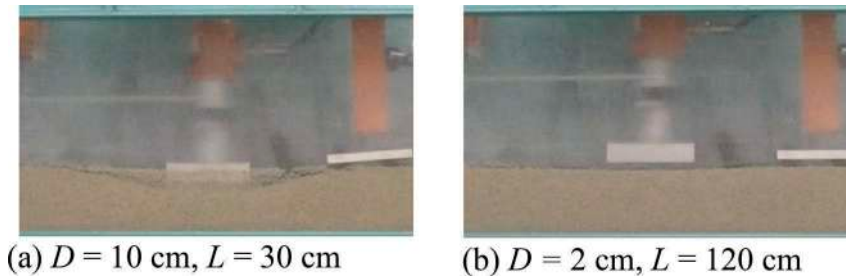


Photo 1. State of settlement of the loaded plate after repeated loading.

4 CONCLUSIONS

In this study, the importance of base course reinforcement in extending the service life of asphalt pavement was investigated by a model test using a small soil box. Therefore, the laying of geotextile was considered as a method of base course reinforcement. In this model test, the type of geotextile, its location, and length were investigated by static and cyclic loading tests. As a result, the following conclusions were obtained.

1. Geotextile is a material that can exhibit a friction effect due to a certain load displacement and can be expected to have a deformation suppressing effect when laid on the base course.
2. Geonet is a reinforcing material that can be expected to have a friction effect due to the meshing effect with the base course material.
3. Woven fabric with high tensile strength has the highest displacement suppression effect, and it can be expected to suppress deformation due to traffic load on the base course material. It can also be confirmed that the suppression of load displacement depends on the magnitude of the apparent internal friction angle and cohesion obtained by the pull-out test of woven.
4. With the decrease of laying depth of the geotextile, the load is distributed more to the evenly distributed load, the ground supporting force is increased, and the reinforcing effect is better.
5. Regarding the geotextiles put in a low laying depth, with the increase of laying length, the reinforcement effect increases because of the frictional force against the ground material, because the tensile effect of the material is generated by the frictional force.
6. If the laying depth is reduced, the effect is good even when the laying length of the geotextile is short.

In this study, silica sand was used due to the size of the model soil tank and the capacity of the loading device. Therefore, the effect of various reinforcement by geotextile will be completely different, and probably the optimal position of geotextile will also be different. The amount of deformation at which the geotextile can function as reinforcement in the base course also needs to be investigated. In the future, we plan to conduct field tests using actual base course material (crushed stone), considering rainwater infiltration through cracks in the asphalt surface layer.

REFERENCES

1. Takahashi S., Ono Y., and Sato M.: Field survey to identify the important key factors for long term durability of asphalt pavement on expressways in Japan.: *Journal of Japan Society of Civil Engineers* Vol.71, No.3, pp.93–101, (2015)(in Japanese).
2. Zomberg, J.G., Roodi, H., Sankaranarayanan, S., Hernandez-Uribe, L.: *Geosynthetics in roadways: impact in sustainable development.*: *Proceedings of the 11th International Conference on Geosynthetics* (2018).
3. Yamauchi, T.: *Geotextiles, -State of the art-*. *Journal of Japan Society of Civil Engineers* 370(III-5), 27–38 (1986) (in Japanese).
4. Takahashi, Y., Hazama, A., Tachibana, T., Kaneko, K., Kumagai, K.: *Experimental study on stability of reinforced soil wall using a high strength geotextile.* *Geo-synthetics Engineering Journal* 23, 155–160 (2008) (in Japanese).
5. Hirao, K., Yasuhara, K., Tanahashi, Y., Takaoka, K., Nishimura, J.: *Bearing capacity characteristics of model soft ground with reinforced geotextiles.* In: *Proceeding of Geotextile Symposium 7*, 1–9 (1992) (in Japanese).
6. Hirakawa, D., Miyata, Y.: *High stabilization of asphalt pavement by geogrid reinforcement.* *Geosynthetics Engineering Journal* 29, 139–146 (2014) (in Japanese).

Study of the mechanical behaviour and self-cementing properties of recycled crushed concrete aggregates

C. Wang, C. Chazallon & S. Mouhoubi

Université de Strasbourg, INSA de Strasbourg, CNRS, ICube, Strasbourg, France

P. Hornych

MAST-LAMES, Gustave Eiffel University, Bouguenais, France

P. Jing

College of Metropolitan Transportation, Beijing University of Technology, Beijing, China

ABSTRACT: Recently, the use of recycled crushed concrete aggregates (RCA) as a substitution of natural aggregates (NA) in unbound granular layers has become more popular, and can contribute for an economic and environmental sustainability of road and highway construction. Generally, the unhydrated cement in the adhered mortar of the RCA can lead to a growth in stiffness and strength in unbound layers, which is known as the self-cementing properties. However, this mechanism has not been thoroughly studied. In this study, samples of two different RCAs (old and fresh crushed concrete aggregates) after different curing time (1 day, 28 days and 180 days) are tested to study the self-cementing properties using the laboratory monotonic triaxial test and repeated load triaxial test (RLTT) which is used for the study of short-term and long-term mechanical behaviours of these recycled crushed concrete aggregates.

Keywords: Recycled concrete aggregate, resilient behavior, self-cementing properties, unbound granular material, repeated load triaxial test

1 INTRODUCTION

Each year, the economic and human activities produce a large amount of construction and demolition wastes (CDW). In 2014, over 800 million tonnes of construction and demolition wastes were generated in Europe (Saez & Osmani, 2019). Concrete wastes are main components and represent up to 75% of total CDW by weight (Nwakaire et al., 2020). These wastes are traditionally disposed in landfills which not only increase the costs of disposal but also raise the environmental concerns. As a consequence, the reuse of recycled concrete aggregates (RCA) produced by crushing concrete wastes as unbound granular materials in unbound pavement layers has become more popular in last 20 years (Arulrajah et al., 2018; Esfahani, 2020; Monroe et al., 2021; Yaghoubi et al., 2018).

RCA is composed of original NA and attached cement paste that retains some unhydrated cement. When RCA is used as unbound granular materials in pavement, after the compaction, the unhydrated cement in the attached cement paste will react with water and cause the secondary hydration of RCA. Hence, the stiffness and strength of unbound layers with RCA increase over time, which is known as self-cementing properties (Arm, 2001; Jitsangiam et al., 2015; Poon et al., 2006; Sangiorgi et al., 2015). Although many studies have been conducted to study the performance of RCA as an unbound granular material and found that the

performance of most RCA is comparable to that of NA (Arulrajah et al., 2012; Arulrajah et al., 2013; Lu et al., 2021; Saberian et al., 2018), the influence of the self-cementing properties on mechanical behavior of RCA has not been thoroughly studied.

The aim of this paper is to study the self-cementing properties and its effects on the mechanical behaviours of RCA. In this test, the pH value of two different RCA materials (old and fresh crushed concrete aggregates) are measured to evaluate their self-cementing properties. After that, the short-term and long-term mechanical behaviours of RCA materials after different curing time (1 day, 28 days and 180 days) are tested by monotonic triaxial test and repeated load triaxial test (RLTT).

2 MATERIALS AND METHODS

2.1 Materials

In this study, two different RCA materials obtained from demolished buildings and crushed in recycling plants in Strasbourg, France, are tested:

- Old RCA was crushed eight years ago and stored in plastic bags, named ORCA.
- New RCA was crushed recently, named NRCA.

The main properties of two RCA materials are summarized in Table 1. The particle size distributions and Modified Proctor curves for ORCA and NRCA are shown in Figures 1 and 2. The maximum particle size is 20mm.

2.2 Self-cementing properties

The self-cementing properties of RCA are evaluated by pH value that could indicate the presence of unhydrated cement (Poon et al., 2006; Prosek et al., 2020). For pH value measurement,

Table 1. Properties of RCA materials.

Materials	Particle density-coarse (10-20mm) Mg/m ³	Water absorption-coarse (10-20mm) %	Fine content (63µm) %	Grading mm	pH
ORCA	2.57	4.30	2.2	0/20	10.53
NRCA	2.65	4.64	2.1	0/20	13.07

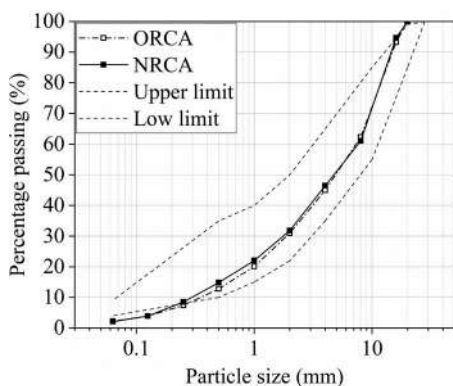


Figure 1. Particle size distributions of ORCA and NRCA.

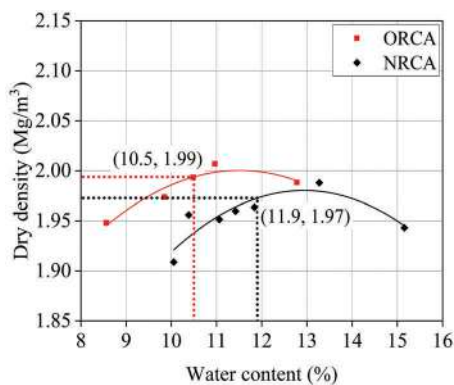


Figure 2. Modified Proctor curves of ORCA and NRCA.

30g of the air-dry RCA fines (0-2mm) and 75g of distilled water are mixed for 2 minutes (BS 1377-3, 2018). The pH value of each suspension is measured after 24h. The pH values of two RCA materials are provided in Table 1. The results show that the pH value of the solution prepared with NRCA is the highest compared to that of ORCA. This result is expected because after eight years of storage, the ORCA is carbonated and some unhydrated cement in the ORCA has already reacted with moisture. This implies that the NRCA contains more hydration products and exhibits very obvious self-cementing properties.

2.3 Specimen preparation

The mixtures are prepared with a water content equal to optimum Proctor moisture content minus 1%, and the dry density is obtained from the Proctor curve, as shown in Figure 2. The targeted water content and targeted dry density for each RCA are summarized in Table 2. The samples are compacted at a diameter of 150mm and a height of 285mm with vibrating hammer in 7 layers. After compaction, the samples are wrapped in plastic foil and stored indoors for 1 day and 28 days (180 days for NRCA) to study the short-term and long-term mechanical behaviours of RCA.

Table 2. Targeted water content and dry density.

Materials	Optimum moisture content (%)	Maximum dry density (Mg/m ³)	Targeted water content (%)	Targeted dry density (Mg/m ³)
ORCA	11.51	2	10.5	1.99
NRCA	12.93	1.98	11.9	1.97

3 MONOTONIC TRIAXIAL TESTS

The monotonic triaxial tests are used to study the short-term mechanical behaviour and to determine the failure line of each RCA. In monotonic triaxial tests, three different confining pressures (20 kPa, 40 kPa and 70 kPa) are applied to the samples after curing for 1 day. The confining pressures correspond to the typical stresses obtained in a pavement base layer. The tests are performed under drained conditions at the shearing rate of 0.3 mm/min until failure.

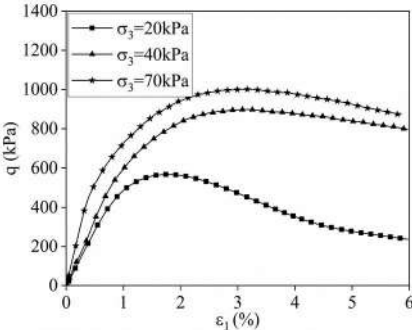


Figure 3. Stress-strain curves of NRCA.

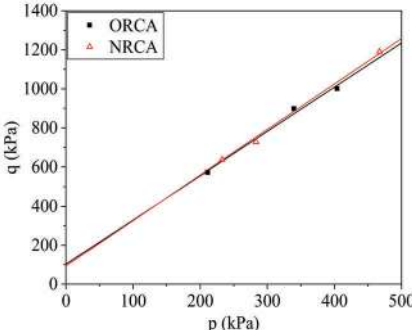


Figure 4. Failure lines of the ORCA and NRCA.

An example of stress-strain curves under different confining pressures of NRCA is shown on Figure 3. The results of monotonic triaxial tests allow to determine the failure line in the p, q stress space and calculate the friction angle φ and cohesion c of each material, as shown in Figure 4 and Table 3. The results show that the failure line, friction angle φ and cohesion c of ORCA and NRCA are similar.

Table 3. Friction angle φ and cohesion c of RCA materials.

Materials	φ (°)	c (kPa)
ORCA	57	62.5
NRCA	55.3	66

4 REPEATED LOAD TRIAXIAL TESTS

The repeated load triaxial tests (RLTT) are used to study the long-term mechanical behaviour of RCA materials after curing for 1 day and 28 days (180 days for NRCA). In this study, RLTTs are carried out following the European Standard NF EN 13286-7 (2004), which consists of a conditioning phase and followed by a resilient phase. The axial strains and radial strains are measured with Hall effect displacement transducers instrumented on the specimen.

4.1 Conditioning phase

In the conditioning phase, to stabilize the permanent strains, the sample is subjected to a constant confining pressure ($\sigma_3=70$ kPa) and a cyclic axial load ($\Delta q=340$ kPa) at the frequency of 1Hz for 20000 loading cycles. The deviatoric stress q and mean normal stress p are defined by:

$$q = \sigma_1 - \sigma_3 \quad (1)$$

$$p = \frac{\sigma_1 + 2\sigma_3}{3} \quad (2)$$

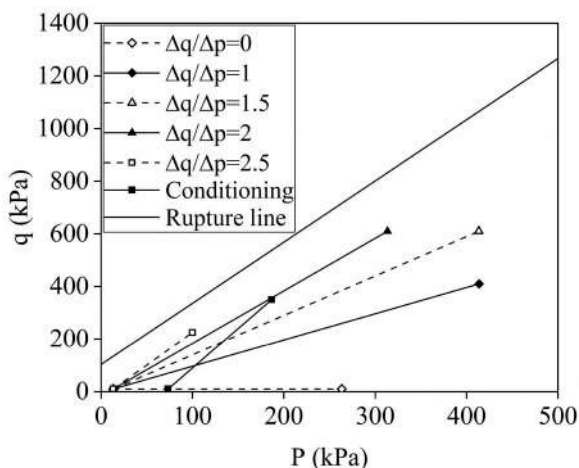


Figure 5. Stress paths for repeated load triaxial test (maximum loading).

where σ_1 is the vertical stress and σ_3 is the confining pressure. The stress path for the conditioning phase is shown in Figure 5.

Figure 6 shows the permanent axial strain ϵ_1^p evolution of RCA materials after different curing time. Since self-cementing properties of ORCA have a negligible cementation effect on permanent deformation, NRCA were cured for 180 days instead of 28 days. Each ϵ_1^p represents the mean value of two or three specimens. Since all the testing parameters, such as particle size distribution, water content (optimum moisture content minus 1%) and dry density (maximum dry density at the targeted water content) are the same for both RCA materials, the ORCA and NRCA curing for 1 day have the similar ϵ_1^p , as shown in Figure 6. After curing 28 days, ORCA presents a similar level of the ϵ_1^p compared with that of ORCA curing for 1 day. In contrast, the ϵ_1^p of NRCA is much lower after curing for 180 days. The decrease of ϵ_1^p is attributed to the presence of unhydrated cement in the NRCA and decreased water content. The results indicate that the influence of self-cementing properties on permanent deformation of NRCA is significant.

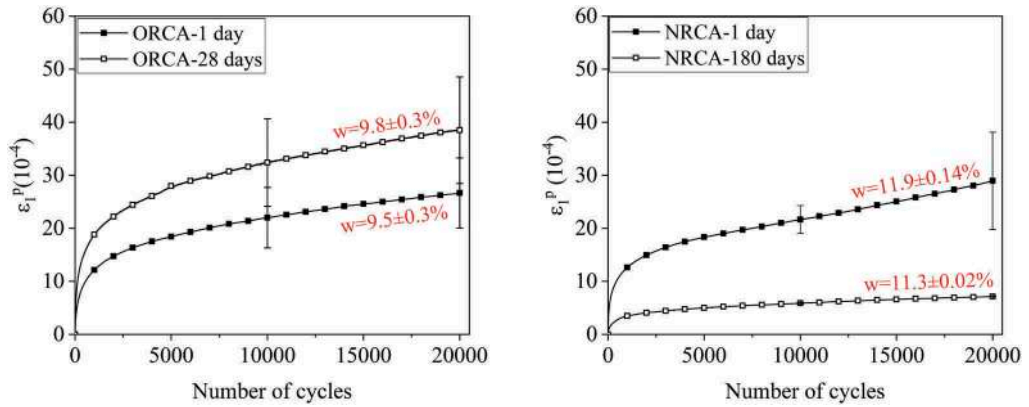


Figure 6. Permanent deformations of RCA materials curing for 1, 28 and 180 days.

4.2 Resilient behavior

For the resilient behavior study, the tests are conducted with a variable confining pressure, where both the confining pressure and the axial load are cycled in phase, after the conditioning phase. Five stress paths ($\Delta p/\Delta q=0, 1, 1.5, 2, 2.5$), with a high stress level, are applied on the same sample at the frequency of 0.1 Hz. Each stress path contains 100 loading cycles, and the last five cycles in each stress path are used to calculate the resilient strains. The stress paths for the resilient phase are also shown in Figure 5.

The resilient deformation behaviour is presented by the resilient modulus E_r , resilient deviatoric strain ϵ_q^r and the resilient volumetric strain ϵ_v^r , which are defined as:

$$E_r = \frac{\sigma_1^{r^2} + \sigma_1^r \sigma_3^r - 2\sigma_3^{r^2}}{\sigma_1^r \epsilon_1^r + \sigma_3^r \epsilon_3^r - 2\sigma_3^r \epsilon_3^r} \quad (3)$$

$$\epsilon_q^r = \frac{2(\epsilon_1^r - \epsilon_3^r)}{3} \quad (4)$$

$$\epsilon_v^r = \epsilon_1^r + 2\epsilon_3^r \quad (5)$$

where ϵ_1^r is the resilient axial strain and ϵ_3^r is the resilient radial strain.

The evolution of resilient modulus E_r for ORCA and NRCA with increasing curing time are shown in Figure 7. The results indicate a clear increase in stiffness of NRCA with curing

time, mostly because of the rehydration of unhydrated cement in the NRCA. Similar results for RCA were also observed by Arm (2001) and Jitsangiam et al. (2015). However, there is no increase of E_r for ORCA.

Figures 8 to 11 present the resilient deviatoric strain ϵ_q^r and the resilient volumetric strain ϵ_v^r for ORCA and NRCA after different curing time (1 day, 28 days and 180 days). The results show that the resilient deformation behaviour of RCA after different curing time is very similar to that of unbound granular materials (UGM) whose resilient deformation is strongly non linear (Hornych et al., 1998; Jing et al., 2017). For this reason, the Modified Boyce model is used to describe the resilient behaviour of RCA (Gaillard et al., 2019; Hornych et al., 1998) and calculate the characteristic resilient modulus E_c defined as the resilient modulus determined for the stress $p=250$ kPa and $q=500$ kPa.

The average parameters of the Modified Boyce model as well as the E_c obtained for all the tests are summarized in Table 4. As expected, the E_c of NRCA increased from 382 MPa to 455 MPa after curing 180 days. Furthermore, a good agreement between the experimental results and predicted results are obtained with this model. The parameters of the ORCA and NRCA after curing different time are of the same order of magnitude.

Table 4. The modified Boyce model parameters for ORCA and NRCA.

Material	Curing time day	Ka MPa	Ga MPa	n	γ	Correlation	E_c MPa
ORCA	1	54.01	54.03	0.52	0.66	0.926	379
	28	46.12	51.85	0.48	0.69	0.914	348
NRCA	1	39.67	51.80	0.47	0.64	0.949	382
	180	33.06	54.99	0.51	0.55	0.904	455

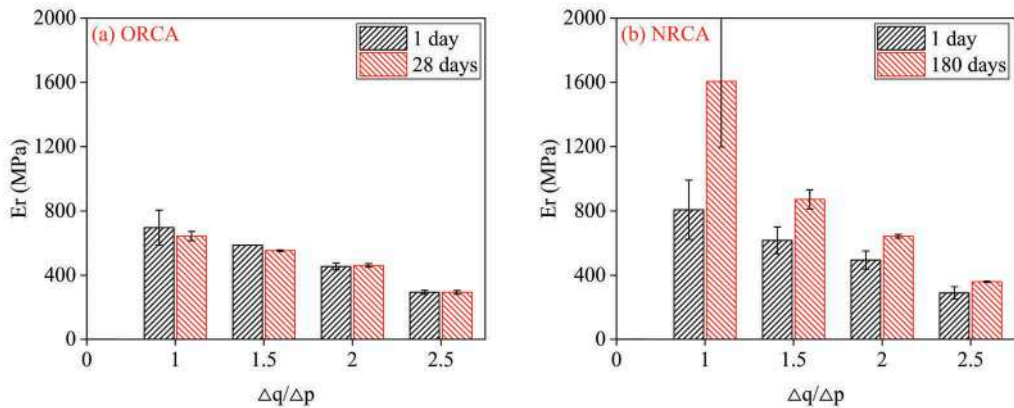


Figure 7. Resilient modulus E_r of ORCA and NRCA curing for different time.

Besides, the influence of self-cementing properties on the resilient strains for these different RCA is quite different. For ORCA which exhibited poor self-cementing properties the ϵ_q^r and ϵ_v^r are the same after curing 1 day and 28 days. However, for NRCA, there are large decrease of ϵ_q^r and increase of ϵ_v^r after curing 180 days. Generally, for RCA materials which have strong self-cementing properties, the resilient axial strain ϵ_1^r decreases after curing which leads to an increase of stiffness. However, a clear increase of resilient contractant behavior ϵ_v^r is also observed in this study, with increasing compressive radial strains ϵ_3^r for the cured NRCA, as shown in Figure 11. The results indicate that the influence of self-cementing properties on the resilient behaviour of NRCA is significant.

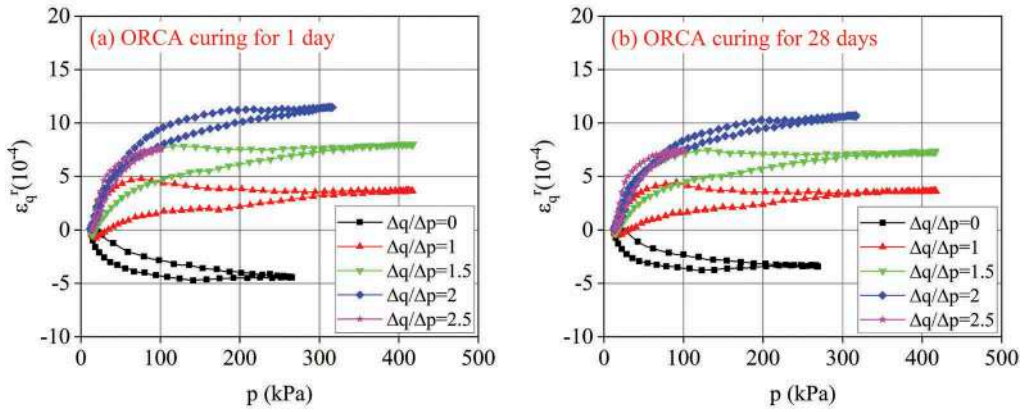


Figure 8. Deviatoric strain ε_q^r of ORCA curing for 1 day and 28 days.

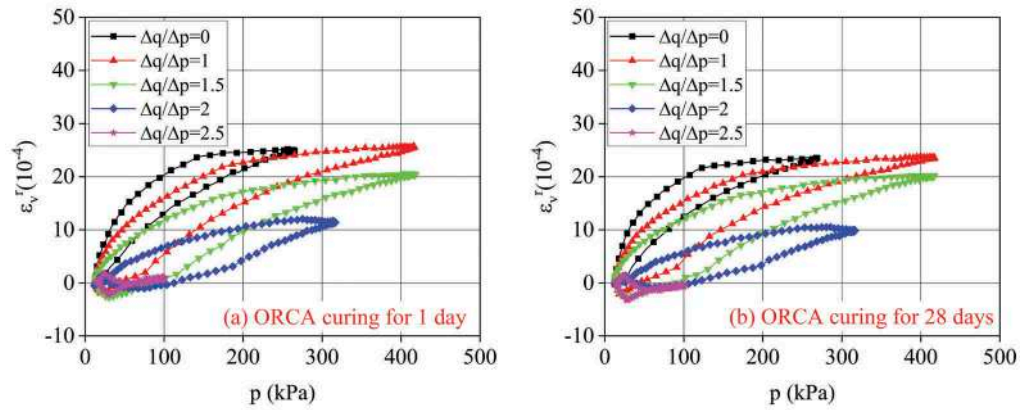


Figure 9. Volumetric strain ε_v^r of ORCA curing for 1 day and 28 days.

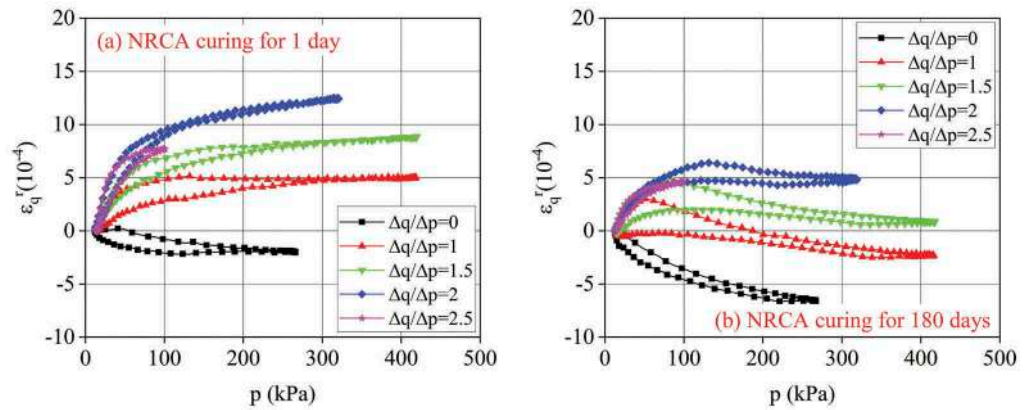


Figure 10. Deviatoric strain ε_q^r of NRCA curing for 1 day and 180 days.

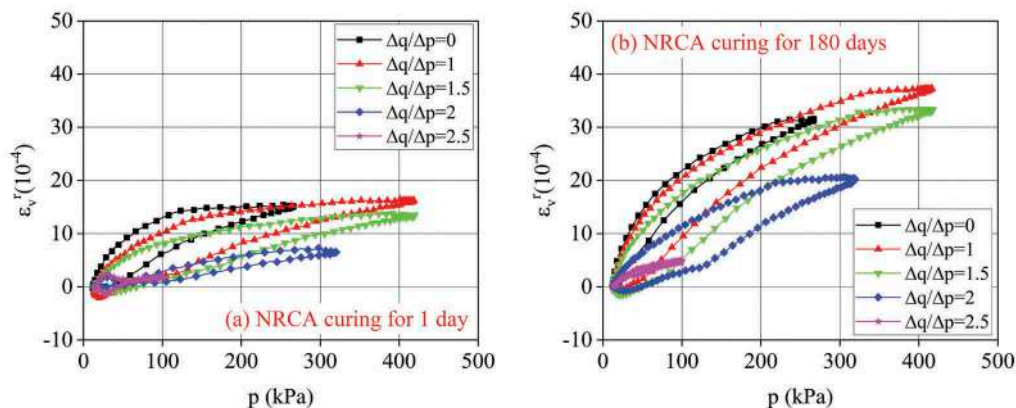


Figure 11. Volumetric strain ϵ_v^r of NRCA curing for 1 day and 180 days.

5 CONCLUSIONS

This work was carried out to study the influence of self-cementing properties on the mechanical behaviours of RCA materials. The self-cementing properties of two different RCA are evaluated by pH value. The short-term and long-term mechanical behaviours of those RCA materials after different curing time are studied by monotonic triaxial tests and repeated load triaxial tests.

The study shows that the NRCA, fresh crushed concrete aggregates, has very high pH value and exhibits very obvious self-cementing properties. However, the ORCA, old concrete aggregates crushed eight years ago, has low pH value and exhibits poor self-cementing properties. It seems, therefore, the unhydrated cement content decreases with increasing storage time.

The RLTT results show that the long-term mechanical behaviour of RCA is greatly influenced by the self-cementing properties. The permanent deformation and resilient deviatoric strain of NRCA decrease while resilient modulus and resilient volumetric strain increases a lot after curing 180 days. However, the permanent deformation and resilient deformation of ORCA have no change after curing 28 days because of poor self-cementing properties.

ACKNOWLEDGMENTS

This work is supported by the China Scholarship Council.

REFERENCES

- Arm, M. (2001). Self-cementing properties of crushed demolished concrete in unbound layers: results from triaxial tests and field tests. *Waste Management*, 21(3), 235–239.
- Arulrajah, A., Imteaz, M., Horpibulsuk, S., Du, Y. J., & Shen, J. S. L. (2018). Recycled concrete aggregate/municipal glass blends as a low-carbon resource material for footpaths. *Road Materials and Pavement Design*, 19(3), 727–740.
- Arulrajah, A., Piratheepan, J., Ali, M. M. Y., & Bo, M. W. (2012). Geotechnical Properties of Recycled Concrete Aggregate in Pavement Sub-Base Applications. *Geotechnical Testing Journal*, 35(5), 743–751.
- Arulrajah, A., Piratheepan, J., Disfani, M. M., & Bo, M. W. (2013). Resilient Moduli Response of Recycled Construction and Demolition Materials in Pavement Subbase Applications. *Journal of Materials in Civil Engineering*, 25(12), 1920–1928.
- BS 1377-3. (2018). Methods of test for soils for civil engineering purposes. Part 3: chemical and electro-chemical testing.
- Esfahani, M. A. (2020). Evaluating the feasibility, usability, and strength of recycled construction and demolition waste in base and subbase courses. *Road Materials and Pavement Design*, 21(1), 156–178.

- Gaillard, L., Chazallon, C., Hornych, P., Quezada, J. C., & Raab, C. (2019). Thermo-hydro-mechanical behaviour of cold reclaimed asphalt aggregates without binder addition. *Road Materials and Pavement Design*, 20, S49–S63.
- Hornych, P., Kazai, A., & Piau, J. M. (1998). *Study of the resilient behaviour of unbound granular materials*. In Proceedings of the 5th Conference on Bearing Capacity of Roads and Airfields, Trondheim, Norway.
- Jing, P., Nowamooz, H., & Chazallon, C. (2017). Effect of Anisotropy on the Resilient Behaviour of a Granular Material in Low Traffic Pavement. *Materials*, 10(12), 1382.
- Jitsangiam, P., Boonserm, K., Phenrat, T., Chummuneerat, S., Chindaprasirt, P., & Nikraz, H. (2015). Recycled Concrete Aggregates in Roadways: Laboratory Examination of Self-Cementing Characteristics. *Journal of Materials in Civil Engineering*, 27(10), 04014270.
- Lu, C., Chen, J. Y., Gu, C., Wang, J., Cai, Y. Q., Zhang, T. T., & Lin, G. (2021). Resilient and permanent deformation behaviors of construction and demolition wastes in unbound pavement base and sub-base applications. *Transportation Geotechnics*, 28, 100541.
- Monrose, J., Tota-Maharaj, K., & Mwasha, A. (2021). Assessment of the physical characteristics and stormwater effluent quality of permeable pavement systems containing recycled materials. *Road Materials and Pavement Design*, 22(4), 779–811.
- NF EN 13286-7. (2004). Unbound and hydraulically bound mixtures – Part 7: Triaxial test under cyclic loading for unbound mixtures.
- Nwakaire, C. M., Yap, S. P., Onn, C. C., Yuen, C. W., & Ibrahim, H. A. (2020). Utilisation of recycled concrete aggregates for sustainable highway pavement applications; a review. *Construction and Building Materials*, 235, 117444.
- Poon, C. S., Qiao, X. C., & Chan, D. X. (2006). The cause and influence of self-cementing properties of fine recycled concrete aggregates on the properties of unbound sub-base. *Waste Management*, 26(10), 1166–1172.
- Prosek, Z., Trejbal, J., Nezerka, V., Golias, V., Faltus, M., & Tesarek, P. (2020). Recovery of residual anhydrous clinker in finely ground recycled concrete. *Resources Conservation and Recycling*, 155, 104640.
- Saberian, M., Li, J., Nguyen, B., & Wang, G. (2018). Permanent deformation behaviour of pavement base and subbase containing recycle concrete aggregate, coarse and fine crumb rubber. *Construction and Building Materials*, 178, 51–58.
- Saez, P. V., & Osmani, M. (2019). A diagnosis of construction and demolition waste generation and recovery practice in the European Union. *Journal of Cleaner Production*, 241, 118400.
- Sangiorgi, C., Lantieri, C., & Dondi, G. (2015). Construction and demolition waste recycling: an application for road construction. *International Journal of Pavement Engineering*, 16(6), 530–537.
- Yaghoubi, E., Disfani, M. M., Arulrajah, A., & Kodikara, J. (2018). Impact of compaction method on mechanical characteristics of unbound granular recycled materials. *Road Materials and Pavement Design*, 19(4), 912–934.

High content of Reclaimed Asphalt Pavement (RAP) in asphalt mixtures – optimal use of rejuvenators

T. Jørgensen & T.H. Fiske

Norwegian Public Roads Administration, Oslo & Trondheim, Norway

R. Telle

Norwegian Road Technology Institute (VTI), Bærum, Norway

ABSTRACT: In 2019 approximately 45 % of RAP was used in new asphalt mixes in Norway. The national objective to implement circular economy, motivates a much higher recycling rate. It is also important that high recycling rates can be made without health and safety, or environmental hazards. The rejuvenated RAP binder in the new mix should not age more than normal for the target bitumen grade.

Norwegian RAPs often consist of relatively modestly aged binder. Quite soft bitumen grades are used, and asphalt wear and tear from studded tyres shortens pavements life. Less use of studded tyres will increase the pavement life, and the use of more deformation resistant pavements do likewise. In the future, RAP-binders will be harder and more aged than today.

A laboratory study simulates 50 % RAP added to fresh asphalt mixture. Recovered bitumen from two RAP-granulates were softened by commercial rejuvenators, to the target penetration grade 160/220. Granulate one was little aged and granulate two were considerable aged. The blends were then blended with an equal amount virgin 160/220 bitumen.

The binder tests on fresh binder; binder after RTFOT-ageing; binder after one and two PAV long term ageing cycles, were: penetration, softening point, Fraass' breaking point, DSR (G*) and MSCRT (Jnr and R%). The blends were tested for water affinity and water susceptibility with a stripping prone aggregate. The test methods used were the Rolling Bottle Test and the Shaking Abrasion test (Vändskak-test).

A practical approach is proposed on how to calculate the proportion of rejuvenator and RAP-binder in the blend, aiming to achieve same viscosity as target bitumen. The calculations are based on expected hardness and viscosity of RAP-bitumen, and viscosity of rejuvenator. Such calculations can be helpful in estimating the suitable rejuvenator dosage in the asphalt mixture.

Keywords: Reclaimed asphalt, bitumen, rejuvenator, test methods, blending

1 INTRODUCTION

1.1 Background

In 2019 approximately 45 % of RAP (reclaimed asphalt pavement) was used in new asphalt mixes in Norway. The national objective to implement circular economy, motivates a much higher recycling rate. It is important that high recycling rates can be made without health and safety or environmental hazards. The rejuvenated RAP binder in the new mix should not age more than normal for the target bitumen grade.

In Norway the normal binder in asphalt concrete (wearing course) is 70/100 for main roads, and 160/220 for secondary roads with lower traffic. A high RAP-dosage in asphalt mixes with 160/220 bitumen will often result in a too high binder content when a softer bitumen grade is added to the RAP. The ability to penetrate and blend with the RAP-granulate binder is also limited. Both drawbacks are mitigated by using a low viscosity rejuvenator. The rejuvenator should increase both blending and dispersion of hard bitumen components of the aged RAP-binder.

Norwegian RAPs often contain relatively modestly aged binder. Modestly soft bitumen grades are used in virgin asphalt, and asphalt wear and tear from studded tyres shortens the pavements life. Penetration ranges of recovered bitumen from 98 RAP-samples are visualised in Figure 1 [KFA, 2019].

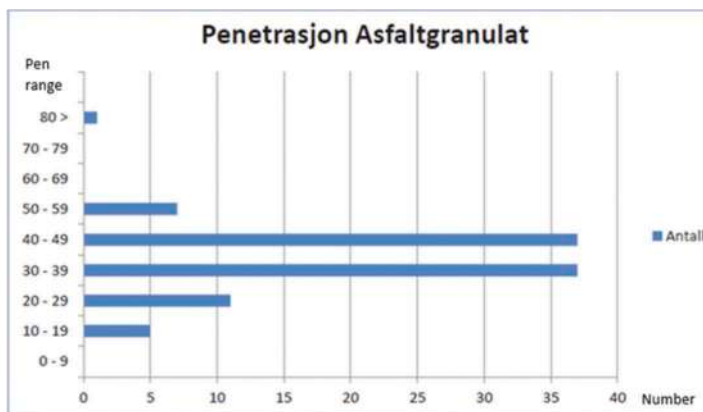


Figure 1. Penetration values of recovered RAP bitumen. Number of results in different penetration ranges.

In Norway, less use of studded tyres and more durable pavements will increase pavement lifetime. RAP-binders will age more and become harder in the future. The benefits of very high recycling rates are both cost savings together with more sustainable roads, as demonstrated by Zaumanis [Zaumanis & al, 2014].

The aim of this project was to assess a selection of rejuvenators. Both the ability to soften aged RAP-binder, and a routine to find the correct dosage to the RAP binder were investigated.

1.2 Project organization & acknowledgements

The project started late 2018 with participation from Norwegian Public Roads Administration (NPRA), Info-centre for recycling of asphalt (KFA), Norwegian Road Technology Institute (VTI) and Nynas Bitumen Norge.

In a preliminary study, laboratory activities were planned, and materials selected. Three rejuvenator products were supplied by their producers together with user information and MSDS (Health and Safety Data Sheet)

VTI and KFA collected RAP-samples and their laboratory extracted and recovered the aged binder. The NPRA's asphalt laboratory carried out binder and adhesion testing. The preliminary study also included a Master thesis [Aslam & Yousef, 2019]. Their report describes plans for the study, and laboratory works in 2019.

In the first round of testing in 2019 a rather soft recovered RAP-binder was used. In 2020 it was decided to extend the investigation with a harder RAP-binder. This second round of testing also included two new rejuvenators.

2 MATERIALS

2.1 Rejuvenators

Rejuvenators are agents intended to restore the rheological properties of the aged binder of the reclaimed asphalt. They cannot bring back the chemical composition of the original binder at production stage [EAPA, 2018]. The rejuvenator shall soften the aged bitumen at low dosages and restore binder properties and performance in the asphalt mix. Thus higher addition rates, above 50 % of RAP are made possible.

Oxidation and other ageing processes lead to increased molecule weight of the largest binder component, asphaltenes [Hunter, Self, & et al., 2015]. The asphaltenes in aged bitumen also tend to cluster and agglomerate in larger structures. A rejuvenating agent should be able to disperse these asphaltene structures, making the colloid stability of the rejuvenated binder more like that of a fresh bitumen.

There are different types of rejuvenators from different raw materials and manufacturing processes. Solvents are not rejuvenators since their effect are temporary. Their blends harden and age faster compared to fresh bitumen.

The products in this study were selected as relevant for the Norwegian market. So far there is little experience with rejuvenators. RAP is often added in low rates, and most RAP bitumen are modestly aged. Table 1 shows materials tested in this study. None of the products are labelled as health hazardous in their safety data sheets.

Table 1. Materials in the study.

Binders and juvenator samples	Origin	Product information
RAP-bitumen	Aged asphalt pavement	Recovered bitumen from asphalt granulate
160/220 bitumen	Fresh	Flash point (Coc) > 220 °C
Rejuvenator Rej1	Refined vegetable oil	Liquid at room temperature. Flash point > 175 °C
Rejuvenator Rej2	Refined tall oil	Liquid at room temperature. Flash point > 270 °C
Rejuvenator Rej3	Refined mineral oil	Liquid at room temperature. Flash point > 210 °C
Rejuvenator Rej4	Modified fat acid	Solid, melting point appr. 60 °C. Flash point > 170 °C
Rejuvenator Rej5	Modified vegetable oil	Liquid at room temperature. Flash point > 250 °C

2.2 Blends of granulate bitumen and rejuvenator

The experimental plan was to simulate 50 % recycling, with the target bitumen 160/220. With a hard granulate bitumen, 160/220 properties can be achieved with a rejuvenator without creating problem with too high binder content in the final asphalt mix. Softening point of the reference 160/220 was target value for the rejuvenated RAP-bitumen. The test samples consisted of 50 % fresh 160/220 and 50 % rejuvenated RAP-bitumen.

3 BLENDING TABLES

With limited amount of recovered granulate bitumen available, it is important to find the correct dosage of rejuvenator spending less material and time. Blending tables were developed, based on 60 °C viscosities of granulate bitumen and rejuvenators [Jørgensen & Fiske, 2021].

Rejuvenator viscosities should be available from the suppliers. RAP-bitumen viscosities were estimated from penetration and softening point data. Viscosity of unmodified bitumen can also be estimated from DSR complex modulus (G^*) values. The blending proportions are calculated by use of formula (1), based on viscosity values in mPas.

$$\log \log (V) = A \log \log V_a + B \log \log (V_b) \quad (1)$$

V: Viscosity of the blend V_a : Viscosity of granulate bitumen V_b : Viscosity of rejuvenator

A: portion of granulate bitumen B: portion of rejuvenator $A + B = 1,00$

Figure 2 shows the percentage of rejuvenator in blends with granulate bitumen of different hardness. The needed percentage of using a softer bitumen grade (250/330) illustrates the large amount needed, compared to the rejuvenators. The blending tables estimate theoretical dosage of rejuvenator to RAP-bitumen. In the next step the value is checked and corrected by trial blends close to the theoretical dosage.

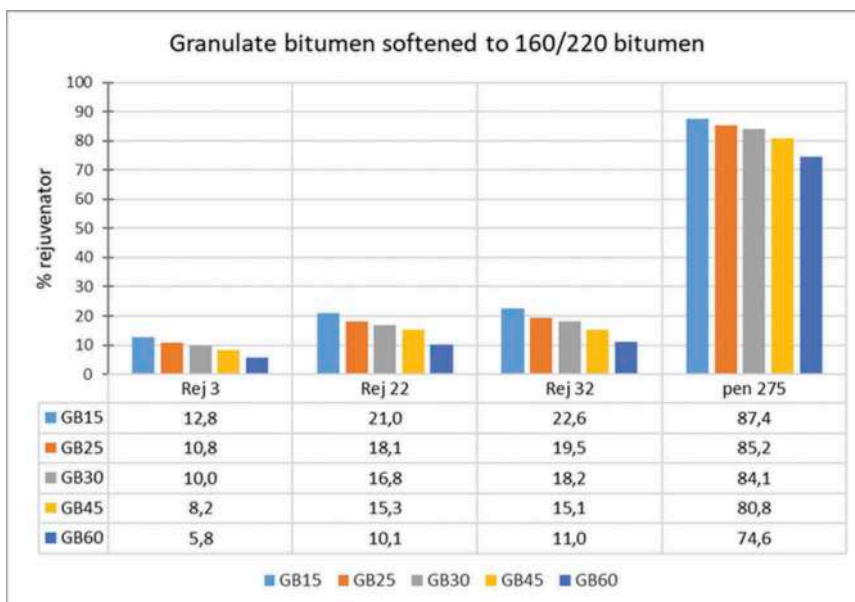


Figure 2. Percentage rejuvenator in blends giving penetration grade 160/220. Granulate bitumen (GB) with given penetration and rejuvenator (Rej) with given viscosity in mPas.

4 LABORATORY TESTING

4.1 Binder testing

EAPA's recommended route for assessing rejuvenators were followed [EAPA, 2018]. Hard granulate bitumen (penetration 24) was blended with rejuvenator and 160/220 bitumen (penetration 160) to give a 160/220 bitumen with softening point 38 °C. European Standards for laboratory testing of bituminous binders were used. The test program is shown in Table 2.

Table 2. Test program.

Test method	Fresh blends	Short term aged RTFOT	Long term aged RTFOT+PAV	Double long- term aged RTFOT+2PAV
DSR Complex modulus, G*	x	x	x	x
Multiple Stress Creep Test (MSCRT Jnr)	x	x	x	x
DSR temperature susceptibility of G* in the range 0 °C – 70 °C	x	x	x	x
Softening point	x	x	x	x
Penetration	x	-	-	-
Fraass' breaking point	-	x	x	-

Water susceptibility (Shaking abrasion test) and adhesion/affinity (Rolling bottle test) testing using a stripping prone aggregate, was carried out. The blending portions of granulate bitumen (RAP-bitumen) and rejuvenator are shown in Table 3. Softening point, penetration and viscosity were tested to confirm that the blend complied with a 160/220. The Rej4 blend was a bit special since this agent has a modifying effect, probably due to its high melting point.

Table 3. Blending portions of granulate bitumen and rejuvenator to restore a 160/220 and test results of the blends.

Rejuvenator	Portion of granulate bitumen	Portion of rejuvenator	Softening point of blend, °C	Penetration of blend, dmm	Viscosity 60°C of blend, Pas *
Rej1	0,926	0,074	37,0	206	66,9
Rej2	0,877	0,123	36,8	201	65,3
Rej3	0,847	0,153	39,8	146	80,2
Rej4	0,885	0,115	41,2	154	32,2
Rej5	0,870	0,130	36,8	200	63,3

DSR measurement of η^ (complex viscosity)

Figure 3 shows results of softening point and of temperatures when the shear modulus (G^*) equals 15 kPa. For unmodified bitumen there is a good correlation between the two methods.

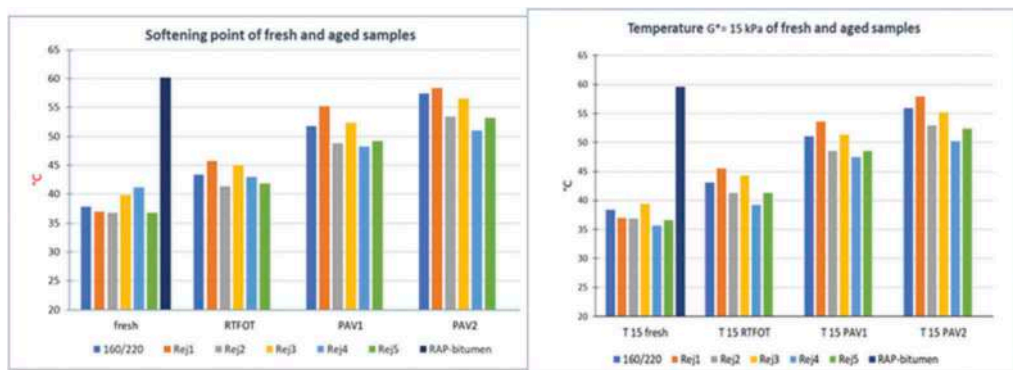


Figure 3. Softening point and temperature where G^* equals 15 kPa of fresh and aged blends.

This good correlation is shown in Figure 4, where the temperature ($G^* = 15$ kPa) against softening point correlates well ($R^2 = 0,971$).

The two results below the trend line are blends with the high melting point rejuvenator. A modifying effect on these blends in this temperature range would be expected.

Fraass' breaking values for RTFOT and one PAV ageing are given in Figure 5. Four of the rejuvenator blends have Fraass' values on same level as the reference.

DSR measurements of temperature susceptibility of G^* was performed with a "temp-ramp" program of the rheometer. Within the temperature range, measurements were made for every 10 °C on the same test specimen. Sufficient equilibrium time and linear viscoelastic range was checked in beforehand. In Figure 6, temperatures where G^* equals 2 kPa, 15 kPa, 50 kPa, 5 MPa and 15 MPa for fresh and aged blends are indicated.

The temperature curve of Rej4 on fresh and RTFO-aged sample differs from the other samples. This is probably due to its high melting point. For PAV-aged samples this deviation has disappeared, and all temperature curves have similar gradient. The temperature curve of recovered RAP-bitumen shows that it is harder than the double PAV-aged samples.

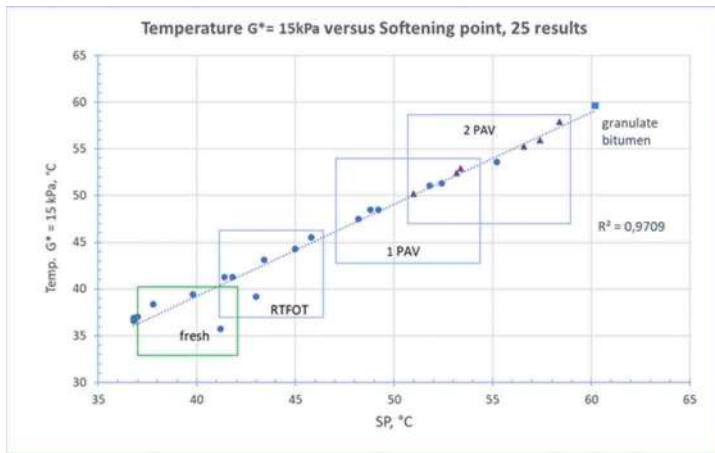


Figure 4. Plot of softening point against temperature ($G^*=15$ kPa) for fresh and aged blends.

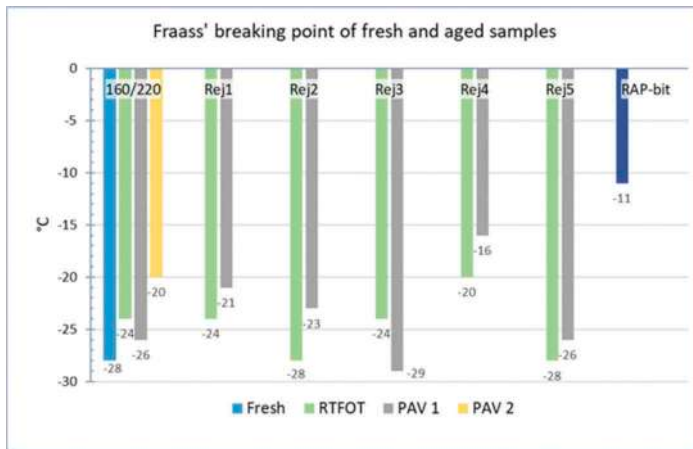


Figure 5. Fraass' breaking point values.

Results from MSCRT-testing are shown in Figures 7 and 8.

The elastic recovery increases markedly through the ageing steps. The J_{nr} -value decreases upon ageing. Hardening and increased elastic recovery of the binder make the J_{nr} -values lower.

4.2 Water susceptibility and adhesion

Water susceptibility was tested with the vändskak test on 0/4 mm asphalt specimens, 30 mm diameter and 27 mm height [Ulmgren, N., 2004]. The test is a modified shaking abrasion test [EN 12274-7, 2005]. Test specimens were water saturated and conditioned at 40 °C in a water bath for 48 hours, before abrasion testing. Test specimens were put in tubes filled with water and rotated 20 rpm for three hours. The abrasion value (% particle loss) was determined by weighing. Figure 9 shows the apparatus and asphalt specimens before testing.

Table 4 and Figure 10 show results from the vändskak test on water susceptibility.

The test results show that no product work as adhesion agent. There was no negative effect on the used adhesion agent (amine).

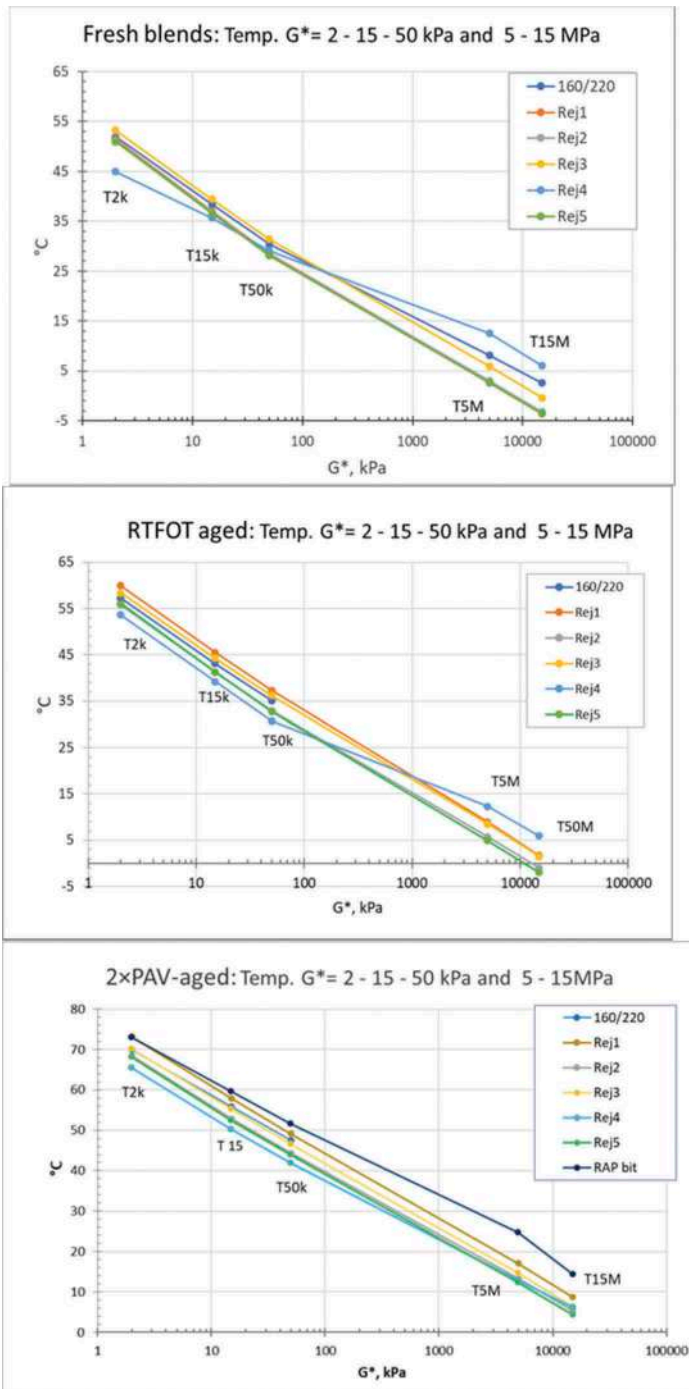


Figure 6. Temperature curves of G^* -values for fresh and aged blends. Temperatures where G^* equals 2 kPa, 15 kPa, 50 kPa, 5 MPa and 15 MPa are indicated.

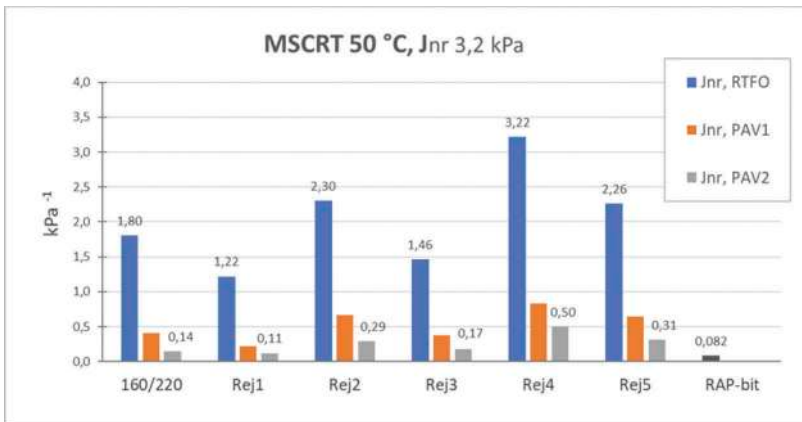


Figure 7. MSCRT-results for Jnr (non-recoverable creep compliance).

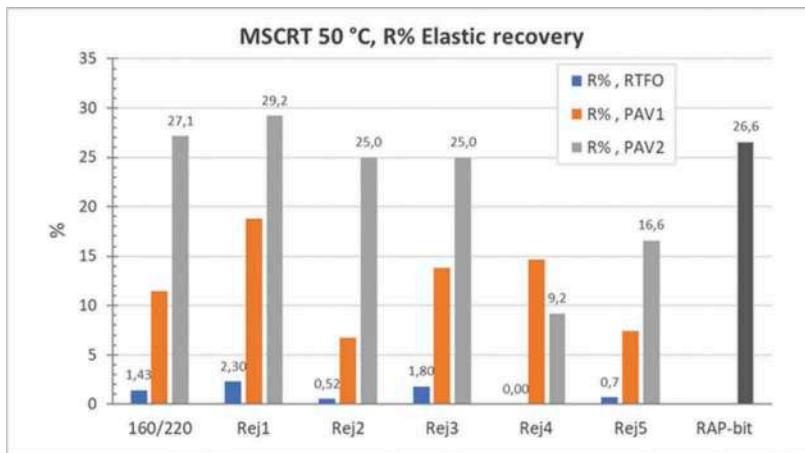


Figure 8. MSCRT-results for R% (recovered strain).



Figure 9. Apparatus and asphalt specimens for the vändskak-test (photo: O. Aslam).

Table 4. Results from vändskak test. Insufficient water susceptibility in red letters.

Blends and additive	Air void, %	Swelling, %	Abrasion, mass %
160/220 w. amine	7,9	4,8	9,8
Rej1 w. amine	8,1	3,8	10,9
Rej2 w. amine	6,8	2,7	7,5
Rej3 w. amine	7,2	3,2	10,1
250/330 w. amine	6,5	4,1	4,3
160/220	6,7	5,2	22,6
Rej1	6,6	5,0	24,4
Rej2	6,8	5,0	22,1
Rej3	8,1	3,7	24,8
250/330	7,5	5,6	21,3

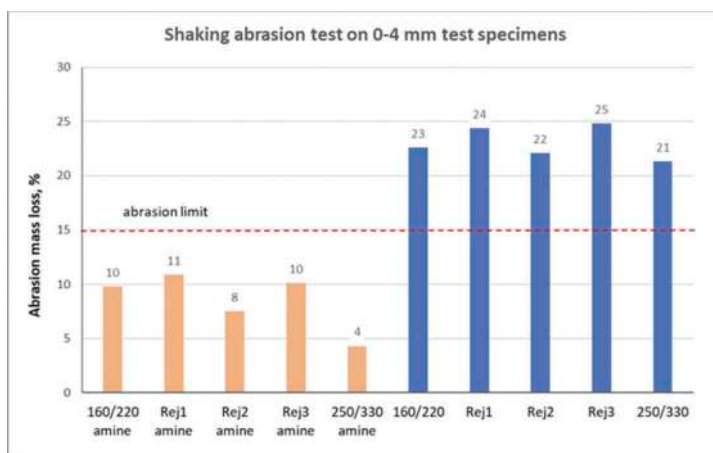


Figure 10. Abrasion values from the Vändskak (Shaking abrasion) test.

The rolling bottle test results in Figure 11 showed almost same results for the rejuvenator blends as for the reference. The aggregate is prone to stripping and adhesion agent is needed. The results of the blends without and with amine confirms that adhesion agent is needed, and that the rejuvenators don't affect the amine negatively.

5 DISCUSSIONS AND CONCLUSIONS

5.1 Comments on binder testing

There was good correlation between softening point and the temperature for $G^*=15\text{kPa}$. This is only valid for unmodified bitumen.

The Fraass' breaking point test is hampered with a rather poor reproducibility of 6°C . A test method giving reliable results and is easy to run is welcomed.

From the DSR G^* measurements, equi-stiffness temperatures can be calculated. The $G^*=15\text{MPa}$ temperatures measured were from -5°C to 10°C (Figure 7). Equi-stiffness temperatures based on DSR G^* , may be used to assess low-temperature stiffness.

DSR G^* temperature curves are useful for binder characterization.

The ageing of the blends differed only a little compared to the reference bitumen.

The blend with Rej4 (high melting point) was stiffer at lower temperatures and softer at higher temperatures. After PAV long-term ageing this effect disappeared.

Rejuvenator blends showed no negative effect in water susceptibility and adhesion tests.

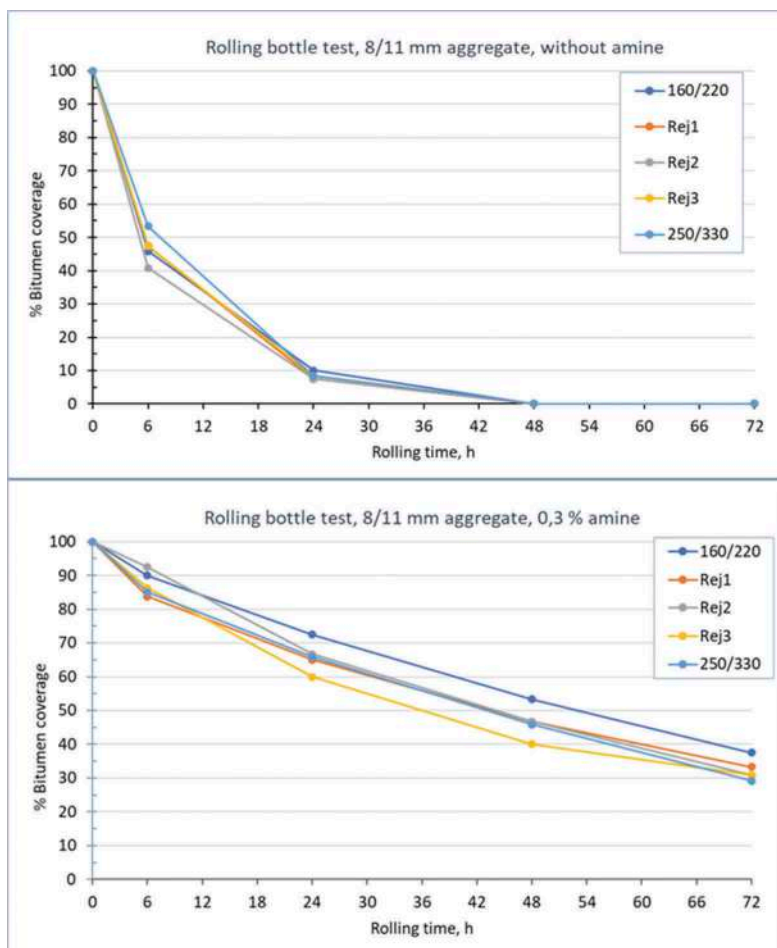


Figure 11. Adhesion (affinity) with rolling bottle test, without and with adhesion agent.

5.2 Binder content for mixes high rate of RAP

The calculated binder content demonstrates the benefit of adding low viscosity rejuvenator to the RAP. For mixes with high RAP-dosage, e.g. 50 % with hard RAP-bitumen, use of a softer bitumen grade is impossible due to excess binder content.

5.3 Conclusions

The product information may not be optimal to cover Norwegian asphalt materials and practice. Softer Bitumen grades than those used in central Europe are used. Less aged RAP-bitumen are softer than normal in central Europe.

New blending tables should ease mix design and planning. Information of the recovered RAP-binder is important. Test methods should be fast and need small amount of sample.

REFERENCES

- Aslam, O., & Yousef, M., 2019. *Effekten av rejuvenatorer på aldet bitumen*. Master thesis. NMBU, Ås, Norway.
- EN 12274-7, 2005. *Slurry surfacing Test methods - Part 7: Shaking abrasion test*. European Committee for Standardization, Brussels, Belgium.

- Hunter, Self, & al., 2015. *Shell Bitumen Handbook, sixth ed.* ICE Publishing, London, UK.
- Jørgensen, T., Fiske, T. H., 2021. *KFA rejuvenatorprosjekt: Laboratorieprøving av blandinger med gjenvunnet granulatbitumen.* Statens vegvesen report no. 734, Norwegian Public Roads Administration, Oslo, Norway.
- KFA., 2019. *Veileder i gjenbruk av asfalt.* Kontrollordningen For Asfaltgjenvinning, Veiteknisk institutt, Bærum, Norway.
- EAPA., 2018. *Recommendations for the use of rejuvenators in hot and warm asphalt production.* European Asphalt Pavement Association. Brussels, Belgium.
- Ulmgren, N., 2004. *The influence of the mastic on the durability of asphalt pavements as studied by the shaking abrasion test.* 3rd Euroasphalt & Eurobitume Congress, Vienna, Austria.
- Zaumanis, M., & et al., 2016. *Towards production of 100 % recycled asphalt.* Eurasphalt & Eurobitume Congress 2012, Prague, Czech Republic.

Polymer modified bitumen for runways containing 60% recycled asphalt

C.P. Plug, A.H. de Bondt & F.R. Bijleveld

Strukton Civiel West bvl/Ooms Producten bv, Scharwoude, The Netherlands

G. van Uden

AsfaltNu, Culemborg, The Netherlands

ABSTRACT: Polymer modified bitumen (PMB) with a high polymer content demonstrated its benefits for high bearing asphalt applications such as runways and taxiways at airports. Runway 18R/36L at Schiphol airport (Amsterdam) was constructed according to this principle in 2002. The asphalt construction for this runway consists of several layers of polymer modified asphalt (PMA). For major maintenance in 2021 about 600,000 m² of the runway and surrounding pavements were replaced with 150,000 tons of new asphalt containing 60% recycled asphalt (RAP) originating from the old PMA asphalt layers.

The use of RAP is common practice in the Netherlands, especially for base and bind layers. New techniques with the pre-treatment of RAP material makes it possible to use the RAP in surface courses as well without quality issues. Furthermore, several studies show that the use of RAP from the old PMA is beneficial for a new asphalt layer.

To maintain the high quality of the PMA containing RAP, strict requirements are needed for the PMB used. Because of changes in bitumen production and crude sources at refineries it has become more difficult to maintain the quality of such binders. For the mentioned project an extensive quality control of the PMB production has been established including selection of the virgin base binder. This quality control provides an optimal homogenous quality of the PMB for the entire project.

For the entire rehabilitation project approximately 3,000 tons of PMB was produced and successfully applied in the new asphalt pavements within a period of 13 weeks. This paper provides an advanced quality control methodology and demonstrates this for an actual runway project in the Netherlands.

Keywords: Polymer modified bitumen, Recycled asphalt pavement, High bearing asphalt, Polymer modified asphalt

1 INTRODUCTION

Since the early 1990s heavily polymer modified asphalt (PMA) is used at Amsterdam Airport Schiphol. Between 1990 and 2000 already over 400,000 tons of PMA has been applied in more than 20 different projects. Among these projects were new pavements like exits and aprons with full depth PMA, and reconstruction of runways and taxiways. Because of the good performances of these PMA pavements, it was decided in 2000 to specify the at that time new runway 18R/36L also with heavily modified PMA, which was completed in 2003. Major maintenance was carried

out on runway 18R/36L in early 2021. For this the old PMA was removed and replaced with new PMA for the base and bind layers in which 60% of the old PMA was reused.

Recycling of asphalt is done on a large scale in the form of partial recycling (PR) in the Netherlands. The percentages of recycled asphalt (RAP) can be without any problems and with little effort up to 60-70% of RAP for asphalt base and binder layers with the use of a parallel drum asphalt mix plant. A high percentage of RAP is also possible for surface courses. Here the quality of the RAP is the restricting factor. The quality depends on the old asphalt layer (grading, type of stone and bitumen content) and the degree of contamination in this layer during milling. For example, by fractionating and sorting the asphalt granulate (according to characteristics such as type of crushed stone and bitumen content), its usability improves and higher percentages of recycling can be achieved (also in surface courses) for new asphalt. Furthermore, recent studies show that the use of old PMA asphalt granulate can even be beneficial for the new asphalt. In combination with a heavily modified PMB and a rejuvenator it was possible to meet the desired specifications for the new base and bind layers of runway 18R/36L at Amsterdam (Schiphol) airport.

To maintain the high quality of the PMA containing RAP, strict requirements are needed for the new PMB used. Because of changes in bitumen production and crude sources at refineries it has become more difficult to maintain the quality of such binders. In this paper the aspects of producing a high quality asphalt containing a high percentage of asphalt granulate will be discussed.

2 RUNWAY 18R/36L 'POLDERBAAN' AT SCHIPHOL

Runway 18R-36R 'Polderbaan' is the westernmost runway at Schiphol Airport. With 3800 meters, the Polderbaan is the airport's longest runway and has a width of 60 meters. The runway was built in the period 2001-2003 (the asphalt layers in 2002 for the main runway and taxi ways) and officially opened on 13 February 2003. The Runway 18R-36R is only used for takeoffs in a northerly direction or for landings from a northerly direction, because of noise regulations for the environment. For this reason there is no taxiway to the northern end of the runway. The number of flight movements from Runway 18R-36R were around 80,000 landings and 65,000 takeoffs in 2018.

The asphalt construction during construction consisted of three open graded polymer modified asphalt layers with a dense graded polymer modified asphalt on top. A (tar-based) anti-skid layer was applied on top of this. The polymer modified bitumen used was a heavily modified PMB (Superpave PG 76-22; Sealoflex SFB 5-50 (HT)) to meet the tight tender specifications for rutting and reflective cracking (Nataraj et al, 2005), see Table 1. The asphalt construction was laid on a foundation of sand and a cement treated base (CTB).

Table 1. Design PMA Specification in 2003.

Description	Test method	Specification
- Permanent deformation at 40°C	EN 12697-25, part B ^{*3}	max 1.0% ^{*1}
- Mix viscosity		min 750 GPa.s ^{*1, 5}
- Permanent deformation at 60°C	EN 12697-25 part B ^{*3}	max 2.0% ^{*1}
- Mix viscosity		min 500 GPa.s ^{*1, 5}
Resistance to reflection cracks		
ITS at 0°C	EN 12697-23	Min 3.15 MPa, Av-3.5 MPa ^{*2}
Toughness at 0°C	EN 12697-23 ^{*4}	Min 11.5 mm/mm ² Av-14.0 mm/mm ² ^{*2}

*1 Average 4 tests

*2 Average 6 tests

*3 Test conditions: $\sigma_c = 0.00$ MPa; $\sigma_b = 0.40$ MPa; $T_1 = 0.2$ s; $T_0 = 0.8$ s; $N = 10,000$; blok puls

*4 Force-displacement curve

*5 Mix viscosity from slope of deformation test

3 REUSE OF POLYMER MODIFIED ASPHALT

Since around the beginning of the 1980s, polymer modified asphalt (PMA) has been used successfully on many large and small projects worldwide. The application of PMA, the lifespan of an asphalt construction can be extended, often in combination with a reduction in thickness. PMA has also proven itself, among other things, in (porous) thin noise reducing layers (thin surfacing), which without polymer modification would have an unacceptably short life-span; a thin surfacing would simply not have existed.

Because of environmental reasons nowadays, questions are being asked whether polymer modified asphalt can be reused as a partial polymer modified asphalt (PR) in new asphalt. Already at the end of the nineties of the last century, extensive research was done into this and the conclusion of this research was that by using PMA granulate, the underlay mixture would have more favorable properties and a higher resistance to permanent deformation than when using unmodified asphalt granulate. Recent research also shows that PMA can be reused without any problems. However, special attention must be paid to relatively fresh PMA granulate. This PMA must first be homogenized before with unmodified asphalt granulate before reuse in order to prevent problems during mixing. It should be borne in mind here that the milling of fresh PMA is of course a rarity and is normally not be done.

3.1 PMA granulate

The most common polymer modifications for a PMA are the SBS (Styrene-Butadiene-Styrene) polymer and the EVA (Ethylene-Vinyl-Acetate) polymer. Both polymers have specific properties and can be applied separately or combined in a PMA, depending on the desired properties and possible national specifications. Which polymer is applied can usually be characterized by means of an FTIR (Fourier Transform Infra-Red) analysis of the recovered bitumen (see Figure 1).

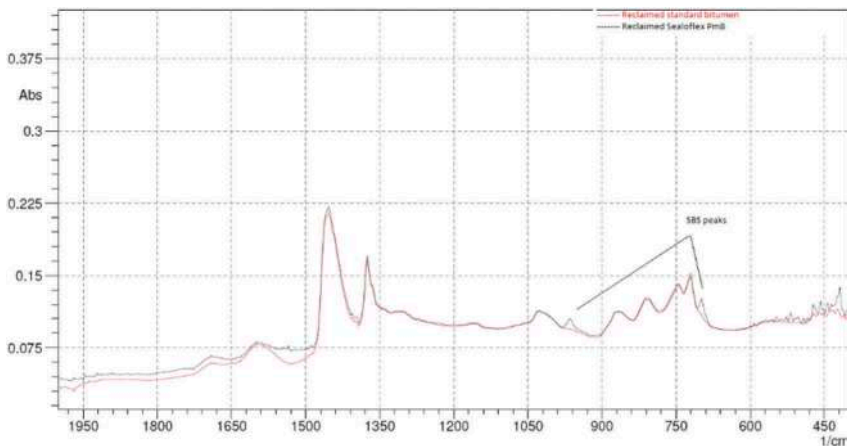


Figure 1. Example FTIR analysis of reclaimed binder from RAP (with and without PMB).

Depending on the age of the PMA, the effectiveness of the polymer will decrease over time. To what extent the effectiveness decreases depends, among other things, on the initial modification and the asphalt type. Under the influence of weather conditions a PMA will slowly age; this will also reduce the effectiveness of the polymer. As a result, the viscosity of the asphalt mixture will change and its workability will become comparable to non-modified asphalt.

Important questions for the reuse of PMA asphalt granulate are: Can the old PMA asphalt granulate be rejuvenated to the functional level of a new asphalt mixture? Does it mix

well with the new binder in the recycling process? or does it result in a 2-phase structure? Various validation projects in the Netherlands have provided answers to these questions. The results of these studies show that PMA asphalt granulate can be reused without any problems, even in Porous Asphalt surface courses (Bochove et al, 2021).

3.2 Case studies reuse of PMA

In 1997, research was carried out into the environmental aspects of old PMA ZOAB granulate (Tauw, 1998). This research showed that the emission of the PMA granulate was on the same level as of non-modified asphalt granulate. This is also to be expected, because the chemical structure of the polymers used (mostly EVA (ethylene vinyl acetate) or SBS (styrene butadiene styrene)) are not chemically different than the components of which bitumen consists.

Also in 1997, the laboratory of the Dutch Road Authorities conducted a research for highly stable asphalt mixture (AC base 22) using 40% old PMA Porous Asphalt granulate. The conclusion of this research was that by using PMA granulate, the mentioned base asphalt mixture had more favorable properties and a higher resistance against permanent deformation than when non-modified asphalt granulate was used (DWW, 1997).

In 2005, an improved version of the above mentioned AC base 22 with 40% PMA Porous Asphalt granulate was used on the Dutch motorway A12 (between Grijsoord-Waterberg). In this project the fresh new bitumen component was also replaced by a polymer modified bitumen. This asphalt mixture was examined intensively during production and processing and no problems were encountered during the implementation (Van Kleef, 2005).

A more recent European study (RECYPMA, 2013) also shows that PMA granulate is a valuable building material for reuse. In this 2-year European study, research was carried out on a laboratory scale into the possibilities of using PMA granulate. The research showed that PMA granulate still contains an active polymer content, which can be beneficial in new asphalt mixtures. For this the PMA granulate has to be properly homogenized and characterized in order to make (optimal) use of the benefits.

As stated reuse of PMA RAB is therefore not a problem, either in theory or in practice. However, special attention should be paid to 'fresh' PMA granulate that has been in the road for less than about 1 year. This PMA granulate may have properties (such as a high viscosity), as a result of which it cannot be mixed by a parallel drum mixing system that is often used in the Netherlands at temperatures of 120 to 130 °C. Such PMA granulate should therefore be homogenized with unmodified asphalt granulate beforehand. The latter is more of a practical problem than a reason why PMA granulate cannot be used in new asphalt.

Furthermore, laboratory tests according to the Dutch CE-marking systematic show that it can be beneficial to use PMA granulate. As can be seen in Table 2, which show the results of 2 Dutch AC 16 surf 40/60 (40% asphalt granulate) mixtures with standard asphalt granulate and PMA granulate according to the Dutch standard RAW specifications 2015.

Table 2. Example effect PMA granulate on asphalt properties AC 16 surf 40/60 (40% RAP).

Asphalt properties	Standard RAP	PMA-granulate	Dimension
Water sensibility ITSR	98	103	%
Stiffness S_{mix}	7200	6970	MPa
Resistance against deformation f_c	0.22	0.08	µm/m/s
Resistance against fatigue ε₆	132	213	µm/m

In particular, the fatigue resistance will increase by applying PMA granulate. A difficulty here is that it is often not known whether asphalt granulate has been modified (and to what extent). A homogeneous PMA granulate will therefore hardly ever be available. Preparing a type test for an asphalt mixture with PMA granulate is therefore only worthwhile if sufficient

homogeneous PMA granulate of the same quality is also available for production. As for renovation of runway 18R/36L at Schiphol this was the case.

3.3 Polymer modified asphalt with high content of RAP

The use of polymer modified asphalt (PMA) is common in heavily loaded asphalt constructions such as runways. The advantages of a PMA is (depending on the polymer modification) that the asphalt lasts longer and/or can be applied in a thinner construction.

By combining a (heavily modified) PMA with 50-60% asphalt granulate (standard unmodified RAP) an asphalt can be produced with excellent properties in comparison with a conventional AC-binder/base asphalt mixture, making it possible to reduce the total layer thickness, resulting in a reduction of the overall Environmental Cost Indicator (lower ECI per m² of asphalt). By applying 50%-60% asphalt granulate, there are no special requirements for the asphalt granulate and this type of asphalt can be produced relatively easily at almost any asphalt plant with a parallel drum system.

In September 2012, this so called hybrid asphalt was applied for the first time on a large scale on the newly constructed road section of the Dutch A4 motorway near Steenberg. By applying this type of asphalt mixture 50 mm thickness of asphalt was saved on this project (based on structural calculations). So in addition to reusing material, savings were also made on new raw materials (Plug et al, 2020).

The same method can be performed with PMA asphalt granulate. The properties of the new asphalt will then also benefit from the polymer modification in the PMA asphalt granulate. An important factor here is that the PMA asphalt granulate is of a consistent quality (from the same source with the same modification). Only then can the added value of the PMA asphalt granulate be included in construction calculations.

4 RUNWAY 18R/36L REHABILITATION PROJECT

A total of approximately 1,400,000 m² of PMA asphalt granulate was selectively milled from the runway and connecting areas after removing the antiskid layer, representing approximately 130,000 tons of asphalt. The asphalt that was selectively milled was partially crushed on site and from there transported to the asphalt plant so that it could be reused for in the new asphalt. For the new asphalt a heavily modified PMB was selected with improved workability at lower application temperatures (Sealoflex SFB 5-90 LT) with the in Table 3 given properties. Added to the PMB was a chemical 'low temperature' additive to achieve improved wetting of the crushed stones and asphalt aggregate during mixing resulting in an overall better workability during paving.

Table 3. Properties selected polymer modified binder.

Properties	Test	Specification	Unit
Penetration	EN 1426	80-120	mm x 0.1
Softening point R&B	EN 1427	≥ 85	°C
Elastic recovery	EN 13398	≥ 90	%
Force ductility at 5 °C	EN 13589	≥ 5.0	J
MSCR J _{NR,3.2 kPa} at 60 °C	EN 16659	≤ 0.1	1/kPa

With the selected PMB a new PMA asphalt for base and bind layers was produced with 60% of the old RAB from the runway in combination with a rejuvenating agent (Anova) to meet the tight tender specifications within a period of 13 weeks without any problems. The properties (according to the Dutch CE-marking systematic) of the used PMA mixtures have been summarized in Table 4.

Table 4. PMA asphalt properties with 60% PMA RAP (Dutch CE type test).

Asphalt properties 60% PMA RAP	Dense PMA	Open PMA	Dimension
Stiffness S_{mix}	4014	4401	MPa
Resistance against deformation f_c	0.05	0.05	$\mu\text{m}/\text{m}/\text{s}$
Resistance against fatigue ϵ_6	291	268	$\mu\text{m}/\text{m}$

In comparison with the properties of the PMA mixtures without RAP (see Table 5), the stiffness of the latter mixtures is lower and the fatigue is higher. Without RAP, the stiffness (around 2800 MPa) is close to the minimum design stiffness, and with PMA RAP the stiffness (around 4000 MPa) is further away from the minimum. The fatigue with PMA RAP is lower than without RAP, but higher than with standard RAP (without polymer modification). However, the fatigue level is high enough because of the total construction on top of a CTB foundation.

Table 5. PMA asphalt properties without RAP (Dutch CE type test).

Asphalt properties	Dense PMA	Open PMA	Dimension
Stiffness S_{mix}	2767	2767	MPa
Resistance against deformation f_c	0.15	0.05	$\mu\text{m}/\text{m}/\text{s}$
Resistance against fatigue ϵ_6	362	336	$\mu\text{m}/\text{m}$

As surface layer a special developed porous friction course (without RAP) was applied (FlightFlex) by the contractor (Santvoort, 2021) without the need of a conventional antiskid layer. Because of the strict regulation for antiskid performance, recycled asphalt could for this project not be used in this layer. Begin May 2021 the rehabilitation project was finished and the runway was put back into operation.

5 QUALITY CONTROL POLYMER MODIFIED BITUMEN

Because of the high amount of PMA asphalt granulate of 60% in the new asphalt mixture strict requirements were needed for the PMB used. Because of changes in bitumen production and crude sources at refineries it has become more difficult to maintain the quality of such binders (Nahar, 2021). In order to guarantee the quality of the PMB to be produced, it is important to know the characteristics of the base bitumen. Deviations in the quality of the base bitumen can have major effects on the properties of the PMB. This is especially the case for specific applications with a high recycled asphalt content. For the production of the specific PMB (Sealoflex SFB 5-90 LT) bitumen from 1 refinery was selected. In the following graphs the variation in properties is given for the relevant specific properties during the production of the PMB.

As can be seen from the Figures 2 and 3 the obtained conventional properties (penetration and softening point) were within tight limits, which were stricter than the European standard for PMBs (European spec EN 14023). This was also the case for the functional properties for cracking (force ductility energy $E_{0.20-0.40\text{m}}$ at 5 °C) and rutting (MSCR $J_{nr,3.5}$ kPa and $R\%_{0.3,5}$ kPa at 60 °C).

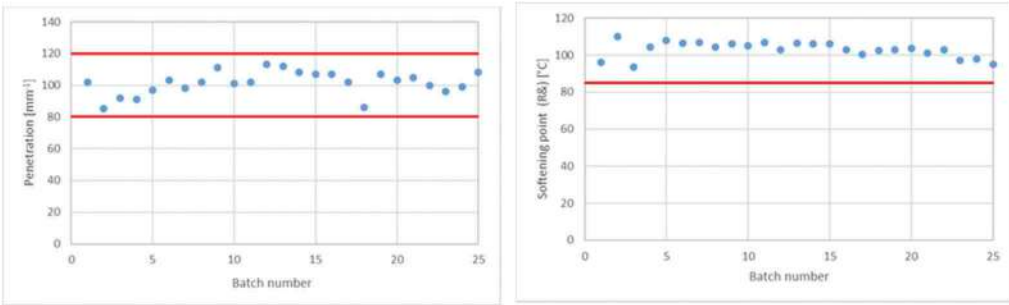


Figure 2 and 3. Obtained penetration and softening point of the produced PMB for the different batches.

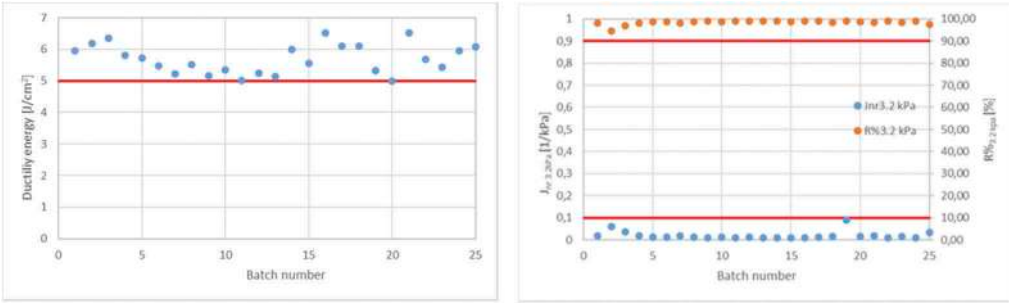


Figure 4 and 5. Obtained force ductility energy ($E_{0,2-0,4m}$) at 5 °C and MSCR $J_{nr,3.5}$ kPa and $R\%_{3.5}$ kPa at 60 °C.

6 CONCLUSIONS

Asphalt with a high percentage of asphalt granulate (RAP) can be used without any problems in heavily loaded constructions such as at airports (runways and taxiways) and motorways. For a good result, the quality of the asphalt granulate is very important, especially with high percentages RAB.

Polymer modified asphalt (PMA) can be reused without any problems, often improving the properties of the newly produced asphalt pavement. To be beneficial the PMA asphalt granulate has to be from the same source (same quality) and homogeneous.

The advantage of using (PMA) RAP compared to a PMA without RAP is that the stiffness of the asphalt mixture is increased compared to a 100% new PMA asphalt. This prevents the stiffness from falling below the design stiffness. The fatigue of the asphalt increases with PMA RAP compared to standard unmodified RAP. However, it is less than with a 100% new PMA mixture. For asphalt layers on a CTB this was within the specifications.

The runway rehabilitation project at Amsterdam Schiphol airport shows that PMA asphalt granulate also can be used for heavy duty run- and taxiways in such a way that the old materials of the runway could be reused in the new runway (so called horizontal recycling). Based on long-term experience with high percentages of RAP in heavy duty roads in the Netherlands, it is expected that this application of high percentage RAP will also be successful for runways.

REFERENCES

- Bochove, G. van; Jol, K.; Vilsteren, I.; Vliet, D. van; Voskuilen, J., 2021. *High-quality reuse of polymer modified asphalt*. 7th E&E Congress, June 2021, Madrid.
- DWW, 1997. *Hergebruik van hoge percentages PMB-ZOAB-granulaat...mogelijk of onmogelijk... (Reuse of high percentages of PMA Porous Asphalt granulate...possible or impossible...)*, Dutch Road authorities (RWS) report, Delft, Netherlands
- Nahar, S.; Teugels, W; Wall, A. van de; Poeran, N.; Vilsteren, I., 2021. *Grip on bitumen: mapping the changes in bitumen market and its impact on performance*. 7th E&E Congress, June 2021, Madrid.
- Nataraj, A.R.; Koning, J.F.A; Voorwinde, M.J., 2005. *Design and Construction of Fifth Runway at Amsterdam Airport Schiphol*. CROW airport conference, Amsterdam, Netherlands.
- Plug, C.P.; Bondt, A.H. de, 2020. *Hoge kwaliteit circulair asfalt (High quality circular asphalt*. CROW infradagen, Ede, Netherlands.
- RECYPMA project, 2013. *Possibilities for high quality RECYcling of Polymer Modified Asphalt*. EU sponsored project.
- Santvoort, M. van, 2021. *Hoge beschikbaarheid en maximale veiligheid Flightflex (High availability and maximum safety Flightflex)*, Heijmans, Rosmalen, Netherlands.
- Tauw report, 1998. *Luchtemissies en arbeidsomstandigheden bij productie en aanbrengen van gerecycled Sealoflex asfalt (Air emissions and working conditions in the production and application of recycled Sealoflex asphalt)*. Report 3690024, Deventer, Netherlands.
- Van Kleef report, 2005. *Hoog stabiele STAB met hergebruik van PMB ZOAB-granulaat (Highly stable AC base asphalt with PMA Porous Asphalt granulate)*. Report 1504607, Vught, Netherlands.

Effect of bio heating oil from biodiesel production on rheological behaviour of bitumen

M. Cabette & J. Pais

University of Minho, Guimarães, Portugal

R. Micaelo

NOVA School of Science and Technology, Caparica, Lisboa, Portugal

ABSTRACT: Bio-materials can replace traditional binders and additives used in the paving industry, which can help to build more resilient transport infrastructures and increase the consumption of secondary materials. Bio Heating Oil (BHO) is a residue of biodiesel production from waste cooking oil and animal fats. It has physical and chemical properties that allow the paving bitumen to improve binder-aggregate adhesion or rejuvenate aged bitumen. The objectives of this work are the study of the rheological and performance characteristics of bio-oil-modified bitumen. A 35/50 paving grade bitumen was modified with five contents of BHO (1, 2, 3, 5, and 10%). The bitumen was studied in unaged and aged conditions to evaluate the BHO ability to act as a rejuvenator of aged bitumen. Ageing treatment was induced by the Rolling Thin Film Oven and Pressure Ageing Vessel protocols. Physical and rheological tests were performed on unaged and aged bitumen. Physical tests include penetration, softening point and viscosity. Rheological behaviour was characterised through strain and frequency sweep tests at different temperatures. Viscoelastic Continuum Damage model was used to analyse the fatigue performance.

Keywords: Bio Heating Oil, Short-term ageing, Long-term ageing, Rejuvenator, Rheological test, Viscoelastic continuum damage

1 INTRODUCTION

The chemical composition of bitumen includes Saturates, Aromatics, Resins, and Asphaltenes (SARA) chemical groups. It can be considered a two-phase material with a liquid phase, called maltenes (saturates, aromatics, and resins), and a solid phase, called asphaltenes (Brovelli et al. 2013). When bitumen starts to be aged (liquid phase oxidised), the bitumen becomes dry and brittle (García et al., 2010; Alakhrass, 2018). Rejuvenators are used to restore the ratio of asphaltenes to maltenes of aged bitumen (García, Schlangen, and van de Ven 2011). The bio heating oil (BHO) is the residue obtained from the distillation of waste cooking oil and animal fats in biodiesel production (Santos et al. 2020). It is composed of less volatile organics and contains some residual Fatty Acid Methyl Ester (FAME).

Researchers have evaluated the effects of some bio-oils as a rejuvenator of aged bitumen. Zargar et al. (2012) and Sun et al. (2016) investigate the use of waste cooking oil as an aged bitumen rejuvenator. Zhang et al. (2018) used wasted wood bio-oil in their

research. Zeng et al. (2018) carried out studies using residue in castor oil, and Zhang et al. (2019) used sawdust bio-oil as a bio-based rejuvenator. It was proven that bio-oil softens aged binders.

Overall, it was found that bio-oil derived from several biomass sources can successfully be used as a bitumen modifier, and it is expected bio-oil to soften the bitumen (Lei et al. 2017; Lei et al. 2018; Zhang, Wang, et al., 2018; Zhang et al., 2019).

Asadi, Tabatabaee and Hajj (2021) concluded that the stiffness of the bitumen could be reduced with low rejuvenator content that may not produce a significant effect on the failure. Some researchers have determined the optimum rejuvenator content based on the penetration or dynamic viscosity of the binder. In contrast, other researchers have investigated rejuvenated binder performance according to the Superpave criteria, Linear Amplitude Sweep (LAS), or Multiple Stress Creep Recovery (MSCR) tests.

The primary purpose of modifiers is to improve the rheological properties of bitumen binders and increase their resistance to fatigue cracking (Hassanpour-Kasanagh et al. 2020). So, this study aimed to (1) investigate the effects of BHO on the rejuvenation of aged bitumen, (2) analyse the fatigue performance of BHO-modified bitumen, and (3) determine the better BHO content to be used in aged bitumen.

2 MATERIALS AND METHODS

2.1 Materials

The study was carried out using a typical paving bitumen, namely a 35/50 pen bitumen which properties are presented in Table 1 in terms of needle penetration, softening point and viscosity. It is a semi-hard bitumen used for hot climatic or heavy traffic conditions.

Table 1. Properties of 35/50 penetration grade bitumen (EN 1426; EN 1427; EN 13302).

Property	Unit	Specification	Measured
Penetration at 25°C	0.1 mm	35-50	36.6
Softening point	°C	50-58	53.2
Complex Viscosity at 150°C	Pa.s	–	0.68

The BHO used in this study resulted from biodiesel production and presented high viscosity due to the reduced amount of FAME and high glycerol. The presence and amount of these two components in the BHO depend on the quality and proportion of used cooking oil and animal fats used in biodiesel production.

To be used at room temperature, 50% of FAME was added to the BHO to produce the rejuvenator/modifier used in this study, which allowed the viscosity presented in Figure 1.

The rejuvenator was applied to three types of samples: unaged, short-term aged, and long-term aged bitumens. Short-term ageing was simulated through the Rolling Thin Film Oven (RTFO) (EN 12607-1), while the long-term ageing was simulated by the Pressure Ageing Vessel (PAV) (EN 14769). The RTFO simulates the binder aged after the mixing, transporting, and compacting processes, and the PAV simulates the long-term ageing equivalent to 5–10 years of in-service pavements.

Unaged bitumen is referred to as BU, RTFO aged bitumen is referred to as BR and PAV aged bitumen is referred to as BP. For each of these bitumens, 0, 1, 2, 3, 5 and 10% of rejuvenator was added, producing 15 binders. Thus, the previous terminology is followed by the rejuvenator content in the sample. For example, an unaged bitumen with 3% of rejuvenator is referred to as BU3.

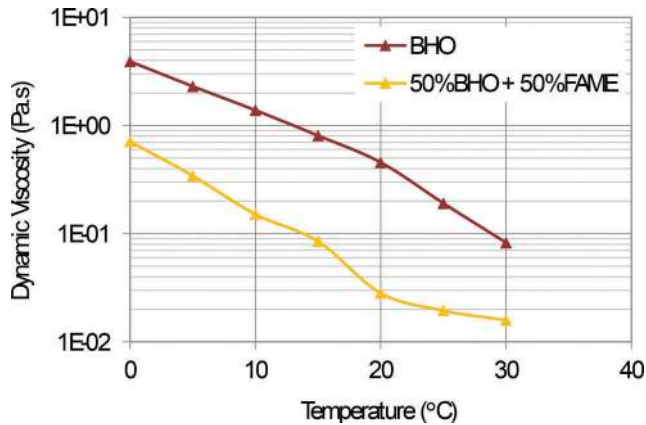


Figure 1. Rotational viscosity of the rejuvenator.

Samples were prepared in a low-shear mixer by blending the bitumen and rejuvenator under 150°C for 5 minutes at 350 rpm.

2.2 Test methods

2.2.1 Physical property tests

The physical properties of bitumen samples were investigated using needle penetration, ring and ball and dynamic viscosity tests. The needle penetration and ring and ball tests were performed following the European standard EN 1426 and EN 1427, respectively. The dynamic viscosity test was measured every 10°C from 100°C to 160°C, following EN 13302.

2.2.2 Linear amplitude sweep test

The mechanical behaviour was evaluated using the Linear Amplitude Sweep (LAS) test consisting of two phases. The first one is a frequency sweep test to determine rheological properties to determine the damage parameter. Then, a second phase consists of a series of oscillatory load cycles at linearly increasing amplitudes at a constant frequency to cause accelerated fatigue damage. The continuum damage approach is used to calculate the fatigue resistance from rheological properties and amplitude sweep results. Results from the LAS test can be used in Viscoelastic Continuum Damage (VECD) model. AASHTO-TP101 presents the test method and VECD analysis. The LAS test was performed at 20 °C.

3 RESULTS AND DISCUSSION

3.1 Physical properties

Penetration test results of unaged and aged bitumens are presented in Figure 2. Penetration increases with the rejuvenator content, meaning that the BHO acts as a bitumen rejuvenator. The evolution of penetration with the rejuvenator content follows an exponential law, with excellent correlation coefficients. It is possible to see the influence of the rejuvenator on the penetration. Based on the obtained results, the increase of penetration (Δpen) can be expressed as:

$$\Delta pen = e^{a \times \Delta RC} \quad (1)$$

where, Δpen is the increase of penetration (mm/10); e is the Euler number; ΔRC is the increase of rejuvenator content (%); a is a statistically determined coefficient. For 35/50 unaged and

short-term aged bitumen, $a = 0.30$; for long-term aged bitumen, $a = 0.27$. On average, the penetration increases about 30% for each 1% rejuvenator added.

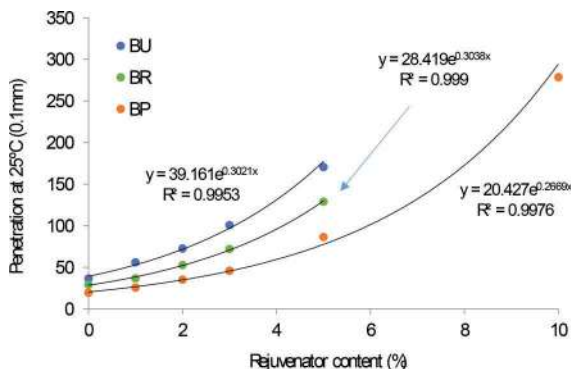


Figure 2. Penetration of the 35/50 bitumen with different rejuvenator content.

The softening point results of unaged and aged bitumens are shown in Figure 3, following a linear law with an excellent correlation coefficient. It is observed a decrease of the softening point when the rejuvenator content increases. On average, the softening point decreases 2.5 °C for each 1% rejuvenator added to the long-term aged bitumen. The softening point decreasing ratio of the other bitumens is 2.3 °C and 2.1 °C for short-term ageing and unaged bitumen, respectively.

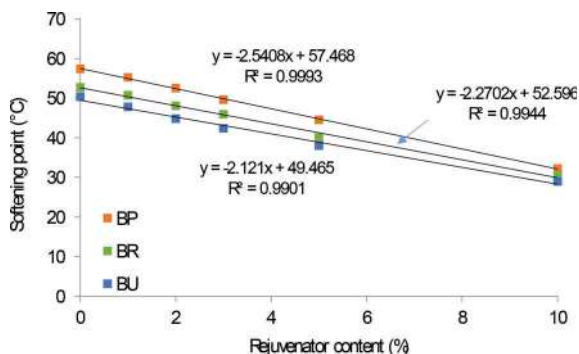


Figure 3. Softening point of the 35/50 bitumen with different rejuvenator content.

Therefore, the higher the dosage of rejuvenator is, the more significant the increase in penetration and the decrease in softening point. It occurs because the volatile component of the bitumen increased and, consequently, a reduction in its stiffness.

The viscosity test results are shown in Figure 4 against the rejuvenator content for temperatures ranging from 100 to 160 °C. These temperatures cover the production, laying and compaction of bituminous mixtures. Results show that the viscosity decreases with the addition of the rejuvenator and follows a perfect exponential law (a straight line in semi-log scale). Also, in a semi-log scale, the viscosity has a linear reduction with the temperature increase. These two trends allowed developing a model to predict the viscosity for 35/50 pen bitumen modified by BHO rejuvenator, as follows:

$$\text{Visco} = a \times e^{b \times RC} \times \left(\frac{t}{100}\right)^c \quad (2)$$

where, Visco is the dynamic viscosity in Pa.s; e is the Euler number; RC is the rejuvenator content in %; t is the temperature em °C; a, b, c are statistically determined coefficients. Based on this model (fitting coefficients listed in Table 2), one can conclude that the viscosity decreases about 15% per each 1% of added rejuvenator.

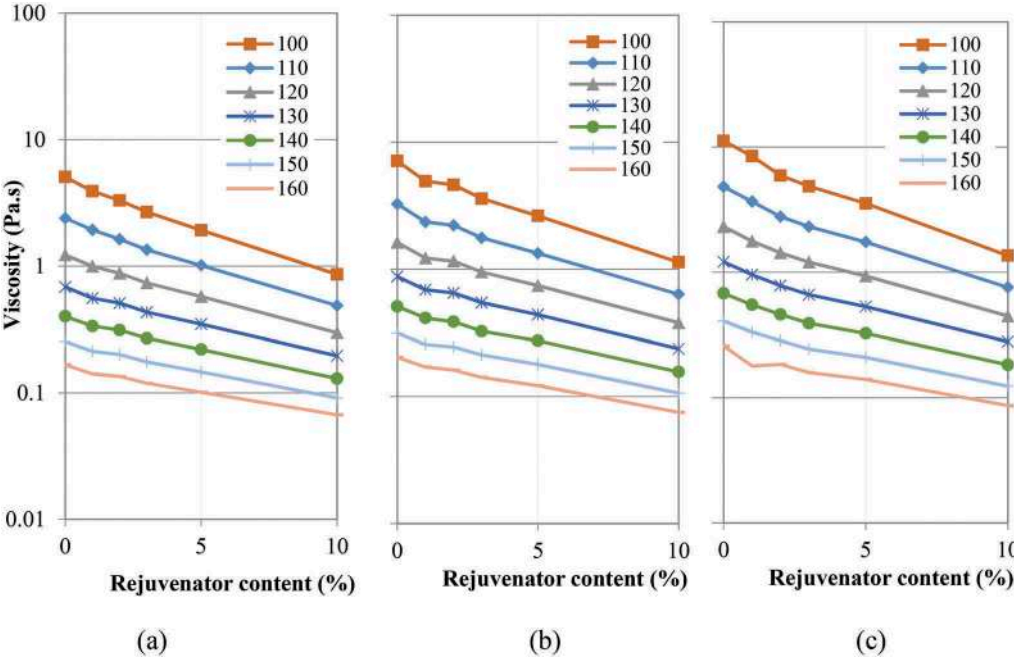


Figure 4. Viscosity of the (a) unaged; (b) short-term aged; and (c) long-term aged bitumen.

Table 2. Coefficients for Equation 2.

Bitumen	a	b	c	R ²
Unaged	3.7022	-0.1367	-6.4446	0.964
RTFO aged	4.8671	-0.1441	-6.5574	0.937
PAV aged	6.7283	-0.1495	-6.8431	0.884

3.2 Rheological and fatigue resistance characterisation

Figure 5 shows the black diagram (complex modulus G^* versus phase angle δ) of the unaged bitumen (BU), short-term aged (BR), and long-term aged (BP) with different rejuvenator content obtained from the frequency sweep at low applied strain that precedes the damage induced strain sweep in LAS test. As expected, the complex modulus increased, and the phase decreased with the ageing treatment. Differently, the rejuvenator caused a reduction of the complex modulus and the increase of the phase angle. This means that the curves move to left and upwards with ageing and to right and downwards with the rejuvenator content added. However, it is noted that the rejuvenator affects more the stiffness modulus than the phase angle. Also, the bitumens with 10% rejuvenator show non-smooth curves that is an indication of non-linear effects and that these binders are more rheologically complex.

Table 3 shows the data of complex modulus G^* and phase angle δ at 10Hz of the unaged bitumen (BU), short-term aged (BR), and long-term aged (BP) with different rejuvenator

content. At 10 Hz, the rejuvenator content required to obtain the same level of complex modulus and phase angle of unaged bitumen is 1-2% and 2-3% with short- and long-term aged bitumens, respectively.

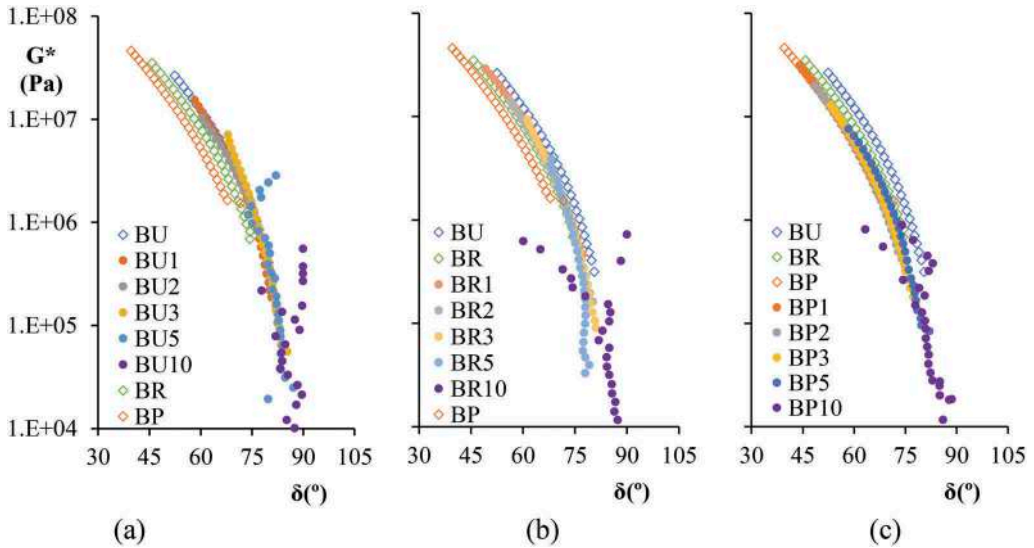


Figure 5. Black diagram of the unaged (BU); short-term aged (BR); and long-term aged (BP) bitumen.

Table 3. Complex Modulus (G^*) and Phase Angle (δ) at 10Hz.

Sample	G^* (Pa)	δ ($^\circ$)	Sample	G^* (Pa)	δ ($^\circ$)	Sample	G^* (Pa)	δ ($^\circ$)
BU0	1.37E+07	58.95	BR0	1.95E+07	51.98	BP0	2.75E+07	45.22
BU1	7.50E+06	63.95	BR1	1.54E+07	55.63	BP1	1.76E+07	49.96
BU2	4.66E+06	67.27	BR2	7.04E+06	62.03	BP2	1.03E+07	54.77
BU3	3.16E+06	71.59	BR3	4.51E+06	65.76	BP3	6.57E+06	58.88
BU5	1.18E+06	74.00	BR5	1.74E+06	71.20	BP5	3.50E+06	65.10
BU10	1.55E+05	89.75	BR10	2.71E+05	73.94	BP10	3.80E+05	83.08

The shear stress versus shear strain of the samples (BU, BR and BP) is shown in Figure 6. It can be seen that stresses sustained by specimens during cyclic loading increase with ageing treatment and decrease with the rejuvenator, which is related with the specimens's stiffness. To determine the specimens's failure in the test is recommended in the literature (Bahia et al. 2013; Micaelo et al. 2015; Zhang et al. 2020) the adoption of the point at which the maximum stress level is attained. In Figure 6(a), the failure strain of BU0 is 8.4% and increases to 9.3%, 9.4%, 10.2%, 10.2% and 13% with the addition of 1%, 2%, 3%, 5% and 10% of rejuvenator, respectively. In Figure 6(b), the failure strain of BR0 is 7.4% and increases to 7.5%, 8.3%, 9.3%, 10% and 10% with increasing rejuvenator content. In Figure 6(c), the failure strain of BP0 is 7.3% and increases to 9.5%, 9.4%, 10.5%, 8.3% and 10.1% with increasing rejuvenator content. From this, it is concluded that ageing treatment made, as expected, the bitumen harder and less ductile, and this is reverted with the addition of bio-oil. The effect of the rejuvenator on the ductility of modified bitumen is especially noted for small rejuvenator contents (1-3%).

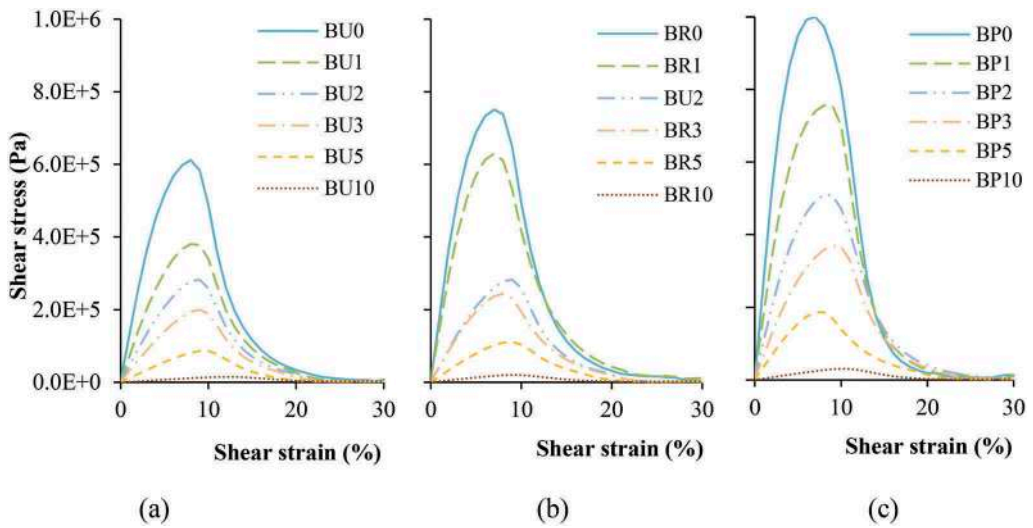


Figure 6. Stress-Strain curves (a) unaged (BU); (b) short-term aged (BR); and (c) long-term aged (BP) bitumen.

To assess the fatigue resistance of bitumens from LAS test the VECD methodology is adopted. In this analysis protocol are firstly determined the material integrity (C) versus damage (S) curves, also referred to as “damage characteristic curves”. Figure 7 shows the effect of the rejuvenator on the damage characteristic curves of bitumens aged to different levels. In the LAS test, the C value (initially 1.0) decreases with increasing loading cycles, and this is related with the growth of the S variable. It is observed that the S value required to attain the same level of C reduction is lower in aged bitumens, and increases with the rejuvenator content. A similar trend is seen with the three bitumens. To quantify the variation in C-S curves with both effects, it was determined the areas under the curves, which are shown in Table 4. The ageing treatment caused a reduction of about 22% in the C-S area, and 2% bio-oil is sufficient to attain the unaged bitumen level.

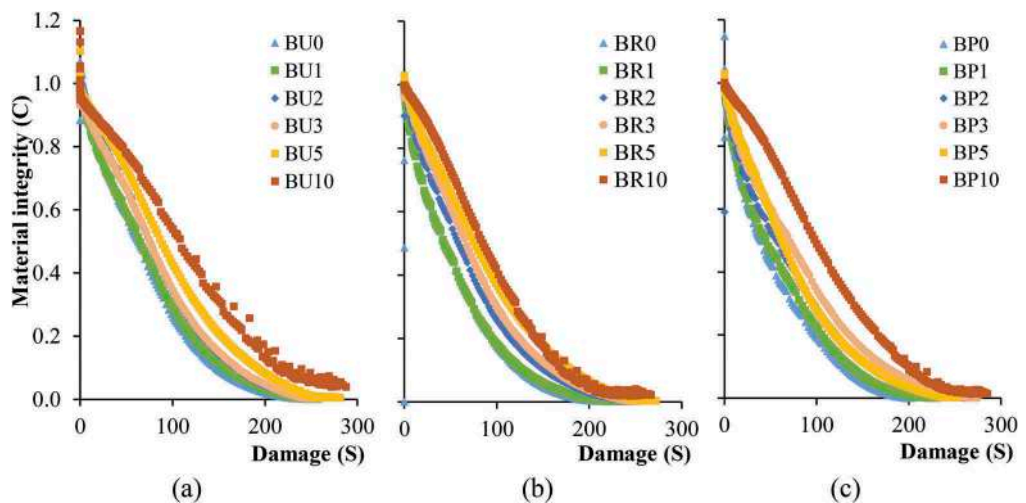


Figure 7. LAS: Material integrity (C) versus damage (S) for (a) unaged (BU); (b) short-term aged (BR); and (c) long-term aged (BP) bitumen.

Table 4. Area bellow C-S curve.

Sample	Area (-)	Sample	Area (-)	Sample	Area (-)
BU0	71	BR0	55	BP0	54
BU1	74	BR1	56	BP1	60
BU2	84	BR2	69	BP2	70
BU3	84	BR3	77	BP3	80
BU5	98	BR5	88	BP5	74
BU10	151	BR10	102	BP10	112

Then, the number of loading cycles (N_f) that the material can sustain at different loading amplitudes are calculated in the VECD methodology. Figure 8 compares the number of loading cycles for two different strain amplitudes (2.50% and 5.00%) of different bitumens. In general, and surprisingly, the fatigue resistance was greater for the long-term aged bitumen, with and without rejuvenator. On opposition, the short-term aged bitumen performed poorly than the unaged bitumen. The results are explained by the sensitivity of the method to the strain level at failure and the C(S) model. BP binders were stiffer than less aged binders (BU and BR), but the strain at failure did not change (reduction) as much as the complex modulus varied. Thus, the determined S value at the failure point was larger than in other bitumens. It is also noteworthy mentioning that the power-law model used to fit C-S curves did not fit well the full range of the curve for some bitumens. Nevertheless, it is observed for the three bitumens (BU, BR and BP) that a small addition of bio-oil increases the fatigue resistance. For the larger rejuvenation contents (5% and 10%), the bitumens performed differently.

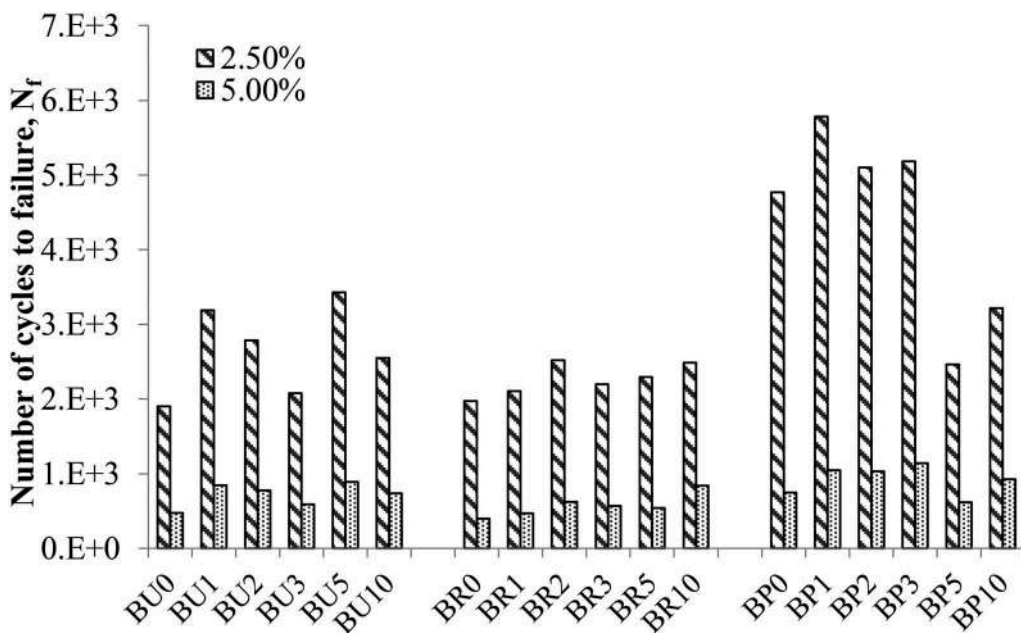


Figure 8. Fatigue resistance of bitumens at two strain levels (2.00% and 5.00%).

4 CONCLUSIONS

This paper aimed to investigate the effects of BHO as a rejuvenator on the physical and rheological properties of aged bitumen. The following conclusions can be drawn:

- The laboratory short-term and long-term ageing processes significantly changed the physical and rheological properties of the unaged bitumen, namely, BU0 that is a 35/50 bitumen grade, were changed after short-term ageing (BR0) to a 20/30 bitumen grade. The increase of the rejuvenator made the higher changed in the physical and rheological properties.
- Adding 1-3% of rejuvenator on the bitumen can restore the physical properties of the aged bitumen, namely, improve the penetration and reduce the softening point and viscosity. Their efficiency to restore the physical properties of the bitumen increase the complex modulus. So, it is also verified that the amount of rejuvenator added must be at least 1 to 3% after ageing to guarantee an adequate penetration value and allow good paving.
- Adding 1-2% rejuvenator in the bitumen, both complex modulus and phase angle of the long-term ageing can be restored to the level of short-term ageing without rejuvenator, which means the optimum dosage of the rejuvenator should be between 1 to 2%.
- Through VECD analyses, the addition of the rejuvenator into the bitumen can increase the fatigue life of the sample. The right amount of 2% until 3% of rejuvenator in the bitumen can increase material integrity.

Based on these findings, the selected amount of rejuvenator that can soften the aged bitumen to a required level, restore the physical properties, and increase the fatigue life, are 2% (by volume of bitumen).

ACKNOWLEDGEMENTS

The authors gratefully acknowledge Fundação para a Ciência e a Tecnologia (FCT) for the financial support (PhD grant reference SFRH/BD/144683/2019).

REFERENCES

- Alakhrass, Mousa Saeed. 2018. "The Effect of Adding Iron Powder on Self-Healing Properties of Asphalt Mixture." The Islamic University–Gaza Deanship.
- Asadi, Babak, Nader Tabatabaee, and Ramez Hajj. 2021. "Use of Linear Amplitude Sweep Test as a Damage Tolerance or Fracture Test to Determine the Optimum Content of Asphalt Rejuvenator." *Construction and Building Materials* 300: 123983. <https://doi.org/10.1016/j.conbuildmat.2021.123983>.
- Bahia, H., H. A. Tabatabaee, T. Mandal, and A Faheem. 2013. "Field Evaluation of Wisconsin Modified Binder Selection Guidelines - Phase II." *Wisconsin Highway Research Program Project, University of Wisconsin Madison*, no. December: 13–86.
- Brovelli, Claudio, Loic Hilliou, Yacine Hemar, Jorge Pais, Paulo Pereira, and Maurizio Crispino. 2013. "Rheological Characteristics of EVA Modified Bitumen and Their Correlations with Bitumen Concrete Properties." *Construction and Building Materials* 48: 1202–8. <https://doi.org/10.1016/j.conbuildmat.2013.07.032>.
- Gao, Junfeng, Hainian Wang, Zhanping You, Mohd Rosli Mohd Hasan, Yong Lei, and Muhammad Irfan. 2018. "Rheological Behavior and Sensitivity of Wood-Derived Bio-Oil Modified Asphalt Binders." *Applied Sciences (Switzerland)* 8 (6). <https://doi.org/10.3390/app8060919>.
- García, A., E. Schlangen, and M. van de Ven. 2011. "Properties of Capsules Containing Rejuvenators for Their Use in Asphalt Concrete." *Fuel* 90 (2): 583–91. <https://doi.org/10.1016/j.fuel.2010.09.033>.
- García, A., E. Schlangen, M. Van De Ven, and G. Sierra-Beltrán. 2010. "Preparation of Capsules Containing Rejuvenators for Their Use in Asphalt Concrete." *Fuel* 184: 603–11. <https://doi.org/10.1016/j.fuel.2010.09.033>.
- Hassanpour-Kasanagh, Sajjad, Perviz Ahmedzade, Alexander M. Fainleib, and Ali Behnood. 2020. "Rheological Properties of Asphalt Binders Modified with Recycled Materials: A Comparison with Styrene-Butadiene-Styrene (SBS)." *Construction and Building Materials* 230: 117047. <https://doi.org/10.1016/j.conbuildmat.2019.117047>.
- Lei, Yong, Hainian Wang, Xi Chen, Xu Yang, Zhanping You, Shi Dong, and Junfeng Gao. 2018. "Shear Property, High-Temperature Rheological Performance and Low-Temperature Flexibility of Asphalt Mastics Modified with Bio-Oil." *Construction and Building Materials* 174 (June): 30–37. <https://doi.org/10.1016/j.conbuildmat.2018.04.094>.

- Lei, Zhang, Hussain Bahia, Tan Yi-qiu, and Cheng Ling. 2017. "Effects of Refined Waste and Bio-Based Oil Modifiers on Rheological Properties of Asphalt Binders." *Construction and Building Materials* 148 (September): 504–11. <https://doi.org/10.1016/j.conbuildmat.2017.05.101>.
- Micaelo, R., A. Pereira, L. Quaresma, and M. T. Cidade. 2015. "Fatigue Resistance of Asphalt Binders: Assessment of the Analysis Methods in Strain-Controlled Tests." *Construction and Building Materials* 98: 703–12. <https://doi.org/10.1016/j.conbuildmat.2015.08.070>.
- Santos, C, J Pais, J Ribeiro, and P Pereira. 2020. "Evaluating the Properties of Bioasphalt Produced with Bio-Oil Derived from Biodiesel Production." In *Lecture Notes in Civil Engineering*, edited by C Raab, vol 76. Springer.
- Sun, Zhaojie, Junyan Yi, Yudong Huang, Decheng Feng, and Chaoyang Guo. 2016. "Properties of Asphalt Binder Modified by Bio-Oil Derived from Waste Cooking Oil." *Construction and Building Materials* 102: 496–504. <https://doi.org/10.1016/j.conbuildmat.2015.10.173>.
- Zargar, Majid, Esmail Ahmadinia, Hallizza Asli, and Mohamed Rehan Karim. 2012. "Investigation of the Possibility of Using Waste Cooking Oil as a Rejuvenating Agent for Aged Bitumen." *Journal of Hazardous Materials* 233–234:254–58. <https://doi.org/10.1016/j.jhazmat.2012.06.021>.
- Zeng, Menglan, Junfeng Li, Wenqiang Zhu, and Yinglin Xia. 2018. "Laboratory Evaluation on Residue in Castor Oil Production as Rejuvenator for Aged Paving Asphalt Binder." *Construction and Building Materials* 193: 276–85. <https://doi.org/10.1016/j.conbuildmat.2018.10.204>.
- Zhang, Hanyu, Kairen Shen, Gang Xu, Jusheng Tong, Rui Wang, Degou Cai, and Xianhua Chen. 2020. "Fatigue Resistance of Aged Asphalt Binders: An Investigation of Different Analytical Methods in Linear Amplitude Sweep Test." *Construction and Building Materials* 241: 118099. <https://doi.org/10.1016/j.conbuildmat.2020.118099>.
- Zhang, Ran, Hainian Wang, Xin Jiang, Zhanping You, Xu Yang, and Mingxiao Ye. 2018. "Thermal Storage Stability of Bio-Oil Modified Asphalt." *Journal of Materials in Civil Engineering* 30 (4). [https://doi.org/10.1061/\(ASCE\)MT.1943-5533.0002237](https://doi.org/10.1061/(ASCE)MT.1943-5533.0002237).
- Zhang, Ran, Zhanping You, Hainian Wang, Xi Chen, Chundi Si, and Chao Peng. 2018. "Using Bio-Based Rejuvenator Derived from Waste Wood to Recycle Old Asphalt." *Construction and Building Materials* 189 (September): 568–75. <https://doi.org/10.1016/j.conbuildmat.2018.08.201>.
- Zhang, Ran, Zhanping You, Hainian Wang, Mingxiao Ye, Yoke Khin, and Chundi Si. 2019. "The Impact of Bio-Oil as Rejuvenator for Aged Asphalt Binder." *Construction and Building Materials* 196: 134–43. <https://doi.org/10.1016/j.conbuildmat.2018.10.168>.

Investigating the use of fly ash for sustainable asphalt binders

R. Melaku, S. Ness, D. Gedafa & N. Suleiman

Department of Civil Engineering, University of North Dakota, Grand Forks, ND, USA

ABSTRACT: The main criteria used in measuring pavement construction effectiveness are sustainability issues related to economic savings and energy and emission reduction. The potential effect of using fly ash in an asphalt binder is the efficient use of existing materials through rework or structural change to ensure that the material's properties are improved, promoting a longer lifespan and enhanced sustainability. The effects of fly ash from five different sources and lime were analyzed for rutting, fatigue cracking, and low-temperature cracking resistance. Two binder grades commonly used in North Dakota were tested: PG 58-28 and PG 64-28. An initial 3%-6% fly ash content by binder weight was evaluated by increasing the fly ash in 1% increments based on literature reviews and laboratory experiments. The effect of fly ash used as a mineral filler on low-temperature cracking resistance for two projects was also investigated. Using 5% fly ash by binder weight resulted in better rutting, fatigue cracking, and low-temperature cracking resistance compared to the control for PG 58-28. Fly ash from Coal Creek Station (CCS) and Ottertail (OTR) resulted in better fatigue cracking and low-temperature cracking resistance than other fly ash materials and lime compared to PG 58-28. An optimum dosage of fly ash can be a sustainable material to replace some asphalt binders used in asphalt pavements.

Keywords: Fly ash, fatigue cracking, low-temperature cracking, rutting

1 INTRODUCTION

The main criteria for the creation of sustainable infrastructures are minimizing environmental impact; using natural resources appropriately; reducing energy consumption; reducing greenhouse gas emissions; limiting pollution, such as air, water, earth, and noise; improving health, safety, and risk prevention; and ensuring a high level of user comfort and safety (Maher et al., 2006). The potential effect of using fly ash as a partial asphalt binder replacement lies in the efficient use of existing materials either through reworking them or changing their structures to ensure that the material's properties are improved to provide longer life and enhance sustainability (Cassar, 2005).

One research study indicated that fly ash mastics are less prone to fatigue damage than limestone filler, exhibiting an increase in fatigue cracking performance; however, this depended upon the type of fly ash and the concentration used with the binder (Bautista, 2005). Asphalt with an addition of up to 6% heavy oil fly ash reduced deformation under traffic loads without affecting fatigue life (Al-Mehthel et al., 2013). The use of Class C fly ash at intermediate temperatures improved aging resistance during mastic testing (Sobolev et al., 2013).

The addition of fly ash improves thermal relaxation, leading to mastics with improved resistance to thermal cracking. Thermal relaxation properties relieve internal thermal stress built up during winter, improving resistance to low-temperature cracking. Class C fly ash

improves resistance to low-temperature cracking; however, no significant increase in stiffness was revealed when using Class F fly ash (Bautista, 2005). Another study revealed that low fly ash concentrations reduce the measured low-temperature stiffness. Class F fly ash exhibited the greatest reduction in low-temperature stiffness (Sobolev et al., 2013). The same study determined that Class F fly ash led to thermal relaxation rate improvements at lower fly ash additions, particularly at 5% of the tested binder.

Plain asphalt binder (PG 58-28), binders containing 5%, 15%, 30%, and 60% fly ash were tested, and the $G^*/\sin(\delta)$ factor was determined at temperatures of 52, 68, 64, and 70°C. The addition of fly ash increased the $G^*/\sin(\delta)$ factor. The addition of Class C fly ash increased the rutting factor, which improved the rutting resistance potential at 58°C. This same improvement occurred with the addition of Class F fly ash. Similar results were obtained with plain PG 70-22 asphalt binder and binders with 5%, 15%, 30%, and 60% Class C and Class F fly ash addition. Adding 15% Class F fly ash improved the grade from PG 70 to PG 76. This same shift occurred with a 30% Class C fly ash addition. The grade increased to PG 64 with a 60% addition of fly ash to the PG 58 binder. This grade change allows us to predict the potential rutting resistance of asphalt mixes with added fly ash (Sobolev et al., 2014). A study by Ramme et al. (2016) also indicated that different fly ash concentrations (5%, 15%, and 30%) increased the rutting factor, improving rutting resistance potential.

Modifying plain asphalt binder with heavy oil fly ash, from 3% wt. to 6% wt, increased the performance grade from PG 64-10 to PG 70-10. With an up to 6% wt. fly ash addition, the rutting potential decreased by 31% without impacting the fatigue resistance (Al-Mehthel et al., 2013). Sobolev et al. (2013) added fly ash to an unmodified binder, one with no polymer modification, which increased the rutting resistance at all concentrations (5%, 10%, 15%, 25%, and 40%) for PG 58-28 and PG 64-28 compared to the virgin binder. Understanding the effect of fly ash on asphalt binder will significantly improve asphalt pavement sustainability.

1.1 Objectives of the study

The main objectives of the study were to:

- Determine the effect of fly ash and lime on fatigue cracking, low-temperature cracking, and rutting resistance for two binder grades.
- Determine optimum fly ash content for cracking and rutting resistance compared to virgin binders.

2 METHODS

The rheological properties of asphalt binders and pastes were determined using a Dynamic Shear Rheometer (DSR). The experimental plan of this study is displayed in Figure 1. Results from this study's Phase II were not included in this paper for brevity.

2.1 Materials

Fly ash was collected from BASIN Electric, Coal Creek Station (CCS), HESKETT, Ottertail (OTR), and MINNKOTA Power Companies in North Dakota. Lime was also used for comparison purposes.

2.2 Binder aging

All five fly ashes (BASIN, CCS, HESKETT, OTR, and MINNKOTA) and lime were used in the binder analysis to determine the optimum dosage that improves the control's rheology. Two binder grades were used for the analysis: PG 58S-28 and PG 64S-28 where S is a designation for a standard traffic loading. The binders were heated at 132 °C before mixing

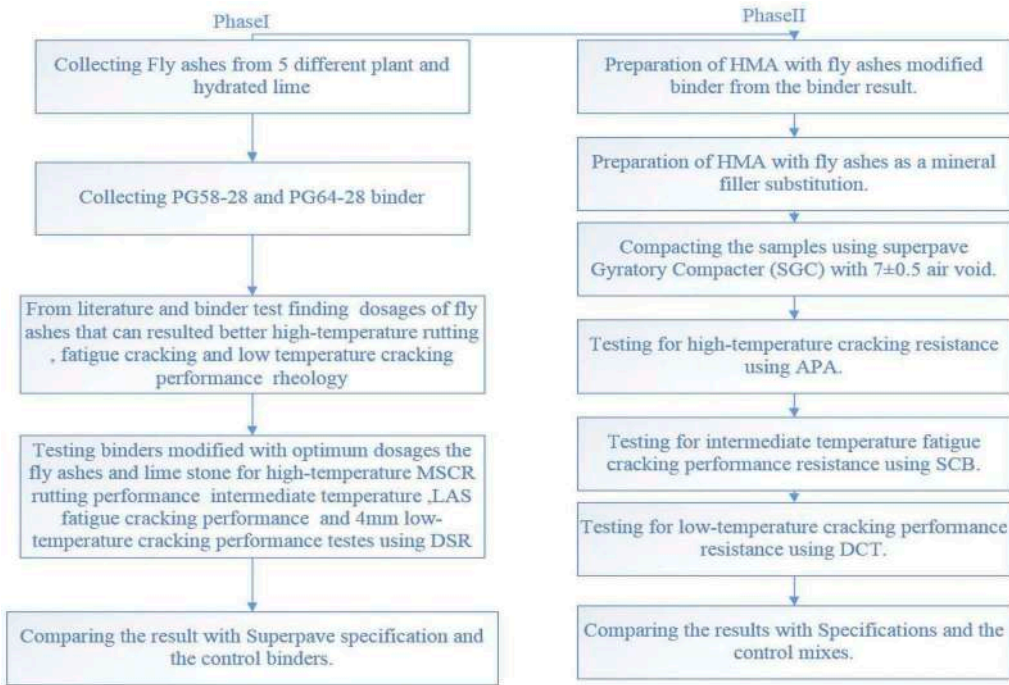


Figure 1. Experimental plan.

to make them workable. The fly ashes were kept at standard temperature (25 °C) before mixing. Trial dosages of fly ash were then added to the binder and mixed with a rapid rotational mixer. The unaged mix sample was removed, and the remaining mix was further aged for short-term and long-term aging analysis.

The Rolling Thin Film Oven (RTFO) test procedure simulated short-term asphalt binder aging, or the aging that happens during construction and placement. Results from this testing method indicate that the asphalt binder's rheological property changes due to conventional hot mixing. The oven was pre-heated for 16 hours before testing to stabilize the testing temperature at 163 °C. Binder was heated in a container with a loose cover so the temperature could exceed 150 °C. Thirty-five (35 ± 0.5) g of the binder were poured into each cylindrical glass container, turned to a horizontal position, and immediately rotated for at least one complete rotation to pre-coat the cylindrical surface. The containers were then filled with asphalt and cooled on a rack for one to three hours. Testing was performed in the oven at a temperature of 163 °C and an airflow of 4000 ± 200 mL/min for 85 minutes following ASTM D2872.

Pressure Aging Vessel (PAV) tests were used to simulate in-service asphalt binder aging with 7 to 10-years of exposure to heat and pressure. This test followed the standard test method outlined in ASTM D6521. Parameters from the manufacturer's manual were used to pre-heat the vessel to a conditioning temperature of 100°C with an air pressure of 2.1 ± 0.1 MPa. Temperatures were selected according to the specifications dictated by ASTM D6373. The RTFO-aged asphalt binder samples were mixed and poured into stainless steel pans, each holding 50 ± 0.5 g. The test was then run for 20 hours ± 10 minutes once the temperature and pressure were stabilized.

2.3 Binder tests

The RTFO and PAV aged samples were used for rutting, fatigue cracking, and low temperature cracking tests. All binder tests were conducted using the Dynamic Shear Rheometer (DSR).

Multiple Stress Creep Recovery (MSCR) is the latest improvement to the Superpave Performance Grade (PG) asphalt binder test following AASHTO T 350 and AASHTO M 332 testing specifications using DSR. This test reports the rutting resistance of the asphalt binder more accurately and is blind to binder modification. The non-recoverable creep compliance at 3.2 kPa (Jnr_3.2) and percent recovery (%R) are the two main parameters used to define the binder's rutting resistance. Jnr_3.2 values of 4, 2, 1, and 0.5 were used as the maximum threshold values for standard, heavy, very heavy, and extreme traffic, respectively. A lower Jnr correlates to a stiffer binder. The RTFO sample with a high temperature grade was used for MSCR analysis.

Linear Amplitude Sweep (LAS) is an improved test to evaluate an asphalt binder's ability to resist fatigue damage. LAS is an oscillatory strain sweep test that generates damage to the binder by linearly applying an increasing load amplitude. The LAS test consists of two steps: a frequency sweep test to obtain information on undamaged material properties and a linear amplitude strain sweep test to obtain information on the binder's damage characteristics. The test is performed on the PAV-aged binder samples at an intermediate temperature. The failure definition for the LAS test is defined as a 35% reduction in the initial modulus. The analysis is performed based on fatigue law parameters A and B, which are model coefficients that depend on the material characteristics. Fatigue-resistant binders tend to have higher A values and lower absolute B values in general. The number of cycles to failure, calculated using Equation (1), is generally used to compare binder fatigue cracking resistance.

$$N_f = A(\gamma_{max})^B \quad (1)$$

Low-temperature resistance was determined using 4 mm parallel plate geometry following the method proposed by Sui et al. (2011). The method allowed us to generate a master curve at low-temperature PG + 10°C. The master curve was used to estimate the relaxation slope (m_r) and relaxation modulus G (t) at 60 seconds. These values were then compared to Superpave PG binder specifications for 4 mm DSR (AASHTO, 2016, FHWA, 2018). The specifications specify a maximum G (t) value of 143 MPa and a minimum (m_r) value of 0.28, which better correlates with creep stiffness, S (t) of 300 MPa, and a creep slope of (m_c) of 0.3. Lower G (t) and higher m_r results indicate a better low-temperature cracking resistance in general.

3 RESULTS AND DISCUSSIONS

3.1 Rutting resistance

The rutting resistance of the original and modified binders was determined using the multiple stress creep recovery (MSCR) test. Figure 2(a) depicts the rutting parameter non-recoverable compliance at 3.2 kPa (Jnr_3.2). The results indicate that a 5% addition of all fly ashes improved the binder's stiffness. The 5% fly ash and lime-modified binders did not experience a grade change; they remained within the standard traffic grade despite increasing stiffness. The stiffness of the control binder improved by 19%, 7%, 24%, 13%, 13%, and 36% due to the addition of 5% BASIN, CCS, OTR, HESKETT, MINNKOTA, and LIME modified PG 58-28 binders, respectively. Lime modification resulted in higher stiffness compared to all fly ash modifiers.

3.2 Fatigue cracking resistance

Linear Amplitude Sweep (LAS) was used to determine the original and modified binder fatigue cracking resistance. Figure 3(a) illustrates the number of cycles to failure (N_f) for the LAS test at 2.5 and 5 microstrains with the PG 58-28 binder. The results indicated that the CSS-modified binder is more fatigue resistant than the control binder at 2.5 macrostrains, whereas the BASIN, OTR, MINKOTA, HESKETT, and LIME modified binders resulted in relatively lower N_f values than the control.

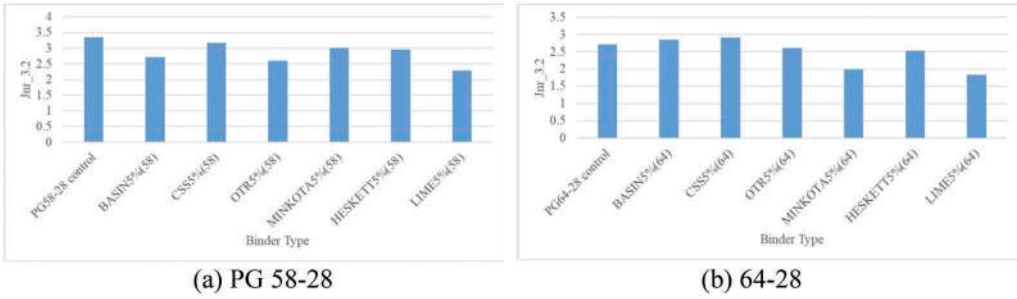


Figure 2. MSCR Jnr_3.2 kPa.

Figure 3(b) displays the number of cycles to failure (N_f) for the LAS test at 2.5 and 5 macro-strains with the PG 64-28 binder. The result revealed that the CSS and OTR modified binders showed similar performances, which was slightly less fatigue cracking resistance than the control binder at 2.5 and 5-micron strains. Fly ash from BASIN, MINKOTA, HESKETT, and LIME resulted in a relatively lower number of cycles to failure than the control.

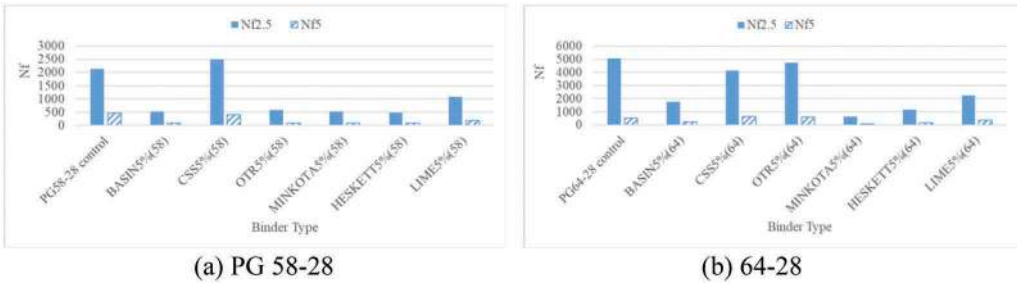


Figure 3. Number of cycles to failure.

3.3 Low-temperature cracking resistance

Figure 4 depicts the relaxation modulus and slope for the fly ash and lime modified PG 58-28 binders, respectively. The relaxation modulus was reduced by 70%, 36%, 35%, 32%, and 68% for BASIN, CSS, OTR, MINKOTA, and LIME, respectively, indicating an improvement in low-temperature cracking resistance, and increased by 30% for the HESKETT fly ash modified binder, indicating a reduction in low-temperature resistance compared to the control binder. The slope results in Figure 4(b) reveal a 15%, 7%, 8%, 10%, and 17% reduction in low-temperature cracking performance for BASIN, CCS, OTR, HESKETT, MINNKOTA, respectively.

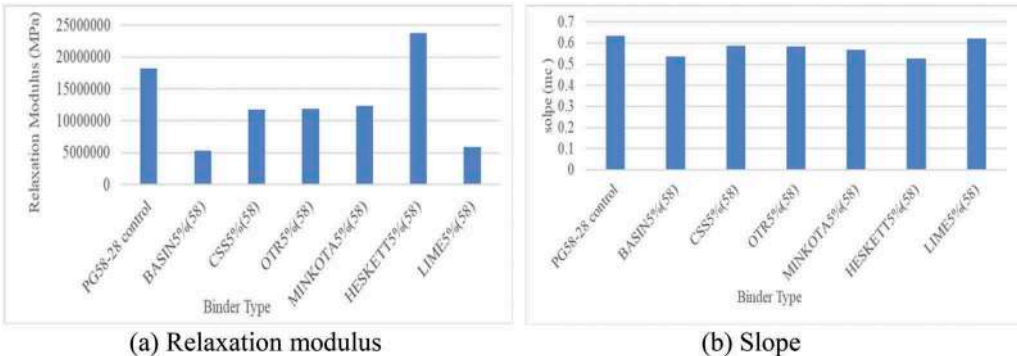


Figure 4. Low-temperature relaxation modulus and slope for PG 58-28.

Figure 5 presents the low-temperature results of fly ash and lime modified PG 64-28 binder. The relaxation modulus result indicates a reduction by 8%, 58%, 35%, and 73% for OTR, MINKOTA, HESKETTS, and LIME, respectively, indicating an improvement in low-temperature resistance. The $G(t)$ increased by 95% and 20% for the BASIN and CSS fly ash modified binders, respectively, exhibiting a reduction in low-temperature cracking performance. The relaxation slope results revealed that the slope reduced by 18%, 24%, and 24% for BASIN, CSS, and OTR fly ash modified binders, respectively, indicating a decrease in low-temperature cracking resistance. There is a slight reduction in low-temperature cracking resistance of HESKETTS and LIME modified binders. The slope improved for MINKOTA modified binders by 2%.

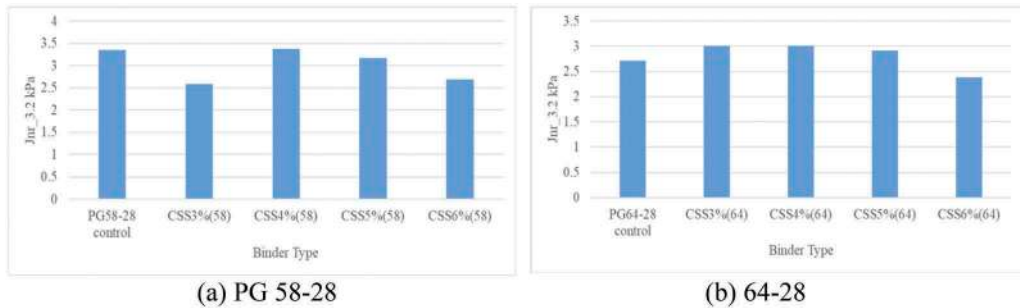


Figure 5. Low-temperature relaxation modulus and slope for PG 64-28.

3.4 Optimum fly ash content

Fly ash from the Coal Creek Station (CCS) was used to determine the optimum fly ash content since it exhibited the greatest improvement in binder cracking and rutting resistance.

3.4.1 Rutting resistance of the CSS modified binder using MSCR

We determined the optimum amount of fly ash content that results in better performance. Figure 6(a) illustrates the result of different CSS modified PG 58-28 binder dosages. The presence of CSS in the amounts of 3%, 5%, and 6% had a stiffening effect, resulting in a $Jnr_{3.2}$ kPa value reduction of approximately 22%, 5%, and 20%, respectively. Modifying the PG 58-28 binder with 4% CSS resulted in a softening effect by increasing the $Jnr_{3.2}$ kPa by approximately 1%.

Figure 6(b) displays the $Jnr_{3.2}$ kPa results for CSS modified PG 64-28 binder. The results indicate that the 6% CCS modification had a stiffening effect by reducing the Jnr value by 12%, whereas 3%, 4%, and 5% CSS modified binders had a softening effect by increasing the Jnr value by 10%, 10%, and 7%, respectively. These results indicate that the stiffness increases with CSS percentage.

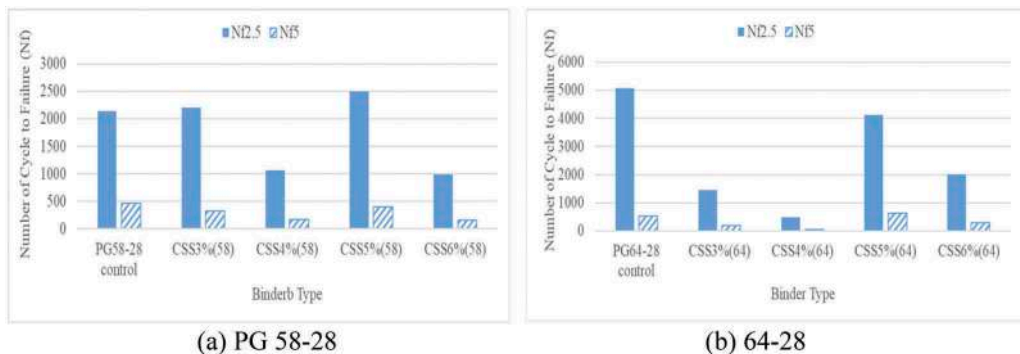


Figure 6. Effect of CCS fly ash on binder rutting resistance.

3.4.2 Fatigue cracking resistance of CSS modified binders using LAS

Figure 7(a) displays the number of cycles to failure for the different dosages of CSS added to the PG 58-28 binder. The results indicate that the optimum percentage of CSS needed to improve the fatigue cracking performance is 5%, resulting in higher resistance than other percentages and the control binder.

Figure 7(b) presents the LAS results for CSS modified PG 64-28 binders. The outcome indicates that the 5% CSS modified PG64-28 binder results in better fatigue cracking resistance than other percentages, but is slightly lower than the control PG 64-28 binder.

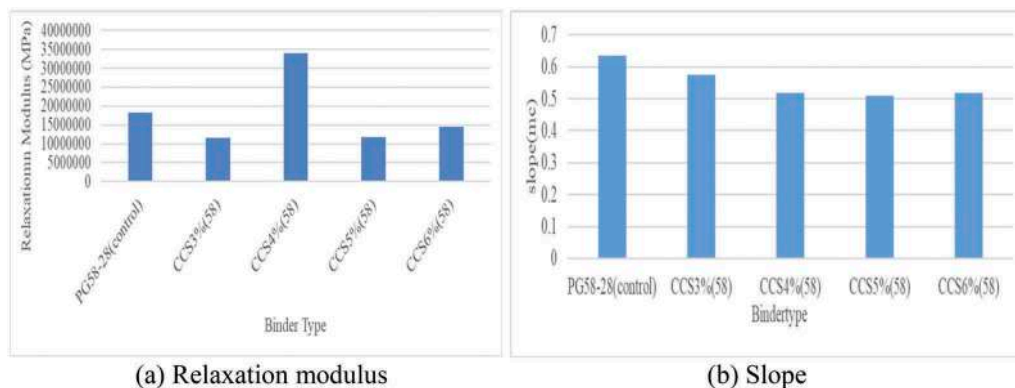


Figure 7. Effect of CCS fly ash on fatigue cracking resistance of binders.

3.4.3 Low-temperature cracking resistance of the CCS modified binders

Figure 8(a) displays the relaxation modulus of the CCS fly ash modified PG 58-28 binders. Fly ash content varied from 0%, or the control, to 6%. The 3% and 5% CCS modified binders had approximately the same relaxation moduli, 36% less than the control binder, indicating a better low-temperature cracking resistance. The 4% CCS modified binder exhibited the least low-temperature cracking resistance.

Figure 8(b) depicts the slope of the CCS modified binders, indicating that all modified binders have a lower slope than the control binder, revealing that it has less low-temperature cracking resistance than the control. The 3% CCS modified binder had better low-temperature cracking resistance than all other modified binders and only 9.4% less resistance than the control binder. All other modified binders exhibited a similar low-temperature cracking resistance: approximately 18% and 9% less than the control and 3% CCS modified binders, respectively. An increase in CCS fly ash content results in a decrease in the slope in general.

Figure 9(a) depicts the relaxation modulus of the CCS fly ash modified PG 64-28 binder. The results reveal that all modified binders have a higher relaxation modulus than the control, indicating that they have less low-temperature cracking resistance. The 5% CCS modified binder had the best low-temperature cracking resistance, an approximate 17% higher relaxation modulus value than the control binder. The 3% CCS and 6% CCS modified binders had nearly the same relaxation moduli, approximately 47% higher than the control binder.

The slope in Figure 9(b) illustrates that all modified PG 64-28 binders have a lower slope than the control, revealing that they are less low-temperature cracking resistant. The 4% CCS modified binder was the best low-temperature cracking resistant binder, approximately 19% lower than the control. The 5% CCS and 6% CCS modified binders had approximately the same slope: 23% and 5% lower than the control binder and 4% CSS modified binders, respectively. There is no clear relationship between CSS fly ash content and the slope.

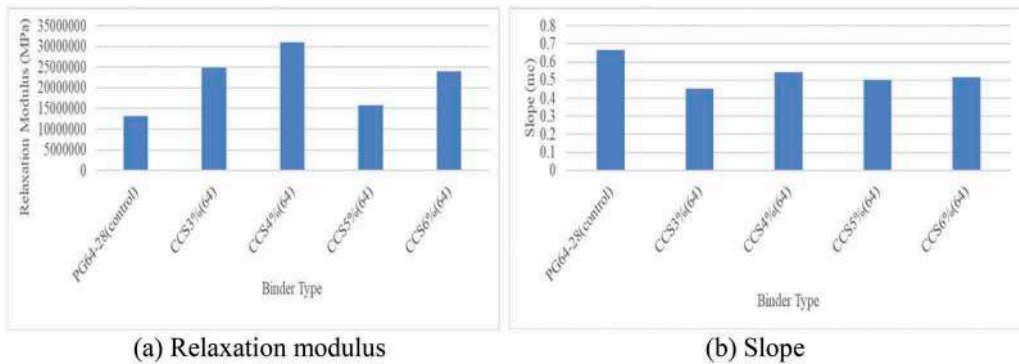


Figure 8. Low-temperature relaxation modulus and slope for the PG 58-28 Binder.

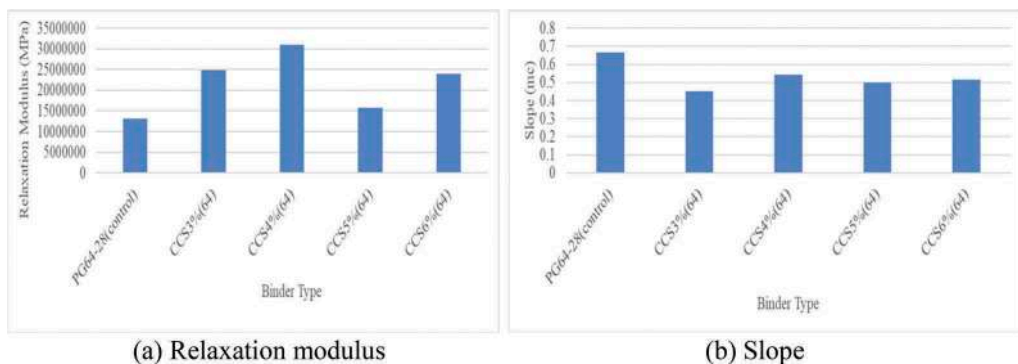


Figure 9. Low-temperature relaxation modulus and slope for the PG 64-28 Binder.

4 CONCLUSIONS AND FUTURE WORK

4.1 Conclusions

Based on this study, the following conclusions can be made:

- Adding 5% fly ash and lime to the PG 58-28 binder increased rutting resistance.
- Adding CSS and BASIN to the PG 64-28 binder improved rutting resistance, whereas all other fly ashes and lime had a softening effect.
- Adding 5% CSS fly ash resulted in a relatively good fatigue cracking resistance for the PG 58-28 binder.
- PG 64-28 CCS and OTR fly ashes resulted in relatively better fatigue cracking resistance.
- The stiffness of the PG 64-28 binder increased with an increase in CSS content.
- The low-temperature binder result for the PG 58-28 binder revealed that 5% CCS is the optimum amount, followed by the 3% CCS modified binder.
- The 4% CCS modified PG 64-28 binder had the optimum content overall.

4.2 Future work

- Determine the viscosity of the original and modified binders.
- Evaluate the performance of the HMA mixes with optimum dosages of fly ash and lime.
- Determine the effect of fly ash and lime as mineral fillers in the mix.

ACKNOWLEDGMENTS

The authors would like to thank the North Dakota Industrial Commission for funding this research under Contract No. FY19-LXXXVII-219. The authors would also like to thank Basin Electric Power Cooperative, Great River Energy, Minnkota Power Cooperative, and Montana-Dakota Utilities Co. for providing fly ash; Pete Lien & Sons, Inc. for providing lime; and Jebro Incorporated for providing asphalt binders.

REFERENCES

- AASHTO, 2016. *Standard Specification for Performance-Graded Asphalt Binder*. Washington, D.C., USA.
- Al-Mehthel, M., Al-Abdul Wahhab, H., and Hussein, I., 2013. *Utilization of Heavy Oil Fly Ash to Improve Asphalt Binder and Asphalt Concrete Performance*. U.S. Patent No. 8,444,761 B2, U.S. Patent and Trademark Office, <https://patentimages.storage.googleapis.com/20/af/c6/4e1e42da99de7d/US8444761.pdf>.
- Bautista, E., 2015. *Experimental Evaluation of the Effect of Coal Combustion Products on Constructability, Damage and Aging Resistance of Asphalt Mastics*. Doctoral Dissertation, University of Wisconsin - Milwaukee, Milwaukee, WI, USA, <https://dc.uwm.edu/cgi/viewcontent.cgi?referer=https://www.google.com/&httpsredir=1&article=1863&context=etd>.
- Cassar, L., 2005. *Nanotechnology and Photocatalysis in the Cementitious Material*. Proceedings of the 2nd International Symposium on Nanotechnology in Construction, Bilbao, Spain, NANOC Centre for Nanomaterials Applications in Construction, 277-283. FHWA, 2018. *User Guidelines for Waste and Byproduct Materials in Pavement Construction*. Publication Number FHWA-RD-97-148, Washington, D.C., USA
- FHWA, 2018. *User Guidelines for Waste and Byproduct Materials in Pavement Construction*. Publication Number FHWA-RD-97-148, Washington, D.C., USA
- Maher, M., Uzarowski, L., Moore, G., and Aurilio, V., 2006. *Sustainable Pavements – Making the Case for Longer Design Lives for Flexible Pavements*. Conference of the Canadian Technical Asphalt Association, CTAA, Charlottetown, Prince Edward Island, Canada, 4456.
- Ramme, B., Covi, A., Faheem, A., and Sobolev, K., 2016. *Fly Ash – An Important Ingredient for Use in Hot-Mix ASHphalt Concrete*. Fourth International Conference on Sustainable Construction Materials and Technologies, Las Vegas, NV, USA, <http://www.claisse.info/2016%20papers/S246.pdf>.
- Sobolev, K., Flores, I., Saha, R., Wasiuddin, N., and Saltibus, N., 2014. *The Effect of Fly Ash on the Rheological Properties of Bituminous Materials*. Fuel, 116, 471–477.
- Sobolev, K., Flores, I., Bohler, J., Faheem, A., and Covi, A., 2013. *Application of Fly Ash in ASHphalt Concrete: From Challenges to Opportunities*. World of Coal Ash Conferences (WOCA), University of Kentucky Center for Applied Energy Research, Lexington, KY, USA, <http://www.flyash.info/2013/012-Sobolev-2013.pdf>.
- Sui, C., Farrar, J., Harnsberger, M., Tuminello, H., and Turner, F., 2011. *A New LowTemperature Performance Grading Method Using 4 mm Parallel-Plates on a DSR*. Transp. Res. Board 91st Annu. Meet. Compend., 43–48.

Comparison of field and laboratory mix performance

J. Liu, R. Melaku, D. Gedafa & N. Suleiman

Department of Civil Engineering, University of North Dakota, Grand Forks, ND, USA

ABSTRACT: Low-temperature cracking, fatigue cracking, and rutting are three common types of distress in asphalt pavements. This study's primary objective was to compare the performance of field and laboratory hot mix asphalt (HMA) mixes in terms of fatigue cracking, low-temperature cracking, rutting, and moisture sensitivity. Performance specifications based on test results and literature reviews were determined, including rut depth for rutting resistance, flexibility index (FI) for fatigue cracking resistance, and fracture energy for low-temperature cracking resistance. Low-temperature cracking, fatigue cracking, rutting, and moisture damage resistances were determined using Disc-shaped Compact Tension (DCT), Semi-circular Bend (SCB), Asphalt Pavement Analyzer (APA), and Indirect Tensile Tests (IDT). Field mix and raw materials to create laboratory mixes were obtained from seven districts in North Dakota. Field mixes were replicated in the laboratory and compacted with $7\pm 0.5\%$ air voids using a Superpave Gyrotory Compactor (SGC). At least three specimens were tested to examine low-temperature and fatigue cracking, four were used to determine rutting resistance, and six were used to investigate moisture damage resistance. The laboratory mixes had a better low-temperature and fatigue cracking resistance, while field mixes generally had higher flexibility indices (FIs). Interstate, interregional, and state corridors have minimum and maximum parameters: maximum rut depths of 7 mm, 8 mm, and 9 mm, minimum FIs of 6, 5, and 4 for good fatigue cracking resistant mixes, and minimum fracture energies of 500 J/m^2 , 450 J/m^2 , and 400 J/m^2 for good low-temperature cracking resistant mixes, respectively.

Keywords: Fatigue cracking, low-temperature cracking, rutting, moisture damage

1 INTRODUCTION

Asphalt plants produce field mixes in large quantities in a short amount of time; therefore, field mix temperature control may not be as accurate as in laboratory specimens. The purpose of comparing field and laboratory mixes is to obtain a higher correlation between the two. There are four primary methods used to fabricate asphalt mixture test specimens: lab mixed and lab compacted (LMLC), plant mixed and lab compacted (PMLC), plant mixed and plant compacted (PMPC), and field cores, which are taken directly from the field (Reyhanech, 2017). Plant mix is referred to as field mix in this study.

Hot mix asphalt (HMA) fatigue cracking, low-temperature cracking, rutting, and moisture damage resistances were analyzed. Several studies have been conducted on lab and field mix performance comparisons. Marasteanu et al. (2012) compared lab and field mix low-temperature cracking performance using Disc-shaped Compact Tension (DCT) and Semi-Circular Bend (SCB) tests. The fracture energy test indicated that

conditioned lab specimens had a high correlation to field specimens. The SCB fracture energy values were comparable in both lab and field specimens. The DCT fracture energy values from the field specimens were generally lower than the non-conditioned lab specimens. Berg (2016) reported that lab mixes had better low-temperature cracking resistance than field mixes based on PG 58-28 and PG 64-28 mixes. Different State Departments of Transportation (DOTs) specified the minimum threshold requirements for low-temperature fracture energy based primarily on traffic level, pavement thickness, and pavement aging type. Minnesota and Iowa State DOTs recommend minimum fracture energies of 400, 460, and 690 J/m², while the Wisconsin DOT recommends 300, 400, and 500 J/m² for low, medium, and high traffic levels, respectively (Bahia et al., 2016, Chelsea, 2016).

Fatigue cracking performance comparisons were completed on 11 plant mix and plant compacted (PMPC) and 11 lab mixed and lab compacted (LMLC) specimens from a New Hampshire State Route 12 construction site using three binder grades: PG 52 -34, PG 58 -28 and PG 64 -28. The study compared the damage characteristic curves (DCC) of the different plant and lab produced mixtures. These results indicated that the lab mix DCC curves were very close and slightly higher than those produced in a plant, suggesting that the lab mixtures had a generally higher fatigue cyclic test performance. The fatigue damage prediction variation was higher for plant mixtures (Reyhanech, 2017). Other studies indicated that the fatigue performance of the lab mix was better overall than the field mix (Berg, 2016, Bahia et al., 2016). Al-Qadi et al. (2015) reported that flexibility indices (FI) of 2.0 and 6.0 appear to be cut-off values distinguishing poor- (less than 2.0), intermediate- (2.0 to 6.0), and high-performing (greater than 6.0) mixes.

The rut depth from the lab mix was relatively lower than the field mix (Choubane et al., 2000). Brown and Cross (1991) stated that there was a low correlation between air voids and rut depths in the lab and field mixes. The maximum limit of the rutting depth for the mixtures was 7 mm for interstate highways based on the rutting performance evaluation of the mixes from North Dakota using an Asphalt Pavement Analyzer (APA) (Suleiman, 2008).

It is essential to ensure that field mixes can be reproduced in the laboratory. The ability to compare field and laboratory mixes is essential to ensure that field mixes, which have properties that are difficult to control, can be replicated in the controlled environment of a laboratory.

The main objectives of the study were to:

- Compare the performance of field and laboratory HMA mixes in terms of fatigue cracking, low-temperature cracking, rutting, and moisture sensitivity.
- Recommend performance specifications of rut depth for rutting resistance, flexibility index (FI) for fatigue cracking resistance, and fracture energy for low-temperature cracking resistance based on test results or literature reviews.

2 METHODS

The field mix and raw materials used for the field mix were collected from North Dakota Department of Transportation (NDDOT) project sites. A total of seven projects from seven NDDOT districts were selected: Grand Forks, Williston, Devils Lake, Bismarck, Valley City, Minot, and Dickinson. Rutting, fatigue cracking, low-temperature cracking, and moisture damage resistance tests were completed using APA, SCB, DCT, and IDT, respectively. The experimental plan of this study is summarized in Figure 1.

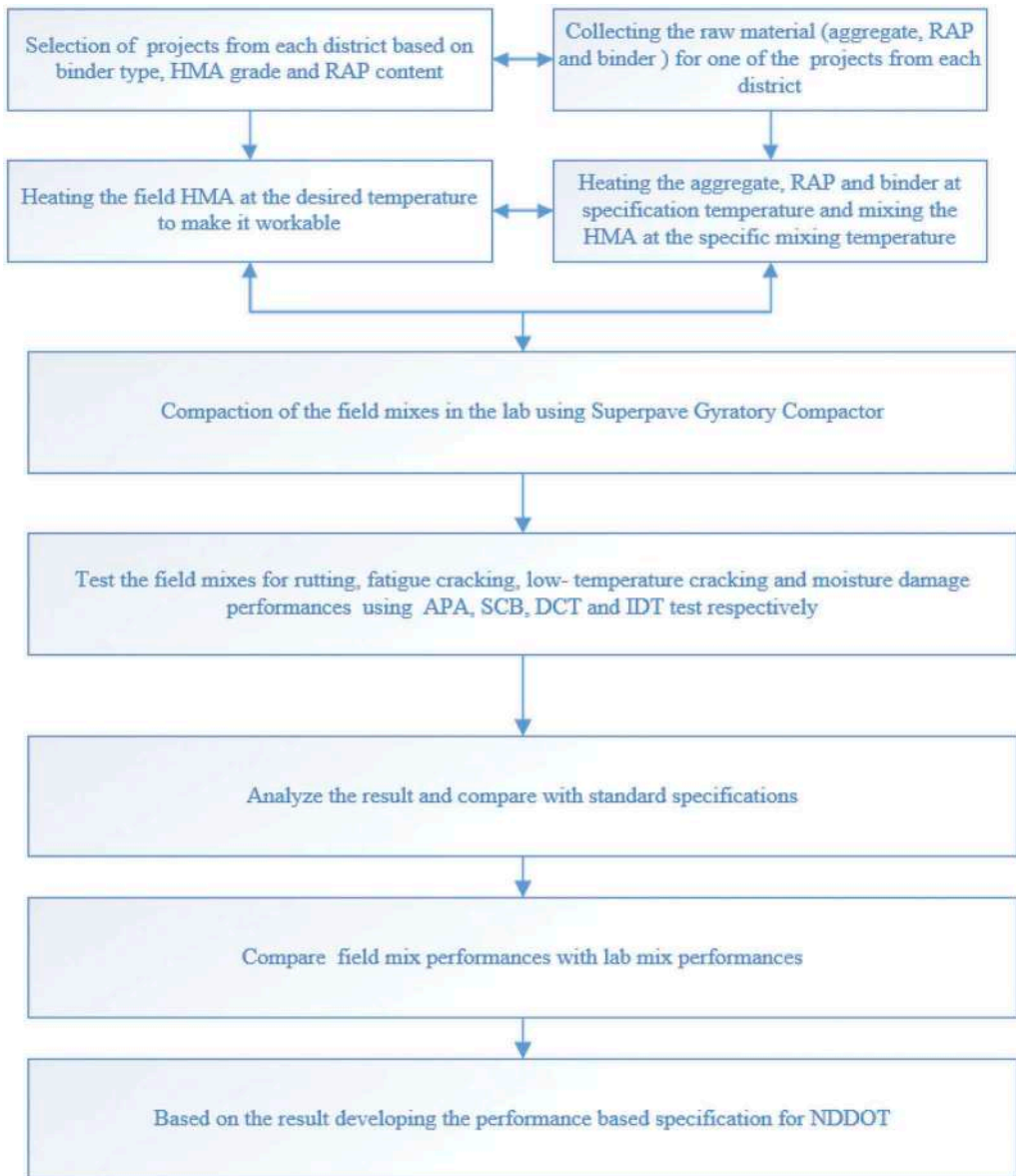


Figure 1. Experimental plan.

2.1 Mix design

The mix designs for all selected projects were obtained from the NDDOT. The same mix designs were adopted to prepare laboratory samples for the projects using the raw materials collected from the field. The mix design parameters for each project are summarized in Table 1, including the abbreviations used to plot the results. Field mixes from different highway classifications (Interstate, Interregional, State, and District Corridor) were obtained and replicated in the lab. Different fine aggregate angularities and binder grades were analyzed. Reclaimed asphalt pavement (RAP) content varied from 0-25%.

Table 1. Project information.

Project Number	Abbreviation	HMA Thick. (mm)	HMA Grade	Binder Grade	% %	
					AC	RAP
SS-2-020(017)027	2-020.027	50	FAA 43	PG 58S-28	5.5	20
NH-1-006(017)042	1-006.042	50	FAA 45	PG 58S-34	6	18
IM-2-094(156)221	2-094.221	65	FAA 45	PG 58H-28	5.2	0
NH-4-052(083)059	4-052.059	50	FAA 45	PG 64-28	5.8	0
NH-NHU-7-002(156)022	7-002.022	175	FAA 45	PG 58V-28	5.5	13
SS-5-008(049)093	5-008.093	75	FAA 43	PG 58S-28	5.5	25
NH-3-003(027)177	3-003.177	75	FAA 42	PG 58S-28	5.7	0

2.2 Mix preparation and calculations

We determined the theoretical maximum specific gravity (G_{mm}) for all field and lab mixes before compaction. AASHTO T209 was followed to determine G_{mm} . Specimen weight was greatly influenced by various factors, such as aggregate density, compaction temperature, compaction revolution, aggregate size, sample mixing, and asphalt content; therefore, we used a trial and error process to determine the appropriate mixture weight that would result in $7 \pm 0.5\%$ air voids for both the field and lab mixes that needed to be compacted. No other calculations were needed for the field mixes since they were already mixed; however, careful remixing was required to minimize weight loss. The mass of the asphalt binder, RAP, and virgin aggregate needed to be determined since all aggregates were pre-blended; therefore, the optimum asphalt content, percent RAP content, and percent virgin asphalt content were recorded on each project sheet.

The field and lab mix samples were compacted using a Superpave Gyrotory Compactor (SGC), following AASHTO T 312. Field mixes were reheated to 143°C , the aggregate blend lab mixes were heated at 163°C for six hours, the asphalt binder was heated at 143°C for no more than one hour, and the RAP was heated at 116°C for no more than two hours. The lab mixes were aged for two hours at 143°C after preparation. The molds, sample trays, mixing bowls, and spoons were heated together in the oven while the HMA sample was heated to ensure consistent temperature throughout compaction. SGC pressure was calibrated to 600 kPa before compaction. An angle of $1.28^\circ \pm 0.03^\circ$ was maintained to simulate a vehicle-tire interaction in the field. Compaction stopped when the desired height was reached: 100 mm, 75 mm, and 95 mm for cracking, rutting, and moisture damage resistance, respectively. The diameter of all specimens was 150 mm.

Bulk Specific Gravity (G_{mb}) and % air voids were determined after proper curing at room temperature. AASHTO T166 and AASHTO T269 were followed to determine G_{mb} and percent air voids, respectively.

2.3 Sample resizing

Fatigue and low-temperature cracking resistance tests were performed by initially compacting samples that were 150 mm in diameter and 100 mm in height, which were further resized to 50 mm in height. Two 25 mm holes were drilled to perform DCT, and a crack mouth opening of 35 mm was created. A 50 mm thick specimen was cut in half, and a crack mouth opening of 15 mm was created at the center of the specimens used for SCB.

2.4 Sample testing

At least 16 specimens were tested for each project's field and lab mixes: three for low-temperature cracking, three for fatigue cracking, four for rutting, and six for moisture damage resistance. Low-temperature cracking, fatigue cracking, rutting, and moisture damage resistances were determined using DCT, SCB, APA, and IDT, respectively. All samples met the $7 \pm 0.5\%$ air void content criterion.

The DCT test was used to determine the low-temperature cracking resistance of the specimens in accordance with ASTM D7313, which determines the fracture energy (G_f). The specimens were conditioned for eight hours at the low-temperature PG +10°C of the binder before and throughout all tests. A constant Crack Mouth Opening Displacement (CMOD) rate of 0.017 mm/s was maintained during the test. Cracks were formed along the cracking mouth during the test, and a graph of CMOD versus recorded load was plotted. The final DCT results were the average values of all individual tests. Fracture energy in J/m^2 was determined by taking the area under the CMOD vs. peak load graph, normalized by the specimen thickness and initial ligament length.

The fatigue resistance test was conducted in accordance with AASHTO TP 124. Sample sizes of 50 ± 2 mm were tested using SCB to determine fatigue cracking resistance using the Illinois-Flexibility Index Tester (I-FIT) protocol. The samples were conditioned for $2 + 0.2$ hours and tested at 25°C. The data from the test were post-processed to calculate the fracture energy and Flexibility Index (FI) using I-FIT software. The fracture energy is the total area under load vs. the displacement curve, and FI is the slope of the curve post-peak load.

The rutting resistance test was conducted in accordance with AASHTO T 340 using dry conditioned specimens. The testing temperature was based on the mixture's virgin binder high-temperature grade. The samples were conditioned inside the APA testing chamber for six hours before testing. A tire pressure of 689 kPa was maintained throughout the test, which was stopped after 8,000 cycles. The final APA results were the average rut depths of four specimens.

The indirect tensile (IDT) strength test was used to determine the moisture-induced damage resistance of the asphalt specimens. AASHTO T 283 was followed to determine moisture damage resistance on specimens that were 95 mm in height and 150 mm in diameter. Six specimens were conditioned and divided into two subsets of three specimens each.

The three dry subset specimens were conditioned at room temperature ($25 \pm 0.5^\circ\text{C}$) in a water bath for two hours. Three wet conditioned samples were placed in a vacuum container to determine the degree of saturation. Samples that passed the saturation requirement were further conditioned in a freezer at -18°C for 16 hours. The samples were conditioned in a 60°C water bath for 24 hours after freezing. The IDT test was then performed on the wet and dry conditioned samples. The maximum compressive load was recorded after vertical cracks appeared, and the tensile strength for all dry and wet conditioned samples was calculated. The tensile strength ratio (TSR) is the ratio of the average tensile strength from the three dry conditioned over the three wet conditioned samples.

3 RESULTS AND DISCUSSIONS

3.1 *Rutting resistance*

Figure 2 depicts the rut depth comparison of the field and lab mixes. The field mixes without RAP were slightly more rut resistant than the lab mixes; however, the results for the mixes containing RAP were not conclusive.

3.2 *Fatigue cracking resistance*

Figure 3 illustrates that the fracture energy of the lab mixes was higher than the field mixes in general, whereas Figure 4 indicates that the FI values of the lab mixes were less than those of the field mixes. This phenomenon could be due to the differences in mixing type, size, mixing time, and aging.

3.3 *Low-temperature cracking resistance*

Figure 5 demonstrates the low-temperature fracture energy of field and lab mixes. The lab mixes that did not contain RAP have higher fracture energy than the field mixes. The field mixes that contained RAP generally had higher fracture energy than the lab mixes.

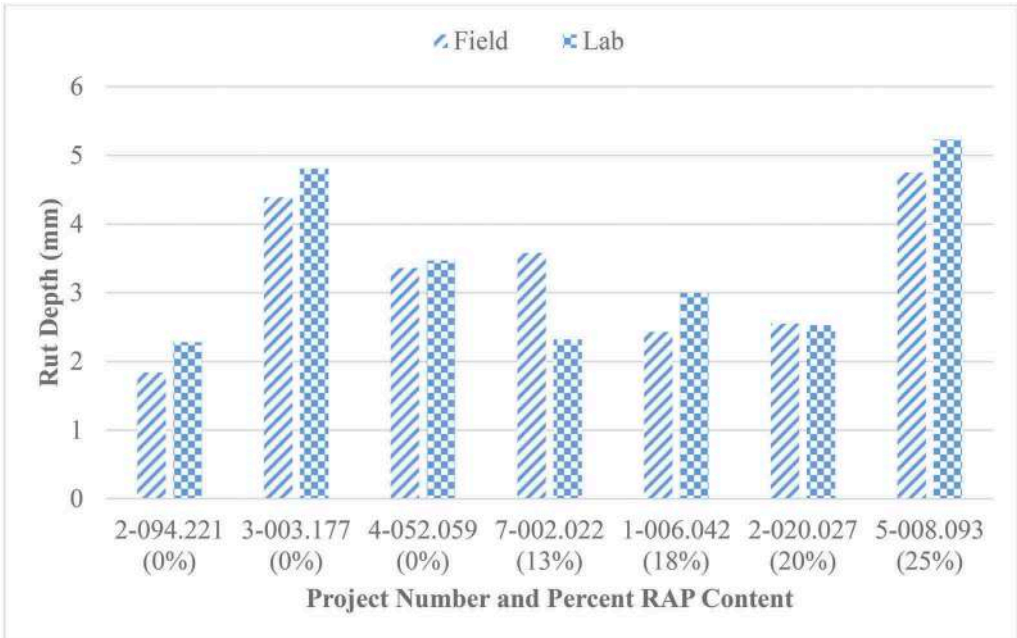


Figure 2. Comparison of rut depth for field and lab mixes.

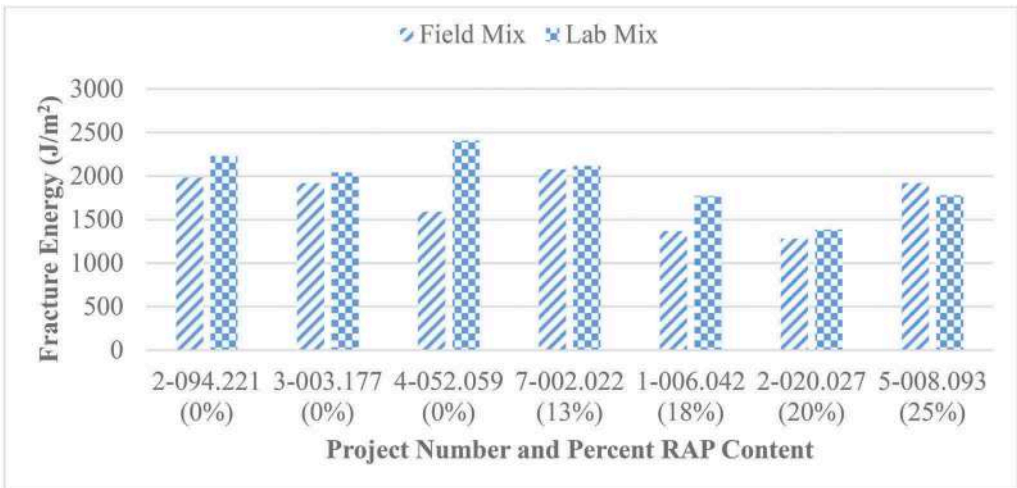


Figure 3. Fracture energy of lab vs. field mixes.

3.4 Moisture damage resistance

Figure 6 displays field and lab mix moisture damage resistance. The field mixes had higher tensile strength ratios for all virgin mixes; however, the results were not conclusive for RAP mixes. This phenomenon could be due to factors such as workmanship, binder content, and gradation that have not been controlled.

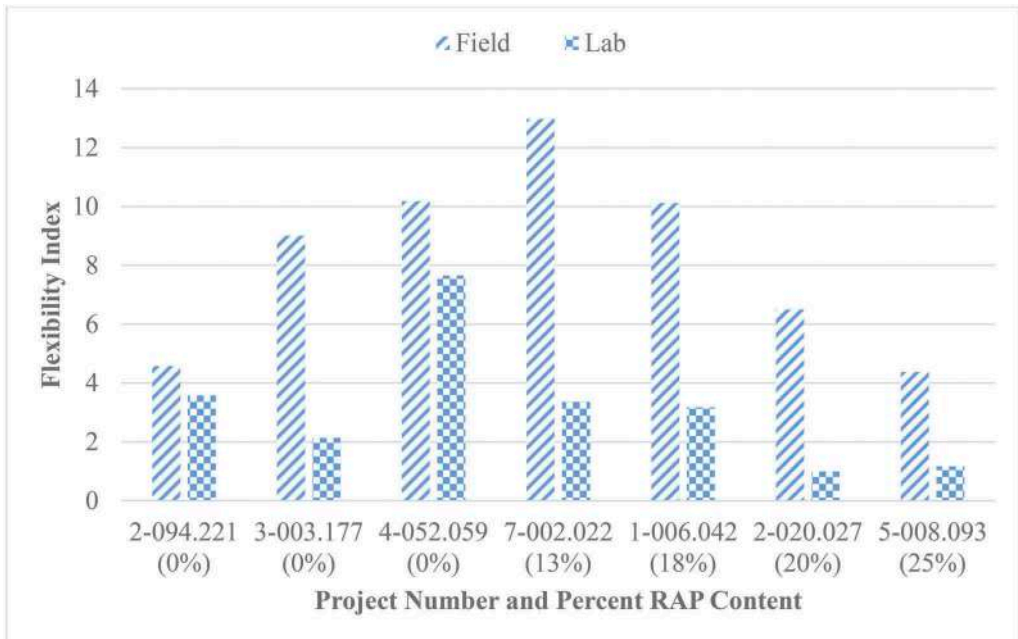


Figure 4. Flexibility index of lab versus field mixes.

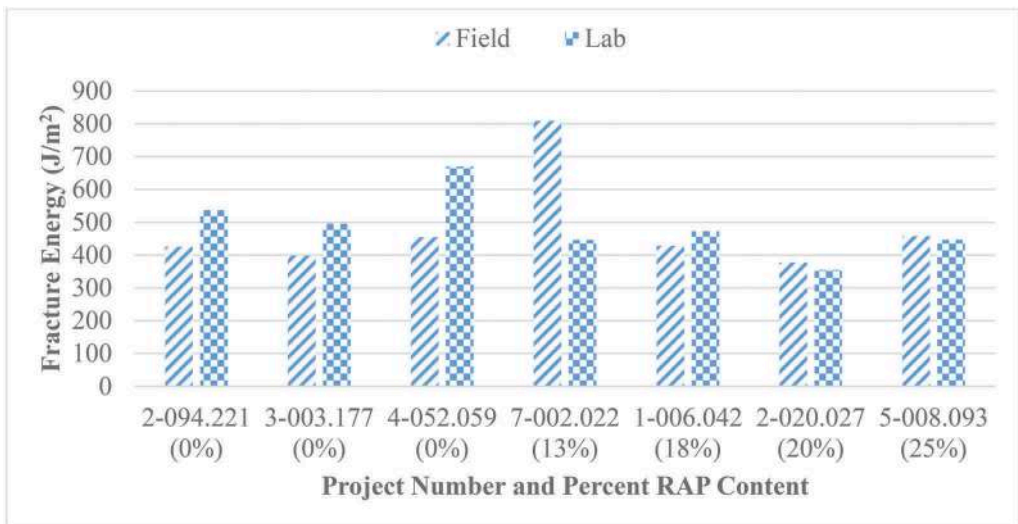


Figure 5. Low-temperature fracture energy of lab versus field mixes.

3.5 Summary of results and minimum specifications

Table 2 lists the summary of results for all projects and recommended limits. The limits were decided based on test results in this project or those reported in the literature review. The state corridor project with FAA 42 is borderline for low-temperature cracking resistance in terms of fracture energy (G_f). The district corridor project with FAA 43 did not meet the minimum specified requirements for low-temperature cracking, which could be due to a 20% RAP content.

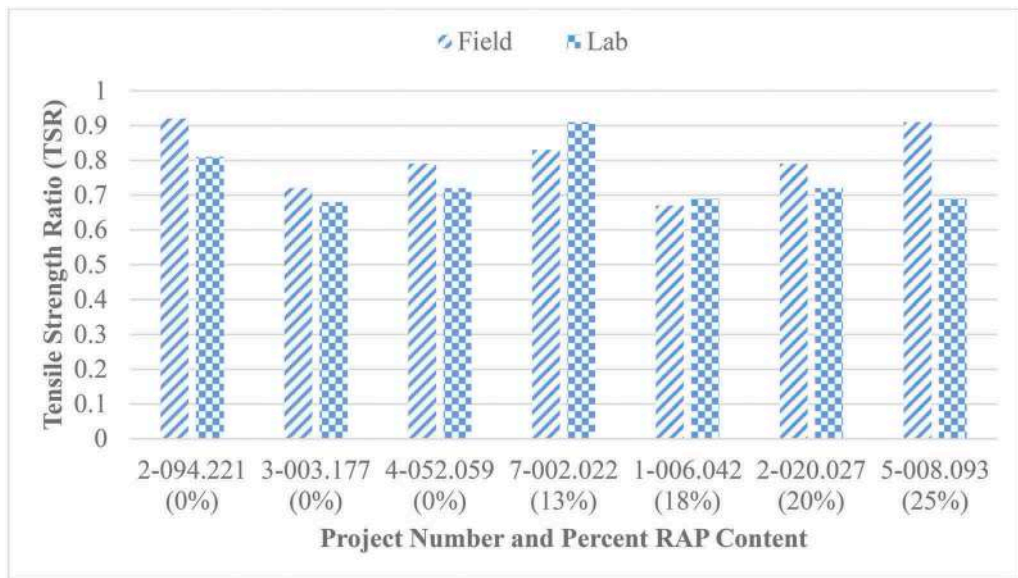


Figure 6. Comparison of moisture damage resistance for field and lab mixes.

Table 2. Summary of results and minimum specifications.

Summary Results						Recommended limiting values				
Project	FAA Type	Oil Type	RAP (%)	Classification	Rut Depth (mm)	FI	G_r (J/m ²)	Rut Depth (mm)	FI	G_r (J/m ²)
2-094.221	SMA	58H-34	0	Interstate	4	40.1	1344	7	6	500
4-052.059	FAA 45	64S-28	0	Interregional	4.3	10.2	546	8	5	450
7-002.022	FAA 45	58V-28	13	Interregional State	3.5	13.0	810			
3-003.177	FAA 42	58S-28	0	Corridor District	4.3	9.0	398			
1-006.042	FAA 45	58S-34	18	Corridor District	2.5	10.1	428	9	4	400
2-020.027	FAA 43	58S-28	20	Corridor District	2.5	6.5	377			
5-008.093	FAA 43	58S-28	25	Collector	4.8	4.4	458			

4 CONCLUSIONS, RECOMMENDATIONS, AND FUTURE WORKS

4.1 Conclusions

The following conclusions based on this study are:

- Rut depth for all samples were well below the maximum rut depth criteria. Field mixes without RAP were slightly more rut resistant than lab mixes.
- Almost all projects satisfied the minimum low-temperature fracture energy requirement of 400 J/m². Lab mixes had slightly higher fracture energy than the field mixes in general.

- The 95% confidence interval for field mix fatigue cracking resistance in terms of fracture energy ranged from 1178 J/m² to 3035 J/m², and the FI ranged from six to nine.
- Field mixes had higher moisture damage resistance compared to lab mixes in general.

4.2 Recommendations

- Maximum rut depths of 7, 8, and 9 mm are recommended for interstate, interregional, and state corridors, respectively.
- Minimum flexibility indices (FI) of 6, 5, and 4 are recommended for good fatigue cracking resistant mixes used on the interstate, interregional, and state corridors, respectively.
- Minimum fracture energies of 500, 450, and 400 J/m² are recommended for good low-temperature cracking resistant mixes used on the interstate, interregional, and state corridors, respectively.

4.3 Future work

- Obtain core specimens from the projects and determine fatigue cracking, low-temperature cracking, and rutting resistance.
- Determine the effects of high RAP content on cracking and rutting using RAP from different sources and mix designs used for different highway classifications.

ACKNOWLEDGMENTS

The authors would like to thank the NDDOT for funding and providing materials for the project. The help provided by the district material coordinators and contractors is greatly appreciated. The tireless efforts of Curt Dunn from the Grand Forks District and Aaron Perez from NDDOT Materials Research, who coordinated with all stakeholders to sample and deliver the materials, are greatly appreciated.

REFERENCES

- Al-Qadi, I., Ozer, H., Lambros, J., El Khatib, A., Singhvi, P., and Khan, T., 2015. *Testing Protocols to Ensure Performance of High Asphalt Binder Replacement Mixes Using RAP and RAS*. Illinois Center for Transportation Series, No. 15-017.
- Bahia, H., Teymourpour, P., Swiertz, D., Ling, C., and Varma, R., 2016. *Analysis and Feasibility of Asphalt Pavement Performance-Based Specifications for WisDOT*. Wisconsin Department of Transportation, Madison, WI.
- Berg, A., 2016. *Cracking and Rutting Performance of Field and Laboratory HMA Mix Designs*. MS Thesis, University of North Dakota, Grand Forks, ND.
- Brown, E. and Cross, S., 1991. *Comparison of Laboratory and Field Density of Asphalt Mixtures*. NCAT Report No. 91-1, Auburn, AL.
- Chelsea, C., 2016. *Cracking Performance Evaluation of Minnesota Asphalt Pavements*. MS Thesis, University of Minnesota.
- Choubane, B., Page, G., and Musselman, J., 2000. *Suitability of Asphalt Pavement Analyzer for Predicting Pavement Rutting*. Transportation Research Record, Vol. 1723, Issue 1.
- Marasteanu, M., Buttlar, W., and Bahia, H., 2012. *Investigation of Low Temperature Cracking in Asphalt Pavements National Pooled Fund Study-Phase II*. Minnesota Department of Transportation, St. Paul, MN.
- Reyhanech, R., 2017. *Cracking in Asphalt Pavements: Impact of Components Properties and Aging on Fatigue and Thermal Cracking*. University of New Hampshire.
- Suleiman, N., 2008. *Evaluation of North Dakota's Aggregate Characteristics and Performance in Locally Produced HMA Mixtures Using the Asphalt Pavement Analyzer*. North Dakota Department of Transportation, Bismarck, ND.

Design and evaluation with balanced performance of recycled asphalt concrete

M.-C. Liao*, J.-W. Shi & W.-H. Gao

Department of Civil and Construction Engineering, National Taiwan University of Science and Technology, Taipei, Taiwan

M.-T. Hung

Department of Civil and Construction Engineering, National Taiwan University of Science and Technology, Taipei, Taiwan

Directorate General of Highways, Taipei, Taiwan

ABSTRACT: The use of reclaimed asphalt pavement (RAP) in new hot-mix asphalt can reduce the consumption of virgin materials required, thereby conserving natural resources and also incentivize circular economy. However, the RAP content together with degree of aged binder activity (DoA) that contributes to the properties of recycled asphalt concrete would considerably affect the mixture design process. In addition, the mixture tests associated with pavement performance should be employed to design recycled asphalt concrete in order to verify the performance-based test methods for routine design of the recycled asphalt mixtures. The objectives of this research were to evaluate the effects of RAP content and DoA on the properties of the recycled asphalt mixtures in terms of rutting and cracking performances. The two pavement-related performance were assessed using wheel tracking test and IDEAL-CT. A clear understanding of design procedure with balanced performance was established based on performance-based test results in order to increase the RAP content in the recycled asphalt concrete without compromising pavement performance. The results indicated that the test data associated with the balanced performance were consistent when the DoA were between 40 and 60% for the recycled asphalt mixtures regardless of the RAP content. However, it should be noted that the asphalt mixtures with higher RAP content (40 and 60%) would be very sensitive to rutting and cracking performance when taking DoA into account. The DoA with underestimation would cause severe rutting distress for the mixture with high RAP content.

Keywords: Circular economy, RAP, balanced performance, DoA

1 INTRODUCTION

Periodically mill-fill operation to resurface badly distressed pavements becomes common because of the advancement of milling machine. However, this routine operation work generates huge amounts of reclaimed asphalt materials (RAP). Thus, RAP has become a viable alternative for pavement construction and rehabilitation. Adding a certain level of RAP content to mix with virgin asphalt materials is a solution to conserve natural resources and incentivize circular economy. However, concern has been raised with a critical issue regarding the degree of blending between the aged and virgin binders. In accordance with ASTM D4887 or AI MS-2, optimum content of virgin binder is determined on the basis of target viscosity of

recycled asphalt binder in terms of total blending scenario. In fact, the assumption of partial blending would be more realistic for the recycled asphalt mixtures (Huang et al. 2005, Huang et al. 2011, Kriz et al. 2014, Yu et al. 2017, Yu et al. 2018). The degree of aged binder activity (DoA) and degree of blending (DoB) have been proposed and defined in previous research (Kaseer et al. 2019, Lo Presti et al. 2020, Yu et al. 2021, Ashtiana et al., 2018; Bressi et al., 2015; Noferini, et al. 2017). The term of DoA can be defined as the amount of recycled asphalt binder (aged binder) that is activated due to mixing temperature or the addition of rejuvenators, while the definition of the DoB is described as the proportion of recycled asphalt binder that blends with the virgin asphalt binder in an asphalt mix. The DoB would be influenced by the mixing temperature, mixing time, RAP content, asphalt content and so on. Nevertheless, the binder blending phenomenon is quite complex due to the fact that the RAP content, mixing temperature, mixing time, aged binder behavior and rejuvenator properties would influence the DoA and DoB (Pires et al. 2021, Riccardi et al. 2016).

This research was to investigate the effects of RAP content and degree of aged binder activity on the performance of the recycled asphalt mixtures. The pavement performance-related parameters including CT-index and rut depth were used to characterize the properties of the recycled asphalt mixtures. A clear understanding of the balanced mix was established in order to increase the RAP content in the mixtures without compromising pavement performance.

The objective of the study are: (1) to investigate the effect of RAP content on the performance of recycled asphalt mixtures, (2) to evaluate the influence of DoA on the performance of recycled asphalt mixtures, and (3) to analyze balanced performance in terms of rutting and cracking.

2 MATERIALS AND METHODS

2.1 *Materials*

The laboratory experiments included twenty-five combinations of RAP contents and DoAs. Four RAP concentration levels ranging from 20 to 60 % were added to the virgin mixtures, while six levels of DoAs between 0 and 100% were also considered in this study. The asphalt mixture with 0% RAP was included as a control mixture for comparison purpose. In addition, the RAP with asphalt content of 3.6% was obtained using solvent extraction method. The recovered asphalt binder from the RAP had a penetration value of 23 (d_{mm}) and 60°C viscosity of 30,000 poise. In addition to the aged binder, the AC-20 grade virgin asphalt binder was employed in this investigation.

The dense graded asphalt mixtures were manufactured with a nominal maximum aggregate size of 19 mm as per ASTM D3515. The natural mineral aggregate including fine and coarse particles was crushed limestone provided from one quarry source. The asphalt mix design results for the asphalt mixtures were determined by conducting conventional Marshall mixture design process. Optimum asphalt contents for the mixtures were determined to correspond with target air void content of 4%. The specimens at optimum asphalt contents were then prepared for further testing as required. Triplicate specimens were tested for each asphalt material considered in this study. Table 1 shows the aged and virgin binder contents for the respective recycled asphalt mixture. The 0% DoA represented the black rock scenario, while 100% indicated total blending situation in the mixes. It can be found that a decrease in virgin binder content with increasing the DoA, indicating the fact that more aged binder were activated. As increasing RAP content, the virgin binder content decreased. It is noted that the total asphalt content of all asphalt mixtures was fixed at 4.7%.

2.2 *Indirect tensile asphalt cracking test (IDEAL-CT)*

Indirect tensile asphalt cracking test (IDEAL-CT) was performed on the compacted specimens in order to evaluate the resistance to cracking of the recycled asphalt mixtures. Based on the ASTM D8225, the compacted cylindrical specimens were prepared, having a diameter of 100 mm and 63.5 mm thick with the design air void of 4%. The test was performed at a temperature of 25oC

Table 1. Binder contents for the recycled asphalt mixtures.

RAP (%)		0% RAP Control		20% RAP		30% RAP		40% RAP		60% RAP		
		Virgin binder (%)	Aged binder (%)	Virgin binder (%)	Aged binder (%)	Virgin binder (%)	Aged binder (%)	Virgin binder (%)	Aged binder (%)	Virgin binder (%)	Aged binder (%)	
DoA (%)	black rock	0%	4.7	0	4.7	0	4.7	0	4.7	0	4.7	0
		20%	-	-	4.56	0.14	4.48	0.22	4.41	0.29	4.27	0.43
	partial blending	40%	-	-	4.41	0.29	4.27	0.43	4.12	0.58	3.84	0.86
		60%	-	-	4.27	0.43	4.05	0.65	3.84	0.86	3.4	1.3
		80%	-	-	4.12	0.58	3.84	0.86	3.55	1.15	2.97	1.73
		100%	-	-	3.98	0.72	3.62	1.08	3.26	1.44	2.54	2.16
full blending												

under a constant loading rate of 50.8 mm/min. The aim of the test was to determine the cracking tolerance index of CT-index for the asphalt mixtures. Three primary parameters used to determine the CT-index include fracture energy (G_f), the 75% post-peak slope (M_{75}) and 75% displacement (L_{75}). In addition, the geometric properties of specimen diameter (D) together with thickness (t) were also incorporated in the calculation. Therefore, the CT-index can be obtained from the following equation:

$$CT_{index} = \frac{t}{62} * \frac{G_f}{|M_{75}|} * \frac{L_{75}}{D} * 10^6 \quad (1)$$

2.3 Wheel tracking test

The wheel tracking test was conducted at 25°C in a temperature controlled chamber in order to assess the rutting performance of the recycled asphalt mixtures. The wheel tracker consisted of a loaded wheel which bore on the cylindrical specimen housed in a 150 mm diameter and 75 mm deep steel mold on a reciprocating table. The table moved backwards and forwards at a rate of 26 cycles per minute. The wheel was rolled on the surface of the specimen with a specific travel length. The standard loading pressure was 700 kPa. After 6,250 cycles, the vertical deformation induced at the middle point of the specimen was recorded.

2.4 Cantabro abrasion test

The Cantabro abrasion test was conducted at 25°C to evaluate the resistance to ravelling property of the asphalt mixtures. The compacted specimen was tumbled inside a Los Angeles abrasion drum without the charge of steel balls for 300 revolutions at a speed of 30 rpm. The percentage of weight loss during the abrasion process was used to represent the ravelling characteristics of the asphalt mixtures. The percentage of weight loss is ratio of specimen weight loss to initial specimen weight.

3 RESULTS AND DISCUSSION

3.1 Properties of RAP material

Although the RAP binder content of 3.6% and 60°C viscosity were found, the mix properties were addressed in this study. Prior to performing mix design for producing the recycled

asphalt mixtures, the balanced performance of the RAP material was evaluated by means of wheel tracking, IDEAL CT and Cantabro abrasion tests. The cylindrical specimens with 100% RAP were prepared. Figure 1 shows the balanced performance in terms of rutting, cracking and raveling properties for the RAP compacted mixtures. It is found that the RAP can not satisfy the requirements of the cracking resistance and raveling property although the low rutting depth was observed. The performance can be expected because the aged binder was incapable of providing sufficient adhesive and cohesive properties to the asphalt mixture. It is necessary to include fresh binder in order to lubricate the RAP and improve the performance of the asphalt mixtures. In addition, the rutting performance of the RAP mixture became worse after the recycled asphalt mixtures experienced the moisture condition.

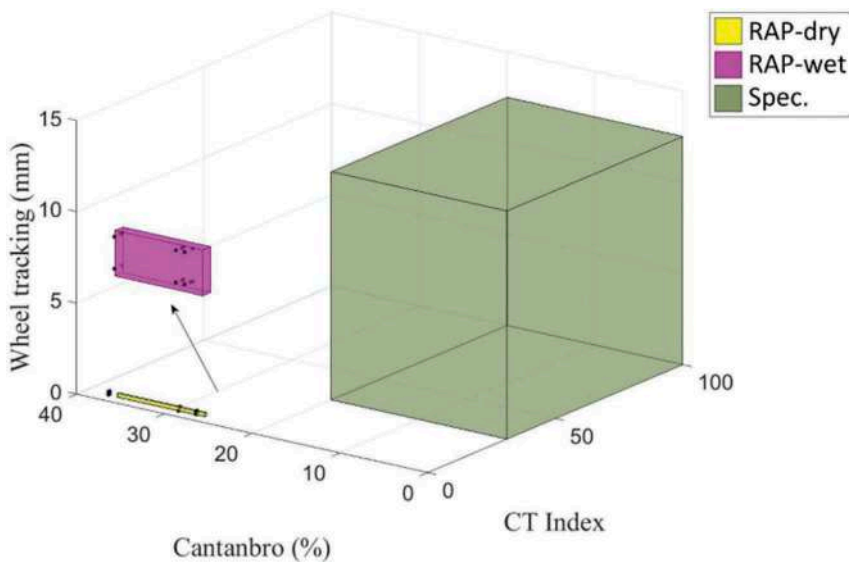


Figure 1. Balanced Performance characteristics of 100% RAP Mixtures.

3.2 Mix design of recycled asphalt mixtures

Figure 2 shows the design grading curve for the dense-graded recycled asphalt mixtures tested and control mix in this study. The passing percentages of aggregate particles were controlled at the midpoints between the upper and lower specification limits at the critical sieve sizes. Marshall mix design was conducted to produce cylindrical specimens, and the target air void of 4% was achieved using a gyratory compactor to compact the specimens. Table 2 lists the results for the control mixture, and all values meet the requirements. The optimum binder content was selected at 4.7%. Therefore, all of the recycled asphalt mixtures had the total binder content of 4.7%. It is noted that the addition of virgin binder content to the mixture were varied. As the DoA were changed, different quantity of active aged binder was contributed to the mixture.

3.3 Effect of RAP content

CT-index results plotted against indirect tensile strength were plotted in Figure 3. It is noted that the higher CT-index value represents the better cracking resistance and the minimum value of CT-index should be 31 as per ASTM D8225. An increase in CT-index with decreasing the indirect tensile strength was found, indicating that the softer mixture appears to improve

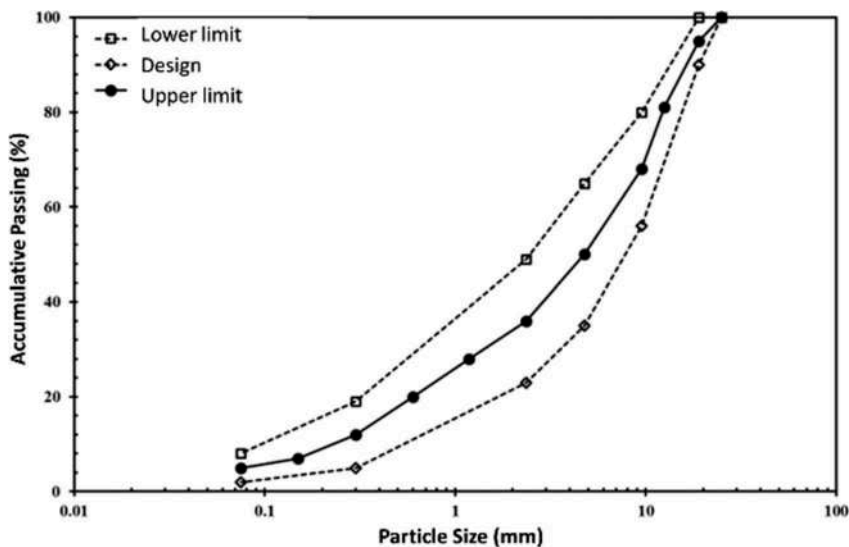


Figure 2. Design Gradation for the NMAAS 19 mm recycled asphalt mixtures.

Table 2. Mixture design results for the control mixture.

Property	Spec.	Results
Asphalt Content (%)	4~10	4.7
Stability(kgf)	≥ 817	1,125
Flow (mm)	2~3.5	2.6
Air Void(%)	3~5	4
VMA (%)	≥ 12	16
VFA (%)	65~75	72.5

resistance to cracking. In general, the asphalt mixtures containing 20 to 40% RAP had consistent data, whereas the scattered results were exhibited for the 60% RAP mixtures. It is observed that the test results of CT-index were in the wide range between 0 and 250 for the mixtures with 60% RAP. Thus, the HMA with higher RAP content appeared to be sensitive to cracking resistance. Although the indirect tensile strength values were relatively lower for the mixtures with 20 and 40% RAP contents, the CT-index values were consistent and generally met the minimum requirement of 31. Some CT-index values were lower than 31 due to the high DoA values. An increase in DoA represents the more aged binder was active to join the binder blending. As less addition of virgin binder incorporated, the aged binder should predominate the behavior of cracking resistance.

3.4 Effect of degree of activated aged asphalt

Figure 4 displays the relationship between CT-index and indirect tensile strength in terms of the DoA effect. It can be seen that an increase in CT-index with reducing the DoA. Low DoA indicated the fact that no aged binder was active and the more virgin binder should be added to the mixture, thereby improving the cracking resistance. In general, mixtures with the DoA lower than 60% can meet the minimum CT-index value of 31. Higher DoA assumption would lead to high tensile strength but low resistance to cracking. As the DoA were greater than 80%, the mixtures with low CT-index values cannot satisfy the requirement of 31. In addition,

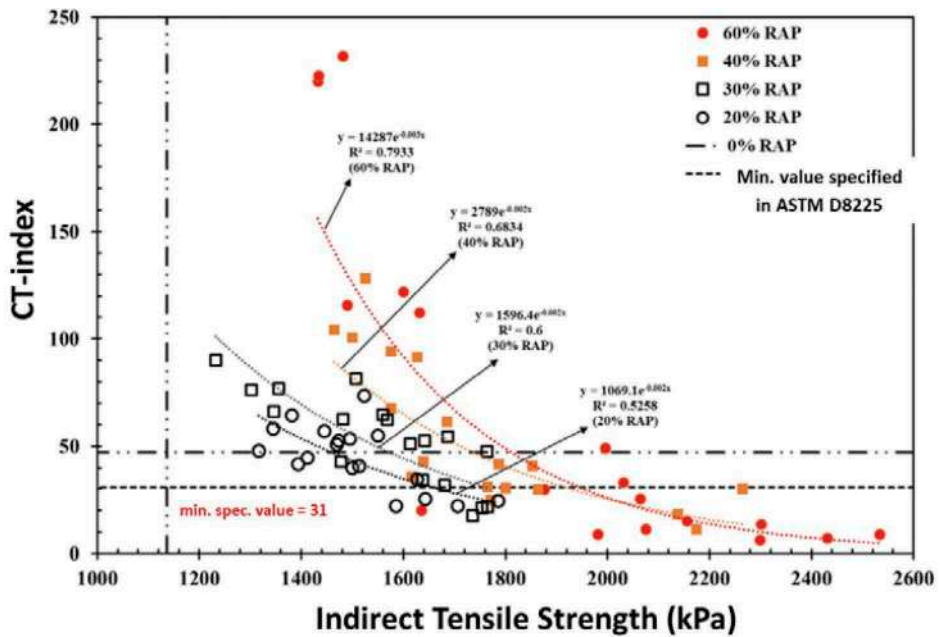


Figure 3. Effect of RAP content on CT-index and indirect tensile strength for the recycled asphalt mixtures.

the CT-index value for the mixture with DoA of 40% appeared to be similar to those for the control mixture. Additionally, the scattered results were shown for the mixtures with 0 and 20% DoA although the reduction in DoA increased the CT-index. It can be interpreted that the more additional virgin binder included would result in the mixture being more sensitive to cracking performance.

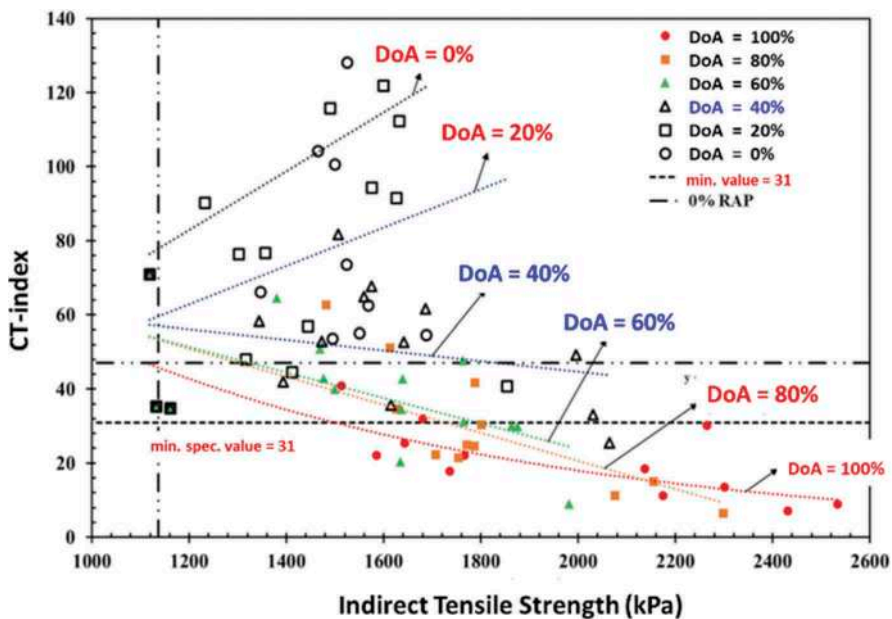


Figure 4. Effect of DoA on CT-index and indirect tensile strength for the recycled asphalt mixtures.

Figure 5 shows the CT-index data against DoA. In terms of the minimum CT-index requirement, the CT-index for the recycled asphalt mixtures should be greater than 31 in order to ensure the satisfied cracking resistance. When adding higher RAP contents of 40 and 60%, the upper limits of the DoA were 70 and 50%, respectively. It can be concluded that the DoA value should be decreased when increasing RAP content. This is due to the fact that the more RAP was incorporated in the mix, however, only less virgin binder can be blended with aged binder.

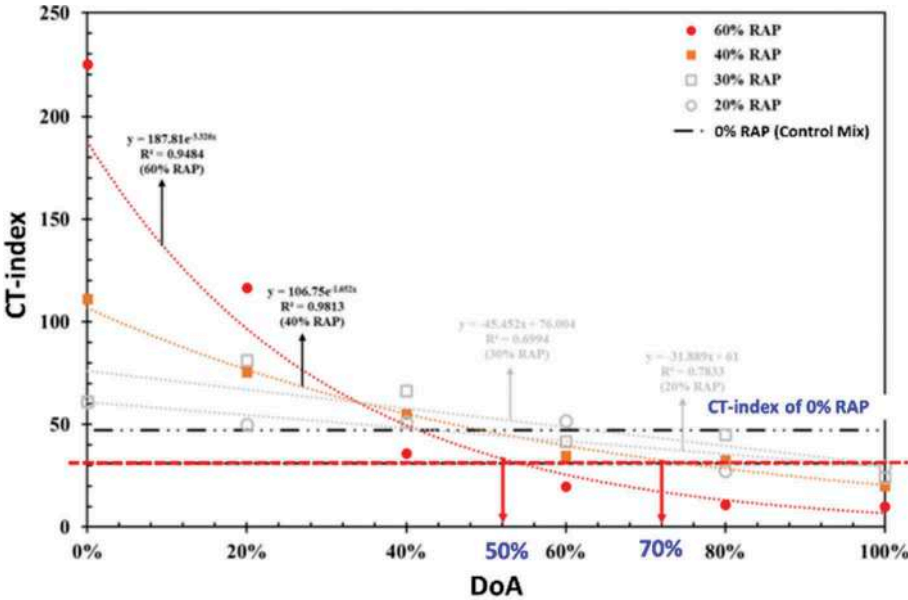


Figure 5. Estimation of DoA for the recycled asphalt mixtures.

Figure 6 exhibits the relationship between CT-index and RAP content, and the CT-index of 31 was used as benchmark. Generally, the use of RAP would be restricted as assuming the higher DoA value. When assuming the DoA values of 100, 80 and 60%, the maximum RAP content should be restricted at 20, 30 and 45%, respectively. It indicates that only 20% RAP content can be added to the asphalt mixture in the case of total blending scenario.

3.5 Balanced performance of recycled asphalt mixtures

Figure 7 shows the balanced performance with the cracking resistance against permanent deformation. An increase in CT-index was obtained with an increase in rut depth. The results can be expected because more virgin binder was incorporated into the mixture. It is found that the test results associated with the balanced performance were consistent when the DoAs were between 40 and 60% for the recycled asphalt mixtures regardless of the RAP content. However, it should be noted that the asphalt mixtures with higher RAP content (40 and 60%) would be very sensitive to rutting and cracking performance when taking DoA into account. The DoA with underestimation would cause severe rutting distress for the mixture with high RAP content.

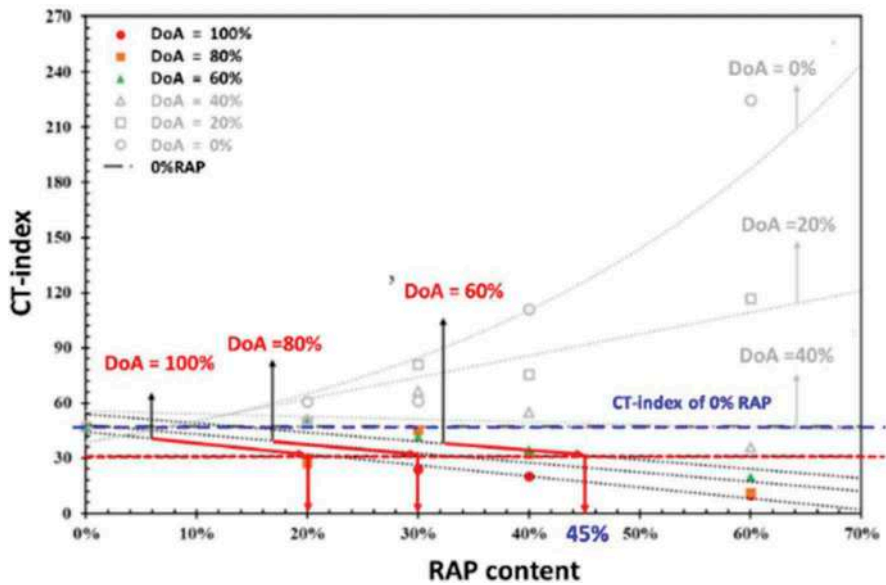


Figure 6. Estimation of RAP content for the recycled asphalt mixtures.

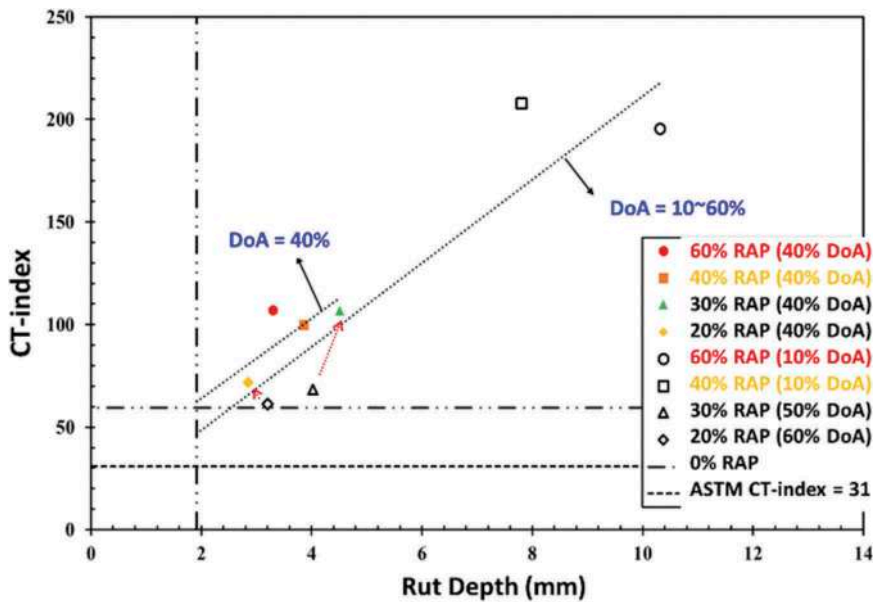


Figure 7. Balanced performance for the recycled asphalt mixtures.

4 CONCLUSIONS

This research was to evaluate the effects of RAP content and DoA on the properties of the recycled asphalt mixtures in terms of cracking resistance and rutting performance. According to the test results, the following conclusion can be drawn. It should be noted that the finding is only applicable to the RAP and other materials used in this study.

- At lower RAP content (20%, 30%), consistent test results were found and the CT-index values met the minimum requirement of 31.
- When asphalt mixture with high RAP content, the scattered results are displayed in terms of CT-index performance.
- The asphalt mixtures with 40 to 100% DoA displayed consistent results, whereas the mixtures with 0~20% DoA appeared scattered data because more virgin bitumen was included in the blending system.
- HMA with high RAP content was sensitive to rutting and cracking performance due to the uncertainty of the DoA.

REFERENCES

- Ashtiana, M., Mogawer, W. and Austerman, A., 2018. A Mechanical Approach to Quantify Blending of Aged Binder from Recycled Materials in New Hot Mix Asphalt Mixtures, *Transportation Research Record*, 2672(28), pp.107–118.
- Bressi, S., Dumont, A. and Pittet, M., 2015. Cluster Phenomenon and Partial Differential Aging in RAP Mixtures, *Construction and Building Materials*, 99, pp.288–297.
- Huang, B., Li, G., Vukosavljevic, D. Shu, X. and Egan, B., 2005. Laboratory Investigation of Mixing Hot-Mix Asphalt with Reclaimed Asphalt Pavement. *Transportation Research Record: Journal of the Transportation Research Board*, 1929(1), pp. 37–45.
- Huang, B., Shu, X. and Vukosavljevic, D., 2011. Laboratory Investigation of Cracking Resistance of Hot-Mix Asphalt Field Mixtures Containing Screened Reclaimed Asphalt Pavement. *Journal of Materials in Civil Engineering*, 23(11), pp. 1535–1543.
- Kaseer, F., Arámbula-Mercado, E. and Martin, A. E., 2019. A Method to Quantify Reclaimed Asphalt Pavement Binder Availability (Effective RAP Binder) in Recycled Asphalt Mixes. *Transportation Research Record: Journal of the Transportation Research Board*, 2673(1), pp. 205–216.
- Kriz, P., Grant, D., Veloza, B., Gale, M., Blahey, A., Brownie, J., Shirts, R. and Maccarrone, S., 2014. Blending and Diffusion of Reclaimed Asphalt Pavement and Virgin Asphalt Binders. *Road Materials and Pavement Design*, 15, pp.78–112.
- Lo Presti, D., Vasconcelos, K., Orešković, M., Pires G. M. and Bressi, S., 2020. On the degree of binder activity of reclaimed asphalt and degree of blending with recycling agents. *Road Materials and Pavement Design*, 21(8), pp. 2071–2090.
- Noferini, L., Simone, A., Sangiorgi, C. and Mazzotta, F., 2017. Investigation on Performances of Asphalt Mixtures Made with Reclaimed Asphalt Pavement: Effects of Interaction between Virgin and RAP Bitumen”, *International Journal of Pavement Research and Technology*, 10, pp.322–332.
- Pires, G., Lo Presti, D. and Airey, G., 2021. A Practical Approach to Estimate the Degree of Binder Activity of Reclaimed Asphalt Materials.” *Road Materials and Pavement Design*, 22(5), pp. 1093–1116.
- Riccardi, C.B., Carrión, A.J., Presti, D.L., Falchetto, A.C., Losa, M. and Wistuba, M., 2016. A New Procedure to Determine the Rheological Properties of RAP Binder and Corresponding Bituminous Blends, *Construction and Building Materials*, 154, pp.361–372.
- Yu, S., Shen, S., Zhang, C., Zhang, W. and Jia, X., 2017. Evaluation of the Blending Effectiveness of Reclaimed Asphalt Pavement Binder. *Journal of Materials in Civil Engineering*, 29(12), pp. 04017230.
- Yu, S., Li, P., Zhang, Z. and Shen, S., 2021. Virgin Binder Determination for High RAP Content Mixture Design. *Journal of Materials in Civil Engineering*, 33(6), 04021112.
- Yu, S., Shen, S., Zhou, X. and Li, X., 2018. Effect of Partial Blending on High Content Reclaimed Asphalt Pavement (RAP) Mix Design and Mixture Properties. *Transportation Research Record: Journal of the Transportation Research Board*, 2672(28), pp. 79–87.

Resilient and permanent deformation of foam glass aggregates assemblies

E.L. Pérez-González, J.-P. Bilodeau, P. Segui & G. Doré

Department of Civil Engineering and Water Engineering, Université Laval, Québec City, Canada

ABSTRACT: Foam glass aggregates is a material produced from mixing and baking glass residues with a foaming agent at high temperatures. The resulting product is a lightweight and insulating material with limited mechanical characteristics, characterized by unconnected millimetric and micrometric alveoli. The production of foam glass aggregates can help to resolve the recycled glass management issue in some countries, while contributing to the need of light, insulating and draining materials in civil engineering. Foam glass aggregates can be used in numerous applications, among them within the flexible pavement layered systems as insulation layers. In cold regions, this technique helps controlling frost penetration in frost sensitive subgrade soils, thus reducing the impact of freezing and thawing cycles responsible for the winter differential heaving and the spring bearing capacity loss experienced on the road network. The impacts of freezing and thawing on flexible pavements in northern countries are among the main causes of the ride quality and general condition deterioration. However, because of its intrinsic characteristic, the use of foam glass aggregates for pavement insulation requires a good assessment of the mechanical response and performance for adequate pavement design and performance, as well as for adequate mechanical protection of the insulation layer. A laboratory study was undertaken to document the resilient modulus and permanent deformation behaviour of three foam glass aggregates from different processes using test methods adapted from AASHTO T307 and EN13286-7. These tests allowed obtaining the essential material parameters to predict the non linear response of foam glass aggregates and quantify the stress dependency, as well as to predict the permanent deformation and the expected ranges of behaviour with respect to stress.

Keywords: Foam glass aggregates, resilient modulus, permanent deformation, cyclic triaxial

1 INTRODUCTION AND PROBLEM STATEMENT

Pavement engineering in northern climates often requires insulation layers in the flexible layered system to protect the infrastructures against adverse effects of frost action (Doré and Zubeck, 2009). One of the main effects of frost action is the frost heaving of sensitive subgrade soils (Konrad, 1999). When negative temperatures occur in those frost-sensitive soils, and in the case of water availability in the system, the formation of ice lenses and related surface heaving can occur. In addition to the increased transversal and longitudinal surface distortions induced by frost heaving and the formation of ice lenses, the increased overall water content and the decreased density in the subgrade soil is likely to create weakened mechanical conditions during spring thaw (Doré and Zubeck, 2009). Therefore, subgrade protection against frost action may be required. This can be achieved with increased pavement embankment thickness or with the use of extruded polystyrene panels (Bilodeau et al., 2016).

Foam Glass Aggregates (FGA) is a poorly-graded, coarse sized, cohesionless and light-weight insulation material made from recycled glass of various origins (Segui et al., 2019). The glass is mixed with about 2% of a foaming agent, and when baked at high temperatures, the glass and the foaming agent react together, resulting in a lightweight and insulating material characterized by unconnected millimetric and micrometric alveoli (Segui et al., 2019). FGA's thermal properties make it a good insulation material for pavements in cold regions.

Insulation layers are often positioned in the layered materials system of pavements, and thermal, mechanical and frost hoar criteria are considered for design (St-Laurent, 2006). This position in the layered flexible pavement systems requires a good knowledge of the mechanical properties of FGA. The resilient modulus and permanent deformation mechanical behaviour are of great importance for the design and performance of pavements. Segui et al. (2019) presented the mechanical response of an FGA tested with a cyclic triaxial procedure, heavy vehicle simulator (HVS) on an indoor test track and falling weight deflectometer on a real-scale experimental pavement. Values varying between 40 to 100 MPa were measured in these experimental conditions, which also is also in the range of similar laboratory measurements obtained by Yousefi (2016). Even if these stiffness values are within a moderately wide interval, they are reasonably consistent considering the differences in FGA materials, test procedures, as well as other sources of variability between samples. Nevertheless, the results presented by Segui et al. (2019) were obtained on only one source of FGA.

This article aims to study the mechanical performance of FGA, as described by its resilient modulus and permanent deformation. In this study, three types of FGA were studied to identify the influence of the production process of the FGA on the mechanical response of the FGA, and finally on how this influences the service life of flexible pavement in service.

2 MATERIALS AND METHODS

Two grain-size distributions were tested, 0-31.5 mm and 20-31.5 mm, for three different FGA. The FGA materials differ based on the method and foaming agents used. In this project, FGA materials referred to as Grey, Red and Black were tested. Figure 1 presents the sampled grain-size distributions (>5mm) prior sieving to obtain the desired gradations. Figure 2 shows the details of these FGA at different scales.

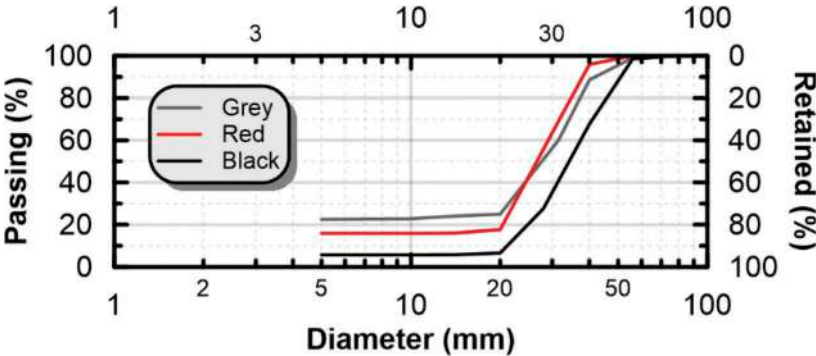


Figure 1. Grain size distribution for FGA considered.

The FGA were tested in the geotechnical laboratory of Laval University. The resilient modulus (E_r) under repeated deviatoric load in a triaxial apparatus was measured following the standard AASHTO T307-99 (AASHTO, 1999) for granular base and subbase materials for a sequence of 15 stress states. The permanent deformation (ϵ_p) was measured with respect to EN 13286-7 (CEN, 2003) using a low-stress level multistage procedure for up to twelve stress states.

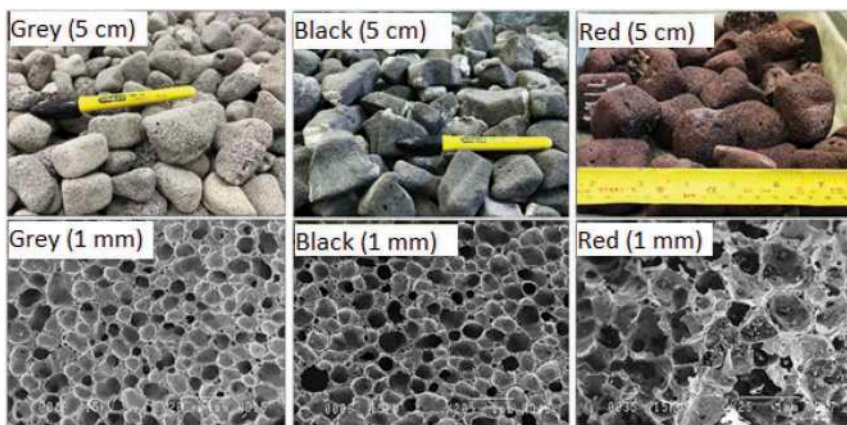


Figure 2. FGA Grey (left), FGA Black (middle), and FGA Red (right), in 5cm and 1mm scales.

FGA is a cohesionless material, so some adaptations were developed to build the sample inside a 150 mm diameter and 300 mm height \pm 10 mm cylindrical mold. FGA is placed in water for 24h and allowed to drain for 1 min. After compaction in 7 layers with a vibratory hammer inside the mold, the mold is placed in a freezer for 24h. The sample was unmolded frozen, and wrapped with a woven plastic fabric to protect the membrane. Finally, the sample was placed in the pressure cell, thawed and consolidated for 24h before the test. Figure 3 presents the triaxial setup and a few sample preparation steps.

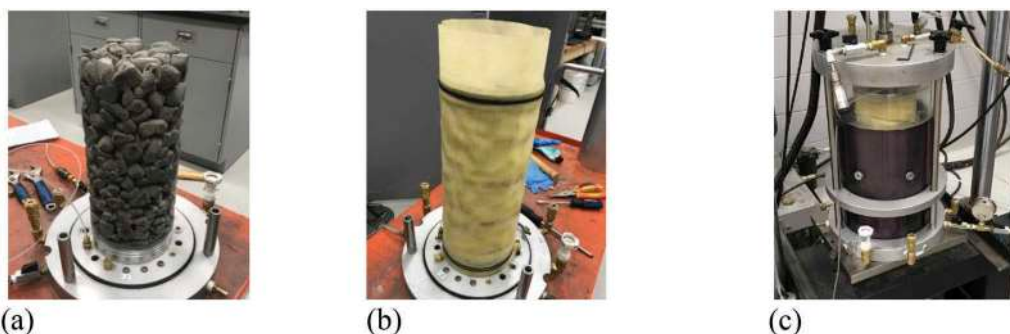


Figure 3. (a) compacted sample, (b) sample with membrane, (c) sample in triaxial chamber.

The stress dependency of E_r can be expressed as a function of the sum of the principal stress (θ , kPa) and of the octahedral shear stress (τ_{oct} , kPa) using the generalized model proposed in NCHRP 1-28A (NCHRP, 2004), which is defined with

$$E_r = k_1 Pa \left(\frac{\theta}{Pa} \right)^{k_2} \left(\frac{\tau_{oct}}{Pa} + 1 \right)^{k_3} \quad (1)$$

in which Pa is the reference atmospheric pressure and k_1 , k_2 and k_3 are regression coefficients.

The multistage low-stress level permanent deformation procedure consisted of various load stages with a maximum of 10^4 cycles (N). The following stage was initiated when 0.5% of permanent deformation was achieved during a specific load stage. The time hardening approach (Pérez-González et al., 2021; Rahman and Erlingsson, 2015) was used to model ϵ_p with respect to N and stress level. This approach can be defined with

$$\varepsilon_p = a(N_0 + N_i^{eq})^b \quad (2)$$

where a and b are model parameters, N_0 is the number of cycles in the stress path from zero, N_i^{eq} is an adjustment factor for a number of cycles in stress path i .

3 RESULTS AND ANALYSIS

Different FGA specimens were studied in the laboratory. Table 1 summarizes the densities of the compacted FGA samples.

Table 1. Densities of FGA compacted specimens.

	Group A		Group B	
Test	Resilient modulus	Permanent deformation	Resilient modulus	Permanent deformation
Grey	370 kg/m ³	534 kg/m ³	324 kg/m ³	342 kg/m ³
Black	312 kg/m ³	272 kg/m ³	231 kg/m ³	222 kg/m ³
Red	540 kg/m ³	286 kg/m ³	533 kg/m ³	540 kg/m ³

3.1 Resilient modulus

Laboratory measurements of the resilient modulus were performed on the different FGA. Figure 4 shows the trend described by E_r in relation to the stress states, and the parameters of the NCHRP generalized model (Equation 1) for each FGA. In order to present the results in a clearer manner, the materials are considered as two groups, identifying as group A the FGA with particle sizes 0 mm - 31.5 mm, and group B the FGA with particle sizes 20 mm - 31.5 mm. The results of the laboratory measurements are summarized in Figure 4. The trend shown in Figure 4 seems to indicate an equivalence of the E_r value for different FGAs. To evaluate whether the mechanical performance is significantly different for FGA with different types of foaming additive and particle size, a t-test hypothesis test was performed. For this, the linear regression described in Equation 3 is used as reference:

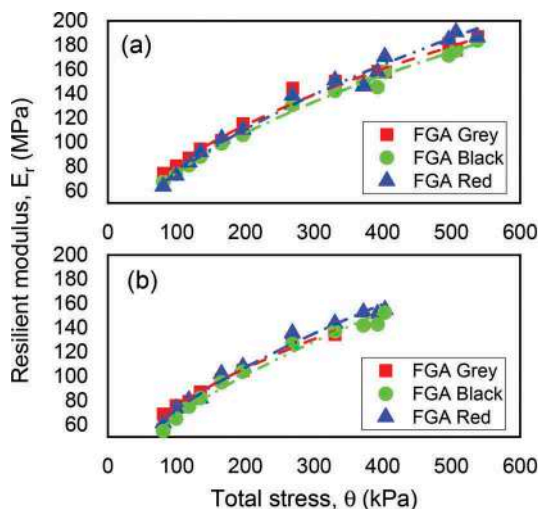
$$Er_i = \beta_1(Er_j) + \beta_2 \quad (3)$$

Where, Er_i and Er_j are the two resilient modulus to be evaluated, β_1 is the slope and β_2 is the intercept of the model. The response, described by the resilient modulus, is considered equal when the slope (β_1) is equal to one, and the intercept (β_2) is equal to zero. The E_r values to be compared are calculated using Equation 1 and the parameters for each FGA. A t-test with a significance level of 5% ($\alpha=0.05$) is used to assess whether these parameters differ statistically from equality (i.e. $\beta_1 \neq 1$ and $\beta_2 \neq 0$). A critical t-value of $t_{0.975} = 2.179$ is used as a reference for the hypothesis test. The results of this analysis are shown in Table 2.

The results summarized in Table 2 show that the mechanical response, described by their resilient modulus of each FGA studied, cannot be considered equal, because in no case the condition $-t_{0.975,12} \leq t_{\beta_i} \leq +t_{0.975,12}$ is satisfied simultaneously for β_1 and β_2 . This inference is relevant for the phase of material characterization. However, the influence of this on pavement life will be evaluated in a later section.

3.2 Permanent deformation

The previously described protocol was followed for the determination of permanent deformation. Figure 5 shows the accumulation of permanent deformation measured in the laboratory.



Group A				
	k_1	k_2	k_3	R^2
Grey	808.4	0.479	0.035	0.990
Black	768.2	0.552	-0.095	0.998
Red	752.5	0.565	-0.004	0.990

Group B				
	k_1	k_2	k_3	R^2
Grey	792.8	0.570	-0.210	0.996
Black	674.5	0.609	-0.040	0.987
Red	729.0	0.575	-0.021	0.987

Figure 4. Resilient modulus as a function of Bulk stress: (a) FGAs group A, (b) FGAs group B.

Table 2. T-statistics for equation 3 parameters in different FSG cases.

		Group A			Group B		
		Grey	Black	Red	Grey	Black	Red
Group A	Grey	-	$t_{\beta_1} = 13.1$ $t_{\beta_2} = -37.8$	$t_{\beta_1} = 25.1$ $t_{\beta_2} = -26.3$	$t_{\beta_1} = -2.8$ $t_{\beta_2} = -6.3$	$t_{\beta_1} = 13.9$ $t_{\beta_2} = -28.1$	$t_{\beta_1} = 21.0$ $t_{\beta_2} = -32.6$
	Black	$t_{\beta_1} = 13.1$ $t_{\beta_2} = -37.8$	-	$t_{\beta_1} = 16.6$ $t_{\beta_2} = -16.7$	$t_{\beta_1} = -7.5$ $t_{\beta_2} = -3.6$	$t_{\beta_1} = 9.2$ $t_{\beta_2} = -20.9$	$t_{\beta_1} = 13.3$ $t_{\beta_2} = -21.9$
	Red	$t_{\beta_1} = 25.1$ $t_{\beta_2} = -26.3$	$t_{\beta_1} = 16.6$ $t_{\beta_2} = -16.7$	-	$t_{\beta_1} = -13.8$ $t_{\beta_2} = 2.0$	$t_{\beta_1} = -17.8$ $t_{\beta_2} = -72.8$	$t_{\beta_1} = -232.2$ $t_{\beta_2} = -960.2$
Group B	Grey	$t_{\beta_1} = -2.8$ $t_{\beta_2} = -6.3$	$t_{\beta_1} = -7.5$ $t_{\beta_2} = -3.6$	$t_{\beta_1} = -13.8$ $t_{\beta_2} = 2.0$	-	$t_{\beta_1} = 8.2$ $t_{\beta_2} = -17.4$	$t_{\beta_1} = 10.2$ $t_{\beta_2} = -17.4$
	Black	$t_{\beta_1} = 13.9$ $t_{\beta_2} = -28.1$	$t_{\beta_1} = 9.2$ $t_{\beta_2} = -20.9$	$t_{\beta_1} = -17.8$ $t_{\beta_2} = -72.8$	$t_{\beta_1} = 8.2$ $t_{\beta_2} = -17.4$	-	$t_{\beta_1} = 4.5$ $t_{\beta_2} = -40.0$
	Red	$t_{\beta_1} = 21.0$ $t_{\beta_2} = -32.6$	$t_{\beta_1} = 13.3$ $t_{\beta_2} = -21.9$	$t_{\beta_1} = -232.2$ $t_{\beta_2} = -960.2$	$t_{\beta_1} = 10.2$ $t_{\beta_2} = -17.4$	$t_{\beta_1} = 4.5$ $t_{\beta_2} = -40.0$	-

From the results obtained in the laboratory (Figure 5), the black FGA is the least favorable material in terms of permanent deformation. For this material, unlike the other types of FGA, lower number of loading cycles were applied. This is because in a multistage permanent deformation test, such as the one used in this study, the stress state must be changed to the following sequence upon reaching a deformation of 0.5% in one sequence. This is to preserve the specimen for as many sequences as possible. For the black FGA of both particle size groups studied, the loading sequences reached this limit when applying less than 200 loading cycles, and the maximum strain limit of 3% was reached in less than 700 loading cycles.

On the other hand, for FGA Grey and FGA Red, those belonging to group A showed better performance, reaching the deformation limit of 3% after twice as many loading sequences as the FGA belonging to group B. The permanent deformation results allow confirming the findings pointed out in the resilient modulus behavior. The mechanical performance of the FGA is conditioned by the grain size and the foaming agent used.

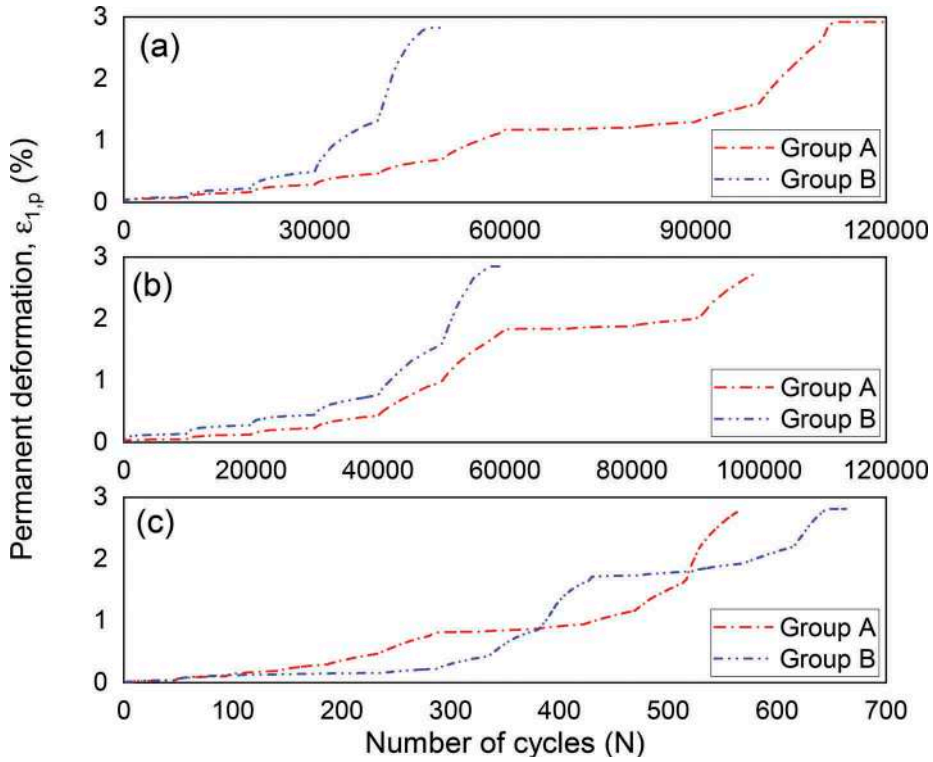


Figure 5. Permanent deformation results: (a) FGA Grey, (b) FGA Red, (c) FGA Black.

Based on the laboratory results, the parameters of the permanent deformation power model (Equation 2) were calculated for each loading sequence. A general equation was developed to associate these parameters (a and b) to the stress states to which the FGA was subjected. To maximize the usefulness of the available data, the models were fitted for each type of FGA, without discretizing by grain size. Equations 4 and 5 describe these correlations. Table 3 summarizes the parameters associated to each FGA. Figure 6 shows the fit between the proposed equations and the parameters calculated from laboratory measurements.

$$a = \alpha_1 (\sigma_3)^{\alpha_2} (q)^{(\alpha_3 \sigma_3 + \alpha_4)} \quad (4)$$

$$b = (\beta_1 \sigma_3 + \beta_2) e^{(\beta_3 \sigma_3 + \beta_4)(q)} \quad (5)$$

Table 3. Adjustment coefficients to calculate parameters a and b with equation (4) and (5).

	α_1	α_2	α_3	α_4	R^2
FGA Grey	$6.972 \cdot 10^{-19}$	11.106	-0.064	1.775	0.9048
FGA Black	$1.888 \cdot 10^{-09}$	2.333	-0.013	2.035	0.9624
FGA Red	$3.544 \cdot 10^{-35}$	20.845	-0.122	4.633	0.8883
	β_1	β_2	β_3	β_4	R^2
FGA Grey	$-4.990 \cdot 10^{-03}$	0.226	$1.400 \cdot 10^{-03}$	-0.030	0.9583
FGA Black	$-5.962 \cdot 10^{-04}$	0.038	$1.653 \cdot 10^{-04}$	-0.008	0.8788
FGA Red	$-1.728 \cdot 10^{-03}$	0.078	$1.065 \cdot 10^{-03}$	-0.002	0.8754

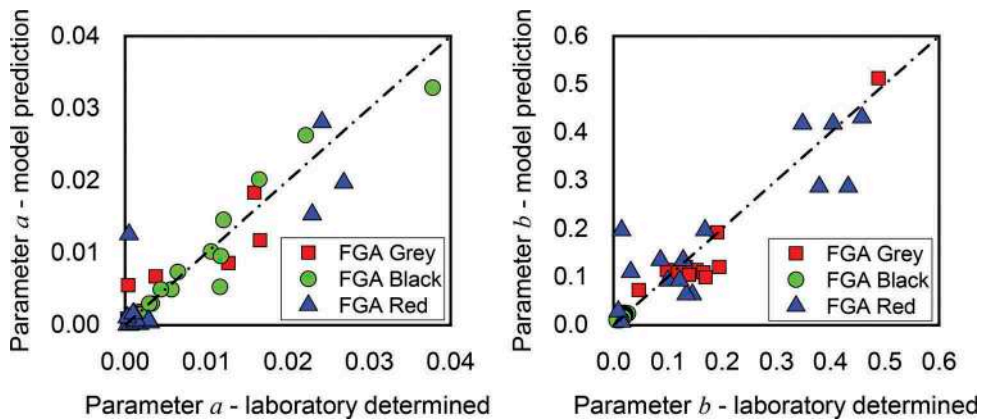


Figure 6. Fit between parameters a and b calculated with laboratory data and predicted with Eq. 4 and Eq.5.

4 CONCLUSIONS

In this research, three different types of FGA were characterized in terms of their mechanical response using resilient modulus and permanent deformation. Triaxial tests were performed in the laboratory, and models were adjusted or develop to describe the FGA performance to the stress state to which it is subjected.

Laboratory characterization showed that factors such as a foaming agent or grain size would cause the material to have different mechanical behavior. This difference in behavior was evaluated through statistical inference in the case of E_r and was evident when analyzing the progression of the permanent deformation measured in the laboratory. This aspect was expected since FGA is a cohesionless material; its mechanical performance is a function of its frictional properties in the granular assembly. The texture obtained in the different production processes is different. The packing capacity of the material, and consequently the level of contact between particles, will be affected by their gradation. The variation of the above factors will affect the mechanical performance of the FGA, so different FGA will have a particular performance, as measured experimentally during this study.

FGA materials demonstrate particular E_r and permanent deformation behaviour. However, these differences between FGA types and grain-size distribution do not appear particularly influential once they are considered as a layer in the pavement system. Given this, although characterization of each material is recommended, general models could be developed to describe the mechanical behavior of flexible pavements insulated with FGA.

ACKNOWLEDGMENTS

The authors would like to thank the Natural Sciences and Engineering Research Council of Canada for their financial support, as well as Cascades Canada ULC, Société Via and Tricentris for their technical and financial support. The authors would also like to thank the Ministère des Transports du Québec, the cities of Châteauguay, Québec and Rouyn Noranda for their collaboration. Finally, this project could not have been done without the collaboration of the Chair i3C at Université Laval (<https://i3c.gci.ulaval.ca>).

REFERENCES

AASHTO, 1999. T-307: Method of test for determining the resilient modulus of soils and aggregate materials. American Association of State Highway and Transportation Officials, Washington, DC.

- Bilodeau, J.-P., Doré, G., Drolet, F.P., Chaumont, D., 2016. Correction of air freezing index for pavement frost protection design to consider future climate changes. *Canadian Journal of Civil Engineering* 43, 312–319. <https://doi.org/10.1139/cjce-2015-0475>
- CEN, 2003. Unbound and hydraulically bound mixtures - test methods: Cyclic load triaxial tests for unbound mixtures. Comité Européen de Normalisation.
- Doré, G., Zubeck, H.K., 2009. *Cold regions pavement engineering*. ASCE Press; McGraw-Hill, Reston, VA : New York.
- Konrad, J.-M., 1999. Frost susceptibility related to soil index properties. *Canadian Geotechnical Journal* 36, 403–417. <https://doi.org/10.1139/t99-008>
- NCHRP, 2004. *Guide for Mechanistic-Empirical Design of New and Rehabilitated Pavement Structures* (Final Report No. NCHRP Report 01-37A). Transportation Research Board, Washington D.C.
- Pérez-González, E., Bilodeau, J.-P., Doré, G., 2021. Analysis model for permanent deformation in granular materials under the action of super-heavy vehicles. *Transportation Geotechnics*. <https://doi.org/10.1016/j.trgeo.2021.100536>
- Rahman, M.S., Erlingsson, S., 2015. A model for predicting permanent deformation of unbound granular materials. *Road Materials and Pavement Design* 16, 653–673. <https://doi.org/10.1080/14680629.2015.1026382>
- Segui, P., Bilodeau, J.-P., Côté, J., Doré, G., Ghafari, N., 2019. Thermal Behavior of Flexible Pavement Containing Foam Glass Aggregates as Thermal Insulation Layer. Presented at the The 18th International Conference on Cold Regions Engineering and the 8th Canadian Permafrost Conference, Quebec City, Canada. <https://doi.org/10.13140/RG.2.2.24112.51208>
- Segui, P., Bilodeau, J.-P., Doré, G., 2019. Mechanical Behavior of Pavement Structures Containing Foam Glass Aggregates Insulation Layer: Laboratory and In Situ Study, in: *Cold Regions Engineering 2019*. pp. 213–221. <https://doi.org/10.1061/9780784482599.025>
- St-Laurent, D., 2006. *CHAUSSÉE 2 : Logiciel de dimensionnement des chaussées souples*. Ministère des Transports du Québec: Direction des chaussées, Québec.
- Université Laval, 2019. *Logiciel mécaniste-empirique de conception des chaussées souples : i3C-me*. Université Laval, Québec, QC.
- Yousefi, Y., Schneider, A., Baaj, H., Tighe, S., Youssef, A., 2016. Foam glass lightweight aggregate: the new approach, in: *Resilient Infrastructure*. Presented at the CSCE Annual Conference, London.

Stabilization of expansive clays using recycled glass

R. Barros, H. Yasarer & Y.M. Najjar

Department of Civil Engineering, University of Mississippi, Oxford, Mississippi, USA

ABSTRACT: Millions of tons of glass end up in landfills every year. The glass in landfills can cause puncturing of the geomembrane and/or clay liner, which protects other chemicals from leaking into the soil and ultimately the groundwater supply. In the state of Mississippi, there is no glass recycling facility. Accordingly, all the household and industrial glass waste ends up in landfills, and it can create a potential problem during the landfill's lifespan. Glass is nearly 100% recyclable and can be substituted for up to 95% of raw materials in new glassware. However, this reuse of glass is often limited by the color of the glass containers. Also, the collection, transportation, and processing of glass waste for recycling can be very costly and time-consuming. Repurposing waste glass by integrating it into roadbeds for stabilization would be an efficient, cost-effective, and sustainable solution. However, proving this concept requires a set of laboratory experiments. Utilizing recycled glass can be an alternative method to using lime or fly ash to stabilize the roadbed. In this study, Atterberg limits and the standard proctor tests were performed with bentonite clay and varying crushed glass sizes. The proper mix of recycled glass and bentonite showed promising results in minimizing the liquid limit, plastic limit, and optimum moisture content. The results indicated that recycled glass has a great potential for the stabilization of expansive clays in transportation applications.

Keywords: stabilization, expansive clays, recycled glass, landfills, Mississippi

1 INTRODUCTION

A huge quantity of soil is required for civil engineering projects, such as railways, highways, and embankments. In some locations, the sources of earth materials are far away from the project site and transportation of these resources requires considerable effort. Expansive soils such as high-plasticity clays are not suitable for this purpose; therefore, their treatment is necessary (Ibrahim et al. 2021). Traditionally, to diminish the significant potential for volume change in expansive clay, chemical treatments such as lime and cement have been used (Prusinski and Bhattacharja 1999). Numerous researchers tried to promote solid waste as an alternative construction material to the conventional treatment methods to mitigate the environmental and economic drawbacks. Chemical stabilizers enhance the properties of expansive clay through chemical reactions, whereas with non-chemical stabilizers, soil improvement is achieved by strengthening the soil structure (Yaghoubi et al. 2021). In recent years, several types of solid wastes have been introduced and evaluated as chemical stabilizers, such as fly ash, calcium carbide residue, and lime kiln dust. Several researchers have investigated the improvement of subgrade soils using a combination of chemical and non-chemical stabilizers, such as spent coffee and geopolymers, short polypropylene fibers and polyvinyl alcohol polymer, rice husk ash, and cement, polyethylene terephthalate fiber, and fly ash. For non-chemical stabilizing, researchers have mainly used different types of fibers, such as carpet waste fibers, rubber fibers, and polyester fibers (Yaghoubi et al. 2021). However,

the use of sand-like particles, such as recycled glass, as non-chemical stabilizers has not been well investigated. In 2011, Americans alone contributed approximately 11.5 million tons of glass to landfills and recycled only 3 million tons (Tutor 2018). Glass takes an unknown amount of time to decompose naturally because it requires such high temperatures to melt. The main component of glass, silica sand, is heated to 3500°F to make glass containers. However, glass is nearly 100 % recyclable. Glass can be broken into small pieces called cullet which is then used to make new containers or other glass products, such as tile or abrasives. The use of recycled glass also helps the environment with less waste and emissions of greenhouse gases because the crushed glass can melt at a lower temperature without compromising the quality or strength of the material. It is estimated that recycling one bottle saves enough energy to run a computer for 25 minutes (Recycling 2021). Glass in the landfills also causes concern of possibly rupturing the geomembrane or clay liner that protects the other chemicals of the landfill from seeping into the surrounding soil and groundwater. The downside to recycling glass is most recycling programs only take certain bottles because of glass color. The container would naturally be clear; however certain metals or chemicals can be added to provide a color that can prevent them from being recycled with the clear glass containers. Since glass is made up mostly of silica sand, it is proposed that crushed glass could strengthen the properties of clay in roadbeds. Additionally, this application of recycled glass would not be limited to the color of the glass and would help to protect the environment with the reduction of solid waste. Therefore, this study performed a series of tests on bentonite clay by using different percentages of glass (0%, 5%, and 10%).

2 COLLECTION METHODS

There are three methods to collecting recycled glass in practice. North Carolina has a state-mandated collection method. Businesses that serve alcohol are required to recycle glass bottles. To ensure that this happens, surprise inspections occur and there are penalties in place if the business is not recycling (Eco Cycle 2021). For Wilmington, North Carolina with a population of approximately 110 thousand, 60 bars recycled 2 million bottles of beer and 140 thousand bottles of liquor in a year. California has an incentive-based collection method for recycling glass. A weekly pickup is set up for participating businesses. The businesses are required to separate the bottles from everyday trash. Recycling the glass reduces the frequency of regular trash pickup and the businesses are paid four times a year, earning around \$20/ton of glass recycled (Taylor 2015). One restaurant in San Diego averages 3 tons of glass per month which makes them \$720/year for recycling the glass. New Jersey has a cost reduction-based collection method. A private company collects the glass from bars and restaurants by having an automatic crusher at the locations. Once the container is full, the company replaces it with an empty one, and the glass is sold to another company that uses the glass to make new bottles. This program averages 3 million beer bottles monthly (State of New Jersey 2020).

2.1 *Preparation of glass samples*

For this research, glass was collected mostly from local bars. The containers were soaked in water for approximately 24 hours and the labels were scraped off. The bottles were given time to air dry so the glass would not be sticking to each other when crushed. Two different methods were tried in crushing the glass containers. The first method was placing the container in a mold and releasing a 50 lb. weight onto it. This method is limiting because it requires a lot of strength to release the weight. The second method was placing the glass container inside thick bags and striking it with a small sledgehammer. This required less strength, but over time the glass was poking holes in the thick bags. Once the containers were broken into smaller pieces, the glass was placed into an old proctor mold for the mechanical compactor. Only one large bottle or two beer bottles could be done at a time. Since the job of the compactor is to compact, the glass was stirred after each set of blows so that it would continue being crushed instead of compacted. The glass was then placed in a stack of seven sieves and placed in a mechanical shaker for approximately 15 minutes. The sieve numbers were 4, 10,

20, 40, 60, 140, and 200. The separated glass particles were placed in the respective containers. Using the same type of bottle for consistency, a grain size distribution was done on the crushed glass from the compactor after 50, 75, and 100 blows.

Figure 1 shows that there is a negligible difference between 75 and 100 blows but there is a sizable difference between 50 and 75 blows.

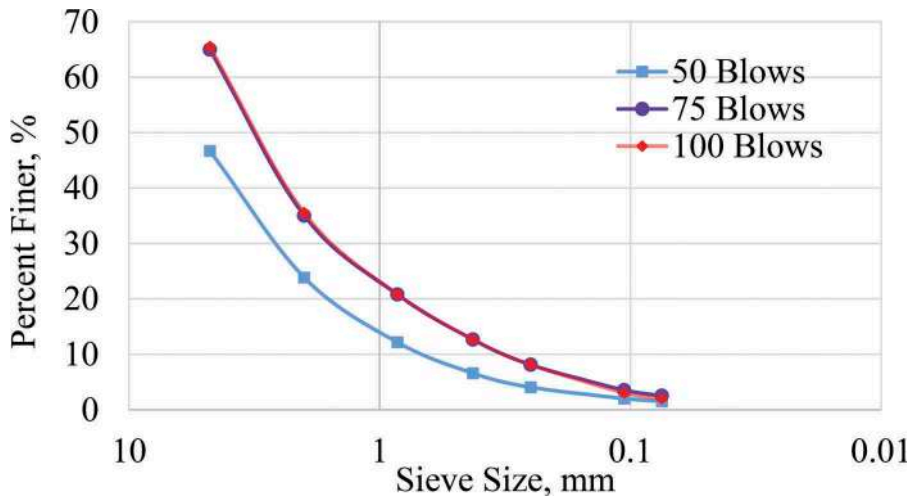


Figure 1. Number of blows, percent finer, sieve size.

3 TEST METHODS

3.1 Atterberg limits

The liquid and plastic limits were tested by both the ASTM D4318 (American Society for Testing and Materials n.d.) and European Standards (EU) BS1377 (British Standards Institution 1990) method for pure bentonite. The ASTM liquid limit method uses the Casagrande device where a section in the middle is removed using the specified tool and the number of blows it takes to close is recorded. A sample is removed after each tries to determine the moisture content. This process is repeated at least four times and there is a recording of at least one above 25 blows and one below 25 blows. The number of blows was then plotted on the x-axis with the respective moisture contents on the y-axis. A line of best fit was added and the equation of the line was used to determine the moisture content at 25 blows. This value is the liquid limit. For the EU liquid limit method, the cone penetrometer was used, where a sample was placed in the brass cup (generally placed in 3 layers and tap compaction with each layer, some moisture contents do not allow for this). The brass cup was then placed underneath the cone. The tip of the cone was lowered to where it just barely touched the sample. There is a displacement reader attached and it should be touching the top of the cone and zeroed out. The cone was then released by pressing and holding the button for a total of five seconds. Then, the displacement was recorded, and a sample was taken out for moisture content. This process was repeated for at least four points and there is a recording of at least one point below 20 mm and one recording above 20 mm. The displacement was then plotted on the x-axis and the moisture content on the y-axis. A line of best fit was added to the plot and the equation of the line was used to determine the moisture content at 20 mm. This value is considered the liquid limit. For the ASTM plastic limit method, water was added to the sample and then rolled into 1/8” threads that are beginning to crack. The standard calls for three sample cans with approximately 6 grams each to determine the plastic limit. In this study, only two sample cans

were used. The EU plastic limit method can be continued from the EU liquid limit. After the liquid limit was done, the sample was recompacted in the brass cup and placed back into position and the displacement gauge was reset. For the plastic limit though, an additional 1.57 N was required and placed on either side of the cone. The cone was dropped for five seconds, and a portion was removed for the moisture content. This process was repeated for a total of at least four points with one recording below and above 20 mm. The same process was used to determine the plastic limit as was for the liquid limit.

3.2 *Standard proctor*

The standard proctor was tested using ASTM D-698 (American Society for Testing and Materials 2003). The goal of the standard proctor is to determine the optimum moisture content (OMC) and maximum dry unit weight. The OMC is important for when other tests need to be conducted in the lab such as direct shear, consolidation, unconfined compression, and triaxial. For each of those tests, the sample must be prepared at the OMC. For pure bentonite, 15% moisture was used for the first point. Lower moistures were attempted but resulted in little compaction and a powdery mess. At 5% increments across six points, the added moisture went up to 40%. Water was introduced to the sample via spray bottle and mixed in as it was introduced. Once fully mixed, the sample was placed into the mold in three approximately equal layers for 25 blows each of compaction. The extension of the mold was then removed, and the soil was leveled with a straight edge. After recording the weight of the soil in the mold, the sample was extruded from the mold using a hydraulic jack. A sample from the center of the mold was collected to determine the actual moisture content. The remaining part of the compacted mold was broken down and mixed back in with the rest of the sample. The process was repeated five more times for a total of six points. From the moisture content and volume of the mold, the dry unit weight was calculated for each point. These points were then plotted and the peak of the curve of the graph is the optimum moisture and maximum dry unit weight.

3.3 *Direct shear*

The direct shear was performed following the ASTM D-3080 (American Society for Testing and Materials 2011) guidelines and was used to find the angle of friction of crushed glass by grain size. The consolidated undrained test setup manufactured by Humboldt (Humboldt 2021) and the respective software were utilized during the testing. The following steps were performed to complete a consolidation and shear testing of a sample. A sample was placed in a shear box mold between two porous stones and two pieces of filter paper. The depth of the mold from the bottom porous stone was recorded for three different places. The depth of the mold from the top porous stone was also recorded for three different places. The diameter of the mold was also recorded and these values were used to find the area of the sample. The shear box mold was then placed in the setup. The associated load for the load sequence was placed on the hanging arm and when the test was started, the arm was released for the load to be applied. After consolidation, the red pins were removed and the sample was sheared. The shear test was run until the deformation reached approximately 30%. The test was done for four load sequences – 0.5 tsf, 1.0 tsf, 2.5 tsf, and 4.0 tsf. Each time the test was performed, the sample was remade. From the Humboldt software, a Microsoft Excel report was generated. This report contains all the data recorded at the specified intervals during the tests. Using the area of the sample and the applied load, the normal stress was calculated. The maximum value of normal and shear stress of each load sequence was plotted together with a linearly fit line. The inverse tangent of the slope is the angle of friction of the sample.

3.4 *Specific gravity*

The specific gravity test follows the ASTM D854-02 (American Society for Testing and Materials 2000) for fine aggregates (passing sieve No. 4). The following steps were performed to determine the specific gravity of a sample. A 1,000 ml pycnometer was filled with water to the line and the

mass was recorded along with the temperature of the water. Then some of the water was poured out to make room for the sample. A 100 ± 10 g sample of glass was added to the pycnometer and then boiled for approximately 10-15 minutes to dry the sample. The sample was then allowed to cool and return to room temperature. Water was added to the 1,000 ml line and the mass was again recorded. The sample was poured into a pan ensuring that all particles were transferred from the pycnometer to the pan and oven-dried. Once dried (approximately 48 hours), the dry mass of the sample was recorded and the specific gravity was calculated. The process has repeated a total of three times and the average specific gravity was taken.

4 RESULTS AND DISCUSSION

4.1 Liquid limit and plastic limit

With pure bentonite, the ASTM and EU methods were compared. For the liquid limit, the ASTM method resulted in 303 and the EU method resulted in 293. The small difference in the two results could be from performance error. The plastic limit result from the ASTM method was 38 but the EU method was 232. Considering the results of the liquid limit, the ASTM result seems to be unreasonable and the EU result is the most feasible. Therefore, the results presented in this study came from the use of the EU method since it was the most effective way to perform the liquid and plastic limit tests. The liquid and plastic limits follow similar trends. Figure 2 shows the liquid limit results of all the completed tests.

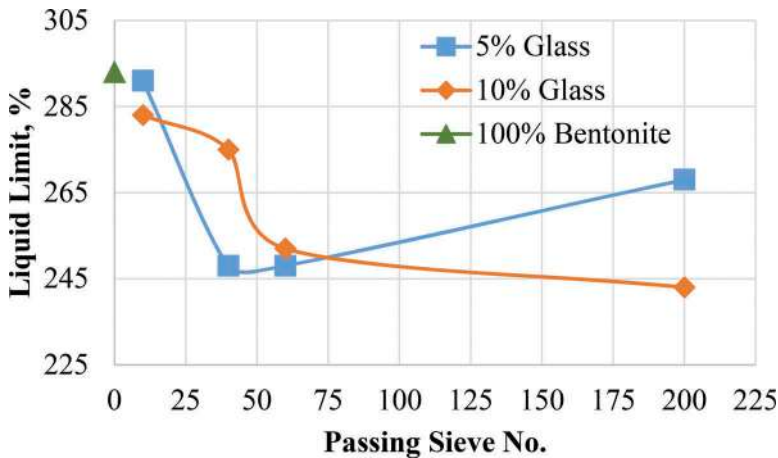


Figure 2. Cone penetrometer liquid limit results, compiled.

The sample with 10% glass passing No. 200 (LL = 243) is the lowest of the liquid limits; however, it is not feasible to use this size glass as it is difficult to crush the bottles to that size. The samples with 5% glass passing No. 40 (LL = 248) and 60 (LL = 248) produce the most feasible liquid limit results. Figure 3 shows the plastic limit results of the completed tests.

The sample with 10% glass passing No. 60 (PL = 179) was the lowest plastic limit. However, the next two lowest were the samples with 5% glass passing No. 40 (PL = 197) and 60 (PL = 195). These values seem reasonable as the glass was mixed with bentonite which is a highly expansive clay material. The liquid and plastic limits were expected to decrease when increasing size glass. However, when glass passing sieve No. 10 was introduced, the liquid and plastic limit both increased instead of decreasing. This could be due to the surface area of the glass particles being larger and not adhering to the bentonite as well as the smaller particles. This could create voids and require more moisture to move throughout the soil states. Both ASTM

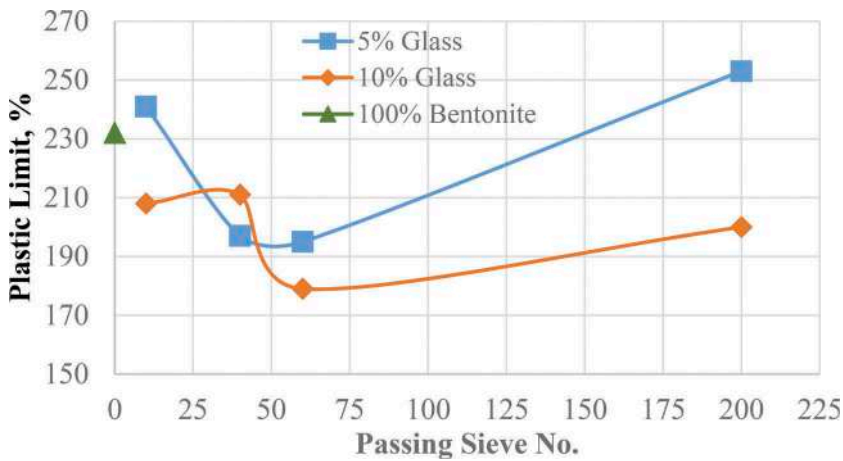


Figure 3. Cone penetrometer plastic limit results, compiled.

and EU methods are subjective to the user with the EU method being less subjective. The ASTM plastic limit requires rolling the sample into very small threads and stopping just when the sample begins to crack. Sometimes the sample can appear to be cracking as if the excess moisture had been removed but has not and should be rolled more. The EU plastic limit requires additional weight which may not be sitting the same way every time. The EU method could also vary from person to person because of how the sample is placed in the brass cup. The ASTM liquid limit is subjective to a person's sight of the gap closing and relying on either a manual count or the motorized clicker.

4.2 Standard proctor

With 5% glass, the optimum moisture content of the samples decreased with the increasing size of the glass. The samples with 10% glass followed the same trend but resulted in higher optimum moisture contents than with 5% glass. The dry unit weights are more sporadic but stay between 77 and 91 pcf. The samples with 5% glass produced higher dry unit weights and lower optimum moisture contents than the pure bentonite sample. The samples with 10% glass produced lower dry unit weights and one higher and one lower optimum moisture content than the pure bentonite sample. These trends can be seen in Figure 4 and Figure 5.

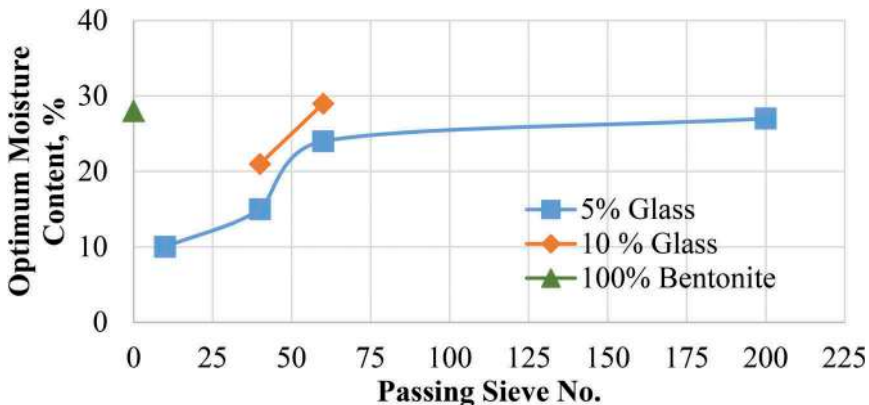


Figure 4. Standard proctor optimum moisture results, compiled.

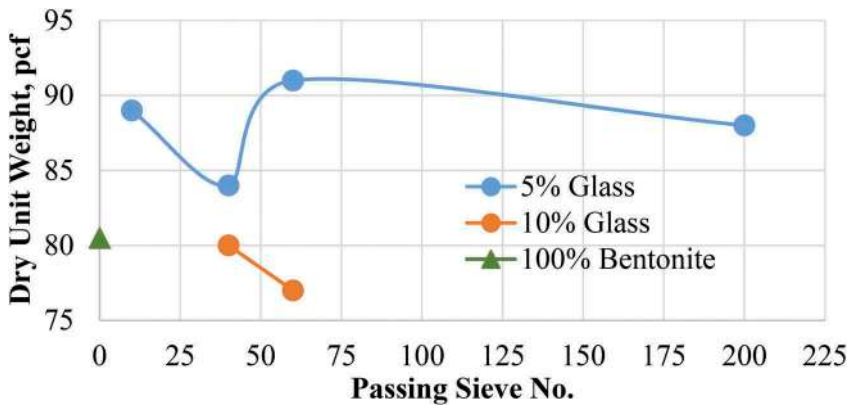


Figure 5. Standard proctor dry unit weight results, compiled.

It is important to note that some of the results appear to have missed the optimum moisture point. Each standard proctor was started at lower moisture contents (7-10%) but the sample would still be very powdery and would not bond together to compact. The optimum moisture content and dry unit weight were estimated with 5% glass passing sieve No. 40 and 10 and with 10% glass passing sieve No. 40.

4.3 Direct shear and specific gravity

The direct shear test was performed on the crushed glass to investigate the angle of friction compared to sand. Table 1 summarizes the direct shear results.

Table 1. Direct shear results, compiled.

Passing Sieve No.	Angle of Friction, °
200	44.64°
60	44.54°
40	44.35°
10	44.35°

The results show that the angle of friction for all tests falls between 44° and 45°. This is consistent with the angle of friction for dense angular sand (Das, 2002). The specific gravity test, also performed only on crushed glass, was performed to investigate how it compares with sand. Table 2 summarizes the specific gravity results.

Table 2. Specific gravity results, compiled.

Passing Sieve No.	Specific Gravity
200	2.05
60	2.42
40	2.54
10	N/A

The results show increasing specific gravity with increasing size. This is reasonable because as the particle size increases, the density is also increasing, and the specific gravity is a ratio of the density of the glass particles to the density of water. According to Das 2013, the typical range for specific gravity of sand is 2.63 – 2.67. The values obtained from the crushed glass are lower which can be valid results or there could be some error. One possible source of error is that a 1,000 mL pycnometer was used instead of a 500 mL pycnometer yet 100 ± 10 -gram sample was still used. Using the sample size designated for a smaller pycnometer in a larger pycnometer could cause the specific gravity results to be less.

5 CONCLUSION AND FUTURE WORK

From the results obtained in this study, it is possible to notice that there is a noticeable difference in the properties of bentonite mixed with crushed glass than from bentonite alone. The following conclusions can be drawn from the outcomes of this investigation:

- **Liquid Limit**
The sample with 10% glass passing No. 200 (LL = 243) had the lowest of the liquid limits; however, it is not possible to use this size glass since it is difficult to crush the bottles to that size. Therefore, the samples with 5% glass passing No. 40 (LL = 248) and 60 (LL = 248) produced the most practical liquid limit results. The use of crushed glass resulted in a reduction of 15.4% for liquid limit compared to the bentonite alone.
- **Plastic Limit**
The sample with 10% glass passing No. 60 (PL = 179) had the lowest plastic limit followed by the samples with 5% glass passing No. 40 (PL = 197) and 60 (PL = 195). These values resulted in a plastic limit reduction of 22.8%, 15.1%, and 15.9%, respectively, compared to the use of bentonite alone.
- **Liquid Limit and Plastic Limit**
The liquid and plastic limits were expected to decrease when increasing size glass. However, when glass passing sieve No. 10 was utilized, the liquid and plastic limit increased. One reason that could have led to the increase of both limits is due to the surface area of the glass particles being larger and not adhering to the bentonite as well as the smaller particles. It could create voids and require more moisture to move throughout the soil.
- **Standard Proctor**
The 5% and 10% glass samples' optimum moisture content decreased with the increasing size of the glass. However, the 5% glass resulted in lower optimum moisture content compared to the 10% glass and bentonite alone.
- **Direct Shear and Specific Gravity**
The results show that the angle of friction is consistent with the angle of friction for dense angular sand for all tests (between 44° and 45°). When increasing size, the specific gravity also increased, which is reasonable since the density is also increasing, and the specific gravity is a ratio of the density of the glass particles to the density of water.
- **Future Work**
The future work for this research includes the unconfined compression and permeability tests, which are rather simple. Also, the consolidation and triaxial tests should be performed but these tests are more complex and time-consuming. Additionally, the research should continue finding an optimum percent of added glass with the simple Atterberg limits and standard proctor as some properties had less of an effect with 10% glass than 5% glass. The tests should also focus on glass passing sieve No. 40 and 60 as those two sizes showed the best results.

REFERENCES

American Society for Testing and Materials. (2000). "D854 - Standard Test Methods for Specific Gravity of Soil Solids by Water Pycnometer." *Astm D854*.

- American Society for Testing and Materials. (2003). "Standard Test Methods for Laboratory Compaction Characteristics of Soil Using (D-698)." *ASTM Standard Guide*, 3, 1–10.
- American Society for Testing and Materials. (2011). "Standard Test Method for Direct Shear Test of Soils Under Consolidated Drained Conditions." *ASTM International*, D3080-11(D3080-11), 343–351.
- American Society for Testing and Materials. (n.d.). "Standard Test Methods for Liquid Limit, Plastic Limit, and Plasticity Index of Soils (ASTM D4318-17e1)." *American Society for Testing and Materials*.
- British Standards Institution. (1990). "Methods of test for soils for civil engineering purposes — Part 5." *British Standard*, (1), 40.
- Das., B. M. (2002). *Soil Mechanics Laboratory Manual, 6th Edition*. Oxford University Press.
- Eco Cycle, S. (2021). "Mandatory Recycling: North Carolina, USA." <<https://www.ecocyclesolutionshub.org/location/mandatory-recycling-north-carolina-usa/>> (Dec. 3, 2021).
- Humboldt. (2021). "Soil Consolidation Testing Apparatus." <<https://www.humboldtmg.com/soil-consolidation.html>> (Dec. 4, 2021).
- Ibrahim, H. H., Mawlood, Y. I., and Alshkane, Y. M. (2021). "Using waste glass powder for stabilizing high-plasticity clay in Erbil city-Iraq." *International Journal of Geotechnical Engineering*, Taylor & Francis, 15(4), 496–503.
- Prusinski, J. R., and Bhattacharja, S. (1999). "Effectiveness of Portland Cement and Lime in Stabilizing Clay Soils:" <https://doi.org/10.3141/1652-28>, SAGE PublicationsSage CA: Los Angeles, CA, 1(1652), 215–227.
- Recycling, E. (2021). "Why Recycle?" <<http://www.edwardsrecycling.co.uk/why-recycle/>> (Dec. 3, 2021).
- State of New Jersey. (2020). "State of New Jersey Recycling Information." <<https://www.nj.gov/dep/dshw/recycling/faq.html>> (Dec. 4, 2021).
- Taylor, M. (2015). "An Analysis of the Beverage Container Recycling Program." (April).
- Tutor, A. (2018). *Stabilization of Highly Expansive Clays using Recycled Glass*.
- Yaghoubi, E., Yaghoubi, M., Guerrieri, M., and Sudarsanan, N. (2021). "Improving expansive clay sub-grades using recycled glass: Resilient modulus characteristics and pavement performance." *Construction and Building Materials*, Elsevier Ltd, 302(May), 124384.

Assessment of construction and demolition waste materials for sublayers of low traffic rural roads

S. Pourkhorshidi & C. Sangiorgi

Department of Civil, Chemical, Environmental, and Materials Engineering (DICAM), University of Bolognas, Bologna, Italy

D. Torreggiani & P. Tassinari

Department of Agricultural and Food Sciences (DISTAL), University of Bologna, Bologna, Italy

ABSTRACT: The need for exploiting massive amounts of natural raw materials for constructing pavements of roads as a key element for development of infrastructures in modern age, together with enormous production amounts of wastes related to civil engineering activities as biggest portion of solid waste generated all over the world, have highlighted the importance of utilizing recycled aggregates of these materials in road pavement layers. The key factor in this quest, is to evaluate load-bearing abilities of various kinds of waste aggregates. Aggregates of reclaimed asphalt, pre-stressed or normal concrete, masonry and demolition waste (CDW) exhibit different behavior under loading after compaction. The ideal situation would be to achieve the densest compacted and durable layer in order to get the highest durability, comparing to traditional road materials. In this study, aggregates from four types of recycled materials are being subjected to study for unbound and cemented pavement layers. Initial laboratory evaluations of size and composition are followed by constructing a field on a subgrade with high non-homogenous surface. Vibrating elastic modulus (E_{vib}) for these materials were determined by Continuous Compaction Control (CCC) Oscillating Rollers. It is observed that, despite the weaknesses arisen from weak components such as masonry and elongated tiles, the stabilized distribution of the particle size can accelerate reaching to final compaction of unbound aggregates with roller passing. This process could be repeated with more or less same pattern in cemented layer, which exhibited an enhanced stiffness and uniformity in order to minimize the weak parts of non-uniform subgrade layer, and provide a high rigid pavement.

Keywords: construction and demolition waste, recycling, continuous compaction control, foundation layers, cemented layers

1 INTRODUCTION

By developing new innovative technologies for road construction in recent years, rollers with continuous compaction control (CCC) capability are more and more utilized for constructing the various layers of pavements. Achieving high efficiency of compaction by these rollers has been a key topic for many researches. Most roller manufacturers follow the corresponding line of evaluating how the soil under compaction reacts to the roller and use this measurement to determine parameters referable to bearing capacity (Dondi et al. 2014).

On the other hand, the need for providing raw materials for pavements is soared in recent decades due to huge amount of road construction all over the world, especially in developing countries, owing to facilitated technological possibilities and solutions. Considering large values of waste materials obtained from civil engineering activities, environmental, sustainability and economic considerations strongly suggest applying recycled construction and demolition waste materials as a substitute of virgin raw materials (Pourkhorshidi et al. 2020, Kovanda 2020, Tansel 2020).

The importance of rural roads in stimulating both economic growth and social development has been observed in many researches (Plessis-Fraissard 2007). The necessity for constructing rural road networks with the most cheap, durable and reliable possible methods with available materials, featured the study of unbound and cement-bound pavements to be used in the rural low-traffic pavements (Del Rey et al. 2016)

Researches on utilizing the recycled solid waste materials of construction and demolition in various layers of road pavements are vastly done all over the world (Barbudo et al. 2012, Gómez-Meijide & Pérez 2014, B. Gómez-Meijide et al. 2016); however, a limited number of them studied using continuous compaction control on recycled materials (Vennapusa et al. 2010). Sangiorgi et al. showed that construction and demolition material (CDW), laid using the same compaction process, could contribute differently to the bearing capacity of a double-layered embankment. Using CCC as an efficient method, they demonstrated that CCC measured E_{vib} moduli increase significantly as CDW compaction progresses. As the number of passes increases, the rate at which stiffness increases diminishes, and there is greater variability in stiffness for each kind of recycled material. Also, Light Weight Deflectometry (LWD) were found to correlate well despite different recorded value sizes for the moduli (Sangiorgi et al. 2015). In another study by Sangiorgi et al., it was concluded that CCC measured moduli shown significant increase with the progress of CDW compaction, even with values being highly affected by the presence of a layered structure and a weak subgrade. Also, the so-called Compaction Paths, starting from loose material values, show different trends of stiffnesses for different layers and materials. LWD measurements were very well correlated comparing to E_{vib} data. They proved that coupling CCC rollers and LWDs' measurements for the evaluation of earthworks should require a minimum CCC- measured value for given compaction amplitude (Sangiorgi et al. 2012).

In this research, an attempt is made to study the evaluation of stiffness by vibratory roller passes on four different recycled materials in unbound conditions, and also to see the stiffness gain in their cement-bound state.

2 MATERIALS

In total, five types of recycled materials obtained from civil engineering activities processed in an Italian high-quality recycling plant near the city of Imola offering licensed recycled aggregates for construction purposes, were utilized for constructing the unbound and cement-bound layers of a trial pavement. All the materials have European certificates and are in the range of 0-30mm size. Three out of five, have stabilized dense gradation envelopes, which make them suitable for being used in pavement applications. The amount of their floating elements is small. The compositions of these materials are listed in Table 1, and their particle size distributions are shown together with the size envelope of Italian authorities for road pavement materials in Figure 1. More technical properties of the materials are given in Table 2.

3 TRIAL FIELD AND COMPACTING METHOD

An experimental site was made in the mentioned recycling plant in Imola, Italy, in a location where high number of heavy trucks pass every working day (at least 5 to 10 heavy lorries each day). The subgrade of the site was constructed in the previous years with very thick

Table 1. Characteristics of the used recycled materials.

Material	Abbreviation	Containing	Composition
Stabilized mix of Crushed concrete and Reclaimed asphalt	ASFC	- Concrete-based building demolition rubble: industrial floors, beams, pillars, etc. - Vineyard poles in reinforced concrete - Asphalt slabs and Reclaimed asphalt pavement	- 50% concrete - 50% RAP
Construction and Demolition waste	CDW	- “Mixed” building demolition rubble not differentiated: brick, concrete, plaster, sand, cement, ceramic, etc. - Ceramic Tiles (ceramic industry waste) - Industrial waste (steel/foundry slag, sandblasting dust)	- 50% demolition mix - 20% ceramic waste - 30% industrial waste
Stabilized Recycled concrete	RCA	- Concrete-based building demolition rubble: industrial floors, beams, pillars, concrete tiles, etc.	- 100% concrete rubble
Stabilized Crushed concrete sleepers	TRV	- Reinforced concrete of Vineyard poles	- 100% concrete rubble from sleepers
Mix of Crushed sleepers and foundry waste	MTRV	- Reinforced concrete of railway sleepers - Industrial waste (steel/foundry slag, sandblasting dust)	- 60% concrete rubble from sleepers - 40% industrial waste

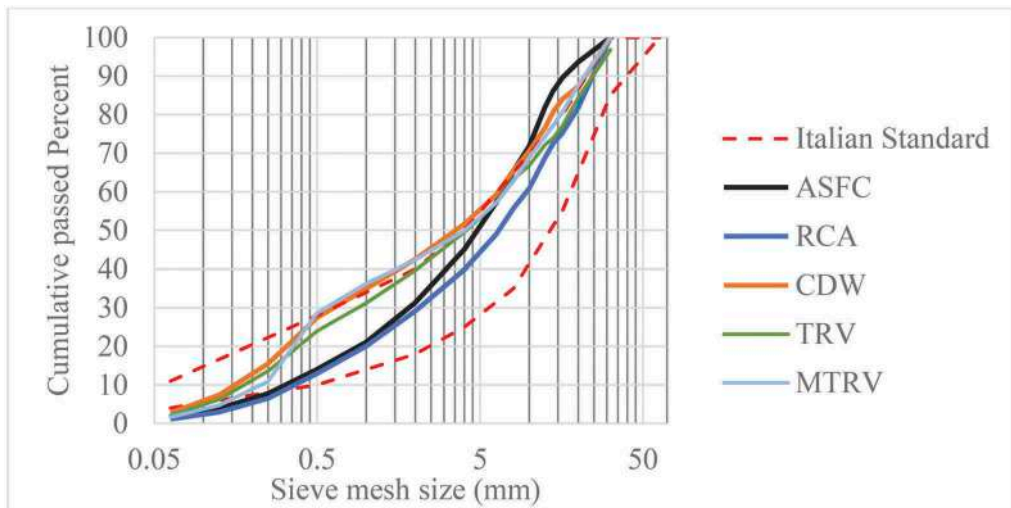


Figure 1. Particle size distribution of recycled materials.

layers of CDW and hardened by passing numerous vehicles including dozers and excavators. Four different layers were identified by means of a specific trench dug to the depth of 1.2 meters (Figure 2). Subgrade was placed in the past as a heterogeneous filling blend of CDW, clayey soil and other waste materials, compacted in several years by the plant traffic. The subgrade surface was roller-compacted and proven in 4 lanes before laying the first layer of new materials.

Table 2. Properties of recycled materials.

Material	Optimum moisture content (%)	MDD (kg/dm ³)	Un-soaked California bearing ratio (%)	Soaked California bearing ratio (%)	Los Angeles index (%)
ASFC	6.27	1.96	92	50	24
RCA	10.80	1.92	165	151	31
CDW	9.55	1.94	159	122	37
TRV	10.85	2.00	202	295	29
MTRV	10.79	1.94	110	150	30

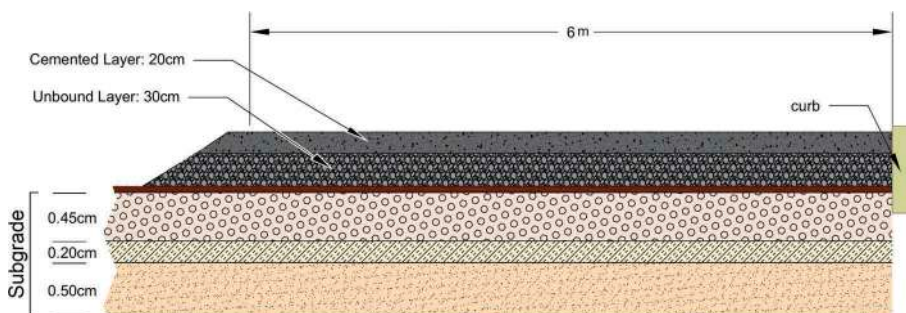


Figure 2. Schematic cross-section of subgrade, unbound and cement-bound layer.

An area 6 meters wide and 36 meters long was chosen for constructing the road and laying the selected recycled materials. The aerial image of the site is shown in Figure 3.



Figure 3. Schematic plan of constructed road and compaction lanes, Left: Sections of unbound materials and three lanes of roller compaction, Right: Cemented layers and lanes.

For target thickness of 30 cm considered for unbound base layer, about 35 cm depth of four type of materials was laid and leveled in the area each for each section length of 9 meters, after aggregates being hauled by loaders. After leveling by grader, the layer was compacted in three lanes by a heavy CCC roller setting a constant vibration amplitude. The subgrade and unbound base layer compaction and test processes were performed by means of a BOMAG

BW219 DH-5 compactor with a drum width of 212cm. Also, the speed and frequency of the roller compactor were controlled and fixed in order to maintain a comparable rolling condition for all three lanes. One each lane, 4 sets of forward vibrating and reverse static compaction were done and the stiffness data were collected.

For the Cement-bound layer, two materials of ASFC (mix of crushed concrete and reclaimed asphalt) and MTRV (mix of crushed sleepers and foundry waste) were selected to be mixed with cement and water, for a target layer of 20 cm thickness. 3% Portland cement was added to the two recycled materials of ASFC and MTRV with an automatic BLEND E050 blending machine, with the capacity of 14m³ of cemented mix (10m³ aggregate and 4 m³ cement). The measured humidity of the mixes were 7.4% and 4.5% for ASFC and MTRV, respectively.

Two cemented materials were laid in parallel as shown in Figure 3, each layer had a width of 3 meters in order to create 8 different layered pavements in the trial site. One lane of vibrating compaction per each cement-bounded material was done by a BOMAG BW174AP-4V AM roller in order to compact and simultaneously evaluate the vibratory stiffness. A Lightweight deflectometry (LWD) was done in between the passes over the cemented material by mean of a ZORN ZFG2000 portable deflectometer.

The specifications of compacting rollers are reported in Table 3.

Table 3. Specifications of roller compactors.

	Subgrade and Unbound Base layer	Cement-bound layer
Model	BOMAG BW219 DH-5	BOMAG BW174AP-4 VAM
Mass	19400 kg	9500 kg
Drum width	212 cm	170 cm
Linear load	60.1 kg/cm	29.8 kg/cm
Roller speed (average)	3.7 km/h	2.4 km/h
Vibration frequency	24 Hz	45 Hz
Manual Amplitude	1.2 mm	0.8 mm

4 RESULTS AND DISCUSSION

The output of the rollers included E_{vib} graphs plot versus the longitudinal position of the roller compactor. The triggering of the data acquisition system was done manually at each forward pass. Data were saved in the cloud and printed on paper for further analysis. Matching of start-end points was made by means of reference points.

4.1 Stiffness variation

The E_{vib} values of the subgrade lanes are shown in Figure 4. The dashed lines show the adjacent sections of the subsequent unbound layer which would be layered in next stage. It is shown that despite revealing an inhomogeneity, stiffness modulus of all lanes follow similar patterns all over the length of the field. At a distance of 14 meters, there was a pipe passing under the subgrade which caused the weakness clearly visible by decrease in the E_{vib} values. The first lane had a lower E_{vib} graph which could be due to proximity to the concrete curb, from which trucks are usually distant for maneuvering. The overall width of subgrade is less than four lanes done with roller drum width of 212 cm, so the drum accelerometer sensor of roller which is located in one side of the drum, had fallen over previously roller-proven lane. Among the sections considered for the next layer of unbound materials, it is more or less obvious that section 2 has the lowest stiffness, while there is a peak in the border of sections 2 and 3.

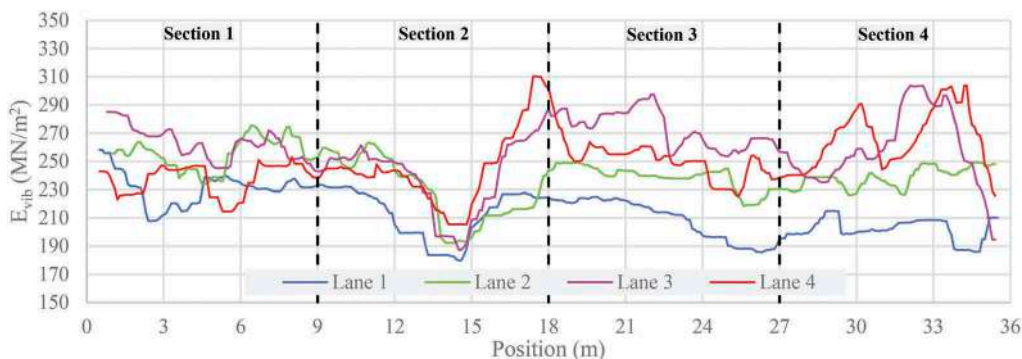


Figure 4. Vibratory modulus of subgrade (4 parallel overlapping lanes).

By constructing the new unbound base layer, another set of E_{vib} data was recorded for three new compaction lanes: east (close to curb), mid and west (the lane with free embankment). These data are shown in the graphs of Figure 5. There are some common details in all three graphs. First, all graphs follow the same pattern comparatively, considering subgrade stiffness inhomogeneity and diversity in materials of sections. For example, the location of weak stiffness regarding to weakness of subgrade under the pipe is obvious in all graphs, in spite of becoming less distinct in the west lane which is far from the curb. Secondly, the value of overall E_{vib} increase by the number of rollers passes. The E_{vib} increasing in various sections are noticeably different. In CDW, the E_{vib} graphs are closer to each other pass 1 to 4, but for other materials, especially RCA, the increase in E_{vib} is clearly visible. This could be related to many factors including the composition of mix constituents and their resistance to fragmentation. For materials with larger quantities of cementitious particles, the resistance to breaking under compaction is higher than CDW which has mainly masonry and bricks particles.

Yellow dashed lines shown the average E_{vib} value of the last pass in each section of material. It is seen that the order of E_{vib} value in the three section of CDW, RCA and ASFC is more or less the same for all lanes: CDW has the lowest value and ASFC has the relatively high average E_{vib} value. The section of TRV show a different behavior in east and west lanes which could be due to the free end edges of the embankment and the effect of subgrade stiffness variations. The relative values of final pass vibration stiffness of each section are not completely in agreement with the materials properties of each sections, which for some CDWs are relatively low (Poon & Chan 2006).

In the east lane, the drastic variations of E_{vib} are seen in first pass, which change to smoother peaks in the last pass (pass 4). However, despite a similar trend is repeated in E_{vib} of west lane, but some new peaks appear by increasing the number of passes. This proves the fact that, at least two different mechanisms contribute to the recorded E_{vib} value: first, the trace of varying stiffness of bottom layers (here: subgrade) on the upper layers, and secondly, the zonal high-compacted small segments created in last passes due to geometrical inhomogeneities in distribution of material layering and leveling.

The E_{vib} graphs of cemented layers are shown in Figure 6. As the material under compaction is unique all over the lane length, any change in the E_{vib} graph along the lane could be explained as the imprint of the base compacted layer on the superimposed cement-bounded layer.

However, the variation of E_{vib} plots in the cement-bound material over the length of the lane are much less than the variations in the unbound base layer, and cemented layers are more homogenous in terms of stiffness. The average value of E_{vib} for the last pass in all the sections (orange dashed lines) are more or less in the same range. This could be described as the positive outcome of well compacted base on the next layer, which provided a more uniform stiffness all over the lane. This homogeneity of stiffness is more evident in cemented MTRV than ASFC.

At the end of the base layer compaction, the mean E_{vib} values increase of approximately 20% with respect to pass 1 which was done over fresh material; it can be stated that each pass

of vibratory compaction increased the E_{vib} of 5%, on average. In studying the CCC method, the achievement of maximum compaction is controlled through the percentage difference between the measured values (MVs) of two consecutive passes: compaction must be continued until the mean roller MV is less than 5% greater than the mean value from the previous pass. For small sites, this guarantees that no further compaction is possible and that if the weak spot tests are positive, than all the area has, on average, sufficient bearing capacity (Sangiorgi et al. 2012). Based on this, it is possible to infer that by only considering above mentioned 5% increment limit rule for the unbound layer, even one pass with the considered energy (frequency and amplitude) appears to be enough, which does not look to be cogent. So, in case of recycled materials, additional tests and methods will be necessary to support the sufficiency of vibratory roller passes for compacting the unbound layer. This is because their stiffness increments could be not fallen in a minimum range by escalating pass number, and persist in later passes.

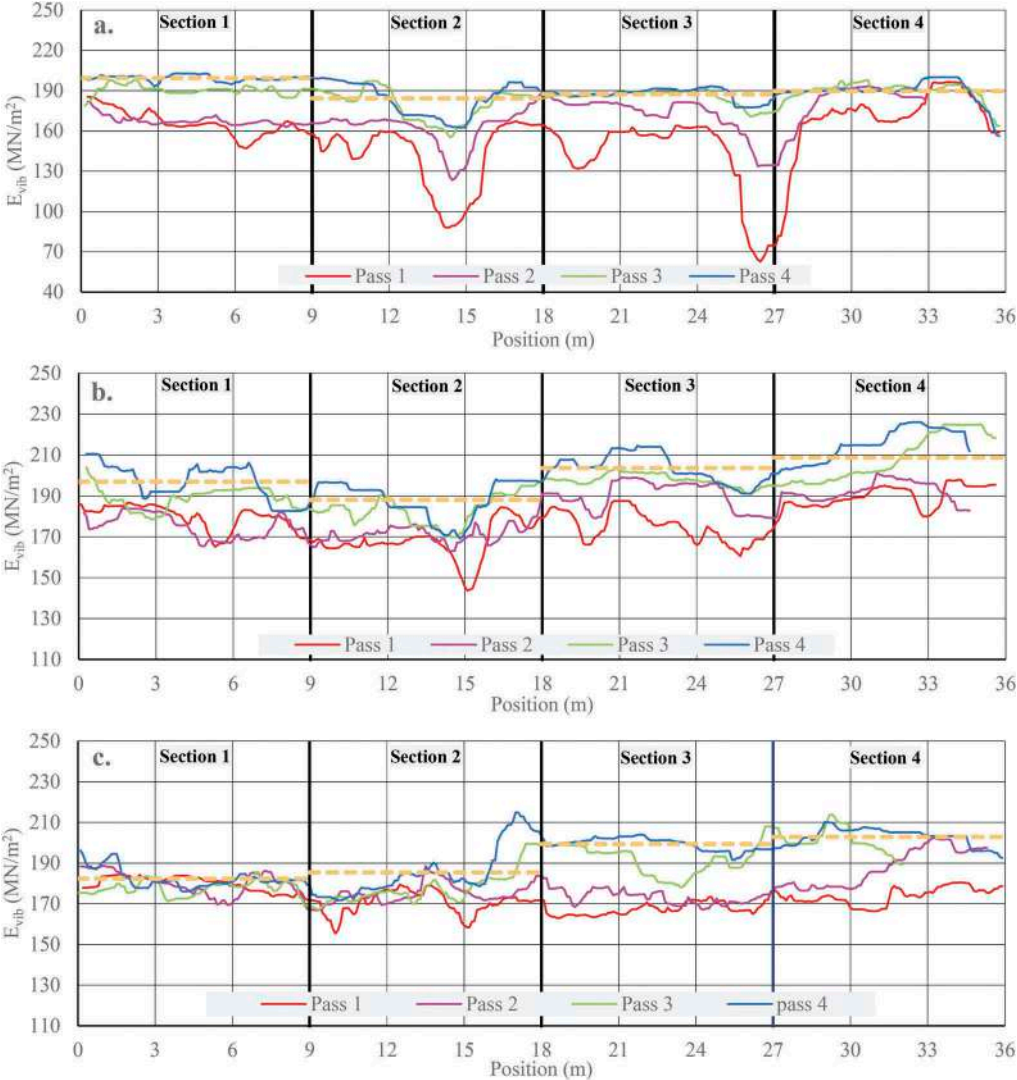


Figure 5. E_{vib} modulus of unbound base layer: a) East Lane, b) Middle Lane, c) West Lane, Section 1: ASFC, Section 2: RCA, Section 3: CDW and Section 4: TRV.

For cement-bound layer, alternatively, the distribution of E_{vib} graph increments is not uniform between passes. It is obvious that in cement-bound layers, the last passes have very close E_{vib} and graphs of final passes become more entangled. Considering that the total number of passes for cement-bound layer is 6, which is more than the passes of unbound layer (4 passes), it seems unlike unbound layer, there would be no increase in E_{vib} graphs of cement-bound layer by any further extra passes of roller. This could be due to the fact that cement-bounded materials reach their final compaction limit in specified roller vibration energy (related to vibration frequency and amplitude) after third pass. The LWD evaluation between each pass (section 4.3) confirms this.

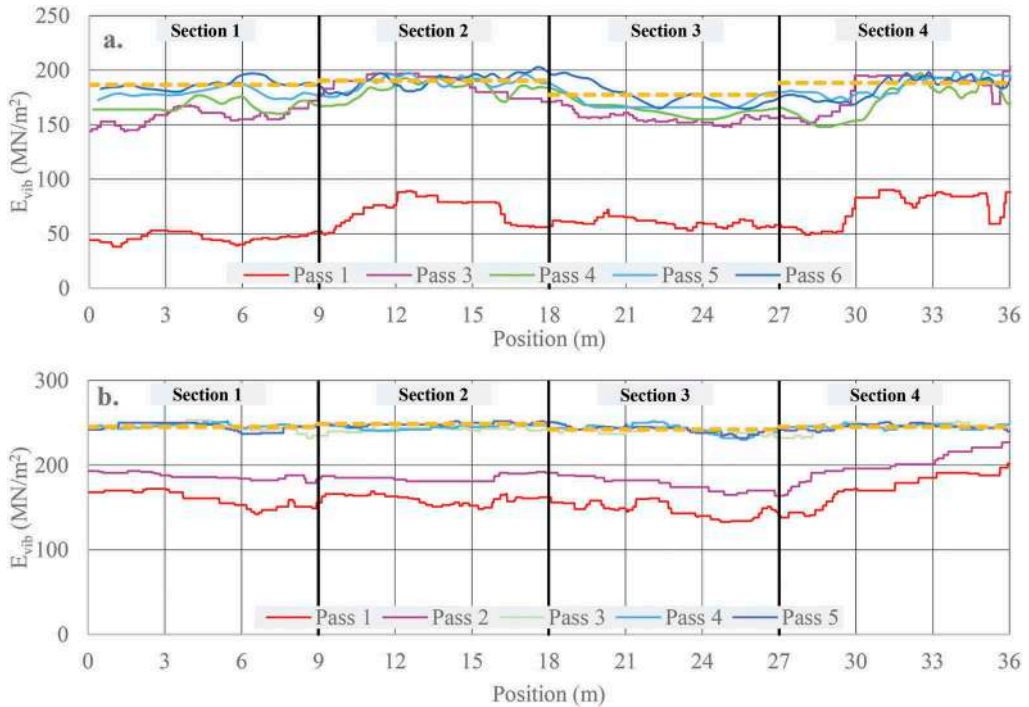


Figure 6. E_{vib} stiffness modulus in the cement-bound layer: a) Lane 1 - Cemented ASFC; b) Lane 2: Cemented MTRV.

4.2 Analysis of compaction development

The evolution of stiffness increase by the number of passes in unbound layer, can be represented in an E_{vib} pass “i” - E_{vib} pass “i+1” graph where the 45° line represents the values of equality between two subsequent vibratory passes, thus meaning that on the diagonal line no increase in stiffness has occurred. The clouds of points tend to get close to the 45° line as compaction progresses. Points below the line represent field positions where E_{vib} reduces from pass “i” to pass “i+1”. This graph shown in Figure 7, where the overall progress can be traced by joining the mean values point of each couple of consecutive passes on the E_{vib} pass “i” - E_{vib} pass “i+1” plane.

This method represents no significant variation in the rate of change between the passes in unbound conditions, which could be in contrast with what could be visually seen in E_{vib} graphs of three roller compaction lanes for all sections. This dissimilarity proves the need for studying details of the stiffness gaining mechanisms in different recycled materials. The separation of different sections data clouds could prove how different materials exhibit different compaction patterns under the vibration of roller in various consecutive passes. An intuitive

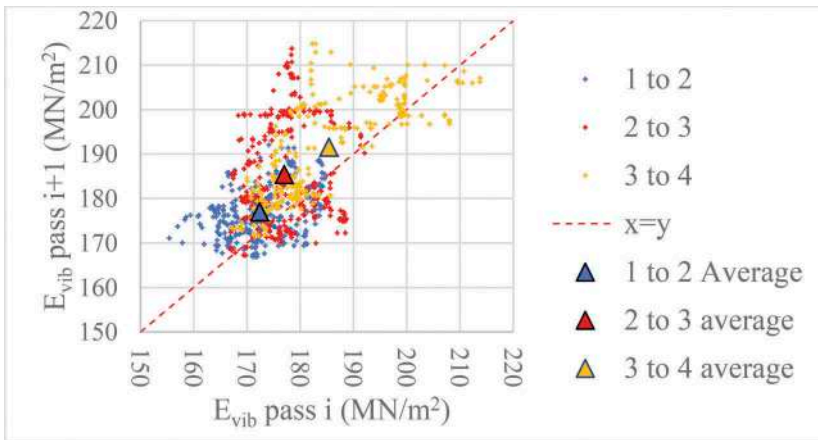


Figure 7. Stiffness values of unbound base layer in pairs of consecutive passes in all sections.

demonstration of the evolution of the stiffness could be given with the Compaction Paths (CP) polyline on each field, as shown in Figure 8.

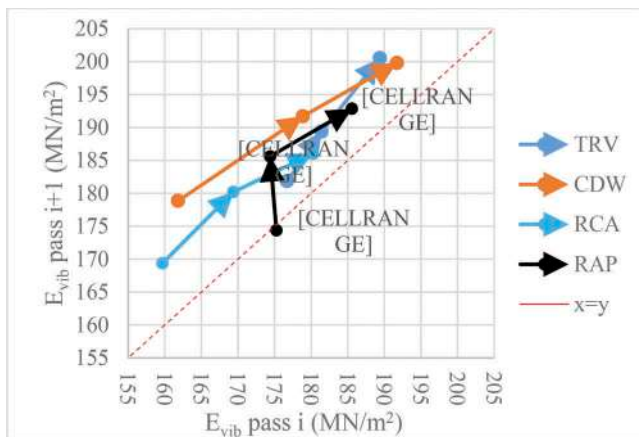


Figure 8. Compaction paths of different materials of unbound base layer.

As it is shown in Figure 8, the changing in stiffness of different materials by applying vibratory pass vary from one recycled material to the another. Considering Compaction path graphs, highest evolution in stiffness by roller compaction happens in CDW (with E_{vib} increase about 25%) and crushed sleepers (with E_{vib} increase of 15%)

The stiffness graphs in CDW became closer to each other in the last passes (3 to 4) than in initial passes (1 to 2). A possible explanation could be due to the type of substances and their portions, which are the only major dissimilarity among the different materials used in this study. CDW contains masonry and brittle tiles which fragmentation under compaction could change their particle size distribution and by increasing the number of passes, vibration could cause rearranging the broken fine particles as the compaction proceeds. This trend is also seen, but to a lower extent, in the RCA. However, in ASFC containing bituminous particles, the behavior is different, while the steps of E_{vib} increment increase in second to third pass and decrease in last ones (3 to 4), and for TRV containing high strength concrete aggregates the increment of stiffness increase pass after pass, making their stiffness development point higher than the 45° line. One possible explanation for extraordinary behavior of ASFC is presence of

two processes working in opposite directions: Bituminous particles of ASFC are less brittle than other components (low Los Angeles test index of ASFC proves this) and they can also damp the energy of vibration due to their visco-elastic nature. This feature can cause the displacement of the aggregates under vibratory compaction in initial passes. This loosening effect can be compensated by the mechanism of filling voids between the aggregates by finer broken aggregates (of other brittle components, such as cemented particles). This improves the compaction degree, diminish the stiffness increment in the last passes and makes the compaction path converge to 45° line.

In crushed sleepers, due to the high strength of source pre-stressed concrete used for manufacturing the railway sleepers, the energy of vibrating compaction roller could not be enough for smashing all coarse aggregates and only minor change in size distribution would happen. This can be followed by eased particle displacement and the process continues in next passes as most coarse aggregates remain, which causes the material gain stiffness by each pass.

4.3 Light weight deflectometry

The evolution of the stiffness of cement-bound layer by the passes measured by LWD point test is shown in Figure 9. It is evident that there is an optimum number of passes for cement-bound layers in order to reach their highest stiffness by vibratory roller compaction. This graph is in agreement with the E_{vib} graphs, where the last passes of the cement-bound layer are very close to each other, and they do not show any extra increment in stiffness by further passes. It is seen that ASFC achieves stiffness by less passes than MTRV in cement-bound layers. Moreover, the rate of reaching the final stiffness from first pass in ASFC is almost twice the one for mixed crushed sleepers. These observations could be an indication of the fact that the compaction energy needed for reaching an optimal compaction in recycled materials with hard high-strength components are higher than those with weaker aggregates.

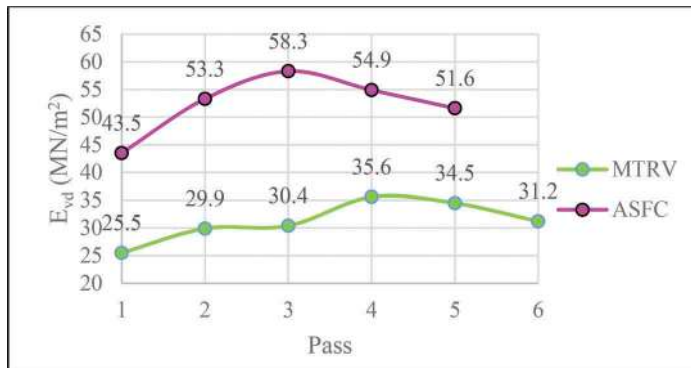


Figure 9. Lightweight Deflectometry test (LWD) results after each roller pass over cement-bound layers.

5 CONCLUSIONS

In this research, five types of recycled aggregates from waste of civil engineering activities were utilized for constructing unbound and cement-bound layers for low traffic roads by using vibratory compaction roller and their embedded CCC systems. The following outcomes can be concluded:

- Different recycled materials exhibit similar behavior with different extent in vibrating roller compaction. Recycled materials with weak components -like masonry and brick aggregates in CDW- could gain stiffness in initial passes due to the fragmentation and change in

aggregate size distribution, however, harder constituents like crushed high-strength concrete aggregates in crushed sleepers cause persisting the stiffness increase rate of the material until later passes of vibrating roller.

- Relying only on the CCC studies could not be sufficient for determining the number of necessary passes for all kinds of recycled material, as even first passes could appear to meet the rule of 5% increment. Therefore, supplementary tests and methods could be required to identify the number of vibratory roller passes for compacting the unbound layer.
- Compaction path shows the change in stiffness of different materials by applying consecutive vibratory passes. These paths vary from one recycled material to the other. CDW and ASFC show highest and lowest stiffness gains by consecutive passes, relatively. This could be due to different strength and brittleness of their constituents.
- Lightweight deflectometry test (LWD) suggests what was visible by E_{vib} records on cement-bound layers: there is an optimum number of passes for cement-bound material to gain stiffness during compaction. Extra passes will not increase the E_{vib} of the compacted material. This number could be different for various materials.

ACKNOWLEDGMENT

The authors acknowledge the Italian companies of C.A.R Inerti srl and BOMAG Italia srl for providing materials, technicians and necessary machinery for experimental field operations of this research.

REFERENCES

- A. Barbudo, F. Agrela, J. Ayuso, J.R. Jiménez, C.S. Poon, 2012 *Statistical analysis of recycled aggregates derived from different sources for sub-base applications*. Constr. Build. Mater. 28, 129–138. <https://doi.org/10.1016/j.conbuildmat.2011.07.035>.
- I. Del Rey, J. Ayuso, A. Galvín, J. Jiménez, A. Barbudo, 2016 *Feasibility of Using Unbound Mixed Recycled Aggregates from CDW over Expansive Clay Subgrade in Unpaved Rural Roads*, Materials (Basel). 9, 931. <https://doi.org/10.3390/ma9110931>.
- G. Dondi, C. Sangiorgi, C. Lantieri, 2014 *Applying Geostatistics to Continuous Compaction Control of Construction and Demolition Materials for Road Embankments*. J. Geotech. Geoenvironmental Eng. 140, 06013005. [https://doi.org/10.1061/\(asce\)gt.1943-5606.0001044](https://doi.org/10.1061/(asce)gt.1943-5606.0001044).
- B. Gómez-Mejide, I. Pérez, A.R. Pasandín, 2016 *Recycled construction and demolition waste in Cold Asphalt Mixtures: Evolutionary properties*. J. Clean. Prod. 112, 588–598. <https://doi.org/10.1016/j.jclepro.2015.08.038>.
- J. Kovanda, 2020 *Raw material consumption or total material consumption? Which indicator is better for evaluating material resource consumption and environmental pressure?*. Environ. Monit. Assess. 192. <https://doi.org/10.1007/s10661-020-08343-w>.
- M. Plessis-Fraissard, 2007 *Planning roads for rural communities*, Transp. Res. Rec. 1, 1–8. <https://doi.org/10.3141/1989-01>.
- C. Poon, D. Chan, 2006 *Feasible use of recycled concrete aggregates and crushed clay brick as unbound road sub-base*, Constr. Build. Mater. 20, 578–585.
- C. Sangiorgi, C. Lantieri, G. Dondi, 2015 *Construction and demolition waste recycling: An application for road construction*. Int. J. Pavement Eng. 16, 530–537. <https://doi.org/10.1080/10298436.2014.943134>.
- C. Sangiorgi, A. Marradi, H. Kloubert, W. Wallrath, 2012 *A ccc experimental site for studying the compaction evolution of C&D materials*. in: Proc. 3rd Int. Semin. Earthworks Eur. Col. FGSV Verlag GmbH, COLOGNE, pp. 115–126.
- B. Tansel, 2020 *Increasing gaps between materials demand and materials recycling rates: A historical perspective for evolution of consumer products and waste quantities*, J. Environ. Manage. 276, 111196. <https://doi.org/10.1016/j.jenvman.2020.111196>.
- P.K.R. Vennapusa, D.J. White, M.D. Morris, 2010 *Geostatistical Analysis for Spatially Referenced Roller-Integrated Compaction Measurements*, J. Geotech. Geoenvironmental Eng. 136, 813–822. [https://doi.org/10.1061/\(asce\)gt.1943-5606.0000285](https://doi.org/10.1061/(asce)gt.1943-5606.0000285).

Utilization of fly ash as a filler in cold bituminous emulsion mix

Deepak Prasad

Department of Civil Engineering, National Institute of Technology Patna, India

Sanjeev Kumar Suman

Department of Civil Engineering, National Institute of Technology Patna, India

Bhupendra Singh

Department of Civil and Infrastructure Engineering, Indian Institute of Technology Jodhpur, India

Nikhil Saboo

Department of Civil Engineering, Indian Institute of Technology Roorkee, India

Ankit Kathuria

Department of Civil Engineering, Indian Institute of Technology Jammu, India

ABSTRACT: Due to its lower production temperature cold bituminous emulsion mix (CBEM) has several environmental and economic benefits over conventional hot mix asphalt. However, its demerits like lower strength, higher moisture susceptibility, and longer curing time make it undesirable for the practitioners. In order to solve these issues, the present study examines the effect of fly ash on the properties of CBEM. In the study, conventional stone dust filler is replaced by fly ash in the proportion of 1%, 2%, 3%, 4%, and 5% by the weight of total aggregates. Marshal stability, retained stability, Indirect tensile strength (ITS), and indirect tensile strength ratio (ITSR) tests are performed. Results obtained from these tests showed that inclusion of flyash improves the mix properties. Further based on the comparison of test results 3% flyash was found to be optimum content.

Keywords: Cold bituminous emulsion mix, filler, stonedust, fly ash

1 INTRODUCTION

India is the world's third-largest coal-fired power producer (Ahn and Graczyk 2012) after China and United States. Due to the inferior quality of the Indian coal, it has a high ash content of about 30-45% as compared to ash produced by good quality coals of about 10-15%. So large quantities of fly ash are generally generated. 217.04 Million tons of fly ash was generated in 2018-19 (Kumar et al. 2017). This fine waste in environment generates some critical issue as it requires large area for disposal, and it further becomes a source of environmental pollution. In India, about 65000 acres of land is being occupied by pond ash (Ram and Masto 2014). Various strategies are used to utilize flyash in diverse areas, such as concrete mix (Amran et al. 2021; De Maeijer et al. 2020), bituminous mix (Mistry and Roy 2021), soil stabilization (Andavan and Pagadala 2020), etc., to lessen the impact of flyash on the environment and to reduce the land requirement for its disposal.

Roads are essential for socio-economic growth of the country because they offer access to resources, employment, and markets (Percoco 2016; Weiss et al. 2015). The majority of roads across the world are flexible pavements containing bituminous mix surface layers. The conventional practice used in flexible pavement construction i.e. hot mix asphalt (HMA) is considered as one of the source of increasing global warming, as it needs an enormous amount of fuel to heat the mix at high temperature which generates high amount of greenhouse gases (Ghale and Pataskar 2017). Thus to deal with the issue researchers and practitioners are adopting different methods. Among these methods one such method is the use of cold mix asphalt (CMA) (Lu et al. 2013). CMA is prepared by mixing the aggregate with bitumen emulsion, cutback or foam. Cold mix prepared using bitumen emulsion is known as cold bituminous emulsion mix (CBEM). Due to its lower production temperature, CBEM production does not need any heating which makes it economical and eco-friendly (Al-Busaltan et al. 2012a). Despite these big advantages, there are some drawbacks associated with CBEM such as like lower initial strength, higher voids, lower moisture susceptibility etc. (Needham 1996; Read and Whiteoak 2003; Thanaya 2007). To increase the field utilization of CBEM, it is important to eliminate these problems. To deal with the above mentioned disadvantages, many researcher have utilized cement as fillers (Al Nageim et al. 2012; Niazi and Jalili 2009; Oruc et al. 2006; Thanaya et al. 2009). The addition of 1-2 % cement in CBEM, have shown significant improvement in initial strength, moisture susceptibility and other properties (Al-Busaltan et al. 2012a; Brown and Needham 2000; Garcia et al. 2013; Thanaya et al. 2009; Singh and Jain 2021). In CBEM, cement acts as a secondary binder and reacts with aggregate in the presence of encapsulated water present in the bitumen emulsion (Bocci et al. 2011; Oruc et al. 2006) and improves the adhesion between aggregate and bitumen. So this indicates that use of cementitious or pozzolanic material may help to deal with the problem associated with CBEM. The use of cement improves the properties but at one hand it increases the cost on the other hand its harmful for the environment. Thanaya (2007) indicated that CBEM containing 2% cement will have the similar carbon footprint as that of the conventional HMA.

Thus there is a need to use an alternate cementitious materials to be used in CBEM. One such material is flyash. In the past numerous studies have used flyash as pozzolanic material in different fields like cement concrete, hot mix asphalt, soil stabilization, etc. There are still very few studies who have extensively examined the effect of flyash as a filler in CBEM. So, the present study aims to examine the effect of flyash (FA), as a filler on the mechanical characteristics and moisture susceptibility of CBEM.

2 MATERIALS

2.1 Aggregates

In this present study single sourced aggregates from local quarry of Bihar, India were used. Aggregates were originated from dolomitic type of rock. Table 1 include conventional properties of aggregates which are within the limits required for bituminous concrete as per MORT&H (2013).

Table 1. Conventional properties of aggregates.

Properties	Values	Standard Used
Impact value (%)	13.05	IS 2386 (Part IV)
Crushing value (%)	13.12	IS 2386 (Part IV)
L. A. abrasion value (%)	17.14	IS 2386 (Part IV)
Water absorption (%)	.46	IS 2386 (Part III)
Specific gravity	2.6	IS 2386 (Part III)
Density (kg/m ³)	2763	IS 2386 (Part III)
Combined flakiness and elongation (%)	20.45	IS 2386 (Part I)

2.2 Fillers

Dolomitic stone dust (SD) and flyash (FA), having specific gravities of 2.67 and 2.32, were used as the conventional and secondary filler materials respectively.

2.3 Binder

Cationic slow setting (CSS-2) emulsion having residual bitumen content of 58.3% was used as binder for preparing mix. The conventional properties of emulsion were determined and are enlisted in Table 2.

Table 2. Conventional properties of emulsion.

Properties	Values	Standard used
Residue on 600 micron sieve (%)	0.045	IS 8887
Viscosity at 25 °C, Saybolt furol viscometer (seconds)	49	IS 3117
Storage stability (%)	17.14	IS 8887
Particle charge	(+)ve	IS 8887
Test on residue	90	IS 1203
Penetration at 25 °C	74	IS 1208
Ductility at 27 °C		

2.4 Water

Potable water was used for the purpose of enhancing the workability of mix before the application of binder. It generally enhances the coating ability of aggregates with binder by providing a wet aggregate surface to the binder.

3 EXPERIMENTAL PROGRAMS

To provide a thorough understanding of the experimental procedure followed in the study, the experimental plan of the study is shown in Figure 1.

3.1 Mix design and specimen preparation

Dense graded bituminous concrete (BC) as given by MORT&H (2013), has been used as the aggregate gradation in the study for the preparation CBEM. The aggregate gradation is shown in Figure 2. For marshal mix design, guidelines given by (MS-14 1997) and MORT&H (2013) were adopted.

CBEM prepared with stone dust as filler material was considered as control mix (unmodified mix). The modification of the CBEM was done by partially replacing the stone dust with flyash by 1, 2, 3, 4, and 5% by weight of total aggregates. The abbreviations used for each set of mix specimen are listed in Table 3. Here CMA denotes cold bituminous emulsion asphalt, prefix to the CMA i.e. U and M mean unmodified and modified respectively, and suffix after CMA i.e. numbers from 1 to 5 represents the percentage of flyash in the mix.

3.2 Marshal stability and retained marshal stability

In this study the ORBC is determined by measuring the maximum soaked marshal stability at different residual bitumen content (Jain and Singh 2021). The dry marshal stability is determined at ORBC. The retained marshal stability is determined by dividing the soaked marshal stability by dry marshal stability. More details on cold mix design procedure are not discussed here for brevity. These details can be found at Jain and Singh (2021).

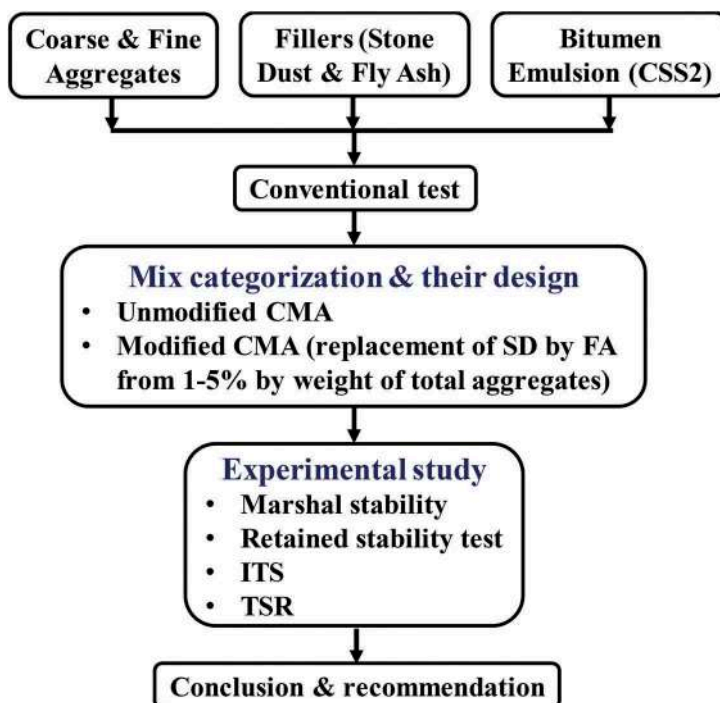


Figure 1. Experimental flow chart of study.

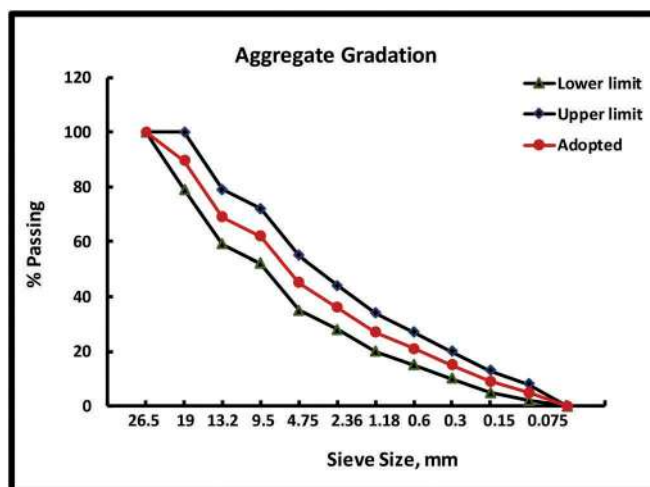


Figure 2. Gradation of aggregates.

Table 3. Abbreviation expressing CBEM type.

% replacement of SD by FA	0	1	2	3	4	5
Abbreviation used	UCMA	FMCMA1	FMCMA2	FMCMA3	FMCMA4	FMCMA5

3.3 Indirect tensile strength and indirect tensile strength ratio

ASTM D6931 was followed to measure indirect tensile strength (*ITS*) of CBEM samples. *ITS* of the bituminous specimen was determined by equation (1)

$$ITS = 2000P/\pi dt \quad (1)$$

Where *P* is the maximum load at failure in N, *d* and *t* are the diameter and thickness of sample in mm, respectively, just before the test.

AASHTO T283 was followed to measure indirect tensile strength ratio (*ITSR*) of CBEM samples. *ITSR* was calculated by using equation (2)

$$ITSR = 100 (ITS)_w/(ITS)_d \quad (2)$$

Where $(ITS)_w$ is the average *ITS* value of wet conditioned samples and $(ITS)_d$ is the average *ITS* of dry conditioned samples.

4 RESULTS ANALYSIS AND DISCUSSION

4.1 Mix design

For CBEM mix design four parameter i.e. initial emulsion content (IEC), optimum premixed water content (OPWC), optimum total liquid content at compaction (OTLC), and optimum residual bitumen content (ORBC) were calculated. IEC and OPWC were found to be 10.3% and 1.5% respectively. Figure 3 shows the variation of OTLC and ORBC of different mix. It can be seen that OTLC increased with increasing flyash content. It may be primarily due to absorptive nature of flyash that need comparatively high amount of water in mixing time (Al-Busaltan et al. 2012b). Figure 3 also shows a decreasing trend of ORBC with increasing flyash content. This behavior can be credited to the lower specific gravity of flyash than stone dust, due to which it occupies higher volume in the compacted mix and leaves lesser space for the bitumen to be accommodated (West and James 2005).

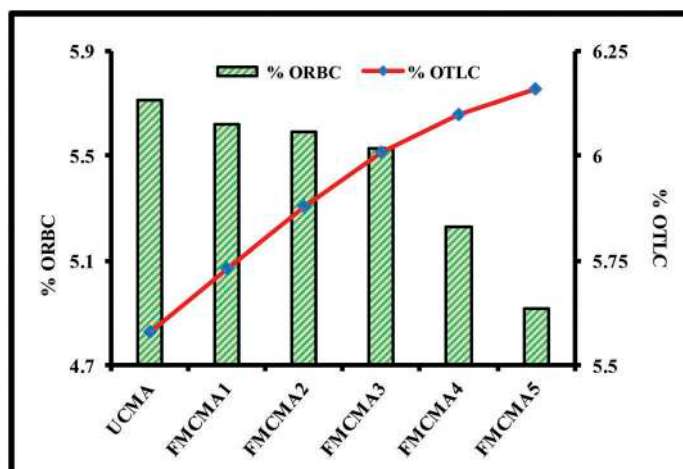


Figure 3. ORBC and OTLC of different mix.

4.2 Marshal stability

Figure 4 Shows the Marshall stability (MS) values of different mixes. Unmodified cold mix asphalt i.e., UCMA was found to have MS value of 6.14 kN, which is significantly lower than the minimum MS value of 9 kN recommended by MORT&H (2013). Lower MS values may be because of the presence of the water in CBEM. Bitumen emulsion contains around 40% water upon that extra water is added to the mix to improve the workability and assist coating. This water generally encapsulate in the compacted mix during early stage and tries to hinder the formation of bituminous bond with mineral aggregates (Jain and Singh 2021) which results in lower strength of the mix.

Replacement of stone dust filler with fly ash filler resulted in increment in MS values of mix. CBEM samples containing 3 % and above flyash (i.e. FMCMA3, DMCMA4 and FMCMA5) were found to have MS values above 9 kN. The improvement in MS value may be due to the stiffening of mix occurred by the hydration of flyash in the presence of encapsulated water, which is considered as a secondary bond in the mix (Al-Busaltan et al. 2012a).

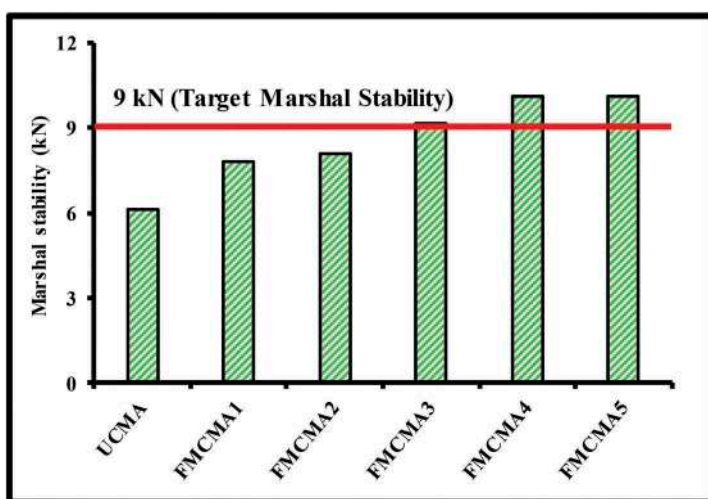


Figure 4. Marshal stability of different mix.

4.3 Marshal quotient

Marshal quotient (MQ) is measured by dividing the MS value by the flow value of the mix. It primarily represents the stiffness of the mix. A higher MQ value signifies a mix having higher stiffness which can distribute the applied load and withstand creep deformation (Arabani and Azarhoosh 2012). It also indicates the resistance to shear stress, permanent deformation, and rutting behaviour of mix (Zoorob and Suparma 2000). However, an extremely high MQ value means a very stiff mix, resulting in distresses like bleeding, fatigue cracking, etc. Mentioning these issues MORT&H (2013) recommends an MQ range of 2–5 kN/mm for bituminous mixes. The marshal quotient of different mix are shown in Figure 5. In this study, UCMA was found to have 1.3 kN/mm MQ value, which indicates a mix having considerably lower stiffness. This is mainly due to the presence of encapsulated water in the compacted mix. However, the incorporation of flyash in CBEM resulted in increment of MQ values. This is because, the flyash utilizes the encapsulated water for the purpose of hydration process (Al-Busaltan et al. 2012a) and form a considerably stiffer mix as compared to UCMA. Here, mix containing $\geq 2\%$ flyash were found to have MQ values of > 2 kN/mm.

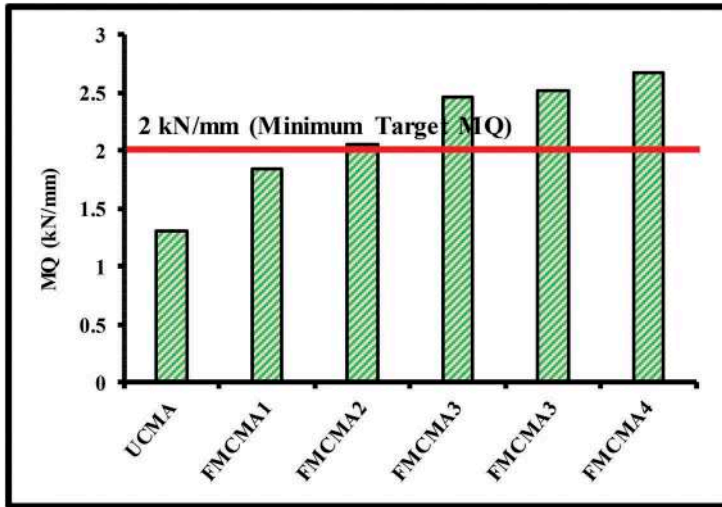


Figure 5. Marshal Quotient of different mix.

4.4 Indirect tensile strength

Figure 6 Shows the variation of ITS with respect to change in flyash content of the mix. From the Figure 6, it can be seen that the ITS values increased with the increase in flyash content. ITS values of mix increased upto the flyash content of 3% and at 4% and 5% flyash content values decreased. Despite decrement FMCMA4 and FMCMA5 samples were found to have ITS values higher than UCMA.

ITS value of UCMA was found to be 365.42 kPa, which increased by 103% for FMCMA3. ITS values of FMCMA4 and FMCMA5 were decreased by 15.54% and 20% as compared to FMCMA3 but were 71.76% and 62.69% were higher than UCMA. The credited for this variation in ITS values can be given to two factors i.e. incorporation of flyash and decreasing ORBC. Incorporation of flyash undergoes hydration by utilizing the encapsulated water present in the compacted mix, resulting in a stiffer mix, which may be validated by MQ values presented in Figure 5. This increased stiffness plays a predominant role upto the flyash

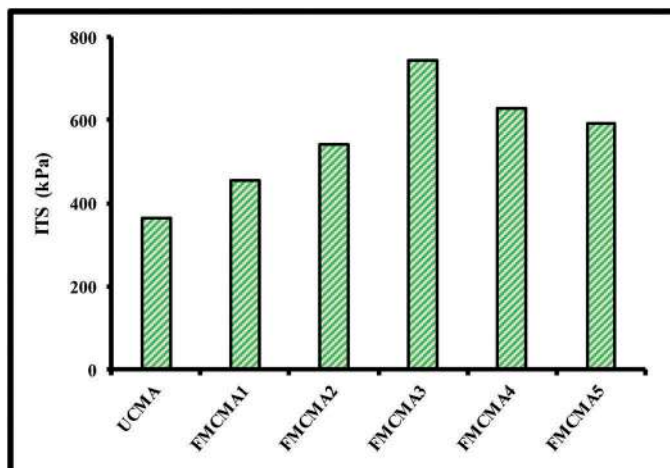


Figure 6. ITS of different mix.

content of 3%. After than the second factor i.e. decreasing ORBC (as shown in Figure 3) overtakes and due to lower binder content in the mix ITS values start decreasing.

4.5 Indirect tensile strength ratio and retained stability

Both the parameter; ITSR and retained stability measure moisture susceptibility of bituminous mix. Figure 7 shows the variation of ITSR of different mixes. ITSR value of UCMA was found to be 41%, which is unacceptable as per MORT&H (2013) recommendations of minimum 80% ITSR value. Samples having flyash content of $\geq 3\%$ were found to be fulfilling the MORTH (2013)'s criteria of 80% ITSR as presented in Figure 7. The ITSR value of FMCMA3 was found to have 84%, which is 105% improved with respect to that of UCMA. For FMCMA4 and FMCMA5 samples ITSR values decreased slightly but the values were still significantly higher than UCMA.

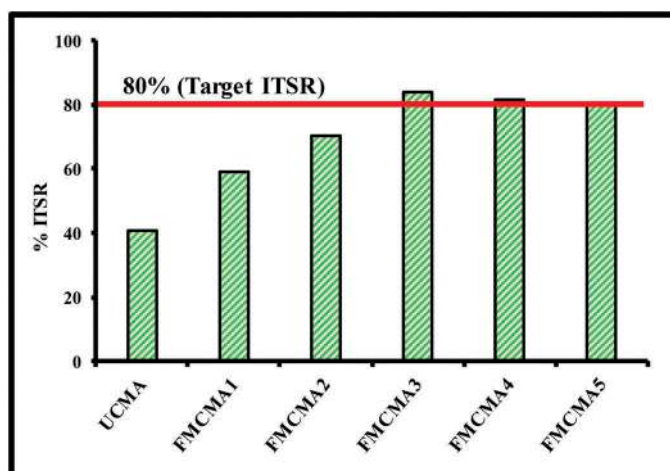


Figure 7. ITSR of different mix.

From Figure 8 it can be seen that retained stability values of the asphalt mix samples kept on increasing with increasing fly ash content. The primary cause of improved moisture susceptibility may be the incorporation of flyash, which utilizes the encapsulated water for its hydration, resulting in an increased curing rate, giving improved strength properties like ITS and marshal stability in early stage even in wet condition. Another author also suggested that the free lime content present in flyash may improve the bitumen aggregate adhesion and durability of asphalt of bituminous mix against moisture (Choudhary et al. 2020).

Comparing ITSR and retained stability results, both showed similar trend up to 3% flyash content i.e., an increasing trend. However, after 3%, ITSR values started slightly decreasing with but retained stability values kept on increasing. This variation may be due to the difference in the loading configuration of both the tests. In ITSR, ITS value is determined by applying point load on diametrically two points on marshal sample so bitumen aggregate adhesion is the dominant factor when it comes to the ITS vales of bituminous samples. Whereas in retained stability test the applied load is diametrical compressive load on the periphery of the sample so retained stability value majorly depends upon the stiffness of the mix. Thus in case of retained stability increasing stiffness of flyash containing samples (as shown in Figure 5) results in increasing values whereas in case of ITSR after 3% flyash content, reduced binder content (as shown in Figure 3) results in reduced aggregate bitumen adhesion so values start decreasing.

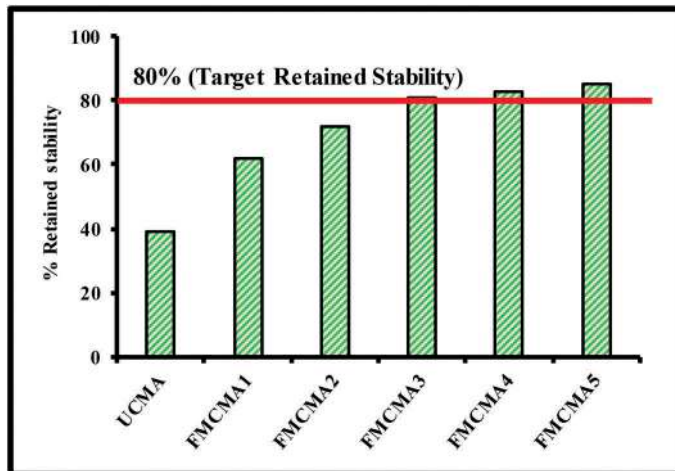


Figure 8. Retained stability of different mix.

5 CONCLUSION

In this study, the conventional filler, i.e., stone dust, is replaced by flyash from 1-5% by total aggregate weight. The mechanical characteristics of unmodified and flyash modified cold mix asphalt were determined and analyzed. Based on the experimental results of this study, the following conclusion are made:

1. The increasing incorporation of flyash in CBEM decreases the optimum residual bitumen content.
2. The marshal stability, marshal quotient, and retained stability increased on increasing flyash content in CBEM, and the maximum value of these parameters was obtained on 5% flyash content.
3. The ITS and ITSR values increased up to the samples containing 3% flyash, and then decreased slightly. This may be credited to lower ORBC values of the samples.
4. Samples containing $\geq 3\%$ flyash satisfied all the criteria given by MoRTH, i.e., minimum marshal stability of 9 kN, marshal quotient value 2 to 5 kN/mm, minimum ITSR and retained stability value of 80%. ITS and ITSR values were maximum at 3% flyash content so keeping all these factors in mind 3% flyash was concluded to be the optimum flyash content for CBEM samples.

The present study includes a single source of aggregate and flyash. Moreover, a single aggregate gradation is also used. Further elaborative studies should be carried out by varying these factors and including more tests to obtain more definitive results.

REFERENCES

- Ahn, S. J., and Graczyk, D. (2012). *Understanding energy challenges in India: policies*. Players and Issues, Paris: International Energy Agency and OECD.
- Al-Busaltan, S., Al Nageim, H., Atherton, W., and Sharples, G. (2012a). *Mechanical properties of an upgrading cold-mix asphalt using waste materials*. Journal of Materials in Civil Engineering, 24 (12),1484–1491.
- Al-Busaltan, S., Al Nageim, H., Atherton, W., and Sharples, G. (2012b). *Green Bituminous Asphalt relevant for highway and airfield pavement*. Construction and Building Materials, Elsevier, 31, 243–250.
- Al Nageim, H., Al-Busaltan, S. F., Atherton, W., and Sharples, G. (2012). *A comparative study for improving the mechanical properties of cold bituminous emulsion mixtures with cement and waste materials*. Construction and building materials, 36, 743–748.

- Amran, M., Debbarma, S., and Ozbakkaloglu, T. (2021). *Fly ash-based eco-friendly geopolymer concrete: A critical review of the long-term durability properties*. *Construction and Building Materials*, 270, 121857.
- Andavan, S., and Pagadala, V. K. (2020). *A study on soil stabilization by addition of fly ash and lime*. *Materials Today: Proceedings*, 1125–1129.
- Arabani, M., and Azarhoosh, A. R. (2012). *The effect of recycled concrete aggregate and steel slag on the dynamic properties of asphalt mixtures*. *Construction and Building Materials*, 35, 1–7.
- Bocci, M., Grilli, A., Cardone, F., and Graziani, A. (2011). *A study on the mechanical behaviour of cement-bitumen treated materials*. *Construction and building materials*, 25(2), 773–778.
- Brown, S., and Needham, D. (2000). *A study of cement modified bitumen emulsion mixtures*. *Asphalt Paving Technology*, 69, 92–121.
- Choudhary, J., Kumar, B., and Gupta, A. (2020). *Utilization of solid waste materials as alternative fillers in asphalt mixes: A review*. *Construction and Building Materials*, 234, 117271.
- Garcia, A., Lura, P., Partl, M. N., and Jerjen, I. (2013). *Influence of cement content and environmental humidity on asphalt emulsion and cement composites performance*. *Materials and Structures/Materiaux et Constructions*, 46(8), 1275–1289.
- Ghale, S. R., and Pataskar, S. V. (2017). *Comparison of Cold Mix and Hot Mix Asphalt*. *International Journal of Engineering Research in Mechanical and Civil Engineering*, 118–121.
- IS 2386 (Part I) (1963). *Indian Standard Method of Test for Aggregates for Concrete, Part-I: Particle Size and Shape*, Bureau of Indian Standards, New Delhi, India.
- IS 2386 (Part III) (1963). *Indian Standard Method of Test for Aggregates for Concrete, Part-III: Specific Gravity, Density, Voids, Absorption and Bulking*, Bureau of Indian Standards, New Delhi, India.
- IS 2386 (Part IV) (1963). *Indian Standard Method of Test for Aggregates for Concrete, Part-IV: Mechanical Properties*, Bureau of Indian Standards, New Delhi, India.
- IS 8887 (2004). *Indian Standard Bitumen Emulsion for Road (Cationic Type) - Specification*, Bureau of Indian Standards, New Delhi, India.
- IS 1203 (1978). *Indian Standard Methods for Testing Tar and Bituminous materials: Determination of Penetration*, Bureau of Indian Standards, New Delhi, India.
- IS 1208 (1978). *Indian Standard Methods for Testing Tar and Bituminous materials: Determination of Ductility*, Bureau of Indian Standards, New Delhi, India.
- IS 3117 (2004). *Indian Standard Bitumen Emulsion for Rural Roads and Allied Applications (Anionic Type) - Specification*, Bureau of Indian Standards, New Delhi, India.
- Jain, S., and Singh, B. (2021). *Cold mix asphalt: An overview*. *Journal of Cleaner Production*, 124378.
- Kumar, S., Mucsi, G., Kristály, F., and Pekker P. (2017). *Mechanical activation of fly ash and its influence on micro and nano-structural behaviour of resulting geopolymers*. *Advanced powder technology*, 28 (3), 805–813.
- Lu, S. M., Lu, C., Tseng, K. T., and Chen, F. (2013). *Energy-saving potential of the industrial sector of Taiwan*. *Renewable and Sustainable Energy Reviews*, 21(10), 674–683.
- De Maeijer, P. K., Craeye, B., Snellings, R., Kazemi-Kamyab, H., Loots, M., Janssens, K., and Nuyts, G. (2020). *Effect of ultra-fine fly ash on concrete performance and durability*. *Construction and Building Materials*, 263, 120493.
- Mistry, R., and Roy, T. K. (2021). *Performance evaluation of bituminous mix and mastic containing rice husk ash and fly ash as filler*. *Construction and Building Materials*, 268, 121187.
- MORT&H. (2013). *Specification of Road and Bridge Work (Fifth Revision)*. New Delhi, India.
- MS-14. (1997). *Asphalt Cold Mix Manual*. Laxington, USA.
- Needham, D. (1996). *Developments in bitumen emulsion mixtures for roads*. University of Nottingham, Nottingham.
- Niazi, Y., and Jalili, M. (2009). *Effect of Portland cement and lime additives on properties of cold in-place recycled mixtures with asphalt emulsion*. *Construction and building materials*, 23(3), 1338–1343.
- Oruc, S., Celik, F., and Aksoy, A. (2006). *Performance of cement modified dense graded cold-mix asphalt and establishing mathematical model*. *Indian Journal of Engineering & Materials Sciences*, 13, 512–519.
- Percoco, M. (2016). *Highways, local economic structure and urban development*. *Journal of Economic Geography*, 16(5), 1035–1054.
- Ram, L. C., and Masto, R. E. (2014). *Fly ash for soil amelioration: a review on the influence of ash blending with inorganic and organic amendments*. *Earth-Science Reviews*, 128, 52–74.
- Read, J., and Whiteoak, D. (2003). *The shell bitumen handbook*. Thomas Telford.
- Singh, B. and Jain, S. (2021). *Effect of lime and cement fillers on moisture susceptibility of cold mix asphalt*. *Road Materials and Pavement Design*, 1–17.
- Thanaya, I. N. A. (2007). *Review and recommendation of cold asphalt emulsion mixtures CAEMS design*. *Civil Engineering Dimension*, 9(1), 49–56.

- Thanaya, I. N. A., Zoorob, S. E., and Forth, J. P. (2009). *A laboratory study on cold-mix, cold-lay emulsion mixtures*. Proceedings of the Institution of Civil Engineers: Transport, 162(1),47–55.
- Weiss, D. J., Nelson, A., Gibson, H. S., Temperley, W., Peedell, S., Lieber, A., Hancher, M., Poyart, E., Belchior, S., Fullman, N., and Mappin, B. (2015). “*A global map of travel time to cities to assess inequalities in accessibility in 2015*.” Nature, 553(7688),333–336.
- West, R. C., and James, R. S. (2005). “*Evaluation of a lime kiln dust as a mineral filler for stone matrix asphalt*.” In Proceedings of National Center for Asphalt Technology. In: The 85th Annual Meeting of the Transportation Research Board, Washington, DC.
- Zoorob, S. E., and Suparma, L. B. (2000). “*Laboratory design and investigation of the properties of continuously graded Asphaltic concrete containing recycled plastics aggregate replacement (Plastiphalt)*.” Cement and Concrete Composites, Elsevier Science Ltd, 22(4),233–242.

Estimation of durability of new surface courses using accelerated load test and expert's opinions

B. Kalman

Swedish National Road and Transport Research Institute, Linköping, Sweden

D. Lo Presti, G. Di Mino & K. Mantalovas

Department of Engineering, University of Palermo, Palermo, Italy

E. Keijzer

Netherlands Organization for Applied Scientific Research, Utrecht, The Netherlands

T. Pary & L. Neves

Nottingham Transportation Engineering Centre, University of Nottingham, Nottingham, England

R. Kleizienė

Road Research Institute, Vilnius Gediminas Technical University, Vilnius, Lithuania

ABSTRACT: There is an increasing interest among road authorities in studying sustainability assessment of road infrastructure. The durability of the surface course is a critical factor in these calculations and must be carefully considered in the analysis. New types of asphalt mixes with the potential to improve the results in the sustainability assessment have no proven track record and are thus more likely not to be used until solid performance data is available. To bridge the gap and diminish the uncertainty about the durability of Green asphalt mixes for surface courses, a combination of laboratory tests and tests in a circular road simulator were performed. Eight mixes were tested in total, four stone mastic asphalt mixes and four porous asphalt mixes. Each group contained a reference mix with well-established performance. The mixes were characterized with dynamic IDT, complex shear modulus and water sensitivity using MiST (moisture induced stress test). Part of the loose mixes was oven aged at 85 °C simulate long term ageing. Plates of aged and virgin mixes were then tested in a circular road simulator in a program set up to check their sensitivity towards rutting, raveling, freeze-thaw cycles, polishing and fatigue. A combination of expert's opinion from academia and national road administrations together with the data from the tests were used to estimate the performance of the new Green mixes.

Keywords: Sustainability, durability, asphalt, service life

1 INTRODUCTION

National Road Authorities in Europe have an increasing interest in implementing sustainability assessment of roads. Service life is a critical parameter in any lifecycle calculation. The lifetime distributions for often used road surface mixes varies across Europe.

Even within a country, the distribution varies with local conditions and with the type of road and traffic volume. New types of asphalt mixes with the potential to improve the results in the sustainability assessment have no proven track record and are thus more likely not to be used until solid performance data is available. To bridge the gap and diminish the uncertainty about the durability of new Green asphalt mixes for surface courses, a combination of laboratory tests and accelerated performance tests could be used.

In this study we have used stone mastic asphalt, SMA, and porous asphalt, PA, as reference materials since there is knowledge about their actual performance in different European countries. The reference SMA was compared to three SMA mixes with potentially higher durability and/or including high percentage of reclaimed asphalt (RA) potentially more sustainable asphalt mixes. The reference PA was compared to three PA with strong fibers or polymer modified binder.

2 MATERIALS AND METHODS

2.1 *Materials*

Four stone mastic asphalt were used in the study. SMA 16; SMA 11 10% RA; SMA 11 40% RA; SMA 8 60% RA

The reference mix was a SMA 16 70/100 with 6,2% binder. The mix was produced in a plant in Sweden. The aggregate was granite from Styvinge in Östergötland. 0.4% cellulose fibers and 0.3% Wetfix BE was added to the mix. Air voids in Marshall compacted specimens was 2.7%.

Two SMA 11 mixes were produced in plants in Denmark. The first mix was a SMA 11 40/60 with 5.8% binder. The aggregate was approximately 70% Hyperit, 20% Labradorit and 10% granite from the RA. 1.5% reactive filler and 1.25% limestone filler was used together with 0.35% Viatorp 66. The mix was produced in Hjallerup. Air voids in Marshall compacted specimens was 2.1 – 2.6%. The second mix was a SMA 11 with 40% RA in the mix. This was also produced in a plant.

The last SMA was a SMA 8 50/70 with 60% RA in the mix. It was produced in the lab. The RA collected from a plant was split into two fractions with a 4 mm sieve. A sieve and binder analysis were made of each fraction. The binder content in the fraction larger than 4 mm was 6.78% and had a penetration value of 18×10^{-1} mm and a softening point of 65,4 °C. For the other fraction, the binder content was 3.85% and the penetration value was 15×10^{-1} mm and a softening point of 68.6 °C.

The 50/70 binder added to produce the SMA 8 60% RA had a softening point of 51.0 °C. 33.4% of the aggregate in the mix were from the larger fraction of the RA and 26.5% of the aggregate in the mix were from the smaller fraction of RA. 54% of the binder in the final mix originated from the RA. To compensate/rejuvenate for the hardened binder in the RA, 0.53% of a VMA additive was used (8.7% of the total binder content) as described in the AllBack2Pave project (Wellner et al. 2015). 0.5% of cellulose fibres were used in the mix. The added aggregate was a granite from Skärlanda in Östergötland.

Four porous asphalt mix were used in the study they are designated: PA 16 or ZOAB+; PA 8 or Fibra 1; PA 8 Panacea or Fibra 3; PA 8 Aramid or Fibra 4.

The PA 16 70/100 with a binder content of 5.5% was produced in the laboratory based the mix detailed by Zhang (Zhang et al. 2018). All coarse granite aggregates 2–16 mm was washed and came from Skärlanda in Östergötland. Sand 0.063–2 mm came from Baskarp. Filler content (Wigro 60K) in the aggregate was 4.7%. 0.3% cellulose fibres were added to the mix.

The Fibra mixes were produced in a plant in Netherlands for the Fibra project (Slebi-Acevedo et al. 2020). Fibra 1 is the standard PA 8 mixture for two layers porous asphalt in

the Netherlands. The binder is a SBS polymer modified bitumen. Fibra 3 is a PA 8 mixture made with 70/100 bitumen and panacea fibres. Fibra 4 is a PA 8 mixture made with 70/100 bitumen and aramid fibres.

2.2 Methods

It is widely thought that ageing of the binder in a pavement layer could have a detrimental effect on the performance of the mix in some. Extensive ageing makes bituminous binders hard and brittle. To what extent the progressive hardening of the binder is a limiting factor for a asphalt layer service life depends on the mix type and the structural properties of the road. To simulate the ageing and to be able to test the mixes in a hardened state we used oven ageing of the loose mixes to simulate the ageing that occurs during service. Oven ageing of loose mix has been used to simulate field ageing has been used in the past for example in (Mollenhauer et al. 2012, De la Roche et al. 2009). We followed these examples and aged loose mix in a tray at approximately 86 °C for seven and fourteen days. The temperature fluctuated in the oven between 84 and 88 °C. These aged mixes are called short- and long-term aged mixes, which should not be confused with the short-term ageing occurring at production of the mix or long-term ageing of binder using a pressure ageing vessel, PAV. The aged batches of the mixes were used together with the un-aged material in the accelerated test.

The binder recovery was performed according to EN 12697-3:2013+A1:2018. Dichloromethane was used as the solvent. During the first phase of the distillation, the oil bath temperature was 85 °C and the applied pressure was 85 kPa. During the second phase, the temperature was 150 °C and pressure was 2.0 kPa. No extra phase was needed for the binder recovery.

Furthermore, the obtained binders were tested for the complex shear modulus G^* and phase angle δ in the linear viscoelastic region with a dynamic shear rheometer (DSR) according to EN 14770:2012. Temperature sweep was conducted at 10 rad/s with a 6 °C interval up to 82 °C. The plate-plate geometry of 25 mm diameter and 1 mm gap was used for the DSR measurement.

The cyclic indirect tensile test was conducted to characterize the stiffness of the asphalt mixtures. The test consists of applying a certain number of cyclic (sinusoidal) loading along the vertical diametral plane of a cylindrical specimen to achieve a constant peak tensile strain along the horizontal diametral plane perpendicular to the loading plane. The test was conducted according to the European standard EN 12697-26:2018 – Annex F. Laboratory compacted specimens having a diameter of 100 mm and thickness of 40 mm were tested at three temperatures (-5, 10 and 20 °C) and 8 loading frequencies (16, 10, 5, 2, 1, 0.5, 0.1, 0.05 Hz).

The dynamic shear modulus test was conducted in accordance with the method and the equipment developed at VTI. According to this method, the two sides of a cylindrical asphalt specimen having diameter of 150 mm and thickness of $\frac{1}{4}$ of the sample diameter is glued to two steel plates using epoxy. The glued specimen is then mounted on the shear box device where one of the plates is rigidly fixed and the other is exposed to a vertical sinusoidal cyclic loading over a range of frequencies. Further details on the testing procedure can be found in (Said, et al. 2013). The dynamic shear testing is usually conducted at four temperatures: -5, 10, 30 and 50 °C, and eight loading frequencies: 16, 8, 4, 2, 1, 0.5, 0.1 and 0.05 Hz.

Accelerated load tests were performed in a circular road simulator, CRS. Asphalt plates were produced from fresh and aged mixes with a roller compactor and a steel frame with the dimensions 50 x 70 x 4 cm. Each plate was trimmed, i.e., two short ends of the plate were cut to create a trapezoidal shape, to make them fit into the track of the circular road simulator. After trimming the plates and fitting them into the track,

joints were filled with mortar and the machine run for a few minutes at elevated temperature to push each plate firmly to the base.

The test in the CRS was divided in three phases:

1. 35 °C in dry conditions. 60 000 laps
2. ~ 0 °C. Seven freeze-thaw cycles in wet conditions. Each cycle started at -2 °C and gradually increased to 2 °C. 120 000 laps.
3. 30 °C in dry conditions with a soft base. Running until pavement failure. 2 000 laps.

In the final phase 3 the plates were released, and a 19 mm cellular rubber sheet were glued to the bottom of the plate and to the base and then fixed to the track. Joints were filled with mortar. Four tires, Cooper Discoverer S/T MAXX, LT 235/85 R16, was used in the for the test in the CRS. This tire type is typically used for SUV. The inflation pressure was 3,5 Bar. Each tyre was loaded with 450 kg.

The full records of the outcome of the laboratory tests can be found in the PavementLCM report (Kalman et al. 2021)

3 SERVICE LIFE OF REFERENCE MATERIAL

The service lives for reference mixes have been reported from different countries multiple times (Christensen et al. 2005, EAPA 2007, Briessinck et al. 2016). Comparing the results from the three studies indicates that there are large differences between the expected service life not only between countries but also between different surveys. A part of the differences in the results could be traced back to how the questions have been asked i.e., if the respondents are reporting the median actual service life or if it is the service life of the best performing roads. For example, Poland reports a service life of 10 years in the heavy traffic lane in the OECD study and 20 years in the PIARC study. Likewise, France reports a service life of 8 years in the heavy traffic lane and 16 years in the fast lane in the OECD study while in the PIARC study the expected service life is 12 years. Service life based on historical data should not be disputed numbers.

Based on historical records the service life distributions could be modelled using a Weibull distribution with increasing failure rate with time.

Historical survival data has two types of events, and each event has an event time. An event is a case if the time for end of life is observed. If rather the time at end of study is observed the subject is still alive, the event is known as censoring. Censored observations contain partial information about the survival time even though end of live is not observed. Survival analysis methods properly take care of both the complete information in the cases and the partial information in the censored observations. Having analytical expressions for the service lives facilitate the possibility to take into account the uncertainty in the lifetimes in life cycle analysis.

In Figure 1 the historical survival records of SMA pavements in Östergötland, Sweden laid from 1980 and onwards on roads with Annual Average Daily Traffic (AADT) volume between 12000 and 16000 is presented as a Kaplan-Meier curve together with the survival curve based on the estimated Weibull distribution. From the figure it can be concluded that the 10% of the SMA surface courses with the longest survival time lasted approximately twice as long as the 10% of the SMA surface courses with the shortest survival time.

4 DISTRESSES TRIGGERING PAVEMENT RESURFACING

Experts from Germany, Denmark, Lithuania, Sweden, Norway, and the Netherlands gave answers to questions which types of surface distress that are typical to causing resurfacing for low, medium, and high-volume roads. All experts except one answered

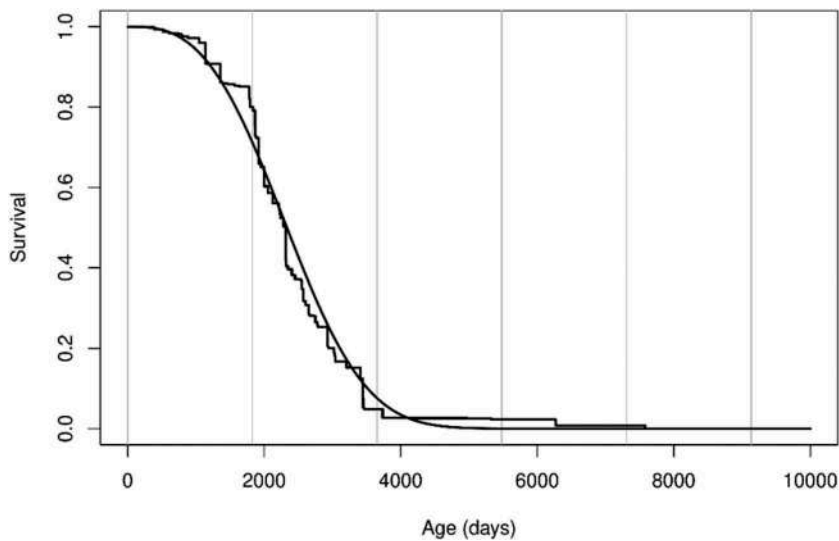


Figure 1. Survival function and the survival curve based on the estimated Weibull distribution for SMA pavements in the county Östergötland, Sweden for roads with AADT between 8000 and 12000.

that there are procedures or databases in their countries where the distresses, and possible other reasons for pavement maintenance operations, are detailed. The respondents were asked to classify each type of distress in terms of how likely it is that its presence triggered the decision to resurface a pavement with SMA or PA. The distresses the respondents could choose among were: Fretting (minor material loss); Ravelling (severe material loss); Rutting; Road wear; Low friction; Cracking (not specified); Transverse cracking; Longitudinal cracking; Edge cracking; Block cracking; Alligator cracking; Other.

The result of the survey regarding high-volume roads is presented in Table 1 for SMA16 or SMA11 and for PA16. Not all experts answered the questions for both types of reference mixes.

In the survey respondents were also asked to estimate how a change in traffic volume or other factors would eventually change the service life. A common assumption in structural road engineering is that the Palmgren-Miner linear damage hypothesis applies, which means that each single loading will contribute to the final failure of the road according to the damage each loading generates.

All experts agree that the service life will only change approximately by 10% (5-15%) if the traffic volume decreases by 25% for a high-volume road with annual average daily flow (AADF) of 8000. If the Palmgren-Miner linear damage hypothesis would apply, the service life would be inversely proportional to the traffic volume. A decrease in traffic volume by 25% would then lead to an increase of the service life by 33% if the traffic would be the only factor responsible for the service life.

For roads with even higher traffic volume, AADF of 16000, the experts have some disagreements in their estimates, but on the average the estimate on how a decrease in traffic volume by 25% would increase the service life is the same: approximately 10%.

For low volume roads with an AADF of 400, there is a shift in the estimates of how that would increase the service life. In this case more experts estimate only a marginal effect (0-5%) on the service life.

From these answers it can be concluded that there are more factors influencing the service than the traffic volume. Factors that usually is mentioned as influencing service life are aging, wet conditions and wet freeze that cycles. Ageing could be caused by exposure to

oxygen and UV radiation. The oxidation rate increases with temperature. It is sometimes postulated that pavements will be able to withstand the loadings of the traffic until the binder have reached a state where it is no longer flexible enough to endure the strains caused by the traffic.

Freeze thaw cycles in wet conditions could have an effect on the properties of asphalt concrete pavements. The experts differed among their estimates about the effect of decreasing the number of freeze thaw cycles in wet conditions. The experts from Norway and Sweden in most cases agree that the service life only increases marginally if number of freeze-thaw cycles decreases. The experts from Denmark and Germany agrees that the effect of freeze-thaw cycles on service life is higher. They estimate that the service life would increase more substantially (approximately 20%) if the number of freeze-thaw cycles decreases by half.

The estimated effect of decreasing the number of wet days by half is on average approximately 10% for high-volume roads although with some variations among the experts.

The number of wet days and the number of freeze-thaw a pavement is exposed to will increase with service life. Oxidative ageing will also increase with service life.

Since experts agrees that a decrease in traffic volume by 25% would only increase the expected service life for high volume roads by approximately 10% (5-15%), instead of 33% which would be expected if service life was only dependent on traffic, it can be concluded that other factors that influences the service life, such as ageing and exposure to wet conditions and freeze-thaw cycles have a substantial influence on the service life.

Table 1. Distress likely to trigger resurfacing of high-volume roads with for SMA16 (or SMA11, or SMA11 10%RA) or PA16. ++ indicates that the distress is likely cause for resurfacing operations. + indicates that the distress is somewhat likely cause for resurfacing operations.

	Denmark	Sweden 1	Sweden 2	Germany	Norway	Lithuania	Sweden 1	Sweden 2	Netherlands	Germany
Answers valid for	SMA11	SMA16	SMA16	SMA11	SMA16	SMA11	PA16	PA16	PA16	PA11
Fretting	++	++			+	++	++			
Ravelling	+	++			+	++	++		++	++
Rutting	+	++	++		++			++		
Road wear		++			+		++	++		
Low friction	+			++		++				
Cracking (not specified)		+		++		++				
Transverse cracking										
Longitudinal cracking		+			+	++				
Edge cracking					+	+				
Block cracking						+				
Alligator cracking		+				+				
Other						+			+	

If the estimates are correct, the calculated 33% increase in service life when traffic volume decrease by 25%, based on Miners' hypothesis would at the same time increase the number of exposures to wet conditions and freeze-thaw cycles by the same amount and ageing would also be increased. If the service life increases only by 10% when traffic

volume decreases by 25%, the number of wet days and number of freeze-thaw cycles would only increase by 10 % which roughly could only explain less than 5% of the difference between the 33 % estimated by Miners' rule and 10% based on experience. From these considerations it is concluded that ageing probably is of major importance for limiting the service life.

5 ESTIMATES OF SERVICE LIFE OF NEW MIXES

To estimate the relative service life of the new asphalt mixtures compared to the reference mixes based on the results from the laboratory studies we must understand the context in which the new mixes is going to be used in, i.e. in which country and which type of road. We also need to have a picture of which type of distresses are common in that context. The latter information was collected in the questionnaire and presented in Table 1.

There are many different mechanisms which potentially and eventually put a limit on the service life of a surface course. Three main components for the degradation of the surface courses are ageing, climate and traffic. Ageing is usually a consequence of oxidation or UV light. Climate puts stress on the road surface through freeze-thaw cycles; presence of water; extreme temperatures and temperature cycles. Traffic induces stresses and strain on the surface course. The surface course is also a part of the road structure and thus protects to higher or lesser extent the other parts of the structure. If other layers in the structure fails, this will eventually have consequences for the surface course.

The results from the questionnaire clearly demonstrated that all three mechanisms, traffic, climate, and ageing are important for the service lives. Thus, any attempt to predict the service life of new mixes needs to address all three factors. To further complicate the situation there are probably positive and negative synergies between the different factors affecting the service life. E.g., ageing usually leads to a stiffening of the binder which in turn could be beneficial for preventing rutting (deformation) but could also be worsening the layer's resistance to withstand fatigue cracking or resist extreme low temperatures.

To summarize the outcome of the experimental studies the new mixes were classified as performing better or worse than the reference mix in each study using a scale with five levels. The compilations are presented in Table 2 and Table 3.

To make the estimations the service lives for the new mixes one needs to compare the relative performance of the new mixes considering the context. In the survey presented in Table 1, there were large differences between different countries regarding the typical distresses that triggers resurfacing. The following example for the situation in Denmark illustrate the procedure:

Typically, high-volume roads with SMA are resurfaced because of fretting/ravelling and to some extent due to rutting and low friction in Denmark. Since the test result regarding friction and ravelling were the same for the new SMA mixes compared to reference SMA, the only important difference between the mixes is their relative performance regarding rutting where the SMA11 10% RA performed better to much better, and the SMA8 60% RA performed worse (in the CRS study) or better (in the shear modulus test) than the reference SMA. The SMA8 60% RA did age considerably faster than the reference SMA. This could have an effect on the long-term durability of the mix.

Hence it is anticipated that SMA11 10% RA have a slightly longer (+5%) service life, that the SMA11 40% RA have the same service life, and that SMA8 60% have slightly lower service life (-10%), compared to the reference SMA. Since the average service life of SMAs on high-volume roads in Denmark is 14 years the estimated service lives of the SMA11 10% RA, SMA11 40% RA and SMA8 60% RA, are 15 years, 14 years and 12 years, respectively for high-volume roads.

Table 2. Relative performance of new SMA mixes compared to the reference SMA16 mix. The relative performance is indicated with -, -, =, +, ++ where - and - indicates much worse and worse, = indicates equal performance and + and ++ indicates better or much better performance.

Test		SMA11 10% RA	SMA11 40% RA	SMA8 60% RA
Climate	Water sensitivity/MIST	=	=	=
Ageing	Short and long term oven ageing	++	++	--
Traffic	ALT/CRS	= ravelling	= ravelling	= ravelling
		= rutting	- rutting	- rutting
		= cracking	= cracking	= cracking
		= friction	= friction	= friction
Traffic/ aging	ALT/CRS aged material	= ravelling	= ravelling	= ravelling
		= rutting	= rutting	= rutting
		+ cracking	+ cracking	- cracking
		= friction	= friction	= friction
Traffic/ climate	ALT/CRS Water sensitivity and freeze-thaw cycles	=	=	- aged material
Traffic	Stiffness modulus/road structure performance	+	=	-
Traffic	Shear modulus/rutting	++	=	+

Table 3. Relative performance of new PA mixes compared to the reference PA16 mix (ZOAB+). The relative performance is indicated as in Table 2.

Test		ibra 1/PA8	Fibra 3/PA8 panacea	Fibra 4/PA8 aramid
Climate	Water sensitivity/MIST	=	=	=
Ageing	Short and long term oven ageing	=	--	--
Traffic	ALT/CRS	+ ravelling	= ravelling	= ravelling
		+ rutting	= rutting	= rutting
		+ cracking	= cracking	= cracking
		+ friction	+ friction	+ friction
Traffic/ aging	ALT/CRS aged material	-- ravelling	-- ravelling	-- ravelling
		+ rutting	+ rutting	+ rutting
		= cracking	= cracking	= cracking
		+ friction	+ friction	+ friction
Traffic/ climate	ALT/CRS Water sensitivity and freeze-thaw cycles	=	=	=
Traffic	Stiffness modulus/road structure performance	-	=	=
Traffic	Shear modulus/rutting	/	+	+

REFERENCES

- Briessinck, M., Moffatt, M., Perveneckas, Z., and Seiler, L. 2016. *Expected Service Life of Wearing Courses*. Paris: PIARC.
- Christensen, J. & et al. 2005. *Economic Evaluation of Long-Life Pavements PHASE 1*. Paris, France: OECD PUBLICATIONS
- De la Roche C. et al., 2009. *Development of a laboratory bituminous mixtures aging protocol*. Procs. Int. Conf. on Advanced Testing and Characterisation of Bituminous Materials.
- EAPA. 2007. *Long-Life Asphalt Pavements – Technical version*. Brussels: European Asphalt Pavement Association

- Kalman B., Ahmed A., Zhu J., Neves L., Rahman S., Eriksson, O. Kleizienė R. and Parry T. 2021. *Deliverable D4.1 – Report on durability data analysis*. Project PavementLCM, Life Cycle Management of Green Asphalt Mixtures and Road Pavements
- Mollenhauer, K., Mouillet, V., Pierard, N., Tusar, M. and Gabet, T. 2012. *Laboratory aging of asphalt mixtures: simulation of reclaimed asphalt and application as test method for durability*. 5th Eurasphalt & Eurobitume Congress. Turkey: EAPA.
- Said, S., Hakim, H., and Oscarsson, E., 2013. *Rheological characterization of asphalt concrete using a shear box*. Journal of Testing and Evaluation, 41(4),602–610. doi:10.1520/JTE20120177
- Wellner, F., Falla, G .C., Milow, R., Blasl, A., Di Mino, G., Di Liberto, C. M. Noto, S., Lo Presti, D., Jimenez Del Barco Carrion, A., Airey, G., 2015. *ALLBACK2PAVE; Deliverable No D2.1; High-content RA warm asphalt mixture design*.
- Zhang, H. Anupam, K., Scarpas, A., and Kasbergen, C., 2018. *Comparison of Different Micromechanical Models for Predicting the Effective Properties of Open Graded Mixes*. Transportation Research Record, 2672(28). doi:10.1177/0361198118794713

Performance characteristics of pavement sub-base containing steel slag

Mahabir Panda, Shubhakanta Barik, Siddhartha Sekhar Mishra, Prateek Kar & Prasanta Kumar Bhuyan

*Department of Civil Engineering, National Institute of Technology Rourkela, Odisha, India
(2nd, 3rd and 4th Ex. PG students of same Institute)*

ABSTRACT: A sub-base is normally a granular layer in a pavement and comprises of aggregates with a specified grading. Good quality aggregates mostly derived from natural stone resources are now a days getting scarce and are becoming too costly in several locations because of longer lead involved. In this regard, engineers and researchers are constantly working on replacing aggregates which constitute bulk of a pavement layer, with alternate and waste materials. This paper deals with utilisation of abundantly and locally available steel slag, an industrial waste of a local integrated steel plant in pavement sub-base, thus not only offsetting the problems such as cost of construction, solid waste disposal problems and environmental concerns, but also helping preservation of natural stone resources for other essential uses. The experimental programme includes grading of available steel slag and normal aggregates, blending of slag with aggregates to achieve the desired gradation, and compaction test to determine the optimum moisture content. The study also includes other important performance characteristics such as expansion potential and CBR besides verifying the hazardous effects of using slag in pavement sub-base. It is observed that the use of aged steel slag results in much better performance characteristics, besides satisfying the environmental requirements, thus providing a solution of building a sustainable pavement in sites not far from steel plants.

Keywords: Slag, XRD analysis, toxicity, CBR, expansion behaviour

1 INTRODUCTION

A sub-base in a pavement is normally a granular layer that bears some amount of stresses and strains caused due to the vehicular loads transmitted through upper layers, and also transmits small amount of stresses to the subgrade. A sub-base used in most of highways comprises of aggregates with a specified grading. Good quality aggregates mostly derived from natural stone resources are now a days getting scarce and are becoming too costly in several locations because of longer lead involved. At the same time, generation of a vast quantity of waste materials from different manufacturing industries like iron and steel, is facing a shortage of dumping space and is also creating severe environmental pollution. In this regard, engineers and researchers are constantly working on replacing aggregates which constitute bulk of a pavement layer, with alternate and waste materials. India is world's 2nd largest producer of crude steel. As on 2019, India produces 12 million tonnes of steel slag annually (IBM 2020). This paper is an attempt to explore replacement of costly conventional aggregates with steel slag produced in huge quantity as a waste from an integrated steel plant located nearby, in pavement sub-base course, as the amount of waste steel slag generated is so vast that it results in dumping problems because of lack of space, and can also be hazardous to the environment.

2 BRIEF REVIEW OF LITERATURE ON USE OF SLAG IN PAVEMENTS

Basic oxygen furnace (BOF) steel slag mainly comprises of silicon, calcium and iron. However, it also contains some trace (potential toxic) elements, like chromium and vanadium, which needs to be verified for acceptable level of concentration (Chaurand et al. 2007). The steel slag aggregate (SSA) was utilised in road construction in Saudi Arabia, which is a by-product of the steel manufacturing process. Two types of SSA materials (0 – 5 mm) and (0 – 37 mm) were used in different combinations with locally available marl, marl fines, and sand, and the CBR values of the optimum blends were found to be very high (Aiban 2006). Pasetto and Baldo (2010) reported that ferrous slags such as blast furnace slag, steel making slag, manufactory and ferroalloy slags are the industrial by-products which can be used in pavement construction because of their wide convenience and scope of applications. The steel slag combined with limestone aggregates were used in different proportions to achieve the desired density and shear strength in Egyptian roads. The BOF slag as well as electric arc furnace (EAF) slag can also be used for road base as well as for road base asphalt concrete. As compared to blast furnace slag, steel slag usually has a higher bulk density and potential expansive nature where volume changes can be noticed up to 10 percent due to the presence of free calcium and magnesium oxides. Before use in construction, suitable ageing or treatment with acids or asphaltic coating should be done to avoid the potential long-term volume changes. The free lime content of steel slag is studied to analyse its expansion behaviour (Emery 1982). He also observed through different investigations that the mixtures of slag and asphalt showed better mechanical characteristics than those containing conventional aggregate and asphalt, satisfying the acceptable criteria for road construction. Wang et al. (2010a) developed a theoretical equation to determine expansion rate of steel slag subjected to load and climatic changes. Volume expansion test was carried out in laboratory and compared with theoretical volume expansion rate which can be deduced from free lime content, specific gravity and bulk specific gravity of slag. It can be seen that, expansion in volume can be absorbed to certain extent by the void volume present in steel slag, and sometimes potential expansion can be almost zero. Shen et al. (2009) aimed at preparing a mix of steel slag, fly ash and gypsum which can be used in base layer of a pavement. After conducting tests for different proportions, the mix having fly ash to steel slag ratio as 1:1, and phosphogypsum dosage as 2.5% makes the optimal mix which resulted in highest strength among other combinations.

2.1 *Objective and scope of study*

Through brief review of literature presented above, it is seen that, most of physical and engineering properties of slag are superior as compared with the natural aggregates. With controlled leaching and expansion characteristics, the use of steel slag in pavement bases/sub-bases can be beneficial from the point of economy, waste utilisation and environment. Keeping in view these facts, the main objective of this study is to explore possible utilisation of abundantly available steel slag for pavement sub-base replacing conventional aggregates to the extent possible. To achieve the above main objective the scope of the present study is as follows.

- i. Collection of steel slag samples from waste dumps
- ii. Characterisation and leachate analysis of steel slag sample
- iii. Grading analysis of collected slag and aggregate samples, and blending of slag and aggregates to satisfy desired grading for subgrade
- iv. Determination of physical properties slag, aggregate and slag-aggregate blends
- v. Study of expansion potential of slag-aggregate blend

3 MATERIALS AND METHODS

The study is divided into three phases. In the first, the chemical composition, phase composition and toxicity characteristics of slag samples are studied. The second phase relates to the

physical properties of slag, aggregates as well as the combination of slag and crushed aggregates to find its suitability for use in the sub-base layer of a pavement. The third phase is regarding free lime content of steel slag and study of its expansion behaviour.

3.1 Characterisation of slag

The dry slag samples were finely grounded to get a homogeneous mixture, and then the samples were analysed using an X-ray fluorescence spectrometer (XRF). The chemical composition of slag samples was analysed and the results are presented in Table 1. The mean chemical composition of 12 slag samples was expressed in terms of percentage of total weight. The chemical composition of slag gives some insight to the performance of the materials in a structural layer. The results show that the slag samples mainly have oxides of iron, aluminium, calcium and magnesium, which provide strength to the material.

Table 1. Chemical composition of slag.

SiO ₂	FeO	Al ₂ O ₃	CaO	MgO	MnO	S	TiO ₂	K ₂ O
26-28	16-25	4.9-7.7	28-34	7.6-11.4	3.6-5.3	0.1	0.59-0.68	0.11-0.18

3.2 XRD analysis

The X-ray diffraction technique was used to determine the phase composition of slag samples. The slag samples were grounded (to pass a standard 75µm IS sieve) and homogenised before analysis. XRD analysis was performed on a PW 3020 Philips diffractometer using Cu K α ($\lambda=0.15405$ nm) radiation. The phases present in the slag sample determined by XRD analysis are illustrated in Figure 1. The XRD patterns of slag sample are quite complex. It shows multiple overlapping of different peaks. This results in presence of a number of different types of minerals in it. As is seen from the figure, a large number of well-defined peaks represent the crystalline structure of the slag. It also represents slow cooling of slag. The intensity of peak also shows major and minor minerals present in it. Most abundant compounds present in this slag are Quartz (SiO₂), Alumina (Al₂O₃), Hematite (Fe₂O₃) and Calcium compounds. Overlapping of peaks and presence of oxides results in difficulty of determination of compounds.

3.3 Scanning Electron Microscopy (SEM)

A Scanning Electron Microscope (SEM) of make and model, JEOL JSM- 6480 LV, EDS was used to capture the micro-structure images of slag samples supplied. The SEM images, as presented in Figure 2 indicate that the steel slag is crystalline in nature. The surface textures of the steel slag are rough and angular. It is seen that some particles are elongated and some are flakey in shape.

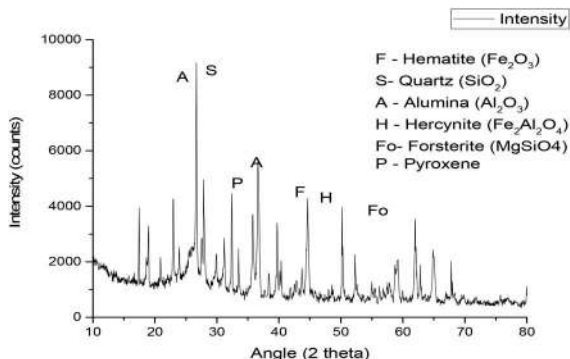


Figure 1. XRD pattern of slag sample.

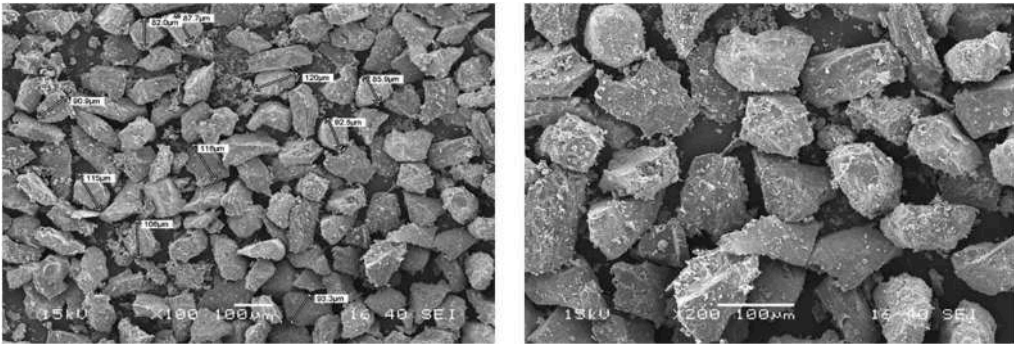


Figure 2. SEM images of steel slag samples.

3.4 Toxic characteristic leaching procedure

Toxicity Characteristic Leaching Procedure (TCLP) is conducted to determine the harmful metals present in slag samples in order to ensure safety in its use in the field. Necessary procedure of sample solution preparation, extraction and filtration has been followed (Environmental Protection Agency (EPA) of United States method 1311 1992, Aiban 2006). Finally, the metals are detected using Atomic Absorption Spectroscope (AAS). The results of quantity of important heavy metals in slag samples following the above procedure are presented in Table 2. It is seen that the results obtained are far below the corresponding permissible limits. In other words, the slag samples contained toxic components below permissible limits for which they can be used in pavement layer without any possible threat of harm to any living plants or organisms.

3.5 Physical properties

3.5.1 Particle size distribution

The gradations of the slag samples and crushed aggregate samples of different nominal sizes, 40 mm, 20 mm, 10 mm, 6 mm and dust were done by sieve analysis using Indian Standard (IS) sieves. The slag samples were blended with crushed aggregate samples for use in filter (lower) layer or drainage (upper) layer of granular sub-base (GSB) to satisfy the desired grading of MoRTH (Ministry of Road Transport and Highways, Govt. of India 2013). For the filter layer a close GSB grading II and for the drainage layer a relatively uniform GSB grading VI was taken as per the said specifications. The grading curves of crushed aggregates and steel slag as supplied are shown in Table 3.

Table 2. Concentration of heavy or toxic elements in leachate water of slag samples.

Toxic element	Pb (Lead) (mg/L)	Cr (Chromium) (mg/L)	Se (Selenium) (ug/L)	As Arsenic) (ug/L)	Hg (Mercury) (ug /L)
Observed concentration	0.127	0	0	0	0.728
Permissible limit	5	5	1	5	0.2

Table 3. Particle size distribution of steel slag and crushed aggregates.

Sieve size (mm)	Per cent passing					
	A40	A20	A10	A6	Stone Dust	Steel Slag
53	100	100	100	100	100	100
26.5	46.82	100	100	100	100	79.69
9.5	0.17	3.6	55.74	100	100	31.56
4.75	0.13	1.25	18.26	87.71	91.36	16.45
2.36	0.13	0.93	5.67	41.41	70.00	10.13
0.425	0.11	0.78	3.55	17.97	41.16	3.77
0.075	0.08	0.52	1.91	4.12	18.44	1.10

The physical properties of slag and crushed aggregates determined by the relevant Indian Standards for use in different layers of sub-base are listed in Table 4.

Table 4. Physical properties of steel slag and crushed aggregate samples.

Property	Steel Slag	Aggregate
Specific gravity (Bulk)	3.28	2.64
Specific gravity (Apparent)	3.5	2.70
Water absorption (%)	1.98	0.46
Liquid limit (%)	27.99	23.17
Aggregate impact value (%)	11.67	14.94
Aggregate crushing value (%)	14.8	14.7
Los Angeles abrasion value (%)	15.76	22.76

3.5.2 Modified proctor test

Modified Proctor test was conducted as per the IS: 2720 (Part 8) (1983) to determine the maximum dry density (MDD) and optimum moisture content (OMC) for a given slag-aggregate sample, so that the same may be used for achieving compaction in the field.

3.5.3 California Bearing Ratio (CBR) test

The CBR values of the combined blend of slag and crushed aggregates were determined as per IS: 2720 (Part 16) (1987).

3.6 Expansion characteristics

Though slag has excellent physical properties, it is the volume expansion that may make it unsuitable for construction applications. The expansion in slag normally occurs due to the presence of free lime. The expansion test was carried out by following the procedures reported in different studies (Emery 1982, Wang et al. 2010]. The mould containing compacted CBR sample was immersed in hot water bath (inside a large steel container). The temperature was maintained at $70 \pm 2^\circ\text{C}$ with continuous supply of air, and the water level was maintained, with temperature readings taken for verification at continuous intervals for seven days.



Figure 3. Expansion test in progress.

4 RESULTS AND DISCUSSION

4.1 Characterization of steel slag used

From the chemical composition as presented in Table 1 and discussed in Section 3.1, it has been observed that the slag used in the study confirms to steel slag that has a principal amount of CaO, SiO₂ and FeO (about 80% by weight) in relevant proportions. From XRD analysis discussed in Section 3.2, the phases are found to be in stable carbonate, hydroxide, silicate or aluminate form which may not cause threat of chemical actions. By using the AAS as discussed in Section 3.4, the concentrations of toxic metals present in leachate water were found to be within the permissible limits of Environmental Protection Agency (EPA) of United States, hence may be considered as safe for use in pavements considering environmental issues.

4.2 Performance characteristics

4.2.1 Blending of steel slag and aggregates

The results of blending of steel slag and crushed aggregate samples determined by following usual theoretical approaches are shown in Table 5. The optimum percentages of steel slag were found to be 58.5% and 90% to satisfy GSB of grading II and grading IV, respectively as per MoRTH (2013), with rest comprising of aggregates of other nominal sizes.

Table 5. Blending of slag and crushed aggregates GSB Grading II and IV (MoRTH, 2013).

Sieve Size (mm)	Grading II		Grading IV	
	Specified Per cent Passing	Blending Proportion (Slag=58.5%+A6=41.5%), Per cent Passing	Specified Per cent Passing	Blending Proportion (Slag=90%+A10=5%+A6=5%) Per cent Passing
53	100	100	100	100.00
26.5	70-100	88.11	50-100	65.64
9.5	50-80	59.95	-	-
4.75	40-65	46.02	15-35	28.00
2.36	30-50	30.16	-	-
0.425	10-15	9.65	-	-
0.075	0-5	2.35	0-5	0.81

4.2.2 Compaction characteristics and CBR of blended mix

For use of materials in a structural layer of a pavement it is essential to ascertain the optimum moisture content (OMC) and compaction conditions (maximum dry density (MDD)) before actual construction. Similarly, in absence of advanced tests for assessment of strength of the granular layer, California Bearing Ratio (CBR) test of sample prepared at its OMC and MDD may be used. The results of optimum moisture content, maximum dry density and CBR values under both unsoaked and soaked conditions for different slag-aggregate blends according to GSB II and GSB IV gradations are given in Table 6.

Table 6. Performance characteristics of blended slag and crushed aggregate samples.

Property	Granular Sub-base Filter layer (GSB II)	Granular Sub-base Drainage layer (GSB IV)
	Slag 58.5% + A6 41.5%	Slag 90% + A10 5% + A6 5%
Optimum moisture content (OMC) (%)	6.24	4.62
Maximum dry density (MDD) (kN/m ³)	24.9	24.7
Un-soaked CBR (%)	128.2	164.4
Soaked CBR (%)	87.1	103.9

4.3 Expansion characteristics

Steel slags have some free lime content which reacts with water, even from atmosphere, to form oxides, as a result creating expansion during this slow reaction. These expansion characteristics cause development of internal stresses in the pavement layer. The amounts of expansion as discussed earlier in Section 3.6 are represented by expansion in percent or expansion ratio, which should be within minimum values for possible use in pavements. The expansion characteristics of slag-aggregate combinations (GSB-II and GSB-IV gradings) determined through the expansion tests are represented in Figure 4. It is to be noted that the top plot refers to the sample without surcharge indicating more expansion behaviour as compared with the bottom plot which refers to the sample with surcharge representing overburden in field situation. It is clearly seen that the expansion of the sample used is quite less for any concern in the field and the given slag-aggregate sample can be used in the pavement sub-base.

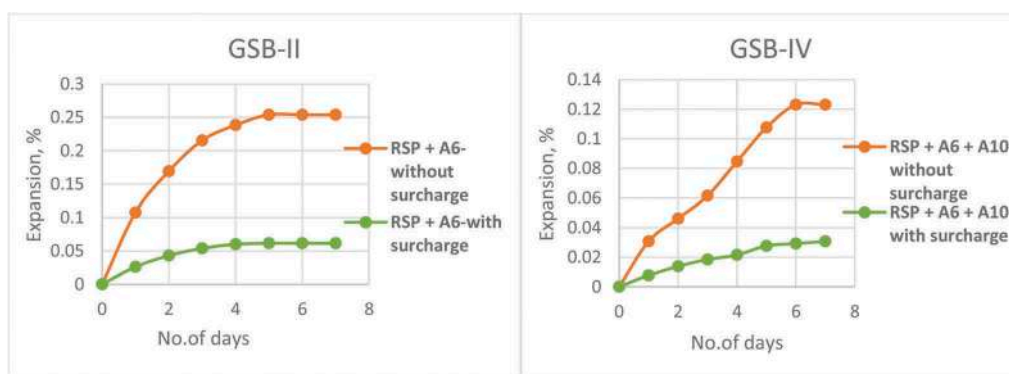


Figure 4. Expansion behaviour of slag-aggregate samples.

5 CONCLUSIONS

From the experiments conducted on the slag and slag-aggregate samples and from the analysis of results of various tests conducted, the following important conclusions are drawn.

- i. The heavy and toxic metals present in the slag leachate water were either zero or negligible, and were within acceptable limits. Hence, there were no potential environmental and health hazards.
- ii. For filter layer and drainage layer of GSB, the optimum concentrations of steel slag were found to be 58.5% and 90% (by weight) satisfying the desired gradings (GSB grading II and grading IV respectively as per the MoRTH specifications).
- iii. Steel slag used was observed to contribute to higher CBR value of the blended sample for GSB.
- iv. The expansion test result of the blended of steel slag-crushed aggregate sample was found to be much below 1% (the limiting value) and can be used in unbound pavement applications.

Considering the above test results obtained through experimental investigations, it is observed that the use of aged steel slag results in much better performance characteristics, besides satisfying the environmental requirements, thus providing a solution of building sustainable pavement sub-base in sites which are close to the steel plants.

REFERENCES

- Aiban, S. A., 2006. *Utilisation of Steel Slag Aggregate for Road Bases*. Journal of Testing and Evaluation, ASTM, Vol 34, No. 1: pp 65–75.
- Chaurand, P., Rose, J., Briois, V., Olivi, L., Hazemann, J. L., Proux, O., Domas, J., and Bottero, J. Y., 2007. *Environmental Impacts of Steel Slag Reused in Road Construction: A Crystallographic and Molecular (XANES) Approach*. Journal of Hazardous Materials, Elsevier, 139.3: pp 537–542.
- Emery, J. J., 1982. *Slag Utilization in Pavement Construction, Extending Aggregate Resources*. ASTM STP 774: pp 95–118.
- Indian Bureau of Mines (IBM), 2020. *Indian Minerals Yearbook 2019 (Part- II: Metals & Alloys)*. 58th Edition, New Delhi.
- IS: 2720 (Part 5), 1985. *Method of Test for Soils: Determination of Liquid and Plastic Limit*. Bureau of Indian Standards, New Delhi.
- IS: 2720 (Part 8), 1983. *Methods of Test for Soils: Determination of Water Content-Dry Density Relation Using Heavy Compaction*. Bureau of Indian Standards, New Delhi.
- IS: 2720, “Methods of Test for Soil (Part 16): Laboratory Determination of CBR”, Bureau of Indian Standards, New Delhi.
- IS: 2386 (Part-I), 1963. *Methods of Test for Aggregates for Concrete: Particle Size and Shape*. Bureau of Indian Standards, New Delhi.
- IS: 2386 (Part-III), 1963. *Methods of Test for Aggregates for Concrete: Specific Gravity, Density, Voids, Absorption, Bulking*. Bureau of Indian Standards, New Delhi.
- IS: 2386 (Part-IV), 1963. *Methods of Test for Aggregates for Concrete: Mechanical Properties*. Bureau of Indian Standards, New Delhi.
- Ministry of Road Transport and Highways (MoRTH), 2013. *Specifications for Road and Bridge Works*. Indian Roads Congress, New Delhi, 5th Revision.
- Pasetto, M., and Baldo, N., 2009. *Experimental Evaluation of High-Performance Base Course and Road Base Asphalt Concrete with Electric Arc Furnace Steel Slags*. Journal of Hazardous Materials, Elsevier, 181.1: pp 938–948.
- Shen, W., Zhou, M., Ma, W., Hu, J., and Cai, Z., 2009. Investigation on the application of steel slag–fly ash–phosphogypsum solidified material as road base material. Journal of Hazardous Materials, Elsevier, 164.1: pp 99–104.
- USEPA, Method 1311, 1992. TCLP – Toxicity Characteristic Leaching Procedure. In: Test Methods for Evaluating Solid Waste. 3rd ed. Washington, DC.
- Wang, G., Wang, Y. and Gao, Z., 2010. *Use of Steel Slag as a Granular Material: Volume Expansion Prediction and Usability Criteria*. Journal of Hazardous Materials, 184.1: pp 555–560.
- Wang, Q., and Yan, P., 2010. *Hydration Properties of Basic Oxygen Furnace Steel Slag*. Construction and Building Materials, Elsevier, 24.7: pp 1134–1140.

Author Index

- Åbele, A. 380
Agardh, S. 87
Alamnie, M. 118
Alrashydah, E. 77
Ashtiani, A.Z. 159
- Baliello, A. 57
Barik, S. 511
Barros, R. 246, 256,
471
Bastola, N.R. 150
Bernava, A. 380
Berzina, R. 380
Bevacqua, M.T. 198
Bhuyan, P.K. 511
Bijleveld, F.R. 418
Bilodeau, J.-P. 463
Boros, Z. 45
Brill, D.R. 159
Broutin, M. 188
Bujoli, B. 332
- Cabette, M. 426
Calçada, R. 168
Capron, I. 332
Castillo-Mingorance, J.M.
128
Chailleux, E. 332
Charoenwong, C. 291
Chazallon, C. 398
Chen, H. 360
Čičković, M. 3, 236
Connolly, D.P. 291
Correia, A.G. 168
Costa, P.A. 168, 291
- de Bondt, A.H. 418
Di Benedetto, H. 188
Di Mino, G. 502
Ding, M. 360
Doré, G. 463
- Elipse, C.A. 138
Elshaer, M.H. 150
- Falla, G.C. 266
Fiske, T.H. 407
Flores, J.M.V. 138
Foshee, M. 108
Freudenstein, S. 207
Fujikawa, T. 387
- Galvín, P. 291
Gambín-Peñalver, J. 313
Gao, W.-H. 454
García-Travé, G. 313
Garg, N. 22
Gaudefroy, V. 332
Gedafa, D. 436, 445
Giacomello, G. 57
Giles, D. 341
Golos, M. 65
Grimshaw, L. 282
- Haritonovs, V. 380
Hayano, K. 322
Hernández-Pérez, M. 313
Herronen, T. 99
Hiekkalahti, A. 99
Hirakawa, K. 387
Hironaka, J. 387
Hoff, I. 118
Hornych, P. 398
Huang, H. 360
Hudson-Griffiths, R. 341
Hung, M.-T. 454
- Isernia, T. 198
Isobe, Y. 387
Ivanova, T. 380
Iwama, M. 322
- Jaskula, P. 65
Jing, P. 398
Jørgensen, P. 220
Jørgensen, T. 407
- Kalman, B. 502
Kar, P. 511
- Kasimova, G.A. 360
Kathuria, A. 491
Kawalec, J. 65
Kazmee, H. 22
Keijzer, E. 502
Khojinian, A. 341
Kim, K.D. 138
Kleizienė, R. 502
Koga, C. 387
Komacka, J. 45
Kotter, F. 207
Kumar, B. 351
- Lee, H.J. 138
Lee, W.S. 138
Leischner, S. 266
Leiva, F. 303
Lenngren, C.A. 178
Lévenard, F. 332
Levenberg, E. 220
Liao, M.-C. 454
Lillin, N. 207
Liu, J. 445
Liu, G. 360
Lo Presti, D. 502
Loizos, A. 370
- Madlangsakay, A.O.
138
Madsen, S.S. 33
Mantalovas, K. 502
Marradi, A. 282
Masad, A. 77
Matintupa, A. 99
Melaku, R. 436, 445
Merijs-Meri, R. 380
Micaelo, R. 426
Mishra, S.S. 511
Mittlmeier, F. 207
Moormann, C. 207
Moreno-Navarro, F. 128,
313
Mouhoubi, S. 398
Murrell, S. 159

Najjar, Y. 246, 256
 Najjar, Y.M. 471
 Ness, S. 436
 Neves, L. 502

 Oeser, M. 266
 Ojum, C. 341
 Ossbahr, C. 87

 Pacheco-Torres, R. 228
 Pais, J. 426
 Panda, M. 511
 Papagiannakis, A.T. 77
 Papavasiliou, V. 370
 Pary, T. 502
 Pasetto, M. 57
 Pasquini, E. 57
 Pedersen, N.L. 33
 Perez, V. 87
 Pérez-González, E.L. 463
 Pérez-Mena, V. 128
 Perslev, R.N.H. 220
 Petiteau, C. 332
 Plug, C.P. 418
 Podolski, C. 3
 Pourkhorshidi, S. 480
 Prasad, D. 491
 Praticò, F.G. 198

 Ramos, A. 168
 Ricalde, L. 22

 Rodriguez-López, C. 313
 Roussel, J.-M. 188
 Rubio-Gámez, M.C. 128, 313
 Rudisch, D. 207
 Rys, D. 65

 Saarenketo, T. 99
 Saboo, N. 491
 Salt, G. 282
 Sangiorgi, C. 480
 Sato, K. 387
 Sauzéat, C. 188
 Segui, P. 463
 Shi, J.-W. 454
 Shimazaki, M. 387
 Simms, M. 341
 Singh, B. 491
 Solanki, P. 275
 Sol-Sánchez, M. 128, 313
 Soto, F.V. 228
 Souliman, M.I. 150
 Speir, R. 159
 Stienss, M. 65
 Subhy, A. 341
 Suleiman, N. 436, 445
 Sultana, S. 246, 256
 Suman, S.K. 491
 Szydłowski, C. 65

 Taddesse, E. 118

 Tassinari, P. 480
 Tauste-Martínez, R. 313
 Taylor, A. 303
 Telle, R. 407
 Timm, D. 108
 Tomás-Fortún, E. 128
 Torreggiani, D. 480
 Tran, T.S. 138

 Uddin, W. 246, 256

 Van Geem, C. 13
 Van Uden, G. 418
 Varin, P. 99
 Verma, G. 351

 Wakabayashi, Y. 387
 Wang, C. 398
 Weise, C. 266
 Wellner, F. 266
 Widyatmoko, I. 341
 Woodward, P.K. 291

 Xie, H. 275
 Xing, H. 360

 Yasarer, H. 246, 256, 471

 Zicans, J. 380
 Žiganova, M. 380
 Zumbo, S. 198